

30

65044

U M I
MICROFILMED 2002

INFORMATION TO USERS

This manuscript has been reproduced from the microfilm master. UMI films the text directly from the original or copy submitted. Thus, some thesis and dissertation copies are in typewriter face, while others may be from any type of computer printer.

The quality of this reproduction is dependent upon the quality of the copy submitted. Broken or indistinct print, colored or poor quality illustrations and photographs, print bleedthrough, substandard margins, and improper alignment can adversely affect reproduction.

In the unlikely event that the author did not send UMI a complete manuscript and there are missing pages, these will be noted. Also, if unauthorized copyright material had to be removed, a note will indicate the deletion.

Oversize materials (e.g., maps, drawings, charts) are reproduced by sectioning the original, beginning at the upper left-hand corner and continuing from left to right in equal sections with small overlaps.

ProQuest Information and Learning
300 North Zeeb Road, Ann Arbor, MI 48106-1346 USA
800-521-0600

UMI[®]

NOTE TO USERS

This reproduction is the best copy available.

UMI[®]

WASHINGTON UNIVERSITY
SEVER INSTITUTE OF TECHNOLOGY

DEPARTMENT OF CHEMICAL ENGINEERING

CHURN-TURBULENT BUBBLE COLUMNS
- EXPERIMENTS AND MODELING -

by

Puneet Gupta

Prepared under the direction of Prof. M. P. Dudukovic' and Prof. M. H. Al-Dahhan

A dissertation presented to the Sever Institute of
Washington University in partial fulfillment
of the requirements for the degree of

DOCTOR OF SCIENCE

May, 2002

Saint Louis, Missouri, USA

UMI Number: 3065044

Copyright 2002 by
Gupta, Puneet

All rights reserved.

UMI[®]

UMI Microform 3065044

Copyright 2002 by ProQuest Information and Learning Company.
All rights reserved. This microform edition is protected against
unauthorized copying under Title 17, United States Code.

ProQuest Information and Learning Company
300 North Zeeb Road
P.O. Box 1346
Ann Arbor, MI 48106-1346

copyright by
Puneet Gupta
2002

WASHINGTON UNIVERSITY
SEVER INSTITUTE OF TECHNOLOGY
DEPARTMENT OF CHEMICAL ENGINEERING

ABSTRACT

CHURN-TURBULENT BUBBLE COLUMNS
- EXPERIMENTS AND MODELING -

by Puneet Gupta

ADVISORS: Prof. M. P. Dudukovic' and Prof. M. H. Al-Dahhan

May, 2002
Saint Louis, Missouri

A fundamental understanding of hydrodynamics is critical to the design and scale-up of bubble column reactors. Towards this goal, systematic experimental and theoretical investigations were conducted to improve the diagnostic tools for assessing bubble column hydrodynamics. The first experimental contribution of this study concerns the development of a novel signal-filtration technique to obtain liquid-phase tracer responses from conductance measurements in gas-liquid flows, which are systematically corrupted due to frequent bubble passage over the probe measurement volume. The usefulness of the developed algorithm was demonstrated in a countercurrent trayed bubble column and

extended to study liquid tracer responses in a batch bubble column. The second contribution pertains to the development of a Monte Carlo simulation technique for efficient non-invasive tracking of a radioactive tracer particle. The developed simulation tool was integrated for simulating detector responses in a multi-detector setup and used to study the effect of media-density distribution on detector efficiencies. The developed technique was further validated against experimental data and applied to a gas-liquid flow in a stainless steel bubble column. Lastly, protocols were developed for executing radioactive tracer tests and γ -scans on pilot-scale bubble columns and data interpretation.

The second part of this study deals with developing a consistent hydrodynamic formulation based on the Euler-Euler two-fluid approach for modeling gas-liquid flows in bubble column reactors. The predicted phase recirculations were subsequently coupled with species transport equations for a gas tracer based on two competing models. The first assumes that the gas-phase hydrodynamics is represented by a single bubble size, whereas the second assumes a radially varying bubble size. The models were applied for interpretation of radioactive tracer data from a pilot-scale reactor used for methanol synthesis. The first model was extended to interpret gas, liquid and catalyst tracer test data acquired in another pilot-scale reactor used for Fischer-Tropsch synthesis. The predicted phase mixing is presented for a number of operating conditions along with comparison to experimental data. It is concluded that when the regime of bubble column operation is churn-turbulent and substantially removed from the transition regime, the model predictions are in reasonably good agreement with experimental data.

to my parents, brother and soul-mate

Contents

List of Tables.....	ix
List of Figures.....	xi
Nomenclature.....	xx
Acknowledgments.....	xxvii
1. Introduction.....	1
1.1. Motivation.....	1
1.2. State of the Art.....	4
1.2.1. Degree of Mixing in a Bubble Column.....	5
1.2.2. Flow Regimes in a Bubble Column.....	7
1.2.3. Measurement of Backmixing and Liquid Phase Hydrodynamics.....	10
1.3. Research Objectives.....	12
1.3.1. Experimental Objectives.....	13
1.3.2. Modeling and Computational Objectives.....	15
1.4. Thesis Organization.....	16
2. Literature Review.....	17
2.1. Gas Hold-up.....	18
2.2. Liquid Backmixing and Velocity Profiles.....	28
2.3. Mass Transfer.....	32
2.4. Reactor Modeling.....	36
3. Conductivity Probes for Liquid Mixing in Gas-Liquid Flows.....	47
3.1. Introduction.....	47
3.2. Experimental Setup.....	50
3.3. Problem Description.....	54
3.4. Description of the Filtering Algorithm.....	56

3.5. Results and Discussion – Implementation of the Filtering Algorithm.....	57
3.6. Characteristic Response Time of the Conductivity Probes.....	60
3.7. Results and Discussion – Tracer Tests in Counter-Current Staged Bubble Column.....	64
3.7.1. Effect of Gas Sparger Design.....	68
3.8. Results and Discussion – Tracer Tests in a Bubble Column with Batch Liquid...	71
3.9. Conclusions.....	76
4. Monte Carlo Simulations of Scintillation Counting by Cylindrical NaI Detectors.....	78
4.1. Introduction.....	79
4.2. Mathematical Formulation.....	80
4.2.1. Monte Carlo Formulation.....	81
4.2.2. Surface Integration over Detector Solid Angles.....	91
4.3. Results and Discussion.....	92
4.3.1. Accuracy of Surface Integration with Number of Quadrature Points.....	93
4.3.2. Validation of the Developed Code against Existing Simulations.....	99
4.3.3. Effect of Crystal Size.....	99
4.3.4. Effect of Media Density Distribution.....	102
4.4. Conclusions.....	111
5. Radioactive Particle Tracking Using Monte Carlo Simulations of Detector Efficiencies.....	113
5.1. Introduction.....	113
5.2. Radiation Photon Counting.....	117
5.2.1. Computation of Simulated Counts.....	119
5.2.2. Optimization of Detector Parameters.....	120
5.2.3. Generation of Calibration Map – Photopeak Efficiency Database.....	122
5.2.4. Particle Position Reconstruction.....	125
5.3. Experiments.....	126
5.4. Results and Discussion.....	128

6. Modeling Phase Mixing in Bubble Columns Using the Two-Fluid Approach....	138
6.1. Introduction.....	138
6.2. Phenomenological/Mechanistic Reactor Models.....	145
6.2.1. Single Bubble Class Model (SBCM).....	150
6.2.2. Distributed Bubble Class Model (DBSM).....	154
6.3. Two-Fluid Sub-Model for Gas and Liquid Phase Axial Momentum Exchange.....	159
6.4. Parameter Estimation for the Mixing Models.....	168
6.5. Results and Discussion.....	175
6.5.1. Effect of Mixing Length on the Predictions of Liquid Recirculation Rates.....	176
6.5.2. Pilot-Scale Experiments and the Corresponding Model Parameters.....	178
6.5.3. Comparison of Simulated results with Experimental Data.....	187
6.5.3.1. Predictions from Single Bubble Class Model (SBCM).....	194
6.5.3.2. Effect of Bubble Size on Mass Transfer Coefficients.....	197
6.5.4. Comparison of Predictions from SBCM and DBSM.....	199
6.5.5. Parametric Sensitivity Analysis.....	209
6.6. Issues Related to Bubble Size Distribution.....	217
6.7. Final Remarks.....	220
7. Gamma-Ray Densitometry and Radioactive Tracer Studies of a Pilot-Scale Fischer-Tropsch Reactor.....	223
7.1. Gamma-Ray Densitometry Studies During FT-IV Runs at the Alternate Fuels Development Unit (AFDU) in La Porte, TX.....	225
7.1.1. Analysis of Gamma-Scan Data.....	225
7.1.2. Statistical Analysis of the Measured Data.....	231
7.1.3. Suggestions for Improving Data Quality from Future Gamma Scans....	237
7.1.4. Suggested Mock Experiments.....	238
7.2. Radioactive Tracer Studies During FT-IV Runs at the Alternate Fuels Development Unit (AFDU) in La Porte, TX.....	239
7.2.1. Protocol for Data Processing.....	246

7.2.2. Reproducibility of the Measured Tracer Data.....	251
7.2.3. Comparison between Catalyst and “Liquid” Tracer Responses.....	254
7.2.4. Liquid Mixing Model.....	256
7.2.5. Model Equations for Liquid Mixing as a Result of Domain-Splitting....	259
7.2.6. Comparison of Experimental Liquid/Catalyst Tracer Responses with Simulation Results.....	262
7.2.7. Parametric Sensitivity of Simulated Liquid/Catalyst Tracer Responses.....	273
7.3. Radioactive Gas Tracer Studies during FT-IV Runs at AFDU.....	278
7.3.1. Comparison of Experimental Tracer Responses with Simulation Results.....	280
7.3.2. Parametric Sensitivity of Simulated Gas Tracer Responses.....	287
7.4. Summary and Conclusions.....	290
8. Summary and Conclusions.....	295
8.1. Summary and Conclusions.....	295
8.2. Recommendations for Future Work.....	299
Appendix A. Parameter Estimation of Bubble Column Hydrodynamics.....	302
Appendix B. Effect of Boundary Conditions on Simulation Results from Mixing Models.....	305
Appendix C. Comparison of FT-IV Experimental Data with Simulation Results from Mixing Models.....	315
References.....	332
VITA.....	355

Tables

1-1.	Examples of industrial processes in two-phase bubble columns (Luo, 1993).....	3
1-2.	Examples of industrial processes in three-phase bubble columns (Luo, 1993).....	4
2-1.	Mass transfer correlations reported in the literature.....	35
2-2.	CFD studies of bubble column flows.....	46
3-1.	Operating conditions for various tracer experiments.....	54
3-2.	Mixing parameters from the tracer response curves.....	67
3-3.	Peak response parameters resulting from impulse liquid tracer injections in the bubble column without trays.....	76
4-1.	Comparison of different numerical approaches.....	92
5-1.	Results of particle position reconstruction for the CST validation experiment.....	133
6-1.	Estimated gas holdup profile during methanol synthesis at AFDU, La Porte....	179
6-2.	Parameter estimation for SBCM.....	182
6-3.	Parameter estimation for DBSM.....	183
6-4.	Predicted bubble sizes by the SBCM, DBSM and literature correlations.....	184
6-5.	Predicted volumetric mass transfer coefficients by the SBCM, DBSM and literature correlations.....	186
6-6.	Predicted bubble velocities by the SBCM, DBSM and literature correlations...	187
6-5.	Effect of bubble size distribution on volumetric mass transfer coefficient.....	198
7-1.	Details of the reactor geometry and operating conditions during GDT scans....	226
7-2.	Combinations of base scans in gas and liquid employed for statistical study....	232
7-3.	Reactor operating conditions during tracer tests.....	242
7-4.	Input parameters for the liquid and gas mixing models.....	263
7-5.	Computed model parameters for the liquid mixing model.....	265

7-6.	Equations for Single Bubble Class Gas-Liquid Recirculation Model.....	279
7-7.	Computed model parameters for the gas-mixing model.....	281

Figures

1-1.	Schematic of a bubble column configuration.....	2
1-2.	Variables affecting bubble-column phenomena and performance.....	5
1-3.	Flow regimes in vertical bubble column reactors. a) Bubbly b) Homogeneous Bubbling c) Churn-turbulent d) Slug-flow e) Annular (Kastanek <i>et al.</i> , 1993).....	9
2-1.	a) Typical DGD data b) 2-Bubble phase model (Krishna, 2000 ^h).....	22
2-2.	Prediction of the pressure effect on gas holdup (Krishna, 2000 ^h).....	25
2-3.	CT measurements of gas holdup distribution. a-b) 6” diameter stainless steel column (Ong, 1999) c-d) 18” diameter Plexiglas column (Chen <i>et al.</i> , 1999).....	27
2-4.	a) CARPT experimental setup b) Particle trajectory c & d) Typical hydrodynamic information from CARPT measurements (Chen <i>et al.</i> , 1999).....	30
2-5.	Representation of mixing in co-current bubble column with a stirred tank for liquid and plug flow for gas.....	39
2-6.	Mechanistic description of buoyancy induced recirculation and turbulent dispersion in a bubble column reactor.....	42
2-7.	Prediction of liquid phase RTD in a co-current bubble column (Degaleesan, 1997).....	43
3-1.	Schematic of the counter-current staged bubble column process loop and the data acquisition set-up with a sketch of the conductivity probes.....	51
3-2.	Details of the gas distributor. (a) Sparger layout (b) Sparger 1: 40 holes, open area=0.14 % (c) Sparger 2: 200 holes, open area=0.68 % (Gupta <i>et al.</i> 2000; Kemoun <i>et al.</i> , 2001 ^a).....	52
3-3.	Location of the conductivity probes during tracer response measurements.....	53
3-4.	Typical signals measured by the conductivity probe in single and two-phase media.....	55

3-5.	Performance of a standard Butterworth filter of order 2 in filtering conductivity probe signals.....	56
3-6.	Flow chart for the developed filtering algorithm.....	58
3-7.	Performance of the new filtering technique, in conjunction with a Butterworth filter of order 2, in filtering conductivity probe signals.....	59
3-8.	Performance of the standard and new filtering techniques in filtering (a) the numerically generated signal, and (b) raw signal from experimental data.....	61
3-9.	First order model fit of the rise of the conductivity probe signal from the one detected in air to that in tap water.....	63
3-10.	Tracer response curves for the experiments at different operating conditions listed in Table 3-1 with the two probes positioned as in Figure 3-3.....	65
3-11.	Normalized tracer response curves of Figure 3-10.....	69
3-12.	Effect of sparger hole density on tracer impulse responses. a-c) Sparger 1 (40 holes per lateral) d-f) Sparger 2 (200 holes per lateral).....	70
3-13.	Sketch of experimental setup of bubble column with no trays.....	72
3-14.	Liquid tracer responses as a function of gas superficial velocity for the bottom tracer-injection location a) Probe_0 b) Probe_1.....	73
3-15.	Liquid tracer responses as a function of gas superficial velocity for the middle tracer-injection location a) Probe_0 b) Probe_1.....	74
4-1.	Graphical representation of the solid angle subtended by a scintillation detector on a point source for evaluating the surface integrals in Equations 4-1 and 4-2.....	82
4-2.	Various possibilities of the relative orientation of the point source with respect to the detector surface (Beam <i>et al.</i> , 1978).....	86
4-3.	Schematic describing coordinate transformation required in the calculation procedure a) First Coordinate Transform b) Second Coordinate Transform.....	89
4-4.	Distribution of source locations in r - θ plane for error analysis. a) Without media b) With intervening media of the shown density distribution.....	95

4-5.	Variation of relative percent error for source positions in the $r-\theta$ plane.	
	a) Solid Angle. b) Total Efficiency without Media. c) Total Photopeak Efficiency without Media. d) Total Efficiency with Media. e) Total Photopeak Efficiency with Media.....	96
4-6.	Distribution of source locations in $r-z$ plane for error analysis.	
	a) Without media b) With intervening media of the shown density distribution.....	97
4-7.	Variation of relative percent error for source positions in the $r-z$ plane.	
	a) Solid Angle. b) Total Efficiency without Media. c) Total Photopeak Efficiency without Media. d) Total Efficiency with Media. e) Total Photopeak Efficiency with Media.....	98
4-8.	Comparison of simulated results from this work with those of Beam <i>et al.</i> (1978).	
	a) Intrinsic Efficiency. b) Ratio of Photopeak to Total Efficiencies.....	100
4-9.	Dependency of peak-to-total efficiency ratio on crystal size.	
	a) Effect of photon energy. b) Effect of intervening media.....	101
4-10.	Simulation of a 2"x2" detector parameters for source positions in $r-\theta$ plane.	
	a) Employed media density distribution. b) Solid angle.	
	c) Intrinsic Total Eff. (No Media). e) Intrinsic Total Eff. (Media).	
	d) Intrinsic Photopeak Eff. (NoMedia). f) Intrinsic Photopeak Eff. (Media)....	103
4-11.	Simulation of a 2"x2" detector parameters for source positions in $r-z$ plane.	
	a) Employed media density distribution. b) Solid angle.	
	c) Intrinsic Total Eff. (No Media). e) Intrinsic Total Eff. (Media).	
	d) Intrinsic Photopeak Eff. (NoMedia). f) Intrinsic Photopeak Eff. (Media)....	104
4-12.	Simulation of a 2"x2" detector parameters for source positions in $r-\theta$ plane.	
	a) Total Efficiency (No Media). d) Total Efficiency (Media).	
	b) Photopeak Efficiency (No Media). e) Photopeak Efficiency (Media).	
	c) Photopeak to Total Ratio (No Media). f) Photopeak to Total Ratio (Media)..	106

4-13.	Simulation of a 2"x2" detector parameters for source positions in r - z plane.	
	a) Total Efficiency (No Media). d) Total Efficiency (Media).	
	b) Photopeak Efficiency (No Media). e) Photopeak Efficiency (Media).	
	c) Photopeak to Total Ratio (No Media). f) Photopeak to Total Ratio (Media)..	107
4-14.	Comparison of Peak to Total Efficiency ratio with and without media.	
	a) In the r - θ plane. b) In the r - z plane.....	108
4-15.	Variation of Peak to Total Efficiency ratio with source-detector distance.	
	a) In the r - θ plane. b) In the r - z plane.....	109
4-15.	Distance vs. counts calibration curves as constructed in a traditional CARPT experiment simulated using the Monte Carlo method.....	110
5-1.	Schematic representation of events in a CARPT experiment.....	114
5-2.	Traditional CARPT versus Monte Carlo based CARPT.....	115
5-3.	Schematic representation of photon detection by a scintillation crystal.....	118
5-4.	Schematic representation of a Compton scattering event.....	119
5-5.	Sample computational grid for generation of photopeak efficiency database.....	124
5-6.	Experimental setup used for verification of the Monte Carlo simulations.....	127
5-7.	Experimentally determined energy spectrums for the four detectors employed in the validation experiments.....	128
5-8.	Reconstructed particle position over 190 data points acquired every 20 ms.....	130
5-9.	Experimental setup for validation under single phase flow conditions.....	131
5-10.	Reconstructed particle locations from a single-phase experiment.....	132
5-11.	Parity plot of particle coordinates reconstructed using Degaleesan's method and Monte Carlo method for arbitrarily picked sequence of 1000 points in stainless steel bubble column experiment.	
	a-c) All 1000 points d-f) Excluding points near gas-liquid interface.....	135
5-12.	Velocity vector plots computed by the Monte Carlo method in a SS bubble column operated at a U_g of 30 cm/s a)0-180° r - z plane b) 45-225° r - z plane.....	136
6-1.	Schematic representation of the experimentally observed phenomena in bubble columns.....	146

6-2.	Schematic of the bubble column reactor compartmentalization for (a) Single Bubble Class Model (SBCM) (b) Distributed Bubble Size Model (DBSM).....	147
6-3.	Effect of mixing length profile on liquid velocity profiles for 10 cm diameter bubble column operated at $U_{G,sup}=12$ cm/s.....	177
6-4.	Effect of mixing length profile on liquid velocity profiles for a 44 cm diameter bubble column operated at $U_{G,sup}=10$ cm/s.....	178
6-5.	Schematic representation of the pilot-scale slurry bubble column at the Alternate Fuels Development Unit, La Porte indicating the detector levels for measurement of radioactive tracer responses.....	180
6-6.	Schematic representation of the AFDU reactor cross-section along with scintillation detectors and their lead shielding.....	189
6-7.	Monte Carlo simulation to demonstrate the broadening of tracer response. a) Detector Geometry b) Normalized response from a non-ideal imperfectly collimated scintillator.....	192
6-8.	Effect of mixing length profile on a) liquid and b) gas velocity profiles for a 46 cm diameter pilot scale slurry bubble column operated at $U_{G,sup}=22.86$ cm/s....	195
6-9.	Comparison of simulated and experimental radioactive gas tracer responses from a pilot scale slurry bubble column using mixing length formulations proposed by a) Joshi (1980)b) Kumar <i>et al.</i> (1994).....	196
6-10.	Sample calculations of mass transfer parameters for assumed bubble size distribution.....	198
6-11.	Liquid and gas radial velocity profiles for the three different operating conditions.....	200
6-12.	Effect of the axial dimension of the distributor and disengagement CSTs on the simulated gas tracer response curves computed using (a) SBCM; (b) DBSM....	202
6-13.	Effect of Henry's constant on simulated gas-tracer response curves (a)-(c) SBCM; (d)-(f) DBSM ($K_{SB1-LB} = 1 \text{ sec}^{-1}$).....	203
6-14.	Effect of volumetric mass transfer coefficient on the gas-tracer responses for Run 14.8 simulated using SBCM (a)-(c) Level 5 (d)-(f) Level 7.....	205

6-15.	Effect of the bubble-interaction parameter in the DBSM (K_{SB1-LB}) on the simulated gas-tracer response for Run 14.6 (a)-(c) $H=0$; (d)-(f) $H=H^*$	206
6-16.	Effect of the bubble-interaction parameter in the DBSM (K_{SB1-LB}) on the simulated gas-tracer response for Run 14.7 (a)-(c) $H=0$; (d)-(f) $H=H^*$	207
6-17.	Effect of the bubble-interaction parameter in the DBSM (K_{SB1-LB}) on the simulated gas-tracer response for Run 14.8 (a)-(c) $H=0$; (d)-(f) $H=H^*$	208
6-18.	Comparison of tracer response simulated using SBCM and DBSM with experimental data (a)-(b) Run 14.6; (c)-(d) Run 14.7; (e)-(f) Run 14.8.....	210
6-19.	Comparison of the effect of radial eddy diffusivity on the simulated tracer responses with experimental data (a)-(c) SBCM; (d)-(f) DBSM.....	211
6-20.	Comparison of the effect of radiation attenuation on the simulated tracer responses with experimental data (a)-(c) SBCM; (d)-(f) DBSM.....	213
6-21.	Comparison of the effect of radial gas holdup profile on the simulated tracer responses with experimental data (a)-(c) SBCM; (d)-(f) DBSM.....	214
6-22.	Comparison of the effect of radial mixing length profile on the simulated tracer responses with experimental data (a)-(c) SBCM; (d)-(f) DBSM.....	215
6-23.	Effect of the parameter “j” on the TBCM predictions. a) Gas phase recirculation b) Simulated tracer responses.....	219
7-1.	Schematic (not to scale) of the reactor cross-section with the collimated source and detector placed on diametrically opposite sides of the column.....	227
7-2.	Distribution of the chords in the reactor cross-section at which measurements were made along directions A-A and B-B.....	229
7-3.	Mean chordal averaged gas holdup for Scan 1 along Section B (bounded by two standard deviations).....	235
7-4.	Mean chordal averaged gas holdup for Scan 2 along Section B (bounded by two standard deviations).....	235
7-5.	Mean chordal averaged gas holdup for Scan 1 along Section A (bounded by two standard deviations).....	236
7-6.	Mean chordal averaged gas holdup for Scan 2 along Section A (bounded by two standard deviations).....	236

7-7.	Schematic of the slurry bubble column reactor at the AFDU along with the scintillation-detector placement for measuring tracer responses.....	241
7-8.	Effect of the parameter “m” on the radial gas holdup profile for fixed $\bar{\varepsilon}_g$ and $\bar{\varepsilon}_g _{Chord}$ a) Run 16.6 b) Run 16.7.....	244
7-9.	Effect of the parameter “m” on the absolute value of the cross-sectional mean gradient of the radial gas holdup profile for fixed $\bar{\varepsilon}_g$ and $\bar{\varepsilon}_g _{Chord}$	245
7-10.	Radial mixing of “liquid” Mn ₂ O ₃ tracer for Run 16.7 with tracer injected at the bottom center location.....	247
7-11.	Radial mixing of gas tracer for Run 16.7 with tracer injected below the sparger.....	249
7-12.	Result of repeated gas tracer injections for Run 16.6.....	252
7-13.	Result of repeated gas tracer injections for Run 16.7.....	253
7-14.	Result of repeated Mn ₂ O ₃ tracer injections (Center, Bottom) for Run 16.7.....	253
7-15.	Comparison of tracer responses for MnO ₂ and catalyst tracer injections (Center, Bottom) for Run 16.6.....	255
7-16.	Comparison of tracer responses for Mn ₂ O ₃ and catalyst tracer injections (Sidewall, Middle) for Run 16.7.....	255
7-17.	Comparison of tracer responses for Mn ₂ O ₃ and catalyst tracer injections (Center, Bottom) for Run 16.7.....	256
7-18.	Schematic of the model compartmentalization.....	258
7-19.	Comparison of experimental and simulated tracer responses for Run 16.6 (Tracer:- Catalyst; Injection Pt.:- Sidewall-Middle).....	266
7-20.	Comparison of experimental and simulated tracer responses for Run 16.6 (Tracer:- Catalyst; Injection Pt.:- Center-Bottom).....	267
7-21.	Comparison of experimental and simulated tracer responses for Run 16.7 (Tracer:- Catalyst; Injection Pt.:- Sidewall-Middle).....	269
7-22.	Comparison of experimental and simulated tracer responses for Run 16.7 (Tracer:- Catalyst; Injection Pt.:- Center-Bottom).....	270

7-23.	Comparison of experimental and simulated tracer responses for Run 16.7 (Tracer:- Mn_2O_3 ; Injection Pt.:- Sidewall-Middle).....	271
7-24.	Comparison of experimental and simulated tracer responses for Run 16.7 (Tracer:- Mn_2O_3 ; Injection Pt.:- Center-Bottom).....	272
7-25.	Parametric sensitivity of simulated tracer responses for Run 16.6 for Bottom- Center injection of catalyst tracer a)-b) Effect of D_{rr} c)-d) Effect of gas holdup profile e)-f) Effect of mixing length profile.....	275
7-26.	Parametric sensitivity of simulated tracer responses for Run 16.7 for Bottom- Center injection of catalyst tracer a)-b) Effect of D_{rr} c)-d) Effect of gas holdup profile e)-f) Effect of mixing length profile.....	276
7-27.	Parametric sensitivity of simulated tracer responses for Run 16.7 for Bottom- Center injection of Mn_2O_3 tracer a)-b) Effect of D_{rr} c)-d) Effect of gas holdup profile e)-f) Effect of mixing length profile.....	277
7-28.	Schematic of the reactor compartmentalization for the gas-liquid mixing model with interphase mass transfer.....	278
7-29.	Comparison of experimental and simulated gas tracer response curves for Run 16.6 with Henry's constant, $H = 0$	282
7-30.	Comparison of experimental and simulated gas tracer response curves for Run 16.6 with Henry's constant, $H = 0.15$	283
7-31.	Comparison of experimental and simulated gas tracer response curves for Run 16.6 with thermodynamically estimated Henry's constant, $H^* = 0.248$	284
7-32.	Comparison of experimental and simulated gas tracer response curves for Run 16.7 with Henry's constant, $H = 0$	285
7-33.	Comparison of experimental and simulated gas tracer response curves for Run 16.7 with Henry's constant, $H = 0.15$	286
7-34.	Comparison of experimental and simulated gas tracer response curves for Run 16.7 with thermodynamically estimated Henry's constant, $H^* = 0.245$	287
7-35.	Parametric sensitivity of simulated gas tracer responses for Run 16.6 a)-b) Effect of D_{rr} c)-d) Effect of gas holdup profile e)-f) Effect of mixing length profile..	288

7-36. Parametric sensitivity of simulated gas tracer responses for Run 16.7 a)-b) Effect of D_{rr} c)-d) Effect of gas holdup profile e)-f) Effect of mixing length profile..289

Nomenclature

AF	acceleration factor for large bubble rise velocity
a	interfacial area, cm^{-1}
C	concentration, moles/ cm^3 (Chapter 6, 7)
C	number of γ -ray peaks received by the NaI (TI) detector (Chapter 5)
C_D	drag coefficient
C_{ij}	simulated counts
C_{vm}	virtual mass coefficient
c	parameter in the hold-up profile to allow non-zero hold-up at the wall
D_C, D_T	column diameter, cm
DF	density factor for large bubble rise velocity
$D_{L,m}$	molecular diffusivity, cm^2/s
$D_{Lm, \text{Argon}}$	molecular diffusivity of Argon in organic liquids, cm^2/s
\bar{D}_r	radial turbulent diffusivity, cm^2/s
\bar{D}_{xx_1}	axial turbulent diffusivity of small bubbles and liquid going up, cm^2/s
\bar{D}_{xx_2}	axial turbulent diffusivity of small bubbles and liquid going down, cm^2/s
d_b, d_{be}	mean (effective) bubble diameter, cm
$d_{b\text{large}}$	bubble diameter of large bubbles, cm
d, d_n	sparger orifice diameter, mm
d_{eff}	distance travelled in the crystal by an undisturbed γ -ray in the direction (α, θ) , cm
d_i	distance travelled by the γ -ray in the direction (α, θ) through the i^{th} material, cm
d_r	distance travelled by the γ -ray through the media inside the vessel, cm
ds	differential area element around the point P

d_{vs}	Sauter mean bubble diameter, m
E_G, E_L	gas and liquid axial dispersion coefficient, cm^2/s
E_o	Eotvos number
$E(t)$	residence time distribution, s^{-1}
Fr	Froude number
FS	filtered signal, volts
FST	filtered plus thresholded signal, volts
f_a	probability that a γ -ray photon reaches the detector surface
f_d	probability that a γ -ray photon reaching the detector surface has an interaction with the detector crystal
f_p	probability that the interaction is by photo-electric absorption
G	detector gain factor
g	acceleration due to gravity, cm^2/s
H	Henry's constant
H_E	expanded height of gas-liquid mixture in column, cm
H_i	dispersion height, cm
H_0	static height of liquid in column, cm
h	distance between the center of the detector face to the tracer location, cm
K_{SB1-LB}	mass exchange coefficient between upflowing "small" and "large" bubble phases, sec^{-1}
k	mass transfer coefficient, cm/s
I	radiation intensity counts
I_0	initial intensity counts
L	distance between the two probes, cm (Chapter 3)
L	dispersion height between the end-zone CSTs, cm (Chapter 6)
L_c	characteristic turbulent length, cm
l	mixing length, cm (Chapter 6)
l	attenuation path length, cm (Chapter 2)
l_{int}	length through the internals, cm
M_{ij}	measured counts

Mo	Morton number
m	power law exponent in the radial gas hold-up profile
N	total number of photon histories
N_{cali}	number of calibration points
N_g	number of quadrature points in each direction
n	Richardson-Zaki coefficient
\bar{n}	external unit vector locally normal to the detector surface at the point P
P	operating pressure, dyne/cm ²
P_ϵ	photo-peak efficiency for detection of photons of a given energy from a point isotropic source
P_ϵ^*	intrinsic photo-peak efficiency
Q	flow rate, cm ³ /s
R	column radius, cm
R	source strength (activity), disintegrations/second (Chapter 5)
$R(\tau)$	cross-correlation coefficient
Re	Reynolds number
RES	residual in the filtering algorithm, volts
RS	raw signal, volts
R_x	reaction rate, moles cm ⁻³ s ⁻¹
r	radial position in the column, cm
r', r''	radii where the liquid and gas velocity profiles invert
\vec{r}	vector from the point γ -ray photon source to a point P on the exposed detector surface
SF	shape factor for large bubble rise velocity
T	sampling time, s
T_ϵ	total efficiency for detection of photons of a given energy from a point isotropic source
T_ϵ^*	intrinsic total efficiency
TOL	tolerance criterion in the filtering algorithm, volts
t	time, sec

$t_{1/2}$	half life, hours
$U_G, U_{G,sup}$	gas superficial velocity, cm/s
U_{gtrans}	transition superficial gas velocity, cm/s
$U_L, U_{L,sup}$	liquid superficial velocity, cm/s
$U_{L,est}$	average interstitial liquid velocity between the two probes, cm/s
u	velocity, cm/s
$u_{b\infty}$	terminal single bubble rise velocity, m/s
u_0	centerline interstitial liquid velocity, cm/s
\bar{u}	radially averaged mean velocity, cm/s
$ \mu_w $	absolute value of the interstitial axial liquid velocity near the wall, cm/s
V_a	volume of the CSTR representing the distributor zone, cm ³
V_b	volume of the CSTR representing the disengagement zone, cm ³
$V_{b\text{small}}^0$	unhindered rise velocity of a small bubble, cm/s
$V_{b\text{small}}$	rise velocity of dense bubble phase, cm/s
$V_{b\text{large}}$	rise velocity of large bubble phase, cm/s
W_i	solid angle subtended by the i^{th} selection of angles α and θ
w_g	quadrature weights
x	axial position in the column, cm
y_{num}	numerically generated raw signals for Figure 8, volts
y_{raw}	air-water raw signals in Figure 4, volts

Greek Symbols

δ'	thickness of the diffusion layer, cm
ϵ	local phase hold-up
$\bar{\epsilon}$	radially averaged phase hold-up
$\bar{\epsilon}_{g,\text{chord}}$	chordal average gas holdup
$\bar{\epsilon}_{G,\text{Overall}}$	overall gas holdup
$\bar{\epsilon}_{gtrans}$	transition gas holdup

$\tilde{\varepsilon}_g$	parameter in the gas holdup profile related to $\bar{\varepsilon}_g$
$\bar{\varepsilon}'_{g1}$	mean hold-up of up-flowing gas with down-flowing liquid
λ	eddy size, cm
μ_d	total linear attenuation coefficient of the detector crystal
μ_{eff}	effective viscosity calculated from power law model, Pa.s
μ_i	total linear attenuation coefficient of the i^{th} material in the γ -ray path
μ_i^j	j^{th} moment of i^{th} probe
μ_l^m	liquid/slurry viscosity, cP
ϕ	fraction of the column diameter (Chapter 6)
ϕ	photopeak to total efficiency ratio (Chapter 4)
θ	angle along which the photon enters the detector
ρ	density, g/cm ³
σ_j	Compton linear attenuation coefficient of the detector crystal
σ, σ_1	surface tension of the liquid, dyne/cm
σ^2	variance
τ	dead time of the detector, s
τ_j	photoelectric linear attenuation coefficient of the detector crystal
τ_{LAG}	characteristic lag time, s
τ_{Mean}	mean residence time, s
τ_{Norm}	normalization factor for time scale, s
τ^m	viscous shear stress, dyne/cm ²
τ'	turbulent shear stress, dyne/cm ²
ν^m, ν_m	kinematic viscosity, cm ² /s
ν'	turbulent viscosity, cm ² /s
ν^*	number of γ -rays emitted per disintegration
ξ	dimensionless radius
ξ'	dimensionless radius where the liquid velocity profile inverts

ξ''	dimensionless radius where the gas velocity profile inverts
Ω	solid angle subtended by the active crystal volume on the point surface
Ω^*	normalized solid angle
ΔP	pressure drop, dyne/cm ³

Subscripts

ASE	after slurry exit
BSE	before slurry exit
b	bubble
bs	small bubble
CST	well mixed distributor and disengagement zones, a and b
c	contact
DP	differential pressure measurement
f	column full of liquid
g, Gas	gas
ga	gas phase in the distributor zone, CST a
gb	gas phase in the disengagement zone, CST b
g,small	gas in small bubbles
g,large	gas in large bubbles
g,trans	gas phase at transition
g1	up-flowing gas
g2	down-flowing gas
gulu	gas flowing upwards with liquid going up as well
guld	gas flowing upwards with liquid going down
gdld	gas going down with liquid down as well
i	inside
in	reactor inlet
l, L	liquid
la	liquid phase in the distributor zone, CST a

lb	liquid phase in the disengagement zone, CST b
l1	up-flowing liquid
l2	down-flowing liquid
mt	empty column
NDG	nuclear density gauge measurement
o	outside
out	reactor outlet
Slurry	slurry
Slurry+Gas	slurry and gas phases
tp	column with two-phase flow

Acknowledgements

I wish to express my heartfelt gratitude to my advisor Professor M. P. Dudukovic for the opportunity to undertake this work under his supervision. His advice, encouragement of independent thought, and trust in my abilities were invaluable in making this work possible. I would also like to thank my co-advisor Prof. M. H. Al-Dahhan, whose enthusiasm in all aspects of the project made it possible for me to focus positively. Additionally, I would like to acknowledge the members of my committee, namely, Prof. P. A. Ramachandran, Prof. K. J. Myers (University of Ohio, Dayton), Dr. M. Chang (Exxon Research and Engineering) and Dr. B. A. Toseland (Air Products and Chemicals, Inc.) for taking interest in my work, examining my thesis and providing useful comments and suggestions.

I wish to gratefully acknowledge the financial support of the Department of Energy and the industrial participants of the CREL consortium, which made this research work possible. In particular, I would like to thank Dr. B. A. Toseland for the several opportunities to visit the Alternate Fuels Development Unit in La Porte, TX and participate in tracer tests on the pilot-scale slurry-bubble column reactors. In addition, I would like to express my thanks to Dr. Robert Mudde (Technical University, Delft, The Netherlands) for his comments with issues related to CARPT data interpretation and Dr. Yubo Yang (Abbott Laboratories) for providing the original code for Monte Carlo simulations and helping resolve issues during the course of Monte Carlo based particle-tracking project.

Several people at CREL and in the Chemical Engineering Department have made significant contributions in making my work and life at Washington University an enjoyable experience. In particular, I would like to express my gratitude to Ms. Booncheng Ong for constantly encouraging and helping me during the difficult phases of my doctoral program when things were not exactly going right. I also thank Mr. Aravind

Rammohan, Dr. Sujatha Degaleesan, Dr. Jinwen Chen and Dr. Kemoun Abdenour for their help and support in the experimental work on several projects undertaken in the bubble column reactor laboratory. My sincere appreciation also goes to Steve Picker, Pat Harkins and John Krietler for their help during the fabrication of the high-pressure slurry bubble column facility; and Dr. Y. Yamashita and Dr. Eduardo Gomez for their help in resolving numerous computer-related issues in CREL. My sincere thanks also go to Dr. Milind Kulkarni and Dr. Mohan Khadilkar whose help and encouragement was invaluable throughout my stay at Washington University.

I sincerely acknowledge the help and assistance offered by all the past and present members of CREL including Dr. Karthik Balakrishnan, Dr. Zhen Xu, Dr. Sailesh B. Kumar, Dr. Yi Jiang, Dr. Yu Pan, Marco Roveda, Fan Li and many others. I also wish to thank the entire Chemical Engineering Department, particularly the secretaries for their help with numerous formalities. Finally, thanks to my roommates and friends whose company made my stay in St. Louis a pleasant and memorable one.

Last, but not the least, my heartfelt gratitude goes to my parents and my brother for their patience and support and their sustained belief in my abilities that one day I will be writing these sentences.

Puneet Gupta
Washington University, St. Louis
May, 2002

Chapter 1. Introduction

1.1. Motivation

Multiphase reactors are at the heart of chemical reaction engineering. Reactions between gas and liquid are frequently encountered both in chemical and biochemical practice. The classification of gas-liquid reactors is based on the dispersed phase nature and, hence, two main groups of such contactors are defined - *reactors with dispersed gas phase* and *reactors with dispersed liquid phase*. For a majority of gas-liquid reactions, the interfacial mass transfer resistance is concentrated in the liquid phase, leading to the application of reactors with continuous liquid and dispersed gas phase. In cases where the third solid phase is also present, the choice of the liquid as the continuous phase is understandable regarding the requirements of the highest possible solids hold-up and minimum energy consumption for its dispersion. Bubble column reactors are at the forefront of such applications.

Figure 1-1 shows a typical bubble column, where both the liquid and the gas are introduced at the bottom of the column. This reactor configuration has been widely used mainly because of the ease of construction, low cost, simplicity of operation, ability to handle solids, excellent heat and mass transfer characteristics and no direct sealing problems due to absence of mechanically moving parts. Tables 1-1 and 1-2 list some of the industrial applications of bubble columns (Luo, 1993). In addition, new avenues for bubble column application are being regularly explored especially in the biotechnological areas such as effluent treatment, single cell protein production, antibiotic fermentation and animal cell culture (Chisti, 1989). From Tables 1-1 and 1-2, it can be seen that this class of reactors has a wide range of important applications both in the chemical and biochemical engineering fields.

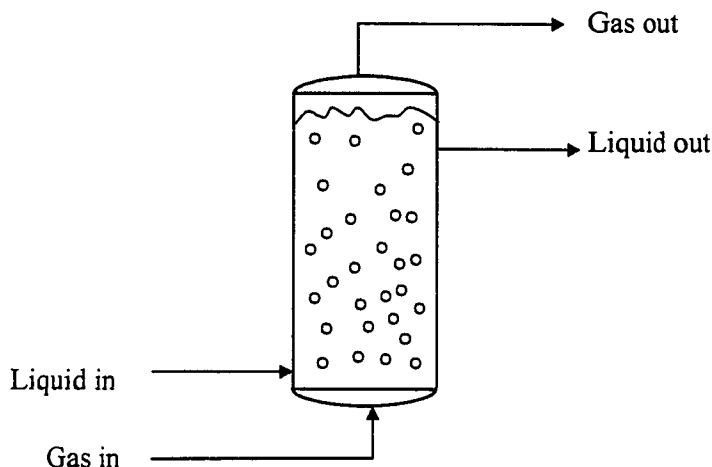


Figure 1-1. Schematic of a bubble column configuration.

In spite of the simplicity in mechanical design, the fluid dynamics associated with the operation of a bubble column reactor are so complex that no reliable fundamental scale-up rules could be established over the past 50 years of research in this area. Moreover, most of the detailed hydrodynamic studies reported in the literature have been conducted using air and water as the two phases with the system operated at atmospheric pressures (Devanathan *et al.*, 1990; Devanathan, 1991; Tzeng *et al.*, 1993; Degaleesan, 1997). However, the chemical industry places demands on operating large diameter bubble columns at high superficial gas velocities under high pressures for gas-liquid systems other than air-water. Under these conditions, bubble columns operate in the *churn-turbulent* regime characterized by frequent bubble coalescence and breakage and a nearly chaotic two-phase system (Vermeer and Krishna, 1981; Wilkinson *et al.*, 1992; de Swart, 1996; Letzel *et al.*, 1997; Chen *et al.*, 1999). The churn-turbulent regime of operation has specifically gained importance with regards to Syngas conversion processes, such as the liquid phase synthesis of methanol and the Fischer-Tropsch (FT) synthesis of heavy paraffins, as alternate sources of fuels (Armstrong *et al.*, 1993; Wender, 1996; Maretto and Krishna, 1999; Krishna *et al.*, 2001). However, given the

current state of technology and fundamental understanding of these complex multiphase flows in general, and their interactions with chemistry in particular, numerous avenues exist for improvements in flow characterization, modeling, design and scale-up of bubble column reactors. The primary motivation of this study is to advance the current state of modeling and characterization of flow and interphase mass transfer phenomena in bubble column systems in accordance with the Department of Energy (DOE) objectives for developing the slurry bubble column technology to process Syngas into value-added chemicals.

Table 1-1. Examples of industrial processes in two-phase bubble columns (Luo, 1993)

Process	Main Product
<i>Oxidation of</i>	
Ethylene (partial)	Vinyl Acetate (Acetaldehyde)
Cumene	Cumene hydroperoxide
Butane	Acetic acid, MEK
Toluene	Benzoic acid
Xylene	Phthalic acid
<i>Wet oxidation of effluents</i>	
<i>Oxychlorination of ethylene</i>	Dichloroethane
<i>Chlorination of</i>	
Aliphatic hydrocarbons	Chloroparaffin
Aromatic hydrocarbons	Chlorinated aromatics
<i>Alkylation of</i>	
Methanol	Acetic acid
Benzene	Ethylbenzene, cumene
<i>Isobutene hydration</i>	<i>tert</i> -Butanol
<i>Oxysulphonation of paraffins</i>	Paraffin sulphonate

Table 1-2. Examples of industrial processes in three-phase bubble columns (Luo, 1993)

Process	Solids
Production of Al-alkyls	Ca(HSO ₃) ₂ as reactant
Coal hydrogenation	Coal particles
SO ₂ removal from tail gas	CaO and CaCO ₃
Wet oxidation of effluent sludge	Sludge
Biotechnological processes	Biomass as reactant
Production of single cell protein	Cells as reactant
Animal cell culture	Cells as reactant
Effluent treatment	Particles as reactant
Polymerization of olefins	Polyolefins
Oxamide synthesis of HCN oxidation	Oxamide
Production of biomass	Biomass as product
Hydrogenation of oils	Catalyst
Coal hydrogenation	Catalyst
Synthesis of methanol	Catalyst
Fischer-Tropsch synthesis	Catalyst
Numerous oxidation and hydrogenation processes	Catalyst

1.2. State of the Art

Figure 1-2 shows the most important design and operating parameters affecting bubble column phenomena and performance. One of the primary tasks in the current methodology of bubble column design involves description of the degree of mixing of each of the involved phases, which is subsequently used along with the chemistry to estimate the reactor performance *viz.* the conversion, yield and selectivity. As with most multiphase flow situations, bubble-column reactors show a large deviation from ideal

mixing (perfect mixing or plug-flow). Moreover, since the fluid-dynamically controlled mixing is only approximately known, the final reactor is generally larger than the preliminary estimates based on ideal flow pattern assumptions. Consequently, much attention has been paid to the experimental determination of mixing parameters describing the state of non-ideal gas-liquid mixing because of the inherent lack of fundamental understanding of the multiphase mixing in bubble column reactors. Better understanding of these phenomena should lead to improved and more economical reactor sizing and performance.

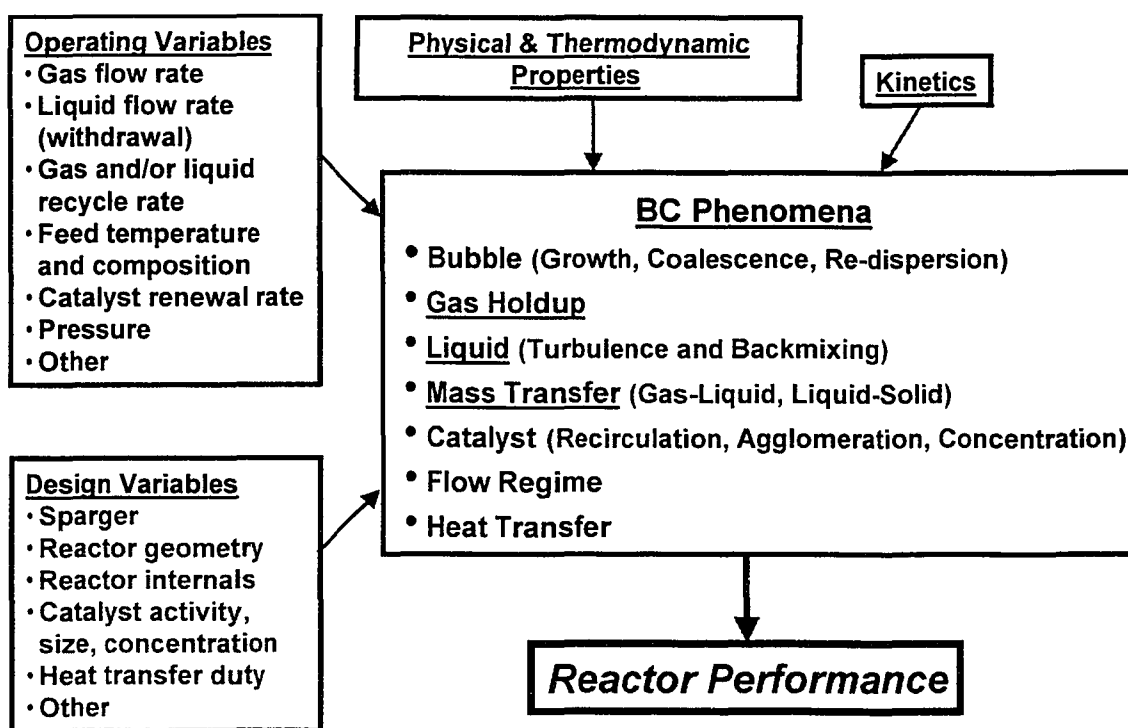


Figure 1-2. Variables affecting bubble-column phenomena and performance.

1.2.1. Degree of Mixing in a Bubble Column

The mixing of individual phases in gas-liquid reactors can be characterized according to the scale of mixing considered -- *micromixing* or *macromixing*. Description of micromixing requires flow quantification at very small scales and of contact times of individual molecules. The extent of micromixing is not quantified by the residence time

distribution and depends solely on the time of association between individualized units of the fluid. Macromixing on the other hand is characterized by the residence time distribution of the phase under consideration. The majority of published literature on mixing has been devoted to studying homogeneous systems, whereas only a limited number of studies have been reported on mixing in heterogeneous reaction systems.

Of the vast amount of literature on the degree of mixing in bubble columns published over the past 30 years, some of the studies that provide insight into the churn turbulent flow regime have been discussed by Kastanek *et al.* (1993). The survey of other studies can be found in the review articles of Mashelkar (1970) and Shah *et al.* (1982). Most of the reported studies have used *axial dispersion* to model the flow. As an alternative, a slug-cell-model was developed by Myers *et al.* (1987) to describe the liquid-phase mixing in churn-turbulent bubble columns. Recently, some efforts have been made to explain the liquid phase flow in terms of a recycle with cross flow model (Degaleesan *et al.*, 1996^b; Degaleesan, 1997). The model predicts well the experimental tracer data when the axial dispersion coefficients in the two liquid regions are taken as the *axial turbulent diffusion* coefficients, and the exchange between the two zones is represented in terms of the *radial turbulent diffusion* coefficient. These turbulent diffusion coefficients were calculated from the velocity fluctuations obtained by the Computer Automated Radioactive Particle Tracking (CARPT) technique. The analysis of experimental results from these studies reported in the literature clearly shows that the axial mixing of liquid in bubble column reactors is decisively influenced by the gas flow rate and reactor diameter. A summary of the correlations for estimating the liquid (E_L) and gas (E_G) phase dispersion coefficients is presented by Kastanek *et al.* (1993).

As compared to the liquid phase mixing, the investigation of gas phase backmixing has received significantly less attention. This is mainly due to the assumption that gas phase is in plug flow in bubble columns of industrial importance. The second reason is that there are considerable problems involved with the determination of reliable gas residence time distribution (RTD) data. The experimental data found in the literature are often contradictory and qualitative conclusions and recommendations are remarkably at variance. These contradictions can be ascribed primarily to the effect of the mode and

quality of inlet gas distribution on the character of gas flow. In general, Kastanek *et al.* (1993) propose that there are two different ways by which the type of distributor and its geometry can influence gas phase backmixing. The main effect is on the formation and stability of homogeneous or turbulent bubbling regime. Second, the working regime of the distributor plate in turbulent bubbling conditions plays an important role, as the non-uniform distribution of the gas induces macro-circulation flow patterns of the liquid phase in the column which in turn contribute to the extent of gas phase backmixing.

1.2.2. Flow Regimes in a Bubble Column

The nature and mechanism of mixing in bubble column reactors is primarily governed by the ensuing flow regime, which in turn is dependent on the employed set of operating conditions. Of the several controllable operating variables, the superficial gas velocity appears to hold the key in dictating the flow regime of operation. Therefore, depending on the gas superficial velocities employed, bubble columns can be operated under two broadly classified regimes: the *bubbly* and the *churn-turbulent* regimes. Some authors also refer to the *homogeneous bubbling* regime which is claimed to provide even better mass and heat transfer characteristics (Kastanek *et al.*, 1993). They point out that this regime should not be confused with the *bubbly* flow regime. The *bubbly* flow regime is stable only at close to atmospheric pressure conditions with gas superficial velocities less than or equal to 3 cm/sec and is characterized by the upward movement of *non-interacting* bubbles through the liquid phase. On the other hand, a high bubble population density characterizes the fully developed *homogeneous bubbling* regime and thereby ensures *close contact* of bubbles in the column. However, because of the almost uniform bubble size distribution and thus a constant bubble rise velocity, almost no mutual interference of bubbles occurs and there is a low degree of macro-turbulence. This in turn results in a uniform radial and axial distribution of the gas hold-up. This regime can exist alternatively with the *churn-turbulent* regime even at gas velocities above 0.1 m/sec, depending on the gas distributor type and geometry, bubble column dimensions and the physical properties of the phases. The *homogeneous bubbling* regime

is less stable than the *churn-turbulent* regime and its existence is limited to a certain upper value of the superficial gas velocity. Beyond this superficial gas velocity, the disintegration of the bubble structure in the column occurs with a subsequent transition to the heterogeneous *churn-turbulent* regime. In general, the conditions for existence of the *homogeneous bubbling* at high gas superficial gas velocities (at which usually the *churn-turbulent* regime would prevail) are a rigidly and firmly mounted column with a sintered plate distributor and a liquid phase with a low coalescing nature. Poulsen and Iversen (1998) found that using punctured rubber-membrane spargers results in the formation of smaller and uniform bubbles even at relatively high superficial gas velocities. This consequently results in approximately doubling of the volumetric mass transfer coefficient as compared to the cases using rigid spargers. Figure 1-3 shows the different regimes that can exist in a bubble column. Besides bubbly, homogeneous bubbly and churn turbulent regimes, two other flow regimes that are known to occur in vertical upward two-phase flows are the *slug* flow regime and the *annular* flow regime. The *slug* flow regime is known to occur only in tall columns of diameter less than 0.15-m where intermittent slugs of bubbles as big as the column diameter rise through the column at regular intervals. On the other hand, the *annular* regime results when the gas velocity is so high that all the gas passes through the core with the liquid pushed to the wall.

In the *homogeneous bubbling* regime, almost a mono-disperse bubble size distribution can be observed. Here, however, the bubbles ascend without significant interactions even at high gas hold-ups, and the buoyancy force corresponding to their size, which generally is affected by the gas distributor type, solely determines their rise velocity. At such conditions, very little axial mixing occurs in the gas phase so that its flow pattern can be well described by the plug-flow model. Consequently, in the homogeneous regime the liquid phase axial dispersion coefficient, E_L , is independent of the gas superficial velocity, and only upon transition to the *turbulent bubbling* heterogeneous regime, one starts seeing a dependency of E_L on U_G . In the heterogeneous regime, however, the axial dispersion in the gas phase is not insignificant and can be ascribed to a bi-disperse distribution of bubble sizes (Vermeer and Krishna, 1981; de Swart, 1996). Clusters of large bubbles rise very fast through the center of the column

with rise velocities of 0.8 - 1.0 m/s for air-water system. The rise velocity of the small bubbles on the other hand corresponds approximately to the buoyancy rate of isolated bubbles (for air-water system $u_{b\infty} \approx 0.2-0.5$ m/s). A few models, other than the axial dispersion model, have been developed to characterize such gas flows (Krishna and Ellenberger, 1996; Krishna *et al.*, 1999^a). The practical use of these models has been hindered by the absence of commonly applicable correlations for the evaluation of model parameters. The axial dispersion model has, thus, been applied in industrial practice for the description of the gas phase RTD even under turbulent bubbling conditions, although its physical basis does not correspond to the flow pattern of the gas phase observed in churn-turbulent bubble columns. Joshi (1982) has presented a survey and critical analysis of the gas phase axial dispersion coefficient, E_G , which has mostly been correlated to gas superficial velocity, gas holdup and column diameter. The ability of the existing correlations to predict accurately the gas axial dispersion coefficient is highly questionable as the predictions of various correlations can differ by an order of magnitude (Fan, 1989).

Flow regimes in vertical upward flow

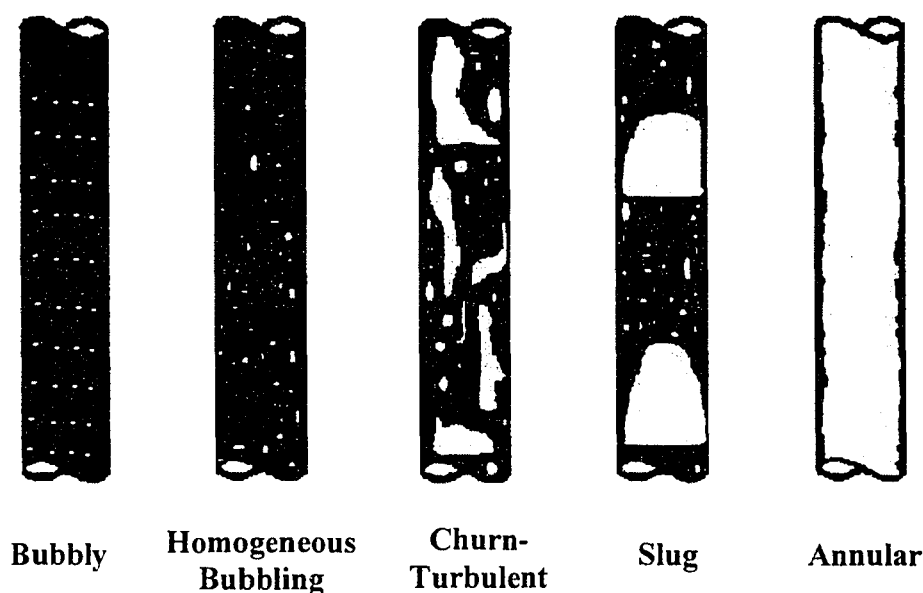


Figure 1-3. Flow regimes in vertical bubble column reactors. a) Bubbly b) Homogeneous Bubbling c) Churn-turbulent d) Slug-flow e) Annular (Kastanek *et al.*, 1993).

Pilhofer (1980) proposed a preliminary criterion for the existence of the homogeneous bubbling regime. This was based on considerations of bubble stability in the column. Some conditions for the existence of homogeneous bubbling regime have also been reported by Kastanek *et al.* (1984). But a general quantitative criterion for the transition between homogeneous and turbulent regime is not available as yet, apparently due to the large number of factors involved and their complex effect on the bubble column hydrodynamics (Letzel, 1997).

1.2.3. Measurement of Backmixing and Liquid Phase Hydrodynamics

The measurement of backmixing in the gas and liquid phases has been primarily achieved using tracer techniques (Molerus and Kurtin, 1986; Kastanek *et al.*, 1993). Overall residence time distribution measurements of a phase in a multi-phase flow situation can be achieved with relative ease when there is a well-defined inlet and a well-defined outlet for the phase under consideration and when a tracer confined to a single phase can be identified. Therefore, overall RTD of the gas phase can be determined by measuring the concentration of the gas tracer in the gas phase outlet following its impulse injection into the gas inlet. Similarly, for a co/counter-current flow of the liquid phase, the overall RTD measurements can be accomplished by measuring the liquid phase outlet concentration of the liquid tracer following its impulse input into the liquid inlet stream. However, finding a suitable gas tracer is not a trivial task because of the finite solubility of most available tracers in the liquid phase that makes the interpretation of outlet gas-phase-tracer concentration subjective because of mass transfer considerations. Contrary to the gas phase, however, the interpretation of the liquid tracer concentration in the liquid phase outlet does not suffer from mass transfer complications, since most of the employed tracers (like solutions of electrolytic salts, fluorescent dyes, radio-tracers, etc.) are non-volatile and do not transfer to the gas phase.

The overall RTD is a very powerful tool for looking at the overall system dynamics of an individual phase. However, for the convection dominated and highly recirculatory flows encountered in bubble column operations, it is of greater interest to

know the localized state of liquid mixing since majority of the mass transfer resistance lies in the liquid phase. These localized measures become even more important when the liquid phase is in the batch mode with no inlet and outlet. Even for co/counter-current flow of the liquid phase, the superficial liquid velocity is much smaller than the recirculation velocities within the reactor domain. Therefore, it is imperative to understand the state of local mixing of the liquid phase in almost all bubble column flow configurations.

Conductivity probes offer the simplest and direct measurement of local liquid-phase-tracer concentration (Boddem and Mewes, 1996). Such measurements are straightforward in single-phase flow situations of the liquid. In spite of being an intrusive measurement, accurate assessment of local liquid mixing is possible by employing appropriately small probes. On the other hand, for gas-liquid flow situations encountered in a bubble column operation, the reliability of such a measurement is marred by the frequent passage of bubbles over the probe measurement volume. Therefore, opportunities exist for developing improved signal processing methodologies to obtain accurate and reliable measurement of local liquid conductance in two-phase gas-liquid flows.

The Computer Automated Radioactive Particle Tracking (CARPT) is one of the most sophisticated, non-intrusive and universal technique for obtaining detailed information on liquid/slurry phase hydrodynamics in high gas volume-fraction flows inside opaque vessels (Devanathan *et al.*, 1990; Devanathan, 1991; Larachi *et al.*, 1994; Degaleesan, 1997; Chen *et al.*, 1999). In such flow situations, other sophisticated techniques like Laser Doppler Anemometry (LDA) and Particle Image Velocimetry (PIV) cannot be fruitfully employed. The CARPT technique provides a Lagrangian trajectory information of a neutrally buoyant radioactive tracer particle by utilizing an array of scintillation detectors mounted strategically around the flow vessel. From such a Lagrangian description, and after considerable data processing (Degaleesan, 1997), one can extract valuable information about the liquid or solid flow field like velocities, turbulent stresses and most importantly the turbulent eddy diffusion coefficients

(Degaleesan and Dudukovic, 1999). This last piece of information is unique to Lagrangian measurements and very important from the point of view of scalar mixing.

Because of the inherent randomness of the radiation emission and detection process, an *ad hoc* methodology of relating the tracer particle position to the scintillation counts registered by the array of detectors is employed in the current generation of CARPT data processing. However, it has been shown by Larachi *et al.* (1994) that a more precise and possibly more accurate method of CARPT data processing is possible using a Monte Carlo based approach to radiation detection. The current *ad hoc* methodology has worked reasonably well for Plexiglas flow vessels that were mostly employed in studies conducted until recently. However, the use of this technique is being pushed to high-pressure and high-velocity situations in stainless steel vessels. It is also proposed to apply the CARPT technique for pilot-scale flow conditions. In such situations where it is not possible to acquire numerous calibration points required by the *ad hoc* methodology, it is imperative to adopt an experimentally simpler simulation-based methodology for effecting a CARPT calibration. Therefore, there are significant benefits of developing simulation capabilities for Monte-Carlo based calibration of the CARPT technique.

1.3. Research Objectives

When bubble columns are operated under churn-turbulent conditions, an increase in mass transfer is observed (Vermeer and Krishna, 1981; de Swart, 1996) in spite of the presence of larger bubbles that tend to reduce the interfacial area for mass transfer. Numerous studies (Azbel, 1981; Sotelo *et al.*, 1994, Saxena, 1995) have been reported in the literature that tried to experimentally determine the volumetric mass transfer coefficients. The end product of most such studies has been the development of empirical or semi-empirical correlations that are justified because of the fact that a lot still remains unknown about the complex hydrodynamics prevailing in the column. The review article by Saxena (1995) on bubble column reactors discusses many of the correlations reported for the volumetric mass transfer coefficient in bubble columns and its dependence on macroscopic hydrodynamic parameters like superficial velocities, gas holdup, bubble

size, column diameter and operating pressure. However, it has been clearly established that it is the hydrodynamics that is responsible for the enhanced mass and heat transfer observed during the churn-turbulent regime of bubble column operation. The present study aims at relating the *hydrodynamics more closely to the mass transfer mechanism, gas-liquid phase mixing and reactor modeling*. In addition, this study also addresses the complexities involved with reliable measurements of two-phase gas-liquid flow phenomena and addresses ways to improve diagnostic techniques for characterizing the liquid phase mixing and particle tracking of the liquid phase motion in bubble column flows. Hence, the research objectives of this work are both experimental and modeling in nature.

1.3.1. Experimental Objectives

I. Development of Conductance Probes for Measurement of Liquid Tracer Responses in Gas-Liquid Flows

Specific objectives are:

- Design experimental test procedures to measure point liquid-tracer concentrations in vertical gas-liquid flows.
- Develop a software based soft-filtering technique to eliminate the systematic signal corruption of the liquid phase conductance when bubbles interact with the probe measurement volume.
- Demonstrate the applicability of the developed measurement and data analysis protocol for tracer studies in a bubble column with batch liquid.

II. Development of a Monte Carlo based Sodium Iodide Detector Calibration Procedure for Radioactive Particle Tracking

Specific goals are:

- Review the literature and develop a simulation tool to estimate counting efficiency of NaI (Tl) scintillation detectors when exposed to a point radioactive source.
- Build capabilities in the Monte Carlo simulation code to account for the presence of intervening media between a point source and a scintillator surface.
- Apply efficient numerical techniques for repetitive evaluations of surface integrals and validate the developed code against published data.
- Develop a Generalized Reduced Gradient (GRG) based optimization protocol to estimate the parameters of a given scintillator by comparison of the detector responses measured experimentally with the computed ones estimated by the simulation tool mentioned above.
- Integrate the optimization and the efficiency simulation tools to estimate detector parameters in a multi-detector setup for tracking a single radioactive tracer particle (point source) inside a vertical cylindrical vessel (like a bubble column).
- Develop methodologies for estimation of tracer particle location from experimental counts data based on a search algorithm that scans the database of computed scintillator efficiencies over the entire vessel volume.
- Test and validate the particle reconstruction algorithms against experimental data.

Many of the objectives stated above were originally proposed by Yang (1997), who was also instrumental in laying the basic framework for the Monte Carlo approach. It was the objective of this work to further develop and implement the original code developed by Yang (1997) to a full-scale bubble column experiment.

III. Development of a Protocol for Radioactive Tracer and γ -Scan Experiments and their Interpretation on Pilot-Scale Bubble Column Reactors

Specific tasks are:

- Analyze γ -densitometry scan data from a pilot scale vessel under reaction conditions and attempt reconstruction of gas-phase distribution inside the vessel.

- Identify shortcomings of the measurement protocol and suggest improvements for future diagnostic efforts.
- Develop a protocol for collection, processing and interpretation of tracer data acquired using radioactive tracers for tagging the gas, catalyst and liquid phases in a hot pilot-scale slurry bubble column operation.

1.3.2. Modeling and Computational Objectives

This part of the work focused on the development of improved models for gas and liquid flow and mixing based on hydrodynamic principles.

Specific tasks are:

- Develop gas and slurry phase recirculation models based on the two-fluid approach. Employ robust numerical schemes for solution of the model equations.
- Study the effect of bubble size distribution on gas recirculation rates predicted by the developed model.
- Develop mechanistic/phenomenological models to describe gas and liquid/slurry phase mixing. Investigate the effect of bubble size distribution on scalar mixing.
- Compare and test the developed models against radioactive tracer data obtained from a pilot-scale reactor during the process of liquid-phase methanol synthesis from synthesis gas.
- Extend the liquid mixing mechanistic model for interpretation of tracer data from the Fischer-Tropsch (FT) synthesis pilot reactor. This is required to account for the slurry exit from the middle portion of the reactor with subsequent recycling at the reactor bottom after separation of the FT wax.
- Analyze the performance of the mechanistic models in simulating gas and liquid/slurry phase tracer responses.

1.4. Thesis Organization

Chapter 2 provides a brief general review of the literature on current research in bubble column reactors while specific topical reviews accompany each subsequent individual chapter. The structure of the thesis is organized so as to present the experimental contributions from this work in the first part followed by the discussion of the modeling efforts in the second half. Chapter 3 covers the developments related to liquid conductance measurements using conductivity probes with example applications to liquid tracer experiments in a bubble column with batch liquid as well as in a staged bubble-column with counter-current flow. Chapter 4 presents the details of the simulation tool for computing scintillator efficiencies using a Monte Carlo method while Chapter 5 provides the details of integrating the Monte Carlo method with the database generation and position rendition algorithms. In addition, Chapter 5 also presents the validation of position reconstruction algorithms with experimental data and an example application to flow mapping in a stainless steel bubble column. On the modeling and computational side, Chapter 6 presents the development of the hydrodynamic model to predict phase recirculation rates using the two-fluid approach and that of the two gas-liquid mixing models based on “single” and “bi-modal” bubble size distributions. Chapter 7 provides the details of the γ -scan and tracer experiments conducted during the FT synthesis at the Alternate Fuels Development Unit (AFDU) as well as comparison of data with modeling and simulation results. Lastly, Chapter 8 provides the conclusions with recommendations and possibilities for future efforts.

Chapter 2. Literature Review

This chapter provides a broad but brief overview of the literature on bubble column hydrodynamics. As mentioned in Chapter 1, the fluid dynamics of bubble columns has been studied in detail in the last several decades and there is a vast body of literature available on bubble column hydrodynamics for different gas-liquid systems. However, the complexity of the hydrodynamics coupled with measurement difficulties has confined most of the earlier studies to measurement of global hydrodynamic parameters like overall gas holdup and volumetric mass transfer coefficient (Mashelkar, 1970; Shah *et al.*, 1982; Saxena, 1995). It was only in the last decade or so that *local quantitative* characterization of the hydrodynamics has become feasible. This has primarily come about as a result of the development of new sophisticated experimental techniques like the Laser Doppler Anemometry-LDA (Mudde *et al.*, 1997), Computer Automated Radioactive Particle Tracking-CARPT (Lin *et al.*, 1985; Devanathan *et al.*, 1990; Moslemian *et al.*, 1992; Yang *et al.*, 1993; Larachi *et al.*, 1994; Limtrakul, 1996; Degaleesan, 1997), Particle Image Velocimetry-PIV (Chen and Fan, 1992; Tzeng *et al.*, 1993; Chen *et al.*, 1994), γ -ray Computed Tomography-CT (Kumar *et al.*, 1995; Adkins *et al.*, 1996; Kumar *et al.*, 1997; Shollenberger *et al.*, 1997), Electrical Capacitance Tomography-ECT (Dickens *et al.*, 1993) and other point probing techniques like optical and conductance probes (Choi and Lee, 1990; Cartelliar, 1992; Chabot and de Lasa, 1993).

Two of the most important hydrodynamic parameters in a bubble column operation, which are both the cause and the effect of a series of complex phase interactions, are the gas volume fraction distribution and the liquid (continuous) phase velocity distribution. These two combined with bubble interactions and levels of liquid

phase turbulence determine the rates of heat and mass transfer and consequently the overall reactor performance (Azbel, 1981; Deckwer, 1992; Sotelo *et al.*, 1994; Krishna and Ellenberger, 1995; de Swart, 1996; Krishna and Ellenberger, 1996; Kojima *et al.*, 1997). While the dynamics of the gas phase *viz.* bubble velocities, bubble-bubble interactions and gas phase mixing are very important as well, these have not received great attention because of the difficulties in measuring gas phase phenomena (Molerus and Kurtin, 1986). Consequently, the gas phase in most studies has been considered to be in plug flow with very little being known of the gas phase velocity distributions. Studies that have tried to address gas phase dynamics have done so by considering a slip velocity (Lockett and Kirkpatrick, 1975), which was assumed either to be a constant or to have a radially varying profile. Some recent studies by Luo (1993), Prince and Blanch (1990) and Svendsen *et al.* (1998) have tried to measure the bubble velocity and bubble-size distributions using probes. These techniques can potentially provide more information on the gas phase dynamics and gas phase recirculation, however, their accuracy and applicability at high superficial gas velocities in churn-turbulent flows remains suspect.

In the following sections, a general review on several essential aspects of bubble column hydrodynamics is presented. Specific topical reviews related to subject matters discussed in different parts of this study are presented in the respective chapters.

2.1. Gas Hold-Up

As mentioned before, the gas volume fraction, also referred to as gas holdup, is probably the single most important parameter governing bubble column hydrodynamics. When referring to gas holdup, one could be addressing either its point value anywhere inside the flow vessel or the average value over the entire flow domain. The former is therefore referred to as the *local gas holdup*, while the latter is usually referred to as the *overall gas holdup*. Therefore, overall gas holdup is equal to the fraction of the total reactor volume occupied by the gas. On the other hand, local gas holdup at an interrogation point is the fraction of an infinitesimal volume around this point that is occupied by the gas phase (Drew, 1983; Kumar, 1994). While the overall phase holdup is

important in determining the gas residence time and the system pressure drop, the local void fraction provides information about the phase interactions, the interfacial areas and phase recirculation; which are all related to the heat and mass transfer mechanisms. Consequently, gas holdup and its distribution have been identified as the most important parameters that govern liquid recirculation in bubble column operation. It is known that the greater the gradients of the radial gas holdup profile, the higher is the intensity of liquid recirculation (Chen *et al.*, 1998), which is one of the important factors responsible for the enhanced mass and heat transfer rates in bubble column operations.

There are various factors affecting gas hold-up profiles and bubble-size distributions, which are indirectly related to the operating flow regime. As described in Chapter 1, the prevalent flow regime in turn depends on the gas and liquid flow rates, liquid properties and the dimensions of the column. The initial sizes of the bubbles and subsequent coalescence and breakup are dependent on the distributor type and the surface tension in the liquid. The prevalent bubble size distribution in the well-developed region, barring the distributor and disengagement zones, is a function of gas and liquid velocities and densities and the liquid viscosity and thus, determines the gas holdup (Joshi, 1998).

As presented in Chapter 1, two different types of flow regimes are generally encountered in bubble column operation, namely, homogeneous and heterogeneous (Ramachandran and Chaudhari, 1983; Kastanek *et al.*, 1993). The homogeneous regime is characterized by small, uniform-sized bubbles that rise without many interactions and is represented by a narrow bubble size distribution. At atmospheric pressure, this usually happens at a superficial gas velocity less than 3 cm/s. As the superficial gas velocity is increased beyond a critical value (roughly 5-8 cm/s for air-water system at atmospheric conditions) a transition to the heterogeneous (churn-turbulent) regime takes place (Kastanek *et al.*, 1993; Joshi *et al.*, 1998). The bubble size distribution in the heterogeneous regime is broader as compared to that in the homogeneous regime (Yu and Kim, 1991; Kang *et al.*, 2000). It has also been frequently reported that this bubble size distribution shows a bi-modality (Tassin and Nikitopoulos, 1995; de Swart, 1996), which is characterized by a distinct presence of large and small bubbles leading not only to

intense liquid turbulence, but also to enhanced bubble-bubble interactions (coalescence-redispersion phenomena).

The operating pressure has a significant effect on the operating flow regime as well as the resulting gas holdup structure. At elevated pressure conditions in the homogeneous regime, the effect of pressure on gas holdup is insignificant (Kölbel *et al.*, 1961; Deckwer *et al.*, 1980). At higher pressures however, the transition from the homogeneous to the churn-turbulent flow regime is delayed to higher superficial gas velocities (Luo *et al.*, 1999). Based on his measurements, Letzel (1997) however suggests that the superficial gas velocity at which transition occurs shows only a slight dependency on pressure with the gas holdup at transition showing a much more pronounced pressure effect. In either case, at higher gas throughputs beyond this transition, gas holdup increases with pressure (Jiang *et al.*, 1995; Adkins *et al.*, 1996; Lin *et al.*, 1998; Fan *et al.*, 1999; Kemoun *et al.*, 2001^a). This increase in gas holdup with pressure is usually attributed to the smaller bubbles that are formed under high-pressure conditions. Jiang *et al.* (1995) reported that a decrease in bubble size results from an increase in pressure, which leads to a narrower bubble size distribution. Oyevaar and Westerterp (1989) reviewed critically the influence of pressure on mass transfer phenomena and hydrodynamics in bubble column. They reported that the initial bubble size at a single orifice decreases with increasing pressure.

It is universally accepted that the increase in gas holdup with pressure is due to the reduction of bubble size and thereby a reduction in bubble rise-velocity. However, two differing hypotheses have been suggested in interpreting the pressure effects on bubble size. According to the first, increasing pressure results in an increase in gas momentum, thereby leading to formation of smaller bubbles (Wilkinson, 1991; Reilly *et al.*, 1994). Jiang *et al.* (1995) on the other hand, attribute the pressure effects to a decrease in interfacial tension with increasing pressure thereby resulting in smaller bubbles. In other words, an increase in system pressure has a similar effect as increasing the gas density, as indicated by the first hypothesis, whereas the latter implies that the decrease in bubble size is due to an inherent instability of bubble size arising from surface tension effects. Letzel (1997) made use of the Kelvin-Helmholtz stability theory

to arrive at a conclusion that bubbles of diameter greater than 2-cm are inherently unstable. These bubbles however do exist because besides continuous breakup of these unstable bubbles there is also a continuous coalescence. The result of these two competing phenomena is an equilibrium bubble size corresponding to the dynamic equilibrium of these two opposing mechanisms. His analysis further concluded that the rise velocity of large bubbles is inversely proportional to the square root of gas density. In the homogeneous regime before transition however, he showed that the swarm velocity of bubbles (which are relatively small being less than 1-cm) has only a weak dependency on gas density. The same effect was observed by Reilly *et al.* (1994) as can be seen from Equation 2-6. This probably explains why the gas holdup in the homogeneous regime is fairly independent of pressure but shows a more pronounced effect in the churn-turbulent regime where large bubbles are known to be present.

For more details and an extensive compilation of the gas holdup literature, the reader is referred to Ong (1999). Her study concluded that most of the reported research in high-pressure bubble-columns has been restricted to the measurement of overall gas holdup with negligible information on spatial distribution of gas holdup. Subsequently, in the absence of any reliable information, the design and scale up of bubble column reactors at elevated pressures utilize the guidelines from detailed experimental data collected at atmospheric conditions. Alternatively, information from the overall gas holdup measurements at elevated pressures can be utilized for such purposes. The measurement of overall gas-holdup is usually achieved using the bed expansion method. If H_0 is the unexpanded height of liquid in the column with no flow of gas, and H_E is the expanded height of the two-phase mixture upon introduction of gas into the column, then the overall gas holdup is given as

$$\bar{\epsilon}_{G,Overall} = \frac{H_E - H_0}{H_E} \quad (2-1)$$

It should be noted that the data from the overall gas-holdup measurements has inherent measurement errors due to a fluctuating gas-liquid/slurry interface leading to uncertainties in determining the expanded height of the gas-liquid mixture (H_E).

Krishna and co-workers (Krishna and Ellenberger, 1995; Krishna *et al.*, 1999^a; Krishna 2000^h; Krishna *et al.*, 2001) have utilized the so-called Dynamic Gas Disengagement (DGD) technique extensively in columns of several different sizes and in liquids of different physical properties to evaluate the holdup distribution of “small” and “large” bubble phases in a churn-turbulent bubble column. They have also investigated the effect of operating pressure and the presence of solid/slurry particles on the structure of gas holdup. The underlying concept of the DGD technique is to monitor the drop in the liquid-gas interface at the top of the column upon shutdown of the gas supply and relate it to the gas holdup structure. Figure 2-1 shows typical data acquired from a DGD experiment along with the two bubble-phase model that has been proposed by Krishna and co-workers. As can be seen from Figure 2-1a, the initial rapid drop in the gas-liquid interface following the shut-off of the gas supply is attributed to the escape of the large bubbles. Subsequently, the gas-liquid interface falls down slowly due to the relatively slower disengagement of the small bubbles.

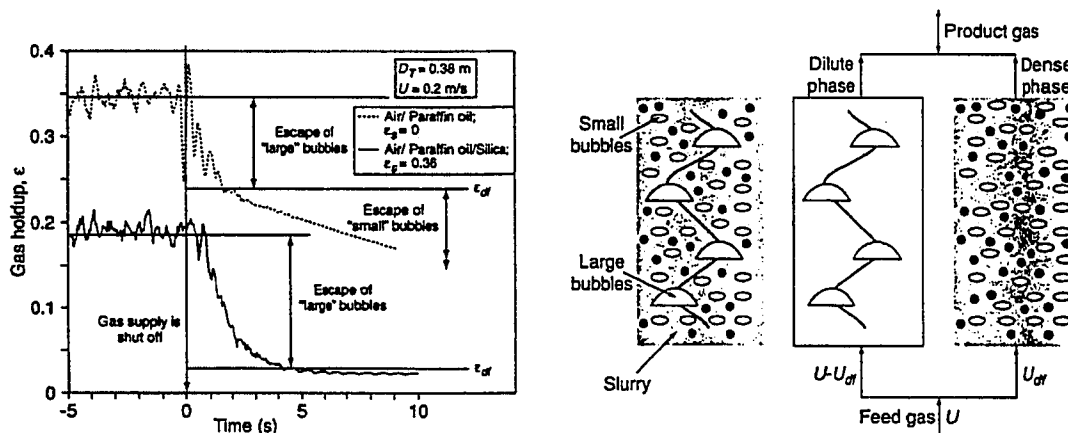


Figure 2-1. a) Typical DGD data b) 2-Bubble phase model (Krishna, 2000^h)

From the extensive data collected by DGD, high-speed photography and Computational Fluid Dynamic (CFD) simulations of bubble movement in liquids using the Volume of Fluid (VOF) model, Krishna and co-workers have proposed the following

methodology for calculating the gas holdup in the small (dense) and large (dilute) bubble phases. In the homogeneous bubbly flow regime, only the small (dense) phase exists and its holdup is given by Equation 2-2.

$$\bar{\varepsilon}_{g,small} = \frac{U_g}{V_{h,small}} \quad \text{for } U_g < U_{g,trans} \quad (2-2)$$

The rise velocity of the dense bubble phase, $V_{h,small}$, is calculated from the correlation proposed by Richardson-Zaki (1954) and is given by Equation 2-3. This phenomenological form essentially modifies the unhindered rise velocity of a small bubble, $V_{h,small}^0$, to account for the hindrance effects arising from the presence of multiple bubbles in a bubble swarm.

$$V_{h,small} = V_{h,small}^0 (1 - \bar{\varepsilon}_g)^{n-1} \quad n = 2 \text{ for air - water systems} \quad (2-3)$$

The superficial gas velocity at which transition to heterogeneous regime takes place, $U_{g,trans}$, is calculated via Equation 2-4.

$$U_{g,trans} = \bar{\varepsilon}_{g,trans} V_{h,small} \Big|_{\bar{\varepsilon}_g = \bar{\varepsilon}_{g,trans}} = V_{h,small}^0 \bar{\varepsilon}_{g,trans} (1 - \bar{\varepsilon}_{g,trans}) \quad (2-4)$$

The gas volume fraction at transition from the homogeneous to the heterogeneous regimes, $\varepsilon_{g,trans}$, and the unhindered rise velocity of a small bubble, $V_{h,small}^0$, are evaluated from the expressions proposed by Reilly *et al.* (1994). Equations 2-5 and 2-6 also capture the effect of pressure via the gas phase density.

$$\bar{\varepsilon}_{g,trans} = 1.16 \sqrt{\frac{\rho_g^{0.96} \sigma_l^{0.12}}{\rho_l}} \quad (2-5)$$

$$V_{h,small}^0 = \frac{1}{2.84} \frac{\sigma_l^{0.12}}{\rho_g^{0.04}} \quad (2-6)$$

In the heterogeneous flow regime, which occurs when the superficial gas velocity is greater than the transition superficial velocity, the holdup of the small bubble phase is

assumed to be the same as the transition gas holdup. Similarly, the superficial gas velocity through the small bubble phase is assumed the same as the transition superficial gas velocity. The bubble size, velocity and holdup of the large bubble phase is calculated from the following relationships (Krishna, 2000^h):

$$d_{b_{large}} = 0.069 (U_g - U_{g_{trans}})^{0.376} \quad (2-7)$$

The rise velocity of large bubbles is influenced by the presence of vessel walls, acceleration due to the presence of other bubbles, and operating pressure via the gas phase density. Therefore, Krishna and co-workers have proposed to modify the rise velocity of single bubbles far removed from vessel walls to incorporate situations encountered in a bubble column flow. Based on the Eotvos number, $Eo = g(\rho_l - \rho_g)d_b^2/\sigma_l$, two different forms have been proposed for the evaluation of the dilute bubble phase velocity.

$$\begin{aligned}
 V_{b_{large}} &= V_{b_{large}}^0 \cdot SF \cdot AF \cdot DF; & DF &= \sqrt{\frac{1.29}{\rho_g}} \\
 AF &= \begin{cases} 2.73 + 4.505(U_g - U_{g_{trans}}) & \text{Low } \mu_l \text{ (like water, } < 3 \text{ cP)} \\ 2.25 + 4.090(U_g - U_{g_{trans}}) & \text{High } \mu_l \text{ (like oil)} \end{cases} \\
 V_{b_{large}}^0 &= \begin{cases} 0.71 \sqrt{gd_{b_{large}}} & Eo > 40 \\ \sqrt{\frac{2\sigma_l}{\rho_l d_{b_{large}}} + \frac{gd_{b_{large}}}{2}} & Eo < 40 \end{cases} \\
 SF &= \begin{cases} 1 & \frac{d_{b_{large}}}{D_T} \leq 0.125, \quad Eo > 40 \\ 1.13 \exp\left(-\frac{d_{b_{large}}}{D_T}\right) & 0.125 < \frac{d_{b_{large}}}{D_T} \leq 0.6, \quad Eo > 40 \\ 0.496 \sqrt{\frac{D_T}{d_{b_{large}}}} & \frac{d_{b_{large}}}{D_T} > 0.6, \quad Eo > 40 \\ \left\{ 1 - \left(\frac{d_b}{D_T}\right)^2 \right\}^{\frac{3}{2}} & Eo < 40 \end{cases} \quad (2-8)
 \end{aligned}$$

From the bubble velocity of the dilute phase, $V_{b_{large}}$, the holdup of the large bubble phase can be evaluated

$$\bar{\epsilon}_{g_{large}} = \frac{U_g - U_{g_{trans}}}{V_{b_{large}}} \quad (2-9)$$

and the total gas holdup is then given by

$$\bar{\epsilon}_g = \bar{\epsilon}_{g_{large}} + (1 - \bar{\epsilon}_{g_{large}}) \bar{\epsilon}_{g_{small}} \quad (2-10)$$

In the above methodology to calculate the gas holdup for a given set of operating and design conditions, Krishna and co-workers point to the extreme sensitivity of the transition velocity to small additions of surface active agents that are not captured in the correlation proposed by Reilly *et al.* (1994). They recommend that the best option is to determine the transition experimentally for the system of interest, as there is no adequate model to predict holdup in the transition regime. Letzel (1997) further points to the difficulties in determining the transition superficial gas velocity from the inflection point in the gas-holdup versus superficial gas velocity curve. To determine the transition point accurately, he used chaos analysis of pressure fluctuation signals. From such an analysis, Kolmogorov entropy was evaluated as a function of gas velocity and transition was indicated by the minimum in the entropy curve. Figure 2-2 shows the comparison of the overall gas holdup predicted by the above-described procedure with the data of Letzel *et al.* (1999). Remarkably, good prediction is reported considering that no experimental data input was used in the estimations.

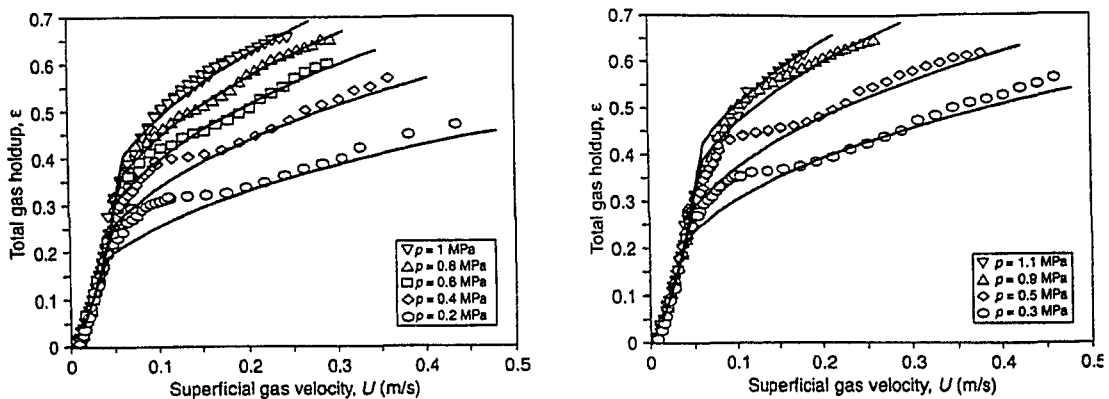


Figure 2-2. Prediction of the pressure effect on gas holdup (Krishna, 2000^h)

The discussion until now has focused on the prediction of overall gas holdup. Other than its overall value, the spatial distribution of the gas volume fraction also has a profound impact on the liquid phase recirculation. When one considers the distribution of gas holdup in a column cross-sectional plane, one finds that in the homogeneous regime, the radial variation of gas holdup is minimal (Hills, 1974; Yao *et al.*, 1991; Kumar, 1994). On the other hand, in the churn-turbulent regime, one observes significant variation of gas holdup in a cross-section, with greater gas holdup in the center than at the wall (Hills, 1974; Yao *et al.*, 1991; Yu and Kim, 1991; Kumar, 1994). It is known that the buoyancy forces resulting from the non-uniform cross-sectional gas holdup distribution are responsible for inducing the liquid recirculation in bubble columns. Since the spatial differences in the magnitude of these forces are small in the homogeneous regime, lower levels of liquid recirculation exist. However, in the churn-turbulent regime, the spatial variation in the magnitude of these forces is significantly larger than in the homogeneous regime and one observes increased intensity of liquid recirculation and liquid turbulence. Computer Tomography provides a very powerful and non-intrusive measure of the long-time averaged gas holdup distribution in a thin cross-sectional slice of a flow vessel, much like an X-ray image that provides information on the internal viscera inside a human body. Figure 2-3 shows the typical gas holdup information that one obtains from such non-invasive Computer Tomographic measurements. This technique uses the γ -ray attenuation measurement to obtain local void fraction information (Kumar, 1994). The basic attenuation phenomenon is described in terms of the Beer-Lambert's law. Accordingly, the absorption of a narrow beam of radiation of initial intensity I_0 by a mixture of gas and liquid with mass attenuation coefficients μ_g and μ_l , and densities ρ_g and ρ_l respectively, is given as

$$I = I_0 \exp\left[-\left(\rho_g \mu_g l_g + \rho_l \mu_l l_l\right)\right] \quad (2-11)$$

where l_g and l_l are the path length of the beam in the gas and the liquid, respectively. In terms of the measured intensities I_p , I_f and I_{mt} corresponding to the test section with the two-phase mixture, full of liquid and completely empty, respectively, the chordal average void fraction is computed from:

$$\varepsilon_g = \frac{\ln(I_p/I_f)}{\ln(I_{mt}/I_f)} \quad (2-12)$$

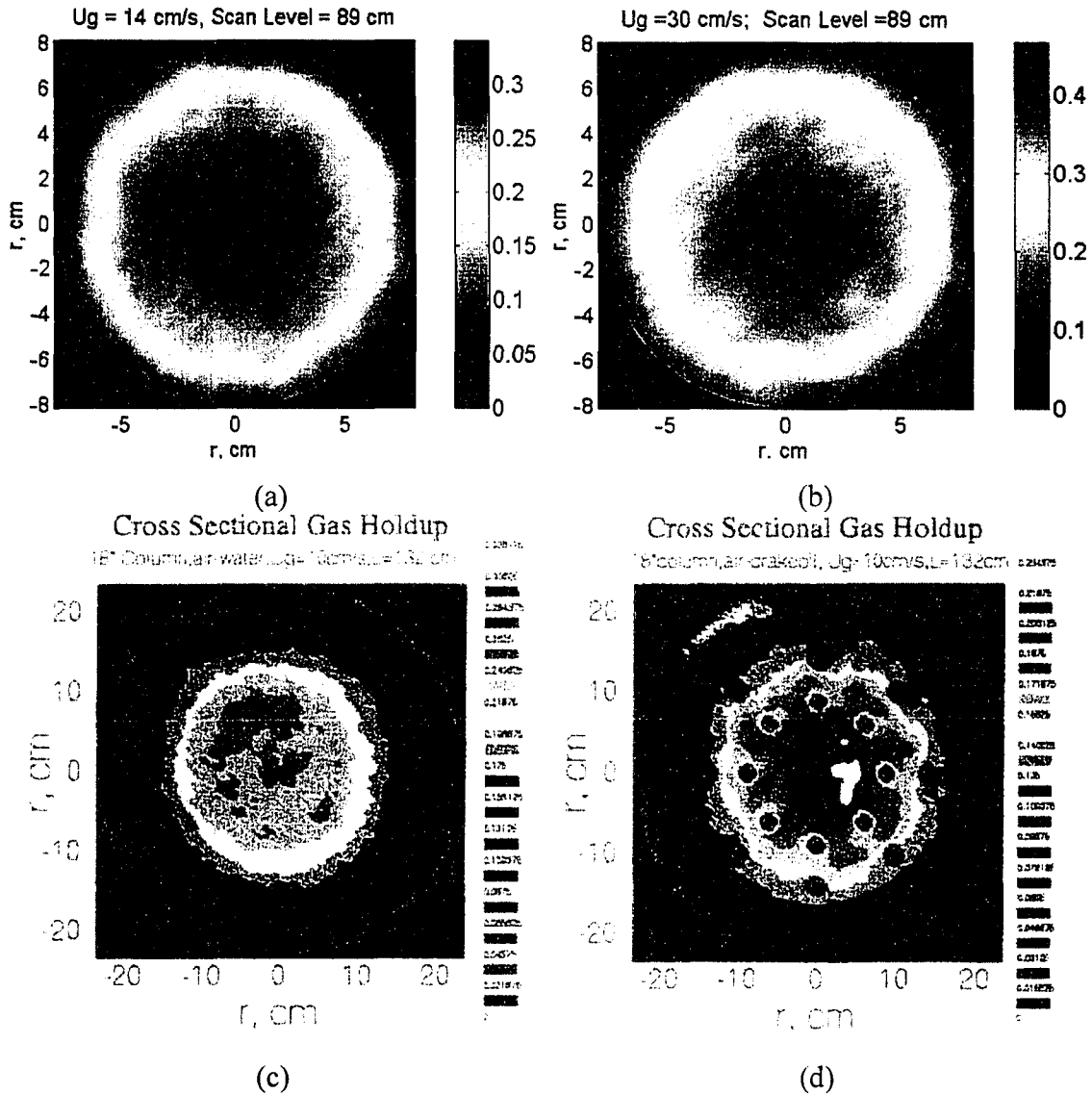


Figure 2-3. CT measurements of gas holdup distribution. a-b) 6" diameter stainless steel column (Ong, 1999) c-d) 18" diameter Plexiglas column (Chen *et al.*, 1998)

Several algorithms can achieve reconstruction of a tomographic image from the multitude of projection measurements acquired during a scan. Kumar (1994) discusses the *pros* and *cons* of some of these algorithms while Shollenberger *et al.* (1997) provides

description of the errors associated with γ -ray attenuation and measurements. This basic principle of attenuation has been coupled with reconstruction algorithms coded in-house to equip the Chemical Reaction Engineering Laboratory (CREL), Washington University, Saint Louis, USA with its CT scanning facility. The greatest advantage of this technique is its ability to probe dense and opaque flows where other non-intrusive techniques based on transmission of light or ultrasonic waves are either inapplicable or they encounter problems due to complex multiple scattering of the transmitted signal. Thus, their application is usually limited to flows in transparent vessels and to operating conditions with low volume fractions of the dispersed phase.

2.2. Liquid Backmixing and Velocity Profiles

It was pointed out earlier that the non-uniformity of the gas holdup distribution in a cross-sectional plane and the resulting spatial differences in the buoyancy force causes the liquid phase to recirculate in order to meet the overall continuity requirements. The greater the gradients in the radial gas holdup profiles, the greater the extent of liquid recirculation (Chen *et al.*, 1998). Scalar mixing in bubble columns is primarily caused by the recirculation developed from radial non-uniformity of gas holdup. Thus, mixing in bubble columns is convection dominated with eddy diffusion being a secondary mechanism to disperse scalars (Degaleesan and Dudukovic', 1999). Unfortunately, most of the studies reported in the open literature on liquid or gas phase mixing in bubble columns have used the axial dispersion model (ADM) to describe the liquid as well as the gas phase backmixing. However, the applicability of ADM to bubble columns has been shown to be suspect (Degaleesan, 1996^b, Degaleesan and Dudukovic', 1999) with the important question being whether the macroscopic circulation due to convection and the eddy dispersion can be lumped into a single parameter, commonly referred to as the effective axial dispersion coefficient. Degaleesan and Dudukovic' (1999) describe the complex way in which the effective axial dispersion coefficient is related to liquid recirculation and axial and radial eddy diffusion. Moreover, the ADM predicts a symmetric distribution of the tracer about the point of injection which is contrary to the

experimental observations where the backmixing in the upper portion of the column is about twice that in the lower portion of the column (Deckwer *et al.*, 1983). Myers *et al.* (1987) argued that at least in the churn-turbulent regime, the ADM is without basis and there is a need for liquid mixing models describing all the pertinent mechanisms. They suggested a phenomenological slug and cell model, which can capture the asymmetry of mixing relative to the tracer injection point. Degaleesan *et al.* (1996^b) have shown that a recirculating cross-flow model can be used very successfully to predict the liquid backmixing in bubble columns. More discussion on the shortcomings of the ADM is presented in Section 2.4.

The Computer Automated Radioactive Particle Tracking (CARPT) as it exists today was developed at CREL by Devanathan (1991) and provides information on the liquid velocities and its recirculation in bubble column flows. It makes use of a neutrally buoyant radioactive tracer particle, the position of which is tracked by a number of scintillation detectors placed strategically around the column. From the instantaneous data on the position of the particle, time averaged velocities can be computed. Accurate time averaging requires an experiment in which data is collected for hours to get sufficient statistics for such computations. Manipulation of the time history of the particle trajectory data leads to estimation of Reynolds stresses and from the calculation of the auto-correlation function, estimates of the eddy diffusivity coefficients can be made (Devanathan, 1991 Degaleesan, 1997). Figure 2-4 shows a schematic of the CARPT setup and typical results that one obtains from processing of Lagrangian trajectory information of a neutrally buoyancy radioactive tracer particle in a bubble column experiment. More details on the CARPT calibration process and radiation simulation are provided in Chapters 4 and 5.

Based on the liquid recirculation pattern observed from experimental data, it can be seen that the physical picture of a time-averaged bubble column flow involves upflow of the liquid in the center and downflow near the walls. Several models have been developed to capture this physical picture for predicting liquid recirculation in the fully developed region of a bubble column flow based on the one-dimensional flow assumption.

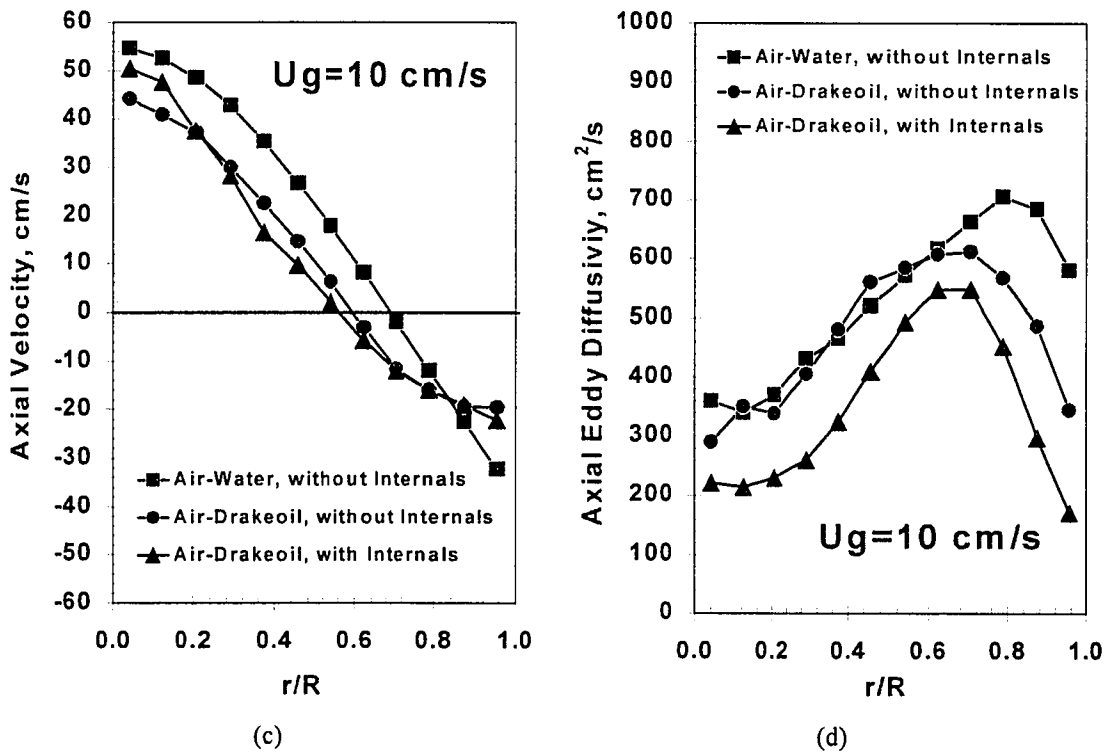
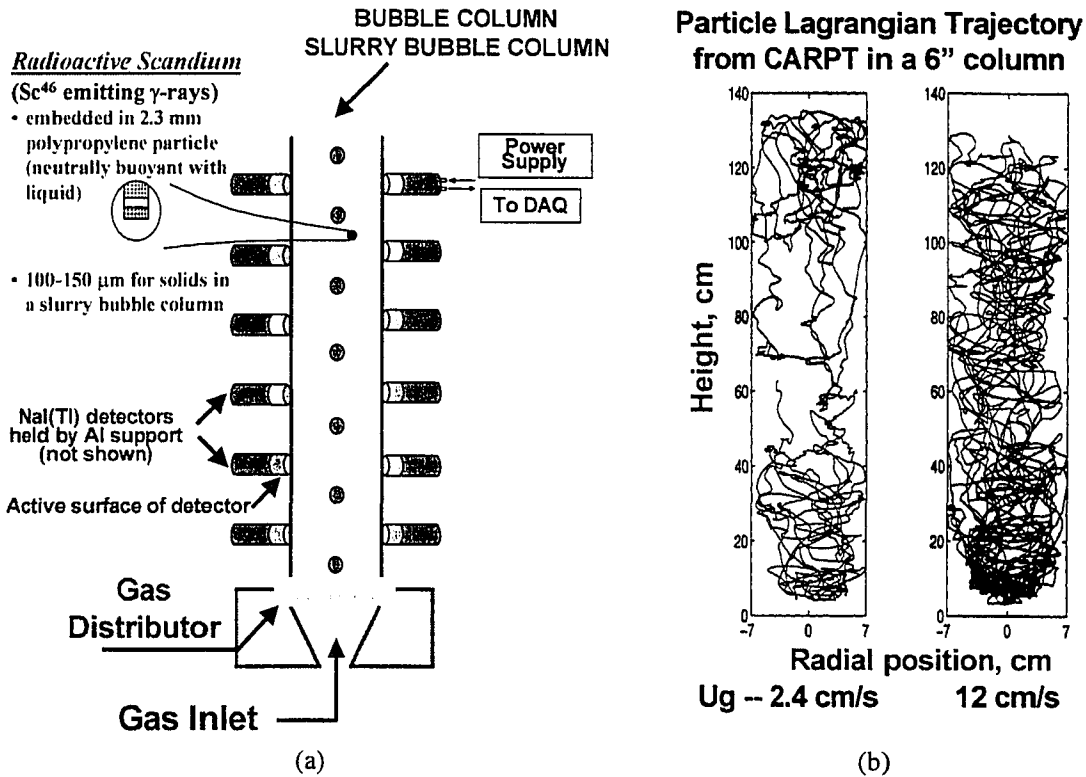


Figure 2-4. a) CARPT experimental setup b) Particle trajectory c & d) Typical hydrodynamic information from CARPT measurements (Chen *et al.*, 1999)

Ueyama and Miyauchi (1979) were the first to propose a correlation for the liquid velocity profile. They assumed that there is a laminar sub-layer near the wall that is thin enough so that the liquid downward velocity in the sub-layer is approximately equal to the wall velocity. Their model equations are presented in Appendix A. Anderson and Rice (1989) proposed a model along similar lines. The main difference in their model, as compared to that of Ueyama and Miyauchi, is that the boundary condition is based on physical reasoning and no empirical constant is involved. They also proposed that there is a thin layer of liquid close to the wall which is in laminar flow and from which the bubbles are excluded. This layer is assumed to extend into the core up to the point of maximum downward liquid velocity. At this point, the shear stress and velocity profiles are matched; and a no slip boundary condition is used at the wall. The equations, derived by them for such a model, are presented in Appendix A as well. These one-dimensional models require as input the information on the radial gas holdup distribution along with a closure for liquid phase turbulence. Ueyama and Miyauchi (1979) as well as Geary and Rice (1992) closed the liquid phase turbulence based on a specified kinematic eddy viscosity.

To include possibilities of other closures for the liquid phase turbulence, Kumar (1994) proposed a modified liquid recirculation model, which can use both the Prandtl's mixing length as well as the eddy viscosity approaches. In his model, the Anderson and Rice (1989) approach is used along with the radial distribution for the void fraction profile obtained from tomographic measurements. Kumar (1994) showed that it is possible to scale-up a bubble-column based on the mixing length theory, when a consistent set of data for liquid velocity and gas void fraction is obtained. A modified version of this approach has been adopted in this work to obtain the liquid velocity profiles for evaluation of the mixing model parameters and details can be found in Chapter 6. Ong (1999) has provided an extensive compilation of the various correlations proposed in the open literature to close the liquid phase turbulence as well as an analysis of their effect on predicted liquid recirculation profiles. In that study, simulations were carried out using the framework of the model of Kumar (1994) that has been modified and extended in this study, details of which are discussed in Chapter 6.

2.3. Mass Transfer

The literature abounds with studies characterizing the overall volumetric mass transfer coefficients and the average specific interfacial area in bubble and slurry bubble columns (Azbel, 1981; Saxena, 1995; Letzel *et al.*, 1999) with numerous correlations being proposed for both the above parameters. The differences among these correlations are significant, principally, because they have been obtained using different diffuser systems, and different range of variables, especially of the gas superficial velocities. Sotelo *et al.* (1994) provided a comprehensive compilation of the available correlations in the literature and the various operating conditions under which these could be used along with the list of gas-liquid systems studied to obtain the correlations. Azbel (1981) derived the expressions for the mass transfer coefficient and the interfacial area, for a non-coalescing and non-breaking bubble swarm, based on an assumed bubble size distribution in a turbulent system. The derived expressions are:

$$a(cm^{-1}) = 2.619 \frac{\bar{\epsilon}_g}{d_b} \quad (2-13)$$

$$k_L(cm.s^{-1}) = const. \frac{D_{L,m}^{1/2}}{(L_c \nu_m)^{1/4}} \left(\frac{\Delta P}{\rho_l} \right)^{3/8} \frac{(1 - \bar{\epsilon}_g)^{1/2}}{(1 - \bar{\epsilon}_g^{2/3})^{1/4}} \quad (2-14)$$

where,

$\Delta P \equiv$ Pressure drop

$L_c \equiv$ Characteristic turbulent length

$D_{L,m} \equiv$ Molecular diffusivity

$\nu_m \equiv$ Molecular kinematic viscosity

Since the derivation for the turbulence parameters is based on dimensional considerations, the equation is correct only up to a constant factor. Based on the experimental results, the constant was found to be 0.12, and comparison of the calculated values with those from other studies for various systems is reasonably good. Kastanek *et al.* (1993) provided a comprehensive review of the various aspects of the modified

Higbie's relation for mass transfer coefficients. For non-interfering bubbles under homogeneous bubbling regime, the contact time of the liquid eddies with the bubbles, t_c , is estimated by the macroscale parameters of bubble diameter, d_b and bubble rise velocity, u_b as

$$t_c = \frac{d_b}{u_b} \quad (2-15)$$

For the turbulent bubbling conditions, however, this simple model fails, as bubbles can no longer be considered non-interfering. In such cases, the contact time is expressed alternatively as (Kastanek *et al.*, 1993)

$$t_c = \frac{d_{be}}{u_{bs}} \quad (2-16)$$

where,

$d_{be} \equiv$ equilibrium bubble diameter from theory of isotropic turbulence.

$u_{bs} \equiv$ rise velocity of the bubble swarm.

Then, the mass transfer coefficient can be estimated from the Higbie's relation

$$k_L = \left(\frac{2}{\sqrt{\pi}} \right) \left(\frac{D_{l,m}}{t_c} \right)^{1/2} \quad (2-17)$$

Even though the contact time, t_c , characterizing the residence time of the micro-eddies at the interface, is expressed by the macro-scale characteristics of the system, the estimates of k_L , for both coalescent and non-coalescent systems with non-viscous liquid phase in the absence of surface active agents, are quite realistic (Kastanek *et al.*, 1993). In the extended models, the effect of a surface diffusion layer, which depends on the presence of surface active agents, is incorporated as well. After expressing the contact time in terms of the macroscopic quantities from the isotropic turbulence theory, one obtains (Kastanek *et al.*, 1993)

$$k_L = \left\{ \frac{\sqrt{\pi} \lambda}{2D_{l,m}^{1/2} \nu_m^{1/2}} + \frac{\delta'}{D_{l,m}} \right\}^{-1} \quad (2-18)$$

where,

δ' \equiv thickness of the diffusion layer

λ \equiv eddy size

In the absence of surface-active agents, the second term in the above equation is dropped. After substituting for the eddy length in terms of the kinematic viscosity and the rate of energy dissipation in the liquid per unit mass of the liquid, expressed in terms of other macroscopic variables, Kastanek *et al.* (1993) obtained

$$k_L = k_1 \frac{2}{\sqrt{\pi}} \left(\frac{D_{l,m}}{\nu_m} \right)^{1/2} \left(g \nu_g \frac{\rho_g}{\rho_l} \right)^{1/4} \left(U_G \frac{(1 - \bar{\epsilon}_g)}{\bar{\epsilon}_g} \right)^{1/4} \quad (2-19)$$

The proportionality constant k_1 was introduced for the contact time. This constant depends on the physico-chemical properties influencing the bubble sizes, especially the surface tension of the liquid, σ and needs to be determined experimentally.

Table 2-1 lists some of the many other correlations reported in the literature on estimating the mass transfer coefficients in gas-liquid systems that can be tried in addition to the ones proposed by Kastanek *et al.* (1993). In the present study on mechanistic reactor modeling, as presented in Chapter 6 of the thesis, the calculation of mass transfer coefficients has been accomplished using Equation 2-17. The contact time, t_c , in this equation is estimated from the bubble size and local gas velocity computed from the one-dimensional two-fluid momentum formulation, which is also presented in Chapter 6. When the approach based on the Higbie's penetration theory cannot be applied due to non-availability of reliable bubble size and velocity information, the correlation of Letzel *et al.* (1999) reported in Table 2.1 can be used for calculating the volumetric mass transfer coefficients as a function of gas holdup in churn-turbulent regime. This correlation also captures the effect of operating pressure via the gas holdup, which shows significant dependency on pressure as discussed earlier.

Table 2-1. Mass transfer correlations reported in the literature

Reference	Correlation
Akita & Yoshida (1973) ($U_G = 0.003 - 0.4$ m/s)	$\frac{k_L a D_c^2}{D_{Lm}} = 0.6 \left(\frac{v_L}{D_{Lm}} \right)^{0.5} \left(\frac{g D_c^2 \rho_L}{\sigma} \right)^{0.62} \left(\frac{g D_c^3}{v_L^2} \right)^{0.31} \varepsilon_g^{1.1}$
Calderbank & Moo-Young (1961)	<i>Small Bubble</i> $(k_L)^s = 0.31 \left(\frac{\Delta \rho \mu_L g}{\rho_L^2} \right)^{1/3} \left(\frac{v_L}{D_{Lm}} \right)^{-2/3}$; $a^s = \frac{6 \varepsilon_g^s}{d_s}$ <i>Large Bubble</i> $(k_L)^l = 0.42 \left(\frac{\Delta \rho \mu_L g}{\rho_L^2} \right)^{1/3} \left(\frac{v_L}{D_{Lm}} \right)^{-1/2}$; $a^l = \frac{6 \varepsilon_g^l}{d_L}$
Deckwer <i>et al.</i> (1981)	$k_L a = 0.00315 U_G^{0.59} \mu_{eff}^{-0.84}$
Fair (1967)	$k_L a = 3.31 \frac{D_{Lm} \varepsilon_G}{d_b^2} \left(\frac{v_L}{D_{Lm}} \right)^{1/3} \left(\frac{d_b U_G}{v_L \varepsilon_g} \right)^{1/2}$
Hikita <i>et al.</i> (1981) ($U_G = 0.042 - 0.38$ m/s)	$k_L a = \frac{14.9 g f}{U_G} \left(\frac{U_G \mu_L}{\sigma} \right)^{1.76} \left(\frac{\mu_L g}{\rho_L \sigma^3} \right)^{-0.248} \left(\frac{\mu_G}{\mu_L} \right)^{0.243} \left(\frac{v_L}{D_{Lm}} \right)^{-0.604}$ $f = \begin{cases} 1.0 & \text{for nonelectrolytes} \\ 10^{0.068 I} & I < 1.0 \text{ kg ion m}^{-3} \\ 1.114 (10^{0.021}) & I > 1.0 \text{ kg ion m}^{-3} \end{cases}$
Kawase <i>et al.</i> (1987)	$\frac{k_L a D_c^2}{D_{Lm}} = \frac{12}{\sqrt{\pi}} B \left(\frac{D_{Lm}}{v_L} \right)^{1/2} \left(\frac{U_G D_c}{v_L} \right)^{1/2} \left(\frac{U_G}{\sqrt{g D_c}} \right)^{1/2} \left(\frac{g D_c^3 \rho_L}{\sigma} \right)^{1/2}$ B = 0.0645 for Newtonian Fluids
Letzel <i>et al.</i> (1999)	$\frac{k_L a}{\varepsilon_g} = 0.5$
Nakanoh & Yoshida (1980)	$\frac{k_L a D_c^2}{D_{Lm}} = 0.09 \left(\frac{v_{eff}}{D_{Lm}} \right)^{0.5} \left(\frac{g D_c^2 \rho_L}{\sigma} \right)^{0.75} \left(\frac{g D_c^3}{v_{eff}^2} \right)^{0.39} \left(\frac{U_G}{\sqrt{g D_c}} \right) \left\{ 1 + C \left(\frac{u_{hs} \lambda}{d_{vs}} \right)^{m-1} \right\}$ $C = \begin{cases} 0 & \text{for inelastic liquids} \\ 0.133 & \text{for elastic liquids} \end{cases}$ $m = 0.55$; $\lambda = \text{characteristic relaxation time}$
Ozturk <i>et al.</i> (1987)	$\frac{k_L a d_b^2}{D_{Lm}} = 0.62 \left(\frac{v_L}{D_{Lm}} \right)^{0.5} \left(\frac{g d_b^2 \rho_L}{\sigma} \right)^{0.33} \left(\frac{g \rho_L^2 d_b^3}{\mu_L^2} \right)^{0.29} \left(\frac{U_G}{\sqrt{g d_b}} \right)^{0.68} \left(\frac{\rho_G}{\rho_L} \right)^{0.04}$
Sotelo <i>et al.</i> (1994)	$\frac{k_L a U_G}{g} = 16.9 \left(\frac{U_G \mu_L}{\sigma} \right)^{2.14} \left(\frac{\mu_L g}{\rho_L \sigma^3} \right)^{-0.518} \left(\frac{\mu_G}{\mu_L} \right)^{0.074} \left(\frac{v_L}{D_{Lm}} \right)^{-0.038} \left(\frac{d_b}{D_c} \right)^{0.908}$

In the above table, the symbols used along with their units are:

d_b	individual and Sauter mean bubble diameter, m
$k_L a$	liquid-phase volumetric mass transfer coefficients, s^{-1}
D_c	column diameter, m
D_{Lm}	molecular diffusivity of dissolved species, $m^2 s^{-1}$
d_o	orifice hole diameter, m
ε_g	gas holdup
σ	surface tension, $N m^{-1}$
ν_L	kinematic viscosity of liquid, $m^2 s^{-1}$
$u_{b\infty}$	terminal single bubble rise velocity, ms^{-1}
ν_{eff}	effective kinematic viscosity of the liquid, $m^2 s^{-1}$
u_G	superficial gas velocity, ms^{-1}
μ_{eff}	effective viscosity calculated from power law model, Pa.s
μ_L, μ_G	molecular viscosity of liquid and gas respectively, Pa.s
ρ_L, ρ_G	density of liquid and gas respectively, kg/m^3

2.4. Reactor Modeling

Reactor modeling in general refers to the mathematical description of transport of chemical species in a given reactor system that includes the production and consumption of the various species via chemical reactions. Since every reaction system has a positive or negative heat requirement; reactor modeling invariably also involves the mathematical treatment of temperature distribution by a balance of the heat loss, production and transport. In all these mathematical descriptions, which could range from simple algebraic forms to more complex ordinary differential equations and ultimately to more complicated partial differential equations, the nature of the mathematical formulation depends upon the level of the hydrodynamic detail that is being modeled for a given reactor configuration. This hydrodynamic description which governs the convective, diffusive and interfacial transport of chemical species and heat in a reactor, is usually modeled separately, and serves as input to the reactor models. The process of hydrodynamic description therefore usually involves the selection of the “level” of detail and subsequent parameter estimation to serve as inputs to the reactor models.

The above mentioned methodology is common to all reactor types with the differences for different reactor types arising from the hydrodynamic flow patterns that exist in a particular reactor type. For example, catalyst particles are stationary in a trickle bed reactor, and therefore, one needs to characterize only the flow and distribution of the gas and liquid reactants in a fixed bed to obtain the hydrodynamic description. On the other hand, if one looks at the hydrodynamics of a slurry bubble column, the catalyst particles are suspended in the liquid medium, and therefore, one needs to characterize the flow of all three phases to accomplish the hydrodynamic description. Flow patterns may be altered by the presence of internals, which might either be present to just serve as media for heat transfer, or alternatively to change the backmixing in order to achieve better conversion and selectivity depending upon the specific reaction system.

Hydrodynamics of multiphase systems is invariably very complicated and in many cases (slurry bubble columns being a good example) not well understood. This lack of understanding of the relevant physics stems from the existence of a multitude of time and length scales at which important physical processes take place. Even though the recent advances in sophisticated measurements techniques have enabled the detection of the large scale phenomena and their subsequent characterization, measurement at relatively small scales under actual operating condition is still in its infancy. It is the modeling of the processes at the small scales and of their coupled interactions with the large scale phenomena that still limits the capability of Computational Fluid Dynamics (CFD) in serving as a standalone tool for prediction of reactor performances. Nevertheless, the advances made in CFD modeling of multiphase flows are providing valuable insights in understanding specific hydrodynamic phenomena; and in certain cases also forming the basis for some sub-grid scale modeling (Krishna, 2000^h).

In this section, some aspects of the various bubble column reactor models that are reported in the literature are reviewed. Mathematical detail has in general been avoided, except where necessary, and the reader is referred to appropriate references for details. The various models that exist in the literature can be classified into three groups depending on the level of detail in the description of hydrodynamics.

Generation I: In these models, the hydrodynamic information is completely lumped into one parameter, which is the overall flow rate of each individual phase. Details of how the phases distribute and recirculate are completely ignored. The two extreme cases of mixing for the fluid are modeled as:

Plug Flow; where there is no backmixing at all and the fluid is assumed to move as a solid body.

Perfectly Mixed Flow; where the fluid is assumed to be perfectly backmixed implying that the concentrations of chemical species, and hence the reaction rates, are the same everywhere in the reactor.

The actual state of mixing in a reactor lies somewhere between these two extremes. For a complete description of the reactor model however, in addition to knowing the degree of backmixing, one also needs to know the gas holdup and the gas-liquid volumetric mass transfer coefficient. Except for reactor models based on Computational Fluid Dynamics, in which gas holdup is computed as part of the solution to the Navier-Stokes equations in the multi-fluid framework, one needs to have an independent scheme for estimation of the gas holdup and volumetric mass transfer coefficients for a given operating condition.

The most commonly used and the simplest reactor model for slurry bubble columns is one in which the solid phase is assumed to be uniformly suspended in the liquid and the pseudo-homogeneous liquid-solid mixture is assumed to be completely back-mixed. On the other hand, the gas is assumed to be in plug flow (refer to Figure 2-5). Unfortunately, the flow patterns of the gas and liquid phases in a bubble column operation are in general far from the idealized descriptions mentioned above. Therefore, alternatives to these idealized conditions need to be employed to describe the state of macromixing. Joshi and Shah (1981) have provided a detailed review of the various hydrodynamic and mixing models that were reported before and in the 1980's. Among the various mixing models that have been reported, the most commonly used one has been the Axial Dispersion Model (ADM) where an effective diffusion is considered to be superimposed on the net convective flow (Zhao *et al.*, 1987; Schlueter *et al.*, 1992; Schlueter *et al.*, 1995).

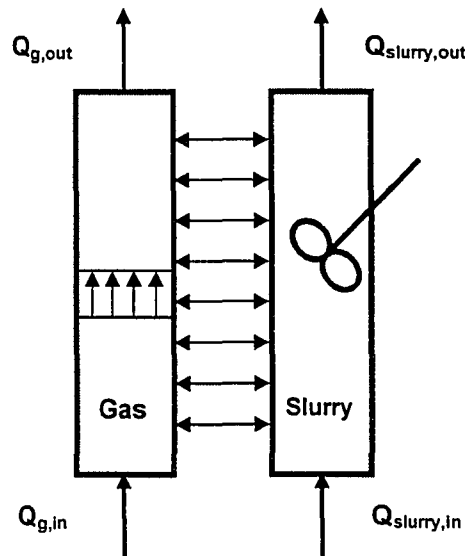


Figure 2-5. Representation of mixing in co-current bubble column with a stirred tank for liquid and plug flow for gas.

The assumption of a homogeneous and uniformly suspended slurry particles is very attractive and is frequently employed as well. However, it is known that even though the particle size of the solid phase ranges from 5-50 μm in most slurry bubble column applications, the solids seem to have an axial distribution as a result of the action of gravity. The distribution of solids in that case is generally described in terms of the sedimentation-dispersion model. Stern *et al.* (1985) considered the axial dispersion in both the gas and liquid phases and accounted for the non-uniform distribution of the catalyst in a reactor model for bubble column in Fischer-Tropsch synthesis. They demonstrated the effect of transport parameters on the conversion of synthesis gas as well as on the axial distribution of the reactants and the products.

The axial dispersion model can equivalently be described in terms of tanks-in-series model (or the cell model) with or without backflow. Both of these models are equivalent with the effective dispersion coefficient being the fitted parameter for the ADM whereas the number of tanks is the floating parameter for the cell model. Schlueter *et al.* (1992) have shown that the numerical treatment of the system of algebraic

equations for the cell model leads to computing times lower by a factor as large as hundred when compared to the computation time for reactor models based on axial dispersion. They show solution examples for methanol synthesis in a slurry reactor, including the description of thermodynamically balanced reactions, as well as of wet air oxidation of sewage sludge under extreme pressure and temperature conditions. Romaninen (1997) discussed a dynamic model that can be used to describe various degrees of backmixing in both co-current as well as countercurrent bubble columns. They used a penetration model for their transient calculations that results in a system of ODEs which were reported to be integrated with a stiff integration algorithm using sparse matrix technique. They discussed the stability problems of the method based on orthogonal collocation and recommended the use of finite difference approach as robust and reliable. Schulzke *et al.* (1998) developed a one-dimensional mathematical model for the dynamic behavior of bubble column reactors to study the absorption of carbon dioxide into aqueous sodium hydroxide solution. Dassori (1998) also reports on the use of modified cell model for the slurry bubble column reactor with significant backmixing in the liquid phase in which interfacial mass transfer and phase distribution are accounted for. In his model, the number of cells determine the degree of coupling among the various hydrodynamic effects and is not related to the extent of backmixing as in the classical models. This model was applied to the hydrocracking of heavy oil fractions. The most recent example of the use of tanks-in-series model with backflow is the work of Debellefontaine *et al.* (1999) in describing wet air oxidation for the treatment of industrial waste-water and domestic sludge. They incorporated the effect of gas holdup, mass transfer and kinetics of the liquid phase reaction as well as of the gas phase thermodynamics using the Peng-Robinson equation of state and Henry's law to describe the equilibrium conditions.

Generation II: The Generation II models are based on some physical picture of the observable phenomena in bubble columns. The observables that have been incorporated into some of these Generation II models are the existence of two bubble classes (Vermeer and Krishna, 1981; Shah *et al.*, 1985; Shetty *et al.*, 1992; Modak *et al.*, 1993; Modak *et*

al., 1994; Maretto and Krishna, 1999; Gupta *et al.*, 2001^a; Gupta *et al.*, 2001^b), and liquid and gas phase recirculation (Degaleesan, 1997; Gupta, 1999; Gupta *et al.*, 2001^b). It is known that the time-averaged liquid recirculation flow patterns in a bubble column reactor are the result of the differences in radial buoyancy forces arising due to the non-uniform distribution of gas phase in the column (refer to Figure 2-6). It is this physical picture that has formed the basis of most of the reactor modeling work accomplished in this study.

In the two bubble class model, the gas phase is assumed to be composed of a dense (small bubble) phase and a dilute (large bubble) phase. Both of these phases are assumed to have interfacial mass transfer with the liquid phase, the mixing in which is also described in terms of the axial dispersion model. The large bubble phase is assumed to have no backmixing and to rise in plug flow whereas the small bubble phase is described in terms of an axial dispersion model. These models, however, still do not treat specifically the recirculation which exists in both the phases due to the strong buoyancy gradients. Nevertheless, these models do indeed take into account some observable phenomena and in general tend to have a slightly better fundamental basis. However, since the axial dispersion model is in principle suitable only for flows which are not far away from plug flow, the application of such models to describe gas and liquid mixing which is a result of convection dominated recirculation provides a complete unphysical explanation of the observed phenomena. Degaleesan *et al.* (1996^b) investigated the applicability of the ADM to characterize the gas and liquid phase mixing in a pilot scale slurry bubble column during methanol synthesis. It was reported that the axial dispersion coefficients obtained from tracer responses at various axial locations in the column show a wide spread and, even though one can in principle fit the axial dispersion model to obtain the effective dispersion coefficient, it would be almost impossible to use the obtained coefficient for scale-up. This has been the greatest shortcoming of the ADM, which has only had success in retrofitting experimental tracer data and has had rather limited success in prediction of reactor backmixing for purposes of design and scale-up. Nevertheless, in spite of its relative mathematical simplicity, it is still being widely used

not as a definitive tool for design, but as a model to provide a first estimate on the bounds of reactor performance.

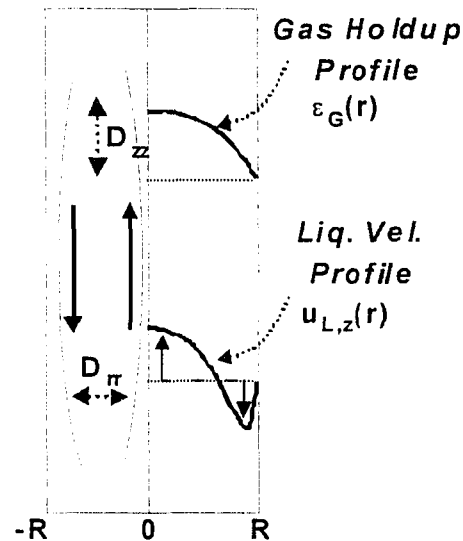


Figure 2-6. Mechanistic description of buoyancy induced recirculation and turbulent dispersion in a bubble column reactor.

Realizing the shortcomings of the ADM in that it lacks a definitive physical basis, work has been going on in our laboratory to incorporate greater information on observable hydrodynamic phenomena into the reactor models. Towards this end, Myers *et al.* (1987) developed a slug and cell model to describe liquid phase mixing and interphase mass transfer with chemical reactions. More recently, Degaleesan (1997) developed a two-dimensional transient-convection-turbulent-diffusion model to describe mixing of tracer concentration in bubble column reactors from fundamental species balances. The basis of the model is the schematic shown in Figure 2-6. The hydrodynamic inputs were obtained from a simplified model for liquid recirculation and an estimation procedure for turbulent diffusion coefficients. It was shown (refer to Figure 2-7) that once the correct and exact hydrodynamic description was provided as input to

the two-dimensional convection-diffusion model, *complete prediction of tracer responses could be accomplished.*

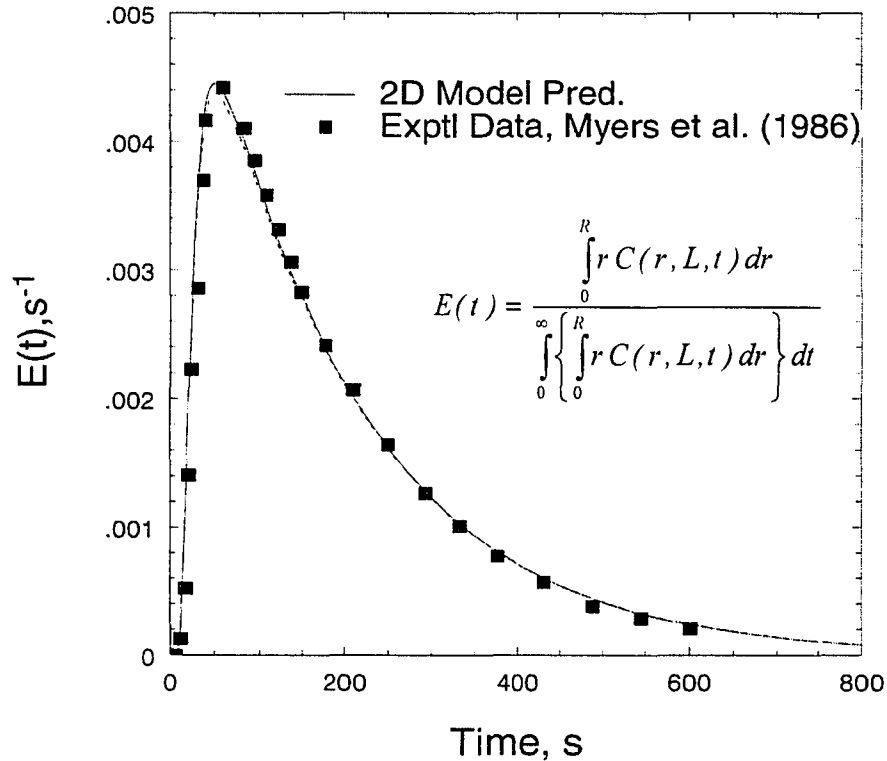


Figure 2-7. Prediction of liquid phase RTD in a co-current bubble column (Degaleesan, 1997)

The model above provided great promise and was successfully used to describe liquid/slurry tracer experiments from a pilot-scale reactor. The efforts in this direction have continued and as part of this study, we have been able to characterize the gas phase mixing on a theoretical basis similar to the one used in the description of liquid phase mixing. The details of the development of the gas phase mixing models, along with comparison of simulation results with pilot scale data, are presented in Chapters 6 and 7. As mentioned before, the Generations I and II models require an independent estimate of gas holdup, and mass transfer coefficients. For purposes of parameter estimation for reactor modeling of bubble columns, the approach of Kirshna (2000^b) for gas holdup and Letzel *et al.* (1999) for mass transfer coefficient presented earlier, is recommended.

Generation III: The Generation III models incorporate detailed fluid dynamic description towards prediction of scalar transport in a multiphase flow situation. These models are referred to as Computational Fluid Dynamic (CFD) models in which the appropriate form of the momentum transport (Navier-Stokes) equations for each phase are solved. The resulting information either provides a very detailed hydrodynamic input to the species transport equations or alternatively the solution of the species transport equations is achieved in a coupled manner with the momentum and energy transport equations. For reaction conditions, as those found in Fischer-Tropsch chemistry as well as most practical reaction systems, this could imply solution of 20-30 species transport equations. Therefore, a completely coupled solution is very computationally intensive and sometimes cannot be achieved in a realistic time-frame. As a result, most applications of CFD to bubble column design are limited to describing the fluid dynamics from which relevant information is passed on to models describing species transport.

The CFD models for bubble column flows specifically and multiphase flows in general are still in their infancy and the literature in this field is limited but is growing at an aggressive pace. One of the first studies reported is the work of Hillmer *et al.* (1984) where a two-dimensional two-fluid dynamic model with account for turbulence through $k-\epsilon$ model was developed for modeling slurry bubble column reactors. This model allows one to investigate the mutual effect of fluid dynamics and chemical reactions. The authors report the development of correlations for calculation of interaction forces between the gas and slurry phase, which is based on experimentally obtained information from reactive multiphase flows. A more recent example is the work of Carbonell and Guirardello (1997) where a Computational Fluid Dynamics approach was applied for the simulation of a slurry bubble column reactor to study the hydroconversion of heavy oils under severe temperature and pressure conditions. Their simulations were carried out in two steps. In the first part of their calculation, the pressure drop in the column as well as the radial distribution of gas and slurry phases holdups and velocities were obtained by solving momentum balances. These calculations provided the hydrodynamic input to a reactor model where a thermal cracking reaction was simulated to predict the conversion of heavy oil to lighter fractions such as diesel and naphtha. Their results show that the

recirculation pattern in the reactor leads to a high degree of backmixing in the slurry phase, and that the temperature and liquid residence time have a profound influence on the oil cracking conversion.

Two different approaches have been adopted to achieve a fluid dynamic description of gas-liquid flows in bubble columns. In the Euler-Euler approach, both phases are treated as pseudo-continuous with their respective physical properties. Coupling and momentum exchange between the phases are obtained via sub-grid scale models to describe phase interactions using a control volume as a basis. In the Euler-Lagrange approach, the continuous (liquid) phase is modeled by a continuum description while the dispersed (gas) phase is modeled as discrete bubbles. As a result, a large number of individual bubbles are tracked and this approach is very computationally expensive. In addition, at large gas volume fractions, an unrealistically large number of notional bubbles need to be tracked to describe the physics accurately. In the absence of reliable breakup and coalescence models, the application of these models have been limited to very low superficial gas velocities (Lapin and Luebert, 1994; Delnoij *et al.*, 1997). In both these formulations, a description of the interactions between the phases is required. Considerable efforts have been devoted to obtaining an accurate description of phase interaction, however, this still remains a very active and young area of research (Jackobsen *et al.*, 1997).

Most computational fluid dynamic studies reported in the literature have focussed on description of the phase distribution and prediction of levels of liquid recirculation in bubble column reactors, and relatively little attention has until now been paid to the effect of mass and heat transport on the hydrodynamics of the bubble column reactors (Jackobsen *et al.*, 1997; Delnoij *et al.*, 1997; Krishna, 2000^b). With the advances of computational efficiency as well as a reduction in costs, it is becoming increasingly possible to have detailed mathematical models for physical processes at various length and time scales and to obtain the solution of these complex system of equations. Various modeling and computational schemes have been developed to address the prediction of bubble column flows and the reader is referred the references listed in Table 2-2 on some recent developments in CFD of bubble column reactors.

Table 2-2. CFD studies of bubble column flows

Reference	Interphase Forces	Turbulence Model	Case Studies	Quantities Reported
^a Grienberger and Hofmann (1992)	Drag Magnus Lift	k- ϵ ,	$D_c = 29$ cm $U_g = 2, 8$ cm/s $U_l = 1$ cm/s	$u_g, u_l, \epsilon_g, k, \epsilon$
^b Ranade (1995, 1997)	Drag Magnus Lift	k- ϵ		$u_g, u_l, \epsilon_g, k, \epsilon$
^c Boisson and Malin (1996)	Drag Virtual Mass Magnus Lift Interfacial Pressure	k- ϵ	$D_c = 13.8, 28.8$ cm $U_g = 4-8$ cm/s $U_l = 0-1$ cm/s	$u_g, u_l, \epsilon_g, k, \epsilon$
^{a,c} Jakobsen <i>et al.</i> (1997)	Turbulent Drag Magnus Lift Virtual Mass	k- ϵ	$D_c = 14$ cm $U_g = 6-14$ cm/s $U_l = 0$ cm/s	$u_g, u_l, \epsilon_g, k, \epsilon$
^d Delnoij <i>et al.</i> (1997)	Drag Virtual Mass Magnus Lift Bubble Collisions	None	Experiments of Becker <i>et al.</i> (1995)	Snapshots of \bar{u}_l and bubble locations
^a Mitra-Majumdar <i>et al.</i> (1997)	Drag Solid Collisions	k- ϵ	$D_c = 15$ cm $U_g = 5-11$ cm/s $U_l = 1$ cm/s	$u_g, u_l, u_s, \epsilon_g$, comparison with experiment
^e Krishna <i>et al.</i> (2000 ^b)	Drag Small and Large Bubble phases	k- ϵ	$D_c = 14-600$ cm $U_g = 1.9-35$ cm/s $U_l = 0$ cm/s	$u_g, u_l, \epsilon_g, k, \epsilon$

^a 2-D axisymmetric, steady, Euler-Euler

^b 2-D transient, Euler-Euler

^c 2-D axisymmetric, transient, Euler-Euler

^d 2-D axisymmetric, transient, Euler-Lagrange

^e 3-D transient, Euler-Euler

Chapter 3. Conductivity Probes for Liquid Mixing in Gas-Liquid Flows

3.1. Introduction

Bubble column reactors have been used extensively in hydrogenation, oxidation, hydroformylation, chlorination, fermentation and natural gas conversion processes to fuels and chemicals. Often it is important to assess the state of mixing of the liquid phase since it is the controlling factor of reactor performance. In bubble columns without baffles or trays, it is typically assumed that macroscopically the liquid is perfectly mixed. When departure from complete backmixing is desired, staging of the bubble columns via trays/baffles is implemented (Shah *et al.*, 1982). The information in the open literature on local liquid backmixing in bubble columns with and without trays is sparse, and as part of this doctoral work, it was undertaken to study it experimentally. In order to accomplish this, a suitable method had to be determined for measuring tracer concentration in the liquid phase, unmasked by the presence of the gas, and to evaluate what state of mixing frequencies can be captured by the selected conductivity measurement equipment. During the course of this work, it was found that the solution to this problem was non-trivial.

Electrical conductance/capacitance probes have been frequently used for the estimation of bubble properties in gas-liquid/gas-solid flows as well as in gas-liquid-solid fluidized beds (Svendson *et al.*, 1998; Gunn and Al-Doori, 1985; Buchholz *et al.*, 1981; Werther and Molerus, 1973). In addition, signals from conductivity probes, which are calibrated to provide instantaneous point phase holdup information, have been used for experimental characterization of regime transitions in multi-phase flows from time-series

data utilizing sophisticated numerical tools (Briens *et al.*, 1996). In several other studies, where the quantity of interest is just the time-averaged phase holdup, probe designs (plate and ring-shaped electrodes) different than those employed for instantaneous conductance measurements have been used (Hu *et al.*, 1985; Andreussi, *et al.*, 1988; Fossa, 1998; Zrymiak and Hill, 1986; Cartellier and Achard, 1991; Tsochatzidis, *et al.*, 1992; Hassan and Rush, 1985).

The conductivity probes can also be utilized to estimate liquid phase velocities and to study local liquid mixing in single as well as two-phase systems by the measurement of liquid phase electrolytic tracer concentrations (Choi, 1996; Boddem and Mewes, 1996; Sokolov and Mashaal, 1990; Rustemeyer *et al.*, 1989; Shah *et al.*, 1978). Traditional application of conductivity measurements involved the characterization of the liquid phase concentrations of the tracer ionic species in solutions devoid of gas. When such measurements are used to obtain the overall liquid phase residence time distribution (RTD) in single-phase flow, little ambiguity is encountered in the interpretation of conductivity-probe signals, as they are free from *biased-noise* contributions, which due to bubble passage, are inevitable in two-phase flow. However, the usual noise contributions associated with the electronics etc. are present irrespective of whether the signals are obtained in a single or a two-phase system. Such noise components are readily removed by using appropriate filters, *viz.*, the filters available in the Signal Processing Toolbox (MATLAB™ Ver. 5).

Experimental evidence indicates that signals acquired using conductivity probes in two-phase gas-liquid flows are corrupted due to significant systematic lowering of the measured conductivity when a bubble hits the probe. This systematic bias in the measured conductance in gas-liquid flows has frequently limited the use of such probes for tracer experiments. As the conductivity of the gas is appreciably smaller than that of the liquid containing an electrolyte as tracer, one observes frequent dips in the measured electrical conductance signal as bubbles pass over the probe measurement volume. If one were to apply standard filtering techniques, one obtains a filtered signal that is always an underestimate of the actual signal, which one would measure if there were no bubbles (gas) present in the system. This is because the noise component, which one is trying to

remove, has a non-zero mean and this causes the filtered signal to under-predict the actual value.

Rustemeyer *et al.* (1989) tried to avoid the signal corruption due to bubble passage by mechanically screening the probe tips. However, the screening of the probe tips to avoid completely the presence of gas can never be perfect, and the signals shown in their article still seem to carry some information due to bubble interaction with the probe tips. Other researchers have tried to resolve the signal corruption due to bubble passage by standard data filtering techniques (Bodden and Mewes, 1996). However, the filtered tracer response seems to have lost some information for the very reasons mentioned above. Standard digital signal filtering procedures assume that the noise component of the signal to be filtered has a zero mean, which happens to be the case only with random noise associated with either the measuring device or fluctuations in the electrical signals. As mentioned earlier, the interaction of the bubbles with the conductivity probes causes a systematic lowering (bias) of the measured signals. If this systematic lowering of the signals were to be considered as noise, the mean of such a noise component is not zero, and standard filtering algorithms do not work very well in removing them. Therefore, interpretation of data from the tracer experiments in gas-liquid flows becomes non-trivial as standard filtering techniques for removing un-biased noise (with zero mean) from the conductivity probe signals are not applicable.

An in-house special purpose software filtering technique has been developed that can effectively tackle the problem of extracting meaningful information about the liquid phase conductance alone from data with systematic corruption obtained in two-phase gas-liquid systems. The advantage of using a software-based filter over a hardware filter is that the acquired signal can be tested against several software filters, whereas a hardware filter permanently filters the original signal, which is no longer accessible for further processing. The filtering technique developed in this work is first demonstrated on numerically generated signals and is subsequently applied to experimental data sets acquired in bubble columns.

3.2. Experimental Setup

Figure 3-1 shows the experimental setup of a counter-current staged bubble column with an inner diameter of 7.5" (19-cm) and overall height of 94.5" (240-cm), which was used to acquire the data sets on which the developed filtering technique is demonstrated. The column is made of clear acrylic and is operated using air as the gas phase while tap water serves as the liquid medium. A shower-type liquid distributor at the top and a gas distributor at the bottom maintain counter-current flow of liquid and gas, respectively. Two air spargers were employed in this study having evenly distributed holes of 0.35 mm in diameter as shown in Figure 3-2. The column was sectioned into four stages by the use of three trays each having 42 holes ¼" in diameter. Several ports were installed in the middle stage and on each side of the tray so that liquid conductivity probes could be inserted for local measurement of liquid-phase tracer concentrations. The entire column was supported at the bottom by the plenum. The conductivity probes (MI-900 Series conductivity electrodes) used in this study were obtained from Microelectrodes Inc. Each probe is interfaced to a 486 PC via a data acquisition board (AT-MIO-16E-10 having a 12-bit resolution and capable of sampling at a rate of 100 kilo-samples/sec) from National Instruments. The probes consist of two electrodes (platinum black coated) approximately 3 mm apart, which are encased in plastic tubing approximately 6mm in diameter and 30 cm in length. The probes are connected to conductance meters (YSI Model 35), and the output from the meters is sent to the data acquisition board.

A pair of conductivity probes was used to acquire the experimental data with the two probes spatially configured as shown in Figure 3-3. In this configuration, the first probe (Probe_0) was positioned in the downcomer region of Tray 2 with the tip of the probe 1.5 cm from the wall and 3.18 cm below Tray 2, whereas, the other probe (Probe_1) was placed in the center of the column 3.18 cm below Tray 1 (as shown in Figure 3-3). These point-measurement of liquid-tracer concentrations were made only with Sparger 2, while for studying the sparger effects, alternate probe locations were employed as discussed in Section 3.7.1. To assess the ability of the developed filtering technique to reliably extract the liquid phase conductance in response to an impulse

tracer injection, three different gas and liquid flow rates were used as summarized in Table 3-1. The table also includes the overall gas-holdup values measured using the bed-expansion method. For the tracer experiments, the liquid stream was not recycled and was discharged into a drain from the liquid outlet.

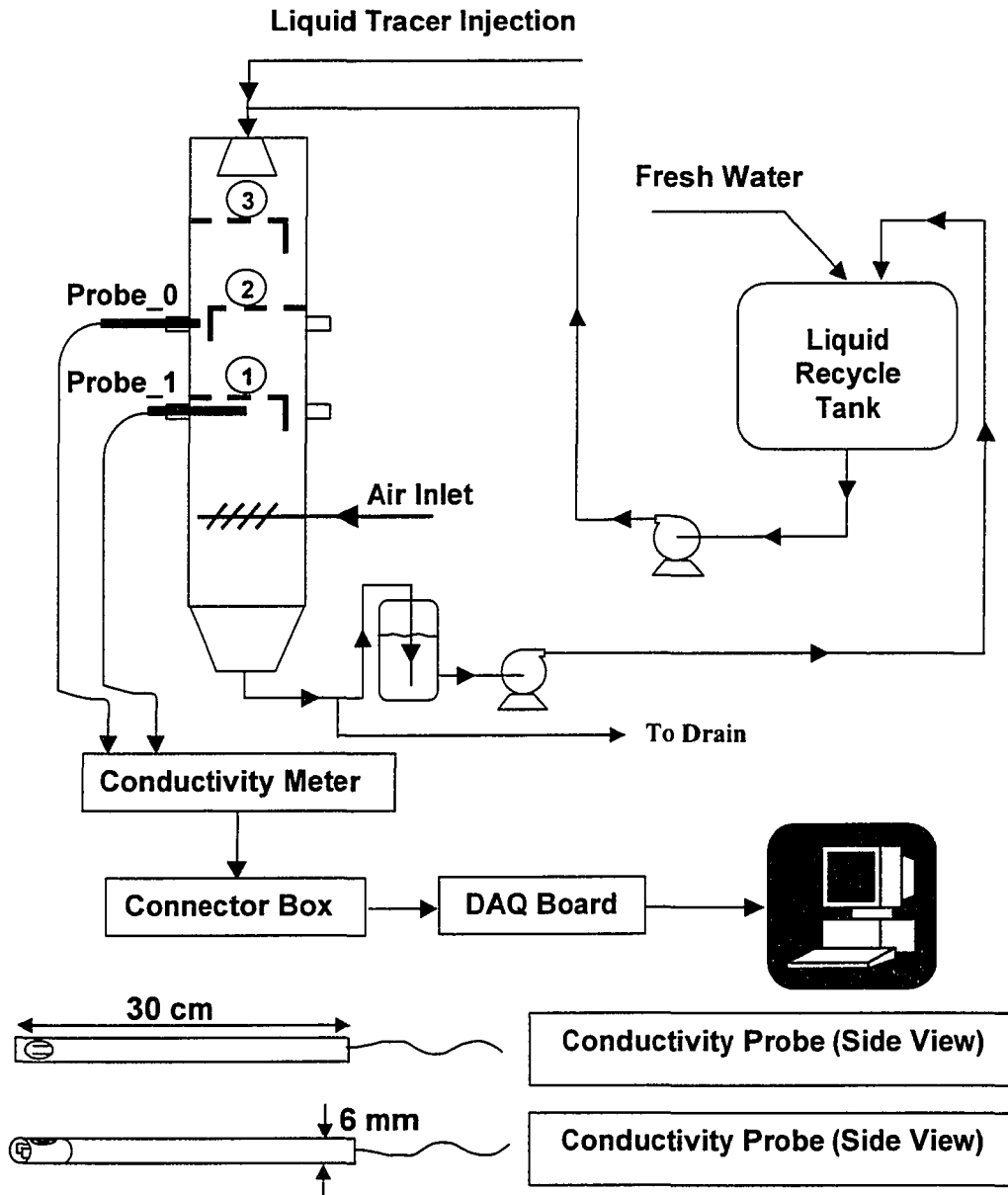
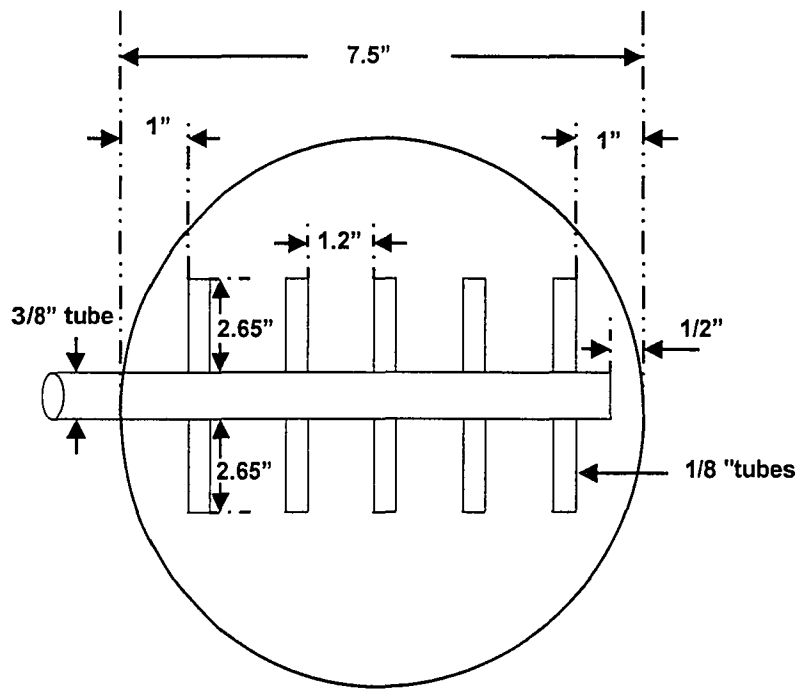
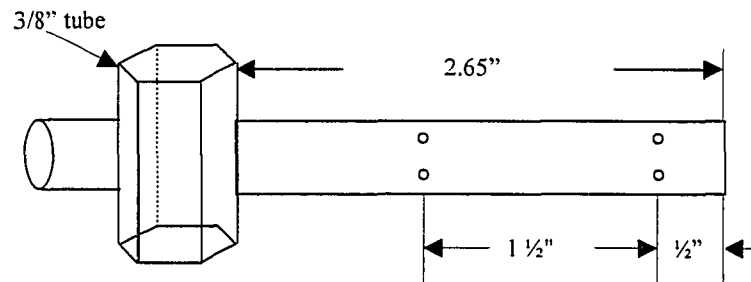


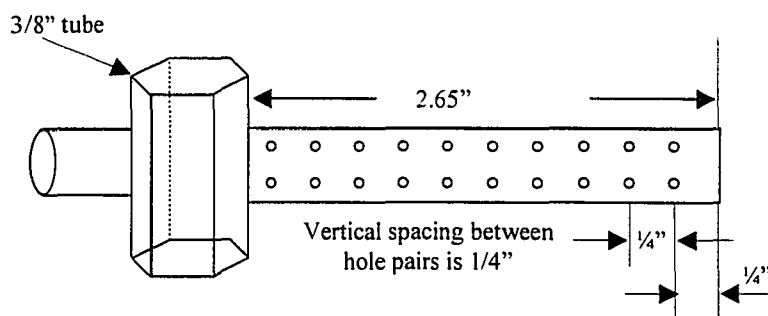
Figure 3-1. Schematic of the counter-current staged bubble column process loop and the data acquisition set-up with a sketch of the conductivity probes.



(a)



(b)



(c)

Figure 3-2. Details of the gas distributor. (a) Sparger layout (b) Sparger 1: 40 holes, open area=0.14 % (c) Sparger 2: 200 holes, open area=0.68 % (Gupta *et al.* 2000; Kemoun *et al.*, 2001^a)

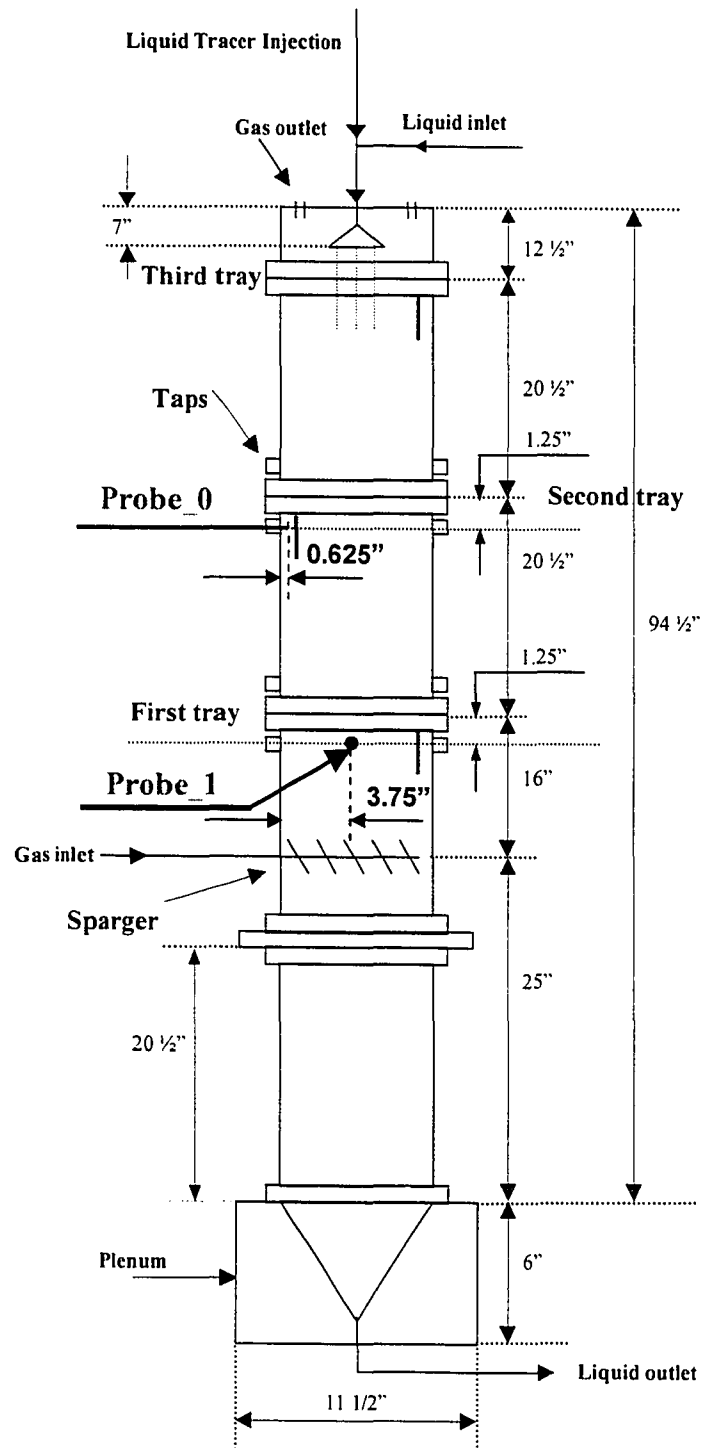


Figure 3-3. Location of the conductivity probes during tracer response measurements.

Impulse tracer injections were made in the liquid inlet stream before the liquid distributor for each of the three operating conditions. The injected tracer consisted of 10-ml of 0.2-gm/ml KCl solution and was introduced at the top of the column into the showerhead with the aid of a syringe. The start of the injection was controlled to the accuracy of a tenth of a second with the help of a stopwatch. The data acquisition system was initiated exactly a minute before the actual injection of tracer was made. This was done to aid in filtering the data later as well as to get an in-situ baseline measurement. The duration of tracer injection was 2.5 ± 0.5 seconds for all the runs.

Table 3-1. Operating conditions for various tracer experiments.

Experiment Number	Flow Rate		Superficial Velocity (cm/s)		Gas Holdup [†] , $\bar{\epsilon}_g$	
	Gas (SCFH)	Liquid (GPM)	Gas	Liquid	Sparger-1	Sparger-2
1	118	2.0	3.25	0.44	0.07	0.11
2	118	6.5	3.25	1.44	0.08	0.12
3	236	6.5	6.51	1.44	0.12	0.20

[†] (Kemoun *et al.*, 2001^a)

Subsequent to this study performed in a tray bubble-column, the liquid tracer measurement technique, as developed in the next few sections, was applied to study the temporal evolution of local liquid-tracer concentrations in a bubble column having no trays and with the liquid in batch mode. The description of the experimental setup for that study is presented in Section 3.8 along with the discussion of the obtained results.

3.3. Problem Description

Figure 3-4 shows the signals obtained from the conductivity probe exposed to three different media, specifically air, water and air-water. The sampling frequency for data acquisition was 100 Hz with a total sampling time of 60 seconds. It can be clearly seen from the figure that the signals obtained from measurements in air and in water

(single-phase measurements) have minimal un-biased noise associated with fluctuations in the supply voltage. However, the signals from the gas-liquid system with turbulent bubbling of gas in batch liquid, show significant systematic lowering of the signal when bubbles interact with the probe surface. Our objective is to be able to extract, from signals acquired in gas-liquid systems, the liquid phase conductance devoid of biased noise resulting from frequent bubble passage over the probe tips.

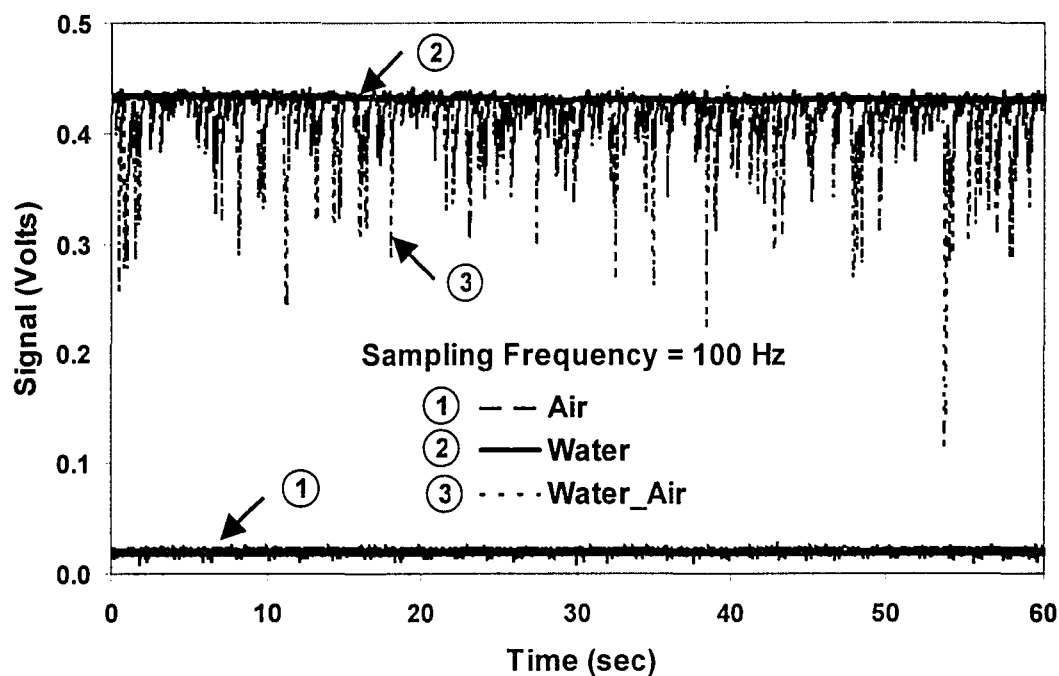


Figure 3-4. Typical signals measured by the conductivity probe in single and two-phase media.

As mentioned earlier, if standard filtering algorithms are employed for data filtering, then the filtered signal is systematically under-predicted. This is shown in Figure 3-5, where a second order Butterworth filter (MATLAB™ Ver. 5) was used to filter the signal from the gas-liquid system, and obtain filtered responses. Two cut-off frequencies (0.5 Hz and 0.05 Hz) were used to filter the signals. It can be seen from Figure 3-5 that in spite of a very low cut-off frequency of 0.05 Hz, the filtered signal is an under-prediction of the signal measured in water. To overcome the difficulty

associated with standard filtering techniques explained above, it was realized that some kind of threshold criterion has to be resorted to so that one is able to get the uncorrupted signal. The details of the developed filtering algorithm and its ability to filter out the biased noise due to bubble passage from the conductivity probe signal are presented below.

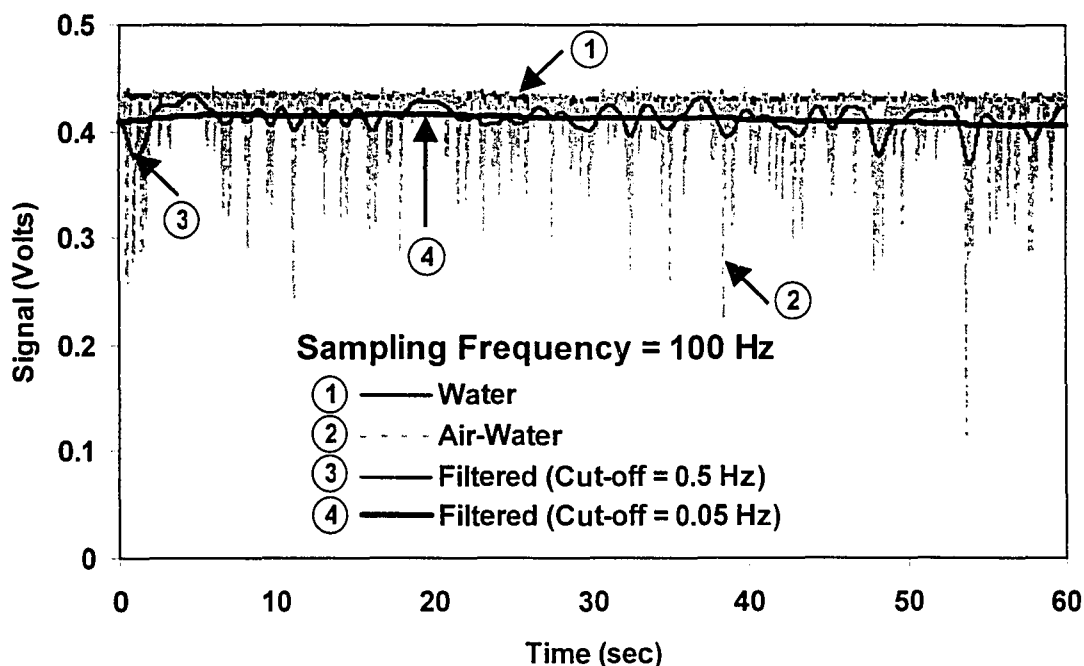


Figure 3-5. Performance of a standard Butterworth filter of order 2 in filtering conductivity probe signals.

3.4. Description of the Filtering Algorithm

The filtering algorithm developed as part of this work involves the steps described below and presented as a flow chart in Figure 3-6. Coupled with the thresholding criterion is the use of Butterworth filters from the Signal Processing Toolbox (MATLAB™ Ver. 5) in the procedure to filter the conductivity-probe signals to remove the biased noise due to bubble passage. The steps involved in this procedure are:

1. The raw signal, $RS(t)$, is first subjected to a regular Butterworth filter to obtain the filtered signal $FS(t)$.
2. The filtered signal, $FS(t)$, is further processed as follows. At each time instant, if the filtered signal, $FS(t_i)$, is lower than the raw signal, $RS(t_i)$, then the filtered response is made equal to the raw signal. However, if at that instant, the filtered signal is higher or equal to the raw signal, the filtered signal, $FS(t_i)$, is accepted as the transformed signal without any modifications. This procedure is referred to as thresholding. The resulting transformed signal, $FST(t)$, is the filtered plus thresholded signal.
3. A residual (RES) is calculated, which is equal to the square root of the sum of the squares of the differences between the raw (RS) and filtered plus thresholded (FST) signals, divided by the total number of data points in the time-series.
4. If this residual is less than a certain tolerance (TOL - 5×10^{-6} volts in this case), then the filtered plus thresholded response is taken to be the final filtered response, otherwise the filtered plus thresholded signal replaces the raw signal, $RS(t) = FST(t)$, and the process is repeated by returning to Step 1.
5. This procedure is continued until the tolerance criterion is met.

The choice of the tolerance (TOL) in general will depend upon the system being studied, and can be estimated from a few test runs in the specific gas-liquid system under investigation. Too strict a tolerance could, however, result in over-smoothing of the signal, and consequently, a loss of information.

3.5. Results and Discussion - Implementation of the Filtering Algorithm

Figure 3-7 shows the results of the above algorithm applied to the raw signal in Figure 3-4. Here we coupled a Butterworth filter of order 2 with the new filtering procedure and performed the filtering operation, using the same two cutoff frequencies (0.5 Hz and 0.05 Hz) to compare the performance of the new technique with that of the standard filter. One can immediately see from the figure that the new filtering algorithm has performed much better in extracting a very reasonably smooth signal from the raw data, and that the final filtered signal is relatively independent of the cutoff frequency.

However, this observation may not be general, as the desired final signal is obvious from visual inspection and is relatively easy to extract as it has insignificant amplitude variation. Therefore, the most important question that remained to be answered was whether this technique could be applied to a signal which resembles a signal similar to the one obtained while measuring the impulse response of an electrolytic tracer in the liquid (water) phase.

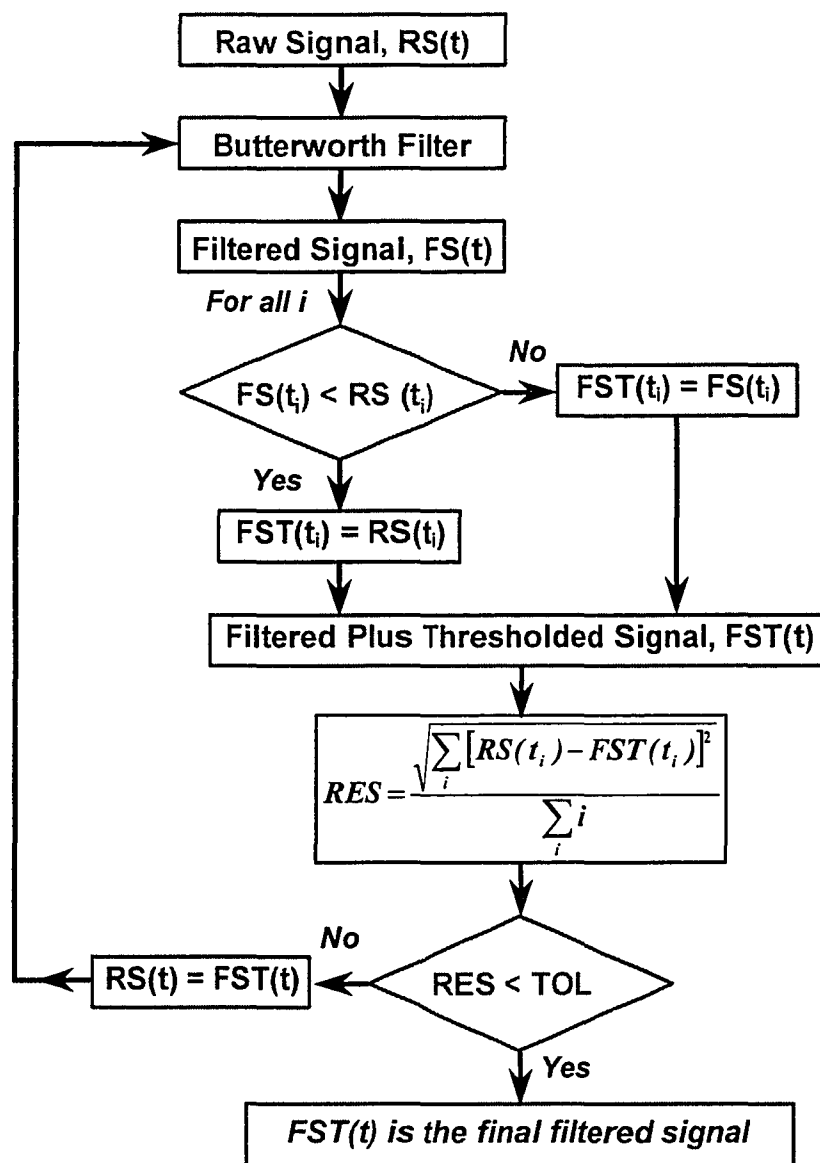


Figure 3-6. Flow chart for the developed filtering algorithm.

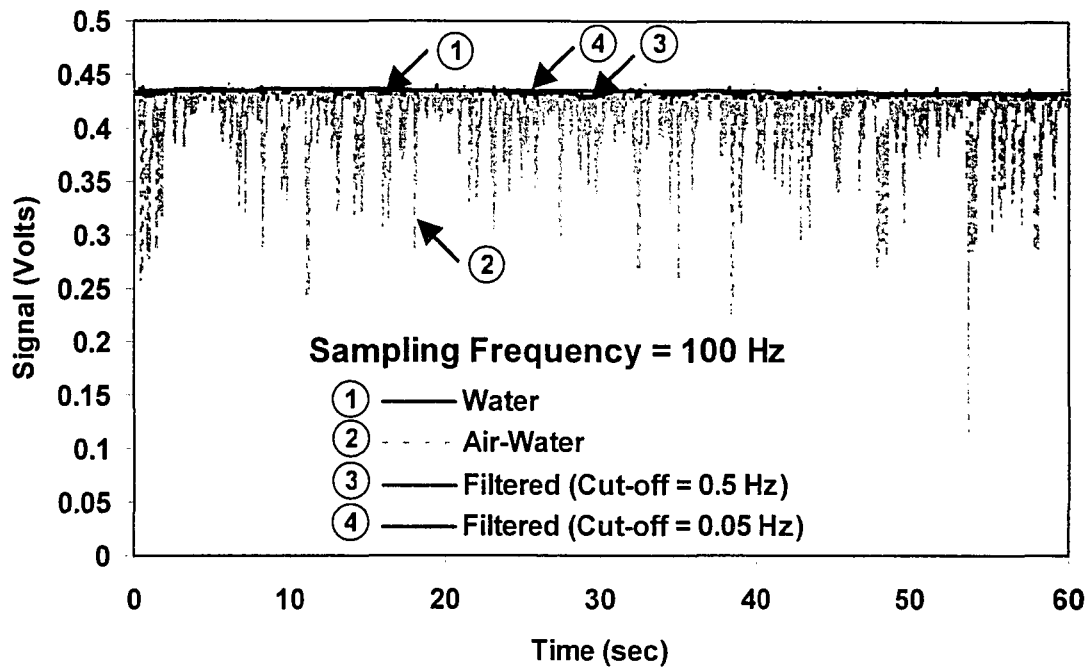


Figure 3-7. Performance of the new filtering technique, in conjunction with a Butterworth filter of order 2, in filtering conductivity probe signals.

To answer this important question, a numerically generated signal resembling a typical response to an impulse tracer injection was created. This signal was then added to the raw air-water signal (shown in Figure 3-4) acquired in a bubbling air-water system. The numerically generated signal was created using the following expression:

$$\left. \begin{aligned}
 y_{mm} &= y_{raw} & t \leq 5 \\
 y_{mm} &= y_{raw} + 4.0 * \left\{ (t-5) * \exp\left(-\frac{t}{2}\right) + (t-5)^3 * \exp\left(-\frac{3t}{2}\right) \right\} & t \geq 5
 \end{aligned} \right\} \quad (3-1)$$

where y_{raw} is the air-water signal in Figure 3-4.

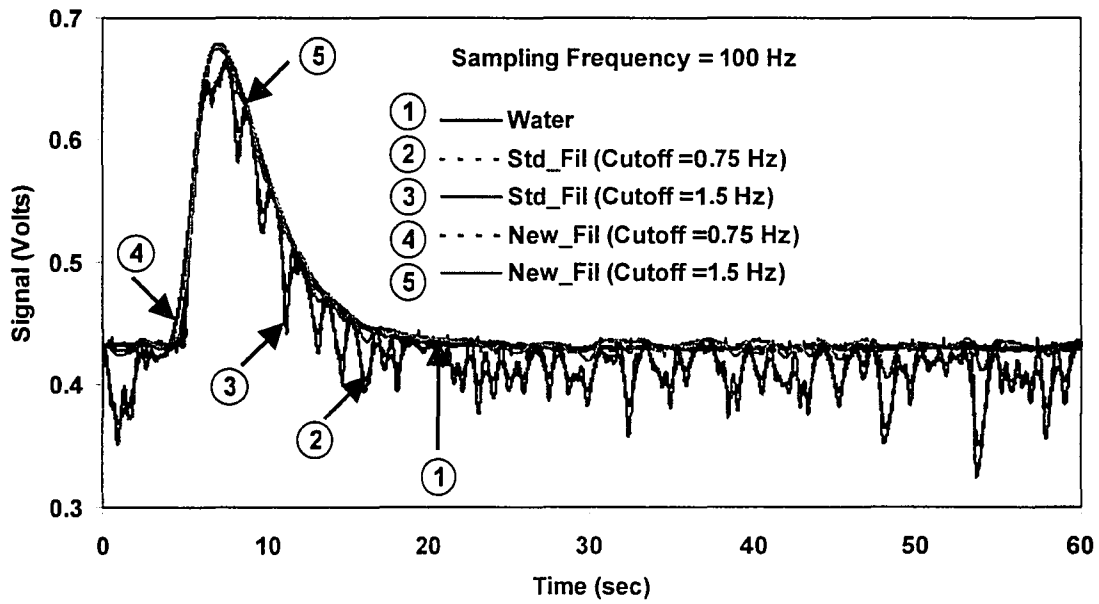
The performance of the standard and new filtering algorithms on the signal obtained from this numerical tracer test is shown in Figure 3-8a. Upon visual observation again, one can see that the new technique has been able to extract the equivalent liquid phase conductance much better than the standard Butterworth filters. Two different cutoff

frequencies were tested to study their effect on the final filtered signals. As before, even with a higher cutoff frequency, the new algorithm performed better than the standard filtering procedure.

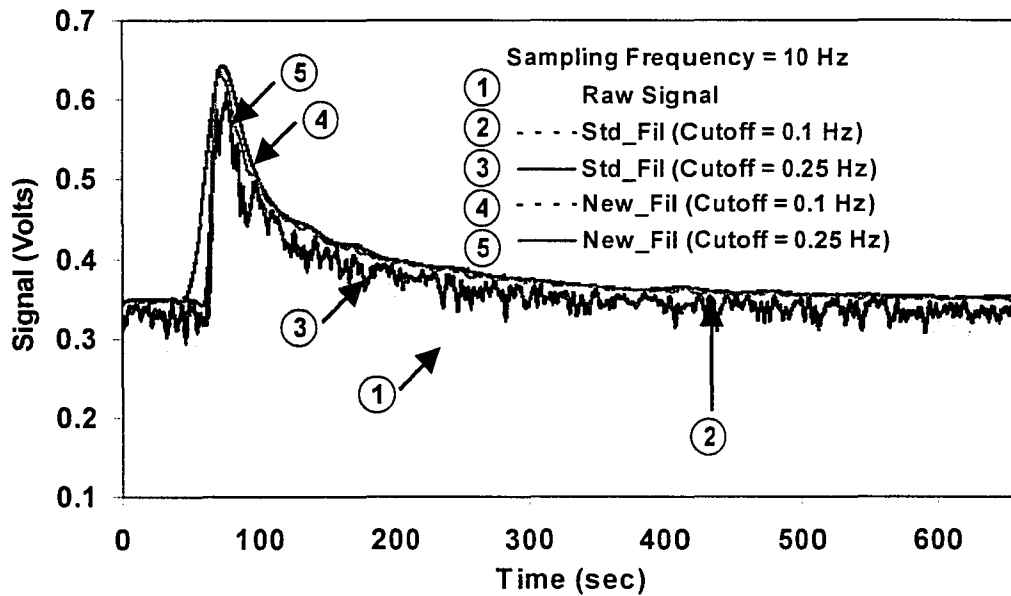
To test the algorithm on an actual experimental data set, the filtering procedure was applied to raw conductivity signal of Probe_0 obtained under operating conditions of Experiment 1 as shown in Table 3-1. From Figure 3-8b, one can see that the algorithm has been successful in producing the desired level of data reduction, while the use of the standard filtering algorithm results in loss of information especially near the peak of the experimental response. Thus, by the above filtering plus thresholding procedure we are retaining frequencies less than or equal to the cutoff frequency as the successively filtered signal relaxes to the final filtered plus thresholded signal. It should be noted from Figure 3-8b that when a cutoff frequency of 0.1 Hz is used in the developed filtering procedure, it results in over-filtering the signal. This in turn results in the leading edge of filtered signal to precede the leading edge of the raw signal, which is not real. Thus, a proper selection of the cut-off frequency is vital to proper implementation of the filtering algorithm.

3.6. Characteristic Response Time of the Conductivity Probes

When acquiring point liquid phase tracer responses, an important issue that needs to be addressed is that of the probe response time. At a sampling frequency of 100 Hz and a total sampling time of eleven minutes needed for the tracer (electrolytic KCl solution) to completely exit the system, an enormous amount of raw data would be acquired. This might not provide any additional information than if the data was acquired at a lower sampling frequency; as a high sampling frequency only results in storage of non-significant data. A sampling frequency of 100 Hz would imply by the Nyquist criterion that one can capture actual phenomena with the frequency-content up to 50 Hz. This would only be true if the conductivity measurement system has an overall response time approximately 3-5 times faster than 20 milliseconds to ensure that the measured signal relaxes to 95-99% (assuming first order response) of the final value when a step change in conductance occurs.



(a)



(b)

Figure 3-8. Performance of the standard and new filtering techniques in filtering the a) numerically generated signal b) raw signal from experimental data.

The characteristic response time of the probes was found experimentally (as is described later in this section) to be around 75 milliseconds (assuming first order response), which corresponds approximately to a frequency of 13 Hz. A characteristic probe response time of ~ 75 milliseconds implies that with such a probe one could confidently monitor a process having a characteristic time of greater than ~ 400 milliseconds. In other words, one cannot expect to capture reliably any phenomena that have characteristic frequencies higher than 2-3 Hz. The characteristic frequency of the tracer washout curves, for typical bubble column experiments, is in the range 1×10^{-3} - 1×10^{-2} Hz. This range is two orders of magnitude lower than the highest frequencies that these probes can capture, implying that the use of these probes for the current work is well justified. Therefore, a sampling frequency 3-5 times the highest characteristic frequency that can be captured with these probes (2-3 Hz) would be approximately 10 Hz. Hence, 10 Hz was chosen as the sampling frequency for all the tracer experiments on the counter-current staged bubble column.

The approximate characteristic-response time of the probes was determined experimentally by modeling the time for the probe signal to rise from that in air to that in tap water by a first order process with zero dead-time. The experiment was repeated five times by dipping the conductivity probe into a beaker containing tap water while recording this temporal variation of the probe signal. The synchronization between the processes of data logging of the probe response with time and the dipping of the probe into the beaker containing tap water was attained with the aid of a stopwatch. The characteristic probe time was subsequently determined by fitting a first order curve to the average of the probe response from the five repetitions. The results of such an experiment are shown in Figure 3-9. Unfortunately, due to the relatively poor de-wetting characteristics of the probes, the reverse experiment to determine the fall time of the probe signal, when the probe is withdrawn out of tap water into air did not yield any useful information.

In general, the choice of the cut-off as well as of the sampling frequencies will depend on the smallest characteristic time-scale (highest frequency) that one is trying to capture from these experiments. It should be pointed out that this method (or for that

matter any other) will lead to significant errors when the highest characteristic frequency that one wants to capture is of the same order as that corresponding to bubble passage, breakup and coalescence. It has recently been reported by Letzel *et al.* (1997) that in bubble columns of industrial importance, characteristic frequencies of $O(10^0 \text{ Hz})$ are related to overall liquid circulation; those of $O(10^1 \text{ Hz})$ are related to bubble passage, coalescence and breakup; while those of $O(10^2 \text{ Hz})$ are associated with the turbulence microscale in the system. Therefore, a natural question to ask is whether similar information could be obtained from the conductivity probe signals acquired in a gas-liquid turbulent bubbling system. If bubbles are expected to exhibit a similar frequency response in this system as the one reported by Letzel *et al.* (1997), then to satisfactorily capture the characteristic frequency due to bubble passage with the conductivity probes, one has to have the characteristic response time of the probe to be at the most 20–30 milliseconds. This obviously is not the time resolution of the probes we are currently using. Thus, one would not be able to distinctly see a frequency corresponding to bubble-passage with these probes; and probes with a better time resolution are required for such a purpose.

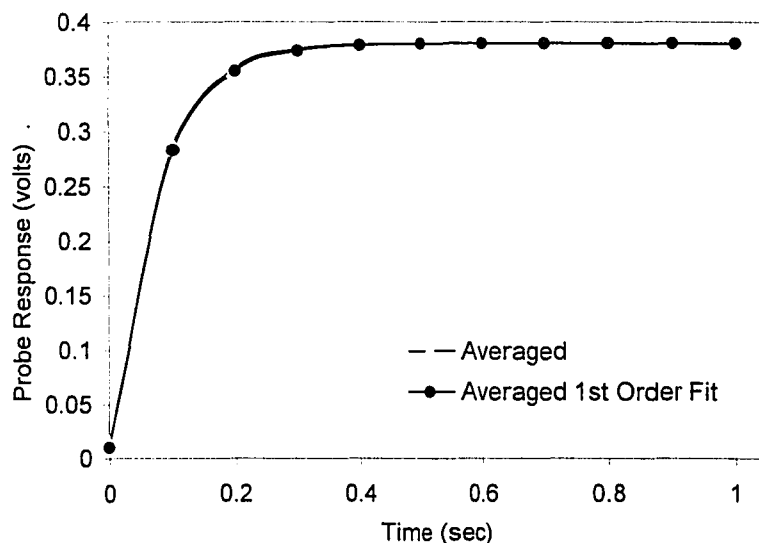


Figure 3-9. First order model fit of the rise of the conductivity probe signal from the one detected in air to that in tap water.

3.7. Results and Discussion – Tracer Tests in Counter-Current Staged Bubble Column

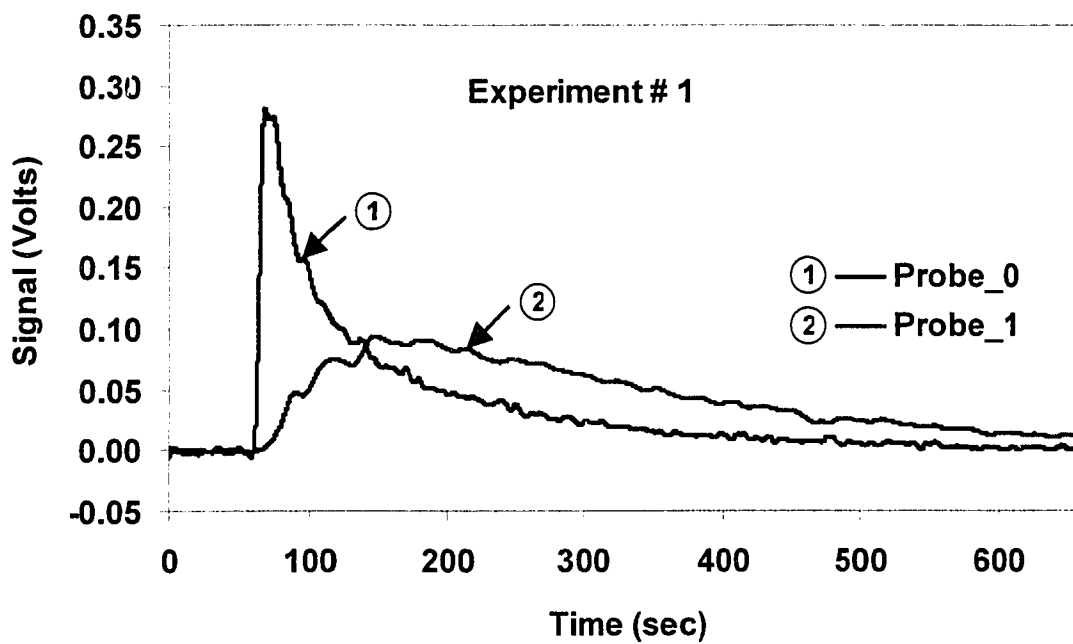
To test the feasibility of the developed filtering technique on experimentally acquired data as opposed to a numerically generated one, impulse tracer injections were made as described in the section on 'Experimental Setup'.

Figure 3-10 shows the tracer response curves for the two probes utilized in studying the inter-stage mixing at the three operating conditions. One can immediately see that the developed filtering technique has been successful in extracting smooth liquid-phase impulse-tracer responses. As can be seen from Table 3-1, experiments 1 and 2 were performed to examine the effect of the liquid flow rate, while experiments 2 and 3 were conducted to characterize the effect of the gas flow rate. Since the liquid flow rate for experiments 2 and 3 was the same, one can see from the Figures 3-10(b) and 3-10(c) that the impulse responses of the two probes in these experiments are very similar even though the gas holdups under these two operating conditions were significantly different. From Figures 3-10a and b, one can also see that the liquid flow rate has a significant effect on the tracer response curves. This comes as no surprise as the tracer response curves have to get washed out approximately three times as fast for a liquid flow rate of 6.5 GPM vs. a flow rate of 2.0 GPM. Additionally, a higher liquid flow rate enhances the radial mixing on the stage and hence, the tracer response curves are washed out almost uniformly throughout the stage.

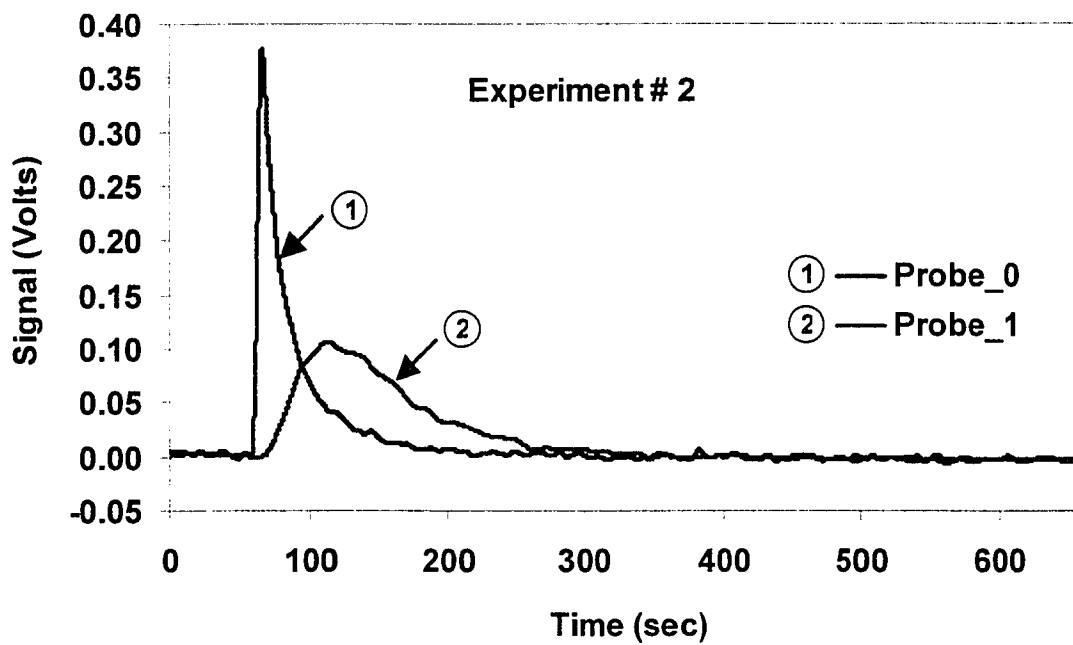
From Figure 3-10, one can also see that the trays provide the desired effect of staging for the liquid phase in the bubble column which inherently results in reduced backmixing. The staging effect can be quantified in terms of the characteristic time delay (τ_{LAG}) between the two signals. This time delay is computed using the cross-correlation technique (Keane and Adrain, 1992) as given by Equation 3.2.

$$R(\tau) = \int_{-\infty}^{\infty} Probe_0(t) * Probe_1(t - \tau) dt \quad (3-2)$$

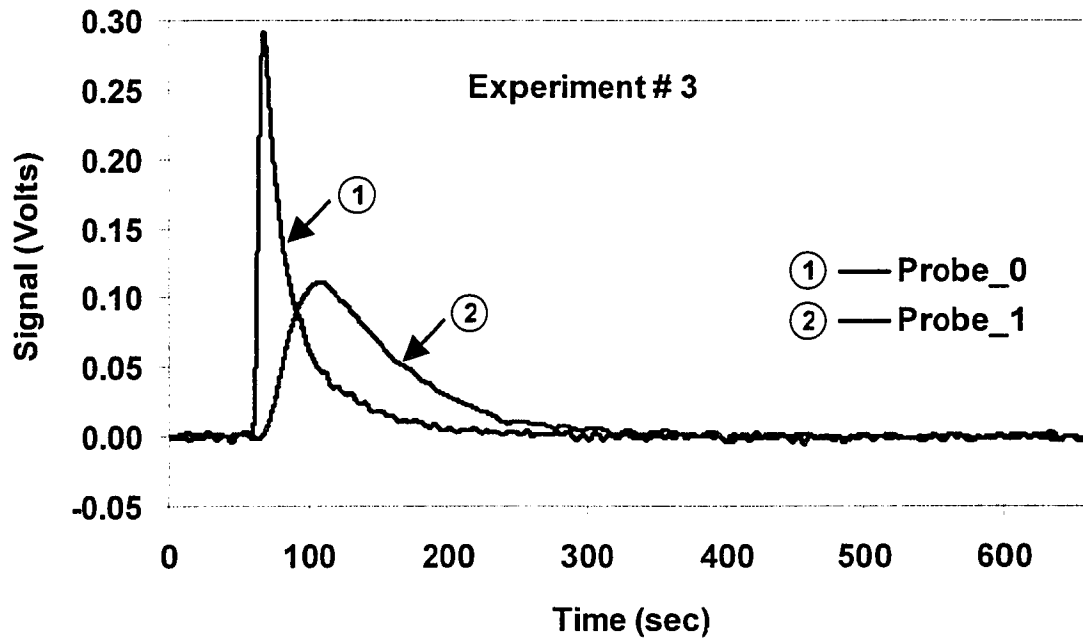
$\tau_{LAG} = \tau$ for which $R(\tau)$ is maximum



(a) $U_G = 3.25$ cm/s, $U_L = 0.44$ cm/s



(b) $U_G = 3.25$ cm/s, $U_L = 1.44$ cm/s



(c) $U_G = 6.51$ cm/s, $U_L = 1.44$ cm/s

Figure 3-10. Tracer response curves for the experiments at different operating conditions listed in Table 3-1 with the two probes positioned as in Figure 3-3.

Table 3-2 shows the characteristic time, at different operating conditions, by which the signals arriving at Probe_1 lag those that arrive at Probe_0. The characteristic lag time can be used to provide an good estimate of the mean interstitial velocity of the liquid phase between the two probes, which is only an estimate of the long-time average velocity between the two points, and not the instantaneous velocity. Knowing the distance between the probes ($L = 20$ inches), the average interstitial liquid velocity between the two probes is calculated as

$$U_{L,est} = \frac{L(1 - \bar{\epsilon}_g)}{\tau_{LAG}} \quad (3-3)$$

The tracer responses presented in Figure 3-10 are further processed to obtain the mean (τ_{Mean}) and dimensionless variance ($\sigma^2_{Dimensionless}$) for both probes at each of the

three operating conditions. These two quantities are defined in Equation 3-4 with the respective value for each tracer response being presented in Table 3-2.

$$\left. \begin{aligned} \mu_i^0 &= \int_0^{\infty} f_i(t) dt \\ \mu_i^1 &= \frac{\int_0^{\infty} t f_i(t) dt}{\mu_i^0} \\ \mu_i^2 &= \frac{\int_0^{\infty} (t - \mu_i^1)^2 f_i(t) dt}{\mu_i^0} \end{aligned} \right\} \Rightarrow \begin{cases} \tau_{Mean} = \mu_i^1 - \mu_i^0 \\ \sigma^2_{Dimensionless} = \frac{\mu_i^2 - \mu_i^0{}^2}{\tau_{Mean}^2} \end{cases} \quad i = \begin{cases} 0 & Probe_0 \\ 1 & Probe_1 \end{cases} \quad (3-4)$$

In the above equation, $f_i(t)$ are the voltage response from the conductivity probes. Additionally, the tracer responses in Figure 3-10 were normalized by the area under the curves, and the time scale was normalized with τ_{Norm} , which is defined by Equation 3-5. The normalized responses are presented in Figure 3-11 for the three operating conditions.

$$\tau_{Norm} = \frac{L(1 - \varepsilon_g)}{U_{L,sup}} \quad (3-5)$$

Table 3-2. Mixing parameters from the tracer response curves.

Experiment Number	1		2		3	
	Probe_0	Probe_1	Probe_0	Probe_1	Probe_0	Probe_1
$U_{G,sup}$ (cm/s)	3.25		3.25		6.51	
$U_{L,sup}$ (cm/s)	0.44		1.44		1.44	
τ_{Norm} (sec)	103		31		28	
τ_{LAG} (sec)	73		40		31	
$U_{L,est}$ (cm/s)	0.62		1.12		1.32	
μ^0 (volts-sec)	21.89	27.17	10.66	12.10	8.48	10.62
$(\mu^0)_{Probe_0}/(\mu^0)_{Probe_1}$	0.81		0.88		0.80	
$(K_C)_{Probe_0}/(K_C)_{Probe_1}$	0.81					
μ^1 (sec)	168.2	285.3	102.6	160.1	97.6	149.7
μ^2 (sec ²)	11632.2	19426.2	3842.1	6261.6	1969.6	4243.8
τ_{Mean} (sec)	117		57.5		52.1	
$\sigma^2_{Dimensionless}$	0.57		0.73		0.84	

It is to be noted that since the two probes utilized in this study had different linear calibration constants, the values of the zeroth moments for the two probes are different. However, since the probe responses are linear, then the ratio of the zeroth moments of the two probes are equal to the ratio of the calibration constants of the two probes. For the precision of the experimental procedure, this seems to be true as can be seen from Table 3-2. From the values of the characteristic times and velocities presented in the table, it can be inferred that there is an indirect liquid flow path from the downcomer of tray-2 to a location beneath tray-1. That is the reason why τ_{Norm} is smaller than τ_{Mean} since a significant portion of the liquid has to travel along the downcomer of tray 1 to be able to reach the Probe_1 location. Another interesting feature emerging from Table 3-2 is the value of the dimensionless variance of the various tracer response curves. The variance at each location is lower than one, which indicates that the flow pattern *between trays* is far removed from being perfectly mixed. However, with increasing gas and liquid flow-rates, the intensity of *inter-stage* mixing increases as can be seen by the consistent increase in the dimensionless variance and in the average interstitial velocity of the liquid phase.

3.7.1. Effect of Gas Sparger Design

It was anticipated that sparger design might have a significant effect on mixing in the liquid phase on a tray in the staged bubble column. As a result, two different sparger configurations, as shown in Figure 3-2, were tested for their effect on liquid mixing on the middle tray. For this purpose, the two probes were located in the center of the column section between trays 1 and 2 with Probe_0 placed just below tray 2 while Probe_1 located just above tray 1. Figure 3-12 shows the tracer response curves obtained at the three operating conditions for these two different spargers. The first important conclusion that can be reached from these results is that relative to the convective time-scale for the column, the differences between the probe responses are negligible, implying close to perfect *intra-stage* mixing on the tray.

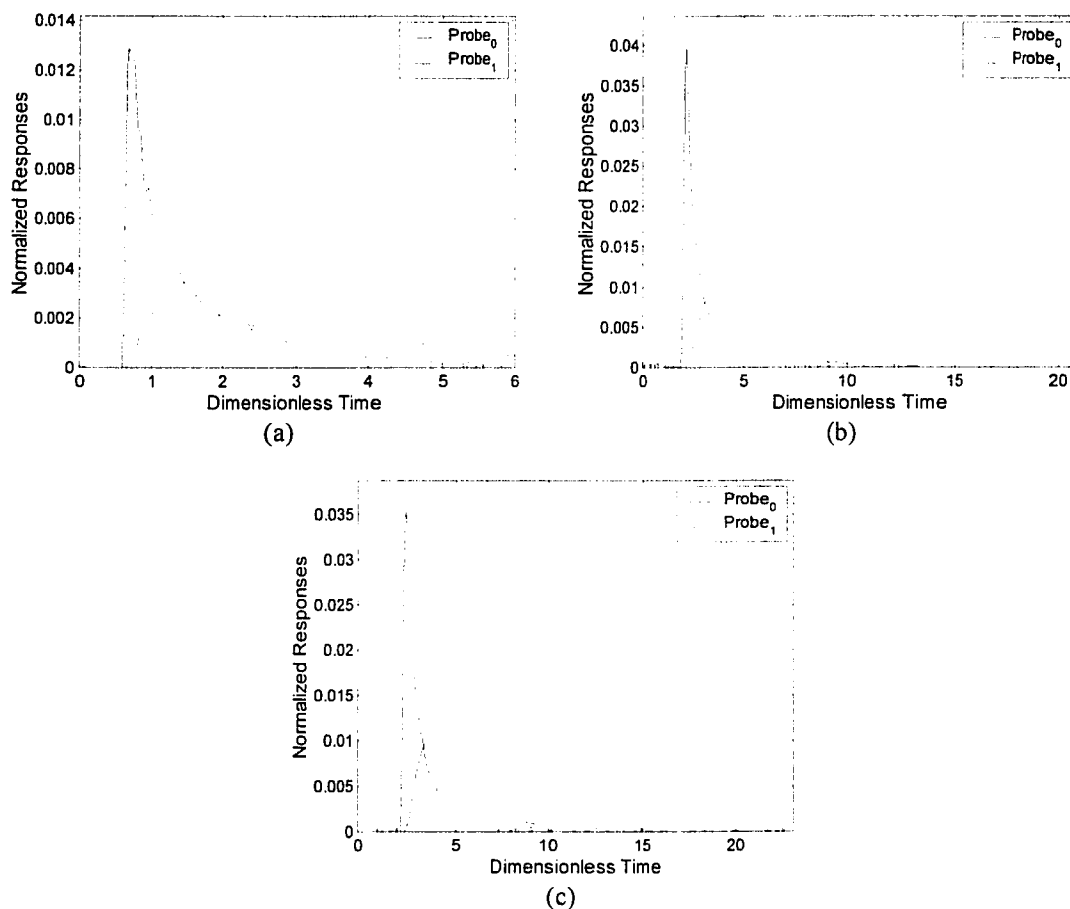


Figure 3-11. Normalized tracer response curves of Figure 3-10.

From Figure 3-12, it can be seen that the sparger has the most significant effect on the local liquid-phase tracer responses at the lowest liquid flow rate used (2 GPM \equiv 0.015 ft/s \equiv 0.44 cm/s). At this liquid flow-rate, the response curves with sparger 1 are noticeably broader than those obtained with sparger 2. This effect is not seen at the highest liquid flow rate used (6.5 GPM \equiv 0.048 ft/s \equiv 1.44 cm/s), irrespective of the employed gas flow rate. This observation is not surprising since the gas holdup for the two spargers are significantly different (refer to Table 3-1), which implies that the tracer is washed out slower for sparger 1 as compared to sparger 2. However, at increased liquid throughput, the differences in the macroscopic liquid flow-patterns arising from the differences in gas holdup diminish, resulting in insignificant differences in tracer washout curves. Qualitatively therefore, the sparger effects at increased liquid throughput are insignificant

and the minor differences that do exist among tracer responses from the two spargers can be quantitatively analyzed from the mixing parameters computed using Equation 3-4.

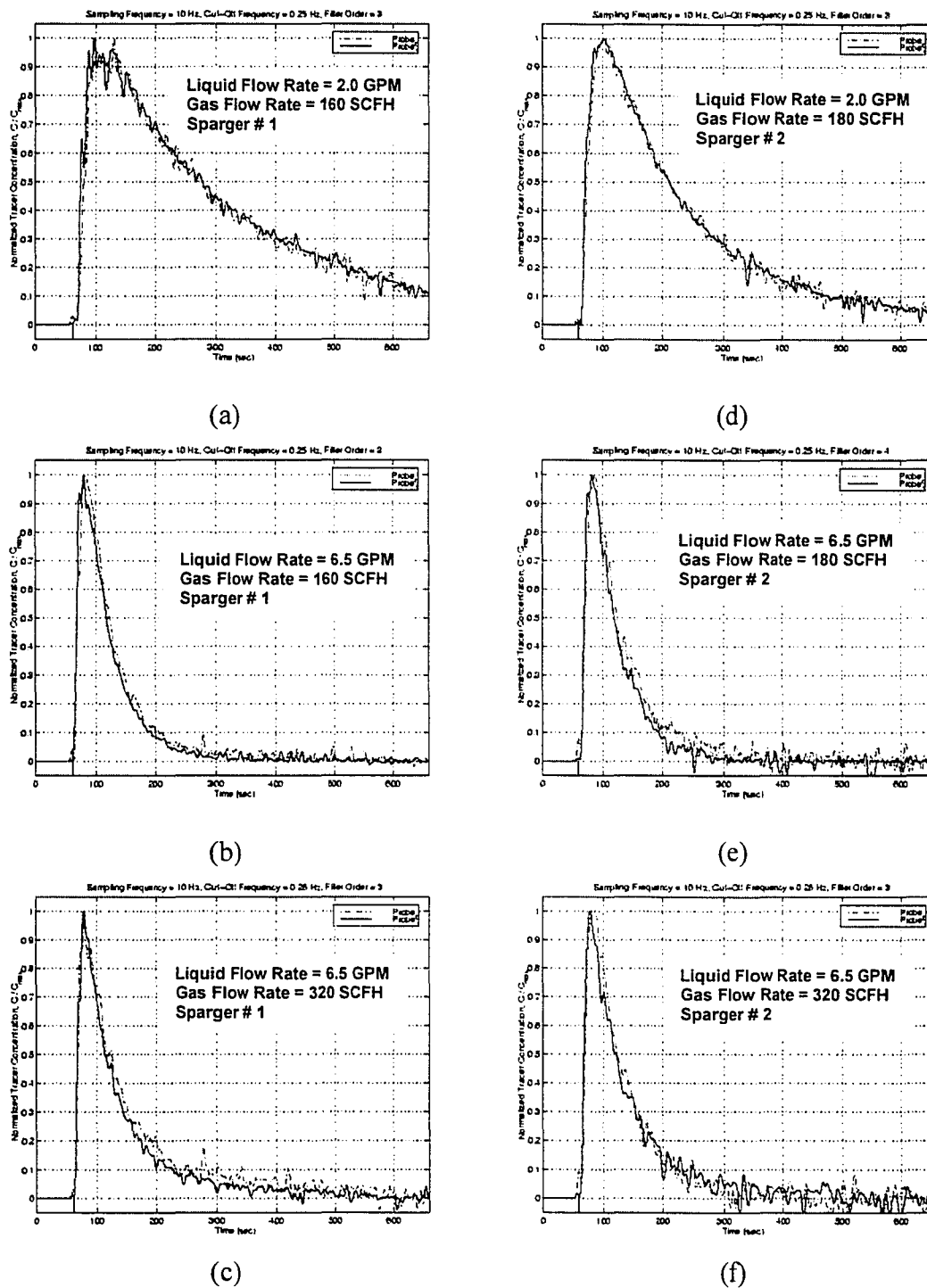


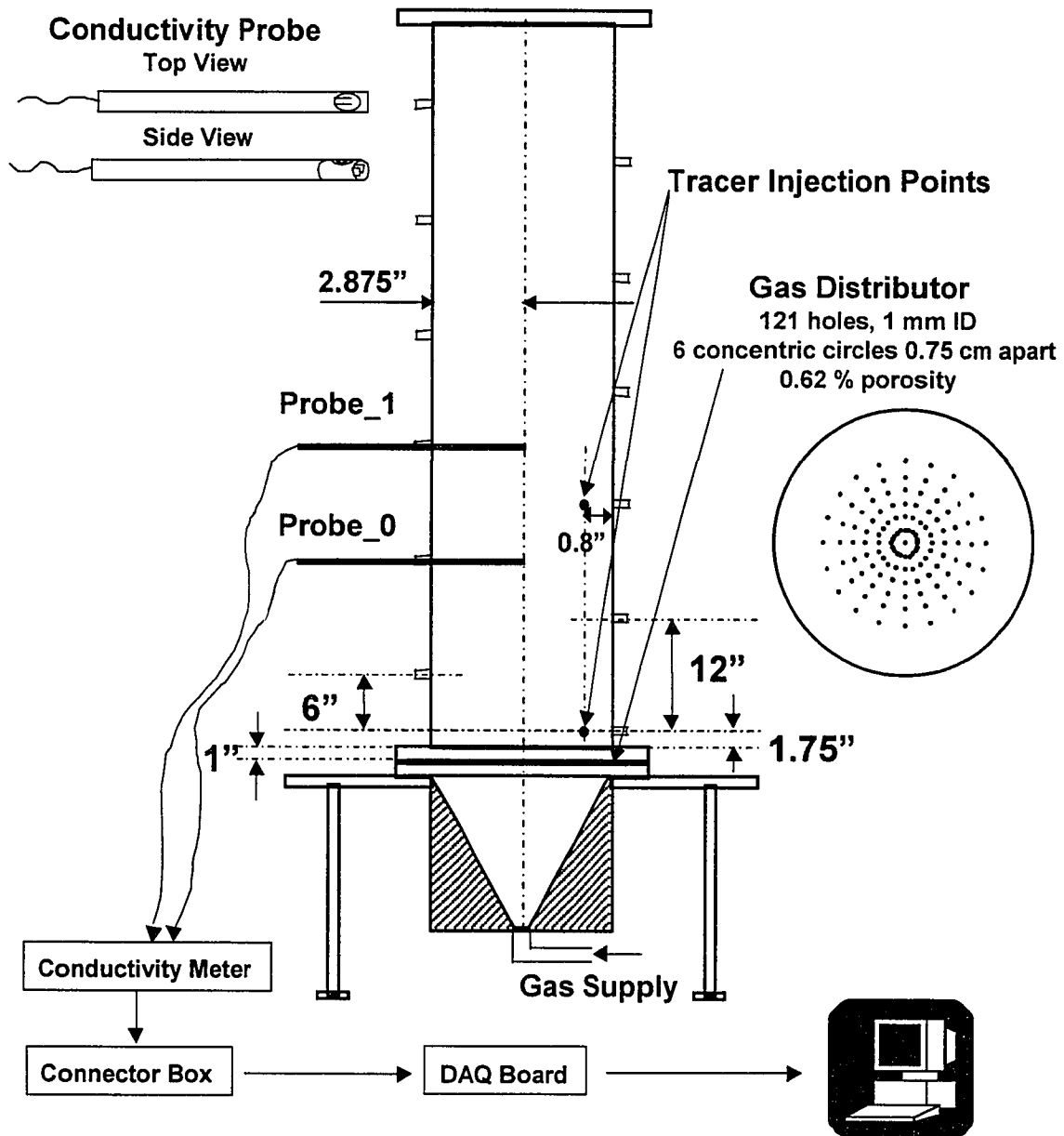
Figure 3-12. Effect of sparger hole density on tracer impulse responses.

a-c) Sparger 1 (40 holes per lateral) d-f) Sparger 2 (200 holes per lateral)

3.8. Results and Discussion – Tracer Tests in a Bubble Column with Batch Liquid

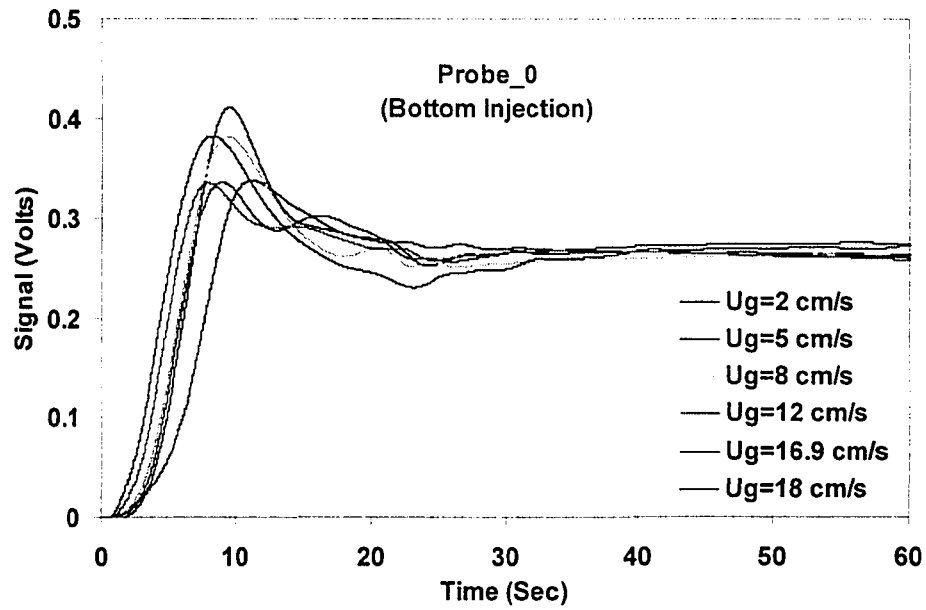
This section briefly describes the application of the filtering algorithm developed in this study to qualitatively investigate liquid mixing in a bubble column with no internals and with the liquid in the batch mode of operation. The column was open to atmosphere during the course of the experimentation with the gas phase being compressed air and the liquid phase being tap water. Figure 3-13 shows the sketch of the experimental setup used for the study along with the sketch of the employed distributor. Two different tracer injection locations were investigated with one being close to the gas distributor and the other being in between the two probes. Because of the limitation of the tracer injection apparatus, the injection points were chosen to be close to the wall as can be seen from Figure 3-13. A range of gas superficial velocities was employed to assess the ability of the probes to capture the liquid-phase tracer responses with increasing gas volume fraction. The acquired signals were processed using the algorithm described in the preceding sections, and the results are presented in Figures 3-14 and 3-15 for the bottom and middle injections, respectively.

From Figures 3-14 and 3-15, the effect of the axial location of the tracer injection point on the resulting liquid tracer responses can be clearly seen. It should be noted that although the tracer injection points are shown to be 0.8” away from the column wall, these are only representative of the location of the tip of the tracer injection-syringe. Since the tracer shoots out horizontally upon application of pressure on the piston of the syringe, the tracer introduction is more likely to be along a line inside the column rather than at only one specific point. Unfortunately, the extent of the tracer injection distribution along this line is controlled by the unknown hydrodynamics in the vicinity of the injection point. Thus, it is not realistically possible to *a priori* obtain a precise estimate of tracer injection dynamics.

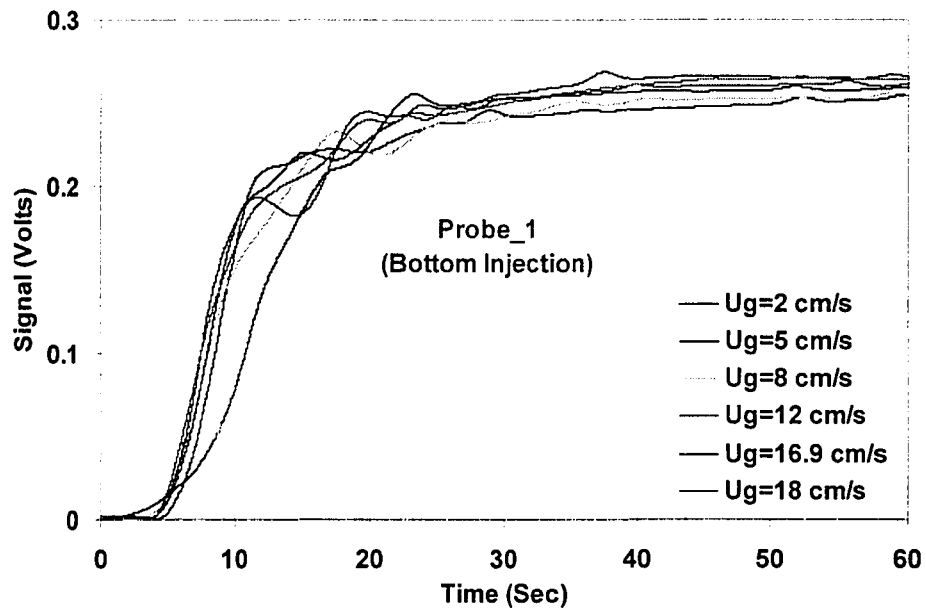


Note: Vertical distance between each port is 12".

Figure 3-13. Sketch of experimental setup of bubble column with no trays.

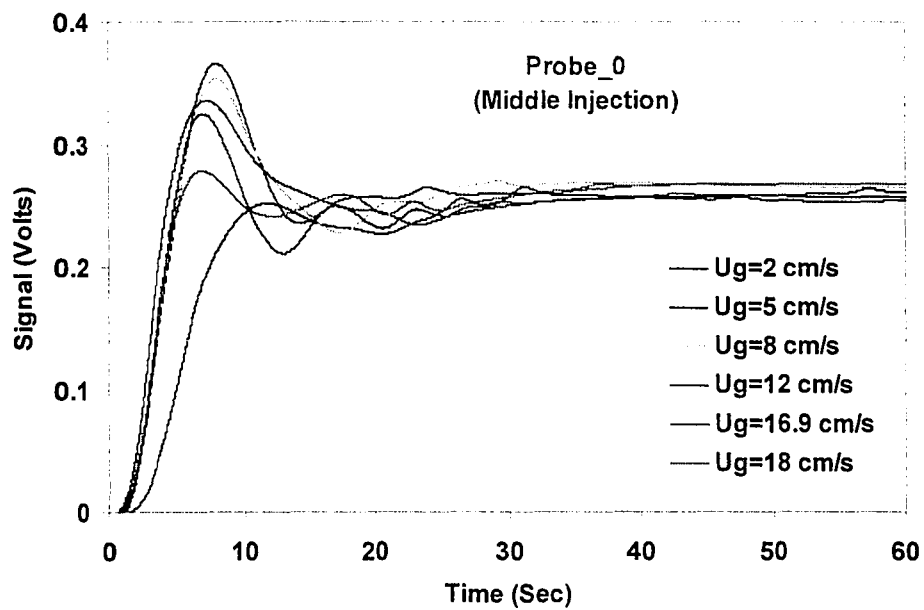


(a)

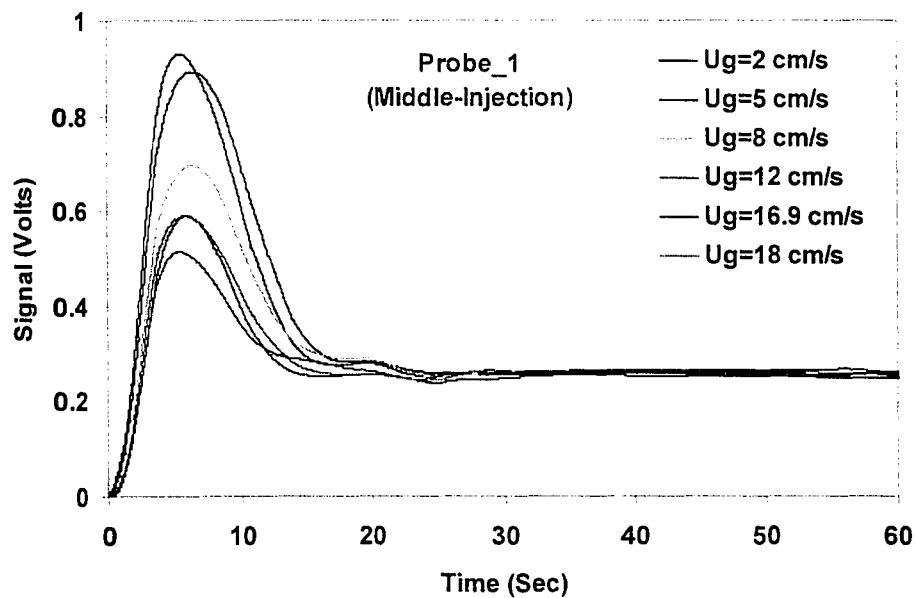


(b)

Figure 3-14. Liquid tracer responses as a function of gas superficial velocity for the bottom tracer-injection location. a) Probe_0 b) Probe_1



(a)



(b)

Figure 3-15. Liquid tracer responses as a function of gas superficial velocity for the middle tracer-injection location. a) Probe_0 b) Probe_1

For the bottom injection location (refer to Figure 3-14), the tracer in its sojourn from the injection point towards the probes located in the center of the column arrives at Probe_0 earlier than Probe_1. This is to be expected since the recirculatory flow of the liquid in a bubble column operation is known to have an upward flow in the center and downward flow near the wall. Other interesting feature to observe from Figure 3-14 is that by the time the tracer reaches Probe_1, it is fairly well-mixed resulting in the absence of the peak that is present in the tracer response registered by Probe_0. Additionally, with increasing gas superficial velocity, the extent of axial mixing increases as can be seen from the arrival time of the tracer pulse at the measurement locations (refer to Table 3-3).

For the middle tracer-injection location, it can be clearly seen from Figure 3-15 that because of the upward flow of the liquid in the column center, Probe_1 receives a clear impulse peak due to majority of the injected tracer being probably caught in the upward flowing liquid. Since the location of Probe_0 is below the tracer injection location, the portion of the peak pulse received by Probe_0 is a combined result of the liquid recirculation superimposed with eddy diffusion (Degaleesan, 1997). Because of the mixing of the tracer, its concentration gets diluted towards its steady value and thus the peak responses recorded by Probe_0 is significantly lower than those recorded by Probe_1. This can be clearly seen from the magnitude of the peak voltage responses of Probe_0 and Probe_1 reported in Table 3-3.

From the figures above, it can also be seen that for all the superficial gas velocities tested, the time to reach close to the steady state tracer levels is in the range of 20-30 seconds. However, the dynamics from the time of tracer injection to the time when tracer concentrations level off shows a clear dependency on the employed gas superficial velocity. Particularly for the superficial gas velocity of 5 cm/s, it can be seen that the peak in the observed response is larger than that for other gas velocities. This implies that mechanisms for mixing of the tracer are suppressed at this gas velocity which is generally considered to lie in the transition regime characterized by higher gas holdups and lower levels of axial and radial mixing (Degaleesan, 1997; Krishna, 2000^h).

Table 3-3. Peak response parameters resulting from impulse liquid-tracer injections in the bubble column without trays.

$U_{G,sup}$ (cm/s)	Bottom Injection (Probe_0)		Middle Injection (Probe_0)		Middle Injection (Probe_1)	
	$Response_{Peak}$ (Volts)	$Time_{Peak}$ (Sec)	$Response_{Peak}$ (Volts)	$Time_{Peak}$ (Sec)	$Response_{Peak}$ (Volts)	$Time_{Peak}$ (Sec)
2	3.38E-01	11.20	3.66E-01	7.93	8.92E-01	6.37
5	4.11E-01	9.50	2.52E-01	11.80	9.30E-01	5.47
8	3.82E-01	9.40	3.54E-01	7.90	6.96E-01	6.33
12	3.36E-01	9.00	3.36E-01	7.20	5.15E-01	5.40
16.9	3.82E-01	8.27	3.25E-01	6.97	5.91E-01	5.93
18	3.35E-01	7.93	2.78E-01	6.90	5.89E-01	5.80

3.9. Conclusions

A new filtering methodology has been developed to extract liquid phase tracer responses from conductance measurements obtained in two-phase gas-liquid systems undergoing turbulent bubbling. By properly choosing a cut-off frequency, and coupling that with the thresholding algorithm described above, one is able to extract reliable information from conductivity probe signals regarding liquid macro-mixing in gas-liquid media. The new filtering approach has been demonstrated through experimental measurements characterizing liquid mixing in a trayed bubble column operated with counter-current flow of gas and liquid. Further, the measurement and signal processing technique developed above was applied to study the effect of gas sparger design on the liquid mixing characteristics of the trayed column. It was found that sparger design had the most pronounced effect only for the lowest liquid superficial velocity employed and was independent of the employed range of gas superficial velocity. Additional investigation of the effect of staging using Computed Tomography has been reported elsewhere (Kemoun *et al.*, 2001^a).

To test the applicability of the filtering algorithm in high volume-fraction flows, an additional application of the developed algorithm was demonstrated by measuring

liquid-tracer responses in a churn-turbulent bubble column without trays. It was found that with increasing gas superficial velocity, the times for arrival of the peak response of the tracer as well as their magnitudes were in general reduced indicating a stronger recirculation implying faster mixing rates. A more quantitative analysis of the tracer curves presented in this work could be accomplished in the future either using simplified mixing models presented in Chapters 6 and 7 or employing full CFD calculations to capture details of the temporal three-dimensional evolution of the tracer. Here, the purpose was to demonstrate the suitability of the developed filtering algorithm at high gas velocities. Combined with the application of smaller probes with shorter response times than those for the probes employed in this study, this new filtering methodology opens the possibility of its use in many potential industrial and research applications.

Chapter 4. Monte Carlo Simulations of Scintillation Counting by Cylindrical NaI Detectors

In this chapter, an efficient computational scheme for surface integration over detector solid angles has been developed for calculation of NaI (Tl) detector efficiencies (Yang, 1997). The scheme, which is based on the Gauss-Legendre quadrature formulation, results in approximately 4-5 times reduction in computational costs as opposed to the traditionally employed Monte Carlo techniques using random sampling. The results from the developed scheme have been validated against previously published work of Beam *et al.* (1978). The scheme has been further extended, by coupling with a coordinate transformation procedure, to calculate detector efficiencies for cases when the point isotropic radioactive source is placed inside a vertical cylindrical vessel containing a liquid or a gas-liquid mixture. The simulation results show that the ratio of the photo-peak efficiency to total efficiency does not change significantly with or without the presence of the intervening medium between the point source and the detector. However, significant variations in the values of the peak-to-total efficiency ratio exist for different source positions relative to the crystal surface. This is an important result for non-invasive tracking of a radioactive particle which utilizes Monte Carlo simulations of detector efficiencies for obtaining, from the time series of tracer particle locations, the quantitative hydrodynamic information inside process vessels for both single as well as two-phase flows.

4.1. Introduction

Gamma-photon pulse detection using inorganic scintillation detectors is usually accomplished by employing NaI (Tl) detectors owing to their high scintillation efficiency (Tsoulfanidis, 1983). The most frequently used detector in photon counting systems is a right circular cylindrical crystal made of sodium iodide (NaI) doped with (Tl). The detectors used in most engineering applications are of 1", 2" and 3" in diameter depending on the particular application, with crystals of larger sizes being employed mostly for monitoring of astronomical radiation (Cameron *et al.*, 1991).

The pulse-detection efficiency of gamma-counting systems depends on the size of the scintillation crystal as well as the energy of the gamma-photons emitted by the source. In addition, the efficiency of detection also depends on the size and shape of the source as well as the intervening medium between the source the detector. Numerical estimation of these efficiencies in the absence of intervening media between the source and the detector has been usually accomplished using Monte Carlo methods (Tsoulfanidis, 1983; Beam *et al.*, 1978; Saito and Moriuchi, 1981). However, information on computation of detection efficiency in the presence of non-uniformly distributed intervening media is rare (Larachi *et al.*, 1994). In applications where the trajectory of a radioactive particle is tracked non-invasively, inside a usually non-transparent vessel with multiphase flow, with the aid of an array of scintillation detectors (Devanathan *et al.*, 1990; Devanathan, 1991; Degaleesan, 1997), the effect of temporally and spatially varying medium on detector efficiency must be estimated. Therefore one needs to devise efficient computation schemes for repetitive evaluation of detection efficiency in particle tracking experiments.

Beam *et al.* (1978) have discussed in detail the basic framework of the Monte Carlo simulation technique for the calculation of total and photopeak efficiencies of right-circular cylindrical NaI (Tl) detectors for arbitrarily located point isotropic sources emitting γ -rays. They show that Monte Carlo calculations can provide detector efficiencies at any specified energy, without resorting to tedious experiments. In this study, this basic framework has been extended to include the presence of non-uniformly

distributed intervening media such as the vessel walls, and the two or three phase mixture in the vessel. In addition, the numerical scheme has been modified to be more efficient by evaluating the surface integrals over detector solid angles using the Gauss-Legendre quadrature formulation (demonstrated originally by Moens *et al.* (1981) for calculation of detector solid angle) instead of the traditional random sampling based Monte Carlo integration. The traditional Monte Carlo based method for calculation of overall detector efficiencies in the presence of intervening media has been employed by Larachi *et al.* (1994). However, they have not included the calculation of photopeak efficiency in their implementation, as they estimate it from the ratio of photopeak to total efficiencies, which they assume to be a constant. It has been shown in this work that the assumption of a constant ratio of photopeak to total efficiencies, *for a fixed relative location of the point isotropic source with respect to the detector*, is well justified for engineering calculations (within a couple percent). However, the ratio does not remain constant for all locations of the point source in the vessel (with a 10-15 percent variation). In other words, the presence or absence of an intervening media does not alter the ratio significantly as long as the source and detector have the same relative positions.

4.2. Mathematical Formulation

The basic framework for this work is based on the study by Beam *et al.* (1978) that presented detailed calculations of detector efficiencies with no intervening medium between the source and the detector. Their development does not include the effects due to the cladding material encasing the scintillation crystal or the photo-multiplier mounting. Some researchers have shown that these effects may be significant when simulating the entire energy spectrum (Nardi, 1970; Steyn *et al.*, 1973; Saito and Moriuchi, 1981). However, if the interest is in simulating only the photo-peak portion of the energy spectrum, the results appear to be insensitive to the inclusion or non-inclusion of the effects of the cladding material in the simulations. This observation is in line with the findings from this work wherein the presence or absence of an intervening medium does not alter significantly the ratio of photopeak to total efficiencies. Therefore, for the

purposes of this work as well, the effects due to cladding and scintillator encasing have not been included in the mathematical formulation. In addition, only Compton and photoelectric interactions of the photons with matter are considered, and production of secondary electrons has been neglected. This implies that the photon energies should be less than 1.022 MeV. This holds true for the average photon energy of the radioactive source of interest to us in particle tracking experiments (Sc^{46}) and therefore, presents no limitation.

4.2.1. Monte Carlo Formulation

The Monte Carlo method consists of tracking a large number of photon histories from emission at the point isotropic source to absorption within the detector volume. Concepts from probability theory (random numbers) are combined with geometrical and transport considerations to locate the photon collision sites, as well as trajectory, energy and direction through each history. A photon history is terminated when either the weight of a scattering interaction (ratio of scattering to total cross-section) or the energy of the photon falls below a specified minimum (e.g. 10^{-10} or 0.01 MeV, respectively). As discussed by Beam *et al.* (1978), three variance reduction steps are employed during each history:

- Each γ -ray is forced to strike the detector.
- Each γ -ray is forced to interact within the bounds of the detector; *i.e.*, photons are not allowed to escape from the detector.
- Each interaction is forced to be a Compton scattering event.

Possibilities of bias due to these variance reduction techniques is eliminated by calculating the appropriate weights for each of the above forced events using well-defined physical and geometrical principles (Beam *et al.*, 1978). These variance reduction techniques coupled with the numerical random sampling experiments provide the detector efficiencies and solid angles as discussed below.

Total and Photopeak Efficiencies

The total and photo-peak efficiencies, respectively, for detection of photons of a given energy from a point isotropic source, can be evaluated by the following integrals:

$$T_{\epsilon} = \iint_{\Omega} \frac{\vec{r} \cdot \vec{n}}{r^3} f_a(\alpha, \theta) f_d(\alpha, \theta) ds \quad (4-1)$$

$$P_{\epsilon} = \iint_{\Omega} \frac{\vec{r} \cdot \vec{n}}{r^3} f_a(\alpha, \theta) f_p(\alpha, \theta) ds \quad (4-2)$$

In these expressions, f_a is the probability that a γ -ray photon reaches the detector surface, f_d is the probability that a γ -ray photon reaching the detector surface has an interaction with the detector crystal, f_p is the probability that this interaction is by photo-electric absorption, \vec{r} is the vector from the point γ -ray photon source to a point P on the exposed detector surface, \vec{n} is the external unit vector locally normal to the detector surface at the point P , ds is the differential area element around the point P , and Ω is the solid angle subtended by the active crystal volume on the point source (Refer to Figure 4-1).

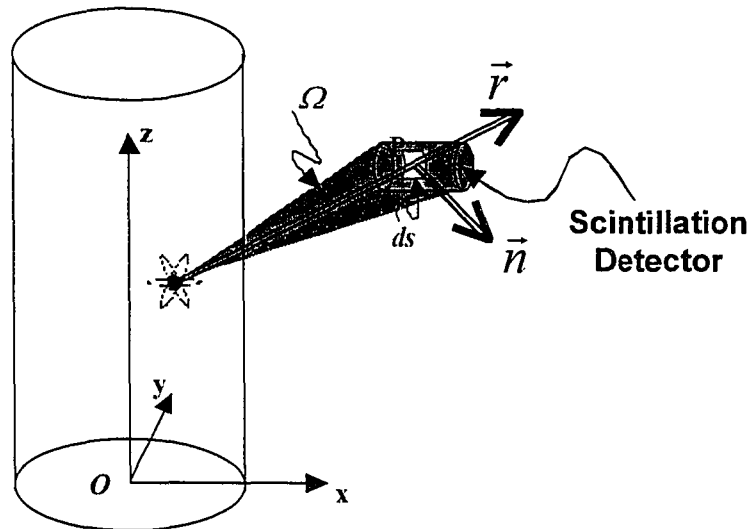


Figure 4-1. Graphical representation of the solid angle subtended by a scintillation detector on a point source for evaluating the surface integrals in Equations 4-1 and 4-2.

Traditional Monte Carlo methods of evaluating the above integrals are based on randomly sampling photon trajectories within the detector solid angle and calculating the average of the integrands (in Equations 4-1 and 4-2) over these samples. The computation of these surface-integrals using different approaches is discussed in detail in a later section. First, we address the evaluation of the various probability functions (f_a, f_d, f_p) appearing in above expressions, which account for the different interactions of the photons with the intervening medium as well as the scintillation crystal in its sojourn from the point isotropic source to the detector.

Photon Interaction with Media in the Vessel and Detector Crystal

The estimation of detector efficiencies takes into account the interaction of the photons with the vessel media and walls and is achieved by calculating the following probability functions:

- a) Probability that γ -rays emitted within Ω would not interact with the reactor media (liquid, gas-liquid, gas-liquid-solid mixture) and the reactor wall, f_a

$$f_a(\alpha, \theta) = \exp\left(-\sum_{i=1}^n \mu_i d_i(\alpha, \theta)\right) \quad (4-3)$$

where, μ_i is the total linear attenuation coefficient of the i^{th} material in the γ -ray path and d_i is the distance traveled by the γ -ray in the direction (α, θ) through the i^{th} material (vessel media, wall, insulation).

- b) Probability of interaction (Compton +Photoelectric) of gamma-rays, emitted within the solid angle, with the detector crystal, f_d

$$f_d(\alpha, \theta) = 1 - \exp(-\mu_d d_{eff}(\alpha, \theta)) \quad (4-4)$$

where, μ_d is the total linear attenuation coefficient of the detector crystal and d_{eff} is the distance traveled in the crystal by an undisturbed γ -ray in the direction (α, θ) .

- c) Probability that γ -rays emitted within the detector solid angle will have a photoelectric interaction with the detector crystal, f_p (Beam *et al.*, 1978)

$$\left. \begin{aligned} f_p &= w_1 \frac{\tau_1}{\mu_1} + \sum_{j=2}^{j=v} w_j \frac{\tau_j}{\mu_j} \prod_{i=2}^{i=j} w_{i-1} \frac{\sigma_{i-1}}{\mu_{i-1}} \\ w_j &= 1 - \exp(-\mu_j d_{eff.j}) \end{aligned} \right\} \quad (4-5)$$

where, w_i is equal to f_d , and d_{effj} is the distance traveled by a γ -ray inside the detector, μ_j is the total linear attenuation coefficient of the detector crystal, τ_j is the photoelectric linear attenuation coefficient of the detector crystal, and σ_j is the Compton linear attenuation coefficient of the detector crystal, all for the j^{th} Compton scattering event. Note that since μ_j , τ_j and σ_j are functions of the γ -ray energy, they have to be recomputed after each Compton interaction of the photon within the detector crystal. Details of the calculation of f_p using the Klein-Nishina differential scattering cross-section are provided elsewhere (Dunn and Gardner, 1972; Shultz and Faw, 1996).

Solid Angle

The calculation of the total and photopeak efficiency inherently requires integration over the solid angle, Ω , subtended by the detector on the location of the point isotropic source. The solid angle in these calculations is also usually calculated by the Monte Carlo method and is given as

$$\Omega = \frac{4\pi}{N} \sum_{i=1}^N W_i \quad (4-6)$$

where, N is the total number of photon histories and W_i the solid angle subtended by the i^{th} selection of angles α and θ (shown in Figure 4-2) and is given as

$$W_i = w(\theta)w(\alpha) \quad (4-7)$$

Angles α and θ are the horizontal and vertical angles which are chosen from rectangularly distributed random number as shown below. Two cases need to be

considered for the position of the point source relative to the detector when sampling the angles α and θ .

- A point source located as shown in Figure 4-2(a) so that the γ -ray photons can enter from the top as well as the side of the crystal.
- A point source located as shown in Figure 4-2(b) so that the γ -ray photons can enter only from top of the detector.

The horizontal angle α is derived from

$$\alpha = \alpha_{max} (2n - 1) \quad -\alpha_{max} \leq \alpha \leq \alpha_{max} \quad (4-8)$$

where n is a rectangularly distributed random number. On the other hand the vertical angle θ , which defines the angle along which the photon enters the detector, is chosen using another rectangularly distributed random number n' .

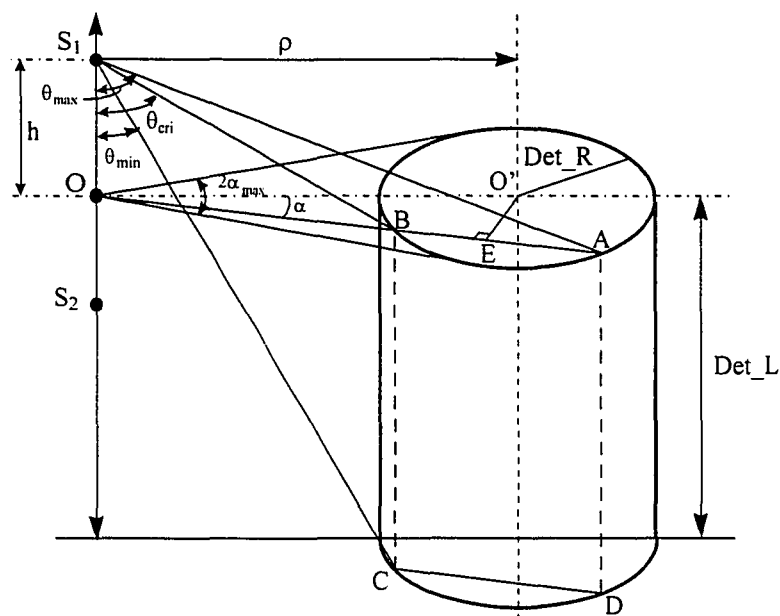
$$\theta = \cos^{-1} \left\{ \cos(\theta_{min}) - n' [\cos(\theta_{min}) - \cos(\theta_{max})] \right\} \quad (4-9)$$

The weighting factors, $w(\alpha)$ and $w(\theta)$, for this selection of α and θ are given by

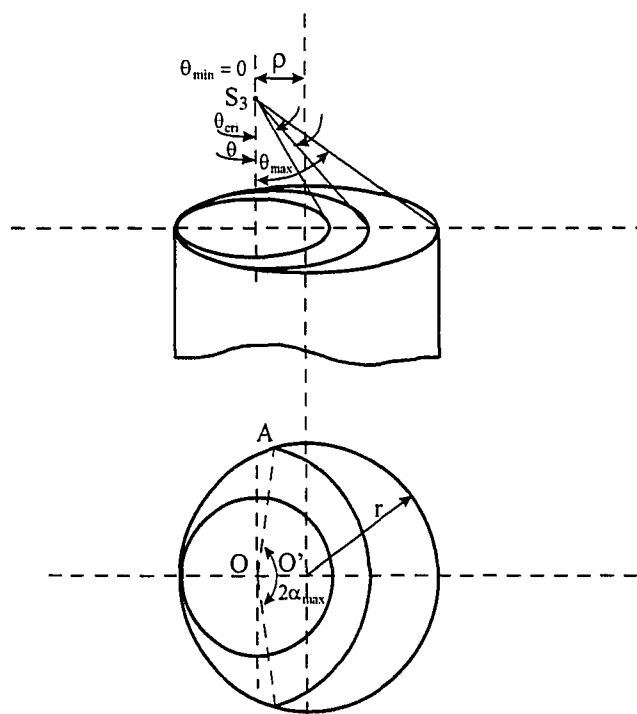
$$w(\alpha) = \int_{-\alpha_{max}}^{\alpha_{max}} \frac{d\alpha}{2\pi} \bigg/ \int_0^{2\pi} \frac{d\alpha}{2\pi} \quad \Rightarrow \quad w(\alpha) = \frac{\alpha_{max}}{\pi} \quad (4-10)$$

$$w(\theta) = \int_{\theta_{min}}^{\theta_{max}} \frac{\sin\theta}{2} d\theta \bigg/ \int_0^{\pi} \frac{\sin\theta}{2} d\theta \quad \Rightarrow \quad w(\theta) = \frac{\cos(\theta_{min}) - \cos(\theta_{max})}{2} \quad (4-11)$$

More details on estimation of α_{max} , θ_{min} , θ_{max} , and θ_{cri} are provided elsewhere (Beam *et al.*, 1978). Here, the focus is on the methodology for calculation of intersection points of a photon trajectory with the vessel walls and the needed coordinate transformations to achieve this efficiently.



(a)



(b)

Figure 4-2. Various possibilities of the relative orientation of the point source with respect to the detector surface (Beam *et al.*, 1978).

Coordinate Transformation Relative to Detector Coordinates

The angles α and θ , as described in Figure 4-2, need to be related to the direction cosines of the γ -ray path from the arbitrary tracer position inside the flow vessel to the entry point on the detector surface. This is necessary for determining the distance a γ -ray travels inside the vessel and through the vessel wall. Since the detector axis for all the detectors are perpendicular to the vessel axis, axes rotations and transformations are implemented to make these calculations tractable.

The origin of the initial coordinate system is the center of the bottom of the vessel, with z -axis in the vertically upward direction along the length of the column, and the x - y plane forming the horizontal cross-section of the column. For any particle position (x_p, y_p, z_p) inside the vessel and detector location (x_c, y_c, z_c) outside the vessel, the following axis rotations and transformations are performed:

First Coordinate Transformation

As shown in Figure 4-3(a), the first transformation is a rotation in the x - y plane by an angle ω' to make the detector axis parallel to the new x' -axis:

$$\omega' = \begin{cases} \tan^{-1}\left(\frac{y_c}{x_c}\right) & x_c > 0 \\ \frac{\pi}{2} & x_c = 0 \\ \pi + \tan^{-1}\left(\frac{y_c}{x_c}\right) & x_c < 0 \end{cases} \quad (4-12)$$

The particle and detector positions in the new coordinate system are (z coordinate remains unchanged):

$$x'_p = x_p \cos \omega' + y_p \sin \omega' \quad y'_p = -x_p \sin \omega' + y_p \cos \omega' \quad z'_p = z_p \quad (4-13)$$

$$x'_c = x_c \cos \omega' + y_c \sin \omega' \quad y'_c = 0 \quad z'_c = z_c \quad (4-14)$$

With this transformation, the distance h between the center of the detector face to the tracer location, and the radius ρ of the tracer from the detector axis are readily calculated:

$$h = |x'_c - x'_p| \quad \rho = \sqrt{(y'_c - y'_p)^2 + (z'_c - z'_p)^2} \quad (4-15)$$

The equations of the circles describing the inside and outside perimeters of the vessel in the horizontal cross section remain the same as in the original coordinate system:

$$x'^2 + y'^2 = R_i^2 \quad \text{and} \quad x'^2 + y'^2 = R_o^2 \quad (4-16)$$

where, R_i and R_o are the vessel inner and outer radii, respectively.

Second Coordinate Transformation

The second transformation, as schematically depicted in Figure 4-3(b), is a rotation of the coordinates in the y' - z' plane by an angle ω'' to make the projection of the 3-D line (x'_p, y'_p, z'_p) to (x'_c, y'_c, z'_c) on y' - z' plane parallel to the new z'' -axis:

$$\omega'' = \begin{cases} \tan^{-1} \left(\frac{y'_c - y'_p}{z'_c - z'_p} \right) & z'_c \neq z'_p \\ \frac{\pi}{2} & z'_c = z'_p \end{cases} \quad (4-17)$$

The particle and detector positions in the new coordinate system are (x' coordinate remains unchanged):

$$x''_p = x'_p \quad y''_p = -z'_p \sin \omega'' + y'_p \cos \omega'' \quad z''_p = z'_p \cos \omega'' + y'_p \sin \omega'' \quad (4-18)$$

$$x''_c = x'_c \quad y''_c = -z'_c \sin \omega'' + y'_c \cos \omega'' \quad z''_c = z'_c \cos \omega'' + y'_c \sin \omega'' \quad (4-19)$$

The equations of the circles describing the vessel perimeters in the new coordinate system now become:

$$x''^2 + (z'' \sin \omega'' + y'' \cos \omega'')^2 = R_i^2 \quad \text{and} \quad x''^2 + (z'' \sin \omega'' + y'' \cos \omega'')^2 = R_o^2 \quad (4-20)$$

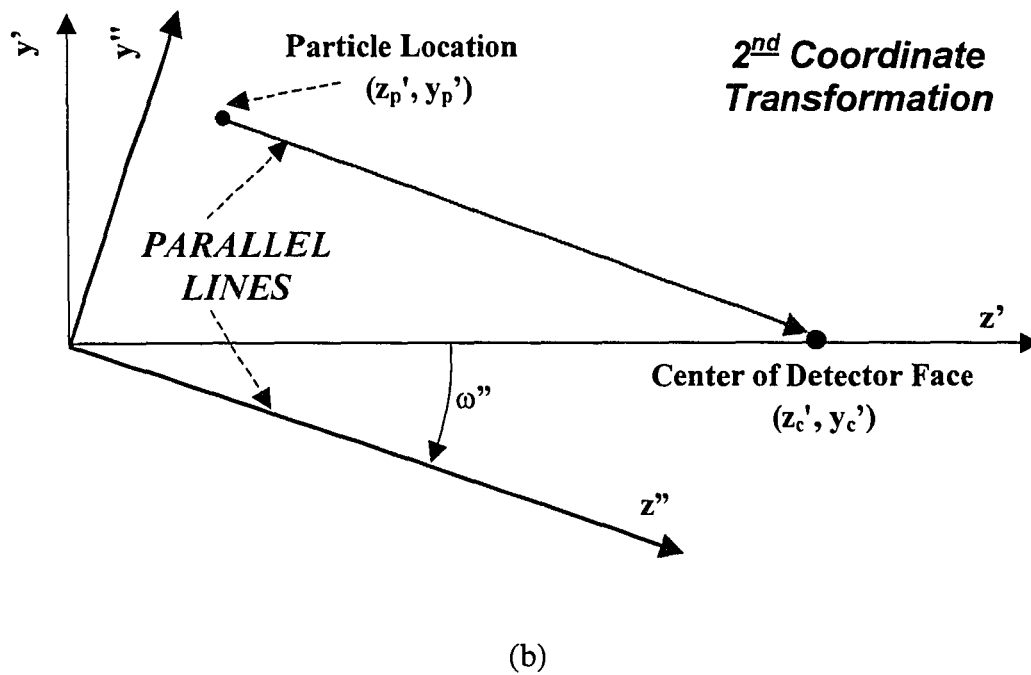
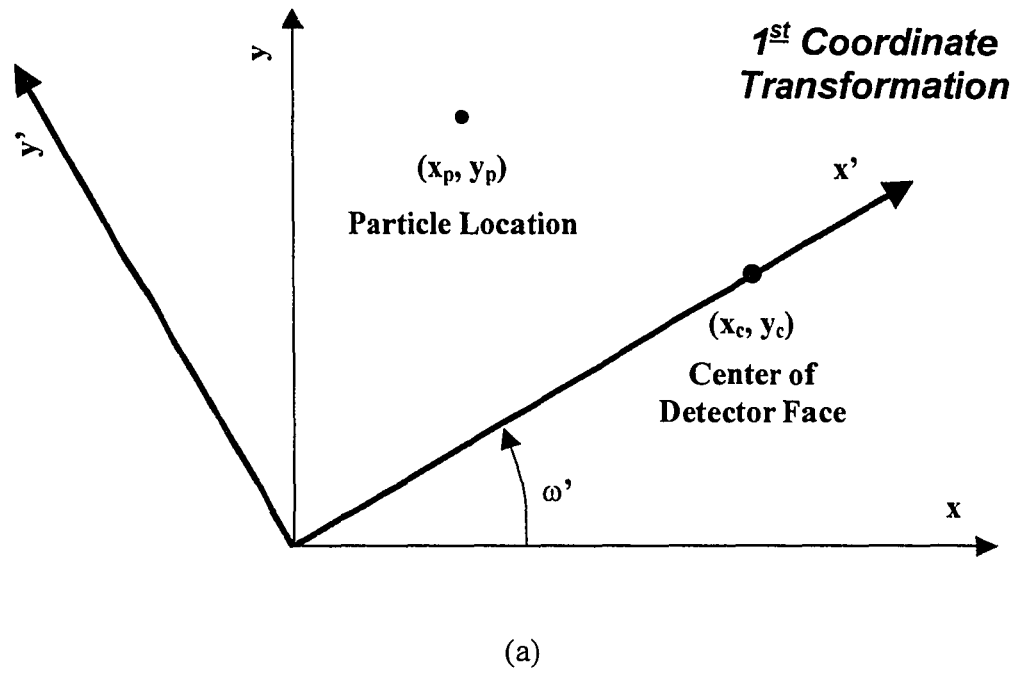


Figure 4-3. Schematic describing coordinate transformations required in the calculation procedure a) First Coordinate Transform b) Second Coordinate Transform.

The direction cosines ($\cos \alpha''$, $\cos \beta''$, $\cos \gamma''$) of the γ -ray path from an arbitrary location of the point isotropic source to the entry point on the detector can now be related to the angles α and θ (from the detector point of view) by:

$$\cos \alpha'' = \cos \theta_1, \quad \cos \beta'' = \sin \theta_1 \sin \alpha, \quad \cos \gamma'' = \sin \theta_1 \cos \alpha$$

$$\text{where } \theta_1 = \begin{cases} \theta & z_p'' \leq z_c'' \\ \pi - \theta & z_p'' > z_c'' \end{cases} \quad (4-21)$$

Therefore, the equation of the line from the point source to the point of γ -ray entry into the detector for a particular choice of α and θ becomes:

$$x'' = x_p'' + t \cos \alpha'' \quad y'' = y_p'' + t \cos \beta'' \quad z'' = z_p'' + t \cos \gamma'' \quad (4-22)$$

where, t is the parameter defining the line in 3-D space.

These linear equations are solved along with the circle equations for the vessel inside and outside perimeters to obtain the intersection points with the vessel inner and outer diameters (ID & OD). Substitution of these linear equations (Equations 4-22) into the circle equations (Equation 4-20) results in quadratic equations in t , which are readily solved. With known values of t , the intersection points of the line between the source and the detector with the vessel inner and outer walls are evaluated. There are two intersection points for each circle equation. The one close to the detector is the true solution, whereas the other is discarded. The distance traveled by the γ -ray through the media inside the vessel, d_r and through the vessel wall, d_w are then determined by the source position and intersection points, i.e.

$$d_r = \sqrt{(x_p'' - x_{id}'')^2 + (y_p'' - y_{id}'')^2 + (z_p'' - z_{id}'')^2} \quad (4-23)$$

$$d_w = \sqrt{(x_p'' - x_{od}'')^2 + (y_p'' - y_{od}'')^2 + (z_p'' - z_{od}'')^2} - d_r \quad (4-24)$$

In the above equations, $(x_{id}'', y_{id}'', z_{id}'')$ is the intersection point with the vessel ID, whereas $(x_{od}'', y_{od}'', z_{od}'')$ is the point of intersection with the vessel OD. With d_r and d_w known, the probability of non-interaction of a particular γ -ray photon history is readily calculated using Equation 4-3. Other details on following the photon history during its sojourn through the detector crystal are the same as presented by Beam *et al.* (1978). This process

of calculating the intersection points of the photon trajectory is repeated for each photon history, and the integrals evaluated for the total and photo-peak efficiencies.

4.2.2. Surface Integration over Detector Solid Angles

In this implementation of the numerical scheme for calculation of the detector efficiencies, instead of choosing the photon trajectories along random directions from a uniformly (rectangular) distributed random number (Beam *et al.*, 1978; Larachi *et al.*, 1994), the angles α and θ are chosen to correspond to the quadrature points of the Gauss-Legendre quadrature formulation. As mentioned earlier, the advantage of such an approach using Gauss-Legendre formulation was first demonstrated by Moens *et al.* (1981). However, their simulations were limited to calculation of the detector efficiencies from sources of finite geometrical dimensions, and the photopeak efficiencies were obtained with the aid of experimental data by assuming that the peak-to-total efficiency ratio is constant. In this work, the calculation of the photopeak efficiency has also been implemented and it is shown in subsequent sections that this approach using Gauss-Legendre quadrature results in an order of magnitude reduction in computational costs, with relative accuracy within a couple of percents. Computationally, this scheme is implemented as follows. If i corresponds to the α -coordinate and j to the θ -coordinate, then

$$x_g(i) = 2n - 1, \quad x_g(j) = 2n' - 1, \quad -1 \leq x_g(i) \leq 1, \quad -1 \leq x_g(j) \leq 1 \quad (4-25)$$

where, the two random numbers, n and n' (Equations 4-8 and 4-9), are replaced with quadrature points, $x_g(i)$ and $x_g(j)$, respectively. Table 4-1 lists the formulation developed in this work and compares it with those of Beam *et al.* (1978) and Larachi *et al.* (1994).

In the equations presented in Table 4-1, N is the total number of photon histories that are simulated for calculation of the detector efficiencies using the traditional Monte Carlo method employing uniform random sampling and may need to be as high as 10,000 to obtain accurate results. On the other hand in the computationally efficient scheme proposed in this work using Gaussian quadrature, N_g is the number of quadrature points

in each direction, with w_g being the quadrature weights, and can be as few as 10 for achieving reasonably accurate results. For more information and details on integration using Gauss-Legendre quadrature, the reader is referred to Press *et al.* (1992).

Table 4-1. Comparison of different numerical approaches.

^a Beam <i>et al.</i> (1978)	^b Larachi <i>et al.</i> (1994)
$\Omega = \frac{4\pi}{N} \sum_{i=1}^{i=N} w(\alpha_i, \theta_i)$	$\Omega = \frac{4\pi}{N} \sum_{i=1}^{i=N} w(\alpha_i, \theta_i)$
$T_c = \frac{1}{N} \sum_{i=1}^{i=N} w(\alpha_i, \theta_i) f_d(\alpha_i, \theta_i)$	$T_c = \frac{1}{N} \sum_{i=1}^{i=N} w(\alpha_i, \theta_i) f_a(\alpha_i, \theta_i) f_d(\alpha_i, \theta_i)$
$P_c = \frac{1}{N} \sum_{i=1}^{i=N} w(\alpha_i, \theta_i) f_p(\alpha_i, \theta_i)$	
This Work	
$\Omega = \pi \sum_{i=1}^{i=N_g} \sum_{j=1}^{j=N_g} w_g(i) w_g(j) w(\alpha_i, \theta_j)$ $T_c = \frac{1}{4} \sum_{i=1}^{i=N_g} \sum_{j=1}^{j=N_g} w_g(i) w_g(j) w(\alpha_i, \theta_j) f_a(\alpha_i, \theta_j) f_d(\alpha_i, \theta_j)$ $P_c = \frac{1}{4} \sum_{i=1}^{i=N_g} \sum_{j=1}^{j=N_g} w_g(i) w_g(j) w(\alpha_i, \theta_j) f_a(\alpha_i, \theta_j) f_p(\alpha_i, \theta_j)$	

^a Effect of intervening media not considered

^b No calculation of photopeak efficiency

4.3. Results and Discussion

The developed numerical scheme as described above has been implemented for calculation of detector efficiencies and solid angles for crystals of three different sizes commonly employed in most applications. The effect of the presence of intervening media between the point source and the detector crystal has also been investigated by considering the point source to be present inside a vertical cylindrical vessel made of stainless steel. Two different media density-distributions have been examined by

considering the column to be either full of water, or having an axisymmetric two-phase distribution of air and water inside the column. The column considered has an internal diameter (ID) of 16.152-cm (6.36”) and an outside diameter (OD) of 16.827-cm (6.625”) with the column wall material having a density of 7.847 gm/cm³. Specific details regarding accuracy of computations, code validation and effect of intervening media on detector efficiencies are discussed in the following sub-sections. Some additional detector quantities, reported in this section but not prescribed in earlier sections, are defined below.

Normalized Solid Angle

$$\Omega^* = \frac{\Omega}{4\pi} \quad (4-26)$$

Intrinsic Total Efficiency

$$T_\epsilon^* = \frac{T_\epsilon}{\Omega^*} \quad (4-27)$$

Intrinsic Photopeak Efficiency

$$P_\epsilon^* = \frac{P_\epsilon}{\Omega^*} \quad (4-28)$$

Photopeak to Total Efficiency Ratio

$$\phi = \frac{P_\epsilon^*}{T_\epsilon^*} = \frac{P_\epsilon}{T_\epsilon} \quad (4-29)$$

4.3.1. Accuracy of surface integration with number of quadrature points

The effect of the number of quadrature points used in each direction to accomplish the surface integration over the detector solid angles is shown in Figures 4-5 and 4-7 for source positions in the r - θ and r - z planes, respectively. The point source locations and the intervening media density distribution used for studying the effect of the number of quadrature points are shown in Figure 4-4 for the r - θ plane and in Figure 4-6 for the r - z plane. These points were chosen so as to be representative of the source locations anywhere inside the vessel, since during a particle tracking experiment, the

tagged tracer particle could visit any portion in the vessel along with the flow. The relative percent error reported in Figures 4-5 and 4-7, in calculating a given quantity for a certain number of quadrature points, is defined as:

$$Relative \% Error_x(N_g) = \frac{X(N_g) - X(N_g = 200)}{X(N_g = 200)} \times 100 \quad (4-30)$$

For analysis of computational accuracy with source locations in the $r-\theta$ plane, one can see from Figure 4-5 that with just ten Gaussian quadrature points in each direction ($N_g=10$), the relative percent error is within $\pm 0.5\%$ in calculation of the solid angle as well as of the total detector efficiency. This is true in the presence as well as in the absence of an intervening medium. Thus, by tracking only a total of 100 photon histories, one can achieve the desired accuracy in the calculation of detector efficiencies. In contrast, a traditional Monte Carlo approach requires a minimum of 1000 histories, with 5,000-10,000 histories being typically employed (Beam *et al.*, 1978; Moens *et al.*, 1981). Therefore, with the use of quadrature integration, one achieves at least an order of magnitude gain in computational speed and an equivalent reduction in costs of solid angle computations. On the other hand, it requires forty Gaussian quadrature points in each direction ($N_g = 40$) are required for photopeak efficiency calculation to ensure that the relative percent error is within $\pm 4\%$ both in the presence or absence of the intervening medium. Compared to traditional Monte Carlo calculations for evaluating photopeak efficiencies, this method is at least 3-5 times more efficient (Beam *et al.*, 1978). The same conclusions can be drawn for analysis of the relative error in the $r-z$ plane, except for one point in the solid angle calculation where the error is about 1.8%. Therefore, based on this analysis, forty Gaussian points were used for calculation of all the results presented subsequently. It should be noted that the rate of reduction of the relative error with N_g for photo-peak efficiency is much slower as compared with the error reduction rates for the solid angle and total efficiencies. This is not surprising since the probability of photoelectric interaction of photons with NaI crystal is a result of the superposition of a number of random non-linear Compton scattering events which occur until either the photon energy is reduced to a specified value or the photon is scattered out of the crystal.

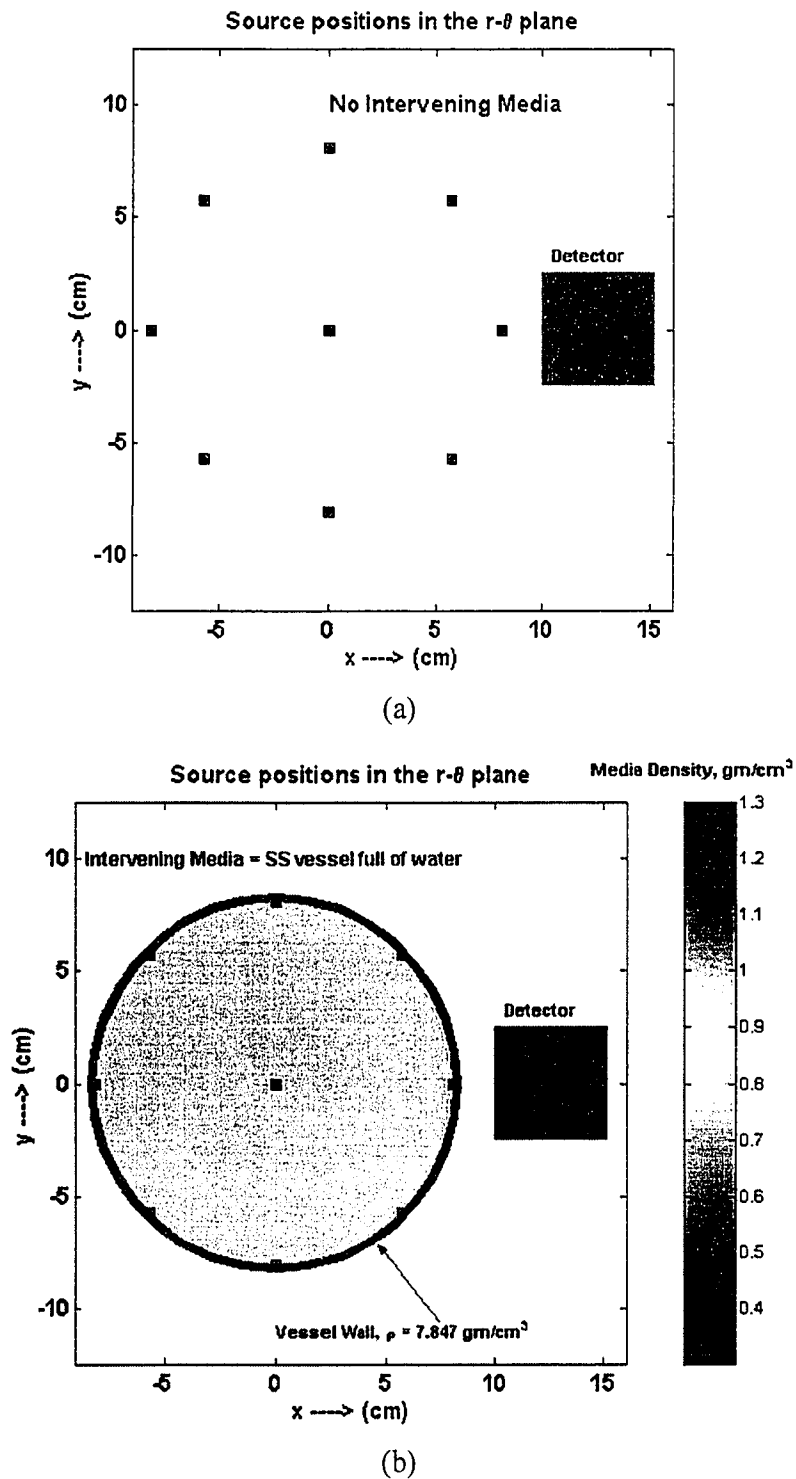


Figure 4-4. Distribution of source locations in r - θ plane for error analysis.

- a) Without media b) With intervening media of the shown density distribution

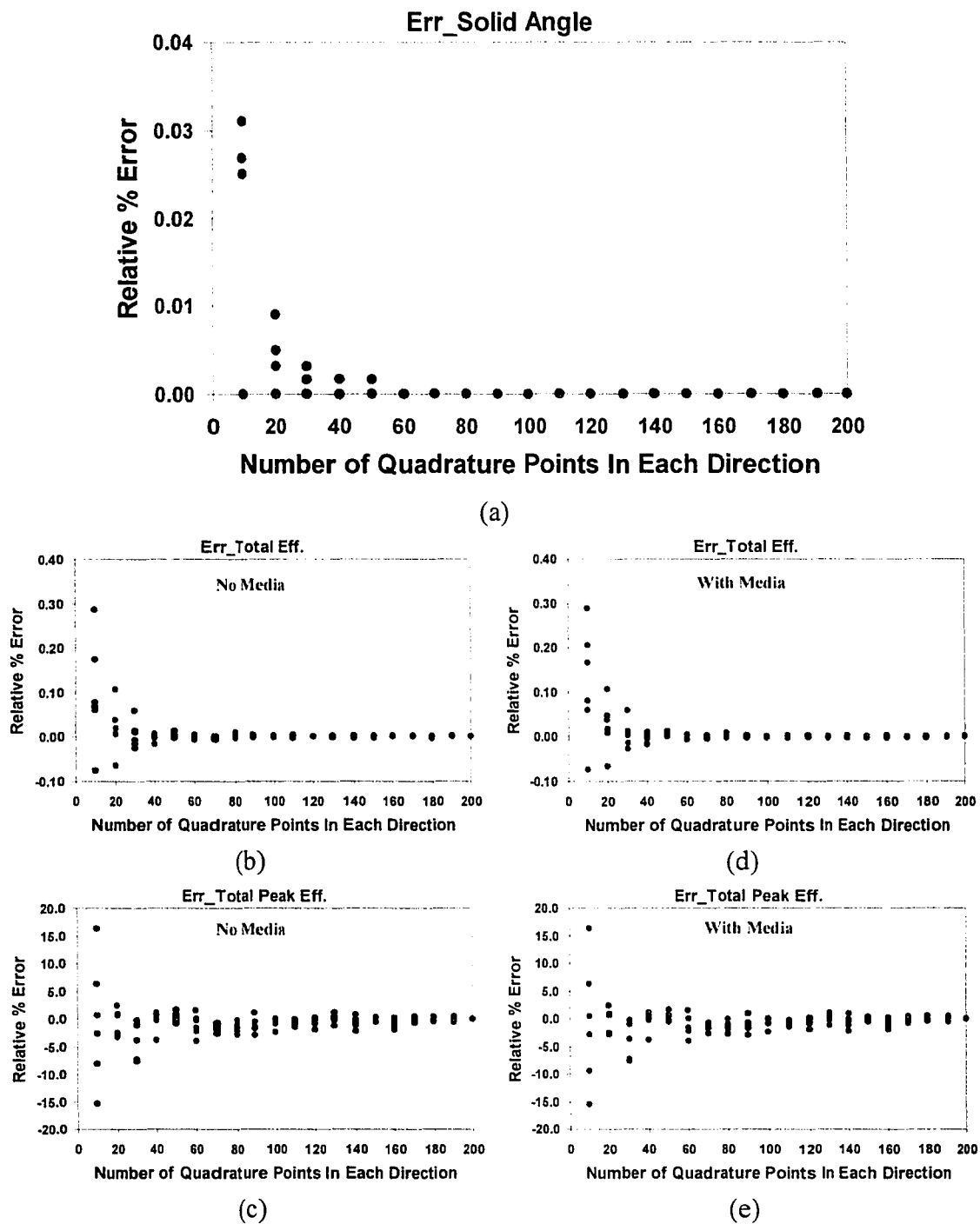


Figure 4-5. Variation of relative percent error for source positions in the $r-\theta$ plane.

- a) Solid Angle.
- b) Total Efficiency without Media.
- c) Total Photopeak Efficiency without Media.
- d) Total Efficiency with Media.
- e) Total Photopeak Efficiency with Media.

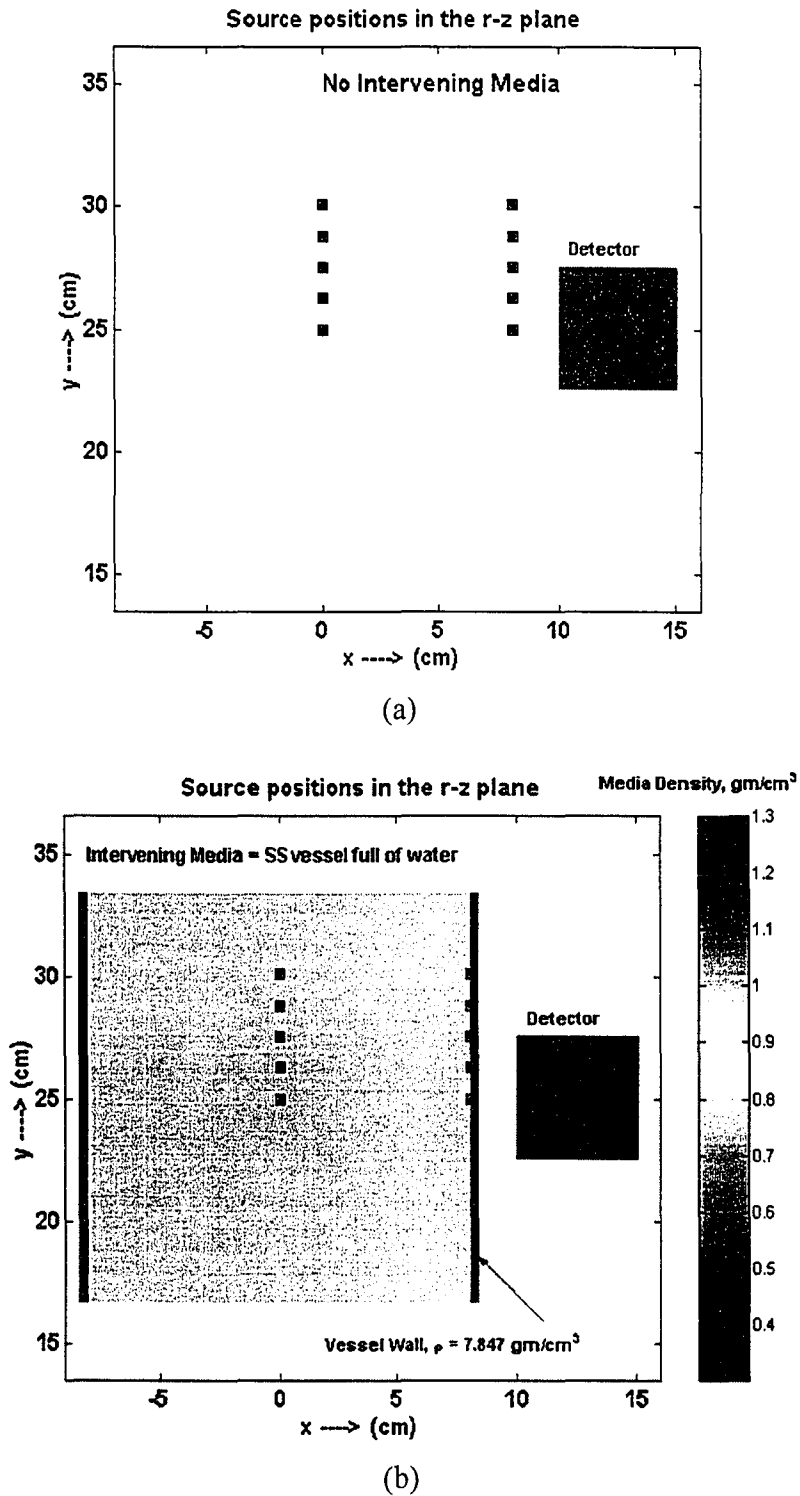


Figure 4-6. Distribution of source locations in r - z plane for error analysis.

- a) Without media b) With intervening media of the shown density distribution

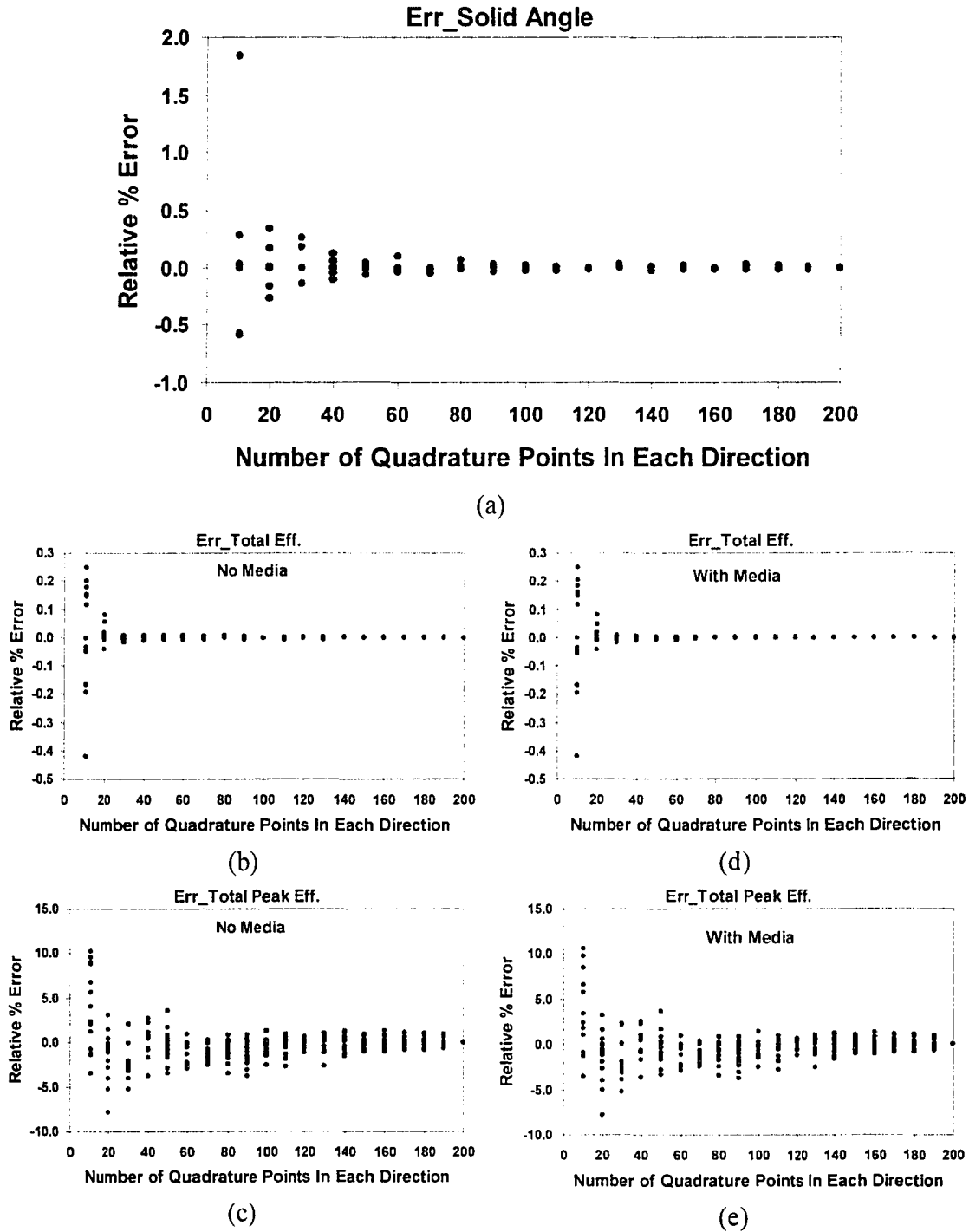


Figure 4-7. Variation of relative percent error for source positions in the r - z plane.

- a) Solid Angle. b) Total Efficiency without Media. c) Total Photopeak Efficiency without Media. d) Total Efficiency with Media. e) Total Photopeak Efficiency with Media.

4.3.2. Validation of the developed code against existing simulations

Figure 4-8 shows the comparison of the simulation results from this work with those of Beam *et al.* (1978) which were obtained using the classical Monte Carlo method for integration over detector solid angles. Figure 4-8a shows the total intrinsic efficiency of a 3"x3" crystal computed by both methods with the point isotropic source located on the detector axis at a distance of 10 cm from the detector circular face. Figure 4-8b displays the simulation results from the two methods for the photopeak-to-total efficiency ratio of a 2"x2" crystal with the point source again located on the detector axis at a distance of 15 cm from the circular face. From these two figures, one can see that the simulations from this work are consistent, with a maximum discrepancy of less than 5%, with those for the test cases available in the literature with a maximum discrepancy of less than 5 %.

4.3.3. Effect of crystal size

The efficiency of a photon counting system depends on the type and size of the employed detector crystal. The effect of the size of the scintillation crystal on the computed photopeak-to-total efficiency ratio, both in the presence as well as the absence of an intervening medium, is examined in Figure 4-9. From Figure 4-9a, one can see that the photo peak-to-total efficiency ratio is nearly independent of crystal size for low energy photons (100 keV), with larger crystals being more efficient as the crystal size increases. The simulations were carried out by placing a point source in the r - θ plane at the locations shown in Figure 4-4. Figure 4-9b shows the peak-to-total ratio for 1 MeV energy photons for the three crystal sizes in the presence and absence of the intervening medium. A significant result that emerges is that this ratio is practically independent of the presence or absence of the intervening medium between the source and the detector. Therefore, for calculations of photo-peak efficiency for a given source location when the intervening medium is changing in time (as would be the case when the point source is placed inside a two-phase flow field and the intervening medium is locally changing continuously), one does not require to repeat the calculation for photopeak efficiency.

Rather, to account for the changing intervening medium, one only needs to calculate the detector **total** efficiency repetitively, which is an order of magnitude cheaper calculation and then obtain the photopeak efficiency from the constancy of the peak-to-total ratio, which can be calculated a priori without the knowledge of the intervening medium. However, a peak-to-total ratio independent of the intervening medium, which is clearly seen in Figure 4-9b for all three crystal sizes, does not imply that the ratio is independent of the location of the source with respect to the detector as is evident from Figure 4-14.

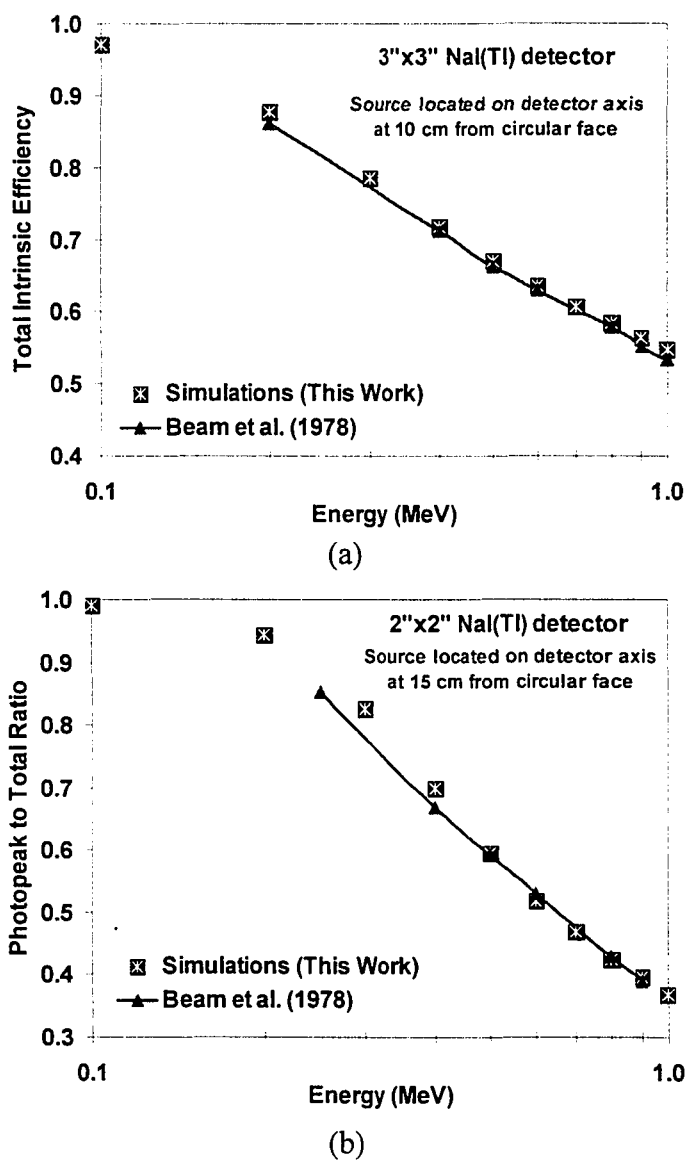
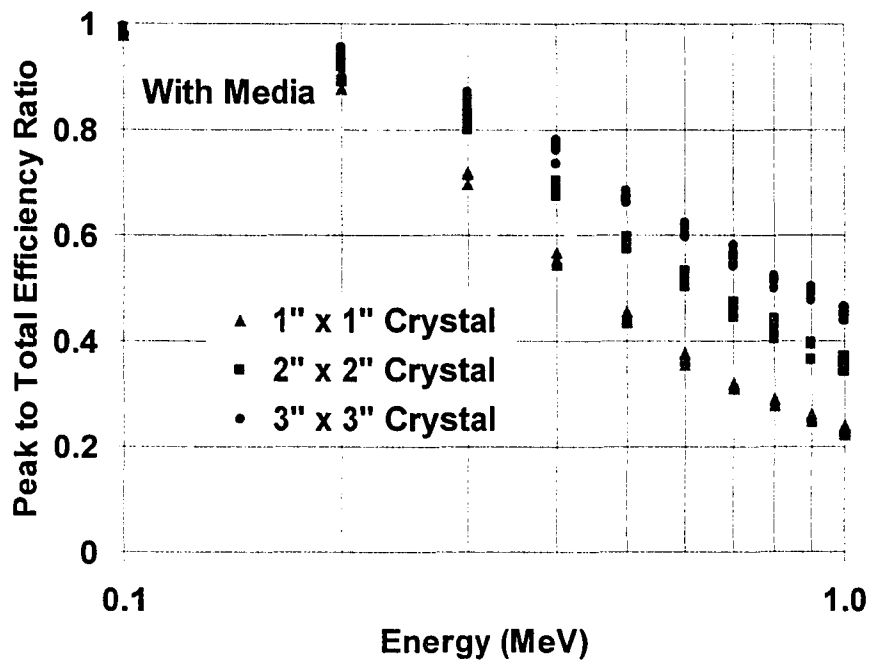
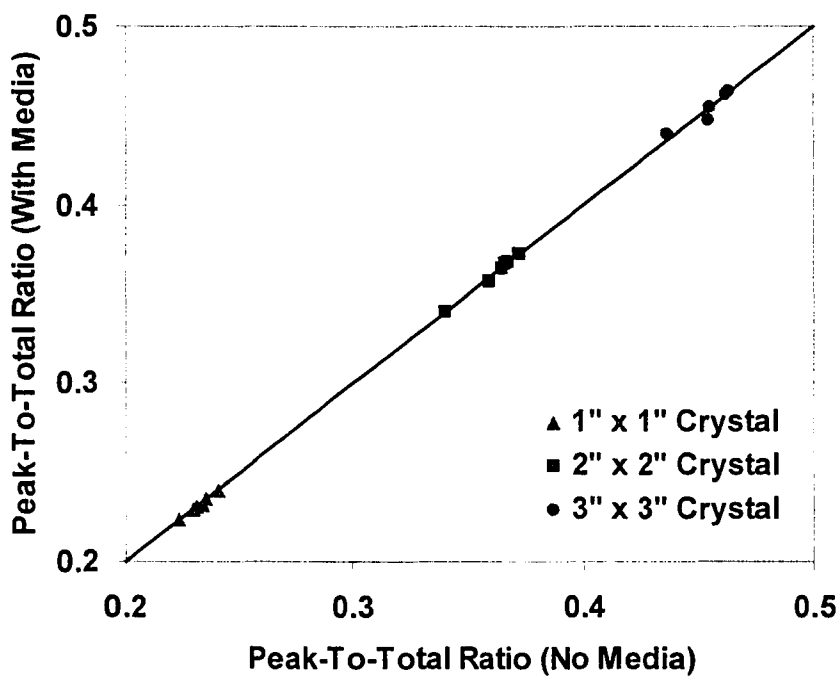


Figure 4-8. Comparison of simulated results from this work with those of Beam *et al.* (1978). a) Intrinsic Efficiency. b) Ratio of Photopeak to Total Efficiencies.



(a)



(b)

Figure 4-9. Dependency of peak-to-total efficiency ratio on crystal size.

a) Effect of photon energy.

b) Effect of intervening media

4.3.4. Effect of media density distribution

The simulation results presented thus far have only considered water as the medium in the vessel implying a constant density distribution inside the vessel. This would be representative of single-phase liquid flows. However, it is of interest to investigate the effect of a distributed media density on the simulated detector efficiencies, which is representative of multi-phase flows in process vessels. For this purpose, the stainless steel vessel mentioned earlier is considered to have a media density distribution as shown in Figure 4-10a for the r - θ plane with the same density distribution represented in the r - z plane as in Figure 4-11a. Figures 4-10b to 4-10f and 4-12a to 4-12f show the simulated detector efficiencies and solid angle for the source locations in the r - θ plane, while Figures 4-11b to 4-11f and 4-13a to 4-13f show the same for the source locations in the r - z plane. The simulations were carried out for photons of average energy 1.005 MeV with the detector being a 2"x2" NaI(Tl) crystal.

From the intrinsic total efficiencies computed in the absence of intervening media, as shown in Figures 4-10c and 4-11c, one can see the edge effects arising due to the finite size of the crystal and crystal boundaries. Figures 4-10c and 4-10e compare the distribution of the intrinsic **total** efficiency in the presence and absence of an intervening medium in the r - θ plane, while Figures 4-11c and 4-11e show a similar comparison in the r - z plane. Along the same lines, Figures 4-10d and 4-10f compare the distribution of the intrinsic **photopeak** efficiency in the presence and absence of an intervening medium in the r - θ plane, while Figures 4-11d and 4-11f show a similar comparison in the r - z plane. From these figures, it can be seen that the presence of an intervening medium has a major impact on the intrinsic total and photopeak efficiencies. Another interesting feature to be observed from the above figures is that the intrinsic detector efficiencies without an intervening medium are at a minimum for source locations right in front of the detector and increase as one moves away from the detector. This is due to the solid angle, which is inversely proportional to the intrinsic efficiencies (Equations 4-27 and 4-28). However, the inclusion of the media effect characterized by the presence of an axisymmetric distribution of density inside the vessel dramatically changes the distribution of intrinsic detector efficiencies as can be seen from Figures 4-10 and 4-11.

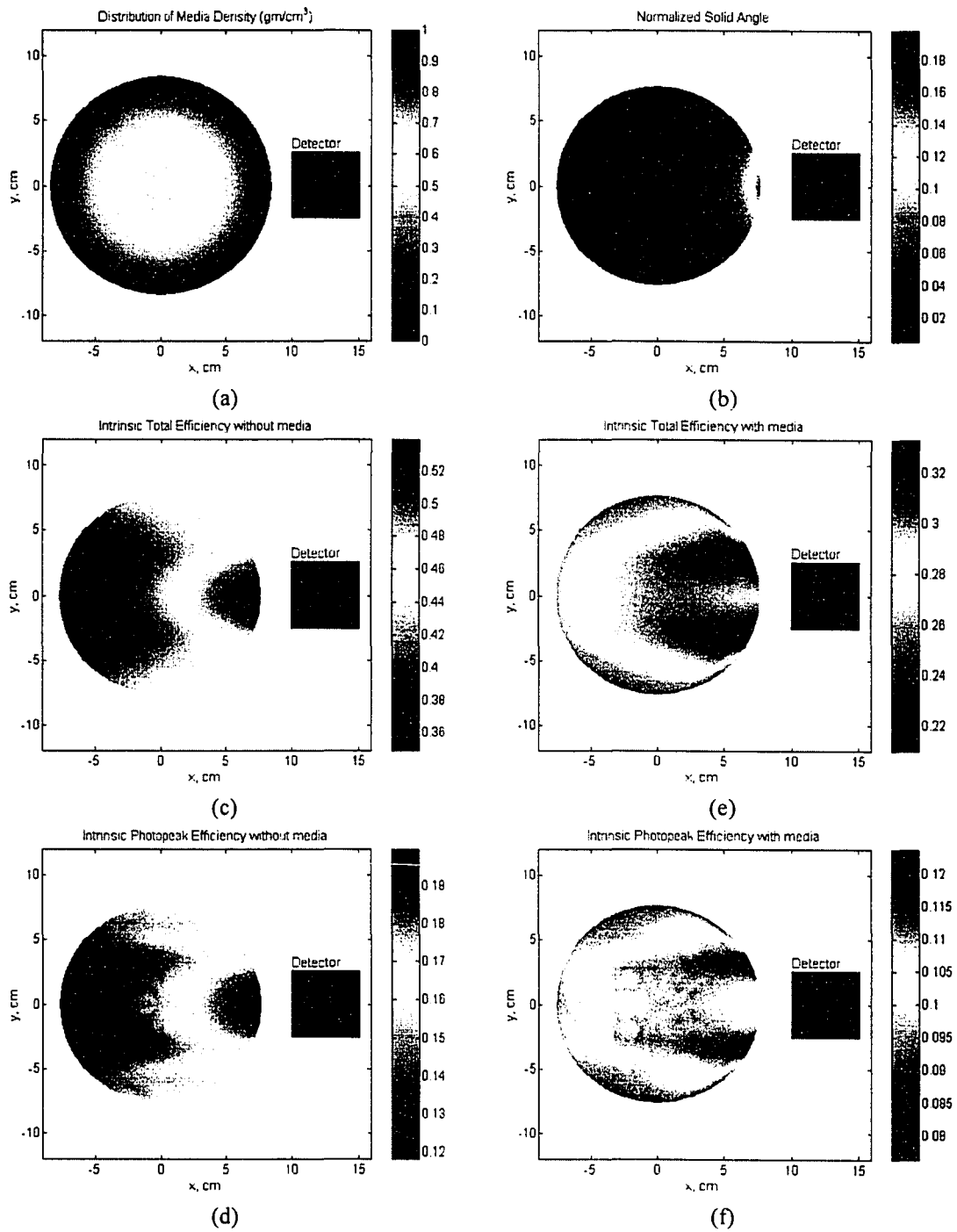


Figure 4-10. Simulation of a 2"x2" detector parameters for source positions in r - θ plane.

- a) Employed media density distribution. b) Solid angle.
 c) Intrinsic Total Eff. (No Media). e) Intrinsic Total Eff. (Media).
 d) Intrinsic Photopeak Eff. (No Media). f) Intrinsic Photopeak Eff. (Media)

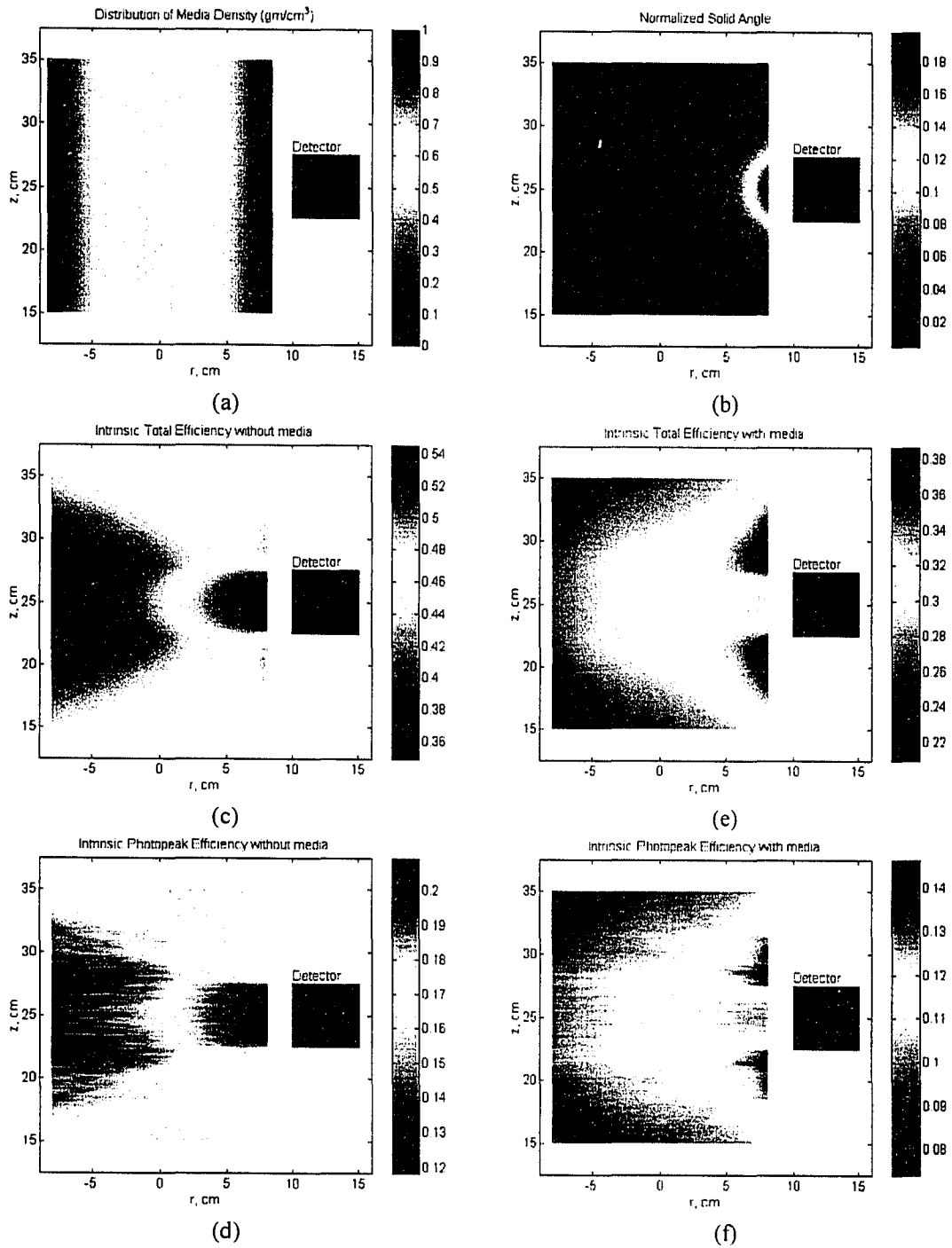


Figure 4-11. Simulation of a 2"x2" detector parameters for source positions in r - z plane.

- a) Employed media density distribution. b) Solid angle.
 c) Intrinsic Total Eff. (No Media). e) Intrinsic Total Eff. (Media).
 d) Intrinsic Photopeak Eff. (NoMedia). f) Intrinsic Photopeak Eff. (Media)

However, in photon counting systems, the quantities of greater interest are the detector absolute efficiencies, which include the effect of the solid angle. These are shown in Figures 4-12 and 4-13 for the r - θ and r - z planes, respectively. From Figures 4-12 and 4-13, the overwhelming effect of the solid angle is evident. Thus, all the intricate features observed in the intrinsic efficiency distributions (as shown in Figures 4-10 and 4-11) are all smeared out and both the total as well as the photopeak efficiencies exhibit the same distribution as the solid angle distribution, true for both the r - θ and r - z planes.

The most important outcome of these simulations is the result shown in Figures 4-12c, 4-12f, 4-13c and 4-13f. These figures represent the distribution of the photopeak-to-total efficiency ratio in the presence and absence of the intervening medium. As can be seen, this ratio is practically independent of the presence or absence of the intervening medium. More importantly, the peak-to-total efficiency ratio is not a constant for various source locations inside the vessel. This feature is shown in greater detail in Figures 4-14a and 4-14b for the source locations in the r - θ and r - z planes, respectively, which show a parity plot of the aforementioned ratio in the presence and absence of the intervening medium. It can be seen, that barring a few outliers, and for engineering purposes, the peak-to-total ratio in the r - θ plane is invariant to the intervening medium. There is, however, a significant variation (~ 10 - 12%) depending upon the specific location of the source in the in the r - θ plane. On the other hand, the result in the r - z plane shows a slight but noticeable skew ($\sim 1\%$) in the peak-to-total efficiency ratio values computed in the presence of the medium as compared to the ones with no intervening medium. However, for all practical purposes, this is negligible as compared to the more significant variation (~ 10 - 15%) that is observed for varying source locations in the r - z plane. The variation of the peak-to-total efficiency ratio with the distance between the detector face and source locations is further analyzed in Figure 4-15. From the figure, it can be seen that the peak-to-total efficiency ratio is lower for source locations closest to the detector. However, no clear trend is evident that could be expressed in terms of a readily identifiable mathematical function. This is true for source locations both in the r - θ and r - z planes as can also be seen from Figures 4-12c, 4-12f, 4-13c and 4-13f.

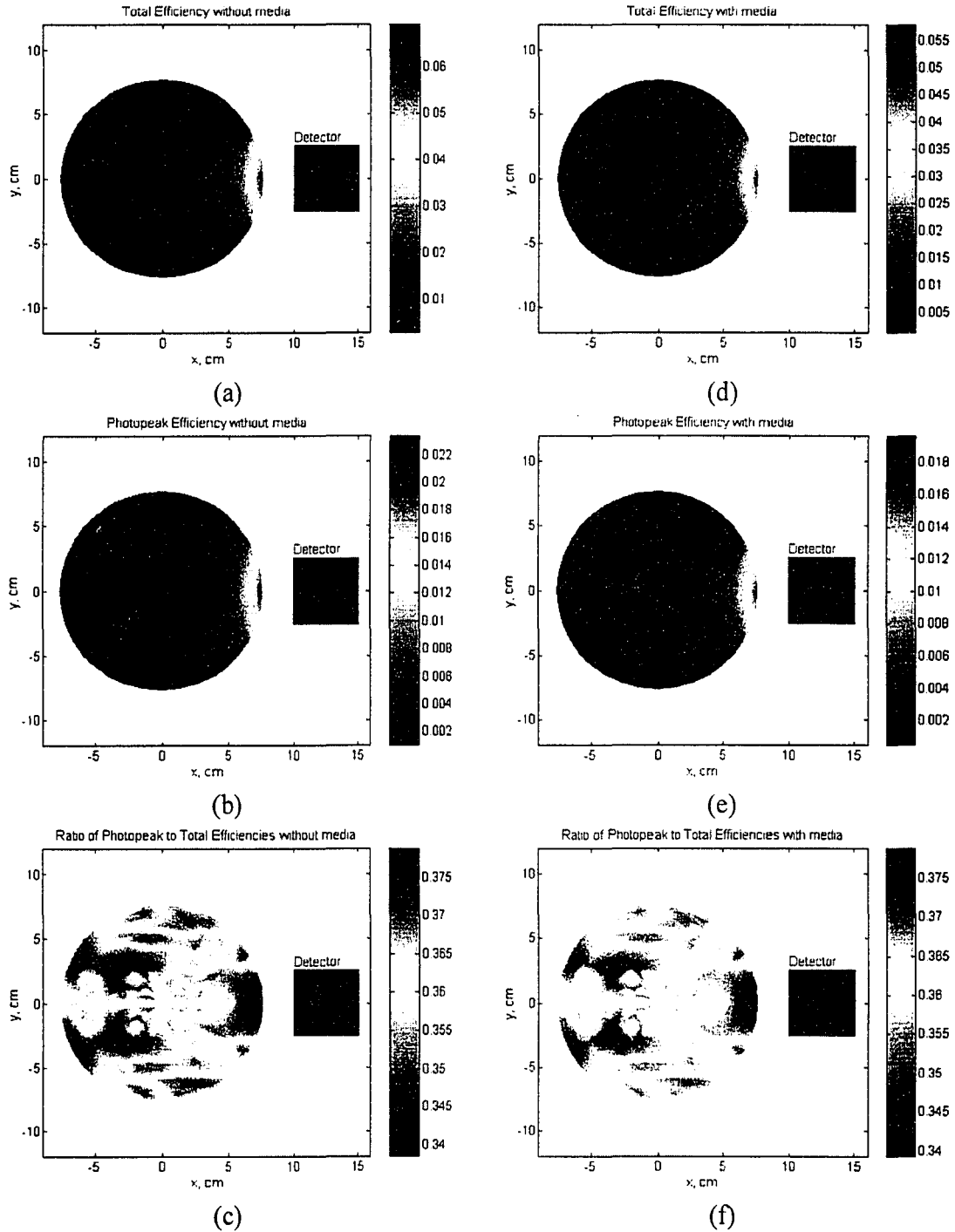


Figure 4-12. Simulation of a 2"x2" detector parameters for source positions in r - θ plane.

- a) Total Efficiency (No Media).
- b) Photopeak Efficiency (No Media).
- c) Photopeak to Total Ratio (No Media).
- d) Total Efficiency (Media).
- e) Photopeak Efficiency (Media).
- f) Photopeak to Total Ratio (Media).

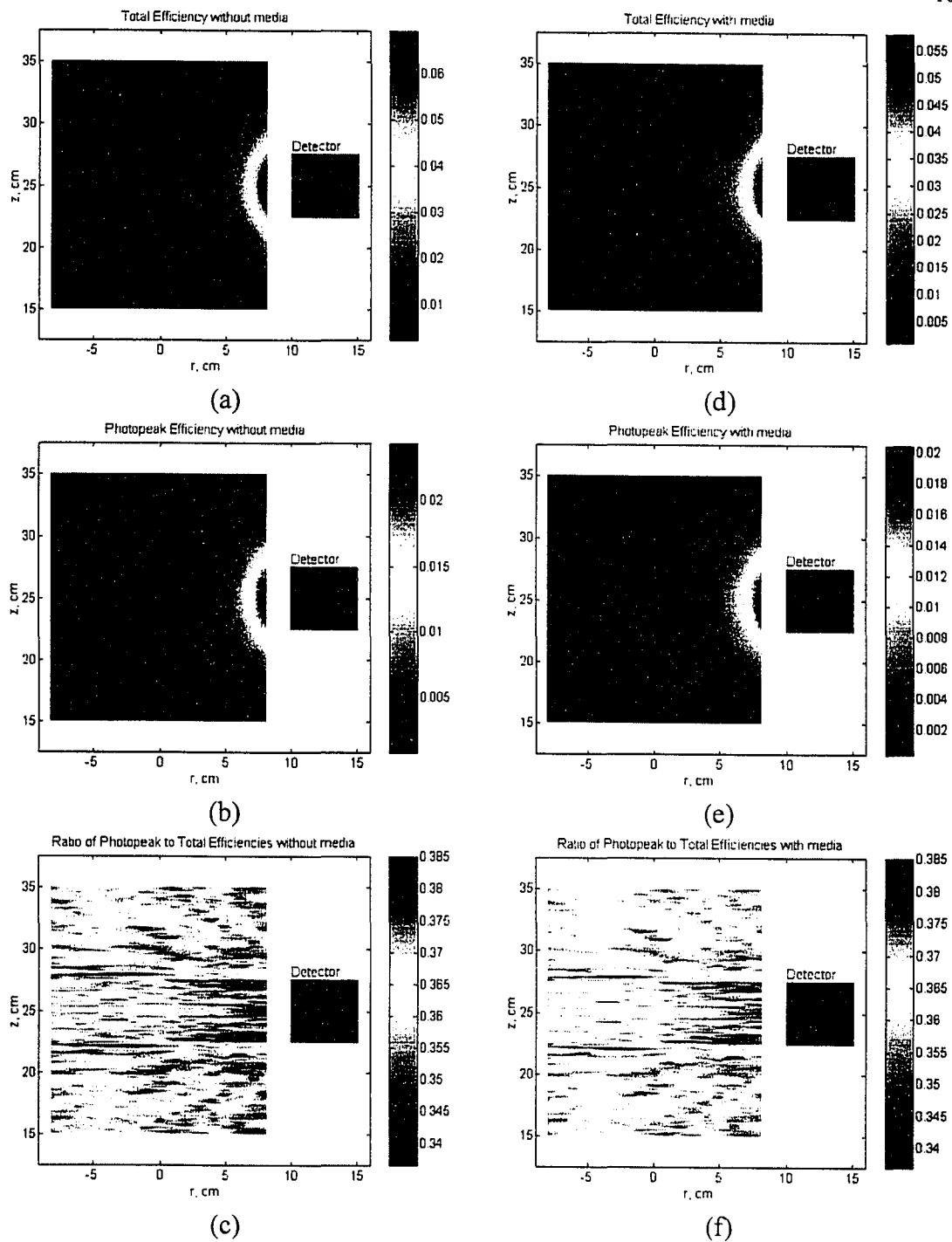
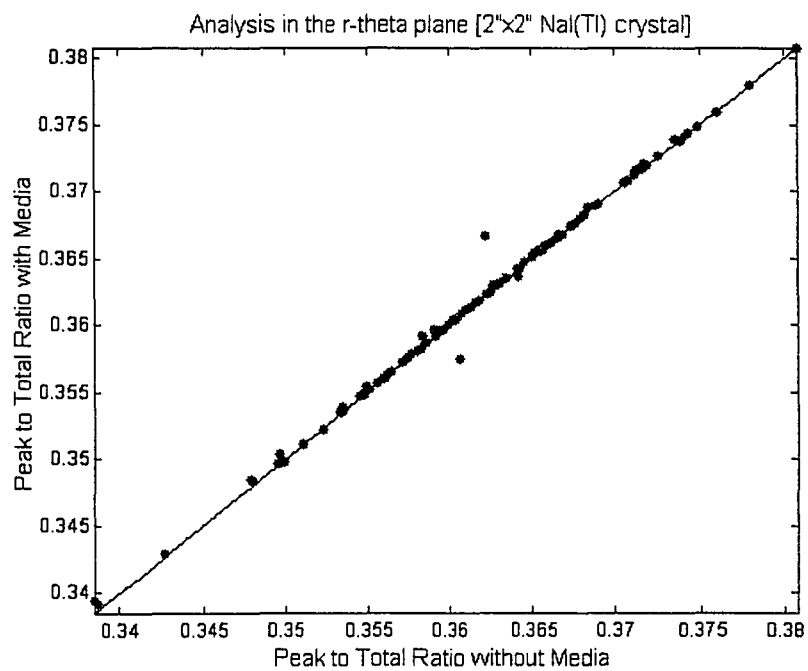
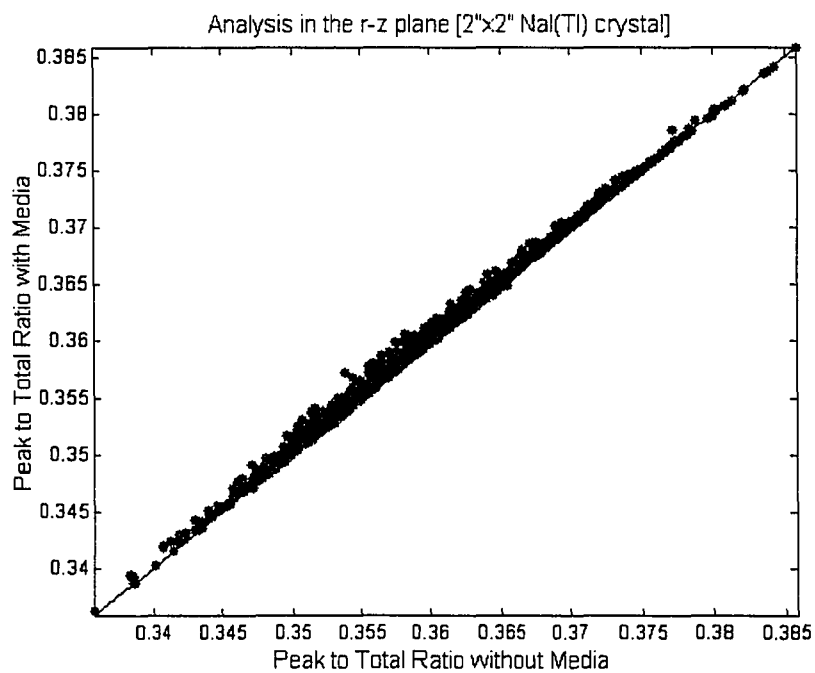


Figure 4-13. Simulation of a 2"x2" detector parameters for source positions in r - z plane.

- a) Total Efficiency (No Media). d) Total Efficiency (Media).
 b) Photopeak Efficiency (No Media). e) Photopeak Efficiency (Media).
 c) Photopeak to Total Ratio (No Media). f) Photopeak to Total Ratio (Media).



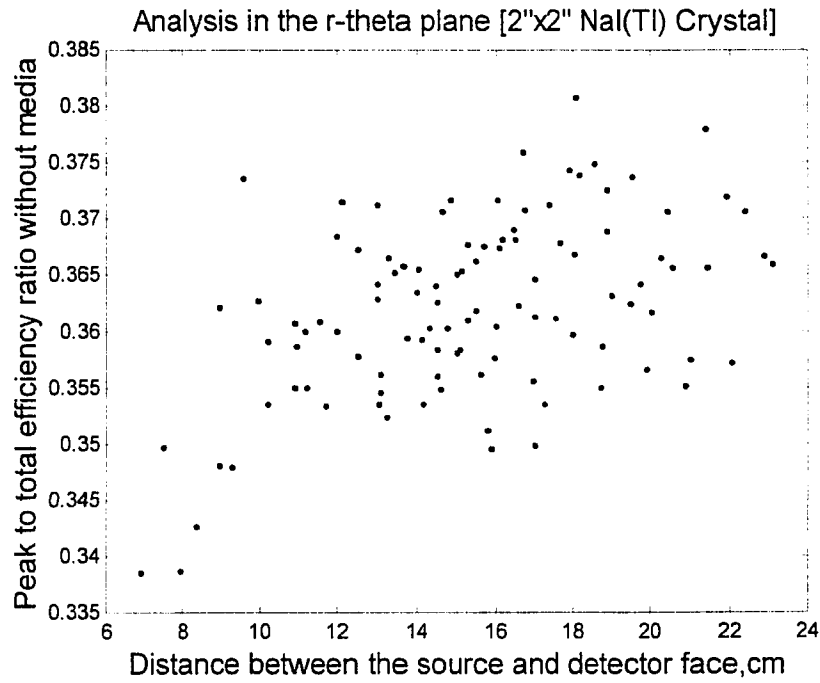
(a)



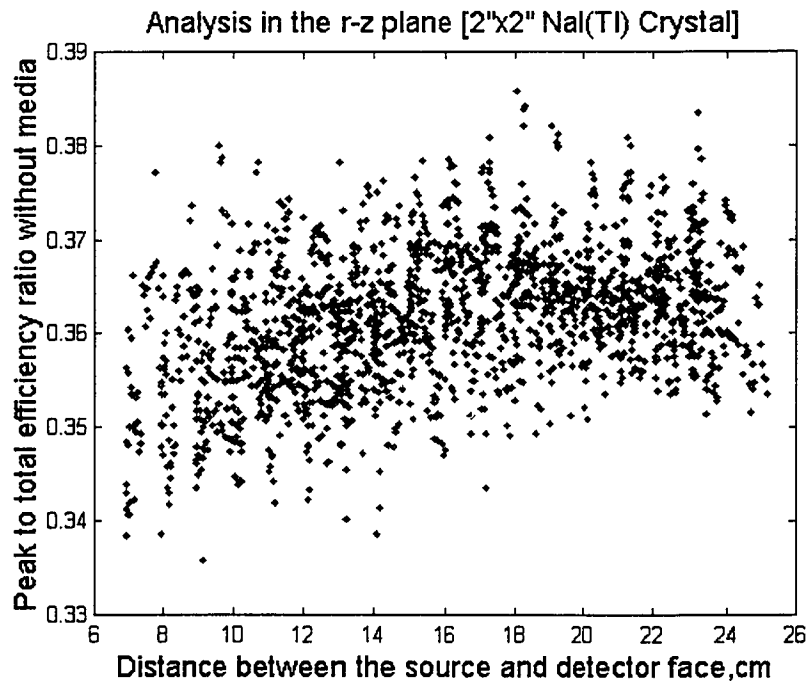
(b)

Figure 4-14. Comparison of Peak to Total Efficiency ratio with and without media.

a) In the r - θ plane.b) In the r - z plane.



(a)



(b)

Figure 4-15. Variation of Peak to Total Efficiency ratio with source-detector distance.

a) In the r - θ plane.b) In the r - z plane.

It should be recognized that this powerful computational tool could be employed for studying many other important variables like the effect of column wall density and thickness on the distance vs. counts calibration maps. This is particularly important when employing a stainless steel (SS) versus a Plexiglas bubble column to investigate bubble column hydrodynamics at high pressures. Figure 4-16 shows typical distance-counts calibration curves obtained in stainless steel and Plexiglas columns computed using the Monte Carlo simulation methodology developed in this chapter.

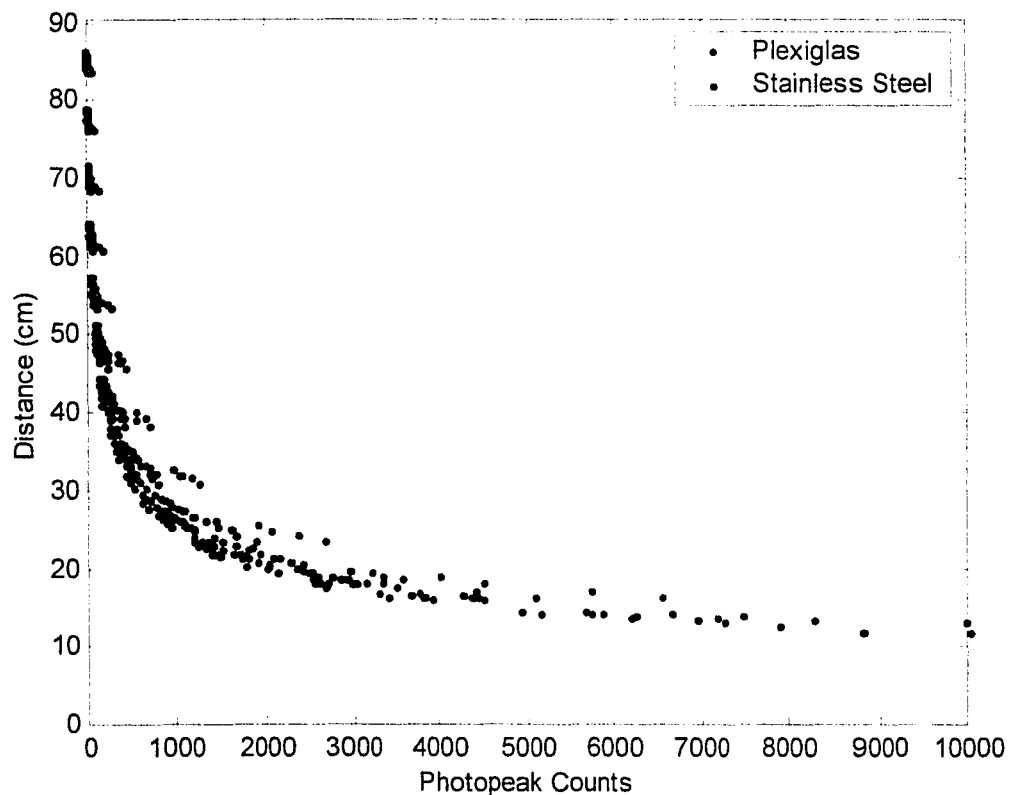


Figure 4-16. Distance vs. counts calibration curves as constructed in a traditional CARPT experiment simulated using the Monte Carlo method.

From Figure 4-16, it can be seen that the calibration curve from a 6" diameter stainless steel column does not exhibit a clear distinction in the counts registered by the

scintillator from calibration points in different axial planes. This however is not the case for the Plexiglas column where not only one can see layers of calibration points indicative of different axial levels (Degaleesan, 1997) but also that the counts are on an average about 15-20% higher than in Plexiglas column. The inability of the SS calibration curve to distinguish among various axial levels could cause problems in a traditional Computer Automated Radioactive Particle Tracking (CARPT) tracer-location reconstruction. Details of this reconstruction methodology have been presented elsewhere (Degaleesan, 1997) with Chapter 5 briefly describing the traditional CARPT methodology along with the Monte-Carlo based reconstruction methodology.

4.4. Conclusions

An efficient Monte Carlo scheme, based on multi-dimensional Gauss quadrature integration, has been developed and implemented for calculation of detector total and photopeak efficiencies for point isotropic sources present inside optically opaque systems for non-invasive tracking of a radioactive tracer particle. It is shown that the presented scheme results in at least an order of magnitude reduction in computing costs for the total detector efficiency with about 3-5 times reduction in computing photopeak efficiency. The developed scheme has been used to study the effect of crystal size and photon energies on the detector efficiencies. It is found that the peak-to-total efficiency ratio is independent of the intervening medium, but is a function of the source location with respect to the detector.

The conclusion about the independence of the peak-to-total efficiency ratio of the intervening medium is a crucial and valuable result for the purposes of non-invasive radioactive particle tracking in opaque multiphase systems. Since the phase distribution inside a vessel with multiphase flow is in general a temporally varying unknown, it is very difficult to estimate the exact instantaneous media density distribution along a photon path in its sojourn from the radioactive tracer particle to the scintillation detector. However, as shown in this study, the peak-to-total efficiency ratio calculation is independent of the media density distribution and thus can be evaluated *a priori* just

based on geometrical considerations. Moreover, the expensive computation of the photopeak efficiency, which has to be evaluated repetitively in a multi-detector particle tracking experiment, can now be replaced with a much cheaper, faster and accurate evaluation of only the total detector efficiencies. These developments and findings from this chapter have been integrated into a generic code for computing detector quantities in a multi-detector setup for tracking a radiotracer particle in single/multiphase flows in vertical cylindrical columns, details of which are presented in the next chapter.

Chapter 5. Radioactive Particle Tracking Using Monte Carlo Simulations of Detector Efficiencies

5.1. Introduction

The Computer Automated Radioactive Particle Tracking (CARPT) has emerged as a unique tool for studying the flow pattern/mixing mechanisms in multiphase reactors with non-transparent walls (Devanathan *et al.*, 1990; Devanathan, 1991; Degaleesan, 1997; Chaouki *et al.*, 1997). Improvements and changes in the CARPT facility have been accomplished from time to time to make it suitable for studies of different multiphase systems. One bottleneck is the need for in-situ calibration procedure. Traditional implementation of the technique requires a tedious and time-consuming calibration procedure at each operating condition in the vessel geometry under investigation. During calibration for a given operating condition, the current state-of-affairs requires the construction of a *distance-count map for each detector*, by placing a radioactive particle, the flow follower, in a few hundred to a few thousand known locations over the entire vessel volume. All the calibration data are taken at the operating conditions of interest in order for the distance-count maps to properly reflect the variations in the density of the media inside the vessel which are dependent on the phase distribution in a multiphase flow situation. Once the entire calibration map is available for each detector, the dynamic position of this tracer particle can be computed from the instantaneous counts data acquired by the detectors. Time-differentiation of the instantaneous position data provides the instantaneous velocity of the particle. The application of the ergodic

hypothesis to the ensemble-averaged velocity data provides the estimation of the time-averaged velocity and turbulence-parameter fields over the entire vessel volume (Degaleesan, 1997). Figure 5-1 schematically represents the sequence of events in a CARPT experiment.

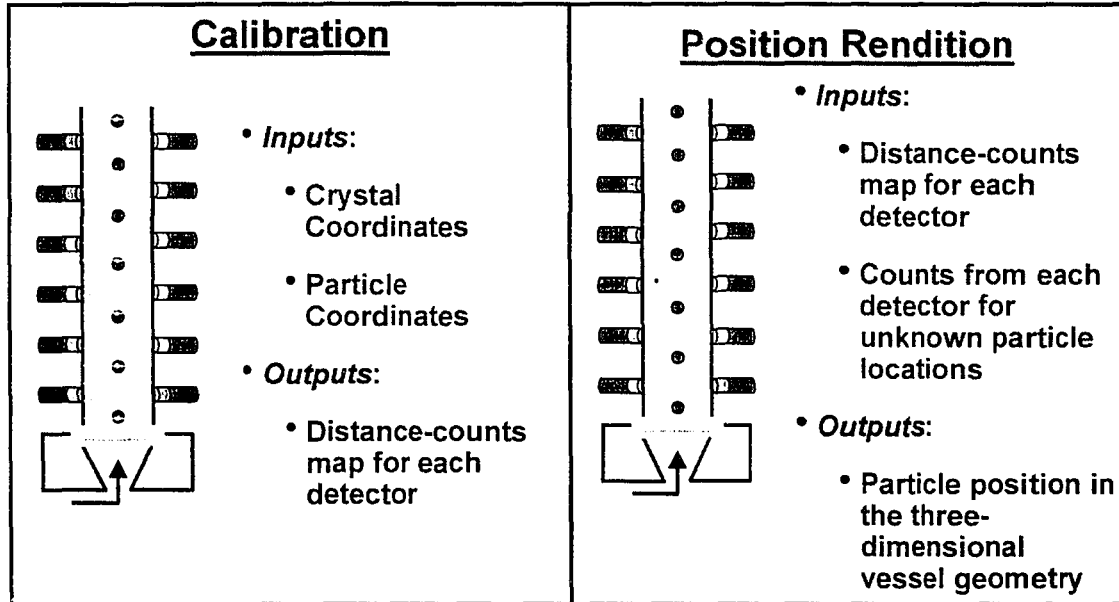


Figure 5-1. Schematic representation of events in a CARPT experiment.

The Monte Carlo simulation of detector photopeak efficiencies, as described in Chapter 4, offers an alternative to this tedious in-situ calibration procedure (refer to Figure 5-2). It is based on an approach where the intensity counts received by a detector are described in terms of a model and was first demonstrated by Larachi *et al.* (1994). This is in contrast to the heuristically based current procedure via in-situ calibration. In other words, the current heuristic calibration approach does not care about the physical processes that occur from radiation emission at the point source to its detection at the scintillator. Rather, it arbitrarily assumes that counts from the point source are only dependent on the *distance* of the point source with respect to the crystal. Since the functionality or dependence of the counts on distance is not known, many calibration locations are needed to map out the *distance-count* map for each detector with acceptable

accuracy over the entire flow domain of interest. However, it is known from Nuclear Engineering principles (Knoll, 1989) that the intensity counts recorded by a scintillation crystal are related in a complex manner not only to the relative position and orientation of the point source with respect to the detector but also to what lies in between the source and the detector – the intervening medium. It is the modeling of this multifaceted relationship among the particle position, crystal size, intervening medium and the count-rate that forms the basis of the model based approach.

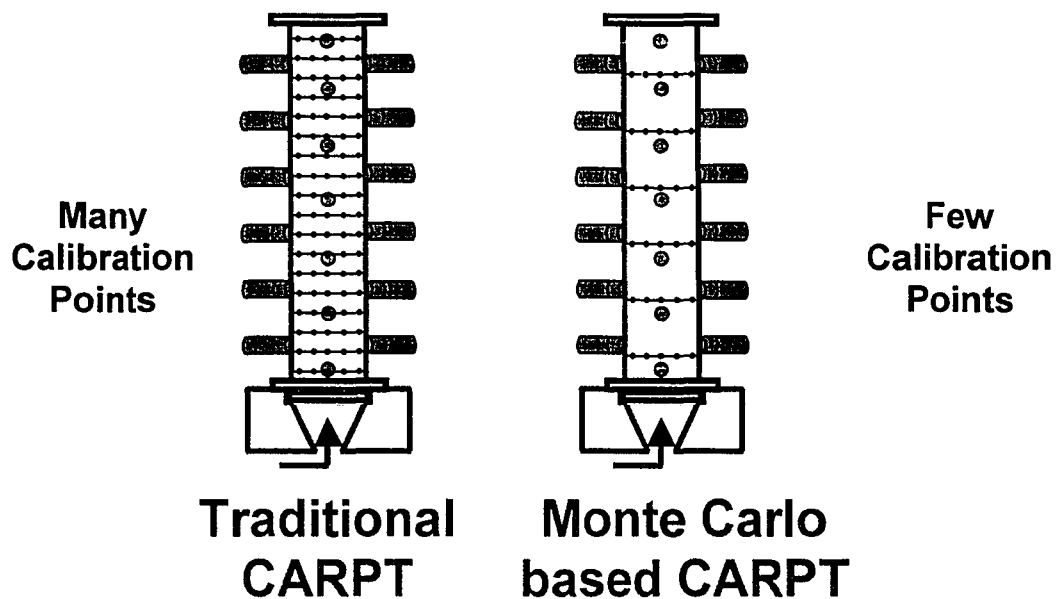


Figure 5-2. Traditional CARPT versus Monte Carlo based CARPT.

The detection of radiation is a very complex phenomenon and it is unrealistic to model the entire radiation-detection process in a real multi-detector system. Therefore, the adopted approach is to have a reasonably accurate model with a few adjustable parameters to achieve a computationally realistic description of the radiation detection process (Tsoufanidis, 1983). Therefore, in a model based calibration procedure, one still requires some experimental data to tune the adjustable model parameters. However, since the number of adjustable parameters is only a countable few, the number of experimental calibration points required is an order of magnitude smaller than those that are required

for a heuristic in-situ calibration. In addition to requiring fewer experimental calibration points, the model-based approach, depending on the accuracy of the fine-tuning of model parameters, has the advantage of determining the dynamic location of the radioactive particle from *a 3-D position-counts map* for each detector. This provides improved accuracy in estimating the particle position from count data received by each detector, since a 3-D mapping is being used for particle-position rendition instead of the 1-D mapping that is used for in-situ calibration.

Irrespective of the calibration approach that is used; the accuracy of position rendition in a CARPT experiment depends heavily on the accuracy and precision with which experimental calibration data is acquired. For the heuristic approach, inaccuracies in positioning the particle during calibration get buried in the arbitrary relationship of the count with source-detector distance and are *probably* less critical. However, for the model based approach, the accuracy of particle positioning is crucial, the lack of which can *cause inaccurate estimates of the model parameters*. Therefore, a description of the mechanics of the particle-positioning procedure at known locations during a calibration is in order here and is discussed briefly. For vessels having transparent walls (made of Plexiglas) and not operated under pressure, calibration is currently achieved by mounting the radioactive particle on fishing lines that are fixed between two grids at the two ends of the column, and manually moving the particle to various locations in the column. For opaque vessels however, which might also be operated under pressure, it is not feasible to use the fishing lines approach. In such situations, therefore, the particle is mounted on a rod and is placed at specified locations using a positioning device driven by computer controlled motors.

While the fishing line methodology is manually tedious, it is far less intrusive than the one using a positioning device with the particle mounted on a rod, and results in *insignificant* effects of the presence of the calibration equipment on the generated distance-counts maps. The fishing line method is also far more accurate as one can position the particle accurately by making taut the pair of strings carrying the particle to withstand the vibrations due to the flow. In addition, there is a visual confirmation of the desired particle position when the vessel wall is transparent. However, since under high-

pressure operation, the particle-on-the-rod is the only feasible calibration methodology, it is necessary that the “attenuation” issue be addressed in order for this calibration method to produce data free from artifacts. Here, the Monte Carlo method presented in Chapter 4 could come to the rescue provided a precise description of the calibration geometry and material of construction is available. Subsequently therefore, future work on Monte Carlo simulations of detector efficiency could quantifiably account for the radiation attenuation arising from the presence of the calibration device.

The in-situ calibration approach has been used in almost all of the work accomplished on Radioactive Particle Tracking (RPT) in CREL and details can be found elsewhere (Devanathan, 1991, Degaleesan, 1997). Here, the focus is on the development of the model based approach and the rest of the chapter will only be discussing the methodology and implementation of this Monte Carlo based simulation approach to achieve calibration and particle position rendition in a CARPT experiment.

5.2. Radiation Photon Counting

The Monte Carlo procedure is based on relating the intensity counts registered by a scintillation crystal from a radioactive point source anywhere in the 3-dimensional space around the crystal to the position of the source once the source strength and the type of intervening medium are known. As mentioned earlier, the radiation pulses recorded by a detector are related in a complicated manner to the medium between the point source and the detector as well as the view factor of the detector from the point source (Tsoufanidis, 1983). Figure 5-3 shows the schematic representation of the photon emission from a radioactive point source, placed inside a vertical vessel with two-phase flow and its subsequent detection at the scintillator-crystal. The spherical surface around the radioactive particle defines its sphere of influence at that radius assuming isotropic medium with the influence getting weaker as the radius increases. The interaction of any 3-dimensional object with this sphere of influence is mathematically characterized in terms of the solid angle. The total solid angle of a sphere is 4π whereas the scintillator crystal volume intercepts only a fraction of this total.

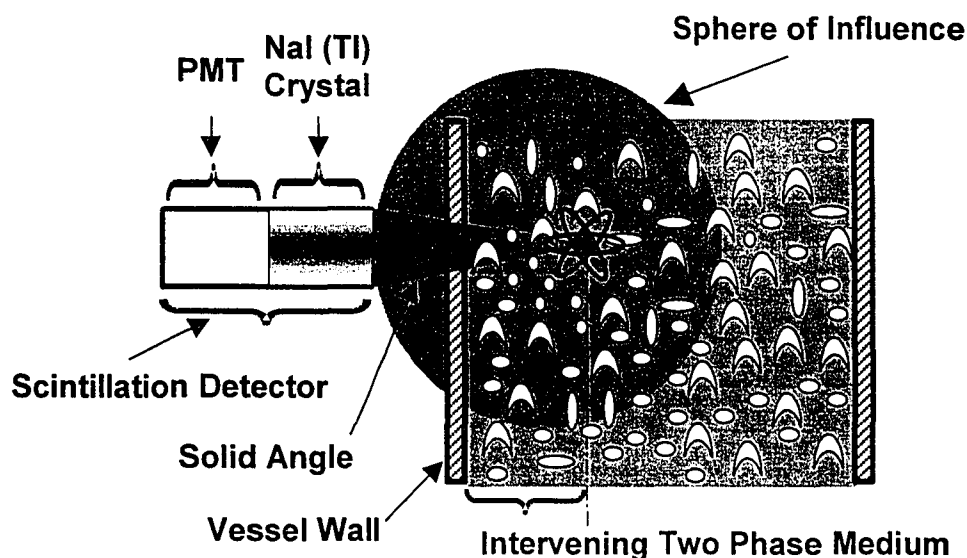
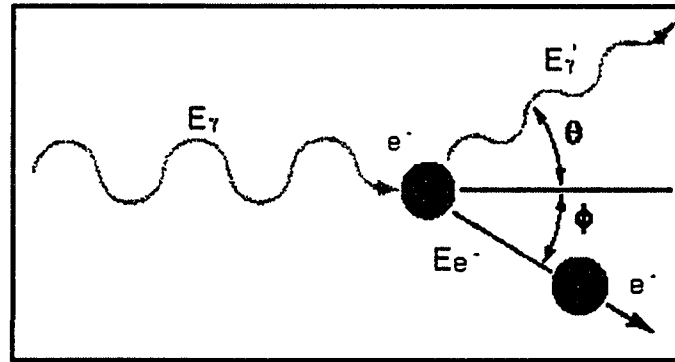


Figure 5-3. Schematic representation of photon detection by a scintillation crystal.

Depending on the source-detector distance, a count rate is registered which also depends on the intervening medium. Therefore after its emission from the point source, a photon encounters interaction with matter (gas, liquid, solid) in its sojourn to the detector which could result in photon getting scattered, reflected or absorbed. Figure 5-4 shows a schematic of the interaction of a γ -ray photon with an electron that results in scattering of both the photon as well as the electron. This type of photon interaction with matter is termed Compton scattering (Knoll, 1989). During this type of interaction, the photon imparts parts of its energy to the electron and changes its direction as shown in Figure 5-4.

There are two other electromagnetic interactions a photon can undergo in its collision with a material electron – photoelectric absorption and pair production. During a photoelectric interaction, the photon collides with an electron to which it imparts its entire energy and thus gets absorbed. During a pair production event, a photon of energy greater than 1.022 MeV interacts with matter to produce an electron and a positron each having an energy of 0.511 MeV. However, for the purposes of tracking Sc^{46} radioactive tracer particle that emits photons having an average energy of 1.005 MeV, one does not need to worry about the pair production events. Therefore, in the simulation tool

developed in this study, only modeling of Compton scattering and photoelectric absorption events has been incorporated.



$$E_{\gamma}' = \frac{E_{\gamma}}{1 + (1 - \cos\theta) \frac{E_{\gamma}}{mc^2}}$$

Figure 5-4. Schematic representation of a Compton scattering event.

5.2.1. Computation of Simulated Counts

As mentioned before, in a CARPT experiment one is interested in estimating the photon counts registered by an array of scintillation crystals mounted around the vessel volume in a specified time interval. In the model-based approach to calibration and particle position rendition, the counts registered for a given point source location are evaluated in a straightforward manner by Equation 5-1. This requires the knowledge of the photo-peak efficiency for each detector that is calculated based on the methodology presented in Chapter 4 for a given location of the tracer particle inside the flow vessel of interest. Equation 5-1 gives the number of γ -ray peaks received by the NaI (TI) detector obeying the non-paralyzable model (Tsoulfanidis, 1983; Larachi *et al.*, 1994) and the detector count is mathematically expressed as:

$$C = \frac{TV^*GRP_{\epsilon}}{1 + \tau V^*GRP_{\epsilon}} \quad (5-1)$$

where

$T \equiv$ sampling time.

ν^* \equiv number of γ -rays emitted per disintegration (2 for Sc^{46}).

$G \equiv$ detector gain factor.

$R \equiv$ source strength (activity), disintegrations/second.

$P_\epsilon \equiv$ photo-peak efficiency or full-energy peak efficiency.

$\tau \equiv$ dead time of the detector.

In the equation above, the Monte Carlo procedure is used to calculate the photopeak efficiency, P_ϵ , for given particle and detector coordinates as well as the density distribution of the intervening medium between the point source and the detector (details are provided in Chapter 4). The tunable parameters in the model-based approach mentioned earlier are the detector gain, G and the dead time, τ . The media density in the flow domain of interest could also be varying and have a parametric form, the parameters of which might also need tuning to give an accurate description of the density distribution of the intervening media. For a two-phase bubble column flow, the variation of the media density is incorporated in terms of a radial profile of the gas holdup (Equation 5-2). It was shown clearly in Chapter 4 that the density distribution of the intervening medium has a profound effect on the detector efficiencies. This effect has therefore, been incorporated in the model-based approach developed as part of this work in terms of a model for the gas volume fraction distribution pertinent to bubble column flows.

5.2.2. Optimization of Detector Parameters

As mentioned above, while estimating the intensity counts, C , from Equation 5-1 in the absence of any experimental data, the gain factor, G and the dead time, τ , are known only approximately. Also, the effective attenuation coefficient for the medium in the vessel depends on the distribution of the vessel media density (which is dependent on the local gas hold-up profile for bubble column flows). The gas holdup profile in fully

developed flow regions in bubble columns can be represented by Equation 5-2 (Kumar, 1994):

$$\varepsilon_g(\xi) = \bar{\varepsilon}_g \left(\frac{m+2}{m} \right) (1 - c\xi^m); \quad \bar{\varepsilon}_g = \bar{\varepsilon}_g \left(\frac{m+2-2c}{m} \right) \quad (5-2)$$

In the above equation, $\bar{\varepsilon}_g$, is the cross-sectional mean gas holdup, ξ is the dimensionless radius, m is the exponent and c is the parameter accounting for the non-zero gas volume fraction at the vessel walls. Although the holdup profile deviates from the form proposed above in some regions of the bubble column, the virtual variations along the column length are not significant except near the distributor and disengagement zones. As the variations in these zones are not well quantified and modeled, the variation of the gas volume-fraction profile with the column axis has been neglected in this work.

In order to get a handle on the correct model parameters for estimating detector counts by Equation 5-1, one has to resort to an optimization (fine-tuning) procedure to get the optimal values of G , τ and the three parameters in the universal gas hold-up profile ($\bar{\varepsilon}_g$, m and c). This is accomplished by comparing the simulated counts for each detector with the experimentally measured ones for a few *known locations* of the point radioactive source of known strength, R . The estimation of the best-fit model parameters for each detector is achieved through a weighted least-squares regression. Therefore, for each detector, the objective function to be minimized, is defined as (Larachi *et al.*, 1994):

$$OBJ_i = \sum_{j=1}^{N_{cali}} W_{ij} \left(\frac{(C_{ij} - M_{ij})}{(C_{ij} + M_{ij})/2} \right)^2 \quad (5-3)$$

M_{ij} \equiv measured counts.

C_{ij} \equiv simulated counts.

N_{cali} \equiv number of calibration points.

$$W_{ij} = \frac{\sqrt{M_{ij}}}{\sum_{j=1}^{N_{cali}} \sqrt{M_{ij}}} \equiv \text{weighting factor for det. "i" \& calibration pt. "j"} \quad (5-4)$$

In the above equations, the subscript "i" is the index identifying a detector in a multi-detector setup while "j" is the index of the known calibration location inside the vessel. The above optimization is implemented through a *Generalized Reduced Gradient* (GRG) method using the code GRG2 (Lasden *et al.*, 1978).

During the regression process, the photopeak efficiency is evaluated repeatedly by the Monte Carlo procedure described in Chapter 4, as it depends on the gas holdup profile the parameters for which keep changing to find their best values for a given detector. When computational resources are limited, one could resort to the following approximation of Equation 4-2 in the evaluation of the photo-peak efficiency without loss of significant accuracy (Larachi *et al.*, 1994).

$$P_{\epsilon} = \iint_{\Omega} \frac{\vec{r} \cdot \vec{n}}{r^3} f_a(\alpha, \theta) f_p(\alpha, \theta) ds \quad \text{Exact Formulation} \quad (5-5a)$$

$$P_{\epsilon} \approx \iint_{\Omega} \frac{\vec{r} \cdot \vec{n}}{r^3} f_p(\alpha, \theta) ds \iint_{\Omega} \frac{\vec{r} \cdot \vec{n}}{r^3} f_a(\alpha, \theta) ds \quad \text{Approx. Formulation} \quad (5-5b)$$

The discretized form of the above approximate integral becomes

$$P_{\epsilon} \approx \frac{1}{4} \sum_{i=1}^n \sum_{j=1}^n w_g(i) w_g(j) w(\alpha_i, \theta_j) f_p(\alpha_i, \theta_j) \times \frac{1}{4} \sum_{i=1}^n \sum_{j=1}^n w_g(i) w_g(j) w(\alpha_i, \theta_j) f_a(\alpha_i, \theta_j) \quad (5-6)$$

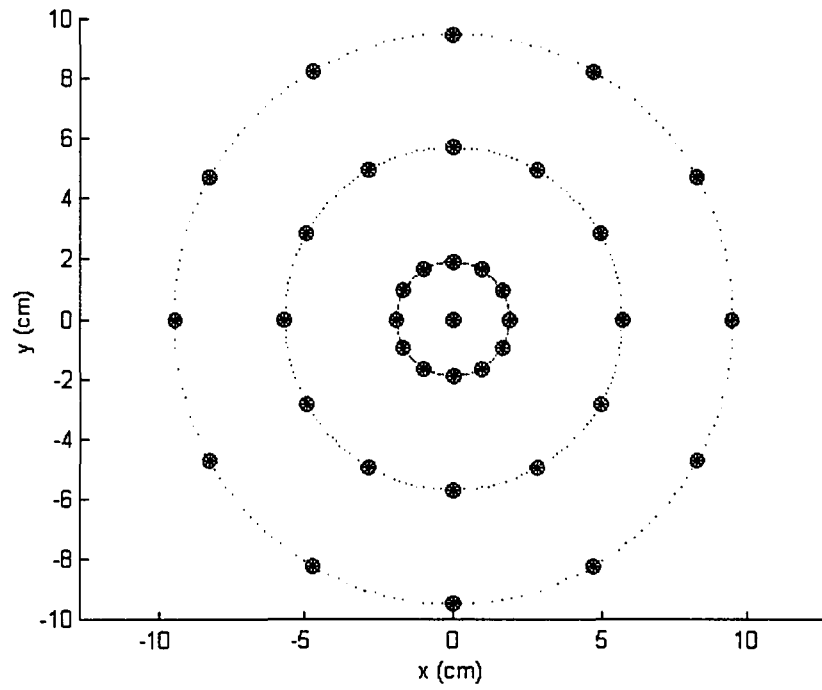
In the approximate formulation, the first term is considered independent of the media density distribution and is held constant during regression of the gas holdup profile parameters. When the results of the computed photopeak efficiency using the approximate formulation are compared to the case when no approximation is used, the differences barely exceed 1%. Thus, the approximation could be used effectively when really large number of calibration points are used or when the availability of computational resources is limited.

5.2.3. Generation of Calibration Map – Photopeak Efficiency Database

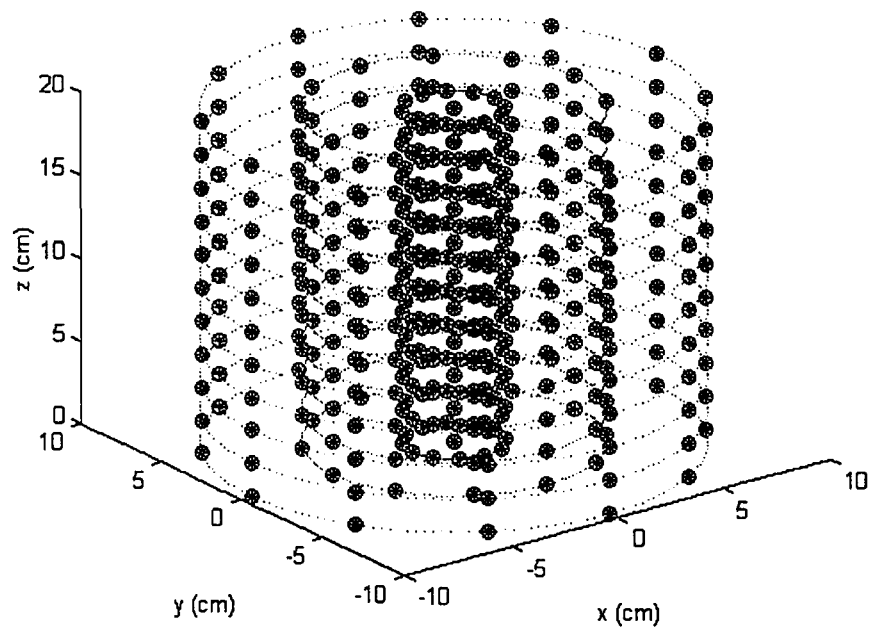
Once the optimization routines converge to provide the optimal values of the optimized parameters (G , τ , $\bar{\epsilon}_g$, m and c) for each detector in a multi-detector CARPT

experimental setup, one can get an accurate description of the counts that will be recorded by a given detector for any particle location inside the column. This description is then used to identify the unknown particle positions based on the counts received by each detector using a χ^2 -minimization procedure as discussed in the next section. Thus, with the optimized detector and gas holdup profile parameters, a detailed calibration map is constructed by *virtually* placing the particle in numerous locations inside the column. This process simulates the process of experimentally generating the calibration map by placing the tracer particle in several hundred to a thousand known locations.

The position rendition process again requires repetitive calculation of the predicted counts using Equation 5-1 along with the optimized parameters over the whole domain while searching for the best "unknown" particle location. Since the evaluation of the photopeak efficiency for multiple detectors (as many as 30) is very expensive computationally, this wasteful and repetitive calculation is by-passed by *a priori* creating a map for the photopeak efficiency for each detector over the whole flow domain. This map is created over a computational grid which could be created for as fine a resolution as desired, limited only by the finite size of the neutrally-buoyant radioactive flow follower, the statistical nature of the radiation, and constraints of computer memory and storage costs. However, for all practical calculations, a grid size of 0.5 cm or larger should be sufficient since a particle location identified on this grid is further refined via a three-dimensional interpolation scheme as discussed in Section 5.2.4. Figure 5-5 shows a sample of the computational grid that could be generated as per the requirements of the particular experiment. Once the grid is generated, the photopeak efficiency at each grid point and for each detector is calculated using the optimal values of the gas holdup profile parameters. These computed photopeak efficiencies are then stored in a database in binary format in order to keep the size of the database file as small as possible. Depending on the size of the flow domain and the number of detectors employed in a CARPT experiment, the size of the photopeak efficiency database file could be anywhere between 10-150 megabytes.



(a)



(b)

Figure 5-5. Sample computational grid for generation of photopeak efficiency database.

5.2.4. Particle Position Reconstruction

Once the calibration map is made available, an actual experiment is carried out in which a neutrally-buoyant tracer is let free in the flow, and the counts emitted by it are registered by each detector at finite time intervals (20 ms for a usual CARPT experiment). Programs have been developed to compute the chi-squared values (refer to Equation 5-7) of the measured counts against those calculated via Equation 5-1 using the optimized values of the detector parameters – G and τ and the photopeak efficiency from the database generated on the computational grid.

$$\chi_j^2 = \sum_{i=1}^{N_{det}} \frac{(C_{ij} - M_i)^2}{C_{ij}}; \text{ for each detector "i" \& computational grid node "j"} \quad (5-7)$$

The grid node location from the photopeak efficiency database, which provides the minimum chi-squared value, is taken as a coarse “maximum likelihood” estimation of the particle position at that instant of time. This search for the least chi-square location among all the grid nodes is done in a sequential manner. If the resolution of the computational grid is not very fine, it may be possible to refine the estimated particle position that is obtained from the sequential search on the computational grid. For this purpose, a 3-D quadratic interpolation of the chi-squared values on the 26 closest neighbors of the above point is implemented. Subsequently, a further refinement of the particle position is obtained by searching for the minimum of the interpolated chi-square function using Powell’s method (Press *et al.*, 1992). This refinement can also be alternatively accomplished using the methodology presented by Larachi *et al.* (1994). A comparative study on the effect of the interpolation scheme on the estimated particle locations could be undertaken in the future to identify the more robust scheme between the two.

The methodology presented above for Monte Carlo simulations based CARPT data processing was developed in modules that were tested individually and subsequently integrated into a comprehensive software package for deploying the “forward” calibration step along with optimization and the “inverse” particle position rendition step. Once the

software was validated against previously published data (refer to Chapter 4), it was necessary to validate the Monte Carlo based scheme against experimental data. The next sections describe the validation experiments in Plexiglas vessels as well as present an example of the application of this approach to a recent CARPT data set in a stainless steel column.

5.3. Experiments

Experimental data for verification of the proposed approach was acquired in a cylindrical Plexiglas column with an I.D. of 7.47" and O.D. of 8.0". The schematic of the experimental setup and data acquisition is shown in Figure 5-6. A set of four 2"x2" NaI (Tl) detectors was used for the data acquisition. The detectors were mounted flush to the column at an axial level of 35.4 cm from the bottom of the column. The detectors were positioned at 90⁰ degrees to each other (in the plane of the detectors). The total column height used for the experiments was 48 cm. Experiments were conducted with an empty column, column filled with water, and with air being sparged into the column filled with water. The objectives of the experiments were twofold. Since the modeled counts belong only to the photopeak portion of the spectrum, the first objective was to determine the correct threshold on the data acquisition system. The second objective was to acquire data at this critical threshold to verify the optimization routines, and to evaluate the particle-position-reconstruction programs against this experimental data.

As mentioned earlier, the Monte Carlo procedure systematically models the photo-peak fraction (or the counts associated with the photo-peak) and it is inevitable that while acquiring the counts during an experimental run, the thresholds and sampling windows are correctly set so as to sample just the photo-peak counts. This is best achieved by measuring the emitted energy spectrum from a point source using a Multi Channel Analyzer (MCA) so that the start and end of the photo-peak could easily be identified. Since Sc⁴⁶ does not emit photons having energy above 1.2 MeV, the possibility of pair production is rare and, therefore, one does not need to worry too much about the end of the photo-peak. The only thing one has to control is the threshold or the

start of the photo-peak, and to adjust the hardware settings correctly so as to properly sample the requisite counts. Experiments were carried out to determine the beginning of the photopeak in the energy spectrum for each of the four detectors.

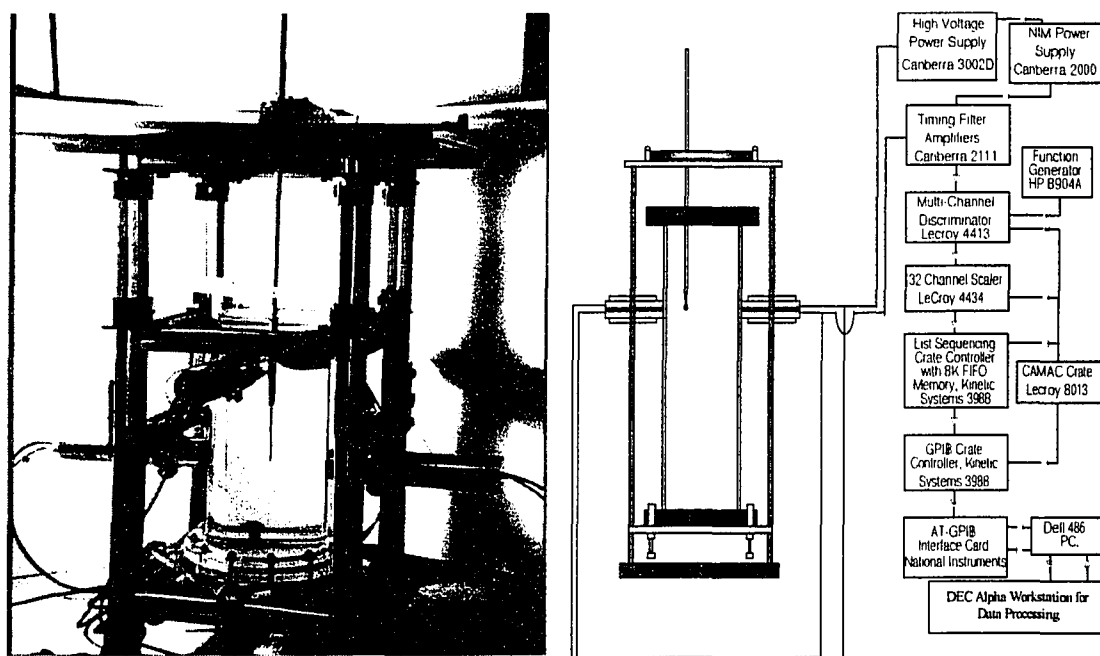


Figure 5-6. Experimental setup used for verification of the Monte Carlo simulations.

Figure 5-7 shows the results of the spectrum analysis for the four detectors used in this study. The radiation counts were acquired by placing the radioactive particle in the center of the column, in the plane of the detectors. It is clear from the figure that a threshold of 300 mV is appropriate as signifying the start of the photopeak portion of the spectrum. The Sc^{46} isotope has two photopeaks at 0.889 MeV and 1.12 MeV, which are evident from Figure 5-7. Depending on the amplifier gain settings, different threshold scales (mV) map to the same scale of γ -ray photon energies. Similar analysis was carried out for other locations of the radioactive source. Though the Compton portion of the spectrum showed dependence on the location of the radioactive source, the photopeak portion of the spectrum was almost independent of the location of the source in terms of the start of the photopeaks. With an identified critical threshold of 300 mV, the data was acquired by placing the radioactive Sc^{46} particle in 27 different locations, at a sampling

frequency of 50 Hz for a total sampling time of 3.84 seconds. These 27 positions were located on 3 planes, one of the planes being the plane of the detectors, with another plane above and one below this plane. In each plane, the data was acquired with the particle placed at the center of the column, and at eight other positions located on a circle of radius 5 cm 45° apart. The strength of the particle used in this study was approximately 95 μCi , the particle was spherical in shape of diameter ~ 2.3 mm.

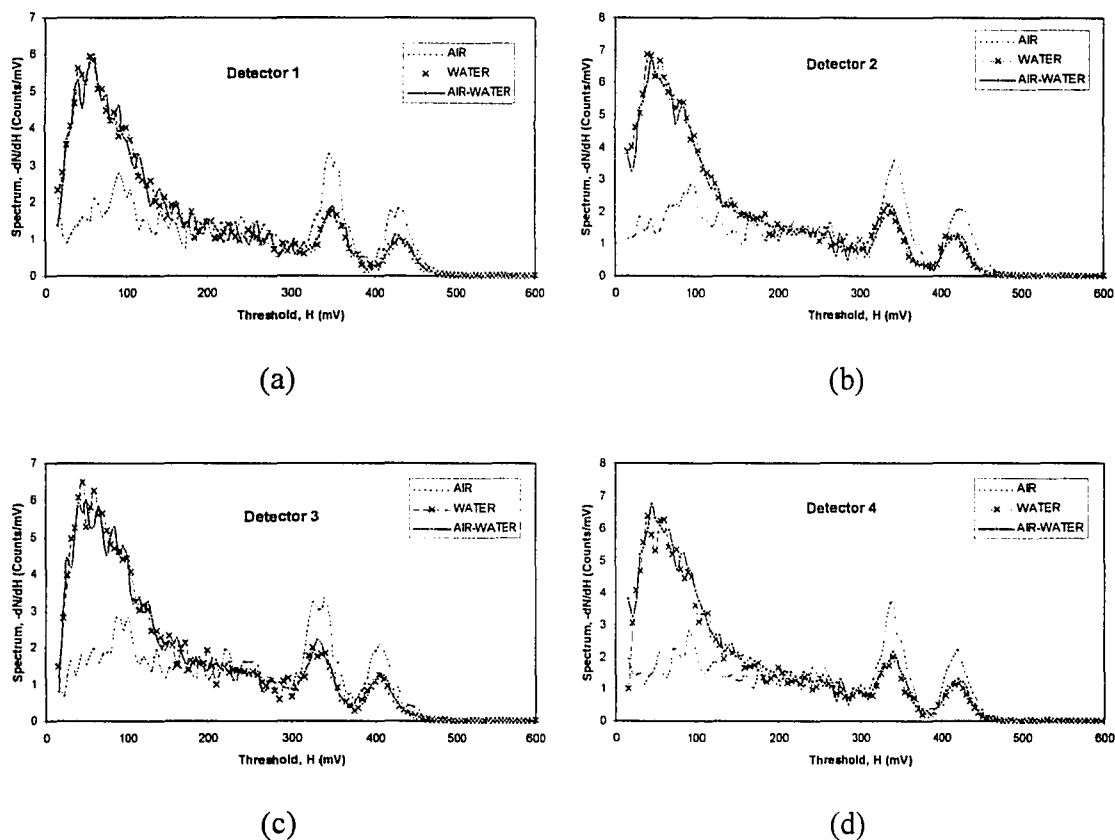


Figure 5-7. Experimentally determined energy spectrums for the four detectors employed in the validation experiments.

5.4. Results and Discussion

Figure 5-8 shows the comparison of the experimentally observed particle position to the one reconstructed by the procedure outlined above. The experiments were

conducted with water as the intervening medium. A resolution of 1 cm was used for generating the 3-D grid over which the particle position is reconstructed. We can see that the position reconstruction in the x-y plane is satisfactory given the grid that was used. However, the resolution in the z-direction is far from satisfactory. Similar trends were observed in an empty column, as well as in one with a gas-liquid dispersion. The reason for this observation is straightforward. A set of four detectors were used to resolve the particle position in the x-y plane, whereas only one level of detectors was used to resolve the particle position in the z-direction -- hence, the observed inaccuracy. It is logical to assert that the z-coordinate reconstruction accuracy would improve considerably if one were to employ multiple detectors in the z-direction.

To acquire greater confidence in the complex sequence of experimental and computational methodology and to address the issues with the accuracy of the z-coordinate reconstruction in the experiment described above, additional experiments were conducted in a single-phase flow situation. The vessel chosen was a stirred vessel shown in Figure 5-9. A total of 16 detectors were used in this setup. As before, proper care was taken to reasonably estimate the threshold for data acquisition in order to ensure that only photopeak counts were acquired. The entire procedure, consisting of the optimization, calibration and position-rendition steps, was applied to the single-phase flow data as was done for the two-phase experiments. 255 data sets were acquired at each of the eight different *x-y* locations on the *z = 10-cm* plane from the bottom of the tank. Table 5-1 lists the actual and reconstructed particle coordinates (along with one standard deviation) while the graphical presentation of the results of particle position reconstruction are shown in Figure 5-10.

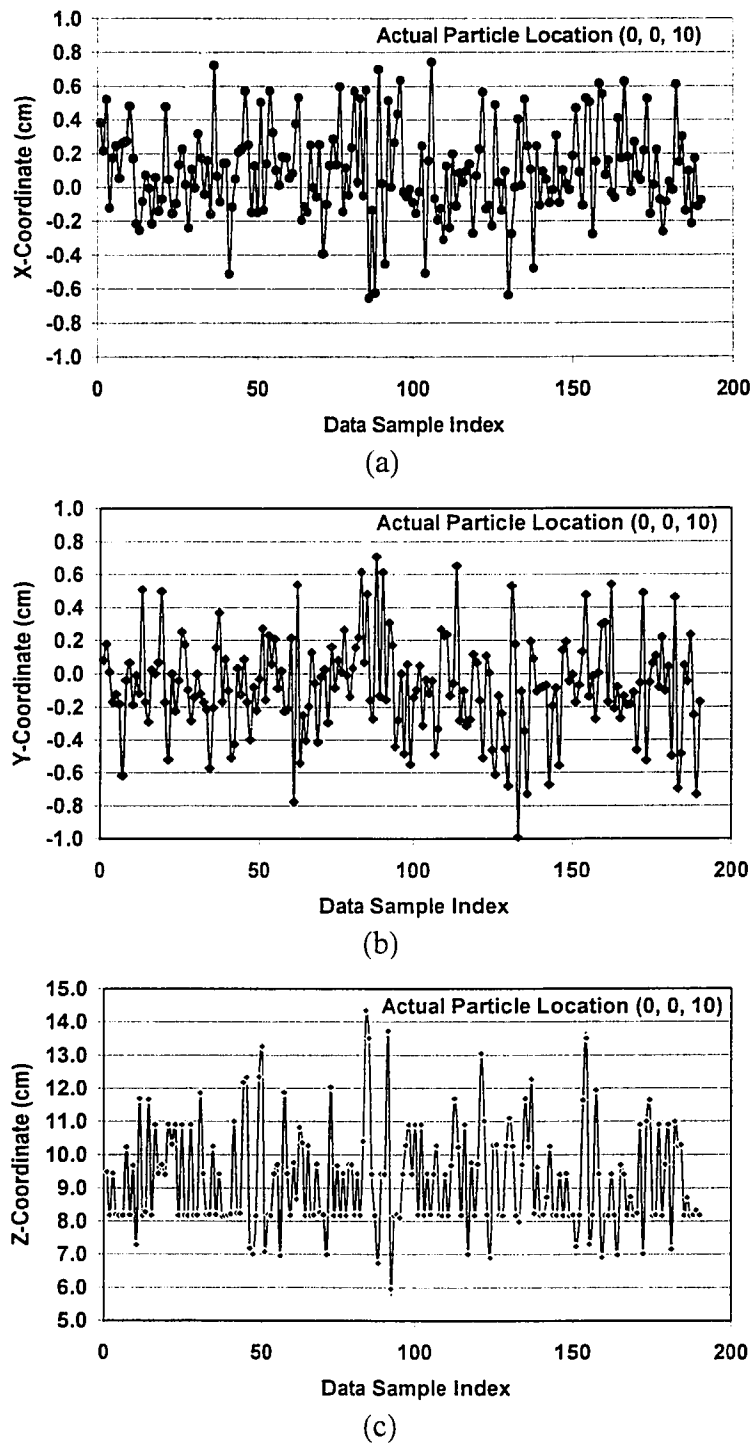


Figure 5-8. Reconstructed particle position over 190 data points acquired every 20 ms

From Figure 5-10 and Table 5-1, it can be seen that the reconstructed x and y coordinates of the matrix of test points is very good as before, and the resolution in the z-

direction has improved considerably. Larachi *et al.* (1994) also point to this observation that in general the estimated z-coordinate has a little bit more error than the x and y coordinates. For the above simulations, details regarding radiation attenuation resulting from the presence of the baffles and the impeller in the vessel were ignored. Therefore, it is possible that the accuracy of the reconstructed particle positions is further improved by accounting for the appropriate geometric features into the simulation scheme. This has not been done in the present study, as the objective here is to demonstrate the application of the Monte Carlo method. Irrespective of the possible improvements that could be accomplished with the incorporation of the geometric detail of the internals in the flow vessel, suitable filtering of the reconstructed positions would definitely result in rectifying the reconstructed position to remove noise caused by the processes of radiation emission and detection (Degaleesan, 1997).

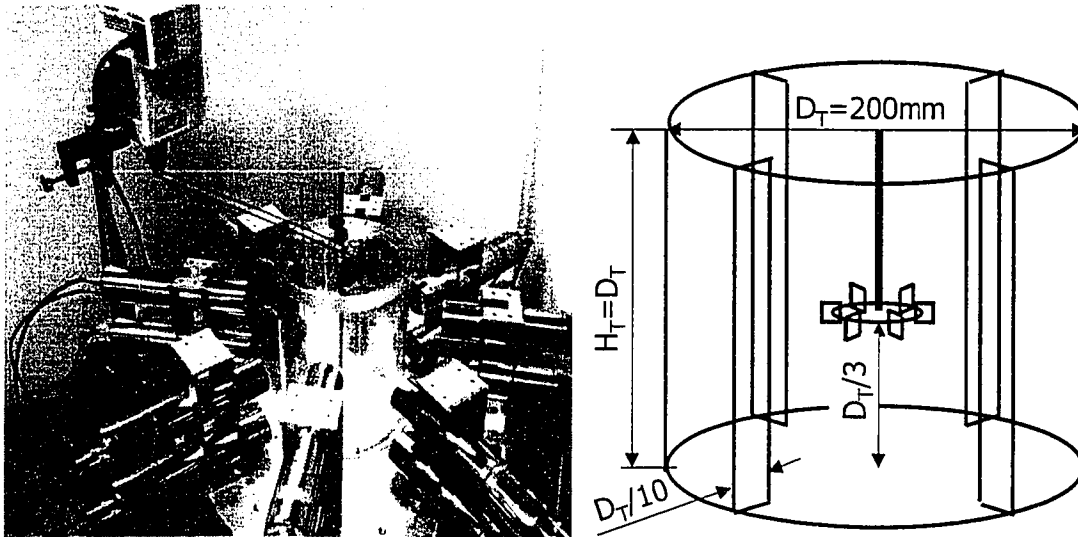
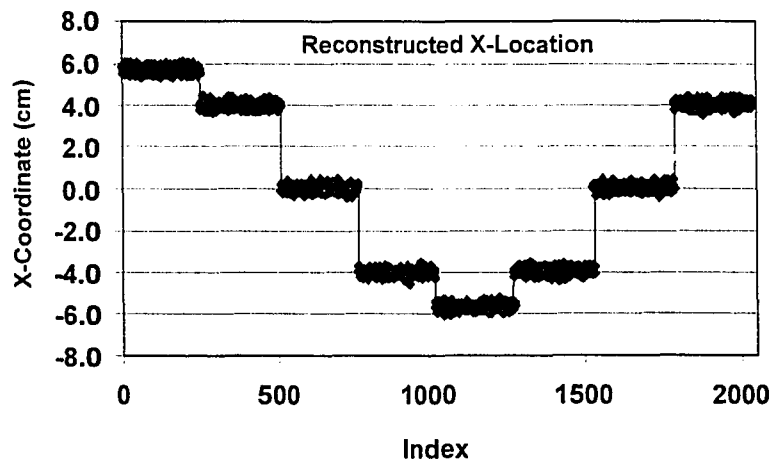
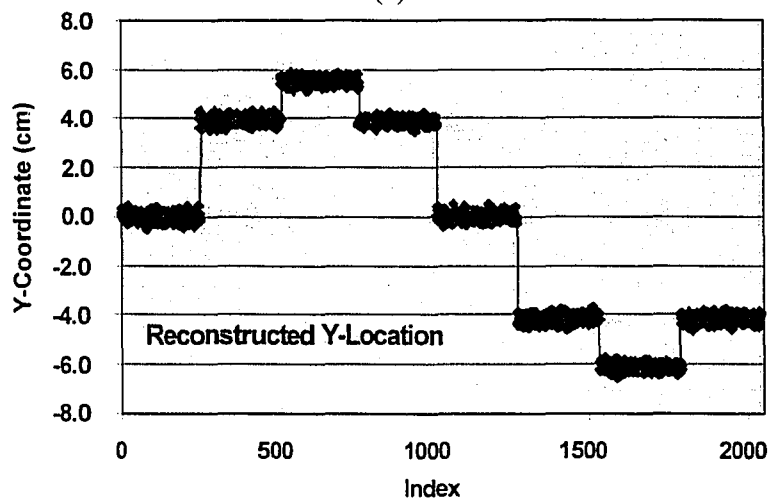


Figure 5-9. Experimental setup for validation under single phase flow conditions.

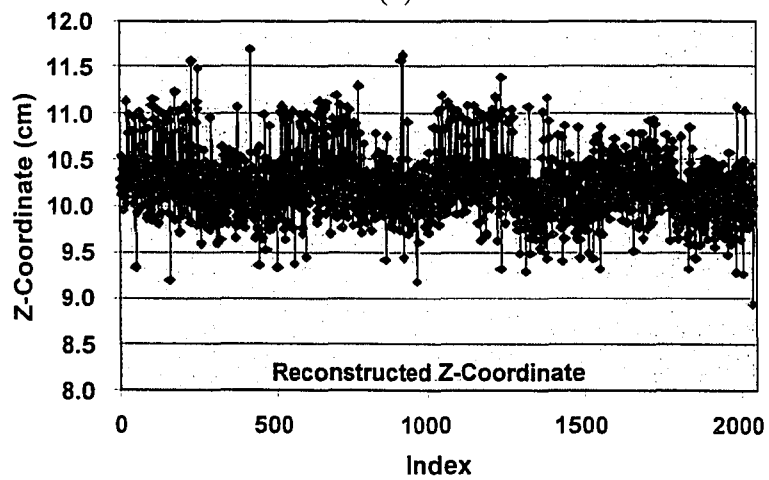
In general however, one should not forget that for realistic flow domains like bubble columns or fluidized beds, the length of the vessel is an order of magnitude larger than the diameter. Thus, a proper way to look at errors would be to scale them by the dimensions of the flow domain. Therefore, errors in x and y coordinates should be scaled with the vessel radius or diameter, and the errors in the z-coordinate by the vessel length.



(a)



(b)



(c)

Figure 5-10. Reconstructed particle locations from a single-phase experiment.

Table 5-1. Results of particle position reconstruction for the CST validation experiment

Index	x-Coordinate (cm)		y-Coordinate (cm)		z-Coordinate (cm)	
	<i>Actual</i>	<i>Computed</i>	<i>Actual</i>	<i>Computed</i>	<i>Actual</i>	<i>Computed</i>
1-255	5.70	5.70 ± 0.16	0.00	-0.03 ± 0.17	10.0	10.36 ± 0.33
256-510	4.03	4.00 ± 0.16	4.03	3.91 ± 0.15	10.0	10.12 ± 0.28
511-765	0.00	0.01 ± 0.16	5.70	5.52 ± 0.15	10.0	10.38 ± 0.36
766-1020	-4.03	-4.00 ± 0.15	4.03	3.88 ± 0.14	10.0	10.15 ± 0.27
1021-1275	-5.70	-5.63 ± 0.14	0.00	0.01 ± 0.16	10.0	10.37 ± 0.34
1276-1530	-4.03	-3.92 ± 0.14	-4.03	-4.16 ± 0.16	10.0	10.08 ± 0.30
1531-1785	0.00	0.03 ± 0.15	-5.70	-6.13 ± 0.14	10.0	10.27 ± 0.25
1786-2040	4.03	4.02 ± 0.15	-4.03	-4.19 ± 0.16	10.0	10.05 ± 0.28

While comparing the results of the above reconstruction to the traditional CARPT methodology, one should keep in mind that the counts used for position reconstruction were acquired at a 50 Hz sampling frequency, while the accuracy of the CARPT technique reported earlier (Degaleesan, 1997) is based on the average counts acquired over a 1.28-seconds period. The reconstructed positions, shown in Figures 5-8 and 5-10, are representative of the randomness associated with the radiation emission and detection process. As mentioned earlier, it is therefore necessary to apply appropriate filtering techniques to the tracer-position data reconstructed from the developed Monte Carlo methodology in order to rectify the spuriously estimated tracer coordinates resulting from the random nature of the radiation emission and detection processes.

These two studies provided the necessary validation of the Monte Carlo technique against experimental data. Further experimentation with more detectors as well as with different data acquisition settings should be carried out to determine the optimal implementation procedure for application of this technique on a regular basis. Here, a very brief example of the application of this approach to process data from a bubble column to map the long-time averaged liquid recirculation velocity is presented. The column, which is 16.2 cm in diameter and is made of Stainless Steel (SS), was operated at a superficial gas velocity of 30 cm/s under atmospheric pressure. Ong (1999) has presented other details regarding the setup of this experiment, which was performed as part of her ongoing doctoral thesis work.

Figure 5-11 shows a comparison of the reconstructed tracer coordinates using the methodology of Degaleesan (1997) and the Monte Carlo method developed in this study. For this purpose, a sequence of 1000 sets of photon counts, measured from 30 detectors that were employed in this experiment, were arbitrarily chosen from the experimental data acquired over a period of 24 hours (equivalent to 4,320,128 total set of counts at a sampling frequency of 50 Hz). From Figures 5-11a-c, it can be seen that the method of Degaleesan has trouble reconstructing particle locations above a z level of 150 cm. For this experiment, the gas-liquid interface was approximately maintained at 180 cm above the distributor (z level = 0 cm). Because of the inaccuracy in the reconstructed z coordinate, the method of Degaleesan also induces large errors in the x and y coordinates. This can be clearly seen from Figures 5-11a-b, where x and y coordinates as large as ± 1000 cm are obtained, which is completely unphysical since the column diameter is 16.2 cm implying that x and y coordinates are confined to ± 8.1 cm. When the particle occurrences beyond a z level of 150 cm are ignored, one observes a consistent agreement between particle positions reconstructed from the Monte Carlo method and those by the method of Degaleesan (refer to Figures 5-11d-e).

When employing the method of Degaleesan, problems similar to the particle occurrences near the gas-liquid interface (beyond z level of 150 cm) are also present when the particle travels close to the distributor region. Such problems are negligible if not completely absent in the Monte Carlo methodology. In addition, the methodology of Degaleesan employed a total of 2646 calibration points while the Monte Carlo method made use of only 306 calibration points to construct the calibration map for each detector. Therefore, the Monte Carlo method in effect results in an order of magnitude reduction in the experimental effort while resulting in better accuracy in particle position reconstruction over the entire flow domain.

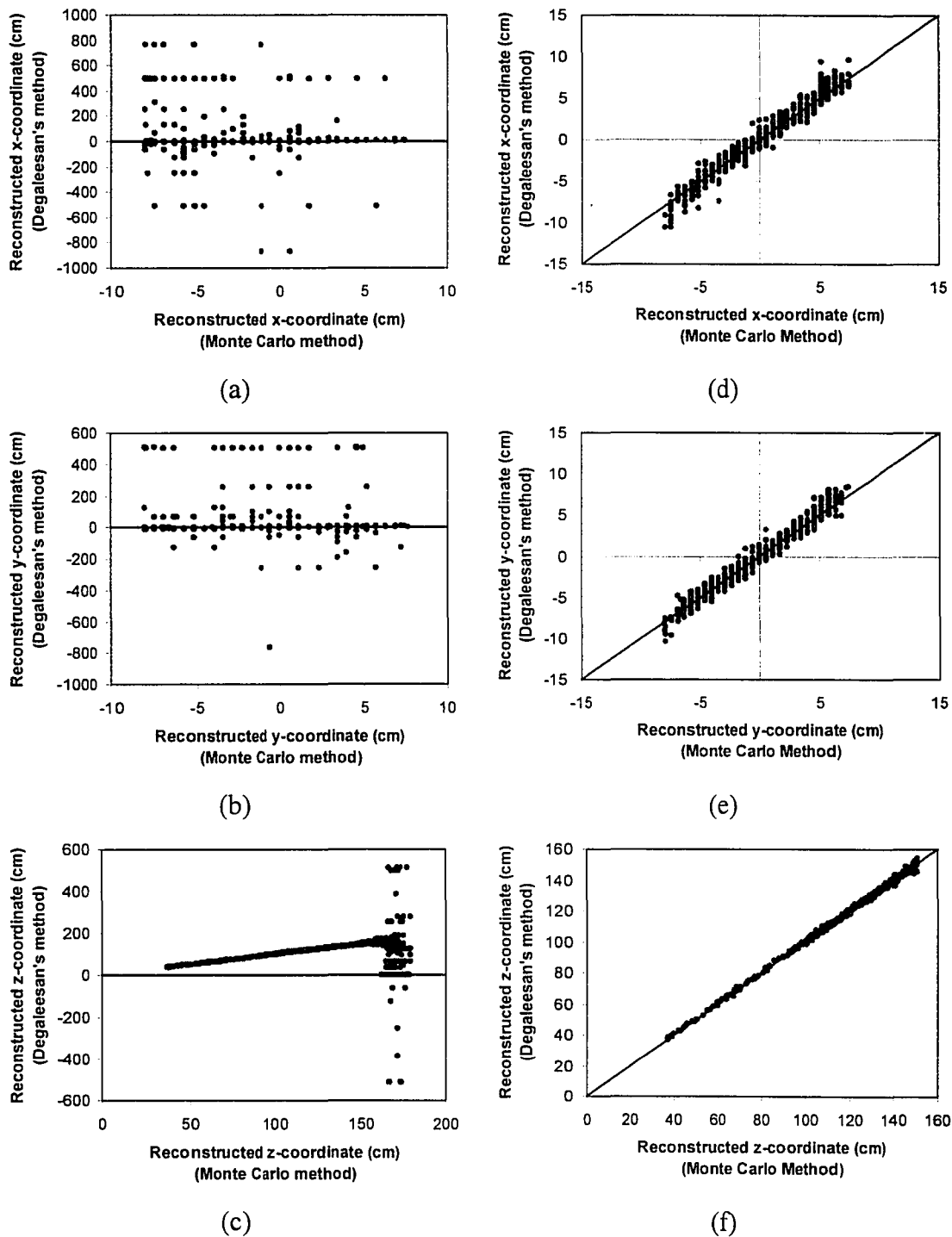


Figure 5-11. Parity plot of particle coordinates reconstructed using Degaleesan's method and Monte Carlo method for arbitrarily picked sequence of 1000 points in stainless steel bubble column experiment.

a-c) All 1000 points d-f) Excluding points near gas-liquid interface

For demonstration purposes, Figure 5-12 shows the long-time averaged velocity vector plot in two different r-z planes. From the figure, it can be clearly seen that the technique has clearly picked up the usually reported liquid recirculation patterns in a bubble column flow with up-flow of liquid in the center of the column and down-flow near the walls. Thus, a successful application of the developed technique to a difficult flow situation has been demonstrated. With this tool available, it should be possible to apply the technique to provide information on the velocity fields in large dense opaque systems, where other non-intrusive techniques are entirely inadequate.

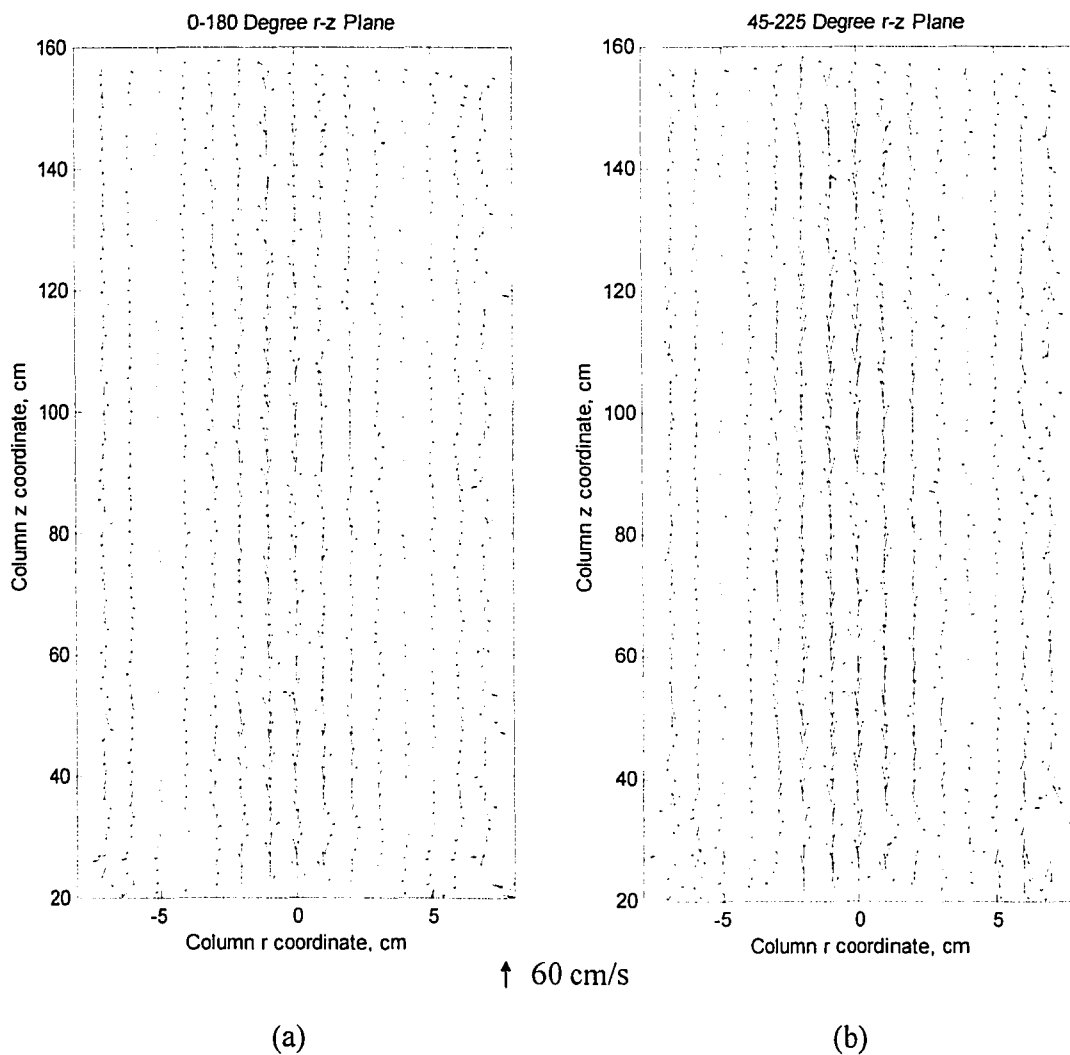


Figure 5-12. Velocity vector plots computed by the Monte Carlo method in a SS bubble column operated at a U_g of 30 cm/s a) 0-180° r-z plane b) 45-225° r-z plane

5.5 Conclusions

In this chapter, the integration of the Monte Carlo simulation tool developed in Chapter 4 has been accomplished to non-invasively trace a radioactive tracer particle inside a flow domain by monitoring the scintillation counts emitted by the tracer with the aid of an array of scintillation detectors mounted strategically around the flow vessel. The position rendition based on the developed Monte Carlo based methodology has been validated against experimental data and has further been applied to successfully trace the radioactive particle in a difficult flow situation resulting from a bubble column operation at a superficial gas velocity of 30 cm/s in a stainless steel vessel. Comparison with the traditional CARPT methodology indicates the robustness of the developed Monte Carlo tool as well as the potential of reduction in experimental efforts to perform a particle tracking experiment.

Several opportunities exist for further improvement of the developed tool. Some of these include:

- 1) Incorporation of radiation build-up in Monte Carlo simulation tool.
- 2) Accounting the axial distribution of gas holdup, which implies axial variation of vessel media density.
- 3) Testing of alternate schemes to refine the particle positions based on the initial crude approximation achieved through χ^2 minimization. Specifically, the methodology proposed by Larachi *et al.* (1994) needs to be tested.
- 4) The dependence of the optimized detector and media density parameter on the form of the employed objective function also needs further investigation.

Based on the results presented in this chapter, it is recommended that for all future processing of the CARPT data, the Monte Carlo based methodology presented in this chapter or refined further by future efforts be employed.

Chapter 6. Modeling Phase Mixing in Bubble Columns Using the One- Dimensional Two-Fluid Approach

The first part of the thesis concentrated on laboratory scale measurements of bubble column hydrodynamics via conductivity probes and Computer Automated Radioactive Particle Tracking (CARPT). Both of these techniques were improved with the efforts described in the previous chapters. In fact the accurate measurement of liquid phase tracer concentration in bubble column flows developed in this work and described in Chapter 3 is a completely new development based on the novel signal filtering procedure. The rest of the thesis deals with addressing the phenomenological modeling of gas and liquid phase flows in bubble columns including the coupling of fluid dynamics and interphase mass transfer in the description of the overall scalar transport processes.

6.1 Introduction

The high reactor volumetric productivity demands of the chemical industry necessitate that bubble column reactors be operated at high superficial gas velocities at high pressures. Additionally, large diameter vessels are typically employed to meet the high production rates. Under these conditions, bubble columns generally operate in the *churn-turbulent* regime characterized by frequent bubble coalescence and breakage and a nearly chaotic two-phase system (Vermeer and Krishna, 1981; Luo, 1993; Krishna and

Ellenberger, 1995; de Swart, 1996; Degaleesan 1997; Krishna, 2000^h). Therefore, for a proper design and/or scale-up of these reactors, it is important that the extent of gas and liquid/slurry phase mixing in these reactors under churn-turbulent conditions is reliably characterized. This chapter provides a brief description of the current methodology for describing inter-phase and intra-phase mixing in bubble columns. One of the primary objectives of this study is to develop physically based models that describe the long-time averaged liquid and gas phase flows occurring in bubble column reactors. Given the fluid dynamic information from the above models, the other objective is to incorporate this information, superimposed with eddy diffusion, into reactor models that are subsequently used to study the impact of fluid dynamics on scalar mixing in bubble column reactors.

Traditionally, the Axial Dispersion Model (ADM) with interface mass transport has been used to describe the degree of backmixing in both phases. Kastanek *et al.* (1993) and Fan (1989) presented detailed reviews of the correlations available for estimating the gas as well as liquid phase effective dispersion coefficients pertinent to the Axial Dispersion Model. However, these correlations are mostly empirical and do not provide reliable estimates for design and scale-up purposes. One of the reasons for the poor predictive capabilities of these correlations is that the ADM is suitable only for modeling of mixing processes in which the flow is not far away from ideal plug flow conditions. Therefore, for recirculation dominated convective flows, such as those occurring in bubble column operation, the application of the Axial Dispersion Model to describe the state of mixing is without a firm physical basis and the model has had success only in fitting the experimental data. Degaleesan *et al.* (1996^a) presented in detail the shortcomings of the ADM applied to liquid and gas tracer data from a pilot-scale slurry-bubble column during liquid phase methanol synthesis at the La Porte Alternate Fuels Development Unit (AFDU). It was shown that the gas and liquid phase dispersion coefficients fitted to the tracer responses, measured at various elevations, did not exhibit a consistent trend, and the values were widely scattered around the estimated means. Moreover, attempts to extract other parameters from the tracer data such as volumetric mass transfer coefficients did not seem to produce consistent results either.

It was subsequently shown in a separate study that the *liquid phase* mixing can be predicted in agreement with experimental data using a two-compartment mechanistic model (Degaleesan *et al.*, 1996^b; Degaleesan, 1997), which accounted for mixing dominated by convective recirculation. Degaleesan and Dudukovic' (1999) also derived the relationship between the liquid phase axial dispersion coefficient and the parameters of the phenomenological recirculation and eddy diffusion model, estimated from the detailed liquid phase hydrodynamics from CARPT, and explained the difficulties involved in obtaining a predictive axial dispersion coefficient. Based on detailed liquid phase hydrodynamics from CARPT measurements, Degaleesan (1997) also developed correlations for predicting the eddy diffusion coefficients (Appendix A). When predictions from these correlations were independently used in the framework of the convection dominated recirculation model, good agreement was achieved between model predictions and liquid-phase tracer data from a pilot scale reactor. It should however be noted that the correlations developed by Degaleesan (1997), for predicting the liquid-phase eddy-diffusion coefficients, are primarily based on data acquired in an air-water system at atmospheric conditions, with no internals and are limited to a maximum superficial gas velocity of 12 cm/sec. For larger diameter vessels operating under pressurized conditions, Degaleesan (1997) used an equivalent superficial gas velocity that leads to the same overall gas holdup in air-water atmospheric systems as the *known* gas holdup in the large diameter vessels. This equivalent superficial gas velocity is subsequently used in the correlations presented in Appendix A to estimate the eddy diffusion coefficients. In addition, a method was also proposed to account for the presence of internal heat exchanger tubes on the radial eddy-diffusion coefficients while the effect of internals on the axial eddy-diffusion coefficients was assumed negligible. In view of this *ad hoc* methodology to account for large vessel diameter, high pressure and presence of internals, uncertainties may still exist when using this methodology for estimating diffusion coefficients in systems other than air-water operating under high-pressure conditions. Nevertheless, given the ever expanding CARPT database, it should become possible in the near future to map out the hydrodynamics of the liquid phase in

bubble column flows resulting from operation at high superficial gas velocities, high pressures and in the presence of significant loadings of slurry particles.

Contrary to the liquid-phase, the modeling of mixing in the gas phase has still not received much attention, with the ADM being used for lack of better alternatives. One of the primary reasons for the relatively limited information on gas phase hydrodynamics is the difficulty associated with reliable gas-phase measurements at high volume fraction of the dispersed phase. In the absence of this detailed information, the characterization of the gas phase dynamics has primarily been limited to the measurement of overall dispersion coefficients in the framework of ADM. Models other than the ADM describe the gas phase dynamics in terms of "small" and "large" bubble classes resulting from a bimodal distribution of bubble sizes, the existence of which is postulated based on Dynamic Gas Disengagement (DGD) measurements (Vermeer and Krishna, 1981; Shah *et al.*, 1985). These two classes of bubbles were shown to coalesce and interact frequently with each other resulting in higher mass transfer rates (de Swart, 1996). However, in spite of a better physical basis resulting from the consideration of a possible bimodal distribution of bubble sizes, these models do not account for the effect of gas and liquid recirculation and turbulence responsible for most of the ensuing mixing.

As discussed in Chapter 2, in contrast to the ADM the Computational Fluid Dynamic (CFD) models provide a rational basis for treatment of bubble column flows. Mathematical modeling and numerical simulation in the framework of the two-fluid model, using multiphase CFD, have recently been used to predict mixing phenomena based on detailed hydrodynamics occurring in large-scale bubble column flows (Krishna *et al.*, 1998). A CFD model, in principle, can provide detailed hydrodynamic information such as velocities, phase fractions, turbulence quantities, etc. at each point in a 3-D domain as a function of time. However, the choice of the correct closures and phase interaction terms needed to yield accurate CFD predictions of flow patterns in churn-turbulent bubble columns is still a matter of art (Boisson and Malin, 1996; Jakobsen *et al.*, 1997; Krishna *et al.*, 2000^b). The primary reason for this situation is that the CFD codes, in general, attempt to predict the macro-scale flow and transport phenomena.

However, these macro-scale phenomena are essentially the result of the complex coupling of the governing phenomena *viz.* bubble-bubble interactions, bubble shape, size and velocity fluctuations, bubble interactions with liquid phase turbulence, etc., which occur on relatively small scales. Unfortunately, measurements at these smaller scales and under actual operating conditions are still in their infancy, with the common measurement techniques being limited to the characterization of the global and large scale phenomena only. Consequently, there is limited experimental information on reliably relating the small-scale phenomena to the macro-scale phenomena, commonly referred to as sub-grid scale modeling. Currently therefore, it is the modeling of the small scale phenomena and their interactions with larger scales that limits the capability of Computational Fluid Dynamics (CFD) in serving as a stand-alone tool for prediction of bubble column reactor performance.

Given the state-of-the art, it is quite likely that fully predictive calculations of reactor performance using multiphase CFD in realistic time frames and with no arbitrary tuning parameters are still decades away. Therefore, until the use of multiphase CFD for reactor design gets well-established, it is desirable to have simplified CFD-like models in conjunction with available experimental observations, which are able to capture most of the observed physical phenomena and provide a reasonably reliable and rational method for design and scale-up. This goal is especially important for reactors involving complex chemistries in industrially relevant very large-scale systems such as those for Fischer-Tropsch synthesis. As mentioned previously, incorporation of the observable physics into such intermediate mechanistic models has been successfully demonstrated in describing the liquid phase mixing of bubble column flows (Myers *et al.*, 1987; Degaleesan *et al.*, 1996^b; Degaleesan, 1997). The primary basis for these liquid-mixing models is the liquid phase recirculation resulting from the gradients in the radial gas-holdup distribution. Superimposed on the recirculation is the radial and axial eddy diffusion resulting from the liquid phase turbulence. These hydrodynamic observations are supported by an extensive experimental database generated by the non-invasive measurement techniques consisting of Computed Tomography-CT and Computer Automated Radioactive Particle

Tracking-CARPT discussed in earlier chapters (Devanathan *et al.*, 1990; Devanathan, 1991; Kumar *et al.*, 1995; Kumar *et al.*, 1997; Degaleesan, 1997; Chen *et al.*, 1998). Thus, an accurate description of liquid phase recirculation and turbulent eddy diffusion results in good predictive capabilities of the liquid mixing model developed by Degaleesan (1997). For most flow situations of industrial relevance, however, detailed hydrodynamic information is usually not available. As mentioned earlier, Degaleesan (1997) has presented a methodology to estimate the liquid mixing model parameters for such cases.

The remarkable agreement between the predictions of the mechanistic liquid mixing model of Degaleesan (1997) with experimental data implies that models which reliably capture the recirculatory flows and superimposed eddy diffusion in bubble columns can be successfully used for predictive purposes. This is the primary motivation for the development of gas phase mixing models presented in the study. As mentioned earlier, since only limited experimental information is available on gas phase hydrodynamics in the churn-turbulent regime, it is necessary to ensure that the gas phase hydrodynamics is at least based on the fundamental principles of mass and momentum conservation. With the primary aim of the present work being the modeling of long-time averaged gas phase recirculation and its interaction with the liquid phase transport processes, the present chapter is divided into several sections. In the first section (Section 6.2), the development of two reactor models describing the transport of a soluble gaseous species is presented while the development of a sub-model for predicting the long time-averaged gas and liquid recirculation velocities is covered in the second section (Section 6.3) of this chapter. The third section (Section 6.4) of the chapter discusses the methodology used in this study to obtain all the parameters of the reactor models presented in Section 6.2 using the results of the predicted recirculation from Section 6.3, the correlations for eddy diffusion coefficients from Appendix A and Higbie's penetration theory for calculating mass transfer coefficients. In the last section (Section 6.5), the developed reactor models are utilized to interpret radioactive gas tracer data from a pilot-scale bubble column operating under conditions of methanol synthesis.

The first of the gas mixing models considered is the Distributed-Bubble Size Model (DBSM), which is based on the assumption that the gas phase dynamics and recirculation can be described in terms of a radially varying mean bubble size, which can be reduced to two bubble classes - a "small" bubble class and a "large" bubble class, with the interaction between the two being modeled using an exchange coefficient (Vermeer and Krishna, 1981; Modak *et al.*, 1994; Krishna and Ellenberger, 1995; de Swart, 1996). The presence of the "large" and "small" bubble phases in a churn-turbulent bubble column open to atmosphere has been widely reported (Krishna *et al.*, 2000^h). However, it is also known that as the system operating pressure increases in churn-turbulent flow, the gas holdup increases due to increased gas density resulting in a reduced bubble size whose distribution becomes narrower (Wilkinson *et al.*, 1992; Luo *et al.*, 1999). Therefore, a second model has been developed where the gas phase dynamics is based just on a single bubble size - Single-Bubble Class Model (SBCM). Both models account for the experimentally observed recirculation in the gas and liquid phases.

The developed sub-models for prediction of liquid and gas recirculation velocity are derived from the Euler-Euler two-fluid representation of the one-dimensional momentum balance equations for the gas and liquid phases (Drew and Passman, 1998); and the liquid phase turbulence is closed in terms of the mixing length. A number of investigators (Kumar *et al.*, 1994; Geary and Rice, 1992; Luo and Svendsen, 1991; Rice and Geary, 1990; Ueyama and Miyauchi, 1979) reported a similar approach to describe only liquid-phase recirculation. In this study, the model equations and closures used for the liquid phase turbulence have been modified. In particular, the momentum balance equations have been derived from the two-fluid equations, and the model has been extended to calculate the radial profile of the axial gas phase velocity in addition to the liquid recirculation profile. As mentioned previously, the recirculation of liquid and gas predicted by these sub-models forms the basis for estimating the parameters of the developed reactor mixing models. In Section 6-4, an alternate methodology of estimating the model parameters based on correlations reported by Krishna and co-workers is examined along with problems in using their method of parameter estimation.

For purposes of evaluating the predictive capabilities of the developed reactor models, data from the gas tracer-experiments has been compared with the simulation results from the mixing models. These radioactive gas-phase tracer experiments were conducted in a pilot-scale reactor at the Alternate Fuels Development Unit (AFDU) in La Porte, Texas during liquid-phase methanol synthesis. A brief summary of these experiments is presented in Section 6.5. The solution of the reactor model equations has been achieved using a robust and completely implicit finite difference scheme. In addition, the sensitivity of the simulation results to the solubility of Ar^{41} in the liquid/slurry and other model parameters has been evaluated. Liquid and catalyst tracer experiments were also performed during these pilot runs, the analysis of which has been reported elsewhere (Degaleesan, 1996^a).

6.2. Phenomenological/Mechanistic Reactor Models

The flow of gas and liquid in bubble column operations is always transient and there is no true steady state operation (Devanathan; 1991; Chen and Fan, 1992; Degaleesan, 1997; Mudde *et al.*, 1997). This is the consequence of the spiraling motion of gas bubbles through the liquid as intermittent helical vortices which are highly chaotic in nature (Letzel, 1997). However, time averaging of such flows (for times as small as 60-120 seconds of CFD data and for progressively longer times of experimental data from techniques like PIV, LDA and CARPT) produces a remarkably predictable symmetric flow pattern of the liquid. The observed time-averaged liquid flow pattern in a typical bubble column operation is represented schematically in Figure 6-1.

The radial distribution of gas holdup depicted in Figure 6-1 is known to result in a single liquid recirculation loop with the liquid rising in the center and flowing downwards near the walls. These observations have been experimentally confirmed repeatedly (Degaleesan, 1997, Chen *et al.*, 1998). The primary cause of the liquid recirculation is the gas-phase, which mostly travels upward through the column center and leaves the reactor. Some small sized bubbles, however, do not possess enough

momentum to leave the reactor and recirculate along with the liquid. In addition to this convective recirculation, momentum transport is caused by the bubble wakes, bubble-bubble interactions, and bubble and shear-induced turbulence, all of which contribute to what is typically called ‘eddy diffusion’. The attempt here is to address whether a model based on the overall time-averaged flow pattern, that accounts for the actual transient nature via eddy diffusivities, is capable of predicting scalar distribution in the reactor. Therefore, the hydrodynamic phenomena in a typical bubble column represented schematically in Figure 6-1, consisting of the radial gas holdup profile that drives liquid and gas recirculation with superimposed axial and radial diffusion, form the basis of the mechanistic reactor models developed in this study. Based on the physical picture depicted in Figure 6-1, the reactor compartmentalization for the Single Bubble Class Model is shown in Figure 6-2a, whereas Figure 6-2b shows the same for the Distributed Bubble Size Model. The DBSM is in essence a modification and extension of the gas-mixing model initially proposed by Wang (1996).

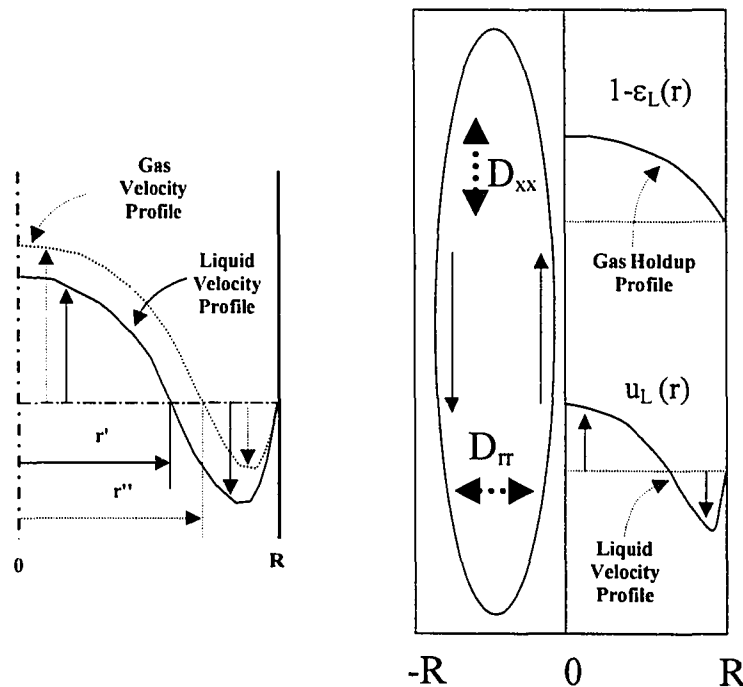
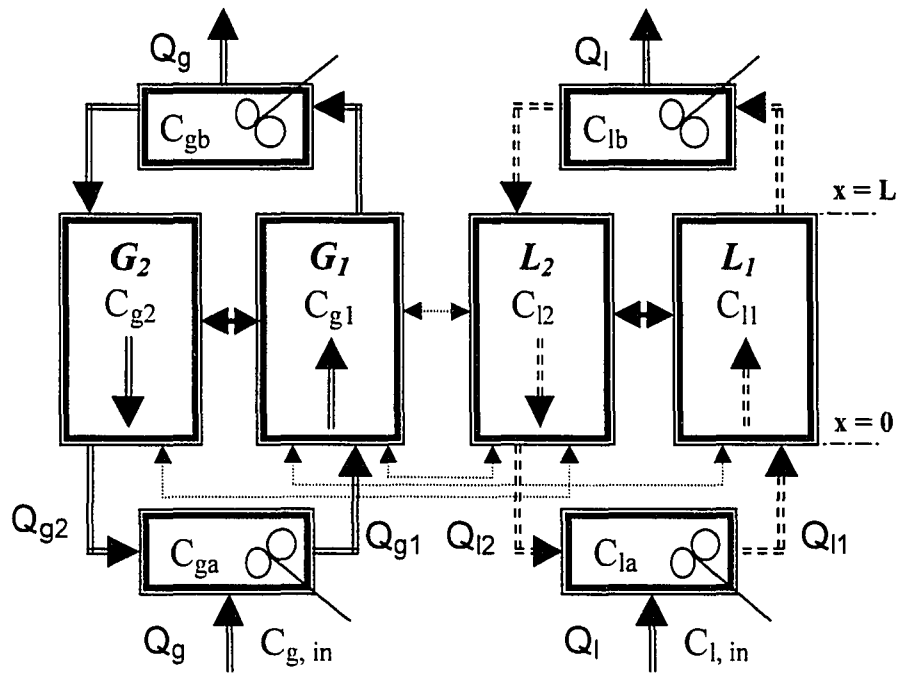
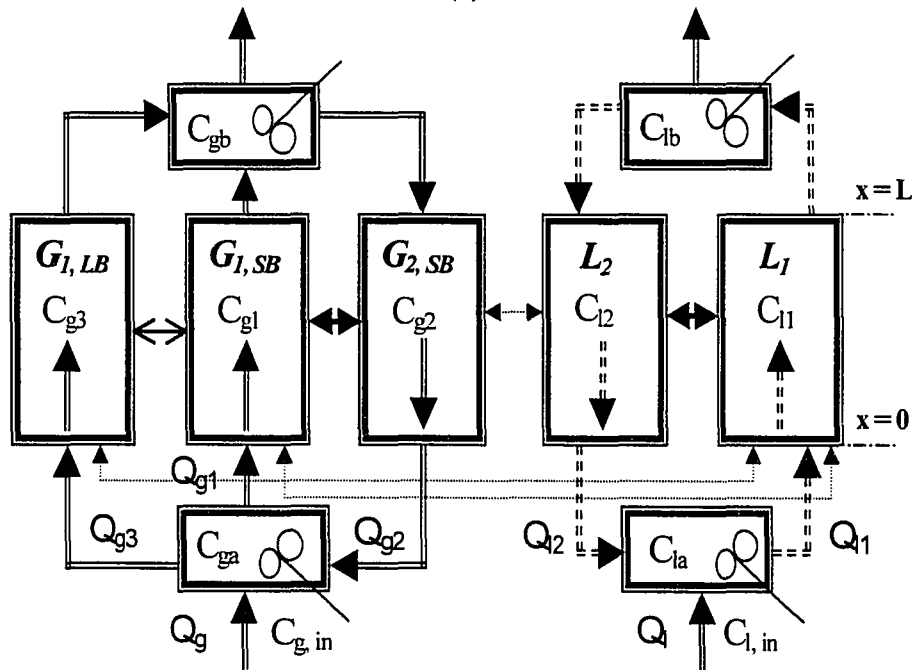


Figure 6-1. Schematic representation of the experimentally observed phenomena in bubble columns.



(a)



(b)

Figure 6-2. Schematic of bubble column reactor compartmentalization for (a) Single Bubble Class Model (SBCM) (b) Distributed Bubble Size Model (DBSM)

It is to be re-iterated that the above physical picture, emerging from numerous experimental studies of liquid recirculation reported in the literature (Nottenkamper *et al.*, 1983; Menzel *et al.*, 1990; Yao *et al.*, 1991; Mudde *et al.*, 1997; Mudde *et al.*, 1998), is confirmed by extensive studies conducted by the non-invasive measurement techniques at the Chemical Reaction Engineering Laboratory (CREL) in Washington University-Saint Louis consisting of Computed Tomography-CT and Computer Automated Radioactive Particle Tracking-CARPT (Devanathan *et al.*, 1990; Devanathan, 1991; Kumar *et al.*, 1995; Kumar *et al.*, 1997; Degaleesan, 1997; Chen *et al.*, 1998). CT provides non-invasive measurement of the long-time averaged, cross-sectional distribution of gas holdup in any reactor cross-section. The details of the γ -ray scanner and associated tomography reconstruction algorithms developed in CREL have been discussed elsewhere (Kumar *et al.*, 1995; Kumar *et al.*, 1997). As discussed in Chapters 2 and 5, the CARPT technique provides information on the long-time averaged liquid velocity profile, turbulent stresses and eddy diffusivities. Details of the principles and methodology of the CARPT technique have also been extensively documented elsewhere (Devanathan *et al.*, 1990; Degaleesan, 1997).

For both the mixing models, the gas phase is assumed to recirculate along with the liquid/slurry phase which has been assumed pseudo-homogeneous for the purposes of this study. The net flow of liquid could be either zero (batch mode of operation) or a co-current up-flow with the net flow of the liquid. In either case, the liquid flow pattern inside the reactor consists of up-flow region (L_1) in the core and down-flow region (L_2) near the wall. The gas phase also has a similar recirculation pattern; with up-flow in the center, and down flow by the wall consisting of bubbles that do not possess sufficient momentum and get recirculated along with the liquid. As can be seen from Figure 6-1, the up-flow liquid region extends from the column center to the radial location, r' while the down-flow liquid zone extends from r' to the column wall. Similarly, the up-flow gas zone extends from the column center to r'' with the down-flow region confined to radial locations from r'' to the wall. As is evident from Figure 6-1, r' and r'' are the radial locations where the radial profiles of the liquid and gas axial velocities become zero.

The manner in which the hydrodynamics of the up-flowing gas is described determines the models presented in Figure 6-2. In the model development for the SBCM, it is assumed that the gas phase dynamics is fully represented in terms of a single mean bubble size both in the core up-flow (G_1) as well as the wall down-flow (G_2) regions. However, it is a common observation in the churn-turbulent regime of bubble column operation (Chen *et al.*, 1994) that the upward flowing gas usually consists of relatively small bubbles trapped in the wakes of the larger fast rising bubbles, and drags the liquid along with it. Therefore, in the development of DBSM, it is assumed that the up-flowing gas in the core of the reactor consists of a lean "large-bubble" phase ($G_{1, LB}$) and a dense "small-bubble" phase ($G_{1, SB}$) (Krishna, 2000^h). Meanwhile the down-flowing gas in the annular region consists only of small bubbles ($G_{2, SB}$) which do not possess sufficient momentum and are therefore recirculated along with the down-flowing slurry.

In both SBCM and DBSM mixing models, the top (disengagement) and the bottom (distributor) zones of height equal to column diameter, D_c , are modeled as being well mixed (Continuous Stirred Tanks – CSTs). Changing the height of these zones between $0.5D_c$ and $2.0D_c$ did not have a noticeable effect on the predicted liquid tracer responses (Degaleesan *et al.*, 1996^b), provided the height of the gas-liquid mixture is much larger than the column diameter (L/D_c is at least 6). This could be attributed to the predominance of the recirculatory flows that primarily govern the characteristic mixing times. For example, if Q_R is the liquid recirculation flow-rate, then the characteristic times for the end zones and the well-developed zones are their volumes divided by Q_R . Since the total liquid volume is constant, a redistribution of the volume among the various zones would probably not affect significantly the overall mixing times. Of course, the well-developed zone should not collapse to zero so that axial and radial dispersion effects are completely eliminated. This, however, is a very simplistic explanation of the effect of the size of end zones on tracer responses and simulation of the model equations should be used to quantitatively assess the different scenarios. It is shown in this study via simulations that as with the liquid phase, the effect of varying the height of these end zones to $0.5D_c$ and $2.0D_c$ on the gas-phase tracer responses is insignificant as well.

6.2.1. Single Bubble Class Model (SBCM)

A differential element along the reactor length in the developed part of the flow, which occupies most of the column, consists of four zones for SBCM into which the reactor cross-section is compartmentalized. By applying mass balances for a soluble species in each of these zones within the differential element, one obtains a set of four transient convection-diffusion Partial Differential Equations (PDEs) with mass interphase transfer and radial exchange between the zones acting as source terms. Additional source terms appear in the form of reaction rates, if simulations are being carried out for a reactive species in a bubble column reactor operated under reaction conditions. On the other hand, the equations describing the dynamics of the perfectly mixed tanks representing the distributor and disengagement zones are only Ordinary Differential Equations (ODEs). Therefore, the reactor model results in a coupled set of four PDEs and four ODEs as summarized below for a representative chemical species. Other details regarding the liquid phase mixing model can be found in Degaleesan *et al.* (1996^b) while those for gas and liquid mixing with interphase mass transfer are described by Gupta *et al.* (2001^a) and are presented in the following sections. The model equations are listed below (refer to Figure 6-2a).

For the gas moving up-wards (G₁)

$$\frac{\partial C_{g1}}{\partial t} = \left\{ \begin{array}{l} \bar{D}_{xx1} \frac{\partial^2 C_{g1}}{\partial x^2} - \bar{u}_{g1} \frac{\partial C_{g1}}{\partial x} - \frac{4(\bar{D}_{rr} \epsilon_g)_{r=r''}}{r'' R \bar{\epsilon}_{g1}} (C_{g1} - C_{g2}) + R_{x,g1} \\ - \frac{k_{gulu} a_{gulu}}{\bar{\epsilon}_{g1}} (HC_{g1} - C_{l1}) - \frac{k_{guld} a_{guld}}{\bar{\epsilon}_{g1}} (HC_{g1} - C_{l2}) \end{array} \right\} \quad (6-1)$$

For the gas moving down-wards (G₂)

$$\frac{\partial C_{g2}}{\partial t} = \left\{ \begin{array}{l} \bar{D}_{xx2} \frac{\partial^2 C_{g2}}{\partial x^2} + \bar{u}_{g2} \frac{\partial C_{g2}}{\partial x} - \frac{k_{gdld} a_{gdld}}{\bar{\epsilon}_{g2}} (HC_{g2} - C_{l2}) \\ + \frac{4r''/R (\bar{D}_{rr} \epsilon_g)_{r=r''}}{R^2 - r''^2} \bar{\epsilon}_{g2} (C_{g1} - C_{g2}) + R_{x,g2} \end{array} \right\} \quad (6-2)$$

For the liquid moving up-wards (L_1)

$$\frac{\partial C_{l1}}{\partial t} = \left\{ \begin{array}{l} \bar{D}_{xx1} \frac{\partial^2 C_{l1}}{\partial x^2} - \bar{u}_{l1} \frac{\partial C_{l1}}{\partial x} + \left(\frac{r''}{r'} \right)^2 \frac{k_{gulu} a_{gulu}}{\bar{\varepsilon}_{l1}} (HC_{g1} - C_{l1}) \\ - \frac{4(\bar{D}_{rr} \varepsilon_l)_{r=r'}}{r' R \bar{\varepsilon}_{l1}} (C_{l1} - C_{l2}) + R_{x,l1} \end{array} \right\} \quad (6-3)$$

For the liquid moving down-wards (L_2)

$$\frac{\partial C_{l2}}{\partial t} = \left\{ \begin{array}{l} \bar{D}_{xx2} \frac{\partial^2 C_{l2}}{\partial x^2} + \bar{u}_{l2} \frac{\partial C_{l2}}{\partial x} + \frac{4r'/R}{R^2 - r'^2} \frac{(\bar{D}_{rr} \varepsilon_l)_{r=r'}}{\bar{\varepsilon}_{l2}} (C_{l1} - C_{l2}) + R_{x,l2} + \\ \left(\frac{r''^2}{R^2 - r'^2} \right) \frac{k_{guld} a_{guld}}{\bar{\varepsilon}_{l2}} (HC_{g1} - C_{l2}) + \left(\frac{R^2 - r''^2}{R^2 - r'^2} \right) \frac{k_{gdld} a_{gdld}}{\bar{\varepsilon}_{l2}} (HC_{g2} - C_{l2}) \end{array} \right\} \quad (6-4)$$

Gas in the distributor zone

$$\frac{dC_{ga}}{dt} = \left\{ \begin{array}{l} \frac{U_G}{\bar{\varepsilon}_g \phi_{in} D_C} C_{g,in} - \frac{U_G}{\bar{\varepsilon}_g \phi_{in} D_C} C_{ga} + \frac{\bar{\varepsilon}_{g1} r''^2}{\bar{\varepsilon}_g \phi_{in} D_C R^2} \bar{D}_{xx1} \frac{\partial C_{g1}}{\partial x} \Big|_{x=0} \\ + \frac{\bar{\varepsilon}_{g2} (R^2 - r''^2)}{\bar{\varepsilon}_g \phi_{in} D_C R^2} \bar{D}_{xx2} \frac{\partial C_{g2}}{\partial x} \Big|_{x=0} - \frac{k_{CST} a_{CST}}{\bar{\varepsilon}_g} (HC_{ga} - C_{la}) + R_{x,ga} \end{array} \right\} \quad (6-5)$$

Liquid in the distributor zone

$$\frac{dC_{la}}{dt} = \left\{ \begin{array}{l} \frac{U_L}{\bar{\varepsilon}_l \phi_{in} D_C} C_{l,in} - \frac{U_L}{\bar{\varepsilon}_l \phi_{in} D_C} C_{la} + \frac{\bar{\varepsilon}_{l1} r'^2}{\bar{\varepsilon}_l \phi_{in} D_C R^2} \bar{D}_{xx1} \frac{\partial C_{l1}}{\partial x} \Big|_{x=0} \\ + \frac{\bar{\varepsilon}_{l2} (R^2 - r'^2)}{\bar{\varepsilon}_l \phi_{in} D_C R^2} \bar{D}_{xx2} \frac{\partial C_{l2}}{\partial x} \Big|_{x=0} + \frac{k_{CST} a_{CST}}{\bar{\varepsilon}_l} (HC_{ga} - C_{la}) + R_{x,la} \end{array} \right\} \quad (6-6)$$

Gas in the disengagement zone

$$\frac{dC_{gb}}{dt} = \left\{ \begin{array}{l} - \frac{\bar{\varepsilon}_{g1} r''^2}{\bar{\varepsilon}_g \phi_{out} D_C R^2} \bar{D}_{xx1} \frac{\partial C_{g1}}{\partial x} \Big|_{x=l} - \frac{\bar{\varepsilon}_{g2} (R^2 - r''^2)}{\bar{\varepsilon}_g \phi_{out} D_C R^2} \bar{D}_{xx2} \frac{\partial C_{g2}}{\partial x} \Big|_{x=l} \\ - \frac{k_{CST} a_{CST}}{\bar{\varepsilon}_g} (HC_{gb} - C_{lb}) + R_{x,gb} \end{array} \right\} \quad (6-7)$$

Liquid in the disengagement zone

$$\frac{dC_{lb}}{dt} = \left\{ \begin{array}{l} -\frac{\bar{\varepsilon}_{l1}}{\bar{\varepsilon}_l \phi_{out} D_C} \frac{r'^2}{R^2} \bar{D}_{xx1} \left. \frac{\partial C_{l1}}{\partial x} \right|_{x=l} - \frac{\bar{\varepsilon}_{l2}}{\bar{\varepsilon}_l \phi_{out} D_C} \frac{(R^2 - r'^2)}{R^2} \bar{D}_{xx2} \left. \frac{\partial C_{l2}}{\partial x} \right|_{x=l} \\ + \frac{k_{CST} a_{CST}}{\bar{\varepsilon}_l} (HC_{gb} - C_{lb}) + R_{x,lb} \end{array} \right\} \quad (6-8)$$

All symbols are defined in the nomenclature.

Initial Conditions

For dynamic impulse tracer tests the initial conditions in all zones of the reactor are those of zero initial concentration of the species to be introduced at time $t = 0^+$ at the reactor inlet.

$$t = 0; \quad C_{la} = C_{lb} = C_{ga} = C_{gb} = C_{l1} = C_{l2} = C_{g1} = C_{g2} = 0 \quad (6-9)$$

The inlet function for describing the introduction of a species at the reactor inlet depends on the simulation objectives. For simulating the distribution evolution of a reactant species under reaction conditions, one would typically have a step change in the concentration of the species at the reactor inlet. However, here we are interested in simulating the distribution of a non-reacting tracer. Additionally, this initial condition for the tracer at the inlet depends on the method of tracer injection, and whether it is an impulse tracer test, or a step-up/step-down tracer test. For the results presented in this study, the experimental impulse input for the tracer runs at AFDU, La Porte have been simulated using a Gaussian function with a tail (Degaleesan, 1997).

$$t \rightarrow 0^+, t > 0; \quad C_{g,in} = \frac{\psi}{\sqrt{2\pi\kappa t}} \exp\left\{-\frac{(\delta - \chi)^2}{2\kappa t}\right\} \quad C_{l,in} = 0 \quad (6-10)$$

Boundary conditions for the fully developed region

The earlier work on the liquid mixing model (Degaleesan *et al.*, 1996^b) and gas-liquid mixing models (Gupta *et al.*, 2001^a; Gupta *et al.*, 2001^b) used the Danckwerts' boundary conditions at the inlet and outlet of the well-developed zones with the understanding that this should guarantee the preservation of mass for each phase. However, upon close examination, it was realized that the boundaries of the well-developed zones with the distributor and disengagement regions are internal and thus don't exactly represent the physical picture representative of Danckwerts' boundary conditions for a closed system. Therefore, the correct boundary conditions to use are of Dirichlet type where the concentrations at the ends of the well-developed zones are matched with those of the well-mixed regions. In other words, the bottom of the fully developed flow zone is the boundary with the CST representing the distributor zone, whereas the top of the fully developed flow zone is the boundary with the CST representing the disengagement zone.

Appendix B presents the analysis of the effect of these two types of boundary conditions on the simulated tracer responses. It was important to compare their effect on simulation results since, as mentioned above, earlier work on these mixing models reported by Degaleesan *et al.* (1996^b) and Gupta *et al.* (2001^a, 2001^b), used the "incorrect" Danckwerts' boundary conditions. Fortunately, for conditions studied in the above reported papers, the effect of boundary conditions on the results was not pronounced and the reported results are valid as shown in Appendix B.

The "correct" Dirichlet boundary conditions used for the well-developed zones are specified below.

Up-flow section of the gas

$$x = 0; \quad C_{g1} |_{x=0} = C_{ga} \quad (6-11)$$

$$x = L; \quad C_{g1} |_{x=L} = C_{gb} \quad (6-12)$$

Down-flow section of the gas

$$x = L; \quad C_{g2} \big|_{x=L} = C_{gb} \quad (6-13)$$

$$x = 0; \quad C_{g2} \big|_{x=0} = C_{ga} \quad (6-14)$$

Up-flow section of the liquid

$$x = 0; \quad C_{l1} \big|_{x=0} = C_{la} \quad (6-15)$$

$$x = L; \quad C_{l1} \big|_{x=L} = C_{lb} \quad (6-16)$$

Down-flow section of the liquid

$$x = L; \quad C_{l2} \big|_{x=L} = C_{lb} \quad (6-17)$$

$$x = 0; \quad C_{l2} \big|_{x=0} = C_{la} \quad (6-18)$$

6.2.2. Distributed Bubble Size Model (DBSM)

In the same manner as for SBCM, applying the mass balance for a soluble species on a differential element along the reactor length in the developed part of the flow depicted in Figure 6-2b yields a set of five transient convection-diffusion Partial Differential Equations (PDEs). The five zones include the liquid flow upward (L_1) and liquid flowing downward (L_2) as in SBCM. Along with the up-flowing liquid, there exists an up-flowing gas zone in the core of the reactor consisting of a lean "large-bubble" phase ($G_{1, LB}$) and a dense "small-bubble" phase ($G_{1, SB}$). Meanwhile the down-flowing gas in the annular region consists only of small bubbles ($G_{2, SB}$) recirculating with the down-flowing liquid. It is to be noted that the description of the three "gas phases" is obtained from a radial distribution of the mean bubble size, as discussed later in Section 6.3. As with SBCM, the source terms appear describing interphase mass transfer and radial exchange between the up-flowing and down-flowing zones. For DBSM however, an additional source term appears in the equations resulting from mass exchange due to bubble-bubble interactions between "large" and "small" bubbles. Moreover, since the

model now incorporates an additional up-flowing gas phase ($G_{1, LB}$) in the well-developed portion of the flow, the equations for the CSTs representing the end zones interact with this additional phase indirectly via the boundary conditions. The model equations for DBSM are presented below (refer to Figure 6-2b):

For the gas in small bubbles moving up-wards ($G_{1, SB}$)

$$\frac{\partial C_{g1}}{\partial t} = \left\{ \begin{array}{l} \bar{D}_{xx1} \frac{\partial^2 C_{g1}}{\partial x^2} - \frac{4(\bar{D}_{rr} \varepsilon_g)_{r=r''}}{r'' R \bar{\varepsilon}_{g1}} (C_{g1} - C_{g2}) + \frac{K_{SB1-LB}}{\bar{\varepsilon}_{g1}} (C_{g1} - C_{g3}) \\ - \bar{u}_{g1} \frac{\partial C_{g1}}{\partial x} - \frac{k_{sulu} a_{sulu}}{\bar{\varepsilon}_{g1}} (HC_{g1} - C_{l1}) - \frac{k_{suld} a_{suld}}{\bar{\varepsilon}_{g1}} (HC_{g1} - C_{l2}) + R_{x,g1} \end{array} \right\} \quad (6-19)$$

For the gas in small bubbles moving down-wards ($G_{2, SB}$)

$$\frac{\partial C_{g2}}{\partial t} = \left\{ \begin{array}{l} \bar{D}_{xx2} \frac{\partial^2 C_{g2}}{\partial x^2} + \bar{u}_{g2} \frac{\partial C_{g2}}{\partial x} + \frac{4r''/R}{R^2 - r''^2} \frac{(\bar{D}_{rr} \varepsilon_g)_{r=r''}}{\bar{\varepsilon}_{g2}} (C_{g1} - C_{g2}) \\ - \frac{k_{suld} a_{suld}}{\bar{\varepsilon}_{g2}} (HC_{g2} - C_{l2}) + R_{x,g2} \end{array} \right\} \quad (6-20)$$

For the gas in large bubbles moving up-wards ($G_{1, LB}$)

$$\frac{\partial C_{g3}}{\partial t} = \left\{ -\bar{u}_{g3} \frac{\partial C_{g3}}{\partial x} - \frac{k_l a_l}{\bar{\varepsilon}_{g3}} (HC_{g3} - C_{l1}) - \frac{K_{SB1-LB}}{\bar{\varepsilon}_{g3}} (C_{g1} - C_{g3}) + R_{x,g3} \right\} \quad (6-21)$$

For the liquid moving up-wards (L_1)

$$\frac{\partial C_{l1}}{\partial t} = \left\{ \begin{array}{l} \bar{D}_{xx1} \frac{\partial^2 C_{l1}}{\partial x^2} - \bar{u}_{l1} \frac{\partial C_{l1}}{\partial x} - \frac{4(\bar{D}_{rr} \varepsilon_l)_{r=r'}}{r' R \bar{\varepsilon}_{l1}} (C_{l1} - C_{l2}) + R_{x,l1} \\ + \left(\frac{r''}{r'} \right)^2 \frac{1}{\bar{\varepsilon}_{l1}} \left[k_{sulu} a_{sulu} (HC_{g1} - C_{l1}) + k_l a_l (HC_{g3} - C_{l1}) \right] \end{array} \right\} \quad (6-22)$$

For the liquid moving down-wards (L_2)

$$\frac{\partial C_{l2}}{\partial t} = \left\{ \begin{aligned} & \bar{D}_{xx2} \frac{\partial^2 C_{l2}}{\partial x^2} + \bar{u}_{l2} \frac{\partial C_{l2}}{\partial x} + \frac{4r'/R}{R^2 - r'^2} \left(\frac{\bar{D}_{rr} \varepsilon_l}{\bar{\varepsilon}_{l2}} \right)_{r=r'} (C_{l1} - C_{l2}) \\ & + \left(\frac{r'^2}{R^2 - r'^2} \right) \frac{k_{sdl2} a_{sdl2}}{\bar{\varepsilon}_{l2}} (HC_{g1} - C_{l2}) + R_{x,l2} \\ & + \left(\frac{R^2 - r'^2}{R^2 - r'^2} \right) \frac{k_{sdl2} a_{sdl2}}{\bar{\varepsilon}_{l2}} (HC_{g2} - C_{l2}) \end{aligned} \right\} \quad (6-23)$$

Gas in the distributor zone

$$\frac{dC_{ga}}{dt} = \left\{ \begin{aligned} & \frac{U_G}{\bar{\varepsilon}_g \phi_{in} D_C} C_{g,in} - \frac{U_G}{\bar{\varepsilon}_g \phi_{in} D_C} C_{ga} + \frac{\bar{\varepsilon}_{g1}}{\bar{\varepsilon}_g \phi_{in} D_C} \frac{r'^2}{R^2} \bar{D}_{xx1} \frac{\partial C_{g1}}{\partial x} \Big|_{x=0} \\ & + \frac{\bar{\varepsilon}_{g2}}{\bar{\varepsilon}_g \phi_{in} D_C} \frac{(R^2 - r'^2)}{R^2} \bar{D}_{xx2} \frac{\partial C_{g2}}{\partial x} \Big|_{x=0} - \frac{k_{CST} a_{CST}}{\bar{\varepsilon}_g} (HC_{ga} - C_{la}) + R_{x,ga} \end{aligned} \right\} \quad (6-24)$$

Liquid in the distributor zone

$$\frac{dC_{la}}{dt} = \left\{ \begin{aligned} & \frac{U_L}{\bar{\varepsilon}_l \phi_{in} D_C} C_{l,in} - \frac{U_L}{\bar{\varepsilon}_l \phi_{in} D_C} C_{la} + \frac{\bar{\varepsilon}_{l1}}{\bar{\varepsilon}_l \phi_{in} D_C} \frac{r'^2}{R^2} \bar{D}_{xx1} \frac{\partial C_{l1}}{\partial x} \Big|_{x=0} \\ & + \frac{\bar{\varepsilon}_{l2}}{\bar{\varepsilon}_l \phi_{in} D_C} \frac{(R^2 - r'^2)}{R^2} \bar{D}_{xx2} \frac{\partial C_{l2}}{\partial x} \Big|_{x=0} + \frac{k_{CST} a_{CST}}{\bar{\varepsilon}_l} (HC_{ga} - C_{la}) + R_{x,la} \end{aligned} \right\} \quad (6-25)$$

Gas in the disengagement zone

$$\frac{dC_{gb}}{dt} = \left\{ \begin{aligned} & - \frac{\bar{\varepsilon}_{g1}}{\bar{\varepsilon}_g \phi_{out} D_C} \frac{r'^2}{R^2} \bar{D}_{xx1} \frac{\partial C_{g1}}{\partial x} \Big|_{x=l} - \frac{\bar{\varepsilon}_{g2}}{\bar{\varepsilon}_g \phi_{out} D_C} \frac{(R^2 - r'^2)}{R^2} \bar{D}_{xx2} \frac{\partial C_{g2}}{\partial x} \Big|_{x=l} \\ & - \frac{k_{CST} a_{CST}}{\bar{\varepsilon}_g} (HC_{gb} - C_{lb}) + R_{x,gb} \end{aligned} \right\} \quad (6-26)$$

Liquid in the disengagement zone

$$\frac{dC_{lb}}{dt} = \left\{ \begin{aligned} & - \frac{\bar{\varepsilon}_{l1}}{\bar{\varepsilon}_l \phi_{out} D_C} \frac{r'^2}{R^2} \bar{D}_{xx1} \frac{\partial C_{l1}}{\partial x} \Big|_{x=l} - \frac{\bar{\varepsilon}_{l2}}{\bar{\varepsilon}_l \phi_{out} D_C} \frac{(R^2 - r'^2)}{R^2} \bar{D}_{xx2} \frac{\partial C_{l2}}{\partial x} \Big|_{x=l} \\ & + \frac{k_{CST} a_{CST}}{\bar{\varepsilon}_l} (HC_{gb} - C_{lb}) + R_{x,lb} \end{aligned} \right\} \quad (6-27)$$

Initial Conditions

As for SBCM for an impulse tracer test, the initial conditions in all zones of the reactor are those of zero initial concentration of the species to be introduced at time $t = 0^+$ at the reactor inlet.

$$t = 0; \quad C_{1a} = C_{1b} = C_{ga} = C_{gb} = C_{l1} = C_{l2} = C_{g1} = C_{g2} = C_{g3} = 0 \quad (6-28)$$

The experimental impulse input for the gas tracer runs simulated using the DBSM is the same as that used with SBCM.

$$t \rightarrow 0^+, t > 0; \quad C_{g,in} = \frac{\Psi}{\sqrt{2\pi\kappa t}} \exp\left\{-\frac{(\delta - \chi)^2}{2\kappa t}\right\} \quad C_{l,in} = 0 \quad (6-29)$$

Boundary conditions for the fully developed region

As before, Dirichlet boundary conditions are used at the inlet and exit of the well-developed zones, to guarantee preservation of mass for each phase. All the boundary conditions used are specified below.

Up-flow section of the gas in small bubbles

$$x = 0; \quad C_{g1} |_{x=0} = C_{ga} \quad (6-30)$$

$$x = L; \quad C_{g1} |_{x=L} = C_{gb} \quad (6-31)$$

Down-flow section of the gas in the small bubbles

$$x = L; \quad C_{g2} |_{x=L} = C_{gb} \quad (6-32)$$

$$x = 0; \quad C_{g2} |_{x=0} = C_{ga} \quad (6-33)$$

Up-flow section of the gas in large bubbles

$$x = 0; \quad C_{g3} |_{x=0} = C_{ga} \quad (6-34)$$

Up-flow section of the liquid

$$x = 0; \quad C_{l1} |_{x=0} = C_{la} \quad (6-35)$$

$$x = L; \quad C_{l1} |_{x=L} = C_{lh} \quad (6-36)$$

Down-flow section of the liquid

$$x = L; \quad C_{l2} |_{x=L} = C_{lh} \quad (6-37)$$

$$x = 0; \quad C_{l2} |_{x=0} = C_{la} \quad (6-38)$$

In the above set of equations, \bar{D}_{xx} and \bar{D}_{rr} are the average axial and radial eddy diffusivities, respectively, which are estimated from a scale-up methodology developed by Degaleesan (1997) from CARPT data. For description of other symbols used in the equations above, the reader is referred to the nomenclature.

For a non-reactive and soluble gas tracer, the simulation results presented in this study have been computed based on the model equations presented above via a completely implicit finite difference scheme (FTCS - first order Forward differences in Time and second order Central differences in Space), which is robust and unconditionally stable. Since for simulation of tracer responses there are no non-linear terms in the equations, one needs to invert the matrix only once. This is accomplished by obtaining the LU decomposition of the matrix resulting from the application of the differencing scheme. The solution at successive times is simply obtained by matrix multiplication of the solution at previous time by repetitive LU back-substitution.

Before one can employ the numerical scheme discussed above for the solution of these reactor model equations, one needs as inputs the hydrodynamic model parameters. As mentioned before, a sub-model for gas and liquid recirculation is needed for this purpose and is discussed below.

6.3. Two-Fluid Sub-Model for Gas and Liquid Phase Axial Momentum Exchange

The starting point in the derivation of the one-dimensional model for the radial liquid and gas-phase velocity profiles is the two-fluid model presented below. The model equations are the result of the ensemble and Reynolds averaged approach of Drew and Passman (1998). Here, the subscript 'l' denotes the continuous liquid/slurry phase, whereas the subscript 'g' denotes the dispersed gas phase, and both phases are considered incompressible.

Equations of Continuity

$$\text{Liquid/Slurry} \quad \frac{\partial \varepsilon_l}{\partial t} + \nabla \cdot (\varepsilon_l \mathbf{u}_l) = 0 \quad (6-39)$$

$$\text{Gas} \quad \frac{\partial \varepsilon_g}{\partial t} + \nabla \cdot (\varepsilon_g \mathbf{u}_g) = 0 \quad (6-40)$$

Momentum Equations

$$\text{Liquid/Slurry} \quad \rho_l \varepsilon_l \left(\frac{\partial \mathbf{u}_l}{\partial t} + \mathbf{u}_l \cdot \nabla \mathbf{u}_l \right) = \left\{ \begin{array}{l} \rho_l \varepsilon_l \mathbf{g} - \varepsilon_l \nabla p - \nabla \cdot (\varepsilon_l \boldsymbol{\tau}_l) \\ - (\mathbf{M}_d + \mathbf{M}_{vm}) - (\mathbf{M}_{Lift} + \mathbf{M}_{Basset}) \end{array} \right\} \quad (6-41)$$

$$\text{Gas} \quad \rho_g \varepsilon_g \left(\frac{\partial \mathbf{u}_g}{\partial t} + \mathbf{u}_g \cdot \nabla \mathbf{u}_g \right) = \left\{ \begin{array}{l} \rho_g \varepsilon_g \mathbf{g} - \varepsilon_g \nabla p - \nabla \cdot (\varepsilon_g \boldsymbol{\tau}_g) \\ + (\mathbf{M}_d + \mathbf{M}_{vm}) + (\mathbf{M}_{Lift} + \mathbf{M}_{Basset}) \end{array} \right\} \quad (6-42)$$

In the momentum balance equations, τ_l and τ_g are the stress tensors representing the normal and shear stresses in the liquid and gas phases, respectively, \mathbf{M}_d is the drag force term, and \mathbf{M}_{vm} is the virtual mass term that arises due to the relative acceleration of the two phases (Drew and Passman, 1998). In more detailed modeling of the momentum exchange between the continuous and dispersed phases, other forces like lift (\mathbf{M}_{Lift}) and Basset-history (\mathbf{M}_{Basset}) are also considered. However, due to lack of good understanding in modeling these forces for high volume fraction flows, these are generally neglected when simulating practical two-phase flow situations. The mathematical representation of

the drag and virtual mass force terms is shown in Equations (6-43) to (6-45), while the reader is referred to Crowe *et al.* (1998) for mathematical representation of the “lift” and “Basset” forces.

$$\mathbf{M}_d = \frac{6\varepsilon_l \varepsilon_g}{\pi d_b^3} \mathbf{F}_d \quad (6-43)$$

$$\mathbf{F}_d = \frac{1}{8} \rho_l \pi d_b^2 C_D |\mathbf{u}_l - \mathbf{u}_g| (\mathbf{u}_l - \mathbf{u}_g) \quad (6-44)$$

$$\mathbf{M}_{vm} = \frac{1}{2} \varepsilon_l \varepsilon_g C_{vm} \left(\frac{D\mathbf{u}_l}{Dt} - \frac{D\mathbf{u}_g}{Dt} \right) \quad (6-45)$$

In the above equations, C_D is the drag coefficient and for sufficiently contaminated systems it is represented by Equation 6-46 (Tomiyama *et al.*, 1995).

$$C_D = \max \left[\overbrace{\frac{24}{Re} (1 + 0.15 Re_b^{0.68})}^{C_{D,2}}, \overbrace{\frac{8}{3} \frac{Eo}{Eo + 4}}^{C_{D,1}} \right] \quad (6-46)$$

where, $Eo = g(\rho_l - \rho_g)d_b^2/\sigma$ is the Eotvos number based on the bubble diameter and the liquid surface tension, and $Re_b = d_b|\mathbf{u}_l - \mathbf{u}_g|/\nu_l^m$ is the bubble Reynolds number.

C_{vm} on the other hand is the virtual mass coefficient that has been discussed by Pan and Dudukovic' (1999).

$$C_{vm} = 1 + 3.32\varepsilon_g + O(\varepsilon_g^2) \quad (6-47)$$

In the well-developed flow region of the column, it has been extensively observed that the flow in the time-averaged sense is axisymmetric with only the axial velocities being non-zero (Degaleesan, 1997). Hence, the time-averaged liquid flow pattern is represented by a single radial profile of the axial velocity. These assumptions are well justified in view of the holdup profile database available at CREL via CT; and the liquid velocity profile database via CARPT (Devanathan *et al.*, 1990; Devanathan, 1991; Kumar *et al.*, 1995; Kumar *et al.*, 1997; Degaleesan, 1997; Chen *et al.*, 1998).

Under these assumptions, the equations of continuity for both the phases (Equations (6-39) and (6-40)) are identically satisfied and one cannot use the traditional approach of solving the Poisson equation for the pressure correction through the use of these continuity equations (as is done in 2-D and 3-D CFD codes). In addition, the left hand side of the momentum equations for both the gas and liquid phases becomes zero, and so does the virtual mass term. Finally, due to no flow in the radial and azimuthal directions, the pressure is assumed to be independent of the radial and azimuthal coordinates, and the pressure gradient term in the momentum equations reduces to dp/dz .

After retaining the non-zero gradients and velocity components in the momentum equations for the two phases, one gets the following simplified equations.

$$\text{Liquid/Slurry} \quad 0 = -\rho_l \varepsilon_l g - \varepsilon_l \frac{dp}{dz} - M_d - \frac{1}{r} \frac{d}{dr} \left(r \varepsilon_l \left\{ \tau_{l,rz}^m + \tau_{l,rz}^t \right\} \right) \quad (6-48)$$

$$\text{Gas} \quad 0 = -\rho_g \varepsilon_g g - \varepsilon_g \frac{dp}{dz} + M_d - \frac{1}{r} \frac{d}{dr} \left(r \varepsilon_g \left\{ \tau_{g,rz}^m + \tau_{g,rz}^t \right\} \right) \quad (6-49)$$

where

$$\tau_{l,rz}^m = -\mu_l^m \frac{du_l}{dr} \quad (6-50)$$

$$\tau_{g,rz}^m = -\mu_g^m \frac{du_g}{dr} \quad (6-51)$$

$$\tau_{l,rz}^t = \overline{\rho_l u_{l,r}^t u_{l,z}^t} \quad (6-52)$$

$$\tau_{g,rz}^t = \overline{\rho_g u_{g,r}^t u_{g,z}^t} \quad (6-53)$$

Since $\mu_g^m \approx O(10^{-1})\mu_l^m$ and $\rho_g \approx O(10^{-1} - 10^{-2})\rho_l$, one can neglect both the molecular as well as the turbulent shear stresses in the gas phase as compared to those in the liquid/slurry phase. Therefore, upon addition of Equations (6-48) and (6-49) one obtains

$$0 = -(\rho_g \varepsilon_g + \rho_l \varepsilon_l) g - \frac{dp}{dz} - \frac{1}{r} \frac{d}{dr} \left(r \varepsilon_l \left\{ \overbrace{\tau_{l,rz}^m + \tau_{l,rz}^t}^{\tau_{l,rz}} \right\} \right) \quad (6-54)$$

In the above equation, the superscripts "m" and "t" refer to molecular (viscous) and turbulent contributions, and ε_g is the radial gas holdup profile, which is represented in terms of the power law function given by Equation 6-55 which fits well the available experimental data (Kumar, 1994; Kumar *et al.*, 1995).

$$\varepsilon_g(\xi) = \bar{\varepsilon}_g \left(\frac{m+2}{m+2-2c} \right) (1 - c\xi^m) \quad (6-55)$$

where, $\xi = r/R$ is the dimensionless radius. Substituting for the radial gas holdup (Equation (6-55)) in Equation (6-54) and using $p' = -dp/dz/\rho_l g$, one gets, on integrating Equation (6-54) with boundary condition $\tau_{l,r} = 0$ at $\xi = 0$,

$$(1 - \varepsilon_g) \tau_{l,r} = \frac{\rho_l g R \xi}{2} (p' - 1) + \frac{(\rho_l - \rho_g) g R \bar{\varepsilon}_g \xi}{2} \frac{(m+2-2c\xi^m)}{(m+2-2c)} \quad (6-56)$$

After anticipating a downward maximum liquid velocity at dimensionless radius $\xi = \lambda$ (which is obtained by an iterative calculation as shown later), one assigns $\tau_{l,r}|_{\xi=\lambda} = 0$. Applying this condition to Equation (6-56) eliminates p' (Equation (6-57)) and yields Equation (6-58).

$$p' = 1 - \bar{\varepsilon}_g \left(\frac{\rho_l - \rho_g}{\rho_l} \right) \left(\frac{m+2-2c\lambda^m}{m+2-2c} \right) \quad (6-57)$$

$$\tau_{l,r}(\xi) = \frac{\rho_l (1 - \gamma) g R c \bar{\varepsilon}_g \xi \lambda^m}{(m+2-2c)(1 - \varepsilon_g(\xi))} \left(1 - \left(\frac{\xi}{\lambda} \right)^m \right) = \rho_l g R \beta(\xi) \quad (6-58)$$

$$\text{where } \beta(\xi) = \frac{(1 - \gamma) c \bar{\varepsilon}_g \xi \lambda^m}{(m+2-2c)(1 - \varepsilon_g(\xi))} \left(1 - \left(\frac{\xi}{\lambda} \right)^m \right) \quad \text{and} \quad \gamma = \frac{\rho_g}{\rho_l} \quad (6-59)$$

To obtain the liquid velocity profile from the above shear stress profile, a constitutive relationship (closure) is needed relating the turbulent shear stresses to the mean liquid velocity profile. The simplest closure in terms of turbulent kinematic viscosity is employed in Equation (6-60).

$$\tau_{l,rz}(r) = -\rho_l(v_i^m + v_i') \frac{du_l}{dr} = -\rho_l v_i^m \frac{du_l}{dr} - \rho_l l^2 \left| \frac{du_l}{dr} \right| \frac{du_l}{dr} \quad (6-60)$$

The turbulent eddy viscosity, v_i' can be closed by a modified mixing length, $l(\xi)$, as given by Kumar *et al.* (1994).

$$v_i' = l^2 \left| \frac{du_l}{dr} \right| \quad (6-61)$$

$$l(\xi) = \left\{ \frac{a(1-\xi)}{(\xi+b)^c} + d(1-\xi)^e \right\} R \quad (6-62)$$

The parameters a , b , c , d and e have been obtained by Kumar *et al.* (1994) after considering extensive data on liquid recirculation velocities and turbulent stresses from CARPT, and experimental results of other researchers who have made measurements of the liquid recirculation velocity and turbulent stresses by other experimental means. For the churn-turbulent regime, these values are $a=7.85$, $b=1.197$, $c=3.078$, $d=-3.809$, $e=2.862$. In this work, two other mixing length models are also used to assess the effect of this parameter on the simulation results. These are the classical mixing length profile of Nikuradse (Schlichting, 1979) for turbulent single-phase pipe flow and that of Joshi (1980) which was proposed for bubble column flows. The reason to test Nikuradse's mixing length correlation is to establish the upper bound on the predicted liquid velocity recirculation.

$$\text{Nikuradse} \quad l(\xi) = \left\{ 0.14 - 0.08\xi^2 - 0.06\xi^4 \right\} R \quad (6-63)$$

$$\text{Joshi} \quad l(\xi) = 0.16 R \quad (6-64)$$

Therefore, by introducing dimensionless radius in Equation (6-60), and upon substitution in Equation (6-58), one obtains the following expression for the liquid velocity gradient

$$\frac{du_l}{d\xi} = \begin{cases} \frac{v_i^m R}{2l^2} \left(1 - \sqrt{1 + \frac{4l^2 gR}{v_i^{m^2}} \beta(\xi)} \right) & \text{for } 0 \leq \xi \leq \lambda \\ -\frac{gR^2}{v_i^m} \beta(\xi) & \text{for } \lambda \leq \xi \leq 1 \end{cases} \quad (6-65)$$

Solution Procedure

The boundary conditions to be used for the solution of the above equations are $u_l = 0$ at $\xi = 1$, and $du_l/d\xi = 0$ at $\xi = 0$. Superimposed on this is the constraint that the overall continuity for the liquid phase must be satisfied (Note that the integral is split at $\xi = \lambda$ which is not the point of inversion of the liquid velocity profile, rather the point of maximum downward liquid velocity).

$$2 \int_{\xi=0}^{\xi=\lambda} \{1 - \varepsilon_g(\xi)\} u_l(\xi) \xi d\xi + 2 \int_{\xi=\lambda}^{\xi=1} \{1 - \varepsilon_g(\xi)\} u_l(\xi) \xi d\xi = U_{L,sup} \quad (6-66)$$

It is this constraint of overall liquid continuity, as expressed by Equation (6-66), that allows one to iterate on λ to obtain a converged solution. The converged value of λ by Equation (6-57) determines p' . The numerical scheme for the solution is as follows.

- Guess a value for λ (generally 0.9 is a good starting point)
- Calculate $u_{l,\lambda}$ by integrating Equation (6-65) from the boundary at $\xi = 1$ to $\xi = \lambda$

$$u_{l,\lambda} = -\frac{gR^2}{v_l^m} \int_{\xi=1}^{\xi=\lambda} \beta(\xi) d\xi \quad (6-67)$$

- To obtain the velocity of the liquid phase in the rest of the domain, integrate Equation (6-65) from $\xi = \lambda$ towards the column center using $u_{l,\lambda}$.

$$u_l = u_{l,\lambda} - \frac{v_l^m R}{2l^2} \int_{\xi=\xi}^{\xi=\lambda} \left(1 - \sqrt{1 + \frac{4l^2 gR}{v_l^{m^2}} \beta(\xi)} \right) d\xi \quad (6-68)$$

- Substitute the radial profile of the axial liquid velocity into Equation (6-66). If Equation (6-66) is satisfied within the tolerance criterion, then the converged solution has been obtained. If the tolerance criterion is not met, then λ is incremented sequentially until convergence is achieved. A word of caution is in

order at this point. The function defined by Equation (6-65) could have steep gradients and proper care must be taken while integrating to obtain an accurate solution.

Once the liquid velocity profile and dp/dz are determined as the converged solution to the one-dimensional liquid circulation model equations, we turn our attention back to the gas phase momentum equation. It should be mentioned that the magnitude of the converged dp/dz is almost equal to the sum of $\rho_l \bar{\varepsilon}_l g$ and $\rho_g \bar{\varepsilon}_g g$. Combining Equations (6-43), (6-44) and (6-49), the expression for the slip velocity, u_s is obtained.

$$u_s = u_g - u_l = \sqrt{\frac{4d_b \left(-\frac{dp}{dz} - \rho_g g \right)}{3C_D \rho_l (1 - \varepsilon_g)}} \quad (6-69)$$

Here, C_D is the drag coefficient, which is a function of the slip velocity as well as of the bubble diameter, and thus has to be obtained through an iterative scheme for a prescribed bubble diameter. The effective bubble diameter for the entire domain is obtained by iteratively searching for that bubble diameter which satisfies the overall gas phase continuity

$$2 \int_{\xi=0}^{\xi=1} \varepsilon_g(\xi) u_g(\xi) \xi d\xi = 2 \int_{\xi=0}^{\xi=1} \varepsilon_g(\xi) u_l(\xi) \xi d\xi + 2 \int_{\xi=0}^{\xi=1} \varepsilon_g(\xi) u_s(\xi) \xi d\xi = U_{G,sup} \quad (6-70)$$

The procedure for obtaining the gas phase velocity profile is based on adjusting the bubble diameter in the drag formulation via an iterative scheme to obtain a solution that satisfies gas phase continuity. For the SBCM, the mean bubble diameter describing the gas phase dynamics is assumed constant in the entire reactor cross-section. For the DBSM on the other hand, a radial variation of the mean bubble diameter with a maximum in the column center is assumed. Since the mean bubble size is assumed to vary with the dimensionless column radius, the mean bubble size distribution is

essentially continuous and hence this model is referred to as the Distributed Bubble Size Model (DBSM). Thus, the bubble size distribution for the two models is:

$$d_b(\xi) = \begin{cases} \bar{d}_b & \text{for use in SBCM} \\ \bar{d}_{G_{1,LB}} (1 - c\xi^m) & \text{for use in DBSM} \end{cases} \quad (6-71)$$

Here, $\bar{d}_{G_{1,LB}}$ is the effective mean diameter of the "large" bubble phase. \bar{d}_b for SBCM and $\bar{d}_{G_{1,LB}}$ for DBSM are parameters that are iterated upon to satisfy the overall gas phase continuity given by Equation (6-70) and are therefore obtained as part of the solution of the sub-model equations for estimating the gas recirculation velocities, as described below. This assumed distribution of bubble diameter, given by Equation (6-71), mimics the radial gas-holdup profile with a relatively flat radial gas-holdup profile implying that the effective mean bubble-size is relatively homogeneous. On the other hand, a large gradient in the radial gas-holdup profile implies greater concentration of gas in the central region of the column resulting from relatively larger bubble voids coexisting with smaller sized bubbles while only the "small" bubble phase is present in the wall region. This assumption of the radial distribution of the long time averaged bubble size is compatible with the non-uniformity in the radial gas-holdup profile.

Following are the steps involved in the iterative procedure to estimate the mean bubble diameter \bar{d}_b for use in SBCM or $\bar{d}_{G_{1,LB}}$ for use in DBSM by converging on gas phase continuity.

- Guess a value for \bar{d}_b or $\bar{d}_{G_{1,LB}}$ (typically start with a very small value)
- Calculate $C_{D,1}$ as defined in Equation (6-46). Since $C_{D,1}$ is independent of the radial coordinate, ξ , as well as of the slip velocity, u_s , once \bar{d}_b or $\bar{d}_{G_{1,LB}}$ is known $C_{D,1}$ is simply evaluated based on the Eotvos number.
- Calculate $C_{D,2}$ as defined in Equation (6-46). Since $C_{D,2}$ is a function both of ξ and u_s , defined by Equation (6-69), it has to be evaluated at each ξ by the following Newton-Raphson procedure

$$u_s^{k+1} = u_s^k - \frac{f(u_s^k)}{f'(u_s^k)} \quad (6-72)$$

$$f(u_s) = u_s - \sqrt{\frac{4d_b \left(-\frac{dP}{dz} - \rho_g g \right)}{3C_{D,2} \rho_l (1 - \varepsilon_g)}} \quad (6-73)$$

$$f'(u_s) = \frac{df(u_s)}{du_s} = 1 - \frac{24}{u_s^2} \left(1 + 0.04695 Re_b^{0.68} \right) \sqrt{\frac{\mu_l^{m^2} \left(-\frac{dP}{dz} - \rho_g g \right)}{3\rho_l^3 C_{D,2}^3 d_b (1 - \varepsilon_g)}} \quad (6-74)$$

- Calculate C_D as the maximum of $C_{D,1}$ and $C_{D,2}$ for each ξ , and subsequently calculate the radial profile of u_s from Equation (6-69).
- Evaluate the gas phase continuity using Equation (6-70). If the gas continuity is satisfied within the tolerance criterion, then the guessed bubble diameter is the correct one, otherwise \bar{d}_b or $\bar{d}_{G_i, LB}$ is incremented and the procedure is repeated until the tolerance criterion is met.

This solution procedure ensures that the gas phase continuity is satisfied as part of the solution. Additionally, it provides an estimation of the bubble diameter, which is subsequently used for calculating mass transfer coefficients. However, it should be noted that the estimated bubble diameter depends on the drag formulation used, and therefore, it is important to use a suitable drag correlation. In principle, any of the available drag forms could be used. This is an issue related to the sub-grid modeling of the phase interaction between the gas and liquid phases and beyond the scope of this work. However, this is an important issue, as it is also relevant to the CFD simulations of flows in practical multi-phase systems. For the purposes of this study, we have adopted the formulation of Tomiyama *et al.* (1995), as it is known to give reasonably good predictions over a wide range of bubble Reynolds numbers. It should also be mentioned that in its current form, the solution of the sub-model equations requires the knowledge of the radial gas-holdup profile; and, therefore, the model is not fully predictive. Recently, Wu *et al.* (2001) developed correlations for predicting the parameters of the radial gas-

holdup profiles in bubble columns and these are presented in Appendix A. Therefore, in the absence of any experimental information on the radial gas-holdup distribution, these correlations could be used as a starting point for the models developed in this study.

Before proceeding further, a precautionary note is in order about the converged liquid velocity profile. From Equation (6-70), it can be seen that if the converged liquid velocity profile is such that the integral, I_1 is greater than $U_{G,sup}$, it implies that an unphysical result has been obtained, since it would mean that in the long-time average sense, the gas phase is moving slower than the liquid, which obviously cannot be the case. The converged liquid velocity profile should therefore be checked for consistency after a converged solution satisfying liquid phase continuity has been achieved. If I_1 greater than $U_{G,sup}$ does indeed occur, it is indicative of gross inaccuracies in the gas holdup profile being used as input for solution of the model equations for liquid recirculation. If such a situation does arise, a remedy could be sought by changing the parameters of the gas holdup profile so as to reduce the magnitude of the gas holdup gradient. This can be achieved by lowering the average gas holdup or alternatively by increasing “m” or lowering “c” (refer to Equation 7-12).

6.4. Parameter Estimation for the Mixing Models

Once the radial profiles of the liquid (slurry) and gas phase velocities are known, the various hydrodynamic input parameters for the mechanistic reactor model can be readily estimated. It should be re-emphasized that the gas and liquid recirculation velocities, obtained from the sub-model presented earlier, satisfy the overall gas and liquid phase continuity and provide a self-consistent approach to parameter estimation. Alternate methodologies to estimate some of the reactor model parameters (interstitial gas phase velocities) like that proposed by Krishna and Ellenberger (1995) may not even satisfy the overall gas phase continuity as shown later in Section 6.5. The liquid and gas velocity profiles obtained from the solution of the two-fluid recirculation model become zero at some distinct radial locations. These are referred to as the inversion points with r'

representing the inversion point, for the liquid velocity, and r'' that for the gas. The inversion points are important in parameter estimation, as they define the boundaries of the up-flow and down-flow zones in the reactor models, *viz.*, core and outlet flow regions for the gas and the liquid. The holdups of the gas and liquid/slurry in the various zones of the reactor are obtained from Equations (6-75) to (6-79) using the measured or estimated gas holdup profile.

Average liquid hold-up in the up-flowing liquid region can be defined as

$$\bar{\varepsilon}_{l1} = \frac{2}{r'^2} \int_0^{r'} (1 - \varepsilon_g) r dr \quad (6-75)$$

Average liquid hold-up in the down-flowing liquid region is

$$\bar{\varepsilon}_{l2} = \frac{2}{R^2 - r'^2} \int_{r'}^R (1 - \varepsilon_g) r dr \quad (6-76)$$

Average gas hold-up in the up-flowing gas region is

$$\left. \begin{array}{l} \text{SBCM} \Rightarrow \bar{\varepsilon}_{g1} \\ \text{DBSM} \Rightarrow \bar{\varepsilon}_{g1+g3} \end{array} \right\} = \frac{2}{r''^2} \int_0^{r''} \varepsilon_g r dr \quad (6-77)$$

Average gas hold-up in the down-flowing gas region is

$$\bar{\varepsilon}_{g2} = \frac{2}{R^2 - r''^2} \int_{r''}^R \varepsilon_g r dr \quad (6-78)$$

Portion of the average gas hold-up in the up-flowing gas where liquid flows downwards

$$\bar{\varepsilon}'_{g1} = \frac{2}{r''^2} \int_{r'}^{r''} \varepsilon_g r dr \quad (6-79)$$

From the converged solutions for the liquid and gas velocity profiles, the average velocities of the gas and liquid in the various zones are evaluated using Equations (6-80) to (6-83), and the mean slip velocity is obtained using Equation (6-84), which is subsequently used to calculate the mass transfer coefficients in the well-mixed end-zones

(Equation 6-93). It should be noted that although the mean slip velocity could be computed by the three different expressions in Equation 6-84, the resulting differences in the computed mean slip velocity are not significant (less than 5%). Additionally, from the simulation results for all cases studied in this study, the actual mean slip velocity (computed using any of the three expressions presented in Equation 6-84) is always smaller than the apparent slip velocity, which is usually defined as $U_{G,sup}/\bar{\varepsilon}_g - U_{L,sup}/\bar{\varepsilon}_L$. It is the apparent slip velocity that is normally used in engineering correlations and this establishes that it does not necessarily represent well the actual slip in the system.

The needed parameters are now obtained as follows:

Average liquid velocity in the up-flowing liquid region is

$$\bar{u}_{l1} = \frac{2 \int_0^r (1 - \varepsilon_g) |u_l| r dr}{r^2 \bar{\varepsilon}_{l1}} \quad (6-80)$$

Average liquid velocity in the down-flowing liquid region is

$$\bar{u}_{l2} = \frac{\frac{2}{\bar{\varepsilon}_{l2}} \int_r^R (1 - \varepsilon_g) u_l r dr}{R^2 - r^2} \quad (6-81)$$

Average gas velocity in the up-flowing gas region is

$$SBCM \Rightarrow \bar{u}_{g1} = \frac{R^2 U_{G,sup} + 2 \int_0^R |u_g| \varepsilon_g r dr}{r^2 \bar{\varepsilon}_{g1}} \quad (6-82)$$

$$DBSM \Rightarrow \bar{u}_{g1+g3} = \frac{R^2 U_{G,sup} + 2 \int_r^R |u_g| \varepsilon_g r dr}{r^2 \bar{\varepsilon}_{g1+g3}}$$

Average gas velocity in the down-flowing gas region is

$$\bar{u}_{g2} = \frac{\frac{2}{\bar{\varepsilon}_{g2}} \int_r^R |u_g| \varepsilon_g r dr}{R^2 - r^2} \quad (6-83)$$

Average actual slip velocity is

$$U_{slip} = \left\{ \begin{array}{l} \frac{2 \int_{\xi=0}^{\xi=1} u_s(\xi) \xi d\xi}{\bar{\varepsilon}_g} \quad \text{No Weighting} \\ \frac{2 \int_{\xi=0}^{\xi=1} \varepsilon_g(\xi) u_s(\xi) \xi d\xi}{\bar{\varepsilon}_g} \quad \text{Weighted by } \varepsilon_g \\ \frac{2 \int_{\xi=0}^{\xi=1} \varepsilon_l(\xi) u_s(\xi) \xi d\xi}{\bar{\varepsilon}_l} \quad \text{Weighted by } \varepsilon_l \end{array} \right\} \leq \frac{U_{G,sup}}{\bar{\varepsilon}_g} - \frac{U_{L,sup}}{\bar{\varepsilon}_l} \quad (6-84)$$

From Equations 6-77 and 6-82, one can see that when using the DBSM, in addition to the assumption of the radial distribution of the mean bubble size (Equation 6-71), one needs two additional assumptions. The first assumption is needed to evaluate the small bubble holdup in the core, $\bar{\varepsilon}_{g1}$ and large bubble holdup, $\bar{\varepsilon}_{g3}$ from $\bar{\varepsilon}_{g1+g3}$, while the second one is needed to calculate \bar{u}_{g1} and \bar{u}_{g3} from \bar{u}_{g1+g3} . The assumptions used in this study are that the small bubble holdup in the core and the wall regions are equal and that the velocity of the large bubble phase in the core is equal to the fraction of the superficial gas velocity defined by the ratio of large to total bubble holdups. Mathematically these assumptions are represented by:

$$\bar{\varepsilon}_{g1} = \bar{\varepsilon}_{g2}, \quad \bar{u}_{g3} = \frac{\bar{\varepsilon}_{g3}}{\bar{\varepsilon}_g} U_{G,sup} \quad (6-85)$$

Alternatively, using the approach of Krishna and Ellenberger (1995), one can assume that $\bar{\varepsilon}_{g1} = \bar{\varepsilon}_{g2} = \bar{\varepsilon}_{g,trans}$ and $\bar{u}_{g3} = (U_G - U_{df}) / \left\{ \bar{\varepsilon}_{g3} (1 - r'^2) \right\}$. However, problems can arise in this method since estimated $\bar{\varepsilon}_{g,trans}$ may be greater than $\bar{\varepsilon}_g$ measured from experiments.

With the volumes and velocities associated with the various compartments of the reactor model estimated, the last set of parameters that needs to be evaluated are the mass transfer coefficients and the interfacial areas for mass transfer. The volumetric mass transfer coefficient is widely studied and reported in the literature and numerous correlations are available for its estimation (Azbel, 1981; Kastanek *et al.*, 1993) as

reported in Chapter 2. However, most of these correlations are empirical in nature with little fundamental basis and, therefore, usually work well only for systems similar to the ones from which data was obtained for their development. To incorporate some level of physics, in this study the mass transfer coefficients are estimated based on the penetration theory of Higbie (Danckwerts, 1970) and the interfacial areas are evaluated using the bubble diameter that satisfies gas phase continuity. Following this methodology, one does not have to depend on empirical correlations for evaluating the mass transfer coefficients and interfacial areas as they can be readily calculated using Equations (6-86) to (6-93). These expressions assume the bubbles are spherical, but one can apply suitable shape factor corrections if needed (Clift *et al.*, 1978). From the expressions for evaluating the mass transfer coefficients and the interfacial areas, one can immediately recognize that for DBSM, one needs an estimate of the average bubble diameter in the reactor as well as the average “small” bubble diameter in the core and the annulus regions. This is accomplished subsequently via Equations 6-94 to 6-98.

Interfacial area for mass transfer from up-flowing gas to up-flowing liquid is

$$\begin{aligned}
 SBCM &\Rightarrow a_{gulu} = \frac{6(\bar{\varepsilon}_{g1} - \bar{\varepsilon}'_{g1})}{\bar{d}_b} \\
 DBSM &\Rightarrow \begin{cases} a_{sulu} = \frac{6(\bar{\varepsilon}_{g1} - \bar{\varepsilon}'_{g1})}{\bar{d}_{G1,SB}} \\ a_l = \frac{6\bar{\varepsilon}_{g3}}{\bar{d}_{G1,LB}} \end{cases} \quad (6-86)
 \end{aligned}$$

$\bar{\varepsilon}'_{g1}$ is the portion of the average gas hold-up in the up-flowing gas region ($\bar{\varepsilon}_{g1}$ for SBCM and $\bar{\varepsilon}_{g1+g3}$ for DBSM) where the liquid flows downwards.

Interfacial area for mass transfer from up-flowing gas to down-flowing liquid is

$$\begin{aligned}
 SBCM &\Rightarrow a_{guld} = \frac{6\bar{\varepsilon}'_{g1}}{\bar{d}_b} \\
 DBSM &\Rightarrow a_{suld} = \frac{6\bar{\varepsilon}'_{g1}}{\bar{d}_{G1,SB}} \quad (6-87)
 \end{aligned}$$

Interfacial area for mass transfer from down-flowing gas to down-flowing liquid is

$$\begin{aligned}
 SBCM &\Rightarrow a_{gdld} = \frac{6 \bar{\epsilon}_{g2}}{\bar{d}_b} \\
 DBSM &\Rightarrow a_{sdld} = \frac{6 \bar{\epsilon}_{g2}}{\bar{d}_{G_2,SB}}
 \end{aligned}
 \tag{6-88}$$

Interfacial area for mass transfer in distributor and disengagement CSTs

$$a_{CST} = \frac{6 \bar{\epsilon}_g}{\bar{d}_b}
 \tag{6-89}$$

Mass transfer coefficient from up-flowing gas to up-flowing liquid

$$\begin{aligned}
 SBCM &\Rightarrow k_{guhu} = \frac{2}{\sqrt{\pi}} \sqrt{\frac{D_{L,m}(\bar{u}_{g1} - \bar{u}_{l1})}{\bar{d}_b}} \\
 DBSM &\Rightarrow \begin{cases} k_{sulu} = \frac{2}{\sqrt{\pi}} \sqrt{\frac{D_{L,m}(\bar{u}_{g1} - \bar{u}_{l1})}{\bar{d}_{G_1,SB}}} \\ k_l = \frac{2}{\sqrt{\pi}} \sqrt{\frac{D_{L,m}(\bar{u}_{g3} - \bar{u}_{l1})}{\bar{d}_{G_1,LB}}} \end{cases}
 \end{aligned}
 \tag{6-90}$$

Mass transfer coefficient from up-flowing gas to down-flowing liquid

$$\begin{aligned}
 SBCM &\Rightarrow k_{gdld} = \frac{2}{\sqrt{\pi}} \sqrt{\frac{D_{L,m}(\bar{u}_{g1} + \bar{u}_{l2})}{\bar{d}_b}} \\
 DBSM &\Rightarrow k_{sdld} = \frac{2}{\sqrt{\pi}} \sqrt{\frac{D_{L,m}(\bar{u}_{g1} + \bar{u}_{l2})}{\bar{d}_{G_1,SB}}}
 \end{aligned}
 \tag{6-91}$$

Mass transfer coefficient from down-flowing gas to down-flowing liquid

$$\begin{aligned}
 SBCM &\Rightarrow k_{gdld} = \frac{2}{\sqrt{\pi}} \sqrt{\frac{D_{L,m}(-\bar{u}_{g2} + \bar{u}_{l2})}{\bar{d}_b}} \\
 DBSM &\Rightarrow k_{sdld} = \frac{2}{\sqrt{\pi}} \sqrt{\frac{D_{L,m}(-\bar{u}_{g2} + \bar{u}_{l2})}{\bar{d}_{G_2,SB}}}
 \end{aligned}
 \tag{6-92}$$

Mass transfer coefficient in distributor and disengagement CSTs

$$k_{CST} = \frac{2}{\sqrt{\pi}} \sqrt{\frac{D_{L,m} U_{slip}}{\bar{d}_b}} \quad (6-93)$$

As mentioned earlier while using DBSM, one needs an estimate of the average bubble-diameter in the various zones of the reactor since the iteration on gas continuity results in the prediction of the maximum bubble size at the column center. This is accomplished by defining a radial profile of the bubble number density function (number of bubbles per unit reactor cross-sectional area) based on the radial gas holdup and bubble size profiles.

$$n_b(\xi) = \frac{4 \varepsilon_g(\xi)}{\pi d_b^2(\xi)} \quad (6-94)$$

From Equation (6-94), the following six quantities are obtained by averaging over the core and outer regions, the boundary between which is ξ'' , the dimensionless radius where the radial gas velocity profile becomes zero.

$$\bar{n}_b = 2 \int_0^1 n_b(\xi) \xi d\xi \quad \Rightarrow \quad \bar{d}_b = \sqrt{\frac{4 \bar{\varepsilon}_g}{\pi \bar{n}_b}} \quad (6-95)$$

$$\bar{n}_{G_{2,SB}} = \frac{2}{(1-\xi''^2)} \int_{\xi''}^1 n_b(\xi) \xi d\xi \quad \Rightarrow \quad \bar{d}_{G_{2,SB}} = \sqrt{\frac{4 \bar{\varepsilon}_{g2}}{\pi \bar{n}_{G_{2,SB}}}} \quad (6-96)$$

$$\bar{n}_{G_{1,SB+LB}} = \frac{2}{\xi''^2} \int_0^{\xi''} n_b(\xi) \xi d\xi \quad \Rightarrow \quad \bar{d}_{G_{1,SB+LB}} = \sqrt{\frac{4(\bar{\varepsilon}_{g1} + \bar{\varepsilon}_{g3})}{\pi \bar{n}_{G_{1,SB+LB}}}} \quad (6-97)$$

In the above equations, \bar{n}_b is the cross-sectional mean bubble number-density and \bar{d}_b is average bubble-diameter over the entire reactor cross-section. Similarly, $\bar{n}_{G_{2,SB}}$ and $\bar{d}_{G_{2,SB}}$ are the mean bubble number-density and bubble-diameter respectively in the wall region,

while $\bar{n}_{G_1,SB+LB}$ and $\bar{d}_{G_1,SB+LB}$ represent the same quantities in the central region. From the above equations, it should be immediately realized that one still needs to extract $\bar{d}_{G_1,SB}$ from known $\bar{d}_{G_1,LB}$ and $\bar{d}_{G_1,SB+LB}$ (the subscript “ $G_1,SB+LB$ ” refers to the combined “small” and “large” bubble populations in the core). This is achieved by utilizing the assumption that the gas holdup of small bubbles is equal in the core and outer region (Equation (6-85)). Stated mathematically, $\bar{\epsilon}_{g1} = \bar{\epsilon}_{g2}$ implies that $\bar{n}_{G_1,SB} \bar{d}_{G_1,SB}^2 = \bar{n}_{G_2,SB} \bar{d}_{G_2,SB}^2$. Therefore, the effective mean diameter of the small bubbles in the core is estimated as

$$\bar{n}_{G_1,LB} = \frac{\bar{n}_{G_1,SB+LB} \bar{d}_{G_1,SB+LB}^2 - \bar{n}_{G_2,SB} \bar{d}_{G_2,SB}^2}{\bar{d}_{G_1,LB}^2} \Rightarrow \bar{d}_{G_1,SB} = \sqrt{\frac{\bar{n}_{G_2,SB} \bar{d}_{G_2,SB}^2}{(\bar{n}_{G_1,SB+LB} - \bar{n}_{G_1,LB})}} \quad (6-98)$$

The above estimation procedure provides all the hydrodynamic model parameters needed as input to solve the SBCM and DBSM reactor model equations describing the transport of a scalar quantity. In the next section, some results are presented first from simulation of the liquid and gas recirculation by the sub-model equations and then from the reactor model describing the gas tracer experiments in a pilot scale slurry bubble column under conditions of methanol synthesis.

There is one more issue with the DBSM that needs to be addressed. It is the effect of the assumed radial profile of the mean bubble size on the computed recirculation rates as well as on the overall scalar mixing in the reactor. The discussion of this issue is postponed to Section 6.6 of this chapter. This has been deliberately done so that the reader gets a better perspective on the issues related to the assumed bubble size distribution after having seen the simulation results from the model development thus far.

6.5. Results and Discussion

For solution of the model equations for gas and liquid recirculation, one needs to know two important inputs - the radial gas-holdup profile and the closure for liquid/slurry phase turbulence. For the purposes of this study, the gas-holdup profile is assumed to be

known from experimental data, though some estimates for the average gas holdup could be obtained from correlations for systems where no experimental data exists (Kastanek *et al.*, 1993; Luo *et al.*, 1999; Kemoun *et al.*, 2001^b; Wu *et al.*, 2001). In such cases, the value of the exponent m in Equation 6-55 is usually assumed in the range of 2-5 (Gharat and Joshi, 1992) and c is assumed to be 1. Or, once the mean gas holdup has been estimated from the appropriate correlation, the correlation of Wu *et al.* (2001) can be used to estimate the radial gas holdup profile, *i.e.*, the parameters " m " and " c " in Equation 6-55. On the other hand, the liquid phase turbulence in bubble column flows is usually assumed as the superposition of the turbulence due to *shear* and that resulting from the highly oscillatory and dynamic bubble motion. The latter contributes to what is frequently referred to as the "bubble-induced" turbulence.

Kumar *et al.* (1994) and Ong (1999) investigated the existing literature on the mixing length correlations relevant to bubble-column flows and found that none of the existing forms matched all the data well. Therefore, based on their own experimental database as well as other data from the literature, Kumar *et al.* (1994) developed a mixing length form represented by Equation 6-62. This is a completely empirical form but is known to provide reasonable estimates of the level of liquid circulation in air-water columns operated at atmospheric pressure. Another very simple form for mixing length (Equation 6-64) has been proposed by Joshi (1980) which also performs reasonably well in predicting the levels of liquid recirculation. Additionally, there is the mixing length correlation of Nikuradse (Schlichting, 1979) developed for turbulent single-phase pipe flows.

6.5.1. Effect of Mixing Length on the Predictions of Liquid Recirculation Rates

The performance of the three proposed mixing length forms (*i.e.* Equations 6-63, 6-64 and 6-62) is tested against two data sets for which measured liquid recirculation profiles are available from CARPT experiments. Figures 6-3 and 6-4 show the relative performance of the three mixing length forms in predicting experimental data for the

liquid phase recirculation. The experimental data is from two different columns with air-water, one of 10-cm diameter and the other one of 44-cm diameter. The superficial air velocity for the former was maintained at $U_{G,\text{sup}} = 12$ cm/s while for the latter it was 10 cm/s. Nikuradse's mixing length (Equation 6-63) always over-predicts the level of liquid recirculation velocity since the effective turbulent viscosity from this formulation is only representative of the shear contribution to the total turbulence as in single-phase flows, and does not account for the increased turbulence generation and dissipation due to the presence of the bubbles. Therefore, for bubble column flows, use of Nikuradse's mixing length in computing the liquid recirculation-velocity profile is not recommended. Modifications to Nikuradse's mixing length could be sought to account for the bubble-induced turbulence, however, the dependence of the mixing length on bubble diameter and its velocity fluctuation is not well-established (Geary and Rice, 1992). The correlations of Joshi (1980), Equation 6-64, and Kumar *et al.* (1994), Equation 6-62, give reasonable predictions for both the cases studied, though the correlation of Kumar *et al.* (1994) seems to do somewhat better.

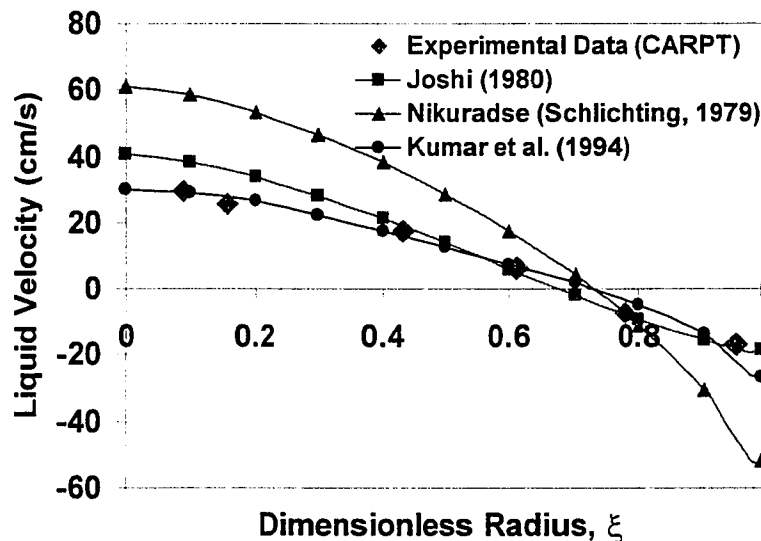


Figure 6-3. Effect of mixing length profile on liquid velocity profiles for 10 cm diameter bubble column operated at $U_{G,\text{sup}}=12$ cm/s.

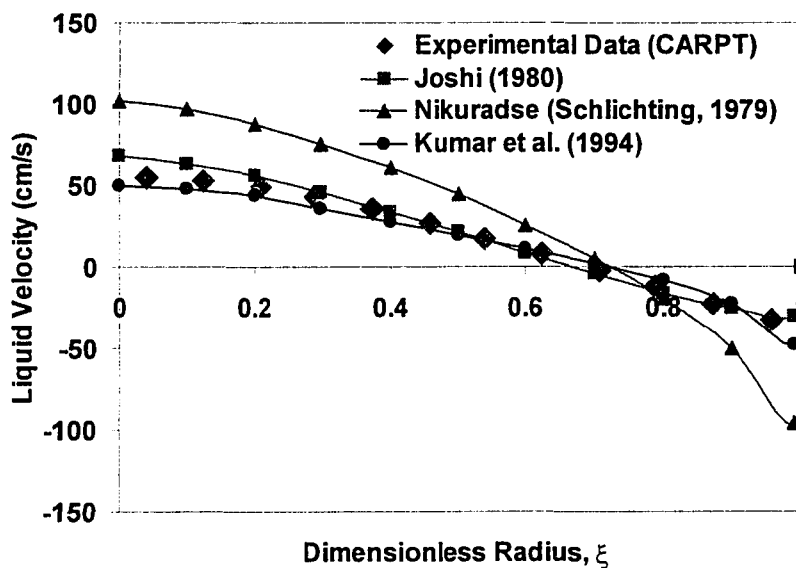


Figure 6-4. Effect of mixing length profile on liquid velocity profiles for 44 cm diameter bubble column operated at $U_{G,sup}=10$ cm/s.

Next, we demonstrate the use of the gas-liquid recirculation sub-model to obtain the hydrodynamic input parameters to the mechanistic reactor models presented earlier; and subsequently, solve these bubble column reactor model equations to predict radioactive gas tracer responses obtained from a pilot scale reactor, details of which are briefly presented below.

6.5.2. Pilot-Scale Experiments and the Corresponding Model Parameters

The experimental data for this study was obtained in a pilot-scale slurry-bubble-column reactor, R1, at the Department of Energy (DOE) facility at La Porte, Texas (Alternate Fuels Development Unit - AFDU). Radioactive gas-tracer measurements were conducted using Ar^{41} in a 46-cm diameter slurry bubble-column. The dispersed gas-slurry height was maintained at approximately 13.25-m during liquid phase synthesis of methanol from Syngas ($CO+H_2$). Experiments were conducted at three different operating conditions listed in Table 6-1 that also presents the estimated physical properties of the

slurry. To estimate the radial gas-holdup distribution in the reactor, Differential Pressure (DP) and Nuclear Density Gauge (NDG) measurements were made along the reactor length. The measurements indicate that the gas holdup in the column was fairly constant except in the distributor and the free board regions. Table 6-1 lists the parameters of the estimated radial gas-holdup profile at the three different operating conditions. Details regarding the estimation of these parameters as well as other details regarding detector calibration and experimental procedure can be found elsewhere (Degaleesan *et al.*, 1996^a; Degaleesan, 1997). From the estimated gas-holdup profile parameters, one can estimate the mean gradient in the gas-holdup profile using Equation 7-12 presented in Chapter 7. The values of the mean holdup gradient for the three operating conditions estimated in this manner are also listed in Table 6-1. As expected, the absolute value of the holdup gradient increases with increased gas superficial velocity and with decreased pressure.

Table 6-1. Estimated gas holdup profile during methanol synthesis at AFDU, La Porte.

Experiment Number	Pressure (MPa)	Temperature (°C)	$\bar{U}_{G,sup}$ (cm/s)	Parameters of Radial Gas Holdup Profile			
				$\bar{\epsilon}_x$	m	c	Mean Gradient (Equation 7-12)
Run 14.6	5.27	250	22.86	0.39	2	0.8444	-0.76
Run 14.7	5.27	250	12.66	0.33	2	0.8908	-0.71
Run 14.8	3.65	250	32.81	0.38	2	0.9433	-0.88

$\rho_L = 0.99 \text{ gm/cm}^3$; $\mu_L = 0.01 \text{ P}$; $\sigma_L = 30 \text{ dyne/cm}$; Mol. Wt._{GAS} $\sim 18 \text{ gm/mol}$; $D_{Lm} \sim 9.43 \times 10^{-5} \text{ cm}^2/\text{s}$

Figure 6-5 shows the schematic of the experimental setup with the gas tracer injected below the sparger in the inlet Syngas stream. The temporal evolution of the tracer inside the reactor was measured using scintillation counters at seven different axial locations with four detectors at each level (see Figure 6-5). Heat exchanger tubes are present inside the AFDU for cooling the reactor medium which gets heated due to the exothermic nature of the reactive system. The reactor is provided with 24 tubes having an outer diameter of one inch, which occupy approximately 7.5% of the cross-sectional area of the reactor, and extend over the entire length of the gas-slurry dispersion.

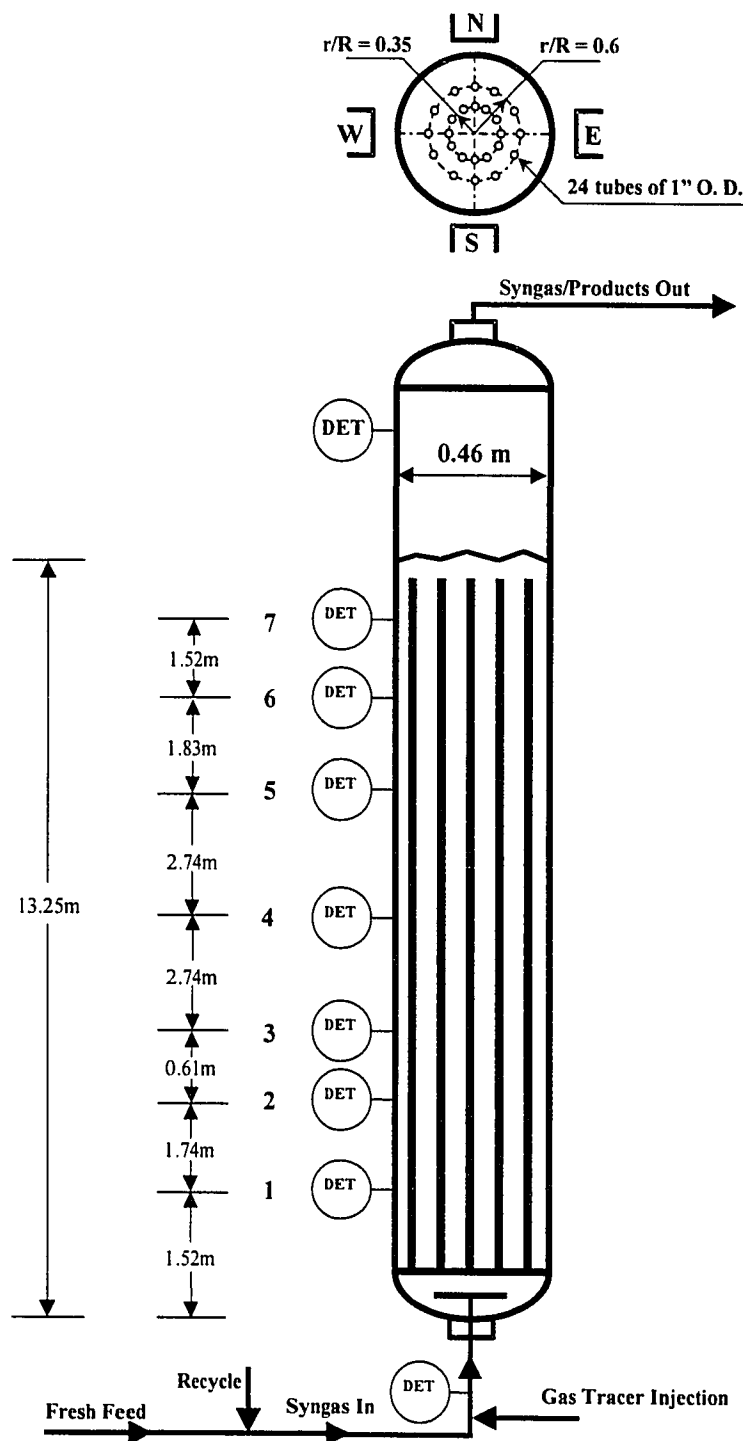


Figure 6-5. Schematic representation of the pilot-scale slurry bubble-column at the Alternate Fuels Development Unit, La Porte indicating the detector levels for measurement of radioactive tracer responses.

From the above table (Table 6-1), one can see that the first two runs (Run 14.6 and Run 14.7) were conducted at higher pressure as compared to Run 14.8. As expected, gas holdup increases at constant pressure with increase in superficial gas velocity. Based on the estimated gas holdup profiles and mean gas holdup gradient, it seems that Runs 14.6 and 14.8 are definitely in churn-turbulent flow. On the other hand, Run 14.7 may be in transition or even in bubbly flow although the correlation of Krishna *et al.* (2000^h) would indicate that the reactor was operating above transition gas superficial velocity for Run 14.7. However, there are no reliable correlations for estimation of transition. It will be discussed later whether these initial observations are supported by additional findings.

With all the operating and physical variables specified, the parameters of the SBCM and DBSM can now be calculated from Equations 6-75 to 6-98 and are listed in Tables 6-2 and 6-3, respectively. For the estimation of the parameters not directly obtained from the solution of the recirculation model, *viz.*, the radial and axial eddy diffusion coefficients, the methodology of Degaleesan (1997) was followed. This involves using an equivalent superficial gas velocity based on the measured gas holdup, which is the superficial gas velocity that would result in the same gas holdup for an equivalent air-water system at atmospheric conditions. Additionally, the radial eddy diffusivities were corrected to account for the presence of internals based on the recommendations by Degaleesan (1997).

As was mentioned earlier, the liquid recirculation model equations were refined in this study based explicitly on the two-fluid equation. This resulted in minor differences in the form of the equation than that used by Degaleesan (1997). When comparing the predicted liquid recirculation velocity ($\bar{u}_{l,r}$) with that computed by Degaleesan (1997) for the same reactor and operating conditions, it is found that the differences between the two for all three operating conditions are less than 2%. Thus, it is fortunate that minor difference in the model equation results only in minor difference in the predicted recirculation rates. However, for all future use of the one-dimensional model liquid recirculation model, it is recommended that the more rigorously derived equations presented in this study be utilized.

Table 6-2. Parameter estimation for SBCM.

Parameter	Equation No.	Run 14.6	Run 14.7	Run 14.8
\bar{d}_b (cm)	6-71	0.61	0.04	2.21
r', r'' (cm)		17.46, 19.19	17.30, 17.71	17.66, 20.08
$\bar{\epsilon}_{11}$	6-75	0.49	0.55	0.48
$\bar{\epsilon}_{12}$	6-76	0.77	0.82	0.82
$\bar{\epsilon}_{g1}$	6-77	0.45	0.43	0.42
$\bar{\epsilon}_{g2}$	6-78	0.26	0.19	0.25
$\bar{\epsilon}'_{g1}$	6-79	0.02	0.004	0.02
\bar{u}_{11} (cm/s)	6-80	45.09	41.60	48.57
\bar{u}_{12} (cm/s)	6-81	38.77	36.58	40.86
\bar{u}_{g1} (cm/s)	6-82	78.27	56.94	104.10
\bar{u}_{g2} (cm/s)	6-83	18.81	23.90	10.66
U_{slip} (cm/s)	6-84	21.54	4.46	37.51
a_{gulu} (cm ⁻¹)	6-86	4.18	65.91	1.09
a_{guld} (cm ⁻¹)	6-87	0.24	0.66	0.05
a_{guld} (cm ⁻¹)	6-88	2.57	28.94	0.67
a_{CST} (cm ⁻¹)	6-89	3.85	51.24	1.03
k_{gulu} (cm/s)	6-90	0.08	0.22	0.06
k_{guld} (cm/s)	6-91	0.15	0.54	0.09
k_{guld} (cm/s)	6-92	0.06	0.20	0.04
k_{CST} (cm/s)	6-93	0.07	0.12	0.05
$\bar{D}_{rr} _{No\ Im.}$ (cm ² /s)	A-9	114	100	112
$\bar{D}_{rr} _{With\ Im.}$ (cm ² /s)	A-9, Degaleesan (1997)	45	35	42
\bar{D}_{xx_1} (cm ² /s)	A-10, A-12	502.08	431.64	506.02
\bar{D}_{xx_2} (cm ² /s)	A-10, A-12	424.22	384.76	402.29

For DBSM, the bubble interaction parameter (K_{SBI-LB}) needs to be additionally specified. Based on the recommendations by de Swart (1996), the effect of K_{SBI-LB} has been investigated in the range 0-1 (1/s).

Table 6-3. Parameter estimation for DBSM.

Parameter	Equation No.	Run 14.6	Run 14.7	Run 14.8
r', r'' (cm)		17.46, 19.09	17.30, 17.55	17.66, 19.48
$\bar{\epsilon}_{11}$	6-75	0.49	0.55	0.48
$\bar{\epsilon}_{12}$	6-76	0.77	0.82	0.82
$\bar{\epsilon}_{g3}$	6-77	0.19	0.25	0.21
$\bar{\epsilon}_{g1} = \bar{\epsilon}_{g2}$	6-78	0.26	0.18	0.23
$\bar{\epsilon}'_{g1}$	6-79	0.02	0.003	0.014
\bar{u}_{11} (cm/s)	6-80	45.09	41.6	48.57
\bar{u}_{12} (cm/s)	6-81	38.77	36.58	40.86
\bar{u}_{g1} (cm/s)	6-82, 6-85	74.11	46.73	94.70
\bar{u}_{g2} (cm/s)	6-83	19.41	25.68	15.27
\bar{u}_{g3} (cm/s)	6-85	85.05	65.91	120.26
U_{slip} (cm/s)	6-84	21.54	4.46	37.51
a_{sulu} (cm ⁻¹)	6-86	1.93	18.96	0.52
a_l (cm ⁻¹)	6-86	1.43	27.46	0.40
a_{suld} (cm ⁻¹)	6-87	0.19	0.27	0.03
a_{sdl} (cm ⁻¹)	6-88	4.26	51.05	1.37
a_{CST} (cm ⁻¹)	6-89	4.01	54.02	1.21
k_{sulu} (cm/s)	6-90	0.07	0.10	0.05
k_l (cm/s)	6-90	0.08	0.23	0.05
k_{suld} (cm/s)	6-91	0.14	0.42	0.08
k_{sdl} (cm/s)	6-92	0.08	0.25	0.06
k_{CST} (cm/s)	6-93	0.07	0.12	0.05
\bar{d}_b (cm)	6-95	0.58	0.04	1.89
$\bar{d}_{G2,SB}$ (cm)	6-96	0.36	0.02	1.00
$\bar{d}_{G1,LB}$ (cm)	6-71	0.81	0.05	3.20
$\bar{d}_{G1,SB}$ (cm)	6-98	0.73	0.06	2.45
$\bar{D}_{rr} _{No\ Int.}$ (cm ² /s)	A-9	114	100	112
$\bar{D}_{rr} _{With\ Int.}$ (cm ² /s)	A-9, Degaleesan (1997)	45	35	42
\bar{D}_{xx_1} (cm ² /s)	A-10, A-12	502.08	431.64	506.02
\bar{D}_{xx_2} (cm ² /s)	A-10, A-12	424.22	384.76	402.29

Table 6-4 lists the bubble sizes predicted by the recirculation sub-model for the SBCM and DBSM. From these values, it is clear that the trend in the estimated bubble sizes is correctly captured for Runs 14.6 and 14.8 that are well in the churn-turbulent flow regime. The bubble sizes estimated for Run 14.7 are unusually small indicating that at superficial gas velocity and operating pressure for Run 14.7, the churn-turbulent flow regime may not have been reached, and use of the holdup profile characteristic of this regime may have skewed the estimation of bubble parameters. Another important observation is that for DBSM, the differences in the estimated large and small bubble diameters is not large, indicating that the hypothesis of the radial distribution of bubble size being similar to the radial distribution of gas holdup might not represent the physical picture accurately. Thus, the assumed parabolic holdup profile for this run may not be correct, as this run seems to be in bubbly flow.

Table 6-4. Predicted bubble sizes by the SBCM, DBSM and literature correlations.

Bubble Size (mm)	Run 14.6 ($U_{G, sup} = 22.86$ cm/s P = 5.27 MPa)	Run 14.7 ($U_{G, sup} = 12.66$ cm/s P = 5.27 MPa)	Run 14.8 ($U_{G, sup} = 32.81$ cm/s P = 3.65 MPa)
\bar{d}_b (SBCM)	6.07	0.39	22.11
\bar{d}_b (DBSM)	5.83	0.37	18.88
$\bar{d}_{G_{1, LB}}$ (DBSM)	8.05	0.55	32.03
$\bar{d}_{G_{1, SB}}$ (DBSM)	7.30	0.57	24.53
$\bar{d}_{G_{2, SB}}$ (DBSM)	3.63	0.22	9.97
$\bar{d}_{b, small}$ (Wilkinson <i>et al.</i> , 1992)	2.40	2.43	2.48
$\bar{d}_{b, large}$ (Krishna and Ellenberger, 1995)	124.98	63.75	178.82
$\bar{d}_{b, large}$ (Krishna, 2000 ^h)	31.91	17.63	40.97
\bar{d}_b (Calderbank and Moo-Young, 1961)	4.55	5.15	3.98

Table 6-4 also presents the predicted bubble sizes for these operating conditions from literature correlations and compares them to those calculated from the SBCM and DBSM models. It can be seen from the table that the predicted bubble sizes are spread over a large range with the correlation of Krishna and Ellenberger (1995) estimating bubble sizes as large as 17.9-cm. In view of this, the bubble sizes predicted by the models proposed in this study are reasonable, except for Run 14.7 for the reasons described above. It can, however, be argued that since there is no independent comparison of the validity of the predicted bubble sizes, and since these are used for calculation of mass transfer coefficients, the predicted $k_L a$ from these bubble sizes may contain large errors. To compare the volumetric mass transfer coefficients estimated by the methodology proposed in this study (and reported in Tables 6-2 and 6-3) with independent estimates, Table 6-5 presents the predicted volumetric mass transfer coefficients for the three operating conditions using the correlations presented in Chapter 2. From this table, one can see that the volumetric mass transfer coefficients predicted by SBCM and DBSM fall roughly in the range of predictions from various correlations. Actually, the values for Run 14.8 are at the low end of the predicted range while those for Run 14.7 are an order of magnitude and more higher than the values predicted by correlations. However, it should be mentioned that the operating conditions for the experiments of this study are outside the range of majority of the data that was used to develop the correlations. Nevertheless, this indicates that our model is very sensitive to the assumed gas holdup profile and the resulting bubble size and there is a need to explore this sensitivity in order to render the proposed model useful. The effect of the assumed gas holdup profile and other input parameters on the computed parameters and tracer responses has been addressed later in the chapter.

To further address the problems encountered with using independent literature correlations for estimation of the reactor model parameters, Table 6-6 presents the velocity of the “large” and “small” bubble phases calculated from literature correlations. Again, the spread in the predicted values is large. In addition, the predictions by Krishna and Ellenberger (1995) don’t even satisfy the overall gas phase continuity. Gas phase

continuity is considered satisfied if the addition of the product of large-bubble velocity with large-bubble holdup and the product of small-bubble velocity with small-bubble holdup is equal to the superficial gas velocity. Moreover, the correlations of Krishna (2000^h) for Run 14.6 predict “small” bubble-phase velocity as slightly greater than that for the “large” bubble-phase. For Run 14.7, the predictions from Krishna’s (2000^h) correlation are simply out of order with the “large” bubble-phase velocity being significantly lower than the “small” bubble phase velocity.

Table 6-5. Predicted volumetric mass transfer coefficients by the SBCM, DBSM and literature correlations.

Volumetric Mass Transfer Coefficient (sec⁻¹)	Run 14.6 (U _{G, sup} = 22.86 cm/s P = 5.27 MPa)	Run 14.7 (U _{G, sup} = 12.66 cm/s P = 5.27 MPa)	Run 14.8 (U _{G, sup} = 32.81 cm/s P = 3.65 MPa)
$(k_L a)_{CST}$ (SBCM)	0.25	6.03	0.05
$(k_L a)_{Fully-Developed}$ (SBCM)	0.31	11.08	0.06
$(k_L a)_{CST}$ (DBSM)	0.27	6.53	0.06
$(k_L a)_{Fully-Developed}$ (DBSM)	0.29	10.15	0.06
Akita & Yoshida (1973)	0.503	0.418	0.475
Deckwer <i>et al.</i> (1981)	0.437	0.308	0.540
^a Fair (1967)	0.144	0.082	0.205
Hikita <i>et al.</i> (1981)	0.590	0.377	0.776
Kawase <i>et al.</i> (1987)	0.007	0.005	0.010
Letzel <i>et al.</i> (1999)	0.195	0.165	0.185
Nakanoh & Yoshida (1980)	0.415	0.230	1.266
^a Ozturk <i>et al.</i> (1987)	0.265	0.160	0.372

^a Requires bubble size, which has been estimated using the correlation of Calderbank and Moo-Young (1961)

In addition to problems with using these correlations, the data in Table 6-6 also points to the unpredictable hydrodynamics prevalent during Run 14.7. Thus, the predictions of bubble-phase velocities by SBCM and DBSM, in addition to being more

consistent are also more physically realistic. For all the literature correlations, the predicted “small” bubble velocity (except for Krishna, 2000^h) is about 21 cm/sec which is the bubble rise velocity of a bubble of ~ 5-mm in diameter (refer to Figure 6-10). However, since the majority of the up-flowing “small” bubbles are in the wake of the fast-rising “large” bubbles, their velocities are expected to be higher. This feature seems to be correctly captured by the models proposed in this study.

Table 6-6. Predicted bubble velocities by the SBCM, DBSM and literature correlations.

Bubble Phase Velocity (cm/s)	Run 14.6 ($U_{G, sup} = 22.86$ cm/s P = 5.27 MPa)	Run 14.7 ($U_{G, sup} = 12.66$ cm/s P = 5.27 MPa)	Run 14.8 ($U_{G, sup} = 32.81$ cm/s P = 3.65 MPa)
\bar{u}_{g1} (SBCM)	78.27	56.94	105.35
\bar{u}_{g1} (DBSM)	74.11	46.73	97.79
\bar{u}_{g3} (DBSM)	85.05	65.91	121.38
$V_{b, large} \equiv \bar{u}_{g3}$ (Wilkinson <i>et al.</i> , 1992)	57.06	39.19	74.83
^a $V_{b, large} \equiv \bar{u}_{g3}$ (Krishna and Ellenberger, 1995)	163.50	116.70	195.50
$V_{b, large} \equiv \bar{u}_{g3}$ (Krishna, 2000 ^h)	31.97	20.46	50.73
$V_{b, small} \equiv \bar{u}_{g1}$ (Wilkinson <i>et al.</i> , 1992)	20.10	20.10	20.32
^a $V_{b, small} \equiv \bar{u}_{g1}$ (Krishna and Ellenberger, 1995)	20.44	20.44	20.70
$V_{b, small} \equiv \bar{u}_{g1}$ (Krishna, 2000 ^h)	32.07	32.07	33.91

^a Does not satisfy overall gas phase continuity

6.5.3. Comparison of Simulation Results with Experimental Data

For comparison of the simulation results with experimental tracer responses, detector level 7 has been chosen in this study. The reason for choosing this elevation is that it is the farthest from the tracer injection location (in the gas distributor) and

therefore the probability of the model assumptions holding true is the greatest. Since the intensity counts measured by a scintillation counter are a complex function of the photon interaction with matter and the detector solid angle, it is not straight-forward to relate the intensity counts to tracer concentration. Moreover, Ar⁴¹, which was used as the gas tracer, has a finite solubility in the slurry mixture and thus its residence time is prolonged by dissolution in the liquid. Therefore, when comparing the simulated results with experimental data at a given axial level, in addition to the contribution of the gaseous tracer at that axial level towards the total scintillation counts registered by the presumably well-collimated scintillation detectors placed at that axial level, one must also include the contribution of the dissolved tracer in the slurry phase at that axial level. Therefore, the total tracer concentration at a given axial location needs to be calculated by summing the tracer concentrations in the gas and the liquid after appropriately weighting them by their respective holdups. Figure 6-6 shows the relative placement of the scintillation detectors with respect to the reactor insulation in one axial plane that was used during the experimentation at La Porte. The figure also shows the various zones into which the reactor cross-section is compartmentalized for modeling purposes. Based on the compartmentalization depicted in Figure 6-6, Equation 6-99a is derived for calculating the total tracer concentration from simulation results at each time instant, which when normalized with its maximum, provides a basis for comparison with normalized experimental data.

$$C_{Total}|_{(t,x)} = \left\{ \begin{array}{l} \left\{ \begin{array}{l} \bar{\epsilon}_{g1} C_{g1}|_{(t,x)} (r''^2) + \bar{\epsilon}_{g2} C_{g2}|_{(t,x)} (1 - r''^2) \\ + \bar{\epsilon}_{l1} C_{l1}|_{(t,x)} (r'^2) + \bar{\epsilon}_{l2} C_{l2}|_{(t,x)} (1 - r'^2) \end{array} \right\} \quad SBCM \\ \left\{ \begin{array}{l} \left(\bar{\epsilon}_{g1} C_{g1}|_{(t,x)} + \bar{\epsilon}_{g3} C_{g3}|_{(t,x)} \right) (r''^2) + \bar{\epsilon}_{l1} C_{l1}|_{(t,x)} (r'^2) \\ + \bar{\epsilon}_{g2} C_{g2}|_{(t,x)} (1 - r''^2) + \bar{\epsilon}_{l2} C_{l2}|_{(t,x)} (1 - r'^2) \end{array} \right\} \quad DBSM \end{array} \right\} \quad (6-99a)$$

However, the relationship of radiation counts registered by the detectors in an axial plane is not linearly proportional to the tracer concentration in that plane but a complex non-

linear function of the tracer distribution and attenuation (described by the Beer-Lambert's law) in the reactor cross-section. Therefore, the use of Equation 6-99a for comparison with experimental data needs to be further verified.

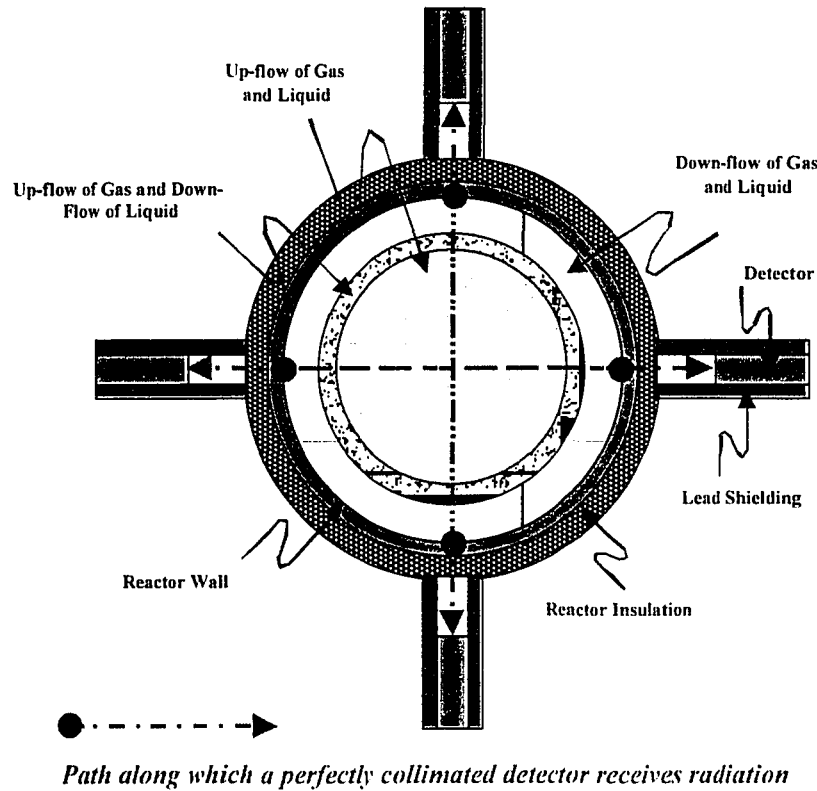


Figure 6-6. Schematic representation of the AFDU reactor cross-section along with scintillation detectors and their lead shielding.

The simplest account of radiation attenuation can be accomplished if one assumes perfect collimation of the detectors. This assumption implies that a detector only receives radiation from the central chord of the reactor cross-section. Thus, the total tracer concentration, at a radial location along the central reactor chord in the axial plane of the detectors at a given elevation, is first integrated along the radial path (r) through the

column center to yield the representative radioactive tracer response at the elevation of the detector plane (Equation 6-99b).

$$\tilde{C}_{Total} \Big|_{(t,x)} = K_{Wall} \int_{-D_c/2}^{D_c/2} C_{Total} \Big|_{(t,x,r)} \exp \left(- \int_r^{D_c/2} \mu_{Total} \Big|_{(\bar{r})} d\bar{r} \right) dr$$

where $C_{Total} \Big|_{(t,x,r)} = \varepsilon_g \Big|_{(r)} C_g \Big|_{(t,x,r)} + \varepsilon_l \Big|_{(r)} C_l \Big|_{(t,x,r)}$ (6-99b)

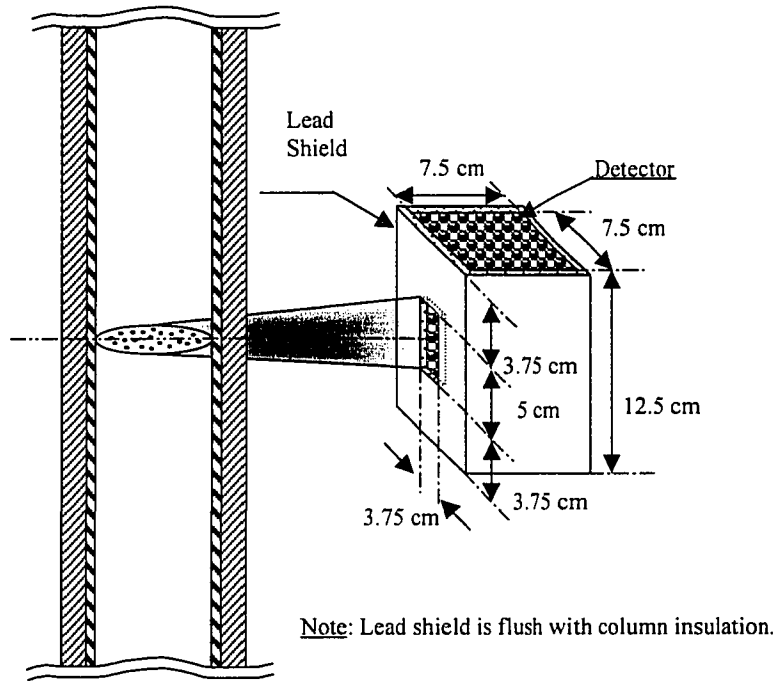
and $\mu_{Total} \Big|_{(\bar{r})} = \mu_g \varepsilon_g \Big|_{(\bar{r})} + \mu_l \varepsilon_l \Big|_{(\bar{r})}$

In the above equation, K_{Wall} is a constant that accounts for radiation attenuation due to reactor wall and insulation. The value of this constant is immaterial since it disappears when the response calculated by Equation (6-99b) is normalized with its maximum. However, it could be calculated if required, provided the thickness of the reactor wall and insulation are known. C_g and C_l in the above equation are the tracer concentration of the gas and liquid phases respectively of that reactor compartment to which the radial location (r) belongs. The comparison of normalized tracer responses calculated from Equations (6-99a) and (6-99b) has been presented later in this section.

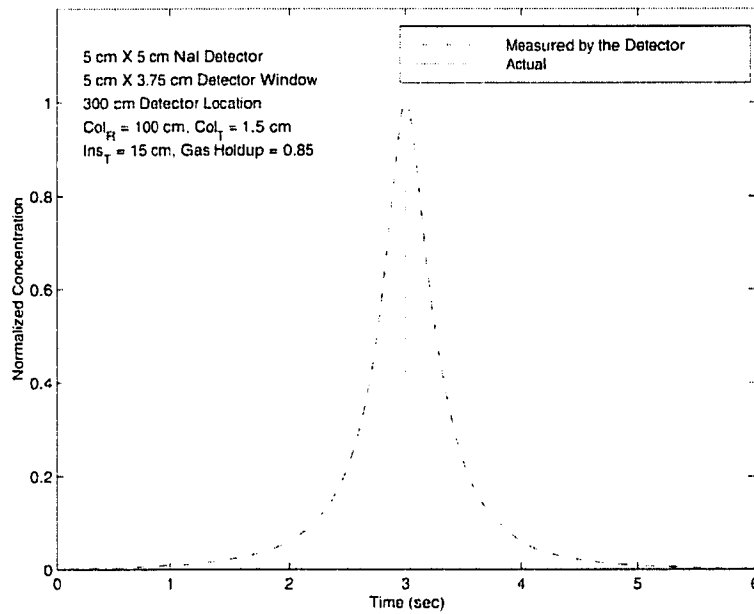
In real world applications, the size of detector collimation is limited due to practical constraints implying that a detector receives radiation from its entire field of view, which results in broadening of the measured tracer responses, as shown in the following example in Figure 6-7. Consequently, for *accurate* comparison of simulation results with experimental data it becomes essential that the contributions of each reactor location towards the registered scintillation counts be considered. This could theoretically be accomplished using the Monte Carlo methodology presented in Chapters 4 and 5 by treating each point in the reactor domain as a point radioactive source and then summing the counts registered by a detector from all points in the reactor. In a multi-detector setup monitoring transient tracer concentrations, such a calculation at each time step would also warrant a precise description of the collimation dimensions and placement with respect to the reactor walls. In addition, all details regarding reactor walls and internals in the field of view would also be needed. Therefore, for practical tracer-data interpretation, this would not be the recommended approach. However, it should be realized that in the

absence of this calculation, the measured tracer responses will be broader than the simulated ones which do not reflect the concurrent contributions from the rest of the reactor. It should also be emphasized that the broadening effects would predominantly originate from the instantaneous axial distribution of the radioactive tracer and minimally from the radial tracer distribution. This can be seen from Figure 6-7 that shows the effect of broadening of a tracer response for an assumed idealized plug flow situation simulated using the Monte Carlo method presented earlier in Chapter 4. Although there is no radial distribution of tracer concentration in an idealized plug flow, the spread in tracer response is still evident. This is indicative of the fact that the origin of this broadening effect is the presence of the radioactive tracer at axial locations other than the axial plane of the detector. Thus, whether one uses Equation (6-99a) or (6-99b), it would not be possible to account for the spread in the normalized detector response. For situations where radial distribution of tracer concentration exists, the use of Equation (6-99b) would only account for a negligible portion of the spread in the measured response. This is shown later while comparing normalized responses evaluated using Equations (6-99a & 6-99b).

For ease of calculating the broadening effect in Figure 6-7, the detector geometry has been approximated as shown in Figure 6-7a. From Figure 6-7b, one can clearly see the effect of non-ideal collimation on the broadening of tracer response. It should be also kept in mind that for a cross-sectionally uniform distribution of radioactivity, approximately 90% of the intensity counts measured by a detector originate from radioactivity near the wall. This is due to the solid angle and detector efficiency effects as presented in Chapter 4. For a sample calculation of the relative contribution to the total counts from various locations in a cross-section, the reader is referred to Degaleesan (1997). It should be mentioned that the broadening of a tracer response as presented in Figure 6-7 represents the upper bound on the broadening effect since the flow is assumed to be an idealized plug flow. When the flow becomes increasingly mixed, the distribution in the tracer concentration diminishes resulting in lesser and lesser broadening. In the theoretical limit of a perfectly mixed flow, this would lead to a zero broadening effect when the transient response measured by a detector is normalized with its maximum.



(a)



(b)

Figure 6-7. Monte Carlo simulation to demonstrate the broadening of tracer response.

a) Detector Geometry

b) Normalized response from a non-ideal imperfectly collimated scintillator

As mentioned above, the response-broadening effect can only be minimized but cannot be eliminated in practical measurement systems unless one is closed to perfectly mixed conditions. Unfortunately, such calculations are prohibitively expensive and require detailed specification of reactor geometry, internals, collimators and detectors. Thus, for the purposes of this study, the normalized tracer concentrations, calculated from Equations (6-99a & 6-99b), have been used to compare with experimental data. The total tracer concentrations, computed by the solution of the model equations, are subsequently normalized by their maximum for comparison with experimental data, which is also normalized with respect to its maximum. The normalized experimental tracer response curves are themselves obtained by averaging the intensity counts registered by the four detectors at the axial plane corresponding to the detector-level of interest. Possible differences among the responses of the four detectors at a given axial level are discussed in Chapter 7. Since the gas, as well as the entrained liquid, moves in a spiraling motion as the gas rises up the column after its introduction at the sparger, radial mixing of the tracer is rapid. The extent of this radial mixing is reflected in the responses observed by the four individual detectors at a given location. For the gas tracer experiments presented in this study, the differences in the normalized responses of the four detectors at level seven are within 5% of each other for majority of the tracer response, and tend to grow for the tail portion of the curves. This should not be surprising since the signal to noise ratio becomes poor for low intensity counts that are recorded by the detectors both when the tracer is approaching the detector plane as well as it leaves it.

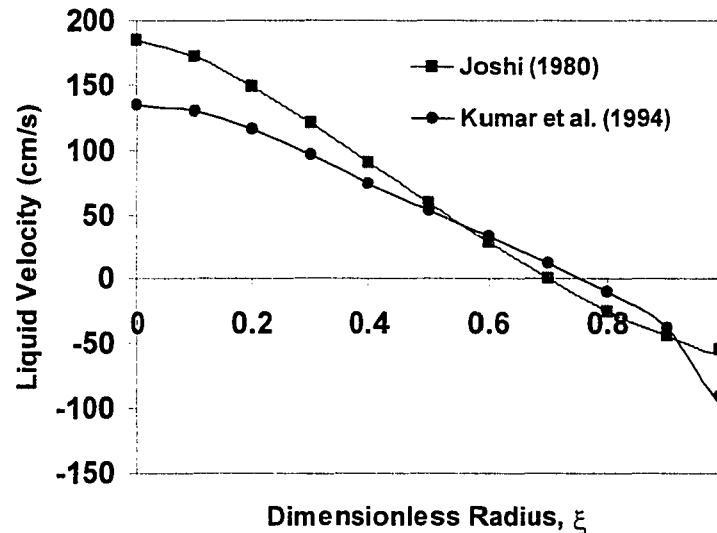
A couple of important points need to be made before one starts comparison of the *cumulative* experimental and simulated tracer responses. First, since the various detectors used in the study are monitoring radiation inside the reactor where strong recirculatory flows are known exist, the measured cumulative response even at “Level 7” cannot be probed to estimate the mean residence time of the gas phase and verify it against the overall mean residence time calculated based on the superficial gas velocity, column length and the mean overall gas holdup. Secondly, for a finite solubility of the gas tracer, the measured responses as well as those estimated from Equations 6-99a and 6-99b

represent not only the transport of the tracer by the gas, but also but the liquid/slurry phase. Therefore, for majority of the simulation results presented in the subsequent sections, it would be far-fetched to speculate whether the simulation results satisfy mass balances. To ascertain the satisfaction of mass balance, the gas mixing model code computes the mass of tracer injected as well as that exiting the reactor. From a multitude of code-verification tests, it has been confirmed that for significantly long times after tracer injection, the total tracer mass input is equal to the total tracer mass output.

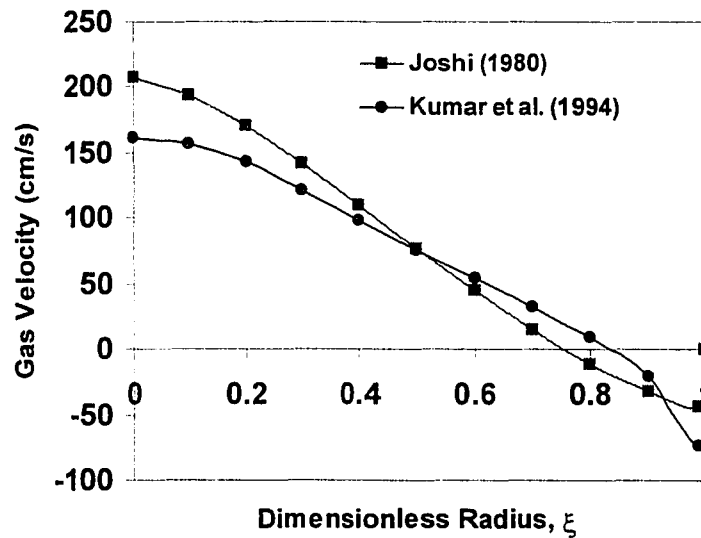
6.5.3.1. Predictions from Single Bubble Class Model (SBCM)

Figure 6-8 shows the predicted liquid (slurry) and gas phase recirculation rates obtained from the mixing lengths of Joshi (1980) and Kumar *et al.* (1994) for the operating conditions of Run 14.6. On the other hand, Figures 6-9a and 6-9b exhibit the comparison of the normalized tracer responses experimental and simulated, obtained using the mixing lengths of Joshi (1980) and Kumar *et al.* (1994), respectively. Several values of the Henry's constant (representing the solubility of Argon⁴¹ in the slurry) were used to simulate the tracer responses due to the anticipated high sensitivity of the model predictions to this parameter. The Henry's constant in this study is *dimensionless* and is defined as the ratio of the Argon molar concentrations in the liquid and gas phase when the two phases are in equilibrium. The thermodynamically estimated value of the Henry's constant under the given operating conditions for Run 14.6 and 14.7 is about 0.17 while it is about 0.12 for Run 14.8. It should be kept in mind that the reactor is operated under high-pressure conditions where the Henry's constant defined above is dependent not only on temperature but also on pressure. For more information, the reader is referred to a basic thermodynamic text (Sandler, 1989). Thus, it is not surprising that the value of the Henry's constant changed for Run 14.8 since the operating pressure was significantly lower. The Henry's constant values were provided by Air Products and Chemicals, Inc. and were estimated using their internal thermodynamic estimation procedures. The estimation procedures involve the assumption about the structure and mean molecular

weight of the slurry mixture; and could deviate from the true value by $\pm 25\%$ to $\pm 50\%$. Therefore, one needs to examine the effect of this parameter on the simulation and the results disclosed in Figure 6-9a,b indicate high sensitivity. The sensitivity to other parameters like the turbulent eddy diffusivities and volumes of the inlet and exit CSTs is relatively insignificant as compared to the sensitivity with respect to the Henry's constant.

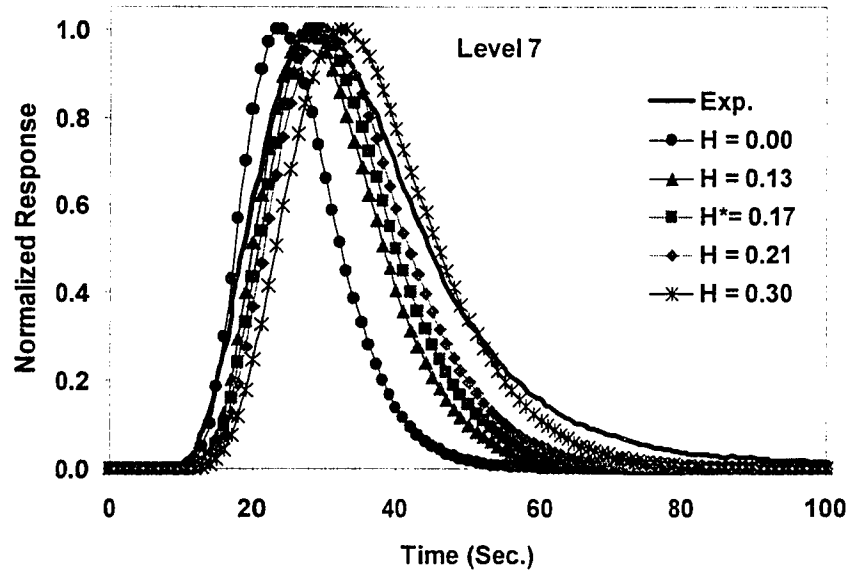


(a)

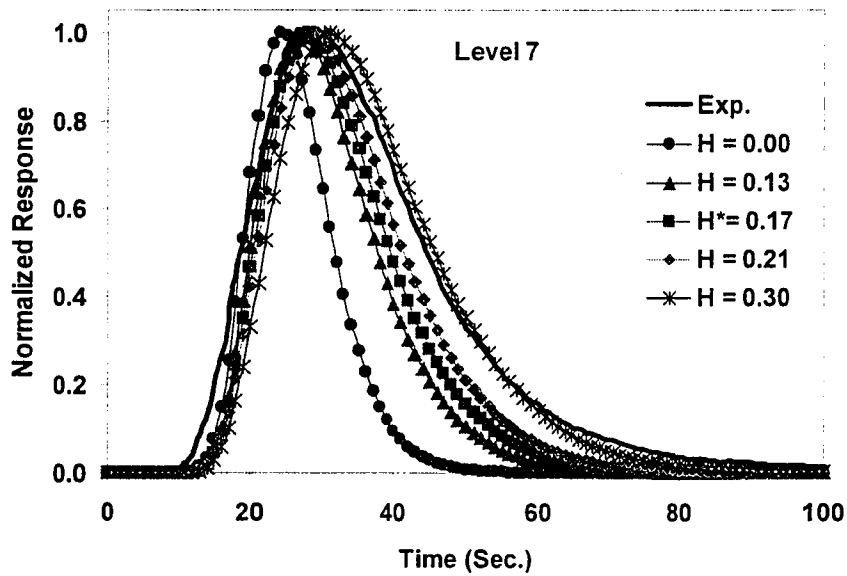


(b)

Figure 6-8. Effect of mixing length profile on a) liquid & b) gas velocity profiles in a 46-cm diameter pilot scale slurry bubble column operated at $U_{G,sup}=22.86$ cm/s.



(a)



(b)

Figure 6-9. Comparison of simulated and experimental radioactive gas tracer responses from a pilot scale slurry bubble column (Run 14.6) using mixing length formulations proposed by a) Joshi (1980) b) Kumar *et al.* (1994).

From Figures 6-9a and 6-9b one can see that the parameters estimated using the mixing length profile of Kumar *et al.* (1994) provide slightly better agreement with the measured tracer responses than those based on the mixing length of Joshi (1980). Particularly for higher values of H (0.21, 0.3) and using the mixing length of Kumar *et al.* (1994), one gets a much closer match of the simulated tracer response with experimental data as compared to that with the mixing length of Joshi (1980). This could possibly be explained based on the results shown in Figure 6-4 where the mixing length of Kumar *et al.* (1994) is shown to provide better predictions of the liquid recirculation profiles as compared to the mixing length of Joshi (1980). In the absence of any obvious advantage in using the mixing length by Joshi and considering the fact that Kumar's mixing length incorporates a wide spectrum of published data on liquid recirculation, ***only the mixing length of Kumar et al. (1994) has been used for all subsequent simulations*** except when comparing the effect of the different mixing lengths proposed by Kumar on the computed tracer responses.

6.5.3.2. Effect of Bubble Size on Mass Transfer Coefficients

It should be noted that a constant bubble size has been used for estimating the " k_L " and " a " in the model equations of the SBCM, which is rarely the case in a real system. Therefore, the effect of a bubble-size distribution on these parameters was investigated using a lognormal distribution with prescribed average bubble-diameter (μ_{db}) and standard deviation (σ_{db}) while holding the gas holdup constant at 0.4. Assuming spherical bubbles, the number of bubbles (n_b) was estimated from the above three quantities. For each bubble diameter (d_b), a corresponding rise velocity (u_b) was calculated using the drag formulation of Tomiyama *et al.* (1995). Based on the bubble diameter and the corresponding rise velocity, the mass transfer coefficient (k_L) and specific interfacial area (a) were calculated based on the concepts outlined in Section 6.4 (Figure 6-10 shows a sample calculation). It was found from these calculations that the volumetric mass transfer coefficient calculated based on average bubble-size and an

average slip-velocity, estimated using this average bubble-diameter, provided the upper bound for $(k_{La})_{avg}$ as compared to $(k_{La})_{pdf}$ computed from the bubble-size and slip-velocity distributions (Refer to Table 6-7). Moreover, as long as the normalized standard deviation for the chosen bubble size distribution remained within 0.1 (for the two mean bubble sizes investigated viz. 0.2 cm and 0.5 cm), this difference was within 10-20%. Therefore, for the high pressure conditions encountered in industrial applications where the bubble sizes are generally in the range from 1-5 mm, the assumption of a constant bubble size for calculation of mass transfer effects is reasonable.

Table 6-7. Effect of bubble size distribution on volumetric mass transfer coefficient.

μ_{db} (cm)	σ_{db}/μ_{db}	ε_g	$k_{La,pdf}$ (s^{-1})	$k_{La,avg}$ (s^{-1})	% Deviation
0.20	0.10	0.40	4.15	4.12	0.67
0.20	0.25	0.40	4.11	4.12	0.29
0.20	0.50	0.40	4.01	4.12	2.69
0.20	1.00	0.40	3.77	4.12	9.13
0.50	0.10	0.40	1.02	1.23	20.80
0.50	0.25	0.40	1.00	1.23	23.34
0.50	0.50	0.40	0.93	1.23	32.82
0.50	1.00	0.40	0.69	1.23	78.43

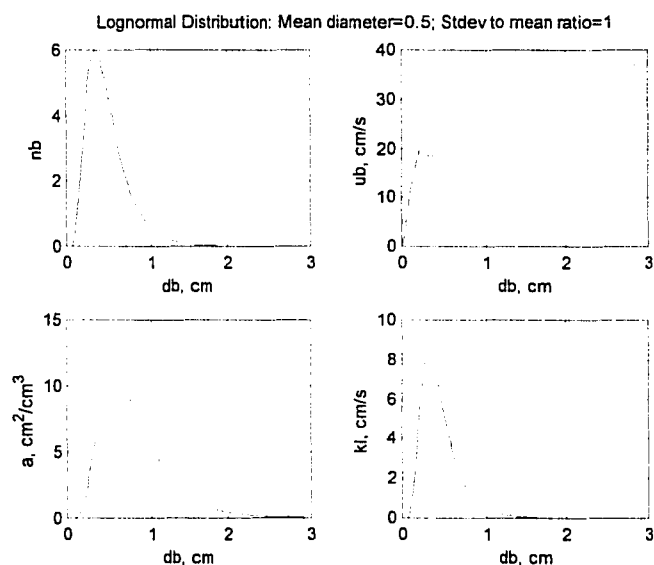


Figure 6-10. Sample calculations of mass transfer parameters for assumed bubble size distribution.

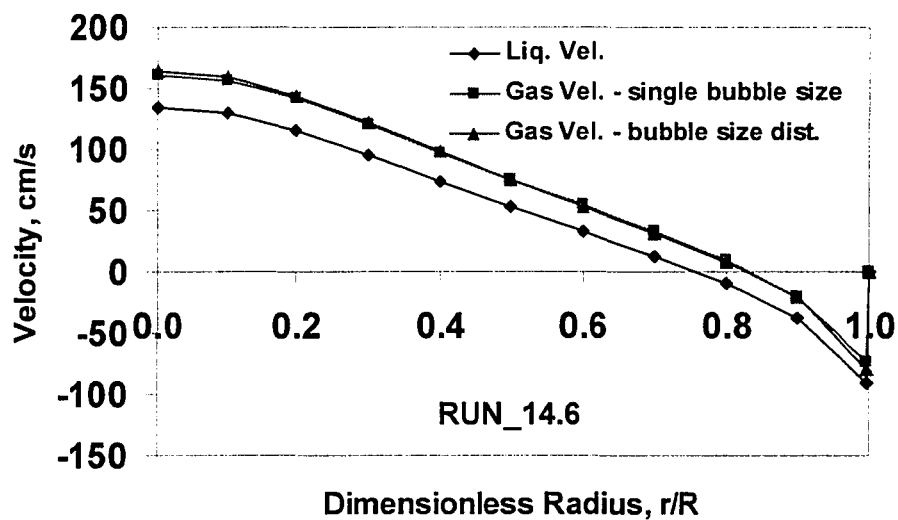
It should be noted that in general an increase in the volumetric mass transfer coefficient results in an increase in the width of the measured tracer response and a reduction of the tail portion of the tracer curve. However, for very high values of the mass transfer coefficient, the spread in the tracer curve around its maximum as well as the tail effect are both reduced. This is illustrated later when comparing the effect of mass transfer coefficients on the predicted tracer responses.

6.5.4. Comparison of Predictions from SBCM and DBSM

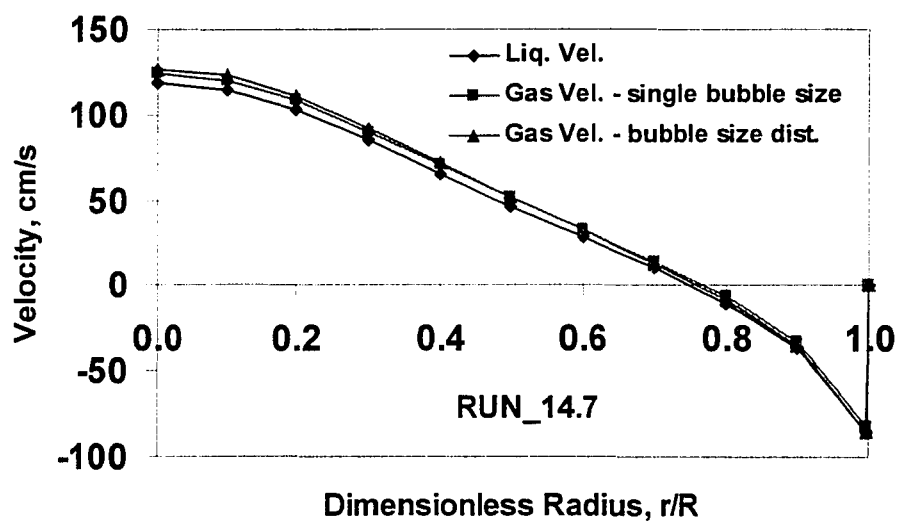
In this section, the effect of the assumed radial distribution of bubble sizes on predicted gas recirculation rates is explained by comparing the results obtained by the SBCM and DBSM. The parameters reported in Table 6-2 and Table 6-3 are used with K_{SBI-LB} assumed to be 1.0 s^{-1} (de Swart, 1996). The effect of using SBCM vs. DBSM on the predictions of experimental tracer data acquired during the AFDU operation under the three operating conditions listed in Table 6-1 is also shown. Figure 6-11 exhibits the radial profiles of the axial time-averaged liquid/slurry and gas velocity profiles computed from the hydrodynamic sub-model for the three operating conditions listed in Table 6-1. Clearly, the computed gas velocity profile is not significantly affected by the nature of the radial distribution of the mean effective bubble-diameter. It is noteworthy that the slip velocity between the gas and slurry phase could be as high as 50-60 cm/s in the column center depending on the superficial gas velocity.

Figures 6-12 to 6-18 present the comparison of the normalized experimental tracer response curves with simulated responses computed from the two models discussed above. The purpose of this comparative study is to evaluate the effect of some of the important model parameters as well as to compare the two models in their ability to predict tracer responses. The effects of some of the other input parameters to the gas-liquid recirculation model on the simulated tracer responses are discussed in the next section (Section 6.5.5). From Figure 6-12, one can see that the effect of the axial dimension of the distributor and disengagement CSTs on the simulated tracer responses

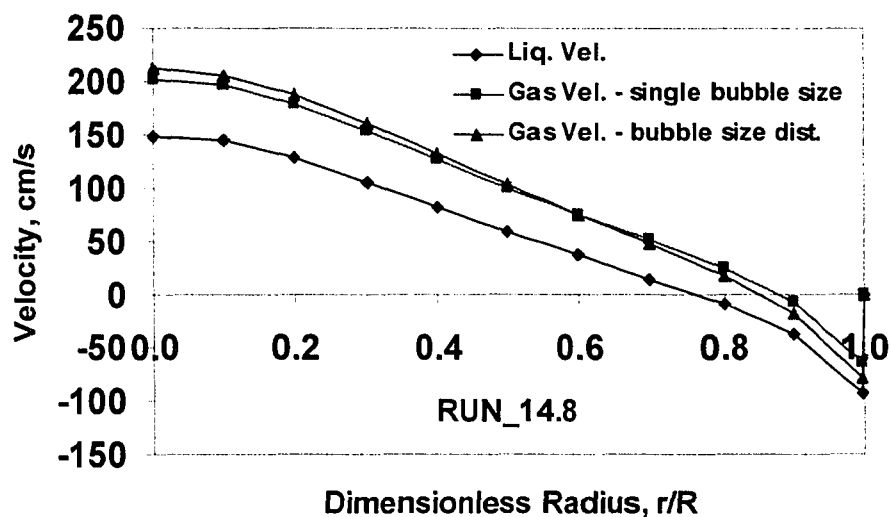
is small for both SBCM as well as DBSM. This result is similar to that of Degaleesan *et al.* (1996^b) for liquid mixing studies in both laboratory as well as pilot-scale columns. Therefore, for all subsequent simulations (Figure 6-13 to 6-15), the height of these regions was set equal to one column diameter. Most importantly, it is evident that both models SBCM and DBSM predict very well the peak of the observed regime in Figure 6-12 for Run 14.6 but the experimental curve is broader for reasons discussed earlier.



(a)



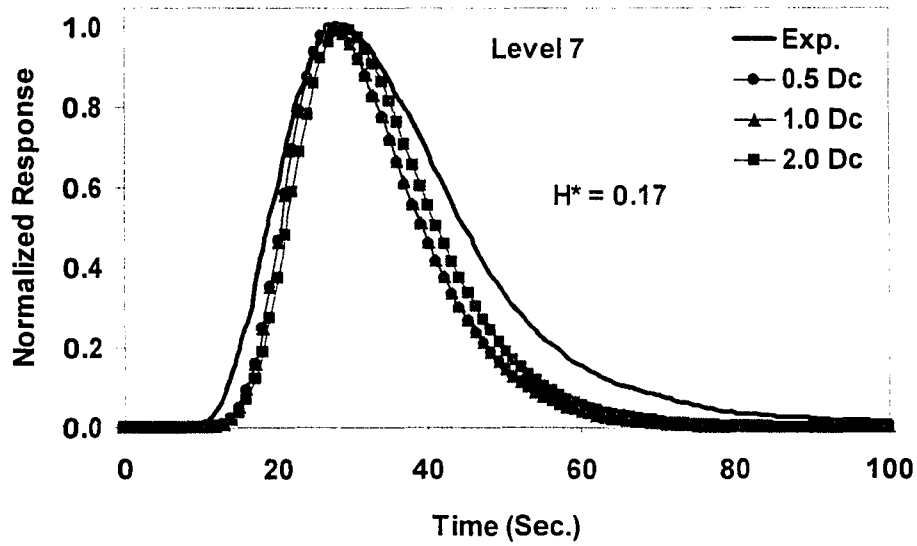
(b)



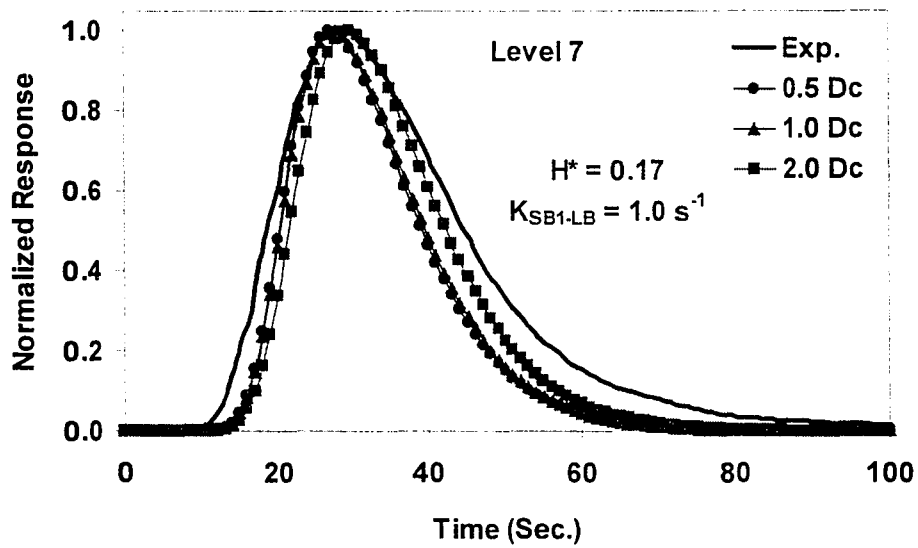
(c)

Figure 6-11. Liquid and gas radial velocity profiles for the three different operating conditions.

As was mentioned previously, the important parameter affecting the spread of the gas-phase tracer-response curves are the Henry's constant (which affects the mean residence time) and the volumetric mass transfer coefficients (which affects the tail portion of the curve). Degaleesan *et al.* (1996^a) also showed that the tracer response curves simulated using the ADM were also very sensitive to these two parameters, however, no consistent trend was found in their estimated values. Figure 6-13 presents the comparison of the simulated and experimental responses for a few values of the Henry's constant. For all the computed results, the mass transfer coefficients and interfacial areas are those reported in Tables 6-2 and 6-3. From the figure, it can be seen that for both SBCM as well as DBSM, Henry's constant can significantly affect the peak arrival time except for Run 14.8 where the effect of the Henry's constant is manifested in the tail portion of the curves. In general, a larger value of the Henry's constant implies that the tracer stays longer in the liquid (slurry) phase resulting in a prolonged residence time.



(a)



(b)

Figure 6-12. Effect of the axial dimension of the distributor and disengagement CSTs on the simulated gas tracer-response curves computed using (a) SBCM (b) DBSM.

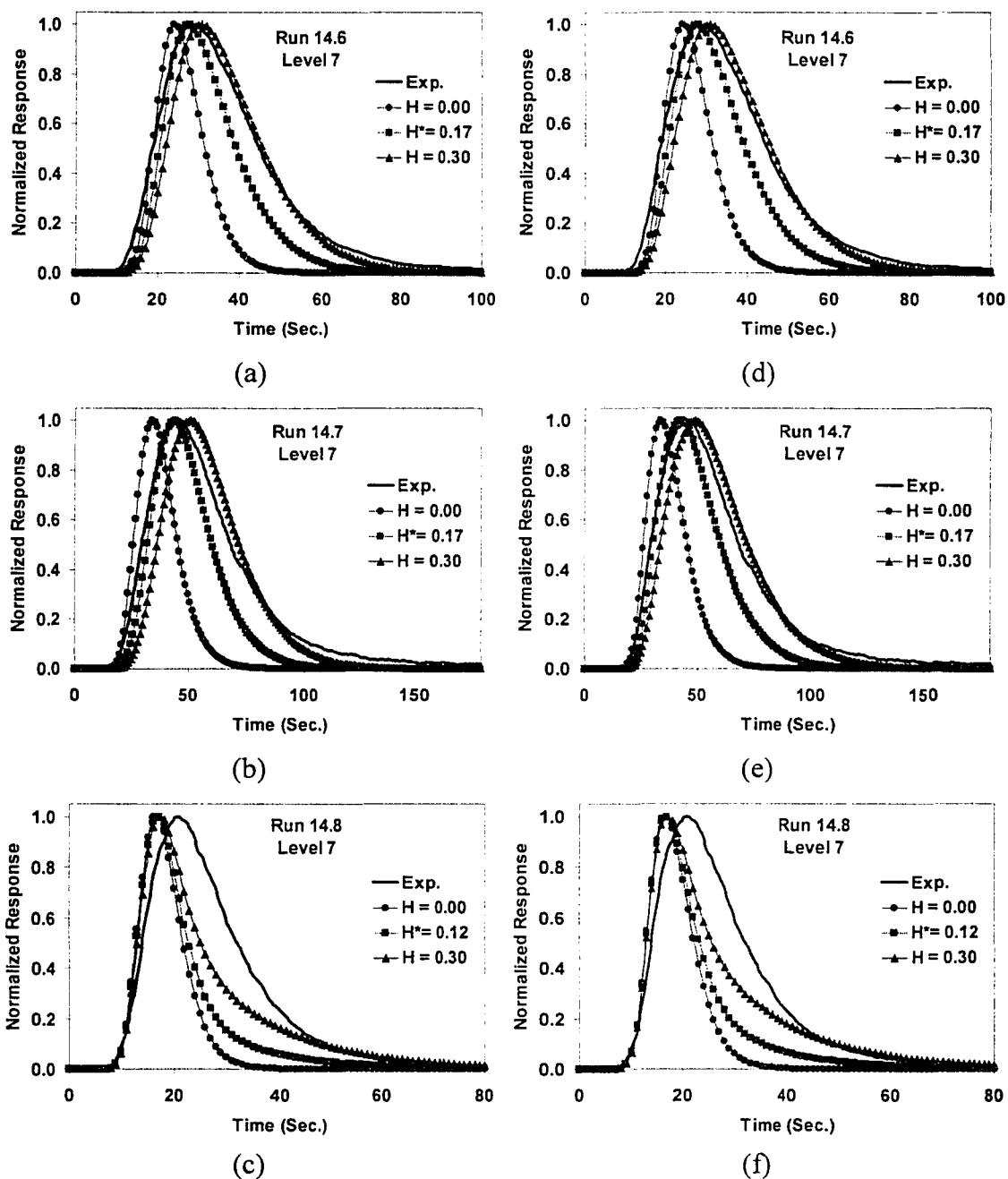


Figure 6-13. Effect of Henry's constant on simulated gas-tracer response curves (a)-(c) SBCM (d)-(f) DBSM ($K_{SB_T-LB} = 1 \text{ sec}^{-1}$).

From the figure above, it can be seen that for Runs 14.6 and 14.7, the simulated tracer curves assuming the thermodynamically estimated value of the Henry's constant

($H^* = 0.17$) result in a good match of the calculated peak arrival times with experimental values and under-estimation of the spreads in the calculated tracer response curves. For Run 14.8 the agreement of calculated and predicted values based on estimated H^* is not that good. It should be re-emphasized here that the measured tracer responses are a result of radiation measurement, which may lead to additional broadening of the tracer responses as discussed earlier depending on the state of mixing prevalent in the reactor. One of the reasons for the poorer predictability of Run 14.8 could arise from the very high superficial gas velocity employed for this experiment. At these high velocities, few drag correlations have been conclusively shown to be reliable in their application to bubble column flows and consequently, the sub-model may be over-predicting the gas phase velocities. This in turn results in smaller values of peak arrival times than the experimentally observed values. Additionally, the high gas phase velocities also imply a larger bubble size that in turn leads to low volumetric mass transfer coefficients. This is evident from Table 6-5 where the value of $k_{L,a}$ is on the lower end of the spectrum predicted by various literature correlations. Thus, because of the low $k_{L,a}$ values computed for Run 14.8, one sees the long tails in the computed tracer responses.

Given that the volumetric mass transfer coefficient for Run 14.8 may be under predicted due to the large bubble sizes computed by the sub-models, it was considered important to evaluate the effect of this parameter on the simulated responses for the conditions of Run 14.8. Figure 6-14 shows the comparison of the simulated responses with varying $k_{L,a}$ values for three different values of the Henry's constant for two detector levels using SBCM. From the figure, it can be seen that as the volumetric mass transfer coefficient increases, the peak of the response curve shifts to larger times. Coupled with an increasing Henry's constant, the tracer response curves get broader with increasing $k_{L,a}$ values. In fact for $k_{L,a}$ of 0.2 s^{-1} and $H=0.3$, the agreement between the simulated responses and the experimental one is nearly perfect. As mentioned earlier, the shift in peak simulated response as well as the overall broadening of the simulated responses with increasing $k_{L,a}$ should not be mistaken for inaccuracies in computations since the computed response is a cumulative result of the tracer in the various gas and slurry zones.

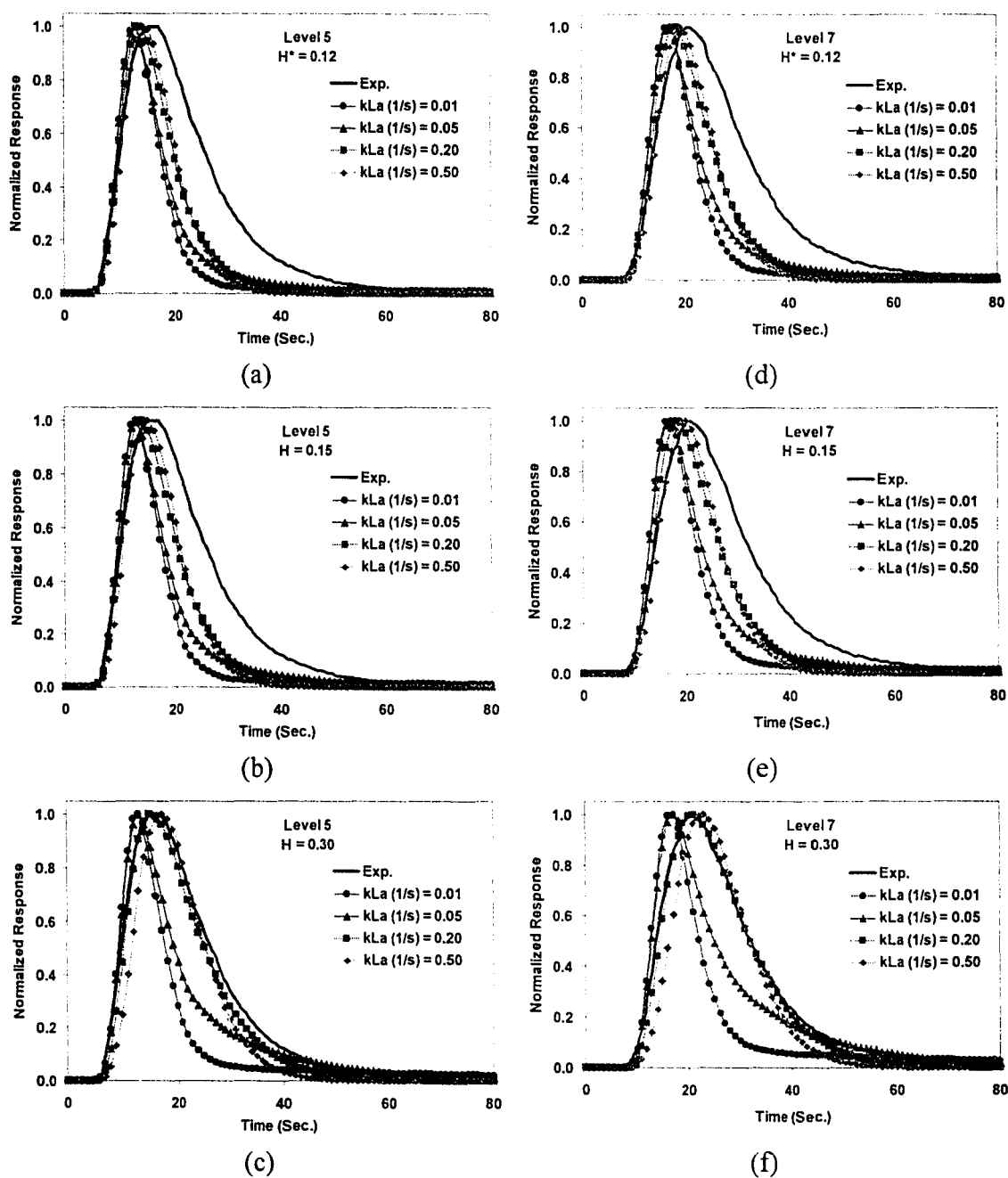


Figure 6-14. Effect of volumetric mass transfer coefficient on the gas-tracer responses for Run 14.8 simulated using SBCM (a)-(c) Level 5 (d)-(f) Level 7.

Figures 6-15 to 6-17 examine the effect of the bubble interaction parameter K ($\equiv K_{SB, LB}$) on the responses simulated by the Distributed Bubble Size Model for Runs 14.6, 14.7 and 14.8 respectively with $K = 0$ implying no bubble-bubble interaction. It can be seen from the figures that the bubble-bubble interactions have a significant effect on the tracer curve in absence of bubble-bubble interaction ($K=0.0$ i.e., for non-interacting small and large bubble phases) especially in the absence of mass transfer. Moreover, there is no noticeable difference in the predicted responses when the interaction parameter is non-zero. In other words, when K is equal to 0.1 s^{-1} , 0.5 s^{-1} or 1.0 s^{-1} all the computed tracer responses collapse into one irrespective of the value of the Henry's constant.

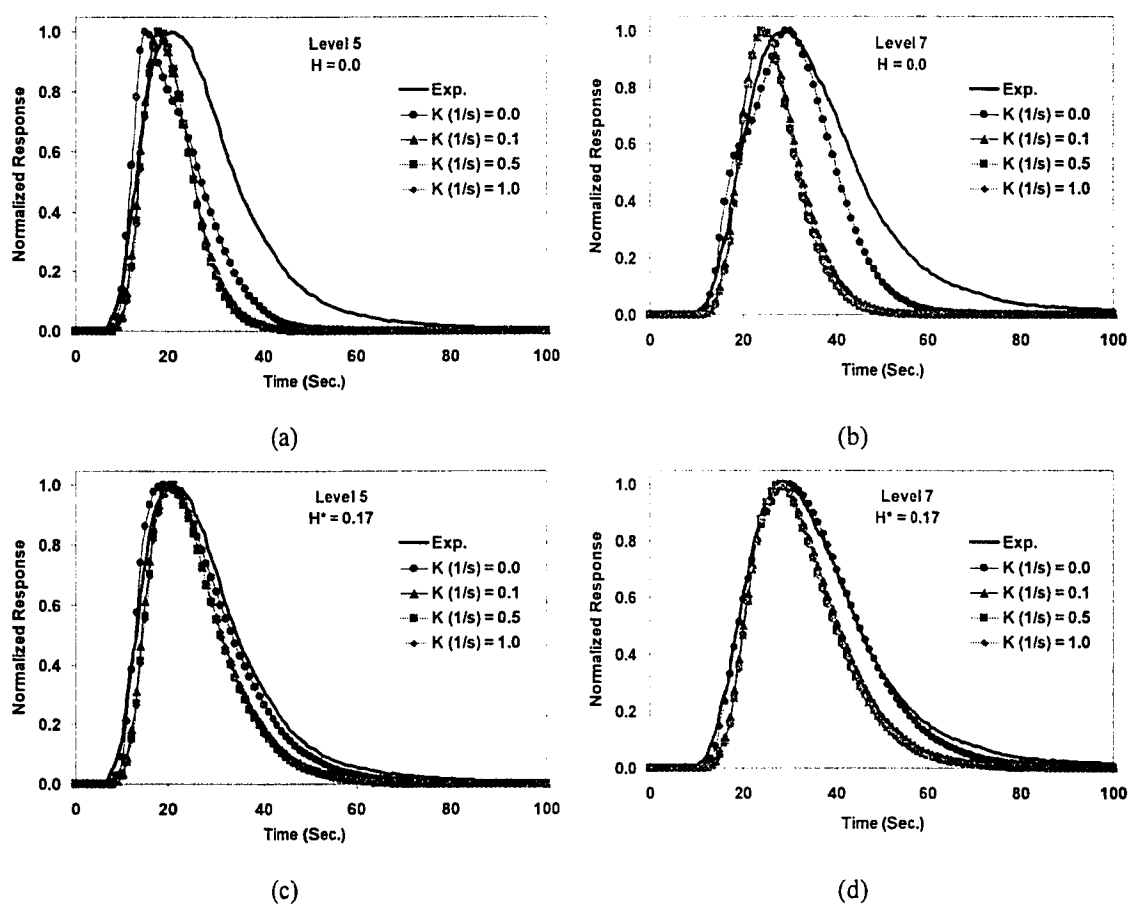


Figure 6-15. Effect of the bubble-interaction parameter in DBSM ($K_{SB, LB}$) on the simulated gas-tracer responses for Run 14.6 (a)-(b) $H=0$; (c)-(d) $H=H^*$.

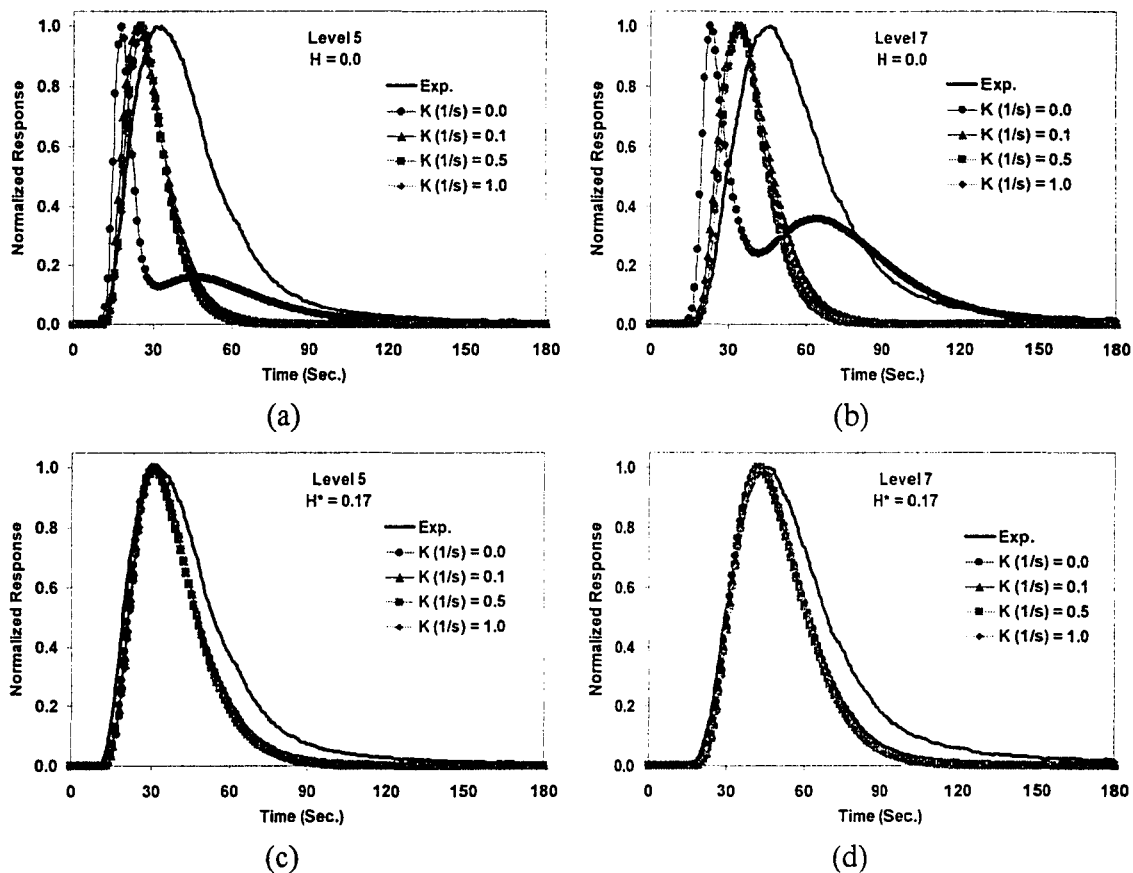


Figure 6-16. Effect of the bubble-interaction parameter in DBSM (K_{SBI-LB}) on the simulated gas-tracer responses for Run 14.7 (a)-(b) $H=0$; (c)-(d) $H=H^*$.

From Figure 6-16, one can see that when the Argon solubility is zero, the large and small bubble phases have independent dynamics in the absence of bubble-bubble interaction. This is clearly seen from the two peaks in the response curves in Figure 6-16a,b. However, in the presence of the gas solubility the two bubble phases interact with each other indirectly when $K=0$. However, the dynamics of that interaction occurs at a time-scale that masks the bubble-bubble interaction effects. This is evident from Figure 6-16c,d where there is virtually no differences in the responses simulated using the four different values of the bubble interaction parameter. Interestingly for Run 14.8, the existence of a finite solubility of the tracer does not result in a complete masking of the bubble interaction effects. On the contrary, for the thermodynamic value of the Henry's

constant and K equal to zero, the agreement between simulations and experiments is very good at detector level 7. This unfortunately is not the case at other detector levels as can be seen from Figure 6-17c. Thus, it is not possible to identify a clear trend in the effect of the bubble interaction parameter on the simulated responses.

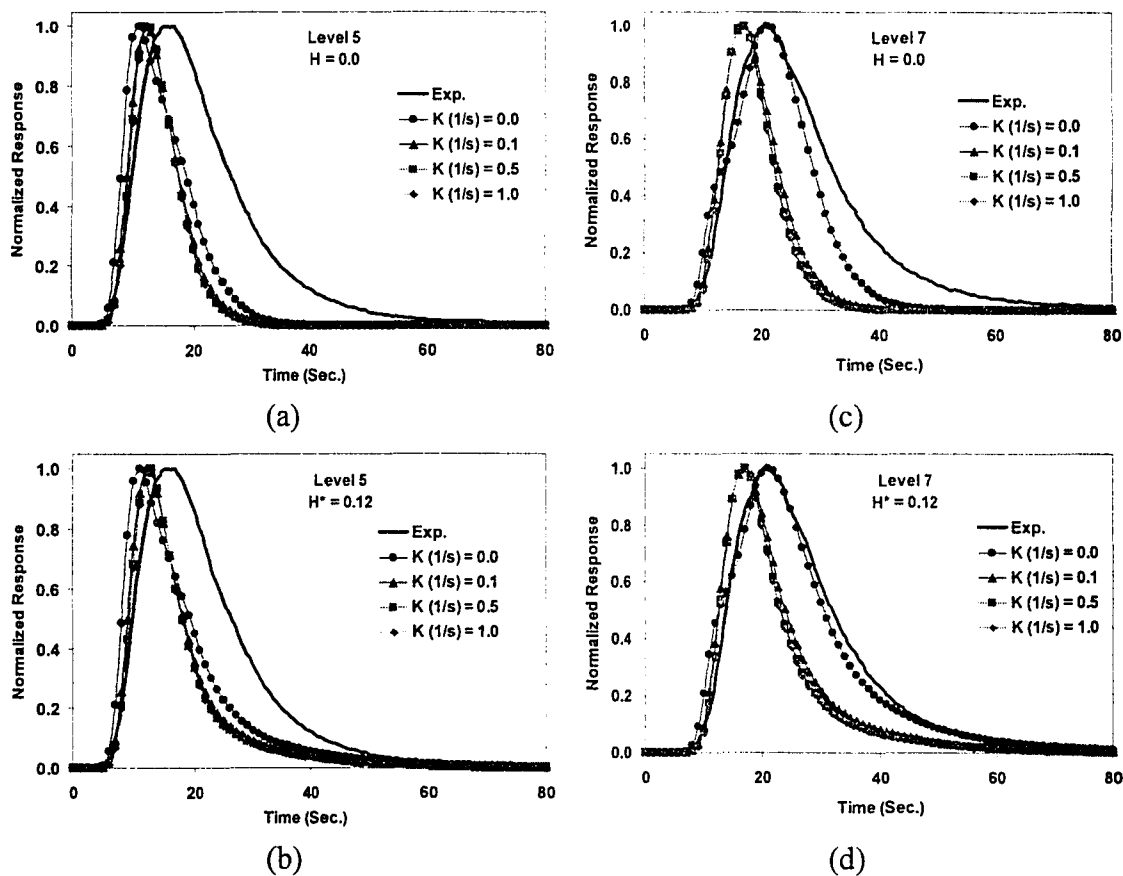


Figure 6-17. Effect of the bubble-interaction parameter in DBSM (K_{SBI-LB}) on the simulated gas-tracer responses for Run 14.8 (a)-(b) $H=0$; (c)-(d) $H=H^*$.

When analyzing the above results, it should also be kept in mind that the average speeds at which the "small" and "large" bubbles travel do not differ by more than 30-45 cm/s as computed from the current parameter-estimation procedure. It is possible that the velocities of the "small" and "large" bubbles may differ much more than assumed here, if computed using literature correlations (Krishna, 2000^h). In that case, the bubble-bubble

interaction parameter might have a more pronounced effect on the simulated tracer responses. However, as mentioned earlier, such correlations for bubble rise velocities are developed without consideration of the inherent recirculatory nature of the flow, and may not provide good estimates for the bubble velocities.

The assumption of the existence of two-bubble classes is also evaluated. Figure 6-18 presents the result of such comparison, where the simulated responses have been computed using $K_{SB-LB}=1.0 \text{ s}^{-1}$. One can see from the figure that the two models do not exhibit any significant differences as far as comparison with tracer response data is concerned. This result is not too surprising as the "small" and "large" bubble phase equations for the DBSM when added together result in the equation describing the dynamics of the up-flowing gas in the SBCM. Therefore, one does not really need to make the assumptions about the bi-disperse bubble size distribution to characterize the gas-phase dynamics, as long as a reasonably accurate description of the recirculation in the gas and liquid phases is incorporated into the reactor model.

6.5.5. Parametric Sensitivity Analysis

Figures 6-19 to 6-22 show the effect of a few input and processing parameters on the computed gas tracer responses. The effect of the radial eddy-diffusion coefficient on the peak and spread of the tracer response can be seen from Figure 6-19. From the figure, it appears that the effect of D_{rr} is minimal on the simulated responses for Run 14.8, while it is most pronounced for Run 14.7. For Run 14.6, the effect is noticeable but not as pronounced as Run 14.7. This trend is possibly due to the degree of recirculatory mixing that is the highest for Run 14.8, then next for Run 14.6 and the lowest for Run 14.7 given the superficial gas velocities at each of the operating conditions.

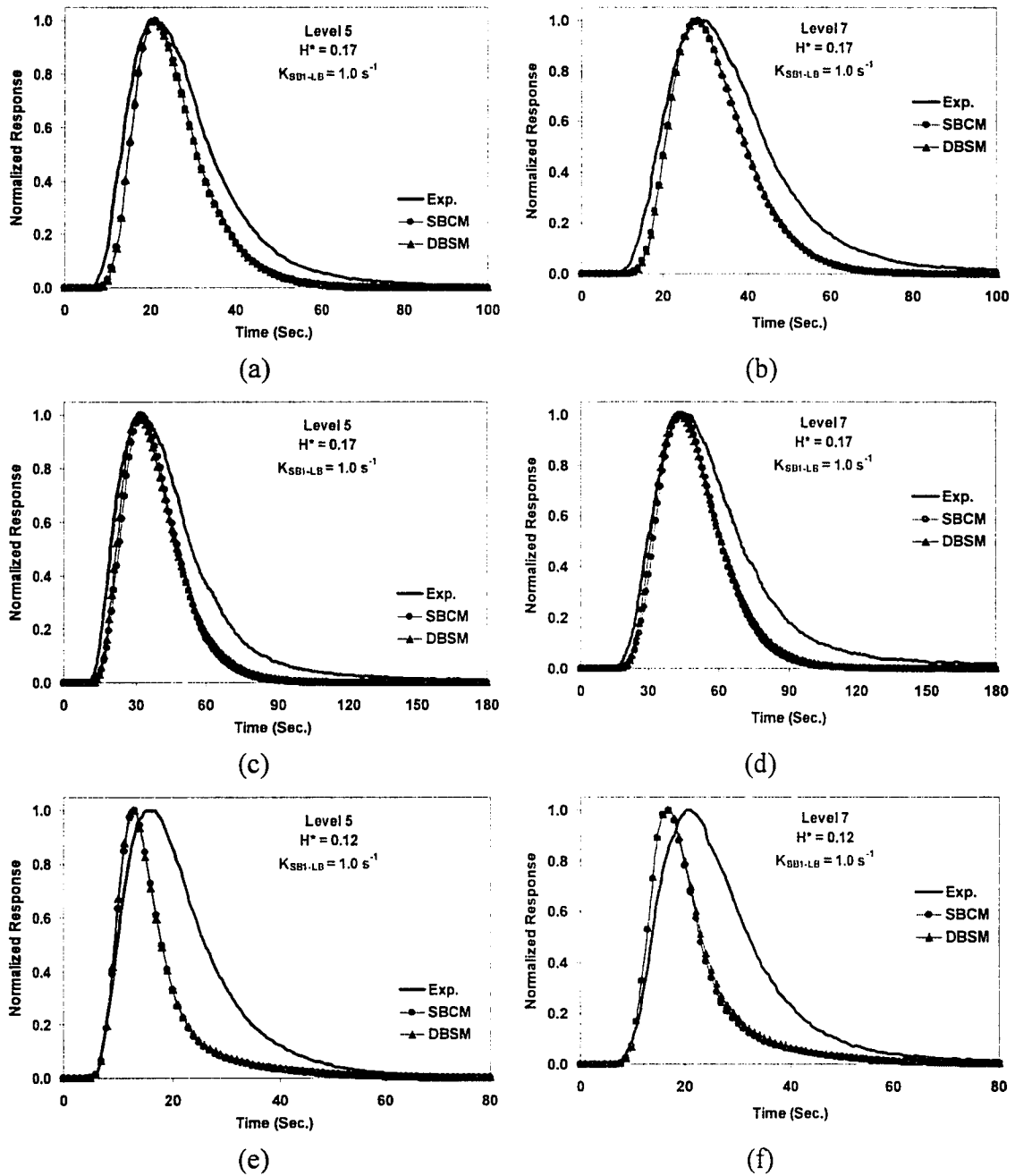


Figure 6-18. Comparison of tracer responses simulated using SBCM and DBSM with experimental data. (a)-(b) Run 14.6; (c)-(d) Run 14.7; (e)-(f) Run 14.8.

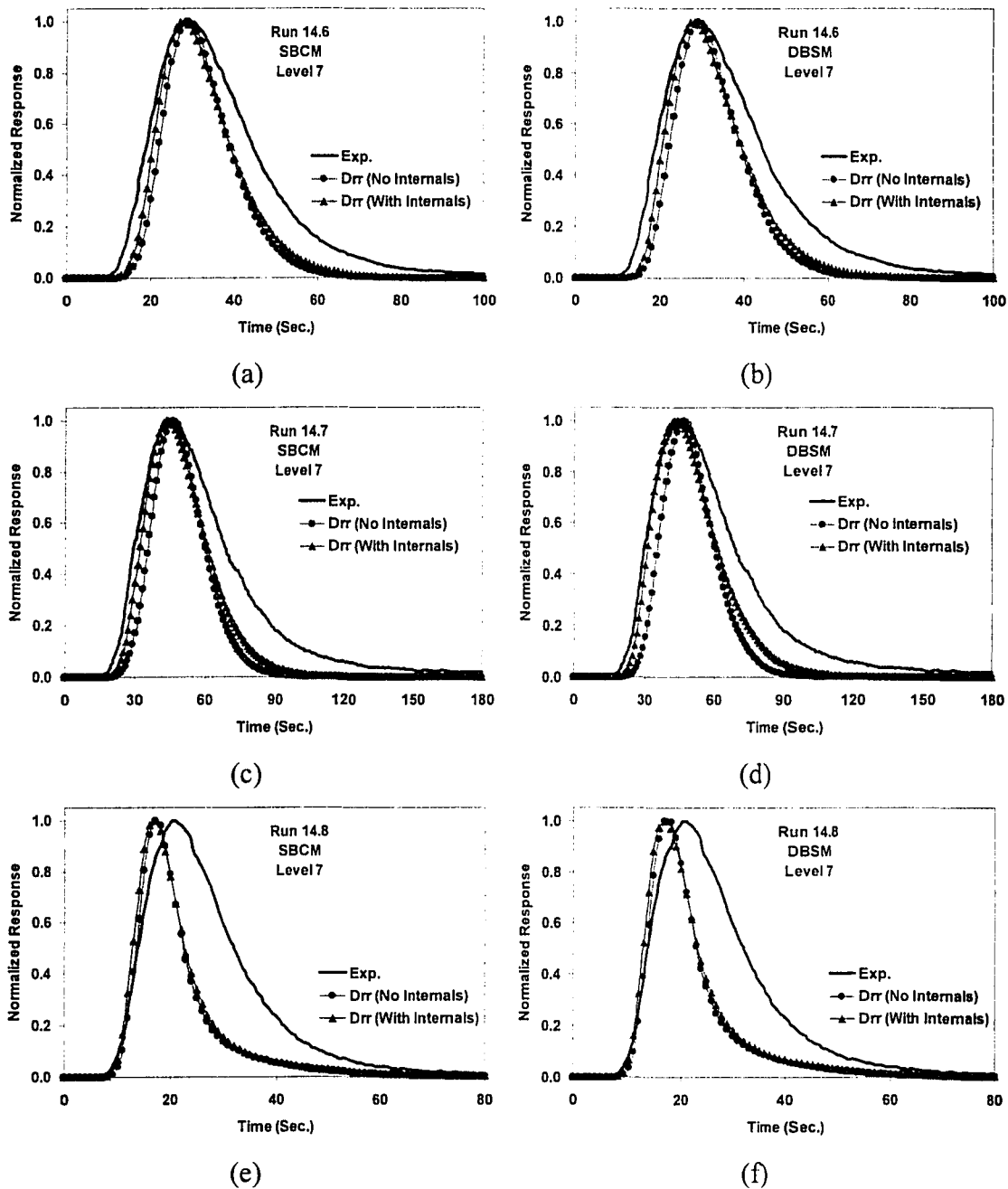


Figure 6-19. Comparison of the effect of radial eddy diffusivity on the simulated tracer responses with experimental data. (a)-(c) SBCM (d)-(f) DBSM.

Based on the above figure, it appears that a lower value of D_{rr} causes the tracer response to arrive earlier as well as to broaden the tracer response curve. Figure 6-20 shows the effect of accounting for radiation attenuation on the computed responses. It can be seen from the figure that the effect of radiation attenuation is negligible, primarily due to the symmetric introduction of the tracer at the sparger. This also points to the high degree of uniformity in the radial distribution of the tracer which is not usually seen in point injections of tracer inside the reactor (refer to liquid/catalyst tracer experiments in Chapter 7).

Figure 6-21 shows the dependence of the simulated tracer response curves on the assumed gas holdup profile. Given the constraints of the cross-sectional and chordal averaged gas holdups from DP and NDG measurements of gas holdup distribution, the exponent “m” in the profile could only be increased to a maximum of 2.25 so as to yield a non-negative radial gas holdup profile. Degaleesan (1997) has recommended a value of 2 for the exponent “m” for all the three runs conducted in this study. Therefore, these two were the obvious choice for parametric evaluation. Additionally, the correlation of Wu *et al.* (2001) suggested that the exponent “m” is in the range 1.2-1.6 pertinent to the operating conditions of the three runs. Thus, an additional value of $m=1.5$ was included in the parametric evaluation of the effect of gas holdup on the simulated responses.

From the above figure, it can be inferred that the gas holdup profile has a negligible effect on the simulated tracer responses for Run 14.7 for both SBCM as well as DBSM. For Run 14.8, the effect of the gas holdup profile is also minimal, with higher values of the exponent “m” leading to slightly greater broadening of the tail portion of the responses. This is particularly so for DBSM than for SBCM. Run 14.6 by far exhibits the most pronounced effect of the gas holdup profile on the shape of the tracer response curve. For an exponent of 1.5, the computed responses are both narrower as well as arrive earlier than the experimental ones. On the other hand, $m=2.25$ results in an excellent agreement of the peak arrival time of the experimental and simulated responses. From these results, it is clear that there are no clear trends as to a preferred value of the exponent in the gas holdup profile. However, based on previous success of Degaleesan

(1997) in simulating liquid tracer responses, a value of 2.0 for the exponent has been used for most of the simulated responses presented in this study.

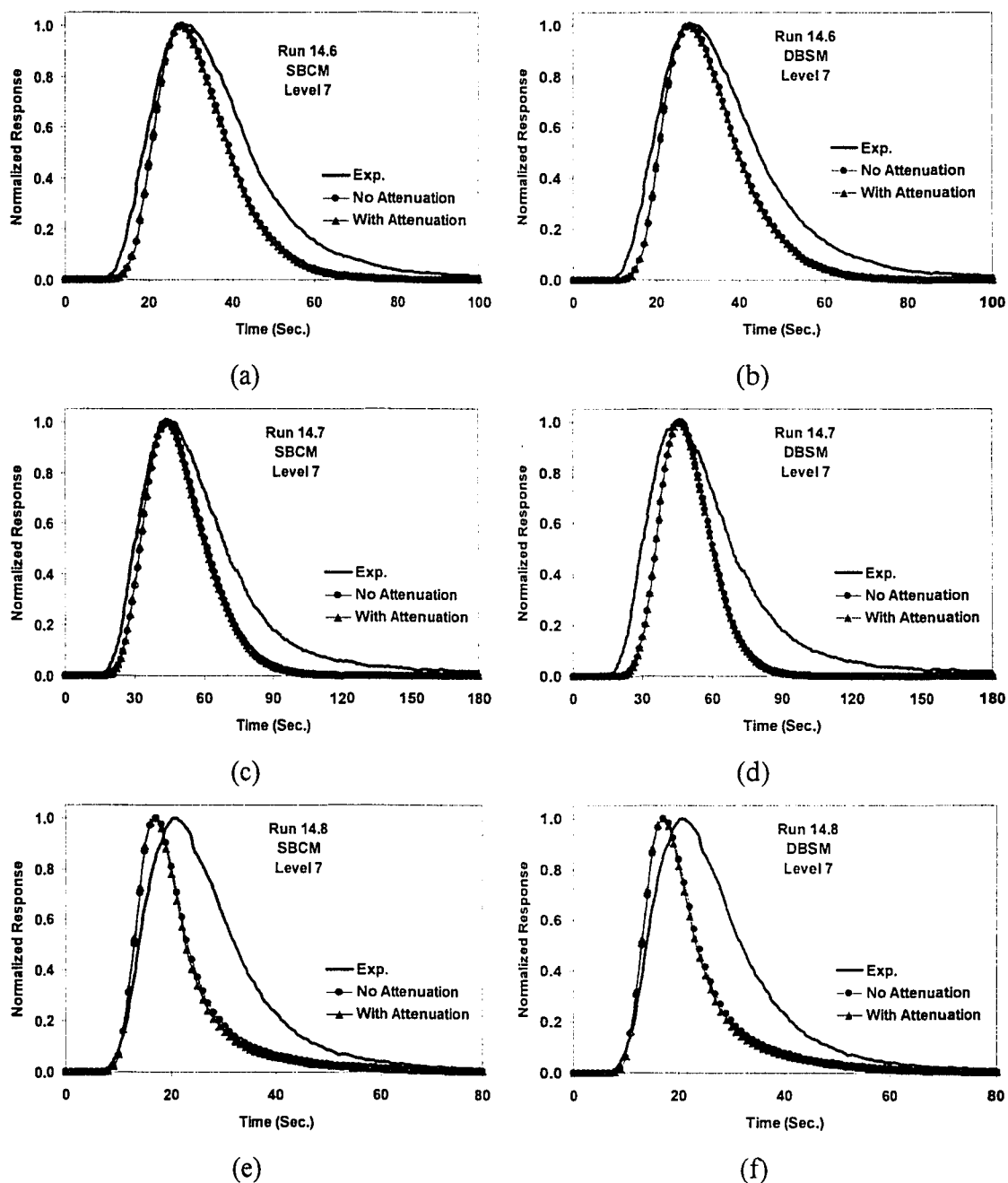


Figure 6-20. Comparison of the effect of radiation attenuation on the simulated tracer responses with experimental data. (a)-(c) SBCM (d)-(f) DBSM.

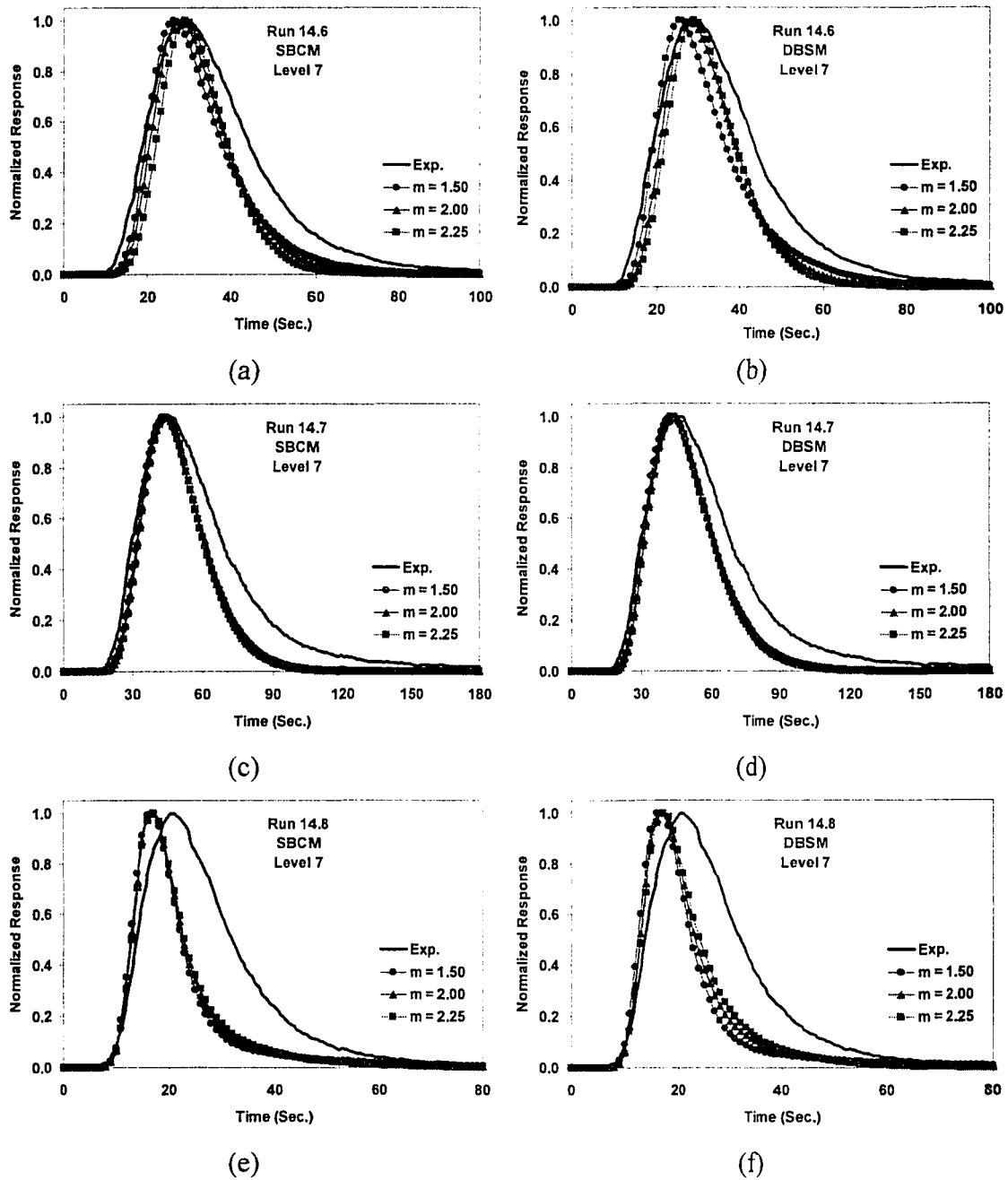


Figure 6-21. Comparison of the effect of radial gas holdup profile on the simulated tracer responses with experimental data. (a)-(c) SBCM (d)-(f) DBSM.

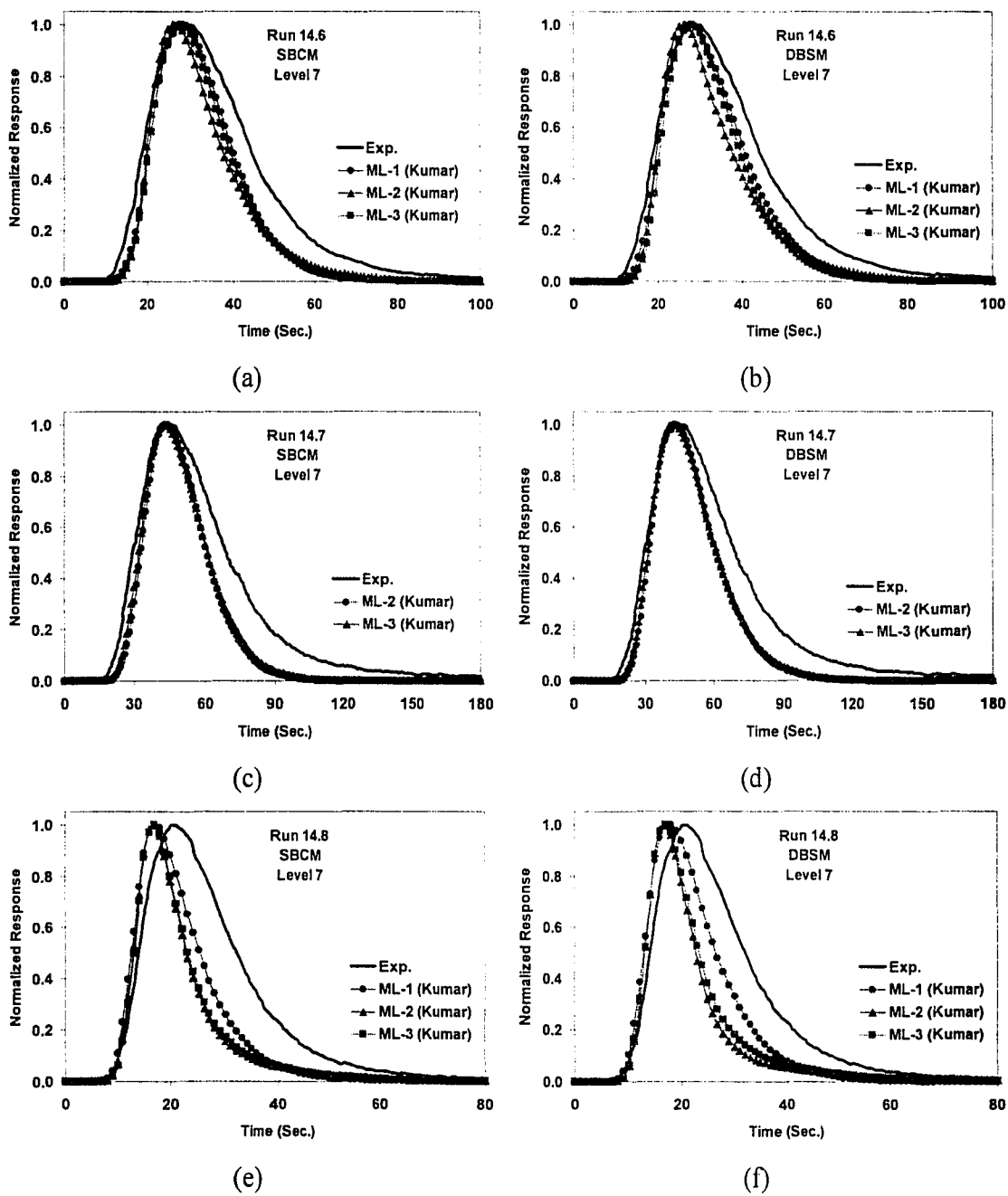


Figure 6-22. Comparison of the effect of radial mixing length profile on the simulated tracer responses with experimental data. (a)-(c) SBCM (d)-(f) DBSM.

Figure 6-22 presents the effect of the mixing length profile on the simulated gas tracer responses. The three mixing length profiles are those from Kumar (1994) who compiled the information on the liquid recirculation velocities and turbulent shear stresses in bubble column flows from the open literature to propose three different mixing lengths. While ML-1 was proposed for bubbly flow situations, ML-2 was that for transition regime and ML-3 for the churn-turbulent regime. For a discussion on these profiles, the reader is referred to Kumar (1994). As with the gas holdup profile, the mixing length profile seems to have negligible effect on the simulated responses for Run 14.7 while its effect on simulated responses for Run 14.6 is marginal and is evident only in the decaying portion of the computed responses. On the other hand, the mixing length profile (ML-1) seems to stretch the computed responses for Run 14.8 and make them broader to bring them closer to the experimental response. The reason for this behavior is that when using ML-1, the computed bubble size that satisfies gas continuity is smaller leading to higher mass transfer coefficients. In general, ML-1 leads to the smallest bubble size, followed by ML-3 with ML-2 resulting in the largest mean bubble size. Since ML-1 is supposed to be representative of the bubbly flow, the computation of a smaller bubble size with its use is logical. However, ML-2 resulting in the largest mean bubble size most likely points to the difficulties associated with reliably defining the transitions regime and subsequently characterizing its hydrodynamics.

Altogether, this indicates that input parameters to the gas-liquid recirculation model have a finite effect on the computed tracer responses. Some parameters like the radial eddy diffusivity affect the tracer responses directly while other like the gas holdup and mixing length profiles affect the computed responses indirectly through computed recirculation, bubble sizes and subsequently mass transfer coefficients. Since there are no obvious choices for these parameters, it is recommended that in a design or an analysis situation, a systematic study of the parametric sensitivity of simulation results be conducted whenever possible.

6.6. Issues Related to Bubble Size Distribution

The radial distribution of the mean bubble size assumed for the DBSM although justifiable in view of the observed radial gas holdup profile, needs more investigation regarding its effect on the prediction of gas-phase recirculation, average diameters of the two bubble classes and overall gas phase mixing. Substitution of the expressions for the radial gas-holdup and bubble-size distributions (Equations 6-55 and 6-71) into the bubble number density function given by Equation 6-94, one gets

$$n_b(\xi) = \frac{4\tilde{\varepsilon}_g(m+2)}{\pi m d_{G, LB}^2} \frac{1}{(1 - c\xi^m)} \quad (6-100)$$

The above equation implies that the bubble number density increases from the column center to the wall. Arguably, this can be justified by claiming that there are many more bubbles by the walls due to presence of very fine bubbles than in the center. However, it may also be argued, since gas holdup is larger in the column center along with the mean bubble size the bubble number density is also at its maximum in the center. In order to provide some flexibility and study the effect between these extreme assumptions, the assumed radial distribution of mean bubble diameter is modified and parametrically represented as

$$d_b(\xi) = d_{b, max} (1 - c\xi^m)^{\frac{1}{j}} \quad (6-101)$$

With this new distribution, the bubble number-density function now becomes

$$\boxed{\times} \quad (6-102)$$

From Equation 6-102, it can be seen clearly that if j is equal to 2, then the bubble number density is constant across the column cross-section. For any value of j greater than 2, the bubble number density decreases from the column center towards the wall, while for j less than 2, the contrary happens. To examine the hypothesis that a larger gas holdup in

the column center, where the mean bubble size is larger, implies that there are more bubbles present at the center, the parametric study of j has been restricted to values of j greater than 2. Of course, as the value of j gets larger and larger, the radial variation of the mean bubble size gets flatter and flatter.

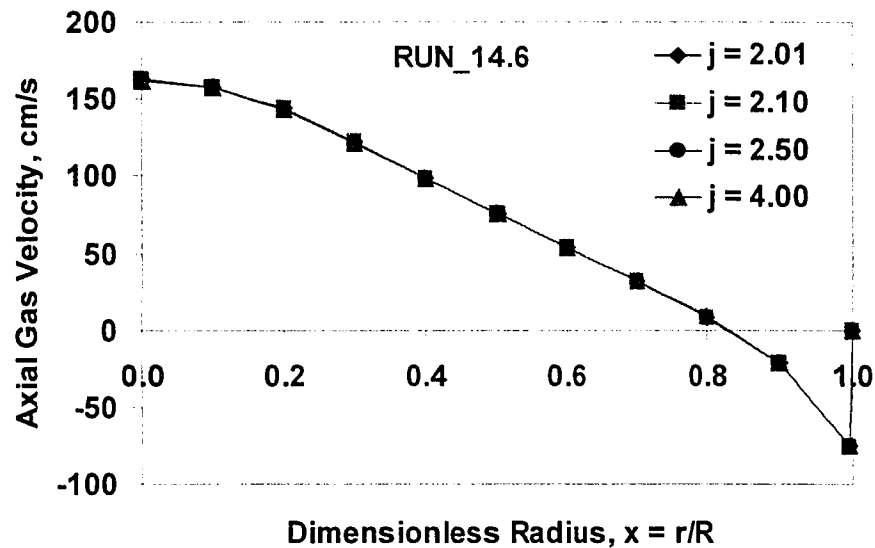
With the bubble number density function forced to be larger in the column center than near the column walls, one is guaranteed that the mean bubble number density in the outer region, $\bar{n}_{G_2,SB}$, computed from Equation 6-96, is less than the mean bubble number density in the core, $\bar{n}_{G_1,SB+LB}$, computed from Equation 6-97. As mentioned earlier, “small” bubble holdups in the “core” and “annulus” regions are assumed equal in DBSM, i.e., $\bar{\epsilon}_{g1} = \bar{\epsilon}_{g2}$. In the methodology presented earlier, this just implies that equality $\bar{n}_{G_1,SB} \bar{d}_{G_1,SB}^2 = \bar{n}_{G_2,SB} \bar{d}_{G_2,SB}^2$ holds but all four quantities - $\bar{n}_{G_1,SB}$, $\bar{n}_{G_2,SB}$, $\bar{d}_{G_1,SB}$ and $\bar{d}_{G_2,SB}$ could be and are different as can be seen from Table 6-4. However, if we impose as another assumption the equality of “small” bubble holdup in the core and the annulus also implies an equality of the average mean bubble diameters as well as the average “small” bubble number densities, then the average bubble number density and size of the “large” bubbles in the core can be readily calculated as

$$\bar{n}_{G_1,LB} = \bar{n}_{G_1,SB+LB} - \bar{n}_{G_1,SB} \quad \text{where } \bar{n}_{G_1,SB} = \bar{n}_{G_2,SB} \quad (\text{assumption}) \quad (6-103)$$

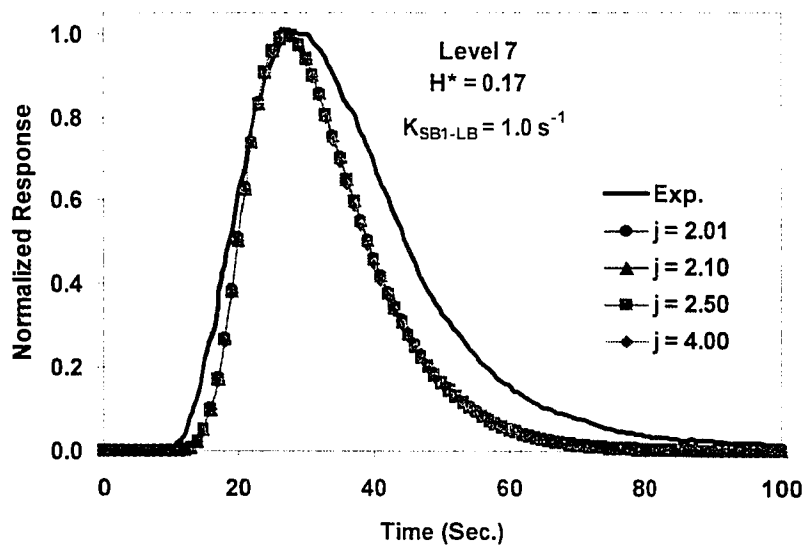
$$\bar{d}_{G_1,LB} = \sqrt{\frac{\bar{n}_{G_1,SB+LB} \bar{d}_{G_1,SB+LB}^2 - \bar{n}_{G_1,SB} \bar{d}_{G_1,SB}^2}{\bar{n}_{G_1,LB}}} \quad \text{where } \bar{d}_{G_1,SB} = \bar{d}_{G_2,SB} \quad (\text{assumption}) \quad (6-104)$$

Based on this new prescription for evaluating the bubble size parameters of the Distributed-Bubble Size Model, the effect of the parameter j on the predicted gas phase recirculation and gas phase tracer response was studied for the operating conditions of Run 14.6 presented in Table 6-1. Figure 6-23 shows the effect of this parameter on the simulation results, which clearly indicates that the choice of the parameter “ j ” doesn’t have any significant effect on the predicted gas phase recirculation. Consequently, there is negligible difference in the predicted DBSM parameters, which translates into

negligible differences in simulated tracer responses. A recommended range of values of “j” is 2.1-2.5 for purposes of simulating gas phase mixing characteristics using DBSM mostly from the point of view of the numerical ease of solution of the model equations.



(a)



(b)

Figure 6-23. Effect of the parameter “j” on the DBSM predictions

a) Gas phase recirculation b) Simulated tracer responses

It is interesting to note the non-dependence of the gas recirculation profiles on the parameter “ j ”. This might be surprising at first sight, however due to the lower bound provided by the radial liquid velocity profile and the upper bound provided by the continuity of the gas phase, the computed maximum bubble size (d_{bmax}) adjusts itself to accommodate changes in the parameter “ j ”. This doesn’t lead to identical bubble size distributions, but the resulting differences in the computed sizes and slip velocity at each radial location are insignificant compared to the magnitude of the respective quantities. Once a nearly identical velocity profile is calculated, most of the model parameters are identical also, which subsequently leads to nearly identical gas tracer responses.

This implies that a consistent prescription of the hydrodynamic inputs to the reactor model should result in reasonable predictions, and provides fundamentally based criteria for design and scale-up. It is also clear that mass transfer plays a significant role in governing the soluble gas tracer distribution when one compares the simulation results for $H = 0$, and non-zero H with the experimental response.

6.7. Final Remarks

In this study, a self-consistent hydrodynamic sub-model has been developed from the two-fluid model equations describing two-phase flow in the Euler-Euler framework. The one-dimensional solution of the model equations provides predictions of the levels of liquid and gas recirculation when a suitable closure for turbulence (like the mixing length formulation of Kumar *et al.*, 1994) is used in the model equations. The hydrodynamic sub-model has been integrated into a four-zone (SBCM) and five-zone (DBSM) mechanistic reactor models describing the distribution, generation and consumption of the reactant species. Comparison of the results from the mechanistic models with experimental gas tracer data indicates a reasonable agreement between the two, provided a correct estimate for the solubility of the gaseous component in the liquid (slurry) is available. When radial gas holdup profiles are known or can be estimated reasonably well, the integrated predictive capabilities of the gas-liquid recirculation sub-model and

the mechanistic reactor model do not suffer from the empiricism of the Axial Dispersion Model, and therefore, provide a fundamentally based methodology for design, synthesis, analysis and scale-up of bubble column reactors.

The comparison of the simulation results indicates that in its current prescription, the DBSM does not present significant benefits over the SBCM. The DBSM does have an additional bubble-bubble interaction parameter between the two-bubble classes, which has an effect on the gas-phase tracer responses primarily in the absence of gas-liquid mass transfer, *i.e.*, for non-soluble gases and for no bubble-bubble interactions. Since it is known that the bubbles flow highly interactively in a churn-turbulent bubble column, it is rather unphysical that no bubble interaction should provide better agreement between simulations and data. Krishna (2000^h) and his coworkers have extensively referred to the existence of two bubble classes in churn-turbulent bubble columns. However, as with DBSM, there exist many uncertainties in their model for predicting the parameters for the two bubble classes. In trying to use a more fundamental approach to predicting the parameters of the two-bubble class model, additional assumptions (some of them not based on any theory) had to be made to arrive at the DBSM formulation. This unfortunately does not land much credibility to the two-bubble class model (DBSM). Therefore, the DBSM use in the future should only be sought once a better physical basis for estimating these parameters has been established.

In summary, this study presents the virtues and current limitations of the 1-D momentum-balance based reactor model. The developed model is self-consistent but needs experimental input (gas holdup profile) and does not always accurately predict independent experimental observations. In this regard, the model needs to be further examined and refined once a better understanding of some of the underlying physics is further understood. Upon further model refinement to improve its predictive capabilities, reaction kinetics could be incorporated into the model equations to provide rational tools for scale-up and prediction of reactor performance.

Several opportunities exist for further exploration in the framework of the reactor models and parameter estimation therein. Some of these are presented below:-

- A systematic analysis of the effect of drag formulation and its interaction with the radial gas holdup and mixing length profiles on the computed gas and liquid phase recirculation should establish the identity of suitable drag correlation for scale reactors.
- Starting with the hypothesis of the existence of “large” and “small” bubble phases, separate momentum equations could be derived for each bubble phase. This would introduce additional bubble-phase momentum exchange terms in the balance equations that would need to be independently prescribed. For these purposes, sub-models can be sought from the bubble coalescence and break-up theories (Prince and Blanch, 1990; Luo, 1993).
- Inclusion of the radial momentum balances for the gas and liquid phase may provide methodologies for predicting the radial gas-holdup profile. Some of the closures for these balances can be extracted from experimental data like CARPT, etc. A successful development in this direction would lead to these models becoming truly predictive.

Chapter 7. Gamma-Ray Densitometry and Radioactive Tracer Studies of a Pilot- Scale Fischer-Tropsch Reactor

With the recent trends and emphasis on employing clean alternate fuels for the automotive industry along with an aggressive search for commercially viable technology to convert abundantly available Natural Gas reserves into desirable value-added chemicals via the Synthesis Gas, the Fischer-Tropsch (FT) synthesis, effected in a slurry bubble column reactor, has emerged as one of the most promising alternatives (Wender, 1996; Sie and Krishna, 1999). As a result, development of a slurry-phase FT process has become of considerable interest to the U.S. Department of Energy (DOE) as part of the Indirect Liquefaction program, which in turn is part of the Coal Liquefaction program sponsored by the Federal Energy Technology Center (FETC). The overall objective of the Coal Liquefaction program is to develop economically competitive and environmentally friendly advanced technology to manufacture synthetic liquid fuels from coal (Bhatt, 1999). In addition, the industrial participants in this program have an interest in developing this technology for remote gas conversion.

Towards this goal, the technology for Fischer-Tropsch (FT) synthesis of desirable hydrocarbons from SynGas (a mixture of hydrogen (H_2) and carbon monoxide (CO) gases in a regulated molar ratio) was demonstrated in a pilot-scale slurry bubble-column reactor at the Alternate Fuels Development Unit (AFDU) in La Porte, Texas (Bhatt, 1999). This study, which was a continuation of earlier studies that had established the “proof-of-concept”, was co-sponsored by the U.S. Department of Energy (DOE), Air Products & Chemicals, Inc. (APCI) and Shell Synthetic Fuels, Inc. (SSFI). As mentioned

previously, gas holdup and catalyst distributions, as well as liquid and gas backmixing, are the result as well as the cause of many complex hydrodynamic interactions that occur in a slurry bubble-column operation and provide the key information in reactor design for a given chemistry. Therefore, in addition to providing the much needed pilot-scale data for potential future commercialization of the technology, some additional objectives of the study were to conduct selected experiments in an effort to improve the overall understanding of slurry bubble-column hydrodynamics under reaction conditions. This is the only part of the study that the Chemical Reaction Engineering Laboratory (CREL) was involved with. Towards this effect, gamma-densitometry scans were obtained under actual reaction conditions to non-invasively establish some measure of the radial profiles of gas holdup. In addition, tracer experiments using radioactive liquid, gas and catalyst tracers were conducted to assess the degree of mixing in the three phases respectively. ICI Tracerco, Inc. executed the actual field measurements during these experiments in La Porte.

The Chemical Reaction Engineering Laboratory (CREL) at Washington University in Saint Louis, Missouri has emerged as one of the primary university-partners in the U.S. Department of Energy's endeavor to continually improve the understanding of slurry bubble column hydrodynamics. A research grant (DE FC22-95 95051) via Air Products and Chemicals, Inc has financially supported CREL efforts which include the analysis of pilot scale tracer and densitometry data from the AFDU. Given the experience with handling such data since 1995, it was a natural choice for CREL to be an active participant in the FT-IV tracer and densitometry studies at the AFDU. The reasons for including this chapter in the thesis should be self-evident. This is the first time that rigorous measurements and modeling of slurry bubble column reactor hydrodynamics have been attempted for a reactor in operating mode of FT synthesis.

In the first part of this chapter, results from gamma-densitometry scans are analyzed for reproducibility to assess the reliability of the measured information and suggest improvements for future scanning of pilot-scale reactors at the AFDU. The second half of the chapter provides the analysis of the radioactive tracer data that includes

- A protocol for processing of the tracer data

- Refinement of the liquid-mixing model presented in Chapter 6 to properly account for the slurry exit from the middle portion of the reactor
- Comparison of experimental tracer data with simulation results from gas-liquid mixing models.

7.1. Gamma-Ray Densitometry Studies During FT-IV Runs at the Alternate Fuels Development Unit (AFDU) in La Porte, TX

As mentioned earlier, γ -ray scans were performed during the demonstration runs of the slurry phase Fischer-Tropsch technology at the Alternate Fuels Development Unit (AFDU), La Porte, Texas, to evaluate the technique as a future non-invasive diagnostic for measurement of cross-sectional gas holdup distribution. The following sections provide some theoretical background in analyzing densitometry data. However, the focus is on evaluating the robustness and reliability of the measurement technique, which has been accomplished using statistical analysis of the measured data. Assumptions made in executing the data processing steps have been clearly stated wherever appropriate.

7.1.1. Analysis of Gamma-Scan Data

Prior to the commencement of the study, an experimental matrix of operating conditions was designed such that it would satisfy the requirements of all the involved parties. The *plan* included operating the reactor at essentially three different *inlet* superficial gas velocity conditions (0.41 ft/sec (12.5 cm/s), 0.62 ft/sec (18.9 cm/s) and 0.72 ft/sec (21.9 cm/s)) with varying ratios of hydrogen and carbon monoxide in the fresh feed gas. The operating pressure for all runs was 710 psig (4.99 MPa). Due to operating constraints, the superficial inlet gas velocity conditions finally employed were 0.41 ft/sec (12.5 cm/s), 0.46-0.48 ft/sec (14.0-14.6 cm/s) and 0.60 ft/sec (18.3 cm/s). To assess the distribution of gas volume fraction in a cross-sectional plane somewhere in the middle of the reactor, where the flow is essentially well-developed, Gamma Densitometry Tomographic (GDT) scans were conducted using a single radioactive source (43 mCi

Co⁶⁰) and a 2" NaI (TI) scintillation detector. Since this was the first time that tomography experiments were being carried out at AFDU in an effort to establish it as a non-invasive tool for monitoring phase distributions, the objectives of the study were modest. Therefore, the scans were executed only at one operating condition (Run AF R16.3B) that corresponded to the highest inlet superficial gas velocity employed of 0.6 ft/sec (18.3 cm/s). Other details are provided in Table 7-1.

Table 7-1. Details of the reactor geometry and operating conditions during GDT scans.

Reactor Inside Diameter	22.5 inches (57.15 cm)
Insulation Outside Diameter	28.0 inches (71.12 cm)
Reactor Total Length	28.3 feet (862.58 cm)
Height of Dispersed Slurry	20 feet (609.6 cm)
Slurry Concentration	24-25 wt %
Internals as Heat Exchangers	22 vertical U-tubes of 0.75 inch SCH 80S pipe with an internal header <ul style="list-style-type: none"> • 12 U tubes near the wall • 10 U tubes near the center • Tubes occupy 9.6% of the reactor cross-section
Average Reactor Temperature	502.1 °F (261.2 °C)
Average Reactor Pressure	710.1 psig (4.99 MPa)
Inlet Gas Superficial Velocity	0.6 ft/sec (18.3 cm/s)
Sparger	Proprietary

Figure 7-1 shows the details of the scanning assembly along with the source and detector collimators in a plane along the reactor cross-section. In this scanning configuration, the source and detector are placed diametrically opposite to each other at a fixed axial elevation and move simultaneously from one end to the other of the reactor cross-section to acquire projection measurements along several chords. From these projection measurements, the chordal gas holdup can be obtained using the Beer-Lambert's law for radiation attenuation (Kumar, 1994). It should be noted that the quality

of the projection measurements is critically dependent on the degree of source and detector collimation as well as on the precision in positioning the source and detector with respect to each other. The reader is referred to Kumar (1994) for an in-depth discussion on the sources of error in a γ -ray tomographic scan.

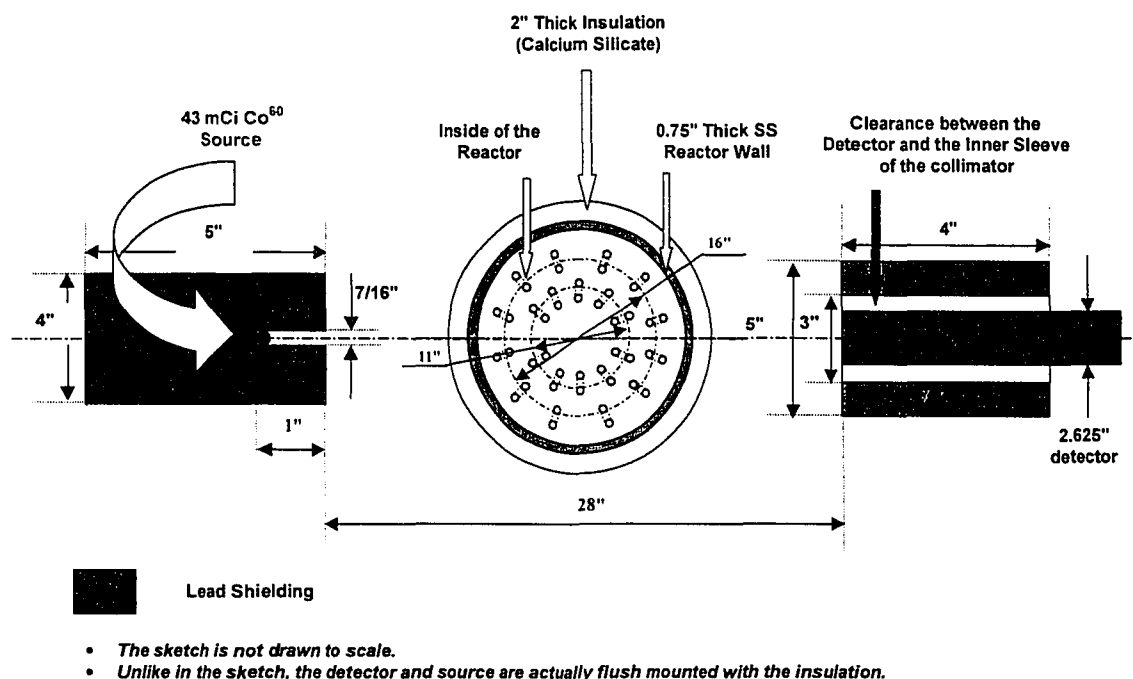


Figure 7-1. Schematic (not to scale) of the reactor cross-section with the collimated source and detector placed on diametrically opposite sides of the column.

Stated concisely, to estimate the chordal average gas holdup from such projection data, the following information is required along each measured chord:

1. Intensity counts (I_{Gas}) with the reactor cross-section filled with just the gas phase (*Base scan in the gas phase*)
2. Intensity counts (I_{Slurry}) with the reactor cross-section filled with just the suspended homogeneous slurry (*Base scan in the slurry phase*)
3. Intensity counts ($I_{Slurry+Gas}$) with the reactor cross-section filled with both the gas and suspended homogeneous slurry under actual operating conditions

From the above three measurements, the chordal average gas holdup can be estimated as:

$$\bar{\varepsilon}_{g, chord} = \frac{\ln\left(\frac{I_{Slurry+Gas}}{I_{Slurry}}\right)}{\ln\left(\frac{I_{Gas}}{I_{Slurry}}\right)} \quad (7-1)$$

Due to practical limitations arising from the flow of SynGas through an empty reactor, the base scans for the gas phase were conducted using Nitrogen flowing through the reactor at ambient conditions instead of the required process gas at operating pressure and temperature. Similarly, the base scans for the suspended homogeneous slurry were substituted for by scans conducted using Durasyn-164 oil at two different temperatures instead of the actual slurry. This oil was used as the liquid phase at start-up when there is no FT wax present in the reactor. Therefore, one needs to correct the radiation intensity counts obtained from the base scans in Nitrogen and Durasyn-164 to get the equivalent base scans in the reactor filled with process gas and reactor filled with slurry, both at the operating conditions at which the three-phase (pseudo two-phase) scans were performed. The procedure for this correction is presented subsequently.

The gamma-densitometry scans were conducted at two angular orientations 90° apart (relative to the reactor cross-section) as shown in Figure 7-2, which also reveals the identities (from -8 to 12 in each direction) of the various chords along which measurements were made. These two scan orientations are referred to as "Section B" and "Section A" in this study to be consistent with the notation provided with the raw data from these experiments. The scans were repeated once for each of the reactor media investigated. Thus, *for each scanning orientation* (Section B and Section A), the following data was collected:

1. Scan 1 and Scan 2 with Nitrogen (at atmospheric condition) as the reactor medium.
2. Scan 1 and Scan 2 with cold Durasyn-164 oil as the reactor medium.
3. Scan 1 and Scan 2 with hot Durasyn-164 oil as the reactor medium.
4. Scan 1 and Scan 2 under the actual operating conditions.

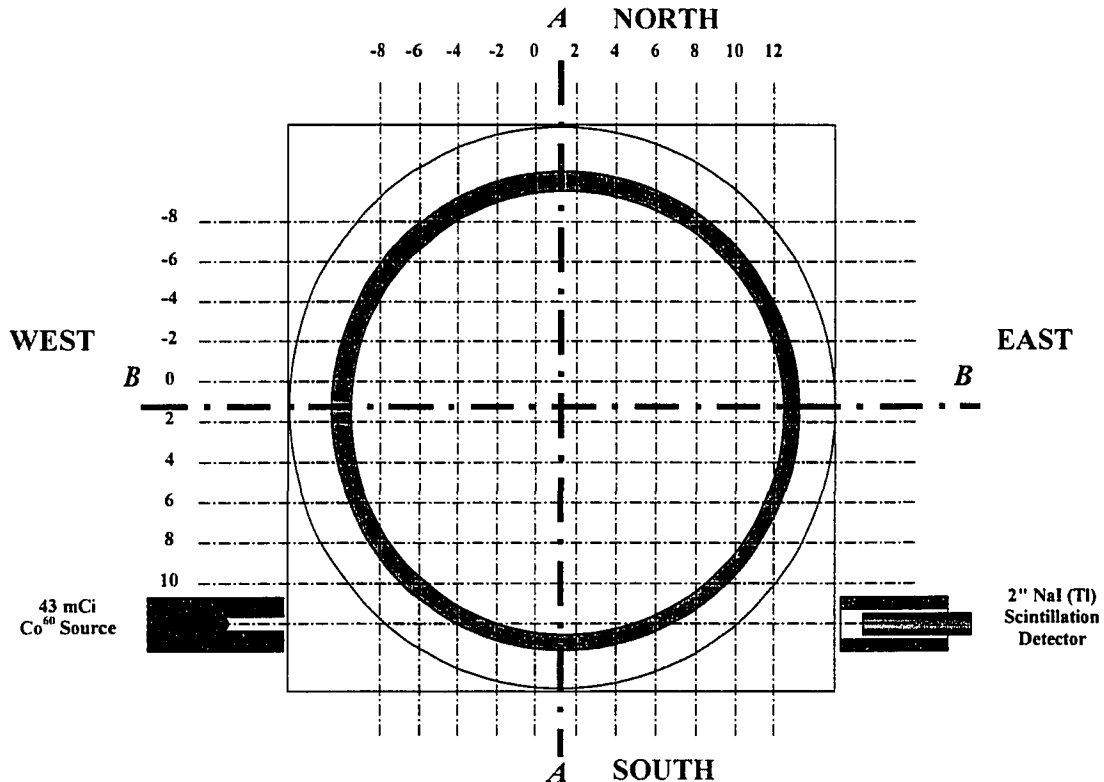


Figure 7-2. Distribution of the chords in the reactor cross-section at which measurements were made along directions A-A and B-B.

For each measurement along a given chord, the source and the detector were manually positioned on diametrically opposite sides of the reactor. However, due to severe space limitations, and given the precision of the mechanical mounting devices for the source and the detector, uncertainties in position and complexities in the analysis of the data collected from these scans were anticipated. Given below is a list of the possible sources of error in the acquired data (in order of their importance).

- Misalignment between the source and detector from one scan to another at a given chord
- Imprecise re-positioning of the source-detector assembly along a given chord from one scan to another
- Presence of numerous (and possibly non-stationary) heat exchanger tubes in the reactor

A brief and illustrative description is provided of a few of the several possibilities of misalignment of the source and detector collimators during gamma scans at the AFDU. From Figure 7-1, one can calculate the maximum offset (calculated to be $\pm 2.7^\circ$ from Equation 7-2) in the orientation of the source-collimator assembly relative to the scanning frame (given that the detector-collimator is perfectly aligned relative to the frame) for the radiation beam to be completely missed by the detector. Since the source strength is large, and no negligible counts are reported for data along any chord, one can say with some certainty that the offset in the angular placement of the source and detector assemblies was less than 2.5° (ICI Tracerco claims the offset to be within $\pm 1^\circ$). However, an angular offset of even a degree or so could cause vastly different attenuation length through the numerous internal heat exchanger tubes. A numerical example is being presented here to illustrate the point in discussion.

$$\theta_{offset} = \tan^{-1}\left(\frac{\pm 2.625/2}{28}\right) = \pm 2.7^\circ \quad (7-2)$$

Let us consider the case of the central chord of the reactor where no internals were present, and let the counts which one would get when the radiation beam is perfectly passing along this central chord be represented by $I_{no\ offset}$. Now, let us consider the case when there was a slight angular offset in the source collimator assembly which caused the radiation beam to pass through several of the internal heat exchanger tubes. Let us denote the length through the internals to be l_{int} , and the counts obtained in this scenario be represented by I_{offset} . Therefore, for the case of the nitrogen scan, the ratio of counts obtained when there is offset to the one when there is no offset is given by Equation 7-3.

$$\frac{I_{offset}}{I_{no\ offset}} = \exp\left\{-l_{int}(\rho_{int}\mu_{int} - \rho_{N_2}\mu_{N_2})\right\} \quad (7-3)$$

The worst case scenario for I_{offset} to be significantly different from $I_{no\ offset}$ would be that this offset causes l_{int} to be equal to several internal HX tube diameters. If we assume that the offset causes the beam to pass through four heat exchanger tubes, then l_{int} would be roughly 3". Using appropriate density and absorptivity values for the internals and nitrogen, one gets from Equation 7-3 the ratio to be 0.72. Thus, a small offset can cause a variability as large as 25-30 %. Additional specific numerical examples can be

analyzed based on geometrical arguments for specific misaligned configurations of the source and detector assemblies. However, the potential for inaccuracies in measurements is immediately evident from this example.

Therefore, in view of the given aforementioned sources of possible errors in the measured data, it becomes necessary to ascertain bounds on the accuracy of these measurements. This has been achieved by several combinatorial evaluations of the experimental data to mimic misalignments resulting from re-positioning of the source detector assemblies. Provided below is a brief description of the analysis of the data from these scans.

7.1.2. Statistical Analysis of the Measured Data

As already mentioned, to get an estimate of the gas holdup along a chord, one measurement is required in the gas phase, one in the slurry phase, and one in the gas-slurry mixture at operating conditions of interest, all executed precisely along the same chord! For a given gas-slurry measurement, the *base* scans in the gas and slurry phases can be chosen from one of the eight (2^3) possible combinations available from the scans in Nitrogen and cold & hot Durasyn-164 as shown in Table 7-2. In other words, for the base scan in the gas phase, one has the choice to either use Scan1 in Nitrogen or use Scan 2 in Nitrogen. Similarly, for the base scan in the slurry phase, one has four choices – Scan 1 or Scan 2 in either hot or cold oil. Therefore, one has a total of eight (two times four) ways in which to choose a set of base scans for the gas and the slurry phases. Then for a projection measurement along a chord under gas-slurry flow conditions, one can employ any of these eight combinations to estimate the chordal average holdup along that particular chord. If the base scan measurements were reproducible; the estimated chordal average gas holdup should be fairly independent of the combination that was used to represent the base scans. Alternatively, if the variation in the estimated chordal average gas holdup (characterized here by two standard deviations implying 95% confidence) is significant, it indicates the poor confidence in the measured data thereby pointing to developmental needs to make this technique reliable.

Table 7-2. Combinations of base scans in gas and liquid employed for statistical study.

Combination Number	Basis for Gas Phase Scan	Basis for Slurry Phase Scan
1	Scan 1 in Nitrogen	Scan 1 in cold Durasyn-164
2	Scan 1 in Nitrogen	Scan 1 in hot Durasyn-164
3	Scan 1 in Nitrogen	Scan 2 in cold Durasyn-164
4	Scan 1 in Nitrogen	Scan 2 in hot Durasyn-164
5	Scan 2 in Nitrogen	Scan 1 in cold Durasyn-164
6	Scan 2 in Nitrogen	Scan 1 in hot Durasyn-164
7	Scan 2 in Nitrogen	Scan 2 in cold Durasyn-164
8	Scan 2 in Nitrogen	Scan 2 in hot Durasyn-164

Therefore, to test for reproducibility, each of these combinations for base scans in Nitrogen and Durasyn-164 was used to estimate the chordal average gas holdup along each chord. In order to estimate this however, the Nitrogen and Durasyn-164 need to be corrected for density so that one obtains the scans representative of the reactor gas and reactor slurry, respectively. The following procedure describes the methodology that was adopted for correction of the base scan data in Nitrogen and Durasyn-164.

- Choose a particular combination (from the possible eight shown in Table 7-2) of the base scans in Nitrogen and in Durasyn-164. A "scan" stands for the intensity counts measured along various chords in one direction (either A-A or B-B).
- For a given chord, let the intensity counts acquired with Nitrogen as the reactor medium be I_{N_2} and those acquired with Durasyn-164 as the reactor medium be $I_{D_{164}}$. Therefore, from Beer-Lambert's law, one has the following relations

$$I_{N_2} = I_0 \exp\left\{-\rho_{ins} \mu_{ins} d_{ins} - \rho_{wall} \mu_{wall} d_{wall} - \rho_{N_2} \mu_{N_2} d_{chord}\right\} \quad (7-4)$$

$$I_{D_{164}} = I_0 \exp\left\{-\rho_{ins} \mu_{ins} d_{ins} - \rho_{wall} \mu_{wall} d_{wall} - \rho_{D_{164}} \mu_{D_{164}} d_{chord}\right\} \quad (7-5)$$

- From Equations (7-4) and (7-5), obtain an estimate of the chord length by Equation (7-6).

$$d_{chord} = \frac{\ln(I_{N_2}/I_{D_{164}})}{(\rho_{D_{164}} \mu_{D_{164}} - \rho_{N_2} \mu_{N_2})} \quad (7-6)$$

- Knowing the chord length from Equation (7-6), use Equations (7-7) and (7-8) to correct for the medium density and estimate the chordal-average counts for the cases when the reactor medium is the process gas and the slurry, respectively at the same operating conditions as the two-phase scan:

$$I_{Gas} = I_{N_2} \exp \left\{ -(\rho_{Gas} \mu_{Gas} - \rho_{N_2} \mu_{N_2}) d_{chord} \right\} \quad (7-7)$$

$$I_{Slurry} = I_{D_{164}} \exp \left\{ -(\rho_{Slurry} \mu_{Slurry} - \rho_{D_{164}} \mu_{D_{164}}) d_{chord} \right\} \quad (7-8)$$

- In Equations (7-4) to (7-5), subscripts "ins" and "wall" refer to the reactor insulation and reactor wall, respectively, μ is the mass attenuation coefficient (cm^2/g) for the specific material under consideration and is estimated by the computational tool (<http://physics.nist.gov/PhysRefData/Xcom/html/xcom1.html>). The estimation procedure requires as input the chemical composition of the material, which is simply the chemical formula in case of pure elements or compounds. For mixtures consisting of more than one compound, the input consists of the chemical formulae of the constituting compounds and elements along with their weight fractions. The mass attenuation coefficients were therefore readily estimated for Nitrogen, Durasyn-164 (assuming its molecular weight to be that of a compound with 80% by weight of C_{30} alkane and 20% by weight of C_{40} alkane) and for the process gas (by evaluating the average chemical composition of the gas in the reactor from the measured inlet and outlet compositions). The mass attenuation coefficient of the slurry was estimated for the Cs^{137} source. However, since a Co^{60} source was employed for the γ -scans, the mass attenuation coefficient of the slurry needs correction to be representative of a Co^{60} source. It was assumed that this correction is given by Equation 7-9 since mass attenuation coefficients are known to depend mainly on photon energy (Tsoulfanidis, 1983).

$$(\mu_{Slurry})_{\text{Co}^{60}} = (\mu_{Slurry})_{\text{Cs}^{137}} \left\{ (\mu_{N_2})_{\text{Co}^{60}} / (\mu_{N_2})_{\text{Cs}^{137}} \right\} \quad (7-9)$$

- All this information was subsequently used for generating the base scans for the process gas and the slurry at the operating conditions of the two-phase scan by Equations (7-7) and (7-8).
- Once I_{Gas} and I_{Slurry} are known for a given chord by the procedure outlined above, the chordal average gas holdup is estimated by Equation (7-1) knowing the

intensity counts registered along the same chord when the reactor medium is a gas-slurry mixture ($I_{Slurry+Gas}$). In this manner, the eight combinations of the base scan data for each chord in both the directions were evaluated against each of the two scans performed under the actual operating conditions to obtain the bounds in the chordal gas holdup estimates.

Figures 7-3 through 7-6 show the range of estimated variations in the chordal average gas holdup from the various combination of the base scans as outlined above. Along each section (B-B and A-A), two scans were acquired under actual process conditions and are referred to as “Online Scan” in the figures. The chord identity (ID) notation is the same as reported along with the original data and the relative placement of the various chords in these two sections have been shown earlier in Figure 7-2. In addition to the chordal averaged gas holdup estimated from the γ -scan measurements at each chord, the dashed lines in the above figures show the chordal averaged gas holdup estimated from the combination of the Differential Pressure (DP) and Nuclear Density Gauge (NDG) measurements. Details of estimating the parameters of the assumed radial gas holdup profile (Equation 7-10) using the DP and NDG measurements are presented later in Section 7.2. Following are the main observations that emerge from these figures:

1. The variations/uncertainties in the chordal averaged holdups estimated from γ -scan measurements are significant. Except for a few central chords, these variations are significantly higher for chords near the walls in Section A-A as compared to those in Section B-B.
2. The expected trend of higher gas holdup in the center of the reactor, as shown by the chordal averaged gas holdups estimated from DP-NDG measurements, is captured by the γ -scan measurements only in Section A-A with the chordal averaged gas holdups from Section B-B being relatively uniform.
3. If results from these two scans are taken at face value, the gas distribution and consequently the flow in the plane of the scans doesn't appear to be axisymmetric which is contrary to most of the evidence from more precise laboratory scale experiments in a similar size vessel (Chen *et al.*, 1998). However, given the

inherent uncertainties in these measurements, any conclusions regarding the asymmetry of long-time averaged gas holdup distribution would be far-fetched.

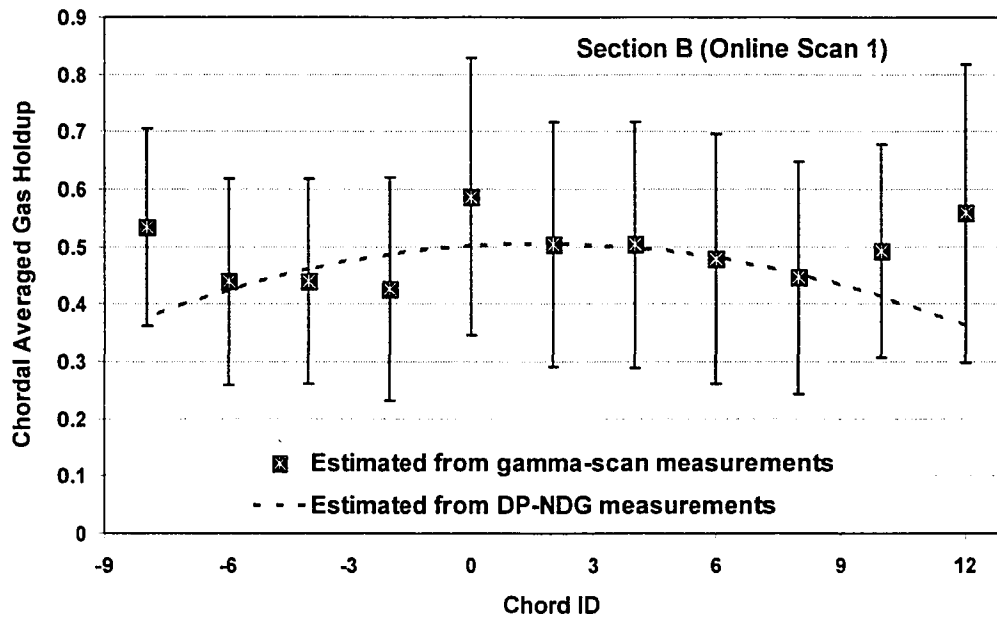


Figure 7-3. Mean chordal averaged gas holdup for Scan 1 along Section B (bounded by two standard deviations).

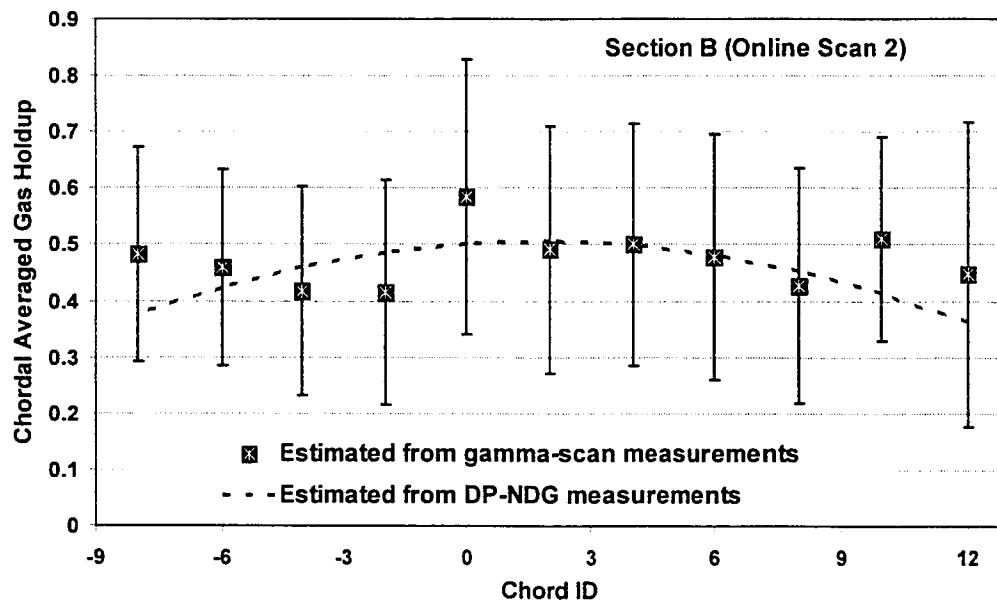


Figure 7-4. Mean chordal averaged gas holdup for Scan 2 along Section B (bounded by two standard deviations).

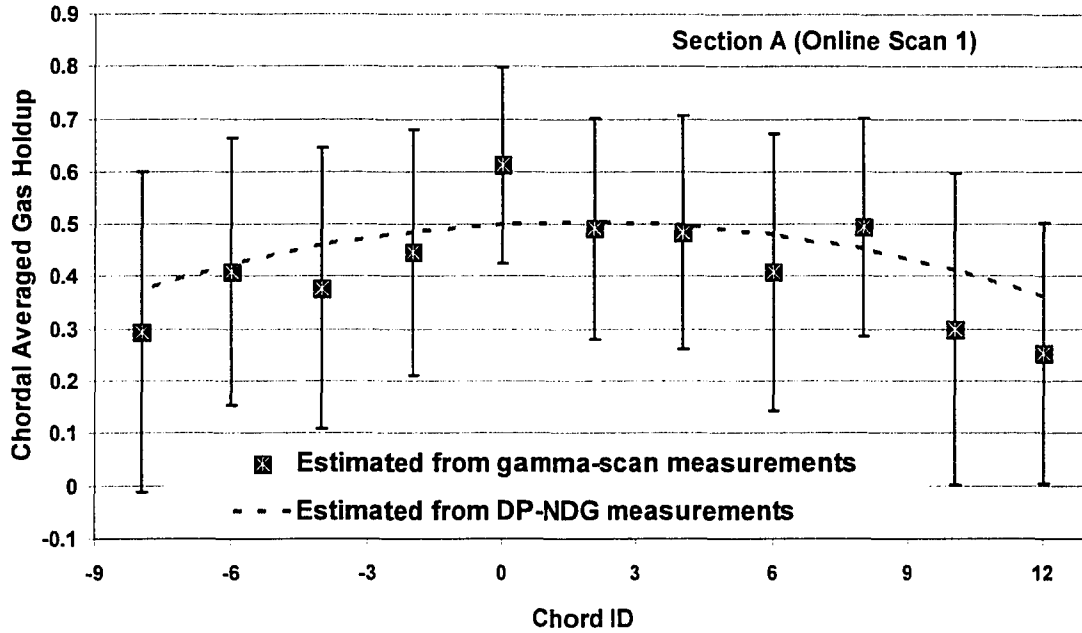


Figure 7-5. Mean chordal averaged gas holdup for Scan 1 along Section A (bounded by two standard deviations).

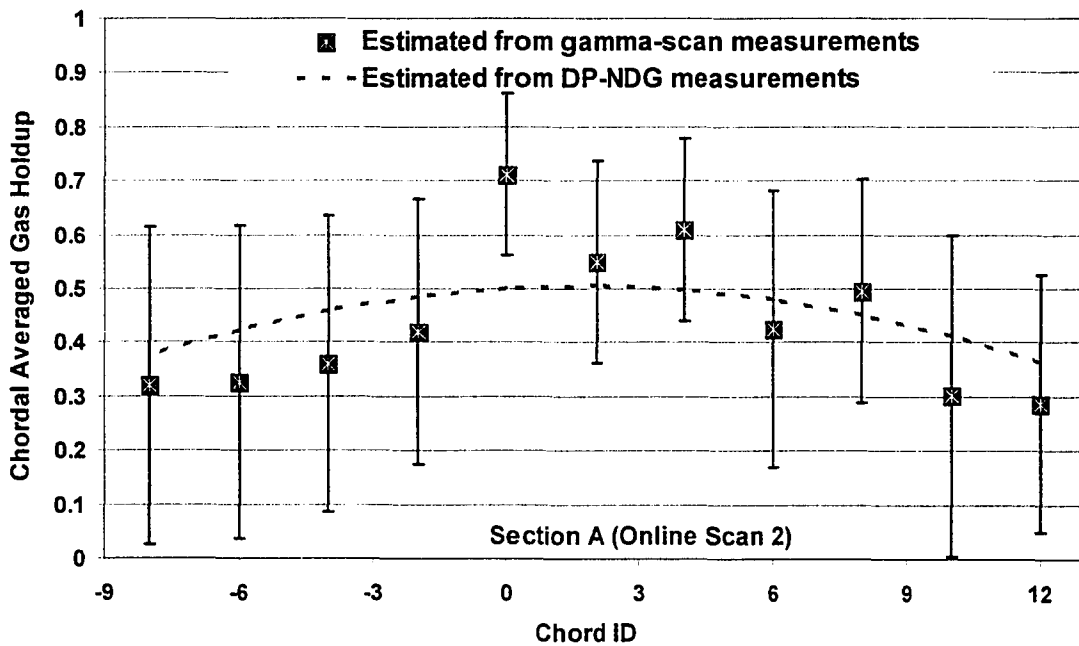


Figure 7-6. Mean chordal averaged gas holdup for Scan 2 along Section A (bounded by two standard deviations).

In view of this analysis, the accuracy and reproducibility of the existing gamma scan technique applied at La Porte appears suspect and no firm conclusions can be drawn regarding the radial gas holdup distribution in the column. Having identified previously the potential sources of errors associated with the current scanning protocol, a few precursory measurements offline become an obvious necessity in order to do better in the future. Presented in the following sub-sections are some suggestions for improving the quality of acquired data from such measurements; and if adherence to a strict protocol is followed based on these suggestions, densitometry measurements hold the potential to become routine for all pilot scale studies at the AFDU.

7.1.3. Suggestions for Improving Data Quality from Future Gamma Scans

To properly execute the densitometry scans on the pilot units at AFDU, the following protocol is recommended and should be followed to improve data quality:

1. Conduct tests on mock-ups of known cross-sections and of known density variations using the same scanning assembly as employed during the previous scans on the La Porte reactor, in order to better understand the effects of source-detector misalignment on the quality of the acquired data.
2. Conduct mockup tests to examine the utility of base scans obtained by using several different fluids and at least two different radioactive sources (Co^{60} , Cs^{137}) and to check the validity of the linear correction schemes (Equations 7-5 to 7-7).
3. Identify axial locations along the reactor where least movement of the internals is expected as the scanning locations. Alternatively, mechanisms to support the tubes inside the reactor could be improved. Currently, the internal heat exchanger U-tubes are mounted on a manifold very near the top of the reactor. At some location in the middle portion of the reactor, they are strapped again. As a result, due to the vigorous flow of the gas and slurry during operation, they sway and move because of the energy of the contacting fluids. Therefore, if locations where the movements are minimal could be identified, the uncertainties resulting from the movement of internal HX tubes could be reduced.
4. Position detector and source with increased accuracy with respect to the reactor.

7.1.4. Suggested Mock Experiments

To estimate the inaccuracies due to source-detector misalignment and re-positioning of the source-detector assembly at a given chord from scan-to-scan, the following experiments are suggested. With the same assembly that was used for the gamma scans at La Porte for FT-IV runs, the following scans should be conducted:

- An empty transparent column (maybe made of Plexiglas) should be scanned several times and the reproducibility in counts checked.
- The same column should then be scanned filled with water. This procedure should also be repeated several times and criterion for reproducibility should be established.
- From these two scans, one should calculate the absorptivity coefficient for water and check it against the theoretical value for the employed radioactive source.
- In the next set of experiments, several repeated scans should be acquired with an empty glass cylinder placed at a known location inside the column filled with water, and the acquired data should be checked for reproducibility in counts. This procedure will enable the assessment of the equipment's ability to measure data capable of capturing the presence of the empty glass cylinder inside the column (which is representative of the internals in the pilot-scale reactors).
- The experiments should also be conducted by performing base scans with fluids other than the one of interest to test the assumptions made in correcting the base scans as done in the current analysis.

In all these scans, one should absolutely ensure that the relative position of the column with respect to the source-detector assembly is never compromised. It is our experience with the tomography setup in our laboratory that even a millimeter or so of misalignment in the column with respect to the scanning assembly causes large variations in the measured gas holdup distributions. In CREL, using a different tomography system, gas holdup profiles are obtained with reproducibility better than $\pm 3\%$ (Kumar 1994).

To summarize, given the accuracy and reproducibility of the existing gamma scan technique applied at AFDU, no firm conclusions could be drawn regarding the radial

holdup distribution in the reactor. Therefore, incorporation of the holdup profile information from these scans in the liquid and gas phase mixing models for prediction of tracer responses cannot be reliably accomplished. However, given the difficult nature of these experiments and numerous constraints due to space and safety, this was a remarkable achievement. It should be evident then that with some dedicated efforts and from the lessons learned during this study, the reliability of the data from this invaluable diagnostic tool could be significantly improved for future pilot scale experiments.

7.2. Radioactive Tracer Studies During FT-IV Runs at the Alternate Fuels Development Unit (AFDU) in La Porte, TX

The second part of the hydrodynamic study at AFDU during FT-IV trial runs was the estimation of backmixing in the gas, liquid and catalyst phases using tracer techniques. Given the hostile operating conditions prevalent in a slurry bubble column reactor, tracing methods using off-the-shelf probes provide little hope. Even if robust probes could be identified, one needs ports to install them at the desired measurement locations. This could be a task that could become very challenging or expensive and is not usually a preferred method. Tracer experiments using radioactive tracers provide a significant advantage in this regard. Being completely non-intrusive, the measurement probes (scintillation detectors) could be positioned at any desired location outside the reactor. The radioactive tracing technique, however, does suffer from the fact that interpretation of the acquired data is not straightforward and requires assumptions about the relationship of the measured signal (radiation counts from the tracer) to the tracer concentration. In standard tracer techniques where there is a linear relationship between the tracer concentration and the tracer property that is actually measured, there is little ambiguity regarding data interpretation. Such, unfortunately, is not the case with radioactive tracer methods because of the complex interactions that a radiation photon undergoes in its sojourn from its source (tracer particles) to its destination (scintillation detectors) as described in Chapter 4. It was shown in Chapter 6 that in the absence of a perfect collimation, the response registered by a scintillation detector is broadened as a result of the counting process and can in principle be modeled if a description of reactor

and collimation geometry as well as distribution of the radioactive tracer is known. This, unfortunately, calls for extensive computing capabilities and is not reasonably simple and realistic to implement. Therefore, as presented in Chapter 6, the simulated normalized responses are compared with equivalent normalized experimental responses.

With the advantages far outweighing the disadvantages, radioactive tracer experiments were conducted at the AFDU, La Porte using gas, liquid and solid radiotracers to assess the degree of backmixing in the three phases. Figure 7-7 shows the schematic representation of the reactor and the array of 2" NaI (Tl) scintillation crystals used for monitoring the temporal tracer distributions at various locations in the reactor. Given the expensive nature of these measurements as well as the time constraints, only two of the three superficial gas velocities were employed for tracer studies. The operating conditions for these two runs (Run 16.6 and Run 16.7) are provided in Table 7-3. The gas tracer was Argon-41 (Ar^{41}) whereas catalyst particles doped with Manganese-56 (Mn^{56}) were used as solid tracer. The "liquid tracer" was a fine powdered oxide of Mn^{56} (Mn_2O_3) suspended in the heat transfer oil, and therefore, was actually a *liquid-like* tracer as opposed to being a true liquid tracer. This tracer was unfortunately employed only for liquid tracer experiments during Run 16.7, since for Run 16.6 a coarser oxide of Mn^{56} (MnO_2) was accidentally used that resulted in tracer plugging in the slurry outlet.

The gas holdup values measured by Nuclear Density Gauge (NDG) and Differential Pressure (DP) also reported in Table 7-3. NDG gives the gas holdup along the central chord of the reactor while DP gives the average (overall or volumetric) gas holdup between the two ports where the differential pressure is measured. For a uniform gas holdup, both of these values are the same. However, when there is a radial distribution of gas holdup with higher holdups in the central region and lower near the reactor walls, gas holdup from NDG is always higher than that measured by DP (Degaleesan, 1997). As mentioned in Chapter 6, a frequently employed radial distribution of gas holdup is given as (Kumar, 1994)

$$\varepsilon_g(\xi) = \bar{\varepsilon}_g \left(\frac{m+2}{m+2-2c} \right) (1 - c\xi^m) \quad (7-10)$$

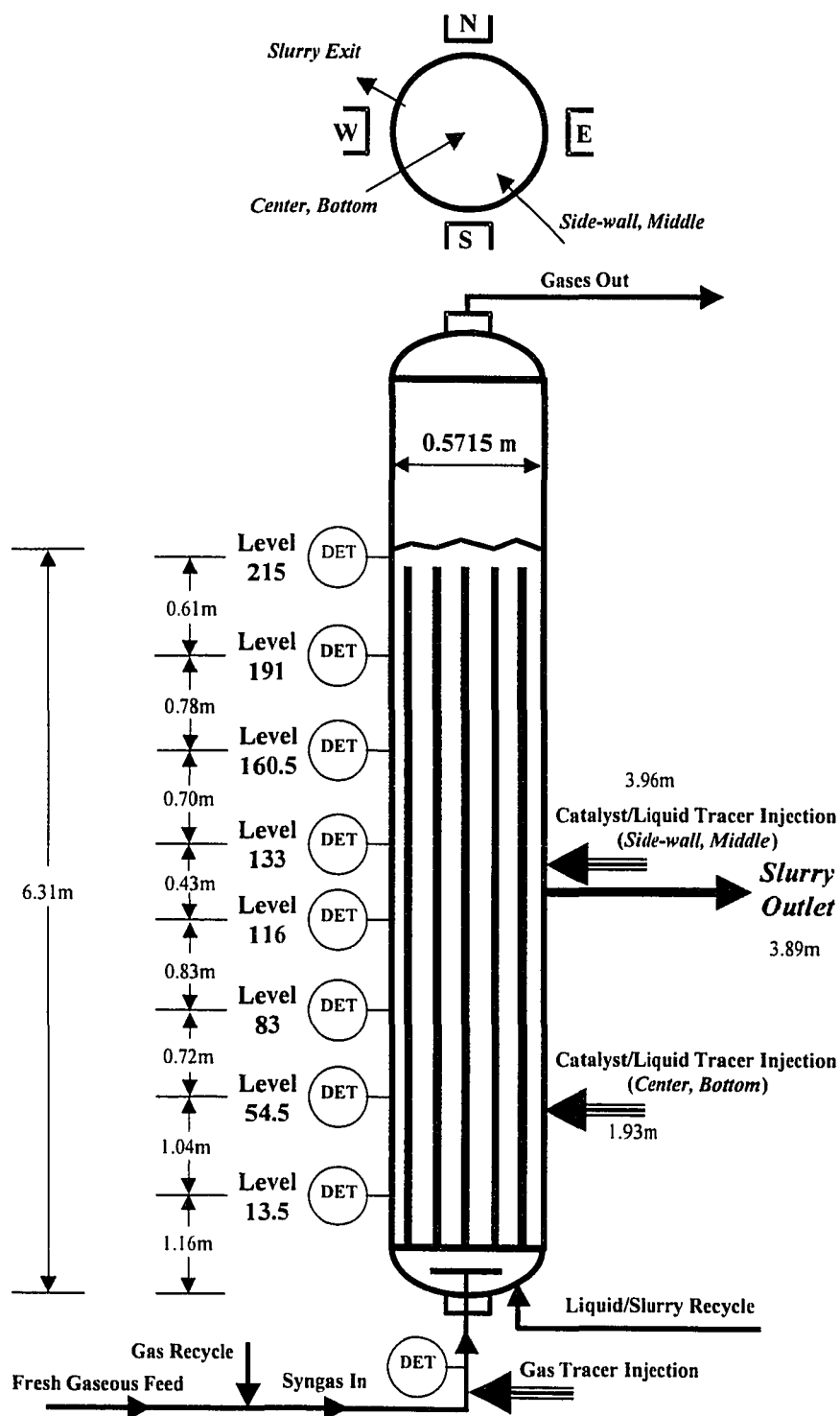


Figure 7-7. Schematic of the slurry bubble column reactor at the AFDU along with the scintillation-detector placement for measuring tracer responses.

In Equation 7-10, $\bar{\varepsilon}_g$ is the cross-sectional average gas holdup, the parameter “c” controls the gas holdup near the wall and can range anywhere from 0 to 1, while parameter “m” can be anything greater than zero. The gas holdup distribution in Equation 7-10 assumes that the long-time averaged gas holdup distribution in the reactor cross-section is axisymmetric. From the results of the densitometry scans presented in Section 7.1, the assumption of axisymmetry of gas holdup cannot be ascertained. However, for a column of 18” diameter and with internal tubes similar to those in the AFDU reactor, CT measurements in CREL established that the distribution of gas holdup was reasonably axisymmetric (Chen *et al.*, 1998). Therefore, in the absence of any better information, the best choice is to assume the validity of the conclusions reached by Chen *et al.* (1998). Consequently, the NDG and DP measured holdups could be related to the gas holdup profile in Equation 7-10 as

$$\bar{\varepsilon}_G|_{DP} = \bar{\varepsilon}_g; \quad \bar{\varepsilon}_G|_{NDG} = \bar{\varepsilon}_G|_{Chord} = \bar{\varepsilon}_g \left(\frac{m+1-c}{m+2-2c} \right) \left(\frac{m+2}{m+1} \right) \quad (7-11)$$

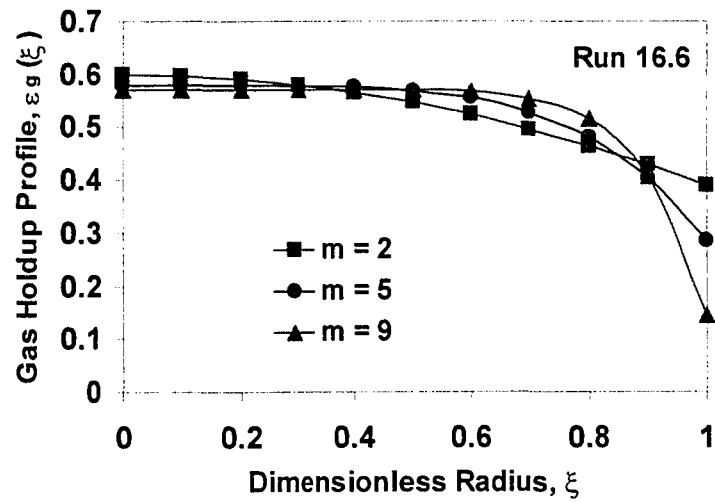
Table 7-3. Reactor operating conditions during tracer tests.

Operating/Measured Parameters	Run 16.6	Run 16.7
Temperature (°K)	532.0	534.2
Pressure (MPa)	4.996	4.997
Inlet Superficial Gas Velocity (cm/s)	12.81	18.23
Outlet Superficial Gas Velocity (cm/s)	9.89	15.21
Average Superficial Gas Velocity (cm/s)	11.35	16.72
Liquid (Slurry) Superficial Velocity (cm/s)	0.727	0.722
Height of Dispersed Media (cm)	631	633
U_{gtrans} (cm/s) – Krishna (2000 ^h)	9.08	9.63
$\bar{\varepsilon}_G$ – Krishna (2000 ^h)	0.437	0.512
$\bar{\varepsilon}_G = \bar{\varepsilon}_G _{DP}$	0.494	0.464
$\bar{\varepsilon}_G _{Chord} = \bar{\varepsilon}_G _{NDG}$	0.529	0.507
m (assumed as suggested by Degaleesan, 1997)	2	2
c, estimated from $\bar{\varepsilon}_G _{Chord}$	0.351	0.435
$\left \frac{d\varepsilon_g}{d\xi} \right $	0.280	0.344

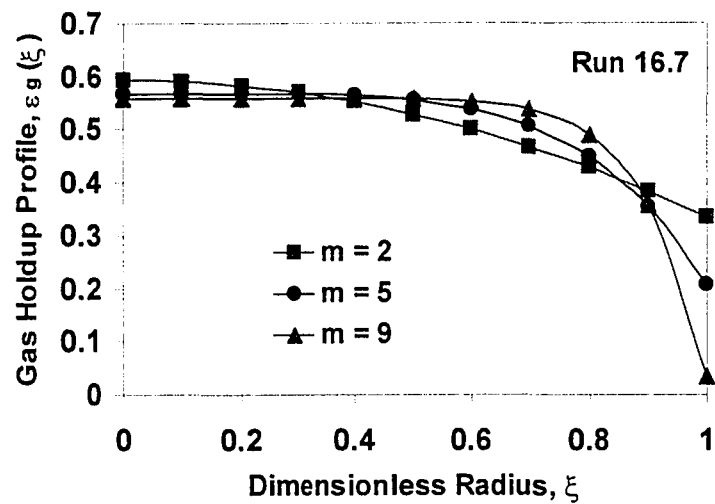
One immediately notes an apparent anomaly that in spite of the operating pressure in Runs 16.6 and 16.7 being the same, Run 16.7, which has a higher gas superficial velocity, recorded a lower gas holdup as compared to that in Run 16.6, which has a lower gas superficial velocity. One cannot suspect inaccuracies in gas holdup measurement since the same trend is recorded by both DP as well as NDG techniques (see Table 7-3). Therefore, the remaining explanation is that the operating conditions of Run 16.6 are close to transition (known to produce a local maximum in the variation of gas holdup with superficial gas velocity), while Run 16.7 is truly churn-turbulent.

Given that three parameters in Equation 7-10 need to be estimated with only two independent measurements (gas holdup from NGD and DP) one is left with no choice but to guess one of them. Degaleesan (1997) suggests to fix “m” as “2” and then use Equation 7-11 to estimate “c”. This reasoning is based on laboratory scale measurements. Therefore, a comparison for various values of “m” on the estimated radial gas holdup profiles is shown in Figure 7-8 for both Runs 16.6 and 16.7. It can be readily seen that “m = 2” provides the most reasonable description of the gas holdup profile as observed from the scans along Section A-A as presented earlier. With increasing “m”, the profiles in the central portion of the reactor become flatter. However, to honor the fixed $\bar{\varepsilon}_g$ and $\bar{\varepsilon}_g|_{Chord}$ obtained experimentally, the gas holdup near the wall becomes increasingly lower and results in steeper gradients in that region. Generally, one thinks of parameter “m” as the primary controller of the gradient of the radial gas holdup profile, with higher values of this parameter resulting in flatter profiles. However, such would be the case only for fixed values of “c” and $\bar{\varepsilon}_g$. To examine the dependence of the cross-sectional mean gradient of the radial gas holdup profile, which is known to be the primary driver for liquid recirculation in bubble columns (Chen *et al.*, 1998) on “m” and “c”, one can derive $\overline{d\varepsilon_g/d\xi}$ using Equation 7-10 as

$$\overline{\frac{d\varepsilon_g}{d\xi}} = -2c\bar{\varepsilon}_g \left(\frac{m}{m+2-2c} \right) \left(\frac{m+2}{m+1} \right) \quad (7-12)$$



(a)



(b)

Figure 7-8. Effect of parameter “m” on the radial gas holdup profile for fixed $\bar{\varepsilon}_g$ and $\bar{\varepsilon}_g|_{Chord}$ a) Run 16.6 b) Run 16.7.

Figure 7-9 shows the effect of the parameter “m” on the cross-sectional mean gradient of the radial gas holdup profile estimated from Equation 7-12. In spite of the profiles being flatter in the central region for higher values of “m”, the overall gradient in the profile increases with “m” which is contrary to the common belief that larger values of “m” result in lower gradients. As mentioned previously, increased holdup gradient

with decreasing values of “m” happens only when the parameter “c” is also fixed which is not the case here. The second interesting result is that in spite of the measured holdups being lower for Run 16.7 (the higher superficial gas velocity condition) as compared to Run 16.6, and irrespective of the value of the parameter “m”, the holdup profile gradient for Run 16.7 is consistently higher than that for Run 16.6. Since it is known that higher superficial gas velocities result in greater liquid recirculation driven by larger gas holdup gradients (Chen *et al.*, 1998), this is in line with such observations.

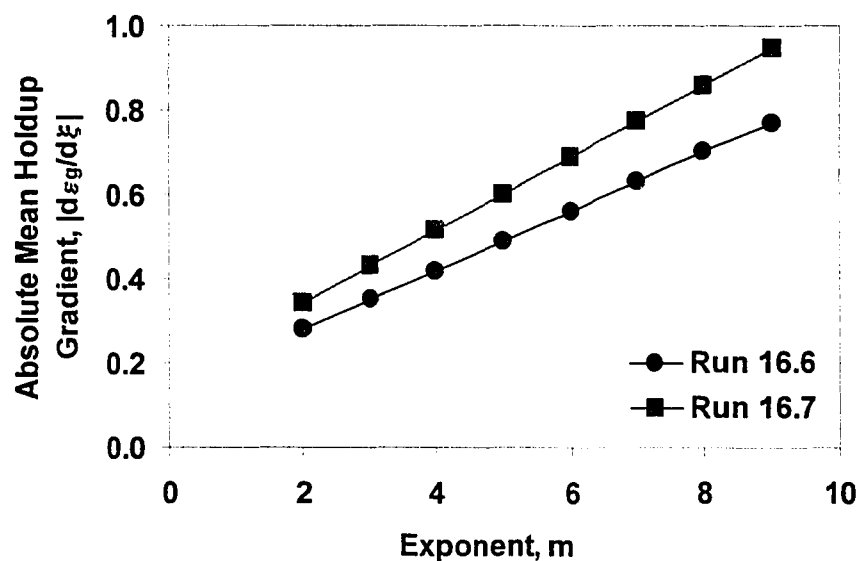


Figure 7-9. Effect of the parameter “m” on the absolute value of the cross-sectional mean gradient of the radial gas holdup profile for fixed $\bar{\epsilon}_g$ and $\bar{\epsilon}_g|_{Chord}$.

Table 7-3 also lists the estimate of the superficial gas velocity at each of the two operating conditions at which transition from bubbly to churn-turbulent flow is assumed to take place. These values have been calculated using the methodology proposed by Krishna (2000^h) as described in Chapter 2. One can see that the superficial gas velocity at the outlet for Run 16.6 is reasonably close to the transition velocity while in Run 16.7 the superficial gas velocity is well above the transition value everywhere in the reactor. Since Run 16.6 is operated close to the transition superficial gas velocity and Run 16.7 well into churn-turbulent flow, this provides the most likely explanation of lower gas holdup

in Run 16.7 than Run 16.6. Since the temperature and pressure conditions during the two runs were nearly identical, one would have expected a very similar transition superficial gas velocity. However, because of the differences in the inlet gas feed concentration, the average molecular weight of the gas is different during the two runs resulting in different gas density and consequently slightly different transition superficial gas velocity. Krishna (2000^h) recommends that transition velocity be actually obtained experimentally by operating the reactor at several different gas superficial velocities. However, this is something that cannot be easily achieved under reaction conditions since variation in gas superficial velocity may not be possible for a stable reactor operation and due to difficulties associated with the measurement of overall gas holdup.

7.2.1. Protocol for Data Processing

The data acquired from radioactive tracer experiments needs to be processed in order to make it suitable for comparison with various flow and mixing models as well as for analysis of flow patterns and mixing in the AFDU reactor during FT synthesis. Since the mixing models are essentially one-dimensional in nature and capture the transient evolution of the tracer responses along the reactor length, it makes sense to average the data from the four detectors in a reactor cross-section at every monitoring plane. However, before that is done, the responses at several axial locations from representative gas and "liquid" tracer tests are examined to address the radial non-uniformity of the tracer distribution. Figure 7-10 shows the detector responses at three different axial levels for the "liquid" tracer test during Run 16.7. Since the tracer is injected slightly below the axial level 54.5 (see Figure 7-7), as marked on the outside tape, using an injection port located southwest in relation to the reactor cross-section, the "South" and "West" detectors located at that axial level record higher intensity counts as compared to the "East" and "North" detectors. However, as one moves away from the injection point, the tracer gets more and more radially mixed and results in uniformity of the counts registered by the four detectors at a given reactor plane. Note however, that the four responses would not become identical since each detector has a slightly different efficiency and therefore responds differently to the same tracer concentration distribution.

Another factor that could result in different intensity counts for detectors having the same efficiencies is the differences in the wall (insulation) thickness and the internal heat exchanger tubes seen by each individual detector, since intensity counts are dependent on the intervening media in a complex manner described in Chapters 4 and 5.

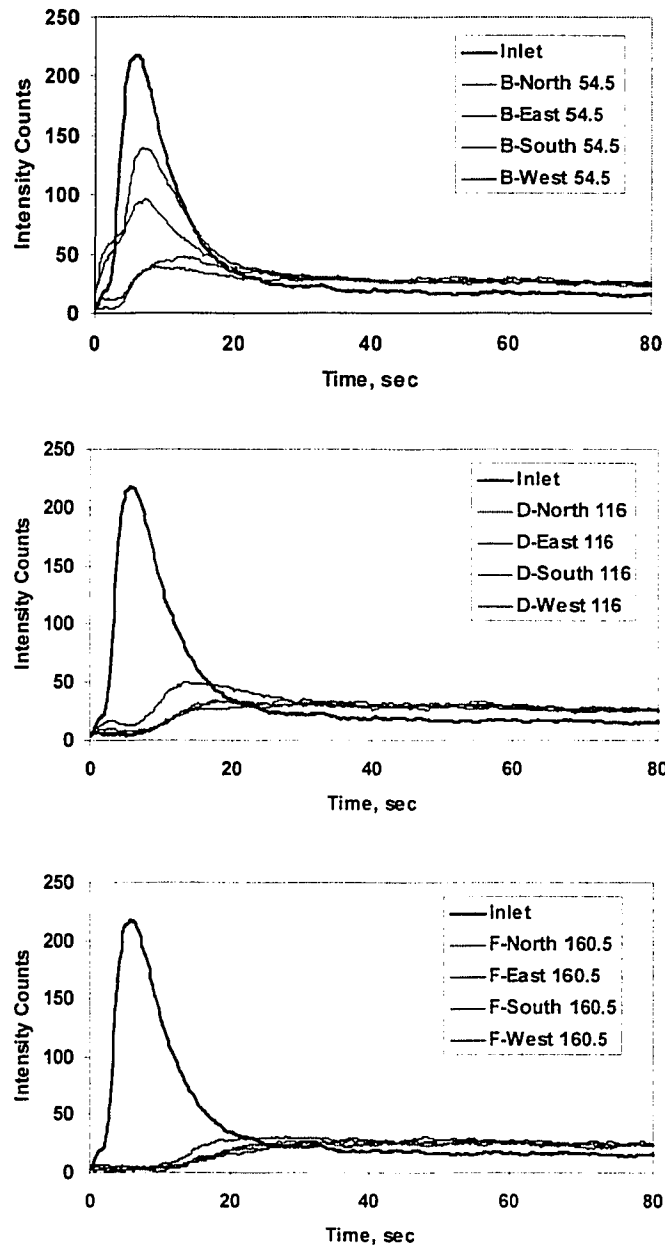


Figure 7-10. Radial mixing of “liquid” Mn_2O_3 tracer for Run 16.7 with tracer injected at the bottom center location.

For the gas tracer responses (see Figure 7-11), the tracer is actually injected before the sparger. As a result of the relatively high pressure-drop across the sparger, the gas tracer gets a chance to get completely mixed before entering the reactor. Therefore, gas tracer responses at a given axial elevation of the reactor are significantly more aligned as compared to “liquid” tracer responses resulting from a point injection of the tracer. The remaining differences are due to variation in detector efficiencies, variation in wall thickness and possibly non-uniform and asymmetric holdup distribution during part of the data record.

Therefore, the assumption of tracer responses being axisymmetric is reasonably good for the gas tracer tests, while the responses resulting from point tracer injection of the liquid/catalyst tracers are significantly asymmetric near the tracer injection point and become more uniform as one moves away from the injection location. However, the mixing models considered in this work are not three-dimensional, and one would require a fully coupled momentum and scalar transport solver to have a chance of capturing the asymmetry in tracer responses. Therefore, the responses at each axial location have been averaged for the purposes of this work. Here we present the various steps involved in pre-processing of the experimental data.

Step 1

The first step in the processing of the data measured in response to tracer injection is to average the responses of the four detectors at a given axial location. The average of the measured intensity counts for each detector is subsequently corrected for the radioactive decay of the tracers (as shown by Equation (7-13)).

$$I_{Corrected} = I_{Measured} \exp(\lambda t) \quad \lambda = \frac{\ln 2}{t_{1/2}} \quad (7-13)$$

The half-lives ($t_{1/2}$) of Ar⁴¹ and Mn⁵⁶ radioisotopes are 1.8223 and 2.5785 hours, respectively (Source: <http://www.dne.bnl.gov/CoN/index.html>).

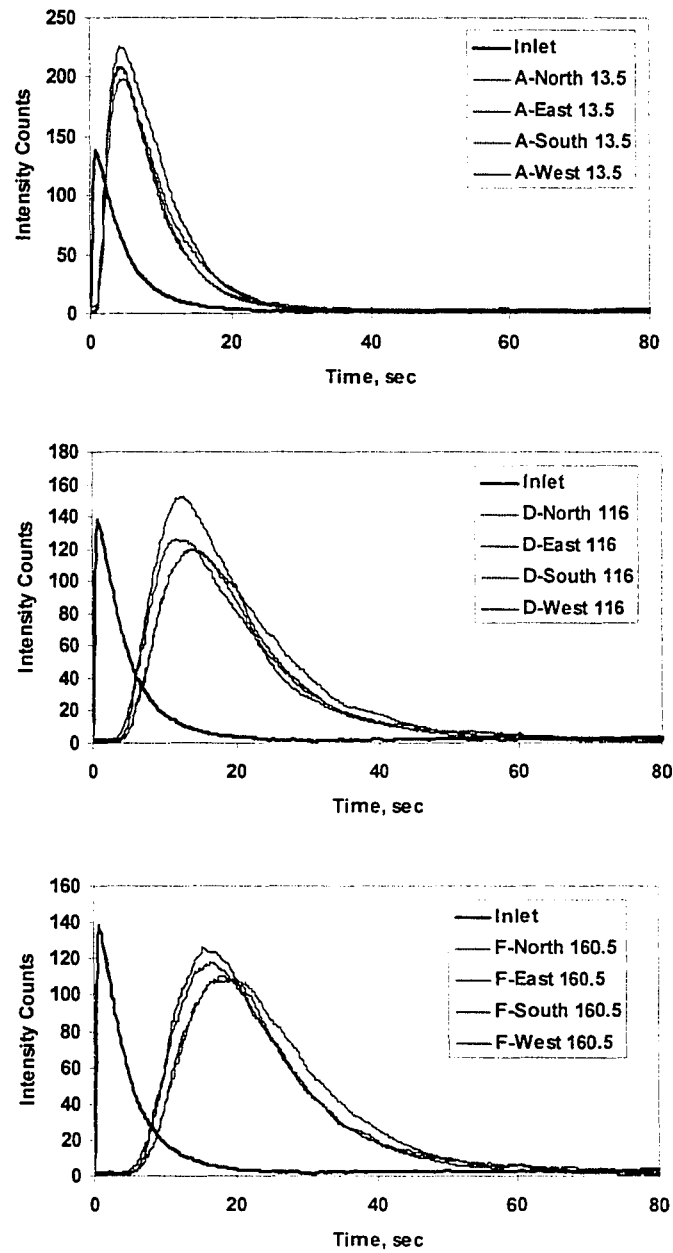


Figure 7-11. Radial mixing of gas tracer for Run 16.7 with tracer injected below the sparger.

Step 2

The next step involves the subtraction of the background counts from the corrected intensity counts obtained from step 1. For the gas tracer experiments, since the

tracer injection vial is sufficiently far from any of the detectors for them to pick-up any spurious radiation, the background count is simply taken as the average of the intensity counts measured prior to the start of tracer injection. This information is available since for all tracer measurements, the data acquisition system is triggered roughly 30-60 seconds before initiating the tracer injection. However, for injections of liquid-like (fine Mn_2O_3 and coarse MnO_2) and catalyst tracers, since some of the detectors are close to the injection vial and can, therefore, pick-up spurious radiation simply due to their proximity to concentrated radioactivity, the background is taken as the minimum counts registered during the entire length of the tracer measurement. This still leaves the spurious pick-up early radiation peak in several detector responses (as shown in Figures 7-14 to 7-17). These spurious peaks can be removed by visual inspection, although a more scientifically based method to accomplish this task may be possible by complete three-dimensional modeling of radiation interaction with the crystal. This is, however, marred by the fact that both the distribution of the radioactive tracer as well as the effective density of the reactor medium between the radioactive tracer source and the detectors are *temporally varying* spatial functions which are unknown, but which are required to accurately implement radiation modeling. Thus, subtraction of pick-up radiation based on visual inspection is a practical solution to this problem.

Step 3

The time series of tracer responses obtained from step 2 can be further processed using simple low-pass Butterworth filters in MatlabTM. This step is particularly crucial if one is to employ the Axial Dispersion Model (ADM) to the measured tracer responses in an effort to extract the effective dispersion coefficient. This is because the ADM tries to fit a tracer response curve to the experimental data by iteratively adjusting the effective dispersion coefficient. Presence of noise in the experimental responses could lead to erroneous results from the optimizer or unusually long computational times during regression. This is not an issue in the current study because the models are completely predictive and nothing is fitted to experimental data. Therefore, this data processing step has not been performed on the tracer responses presented subsequently.

Step 4

Each time series obtained either from step 2 or from step 3, is normalized by the maximum intensity counts in that time-series to obtain the normalized detector responses presented in Figures 7-12 to 7-17. It should be remembered that while comparing these normalized experimental responses with simulation results, the simulated tracer concentration in various portions of the reactor could in principle be related to equivalent scintillation counts via a model for radiation detection as described in Chapter 6.

7.2.2. Reproducibility of the Measured Tracer Data

Figures 7-12 and 7-13 show the tracer responses from repeated gas tracer injections for Runs 16.6 and 16.7, respectively. From these figures one can see that the reproducibility is very good suggesting that it is not necessary to have many repeated gas tracer injections. However, it is advisable that one repeat injection still be done for each operating condition as a check in future gas tracer studies. The reason for good reproducibility is the fact that the gas tracer is injected into the gas feed line prior to the gas sparger. The high pressure drop across the sparger ensures a uniform and reproducible distribution of the tracer in the reactor cross-section at the point of tracer entry into the column, and hence the excellent reproducibility.

For the catalyst and Mn_2O_3 (MnO_2) tracers, however, a point tracer injection is made at the two tracer injection locations shown in Figure 7-7. The flow at these points of tracer entry into the column is continuously changing with time, and therefore, the likelihood of the tracer to encounter the same flow conditions at the instant of tracer injection from repeated tracer injections is small. Therefore, this variable local flow condition at the point of tracer introduction into the system results in a different initial spread of the tracer in the reactor cross-section, and one expects some difference in the recorded tracer responses from repeated tracer injections at the same operating conditions. This is illustrated in Figure 7-14 for Mn_2O_3 tracer injections in the reactor center for Run 16.7. Thus, for point tracer injections, one needs several repeat trials (a minimum of five is recommended) to estimate the ensemble-averaged tracer responses

(refer to Equation (7-14)) for comparison with mixing models which themselves simulate ensemble-averaged quantities.

$$\bar{I}(t)_{Ensemble-Averaged} = \frac{1}{N_{Tracer\ Injections}} \sum_{i=1}^{i=N_{Tracer\ Injections}} I_i(t) \quad (7-14)$$

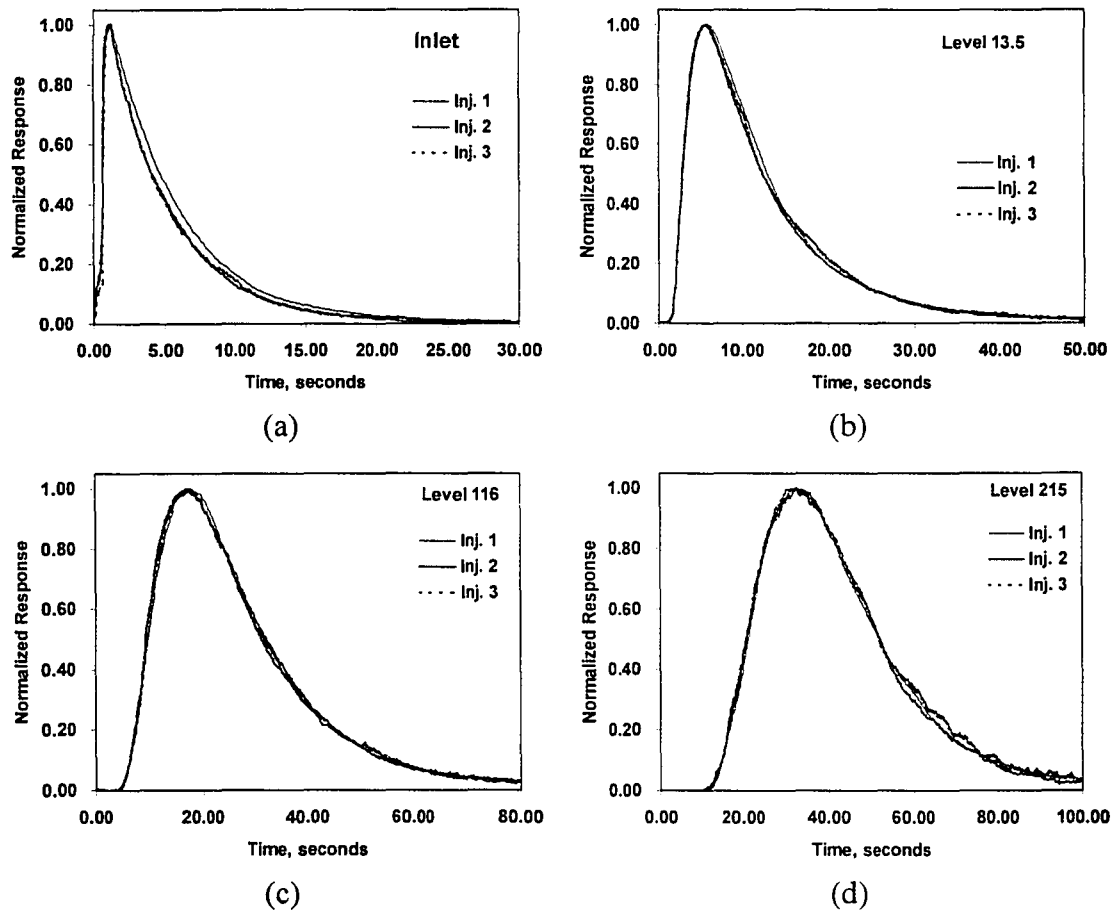


Figure 7-12. Result of repeated gas tracer injections for Run 16.6.

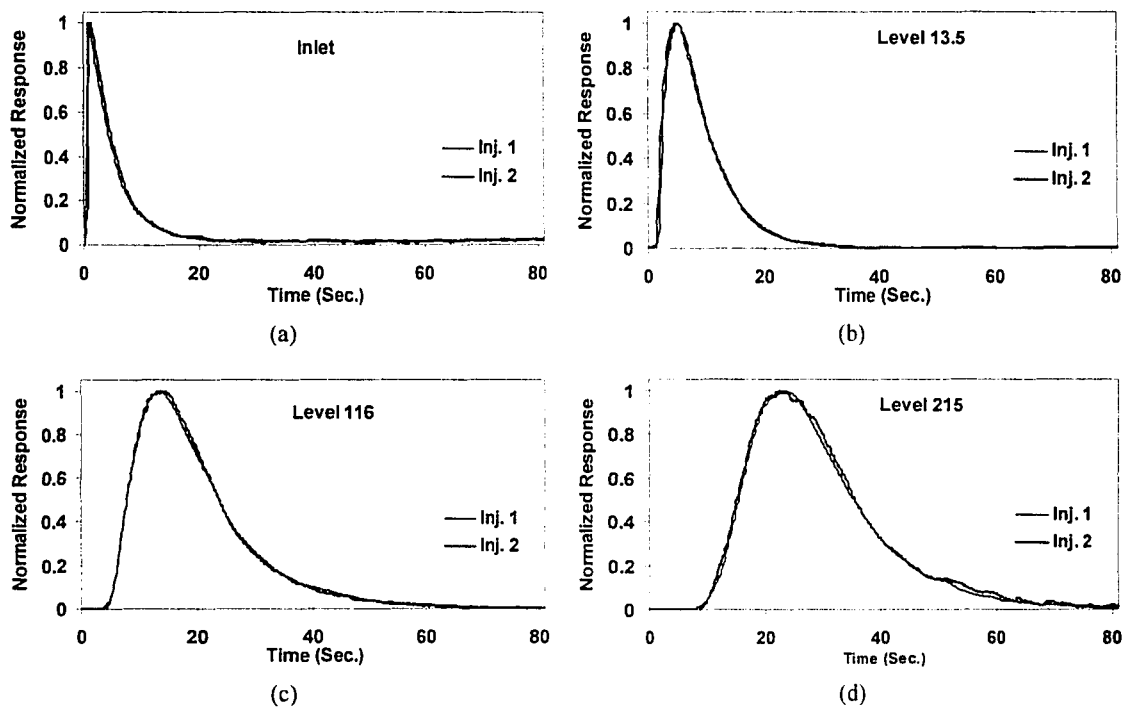


Figure 7-13. Result of repeated gas tracer injections for Run 16.7.

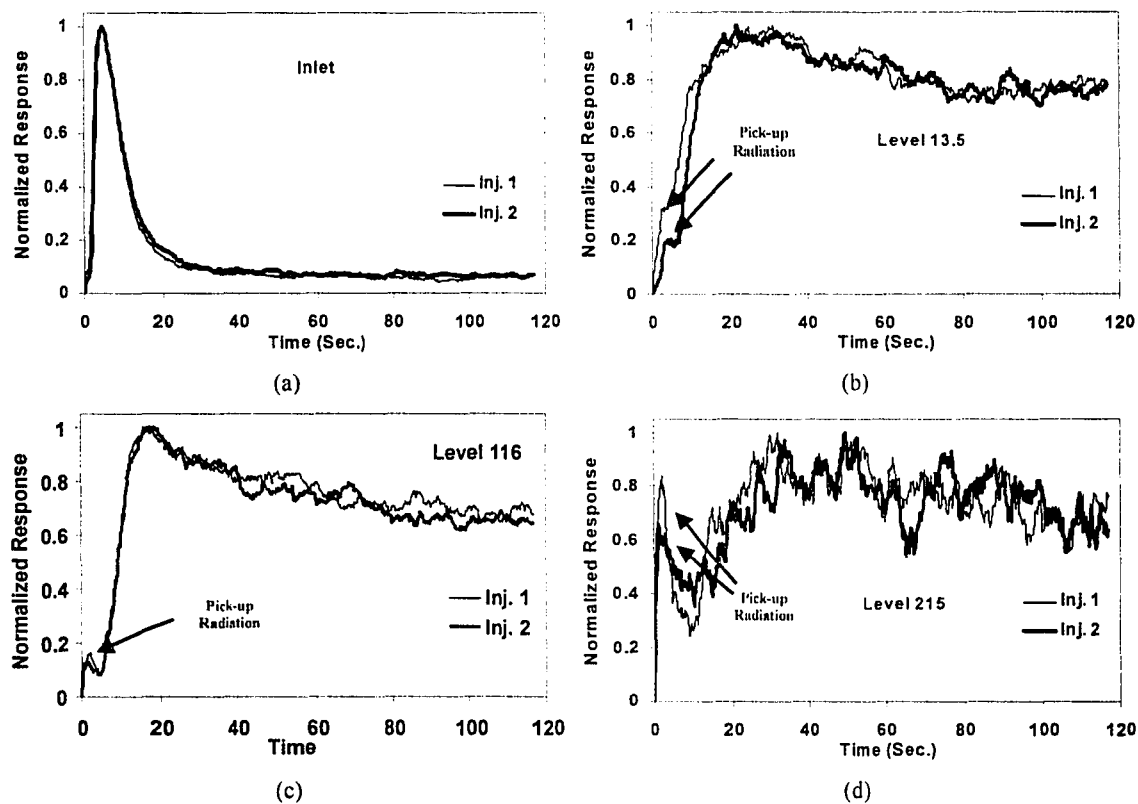


Figure 7-14. Result of repeated Mn_2O_3 tracer injections (Center, Bottom) for Run 16.7.

From Figures 7-14 (b) and (c), it is worth observing that even after 60-80 seconds from the time of tracer injection, the normalized responses have still not become identical. This could be caused by a changing gas holdup structure, which indirectly affects the radiation intensity counts. Alternatively, it could be due to the tracer exiting the flow domain from the slurry outlet (refer to Figure 7-7). Additionally, the response in Figure 7-14 (d) is corrupted by the closeness of the measurement location to the radiation source for the NDG measurements as well as the fluctuating gas-slurry interface.

7.2.3. Comparison between Catalyst and “Liquid” Tracer Responses

Figure 7-15 compares the tracer responses under identical operating conditions obtained in response to fine catalyst and coarse MnO_2 tracers. For conditions of Run 16.6 unfortunately, coarse MnO_2 tracer particles were *accidentally* employed to mimic the liquid phase. However, the large particle size resulted in significant settling of the tracer, and for the sidewall tracer injection, the tracer actually clogged the slurry outlet line as a result of settling. For the center-bottom injection, such a problem was not encountered since the point of tracer injection was significantly away from the slurry outlet. However, one can see from Figure 7-15 that settling of the tracer occurred, and the responses obtained from fine catalyst injection are significantly different from the responses of MnO_2 (coarse particle) injections. Therefore, for comparison with mixing models, this set of data for coarse MnO_2 particles has not been considered.

For tracer experiments under conditions of Run 16.7, which took place on the day following Run 16.6, the *correct* (fine Mn_2O_3) tracer particles were employed to mimic the liquid phase. Comparison of responses (averaged over repeat injections) obtained from catalyst and Mn_2O_3 tracer injections in the sidewall-middle and center-bottom are shown respectively in Figures 7-16 and 7-17. From these figures, one sees that the difference between the catalyst (solid) and Mn_2O_3 (liquid-like) tracer responses, even though clearly present, is within the range of variation in responses from repeated Mn_2O_3 injections as shown in Figure 7-14. This indicates a high probability of a well-suspended catalyst in the liquid medium, and as a first approximation, one is justified in treating the slurry in FT systems as a pseudo-homogeneous phase for modeling purposes.

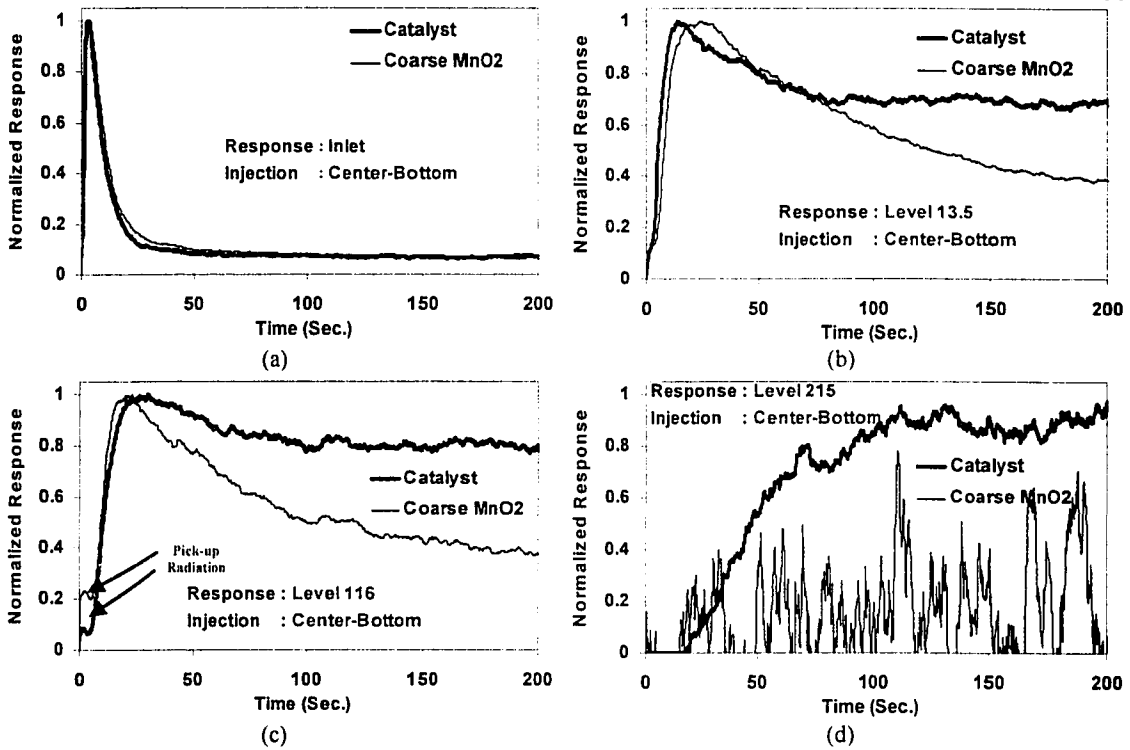


Figure 7-15. Comparison of tracer responses for MnO₂ and catalyst tracer injections (Center, Bottom) for Run 16.6.

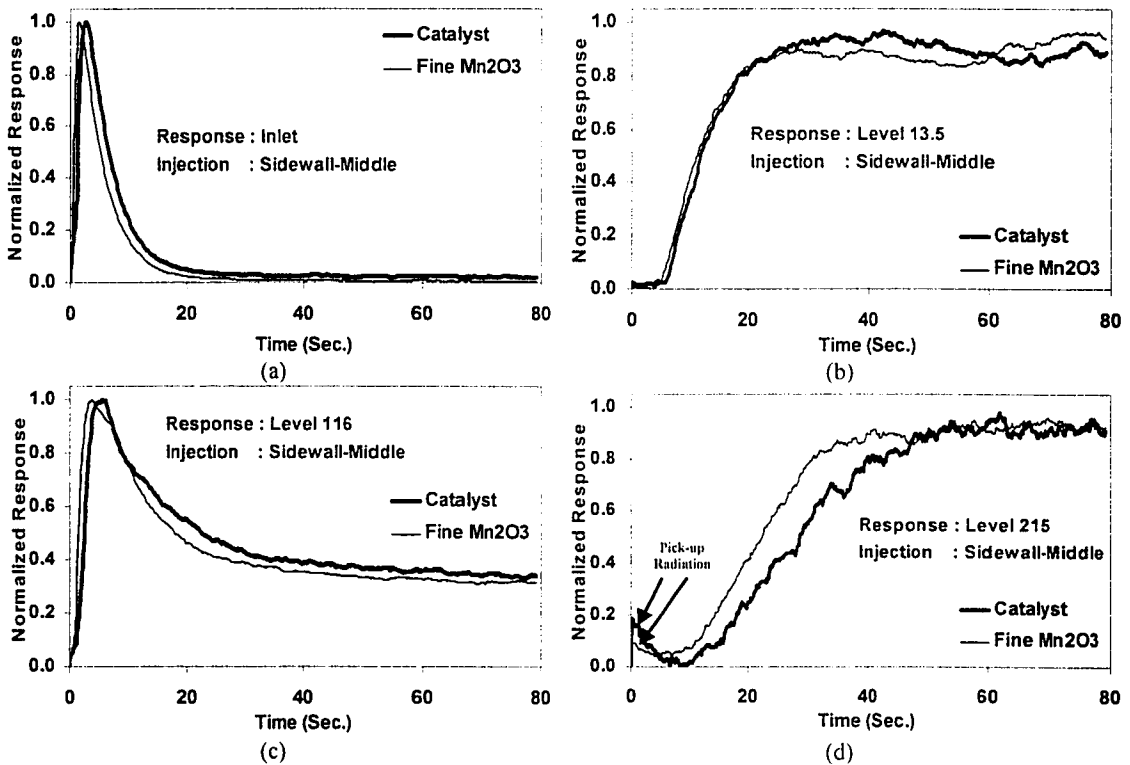


Figure 7-16. Comparison of tracer responses for Mn₂O₃ and catalyst tracer injections (Sidewall, Middle) for Run 16.7.

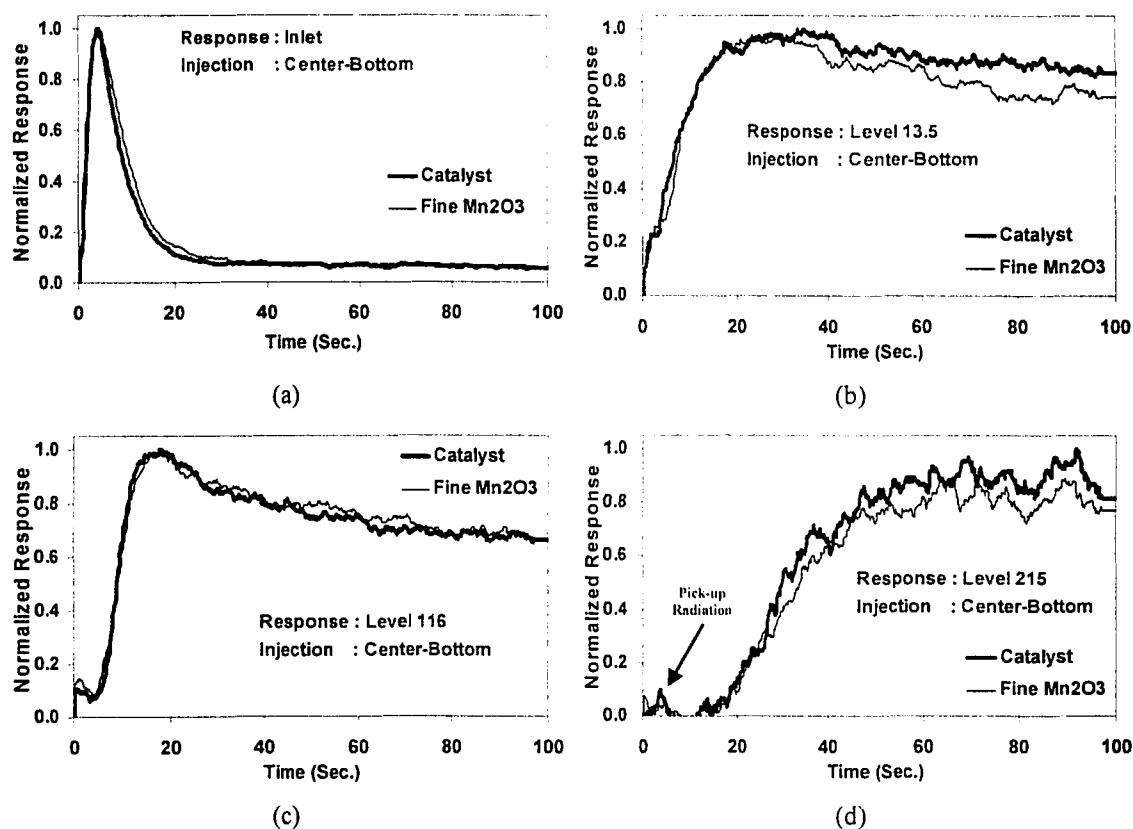


Figure 7-17. Comparison of tracer responses for Mn₂O₃ and catalyst tracer injections (Center, Bottom) for Run 16.7.

7.2.4. Liquid Mixing Model

The radioactive tracer data reported above at the two operating conditions of Table 7-3 has been analyzed using the liquid (slurry) (Degaleesan, 1997) and gas-liquid (slurry) (Gupta *et al.*, 2001^a) mixing and recirculation models developed at CREL. In this chapter, the liquid (slurry) mixing model developed at CREL (Degaleesan, 1997; Gupta *et al.*, 2001^a) is extended to account for the slurry recycle from the middle portion of the reactor. As was discussed in Chapter 6, the above models originally had incorrect boundary conditions which were corrected in the present work (Appendix B). Predictions from the developed model are compared with the Mn₂O₃ “liquid-like” tracer responses for Run 16.7. Since wrong “liquid-like” tracer was employed for Run 16.6, for this run the tracer responses measured using the catalyst tracer are compared with the predictions

from the liquid mixing model. In an earlier study on analysis of tracer data obtained at the AFDU, La Porte during methanol synthesis, the shortcomings of the Axial Dispersion Model (ADM) were discussed (Degaleesan *et al.*, 1996^b). Therefore, the FT-IV tracer data has not been analyzed using the ADM.

As mentioned earlier, Figure 7-7 shows the schematic of the reactor layout with syngas sparged into the bottom of the column where the slurry recycle stream is introduced also. The slurry exits the reactor approximately in the middle portion and flows to a filtration unit where the liquid product is separated from the slurry, which gets recycled back into the reactor. From the responses obtained from the detectors placed at the slurry outlet and at the slurry recycle streams, a lag time of approximately 60 seconds was observed for all tracer injections, which is to be expected since the superficial slurry velocity during the tracer tests was almost identical (0.727 cm/s for Run 16.6 and 0.722 cm/s for Run 16.7). Since the measured liquid and catalyst tracer responses do not appear to reach steady state before 100-120 seconds from the start of tracer injection, one cannot ignore the effect of the slurry recycle, having an approximate recycle-loop residence time of 60 seconds as mentioned above, on the tracer responses simulated using the mechanistic liquid mixing models. To account for the slurry recycle, the mixing model (Degaleesan, 1997) is extended and modified by modeling the slurry recycle loop as a plug flow section with a residence time of 60 seconds. Moreover, it was observed that the experimental response of the product (wax) outlet detector was relatively weak implying that there was insignificant loss of the tracer to the product outlet stream. Therefore, the loss of tracer to the product stream has not been considered in the model by assuming complete recycle of the tracer. Figure 7-18 shows the details of the reactor compartmentalization resulting from the phenomenological picture presented above.

It is to be noted that in the upper portion of the column above the slurry outlet, there is no net flow of the slurry; while in the bottom portion, there exists a net up-flow. Therefore, the reactor model parameters obtained from a sub-model for computing the radial profile of the liquid/slurry axial velocity (Gupta *et al.*, 2001^a), are estimated separately for the upper and lower portions of the column. The reactor compartmentalization sketched in Figure 7-18 results in a coupled system of two ODEs

and two PDEs for the two end CSTs (Continuous Stirred Tanks) and the two well-developed flow zones, respectively. The cell location, at which the slurry exits, patches the different model parameters for the lower and bottom portions of the reactor by mass balance considerations. The tracer concentration in the recycle slurry at the reactor inlet is taken to be the slurry outlet concentration with a time lag of 60 seconds. The resulting set of equations, with appropriate boundary and initial conditions, is solved by a completely implicit finite-difference scheme. Details of the solution procedure and the sub-model equations are presented in Chapter 6. The coupled system of ODEs and PDEs resulting from domain splitting is presented below.

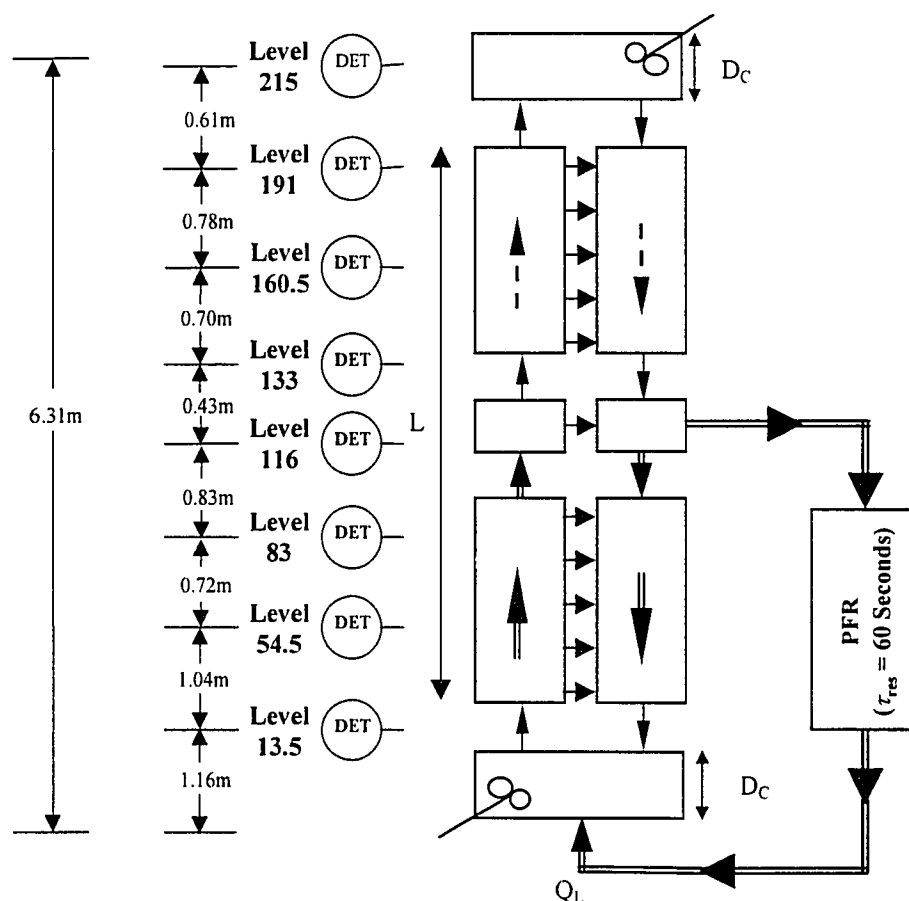


Figure 7-18. Schematic of the model compartmentalization.

7.2.5. Model Equations for Liquid Mixing as a Result of Domain-Splitting

Liquid in the Distributor Zone

$$\frac{dC_{la}}{dt} = \left\{ \begin{array}{l} \frac{U_L}{\bar{\varepsilon}_l \phi_{in} D_C} C_{l,in} - \frac{U_L}{\bar{\varepsilon}_l \phi_{in} D_C} C_{la} \\ + \frac{\bar{\varepsilon}_{l1,BSE}}{\bar{\varepsilon}_l \phi_{in} D_C} \frac{r'_{BSE}{}^2}{R^2} \bar{D}_{xx1} \frac{\partial C_{l1}}{\partial x} \Big|_{x=0} + \frac{\bar{\varepsilon}_{l2,BSE}}{\bar{\varepsilon}_l \phi_{in} D_C} \frac{(R^2 - r'_{BSE}{}^2)}{R^2} \bar{D}_{xx2} \frac{\partial C_{l2}}{\partial x} \Big|_{x=0} \end{array} \right\} \quad (7-15)$$

Fully-Developed Zone of Up-flowing Liquid below Slurry Exit (BSE)

$$\frac{\partial C_{l1}}{\partial t} = \left\{ \bar{D}_{xx1} \frac{\partial^2 C_{l1}}{\partial x^2} - \bar{u}_{l1,BSE} \frac{\partial C_{l1}}{\partial x} - \frac{4(\bar{D}_{rr} \varepsilon_l)_{r=r'_{BSE}}}{r'_{BSE} R \bar{\varepsilon}_{l1,BSE}} (C_{l1} - C_{l2}) \right\} \quad (7-16)$$

Fully-Developed Zone of Down-flowing Liquid below Slurry Exit (BSE)

$$\frac{\partial C_{l2}}{\partial t} = \left\{ \bar{D}_{xx2} \frac{\partial^2 C_{l2}}{\partial x^2} + \bar{u}_{l2,BSE} \frac{\partial C_{l2}}{\partial x} + \frac{4r'_{BSE}/R}{R^2 - r'_{BSE}{}^2} \frac{(\bar{D}_{rr} \varepsilon_l)_{r=r'_{BSE}}}{\bar{\varepsilon}_{l2,BSE}} (C_{l1} - C_{l2}) \right\} \quad (7-17)$$

Fully-Developed Zone of Up-flowing Liquid above Slurry Exit (ASE)

$$\frac{\partial C_{l1}}{\partial t} = \left\{ \bar{D}_{xx1} \frac{\partial^2 C_{l1}}{\partial x^2} - \bar{u}_{l1,ASE} \frac{\partial C_{l1}}{\partial x} - \frac{4(\bar{D}_{rr} \varepsilon_l)_{r=r'_{ASE}}}{r'_{ASE} R \bar{\varepsilon}_{l1,ASE}} (C_{l1} - C_{l2}) \right\} \quad (7-18)$$

Fully-Developed Zone of Down-flowing Liquid above Slurry Exit (ASE)

$$\frac{\partial C_{l2}}{\partial t} = \left\{ \bar{D}_{xx2} \frac{\partial^2 C_{l2}}{\partial x^2} + \bar{u}_{l2,ASE} \frac{\partial C_{l2}}{\partial x} + \frac{4r'_{ASE}/R}{R^2 - r'_{ASE}{}^2} \frac{(\bar{D}_{rr} \varepsilon_l)_{r=r'_{ASE}}}{\bar{\varepsilon}_{l2,ASE}} (C_{l1} - C_{l2}) \right\} \quad (7-19)$$

Liquid in the Disengagement Zone

$$\frac{dC_{lb}}{dt} = \left\{ - \frac{\bar{\varepsilon}_{l1,ASE}}{\bar{\varepsilon}_l \phi_{out} D_C} \frac{r'_{ASE}{}^2}{R^2} \bar{D}_{xx1} \frac{\partial C_{l1}}{\partial x} \Big|_{x=l} - \frac{\bar{\varepsilon}_{l2,ASE}}{\bar{\varepsilon}_l \phi_{out} D_C} \frac{(R^2 - r'_{ASE}{}^2)}{R^2} \bar{D}_{xx2} \frac{\partial C_{l2}}{\partial x} \Big|_{x=l} \right\} \quad (7-20)$$

Initial Conditions

The initial conditions in all zones of the reactor are those of zero initial concentration of the tracer which is introduced at time $t = 0^+$ at the tracer injection point.

$$t = 0; C_{1a} = C_{1b} = C_{11} = C_{12} = 0$$

$$x = x_{inj}, C_{11} = C_{L,inj} \text{ for center injection OR } C_{12} = C_{L,inj} \text{ for sidewall injection} \quad (7-21)$$

For simulating the catalyst and liquid-like tracer responses for the tracer runs at AFDU, La Porte, the experimental *molar input rate* of the tracer has been simulated as a product of a constant (arbitrary) concentration ($C_{L,inj}$) and a volumetric flow rate ($Q_{L,inj}$). This volumetric flow rate of the tracer is time-dependent and is approximated as a Gaussian function with a tail as shown in Equation 7-22 (Degaleesan, 1997). The parameters of this functional form are obtained by curve fitting the experimentally measured input tracer response measured by a scintillation detector placed on the tracer injection port.

$$t \rightarrow 0^+, t > 0; Q_{L,inj} = \frac{\psi}{\sqrt{2\pi\kappa t}} \exp\left\{-\frac{(\delta - \chi)^2}{2\kappa t}\right\} \quad (7-22)$$

Boundary conditions for the fully developed region

As mentioned earlier in Chapter 6, it is tempting to use Danckwerts' boundary conditions at inlet and exit. However, these are not correct in this particular compartmentalization of the reactor as was discussed in Chapter 6. The reader is referred to Appendix B for a comparison of the effect of the boundary conditions on the predicted tracer responses. For the cases considered in this study, the differences between the simulated results from the two boundary conditions are negligible.

The bottom of the fully developed flow zone is the boundary with the CSTR representing the distributor zone, whereas the top of the fully developed flow zone is the boundary with the CSTR representing the disengagement zone. The correct boundary conditions to use are Dirichlet type and are shown below.

Up-flow section of the liquid

$$C_{11} \big|_{x=0} = C_{1a} \quad (7-23)$$

$$C_{12} \big|_{x=0} = C_{1a} \quad (7-24)$$

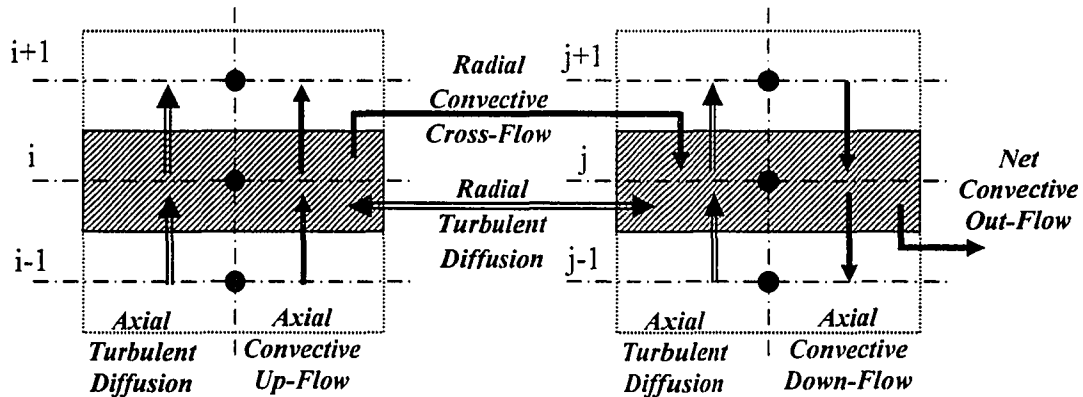
Down-flow section of the liquid

$$C_{11} \Big|_{x=L} = C_{1b} \quad (7-25)$$

$$C_{12} \Big|_{x=L} = C_{1b} \quad (7-26)$$

Numerical Treatment of the Slurry Exit Point

The basis for the mathematical treatment of the slurry exit point is represented in the sketch below, where the index "i" represents the axial slurry exit location in the up-flow region, and "j" that in the down-flow region.



The following equations result from the above representation of the elemental mass balance for the slurry exit node in the up-flow and down-flow regions, respectively. Essentially, the above schematic implies that the difference in the net axial convective plus diffusive flux between the up-flow and the down-flow zones, when subtracted from the net radial flux gives the balance that accounts for the slurry exit concentration and accumulation in the cell representing the slurry exit node.

$$\frac{\partial C_{11,i}}{\partial t} = \left\{ \bar{D}_{xx1} \frac{\partial^2 C_{11}}{\partial x^2} \Big|_i - \frac{\bar{u}_{11,BSE}}{\Delta x} C_{11,i} + \frac{\bar{u}_{11,BSE}}{\Delta x} C_{11,i-1} - \frac{4(\bar{D}_{rr} \varepsilon_1)_{r=r'_{BSE}}}{r'_{BSE} R \bar{E}_{11,BSE}} (C_{11,i} - C_{12,j}) \right\} \quad (7-27)$$

$$\frac{\partial C_{12,j}}{\partial t} = \left\{ \begin{aligned} & \left[\bar{D}_{xx2} \frac{\partial^2 C_{12}}{\partial x^2} \Big|_j + \frac{4r'_{BSE}/R}{R^2 - r'^2_{BSE}} \frac{(\bar{D}_{rr} \varepsilon_l)_{r=r'_{BSE}}}{\bar{\varepsilon}_{12,BSE}} (C_{11,i} - C_{12,j}) \right] \\ & + \frac{\bar{u}_{12,ASE} \bar{\varepsilon}_{12,ASE} (R^2 - r'^2_{ASE})}{\Delta x \bar{\varepsilon}_{12,BSE} (R^2 - r'^2_{BSE})} C_{12,j+1} - \left[\frac{\bar{u}_{12,BSE}}{\Delta x} + \frac{U_L}{\Delta x \bar{\varepsilon}_{12,BSE} (R^2 - r'^2_{BSE})} \right] C_{12,j} \\ & + \frac{(\bar{u}_{11,BSE} \bar{\varepsilon}_{11,BSE} r'^2_{BSE} - \bar{u}_{11,ASE} \bar{\varepsilon}_{11,ASE} r'^2_{ASE})}{\Delta x \bar{\varepsilon}_{12,BSE} (R^2 - r'^2_{BSE})} C_{11,i} \end{aligned} \right\} \quad (7-28)$$

In the above set of Equations (7-15) to (7-28), \bar{D}_{xx} and \bar{D}_{rr} are the average eddy diffusivities from CARPT, which are estimated from a scale-up methodology developed by Degaleesan (1997) (refer to Appendix A).

7.2.6. Comparison of Experimental Liquid/Catalyst Tracer Responses with Simulation Results

Simulations were carried out using the liquid mixing model for the operating conditions of Run 16.6 listed in Table 7-3. Other parameters that were needed to predict liquid and catalyst tracer responses as well as the gas tracer responses presented in Section 7.3 are listed in Table 7-4. As was shown in Chapter 6, since Henry's constant has the greatest effect on the predicted gas tracer responses, a range of values for this parameter was investigated. The sub-model for parameter estimation (Gupta *et al.*, 2001^a) requires as input the radial gas holdup profile, which is given by Equation 7-10. In this equation, the parameter $\bar{\varepsilon}_G$ is the volume averaged mean gas holdup, measured using the Differential Pressure (DP). The parameter “*m*” is the exponent while “*c*” is the parameter that allows for a non-zero holdup at the wall. Earlier in this section, the reasons for fixing the parameter “*m*” as 2 were discussed in view of the suggestions from Degaleesan (1997). Once “*m*” is fixed, “*c*” is readily estimated using the chordal average holdup obtained using Nuclear Density Gauge (NDG) measurements (Equation 7-11). It was pointed out earlier that Table 7-3 reveals a peculiar situation of higher measured average gas holdup ($\bar{\varepsilon}_G|_{DP}$) in Run 16.6, executed at lower superficial gas velocity, than in the

Run 16.7 conducted at higher U_g . Since the pressure and temperature were essentially the same in the two runs, this implies that these conditions are close to transition between bubbly and churn-turbulent flow. In the transition zone, which is known to occur at gas superficial velocities of 3-6 cm/s in water at atmospheric pressure and at much higher gas superficial velocities at elevated pressures, different overall gas holdups are frequently observed and poor reproducibility or multiple holdup values have been reported. This also means that meaningful interpretation of the effect of gas superficial velocity on liquid or gas mixing based on Runs 16.6 and 16.7 is difficult, if not impossible, since the two runs likely did not experience the same flow regime.

Table 7-4. Input parameters for the liquid and gas mixing models.

Input Parameter	Run 16.6	Run 16.7
Radius of the reactor, R_C (cm)	28.6	28.6
Height of Dispersed Media (cm)	631	633
Temperature ($^{\circ}$ K)	532.0	534.2
Pressure (MPa)	5	5
Molecular Weight of Gas (g/mole)	16.99	18.09
ρ_G (gm/cm ³)	0.0192	0.0203
ρ_{SL} (gm/cm ³)	0.795	0.824
μ_{SL} (Poise)	0.025	0.025
σ_{SL} (dyne/cm)	13	13
Inlet Superficial Gas Velocity (cm/s)	12.81	18.23
Outlet Superficial Gas Velocity (cm/s)	9.89	15.21
Average Superficial Gas Velocity (cm/s)	11.35	16.72
Liquid (Slurry) Superficial Velocity (cm/s)	0.727	0.722
$\bar{\epsilon}_G$	0.494	0.464
m	2	2
c	0.351	0.435
$D_{Im, Argon}$ (cm ² /s)	4.41×10^{-5}	4.41×10^{-5}
Henry's Constant, H (ratio of Argon concentration in the liquid to that in the gas at gas-liquid equilibrium)	0, 0.15, 0.248*, 0.35	0, 0.15, 0.245*, 0.35

Table 7-5 lists the parameters computed by the solution of the sub-model equations for predicting liquid recirculation. Since the current model does not handle changing superficial gas velocity due to reaction along the reactor length, a sensitivity analysis of the computed parameters was in order. Thus, for both Run 16.6 and Run 16.7, the model parameters have been computed using the inlet, outlet and average superficial gas velocities. From Table 7-5, one can see that none of the *parameters of the liquid mixing model* are affected by a change in the gas superficial velocity. This is due to the fact that the only parameters affecting liquid recirculation are the radial gas holdup profile and the closure for liquid turbulence. Since both of these are assumed to be independent of the changing superficial gas velocity along the reactor length, the computed liquid recirculation velocities as well as the eddy diffusivities show no dependence on superficial gas velocity given a non-varying gas holdup distribution. In actuality, however, there is a finite variation in the gas holdup along the reactor length that will cause the model parameters to vary from inlet to exit. It should be pointed out though that a change in superficial gas velocity would cause a change in the *parameters of the gas-mixing model*.

Figures 7-19 and 7-20 show the comparison of the simulation results with experimental data for sidewall-middle and center-bottom injections, respectively. One can see from Figure 7-19 that the model predictions for the sidewall-middle injection of the catalyst tracer are distinctly different from the experimental responses. The reason for this significant deviation is the fact that the model assumes a well-developed one-dimensional flow in the region of slurry exit, which obviously is not the case. However, this approximation in modeling the slurry exit is not met when the tracer is injected close to the axial location of the slurry outlet, which happens to be the case with the tracer injected into the reactor sidewall. Therefore, if one observes the comparison of the simulated and experimental responses for the tracer injection into the reactor center-bottom, shown in Figure 7-20, one finds reasonable agreement, especially in the fully developed portion of the flow. In this case, the tracer has sufficient time to mix radially before encountering the slurry outlet stream, and the three-dimensionality of the flow near the slurry outlet does not significantly affect the measured tracer responses.

Table 7-5. Computed model parameters for the liquid mixing model.

Parameter	Run 16.6			Run 16.7		
U_G (cm/s)	12.8	9.89	11.4	18.2	15.2	16.7
<input checked="" type="checkbox"/>	0.494	0.494	0.494	0.464	0.464	0.464
U_{ge} (cm/s)	86.4	86.4	86.4	74.9	74.9	74.9
<input checked="" type="checkbox"/>	0.458	0.458	0.458	0.478	0.478	0.478
<input checked="" type="checkbox"/>	0.564	0.564	0.564	0.607	0.607	0.607
<input checked="" type="checkbox"/>	0.457	0.457	0.457	0.476	0.476	0.476
<input checked="" type="checkbox"/>	0.562	0.562	0.562	0.605	0.605	0.605
<input checked="" type="checkbox"/> (cm/s)	33.6	33.6	33.6	36.2	36.2	36.2
<input checked="" type="checkbox"/> (cm/s)	30.1	30.1	30.1	32.2	32.2	32.2
<input checked="" type="checkbox"/> (cm/s)	33.1	33.1	33.1	35.7	35.7	35.7
<input checked="" type="checkbox"/> (cm/s)	30.7	30.7	30.7	32.8	32.8	32.8
<input checked="" type="checkbox"/>	0.739	0.739	0.739	0.742	0.742	0.742
<input checked="" type="checkbox"/>	0.730	0.730	0.730	0.734	0.734	0.734
<input checked="" type="checkbox"/> (cm ² /s)	624	624	624	601	601	601
<input checked="" type="checkbox"/> (cm ² /s)	606	606	606	573	573	573
<input checked="" type="checkbox"/> (cm ² /s)	604	604	604	585	585	585
<input checked="" type="checkbox"/> (cm ² /s)	624	624	624	590	590	590
<input checked="" type="checkbox"/> (cm ² /s)	153	153	153	146	146	146
<input checked="" type="checkbox"/> (cm ² /s)	60	60	60	55	55	55

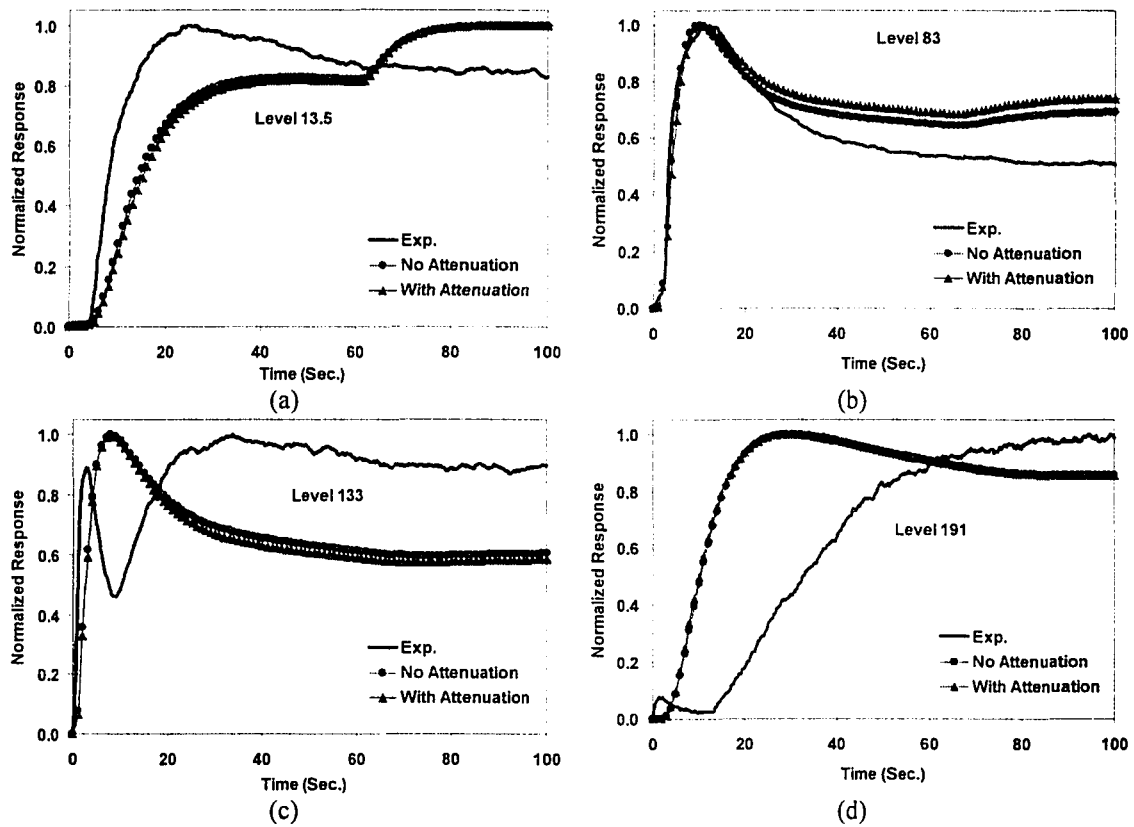


Figure 7-19. Comparison of experimental and simulated tracer responses for Run 16.6 (Tracer: - Catalyst; Injection Pt.: - Sidewall-Middle).

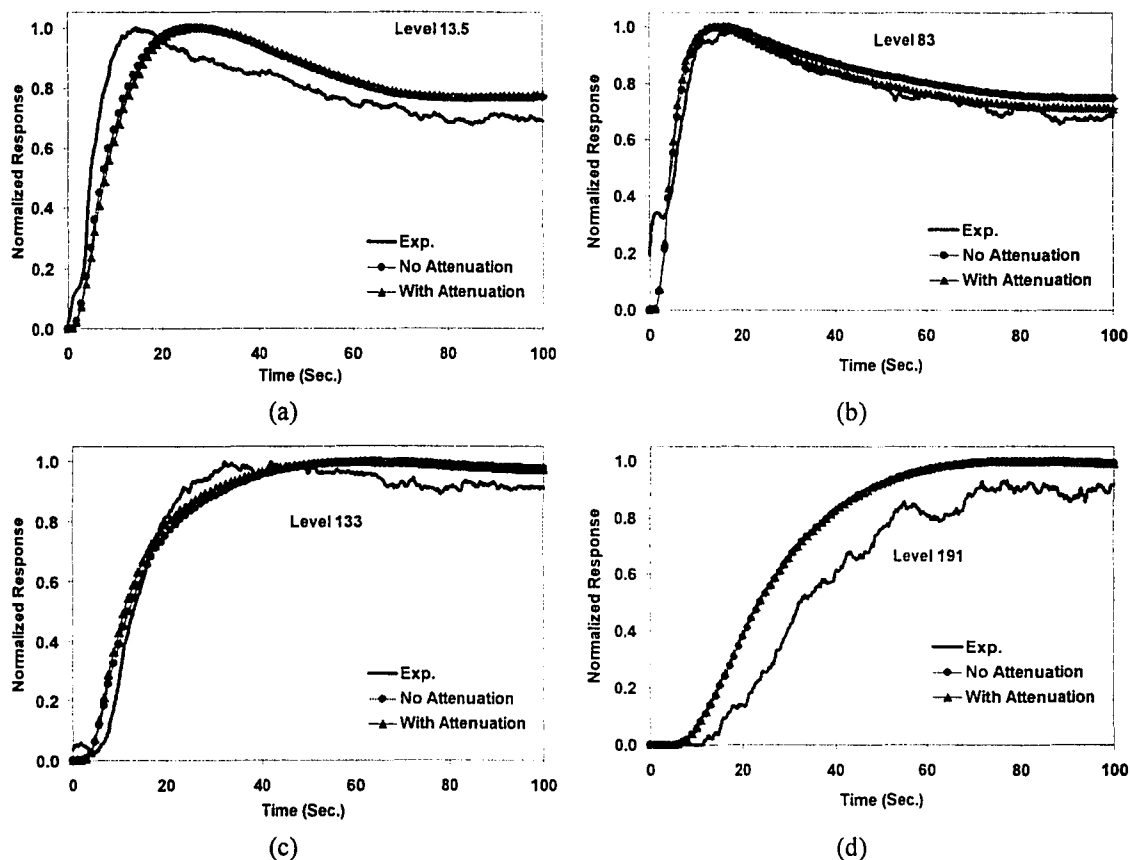


Figure 7-20. Comparison of experimental and simulated tracer responses for Run 16.6 (Tracer: - Catalyst; Injection Pt.: - Center-Bottom).

The comparison of the simulated and experimental results for levels 191 and 215 inches (refer to Appendix C), as referenced on the outside tape, indicates that the simulated tracer responses seem to arrive earlier than the experimental ones. There could be several possibilities which can cause the experimental tracer responses to be detected later at higher column elevations. They are:

1. Existence of a foamy structure at the top of the column, which would prevent the tracer from easily accessing the slurry fluid elements in that zone of the reactor.
2. A significant fluctuation of the gas-slurry interface.
3. Reduction in the superficial gas velocity, U_G , through the upper portion of the column as some amounts of gas leave the column via the slurry exit. This gas is actually re-introduced into the reactor close to the vapor headspace after going

through a gas- slurry separator (degasser). However, this probably results in lowering the superficial gas velocity and consequently the gas holdup in the upper portion of the column. Additionally, the axial and radial eddy diffusivities used in the model simulations are based on a constant (mean) U_G . Therefore, the model parameters could be slightly over-estimated for the upper portion of the column and could explain the earlier arrival of the simulated tracer responses, especially at levels 191 and 215. Unfortunately, there is no readily available information to estimate how much gas bypasses through the degasser.

4. The catalyst tracer particles are more representative of the solids phase while the simulations represent the slurry. There may be some slip between solids and liquid, which could cause the measured responses to rise slower than predicted liquid (“slurry”) response of solids tracer.

This model has been further employed to simulate the tracer responses for Run 16.7 for both the liquid-like (fine Mn_2O_3 powder in heat transfer oil) and catalyst tracers. These results are presented next along with the comparison of the model simulations with experimentally obtained responses. Figures 7-21 and 7-22 show the comparison of the simulation results with experimental data for sidewall-middle and center-bottom injections, respectively, for the catalyst tracer. This comparison reveals that the dominant time constant is captured rather well by the model at all axial detector locations. The agreement between model predictions and data is somewhat better for the center-bottom injection (Figure 7-22) than for sidewall-middle injection (Figure 7-21) since for the former the assumptions of the model are better satisfied (more liquid radial and azimuthal mixing at the location of tracer injection). It should be recalled that this model treats the slurry as a pseudo-homogeneous mixture so that the response of the catalyst tracer is modeled as the liquid (slurry) response.

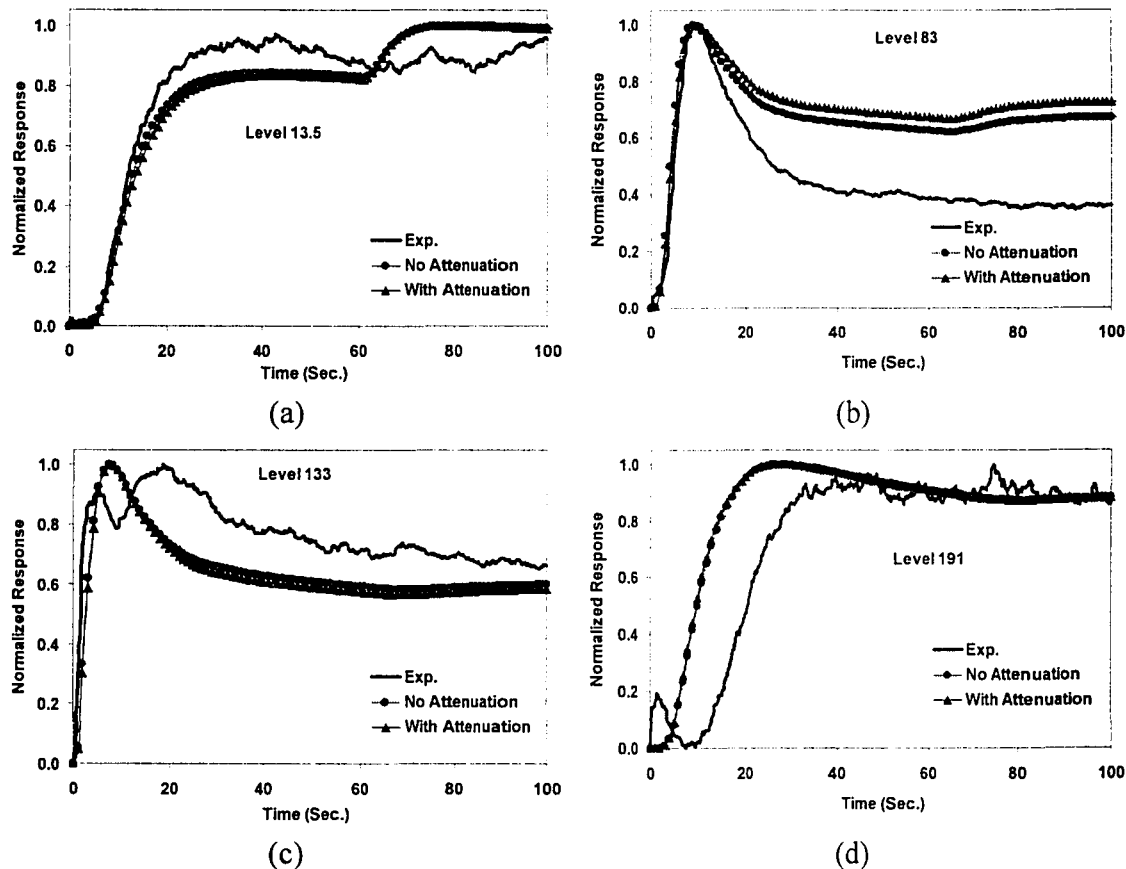


Figure 7-21. Comparison of experimental and simulated tracer responses for Run 16.7 (Tracer: - Catalyst; Injection Pt.: - Sidewall-Middle).

Figures 7-23 and 7-24 show the comparison of the model predictions for the slurry response (same as in Figures 7-21 and 7-22) and the experimental data for the fine Mn_2O_3 tracer that should be fully capable of following the liquid. In general the agreement between data and predictions is even better. One can also see from Figures 7-21 and 7-23 that the model predictions for the sidewall-middle injection, both for the catalyst as well as of Mn_2O_3 tracer, are in fair agreement with the experimental responses as far as the overall mixing time are concerned. This is especially true for the levels 54.5, 83, 116, 133, and 160.5 inches with reference to zero on the outside tape. It should be recalled that this was not the case for the tracer responses obtained for sidewall injections under conditions of Run 16.6. It seems that the higher superficial gas velocity employed during Run 16.7 results in better radial mixing of the tracer even for the sidewall-middle

injection, thus satisfying better the model assumptions. However, even though the agreement is better than for Run 16.6, the proximity of the tracer injection point to the slurry outlet still cannot be completely captured by the employed model. *Consequently, this tracer injection point is not recommended for any future studies with net slurry recycle from the middle portion of the reactor.*

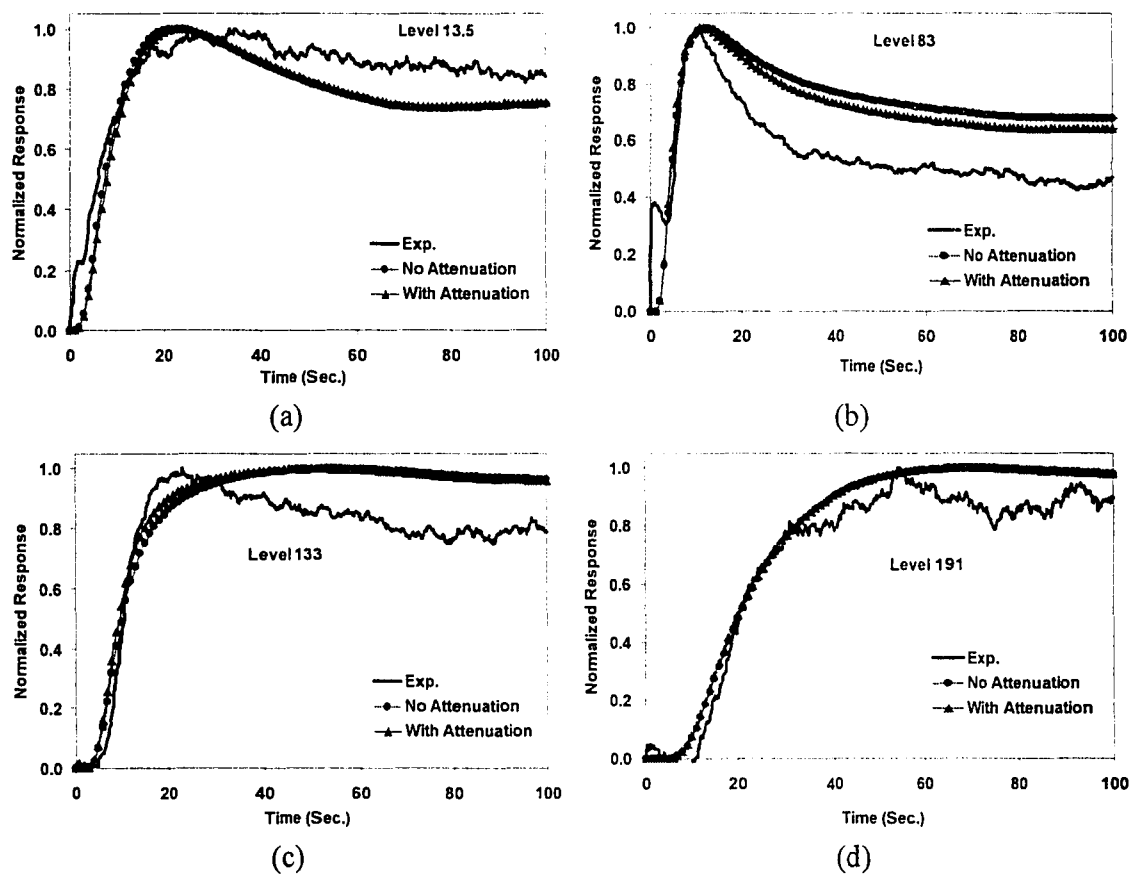


Figure 7-22. Comparison of experimental and simulated tracer responses for Run 16.7 (Tracer: - Catalyst; Injection Pt.: - Center-Bottom).

When one examines the comparison of the simulated tracer responses and experimental ones for the center-bottom injection (both for the catalyst as well as for the Mn_2O_3 fine tracer), one finds better agreement between data and model predictions as compared to the results for the sidewall-middle injection. This is not surprising since for the center-bottom injection, the tracer has sufficiently longer time to disperse radially

before encountering the slurry exit as compared to the sidewall-middle injection. Additionally, the radial mixing for Run 16.7 is enhanced as compared to Run 16.6 due to a higher superficial gas velocity. While comparing the tracer responses with simulation results for the catalyst and fine Mn_2O_3 particles, one finds that the Mn_2O_3 particles seem to trace the liquid better, and consequently, one observes better agreement of Mn_2O_3 responses with simulation results as compared to catalyst responses.

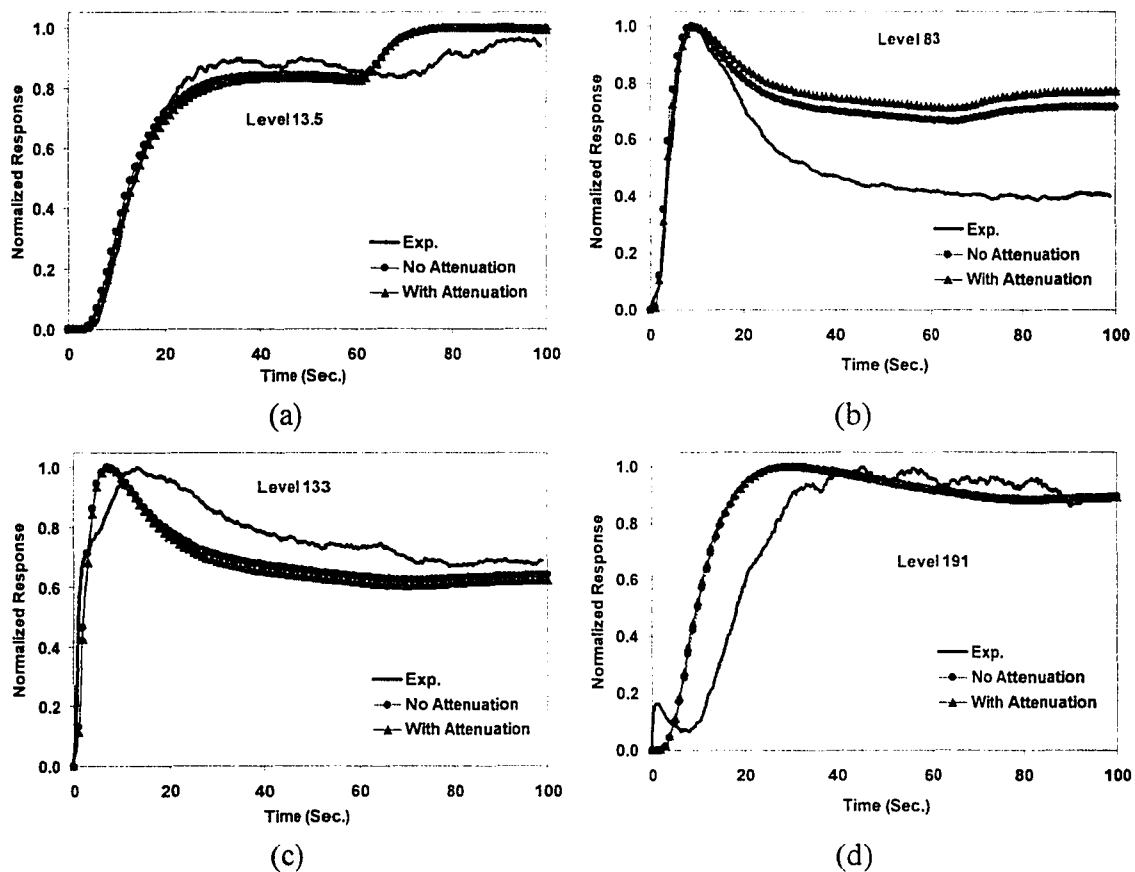


Figure 7-23. Comparison of experimental and simulated tracer responses for Run 16.7 (Tracer: - Mn_2O_3 ; Injection Pt.: - Sidewall-Middle).

As was observed for Run 16.6, again the comparison of the simulated responses and experimental data for levels of 191 and 215 inches (see Appendix C), as referenced on the outside tape, indicates that the simulated tracer responses arrive earlier than the

experimental ones. As mentioned before, these discrepancies between the simulated and measured responses for the top portion of the reactor could result from existence of a foamy structure near the gas-liquid interface and/or from a lower effective superficial gas velocity through the upper portion of the column due to some gas bypassing via the slurry outlet line.

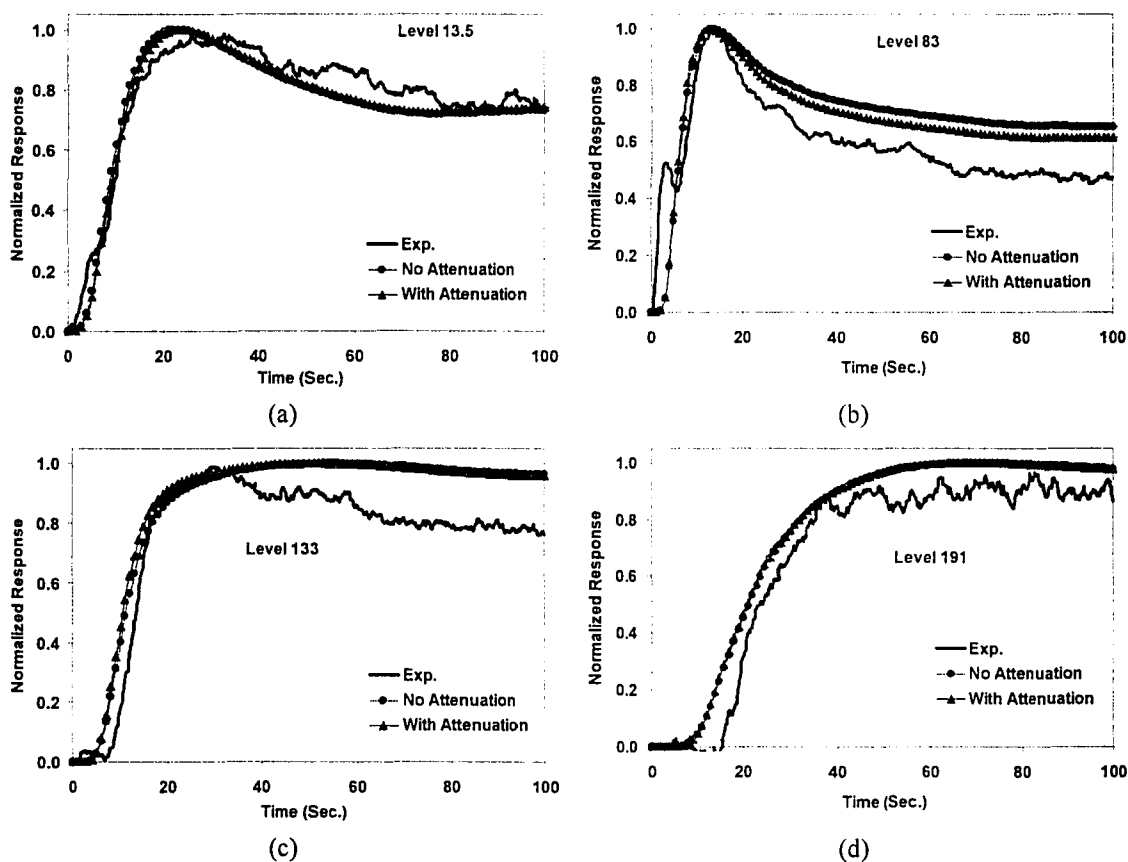


Figure 7-24. Comparison of experimental and simulated tracer responses for Run 16.7 (Tracer: - Mn_2O_3 ; Injection Pt.: - Center-Bottom).

In addition, the experimentally measured response at Level 133 in Figure 7-22 and 7-24 show a loss of tracer as this is very close to the location of the slurry exit. It is also possible that around the slurry exit location there are internals/flanges that obstruct the field of view of detectors at that level and result in a lower count-rate. However, if this were the case, then the count-rate would be lower at all times and would not explain

the observed trend. Thus, the observed trend is most likely the result of a preferential loss of tracer.

For all the simulation results in Figure 7-19 to 7-22 above, the radial eddy diffusion coefficients used to model cross mixing between the up-flow and down-flow liquid zones were estimated based on the scale-up procedure of Degaleesan (1997) as presented in Appendix A. Following her methodology, the estimated radial eddy diffusivities were further scaled down to account for the presence of the internal heat exchanger tubes. Unfortunately, since details on evaluating the shape of the scaled-down radial profile of the D_{rr} due to the presence of internals are not clearly spelled out in the protocol suggested by Degaleesan (1997), a visual approximation of the shape of her profile was used in this study.

In addition to the comparison of the simulated responses with the experimental ones, the above figures also show the comparison of the simulated responses with and without accounting for radiation attenuation by the Beer-Lambert's law as discussed in Chapter 6. In general, the differences between the simulated responses with and without attenuation are minimal indicating that the radial uniformity in the distribution of the tracer is achieved on a much shorter time scale as compared to the time-scale at which the mixing in the axial direction occurs.

7.2.7. Parametric Sensitivity of Simulated Liquid/Catalyst Tracer Responses

As mentioned earlier, the simulated tracer responses are computed from model equations that require as inputs the gas holdup profile, a closure for liquid phase turbulence and an estimate of the radial eddy diffusion coefficient. Even though guidelines are available for choosing the above parameters, these are unfortunately empirically based. It is therefore important to explore the effect of these parameters on the change in trends of the simulated responses. For this purpose, the effect of three different gas holdup profiles, three different mixing length profiles (presented in Chapter 6) and two different radial eddy diffusivities on the simulated responses at two detector levels (83 & 160.5 as measured on the outside tape) is presented below. The experiments chosen for this evaluation are

- Bottom-Center injection of Catalyst tracer for Run 16.6
- Bottom-Center injection of Catalyst tracer for Run 16.7
- Middle-Sidewall injection of Mn_2O_3 tracer for Run 16.7

The effect of the aforementioned parameters on the simulated responses for the above three experiments are presented in Figures 7-25 to 7-27 respectively. From these figures, it can be seen that the effect of the radial eddy diffusion coefficient on the predicted tracer responses is the most pronounced especially for responses resulting from tracer injections at the “preferred” bottom-center location (refer to Figures 7-25b and 7-26b). On the other hand, for the sidewall injection of the tracer, the effect of D_{rr} on the simulated responses is smaller as compared to those resulting from the bottom-center injection. It is therefore important to consider the presence of internals for properly estimating the radial eddy diffusion coefficient that accounts for the radial cross mixing of the tracer. On the other hand, the effects of the mixing length and gas holdup profiles, though significant for some cases, do not indicate a clear choice for either of them across all conditions. Further, it appears that on the whole, a gas holdup profile with “ $m = 2$ ” and the mixing length profile (ML-3), the original choices as model inputs, provide the best comparison of experiments with simulations.

In conclusion, the developed recirculation model, in spite of its simplicity, is successful in capturing the dominant transport time-scale in a complex three-phase multiphase flow accompanied by heat transfer and further complicated by the difficulties associated with interpretation of data from radiotracers. It is hoped that future advancements in understanding of the liquid phase turbulence and its interaction with gas holdup and bubble motion would be beneficial in improving the predictive capabilities of the developed model.

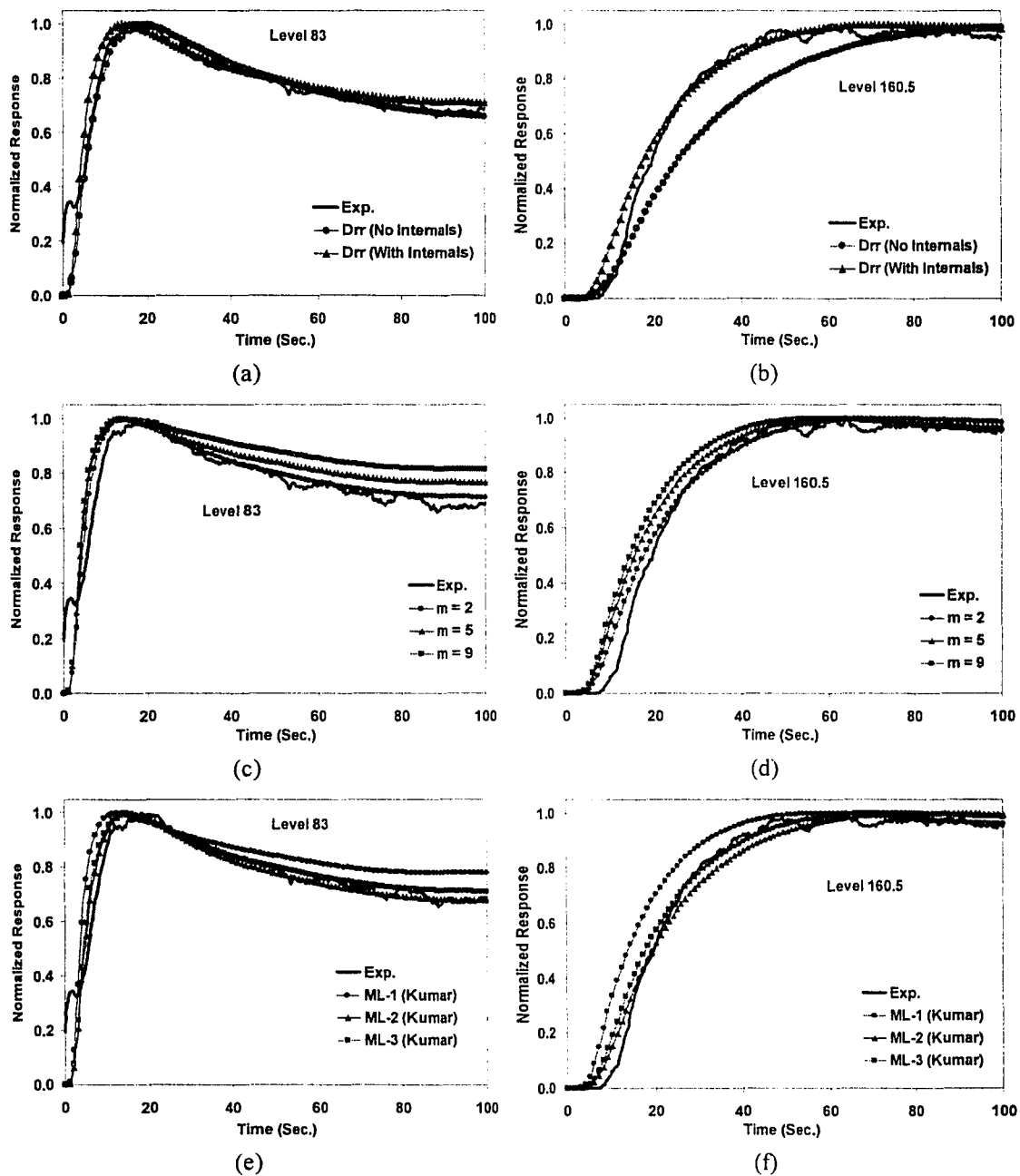


Figure 7-25. Parametric sensitivity of simulated tracer responses for Run 16.6 for Bottom-Center injection of catalyst tracer
 a) - b) Effect of D_{rr} c) - d) Effect of gas holdup profile
 e) - f) Effect of mixing length profile

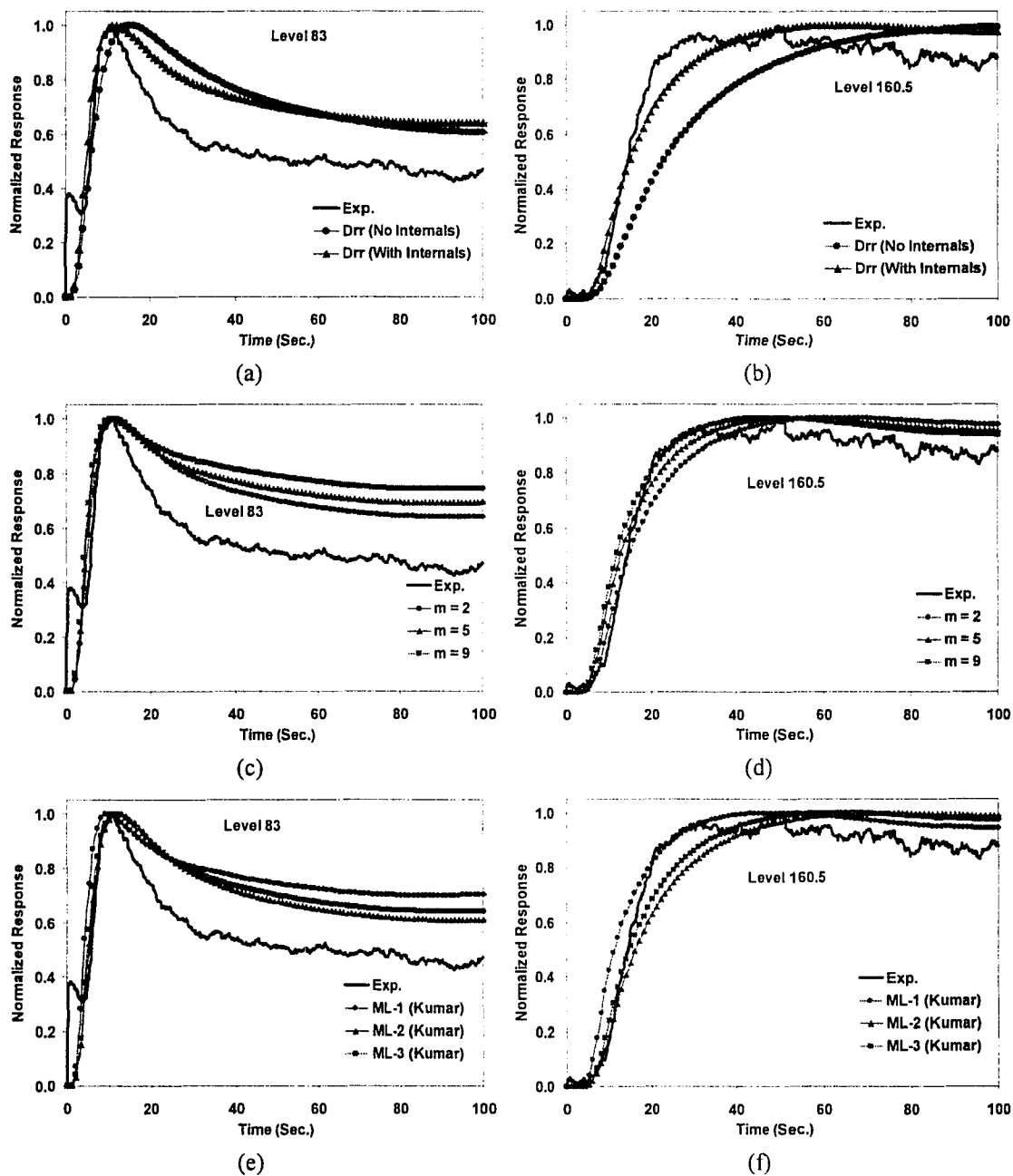


Figure 7-26. Parametric sensitivity of simulated tracer responses for Run 16.7 for Bottom-Center injection of catalyst tracer
 a) - b) Effect of D_{rr} c) - d) Effect of gas holdup profile
 e) - f) Effect of mixing length profile

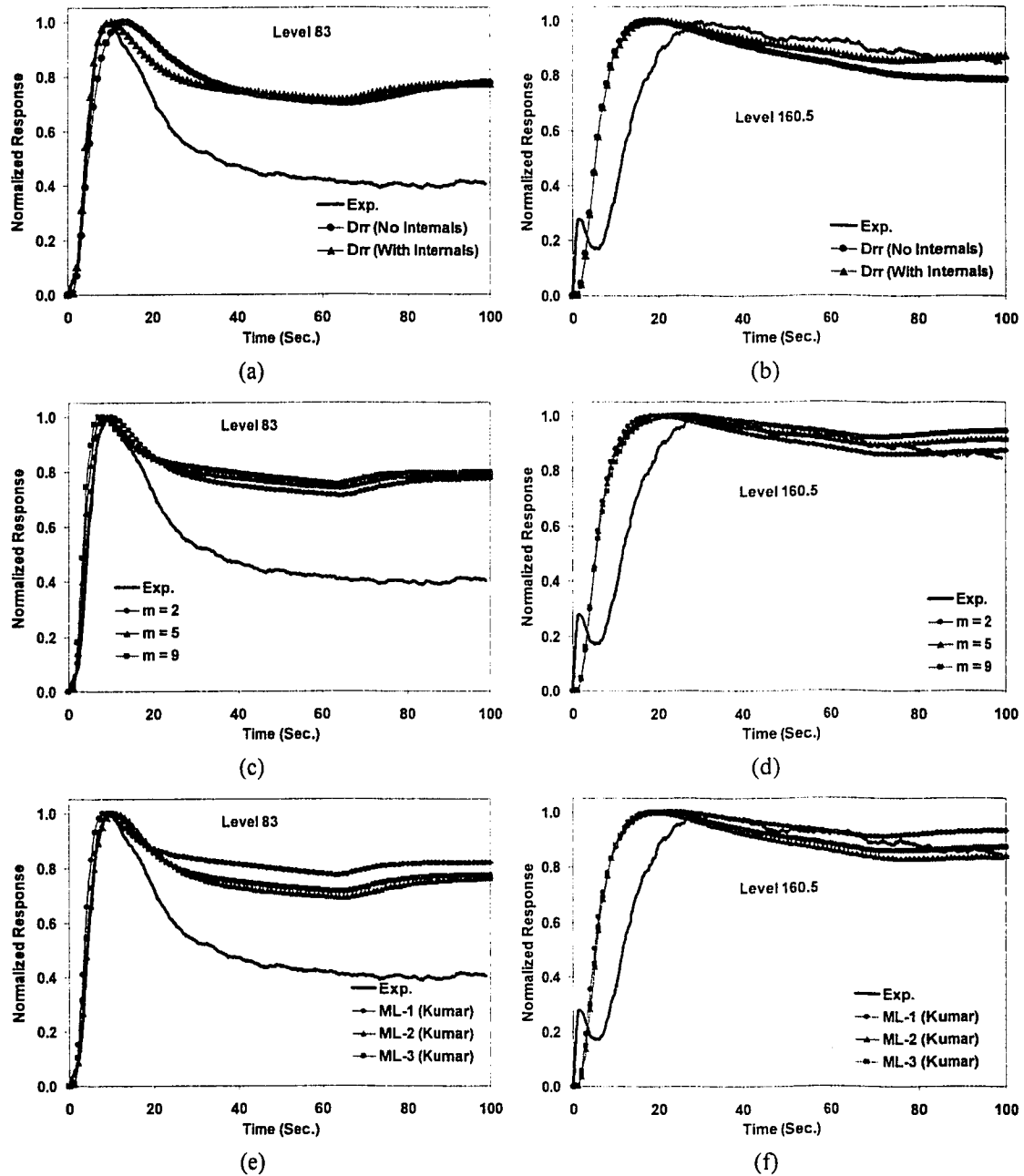


Figure 7-27. Parametric sensitivity of simulated tracer responses for Run 16.7 for Middle-Sidewall injection of Mn_2O_3 tracer

a) - b) Effect of D_{rr} c) - d) Effect of gas holdup profile

e) - f) Effect of mixing length profile

7.3. Radioactive Gas Tracer Studies during FT-IV Runs at AFDU

In this section, the analysis of the gas tracer responses from Runs 16.6 and 16.7 are presented using a mechanistic gas-liquid/slurry mixing model with inter-phase mass transfer to account for the finite solubility of the gas tracer (Ar^{41}). The compartmentalization of the reactor volume is shown in Figure 7-28 and is the same as the Single Bubble Class Model (SBCM) described in Chapter 6, whereas the model equations for each compartment from Chapter 6 are re-stated in Table 7-6 for the sake of completeness.

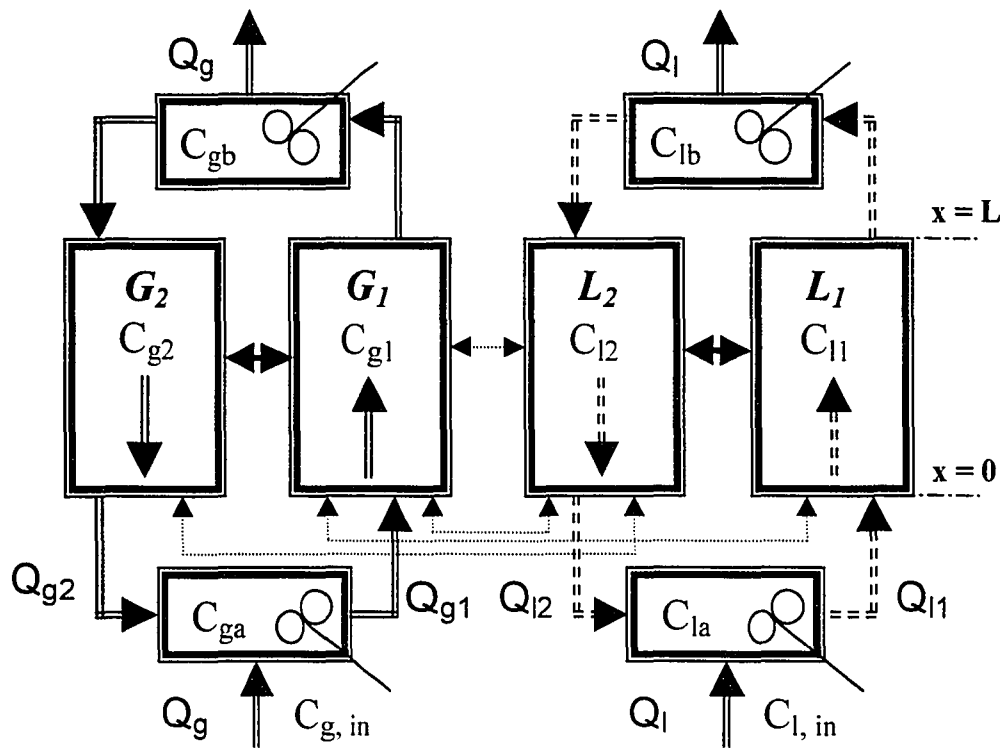


Figure 7-28. Schematic of the reactor compartmentalization for the gas-liquid mixing model with interphase mass transfer.

Table 7-6. Equations for Single Bubble-Class Gas-Liquid Recirculation Model.

$\frac{\partial C_{g1}}{\partial t} = \left\{ \bar{D}_{xx1} \frac{\partial^2 C_{g1}}{\partial x^2} - \bar{u}_{g1} \frac{\partial C_{g1}}{\partial x} - \frac{4(\bar{D}_{rr} \varepsilon_r)_{r=r}}{r'' R \bar{\varepsilon}_{g1}} (C_{g1} - C_{g2}) + R_{x,g1} - \frac{k_{gulu} a_{gulu}}{\bar{\varepsilon}_{g1}} (HC_{g1} - C_{g1}) - \frac{k_{guld} a_{guld}}{\bar{\varepsilon}_{g1}} (HC_{g1} - C_{l2}) \right\}$	
$\frac{\partial C_{g2}}{\partial t} = \left\{ \bar{D}_{xx2} \frac{\partial^2 C_{g2}}{\partial x^2} + \bar{u}_{g2} \frac{\partial C_{g2}}{\partial x} - \frac{k_{guld} a_{guld}}{\bar{\varepsilon}_{g2}} (HC_{g2} - C_{l2}) + \frac{4r'' R (\bar{D}_{rr} \varepsilon_r)_{r=r}}{R^2 - r'^2 \bar{\varepsilon}_{g2}} (C_{g1} - C_{g2}) + R_{x,g2} \right\}$	
$\frac{\partial C_{l1}}{\partial t} = \left\{ \bar{D}_{xx1} \frac{\partial^2 C_{l1}}{\partial x^2} - \bar{u}_{l1} \frac{\partial C_{l1}}{\partial x} + \left(\frac{r''}{r'} \right)^2 \frac{k_{gulu} a_{gulu}}{\bar{\varepsilon}_{l1}} (HC_{g1} - C_{l1}) - \frac{4(\bar{D}_{rr} \varepsilon_r)_{r=r}}{r'' R \bar{\varepsilon}_{l1}} (C_{l1} - C_{l2}) + R_{x,l1} \right\}$	
$\frac{\partial C_{l2}}{\partial t} = \left\{ \bar{D}_{xx2} \frac{\partial^2 C_{l2}}{\partial x^2} + \bar{u}_{l2} \frac{\partial C_{l2}}{\partial x} + \frac{4r' R (\bar{D}_{rr} \varepsilon_r)_{r=r}}{R^2 - r'^2 \bar{\varepsilon}_{l2}} (C_{l1} - C_{l2}) + \left(\frac{r'^2}{R^2 - r'^2} \right) \frac{k_{guld} a_{guld}}{\bar{\varepsilon}_{l2}} (HC_{g1} - C_{l2}) \right. \\ \left. + \left(\frac{R^2 - r'^2}{R^2 - r'^2} \right) \frac{k_{guld} a_{guld}}{\bar{\varepsilon}_{l2}} (HC_{g2} - C_{l2}) + R_{x,l2} \right\}$	
$\frac{dC_{gu}}{dt} = \left\{ \frac{U_{gi}}{\bar{\varepsilon}_g \phi_m D_c} C_{g,m} - \frac{U_{gi}}{\bar{\varepsilon}_g \phi_m D_c} C_{g,u} + \frac{\bar{\varepsilon}_{g1} \cdot r'^2}{\bar{\varepsilon}_g \phi_m D_c R^2} \bar{D}_{xx1} \frac{\partial C_{g1}}{\partial x} \right\}_{x=0} \\ + \frac{\bar{\varepsilon}_{g2}}{\bar{\varepsilon}_g \phi_m D_c} \left(\frac{R^2 - r'^2}{R^2} \right) \bar{D}_{xx2} \frac{\partial C_{g2}}{\partial x} \Big _{x=0} - \frac{k_{cst} a_{cst}}{\bar{\varepsilon}_g} (HC_{gu} - C_{lu}) + R_{x,gu}$	
$\frac{dC_{lu}}{dt} = \left\{ \frac{U_{li}}{\bar{\varepsilon}_l \phi_m D_c} C_{l,m} - \frac{U_{li}}{\bar{\varepsilon}_l \phi_m D_c} C_{l,u} + \frac{\bar{\varepsilon}_{l1} \cdot r'^2}{\bar{\varepsilon}_l \phi_m D_c R^2} \bar{D}_{xx1} \frac{\partial C_{l1}}{\partial x} \right\}_{x=0} \\ + \frac{\bar{\varepsilon}_{l2}}{\bar{\varepsilon}_l \phi_m D_c} \left(\frac{R^2 - r'^2}{R^2} \right) \bar{D}_{xx2} \frac{\partial C_{l2}}{\partial x} \Big _{x=0} + \frac{k_{cst} a_{cst}}{\bar{\varepsilon}_l} (HC_{gu} - C_{lu}) + R_{x,lu}$	
$\frac{dC_{gb}}{dt} = \left\{ \frac{\bar{\varepsilon}_{g1} \cdot r'^2}{\bar{\varepsilon}_g \phi_m D_c R^2} \bar{D}_{xx1} \frac{\partial C_{g1}}{\partial x} \Big _{x=l} - \frac{\bar{\varepsilon}_{g2}}{\bar{\varepsilon}_g \phi_m D_c} \left(\frac{R^2 - r'^2}{R^2} \right) \bar{D}_{xx2} \frac{\partial C_{g2}}{\partial x} \Big _{x=l} - \frac{k_{cst} a_{cst}}{\bar{\varepsilon}_g} (HC_{gb} - C_{lb}) + R_{x,gb} \right\}$	
$\frac{dC_{lb}}{dt} = \left\{ \frac{\bar{\varepsilon}_{l1} \cdot r'^2}{\bar{\varepsilon}_l \phi_m D_c R^2} \bar{D}_{xx1} \frac{\partial C_{l1}}{\partial x} \Big _{x=l} - \frac{\bar{\varepsilon}_{l2}}{\bar{\varepsilon}_l \phi_m D_c} \left(\frac{R^2 - r'^2}{R^2} \right) \bar{D}_{xx2} \frac{\partial C_{l2}}{\partial x} \Big _{x=l} + \frac{k_{cst} a_{cst}}{\bar{\varepsilon}_l} (HC_{gb} - C_{lb}) + R_{x,lb} \right\}$	
$d_B = \bar{d}_B$	
Hydrodynamic Model	
$\varepsilon_g(\xi) = \bar{\varepsilon}_g \left(\frac{m+2}{m+2-2c} \right) (1 - c\xi^m)$	
Liquid Phase	Gas Phase
$0 = -(\rho_g \varepsilon_g + \rho_l \varepsilon_l) g - \frac{dP}{dz} + \frac{1}{r} \frac{d}{dr} \left(r \varepsilon_l \left[\tau_{l,rz}^m + \tau_{l,rz}^l \right] \right)$	$0 = -\rho_g \varepsilon_g g - \varepsilon_g \frac{dP}{dz} + M_d$
$\tau_{l,rz}(\xi) = -\frac{\rho_l \nu_l^m}{R} \frac{du_l}{d\xi} - \frac{\rho_l l^2}{R^2} \left(\frac{du_l}{d\xi} \right)^2$	$M_d = -\frac{3\varepsilon_l \varepsilon_g \rho_l C_{l1}}{4d_B} (u_l - u_g)^2$
$\frac{l(\xi)}{R} = \frac{a(1-\xi)}{(\xi+b)^c} + d(1-\xi)^c$ Kumar <i>et al.</i> (1995)	$C_{l1} = \max \left[\frac{24}{Re} (1 + 0.15 Re^{0.687}), \frac{8}{3} \frac{Eo}{Eo+4} \right]$ Tomiyama <i>et al.</i> (1995)

For details of the derivation of the gas-liquid recirculation model equations, the solution procedure and the parameter estimation, the reader is referred to Chapter 6. Since only a small fraction of the gas escapes along with the slurry through the reactor outlet, this effect has not been incorporated into the gas phase mixing model. While the slurry recycle effect could be safely ignored for the gas phase model, it would not be

appropriate to do so for the liquid phase model. It could be argued that since mass transfer of the gas tracer to the liquid phase is significant, consideration should be given to the effect of the slurry recycle on the gas tracer responses. Similarly, the effect of the changing gas velocity along the reactor could have an effect on the simulated responses, but has not been considered in the model comparisons with data presented in this study. In theory both of these could be achieved but call for significant model and code development efforts. It is proposed that these effects be explored in future continuation of the present work to bring the current mixing models to the next level of sophistication.

7.3.1. Comparison of Experimental Tracer Responses with Simulation Results

Table 7-7 lists the parameters computed by the gas-liquid recirculation model. As for the parameters of liquid/catalyst mixing model, gas-mixing model parameters were computed from the one-dimensional sub-model for three different superficial gas velocities (inlet, outlet and mean) for both Run 16.6 and Run 16.7 to explore their dependence on the changing superficial gas velocity along the reactor length. However, the figures presented subsequently have all been computed using the parameters based on the mean superficial gas velocity. Additionally, the simulated responses account both for the presence of the internals as well as for the radiation attenuation based on the Beer-Lambert's law as presented in Chapter 6.

Figures 7-29 to 7-32 show the comparison of the simulation results using different values of the Henry's constant (H) with experimental tracer data for Run 16.6 in response to the radioactive gas tracer injected below the gas sparger. One can see from these figures that the model predictions are in good agreement with the experimental responses for zero and small values of the Henry's constant at lower reactor levels, while at higher levels, a Henry's constant of 0.15 (dimensionless) seems to bring the predictions closer to data. However, for the thermodynamically estimated Henry's constant ($H = H^* = 0.248$), the predicted responses are slightly delayed in time as compared to the experimental data. The reason for these discrepancies between simulated and experimental responses could lie in the uncertainties associated with the estimated Henry's constant, which influences the mean residence time of the gas species in the reactor. However, in general, there is

good agreement between the simulated and experimental responses for the Henry's constant of 0.15 and 0.248.

Table 7-7. Computed model parameters for the gas-mixing model.

Parameter	Run 16.6			Run 16.7		
	12.8	9.89	11.4	18.2	15.2	16.7
U_G (cm/s)	0.458	0.458	0.458	0.478	0.478	0.478
<input type="checkbox"/> \times	0.564	0.564	0.564	0.607	0.607	0.607
<input type="checkbox"/> \times	0.516	0.524	0.520	0.481	0.488	0.484
<input type="checkbox"/> \times	0.448	0.443	0.446	0.416	0.410	0.413
<input type="checkbox"/> \times (cm/s)	33.6	33.6	33.6	36.2	36.2	36.2
<input type="checkbox"/> \times (cm/s)	30.1	30.1	30.1	32.2	32.2	32.2
<input type="checkbox"/> \times (cm/s)	46.3	42.6	44.4	57.2	52.9	55.1
<input type="checkbox"/> \times (cm/s)	22.5	24.6	23.5	19.9	22.1	21.0
<input type="checkbox"/> \times	0.739	0.739	0.739	0.742	0.742	0.742
<input type="checkbox"/> \times	0.821	0.791	0.806	0.860	0.834	0.845
<input type="checkbox"/> \times (cm ² /s)	624	624	624	601	601	601
<input type="checkbox"/> \times (cm ² /s)	606	606	606	573	573	573
<input type="checkbox"/> \times (cm ² /s)	153	153	153	146	146	146
<input type="checkbox"/> \times (cm ² /s)	60	60	60	55	55	55
<input type="checkbox"/> \times (cm)	0.198	0.122	0.159	1.28	0.632	0.940
k_{gulu} (cm/s)	0.060	0.064	0.062	0.030	0.039	0.034
a_{gulu} (1/cm)	13.3	23.3	17.2	1.82	3.92	2.55
k_{guld} (cm/s)	0.147	0.183	0.163	0.063	0.087	0.072
a_{guld} (1/cm)	2.32	2.53	2.44	0.437	0.715	0.539
k_{gdld} (cm/s)	0.046	0.050	0.048	0.023	0.030	0.026
a_{gdld} (1/cm)	13.6	21.9	16.8	1.96	3.89	2.64
k_{CST} (cm/s)	0.062	0.060	0.062	0.033	0.040	0.035
a_{CST} (1/cm)	15.0	24.4	18.7	2.18	4.41	2.96

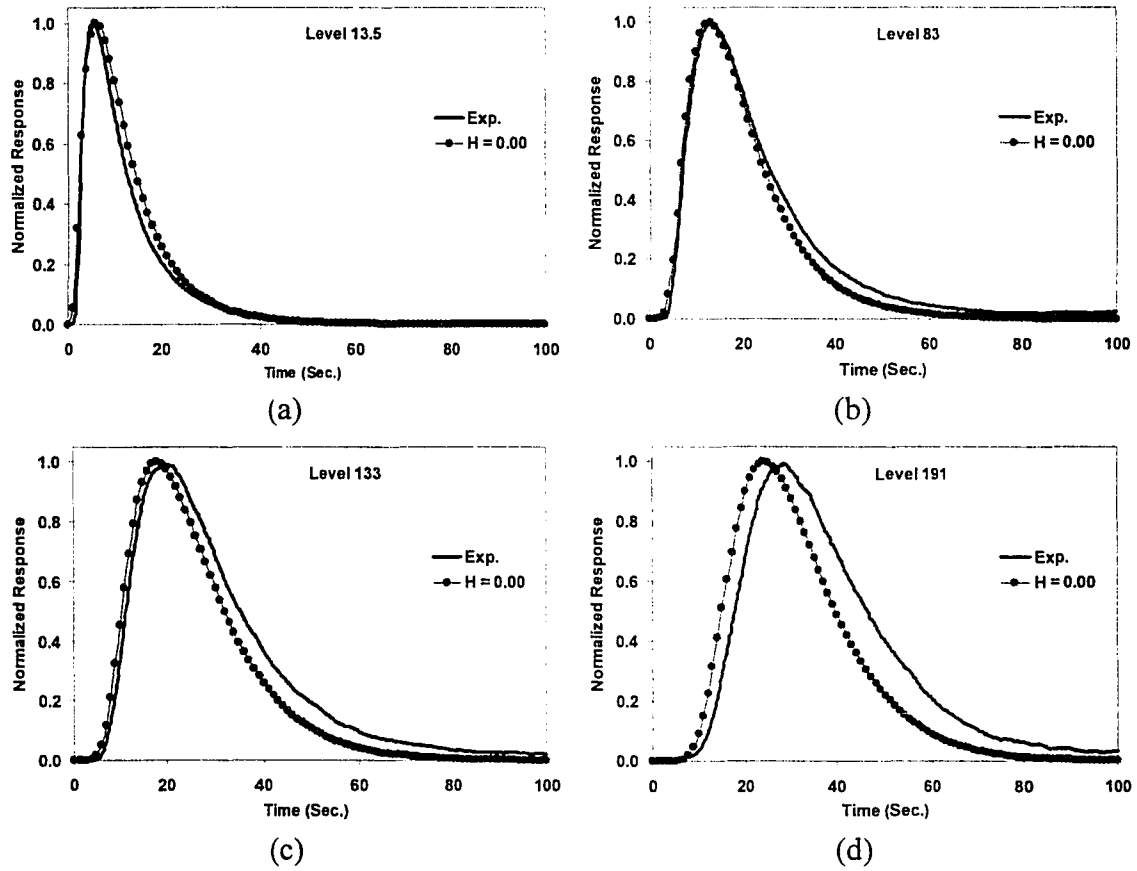


Figure 7-29. Comparison of experimental and simulated gas tracer response curves for Run 16.6 with Henry's constant, $H = 0$.

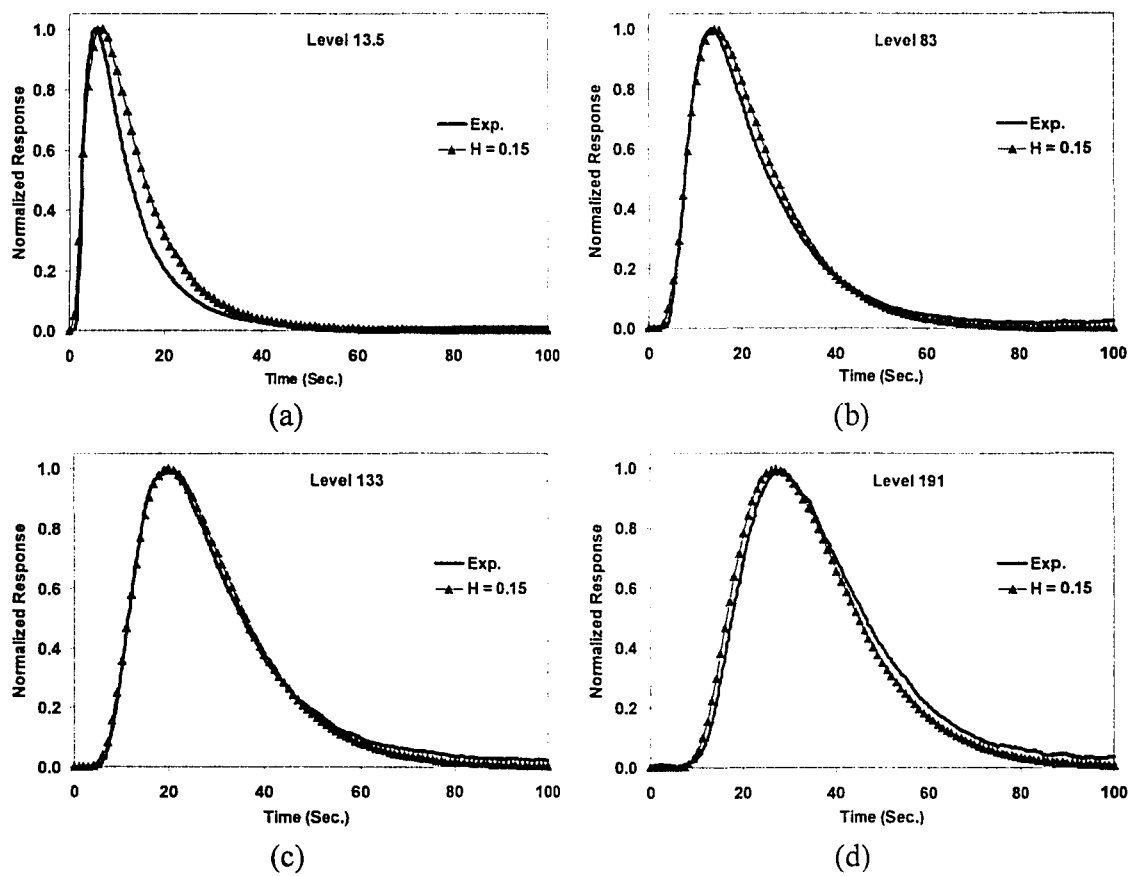


Figure 7-30. Comparison of experimental and simulated gas tracer response curves for Run 16.6 with Henry's constant, $H = 0.15$.

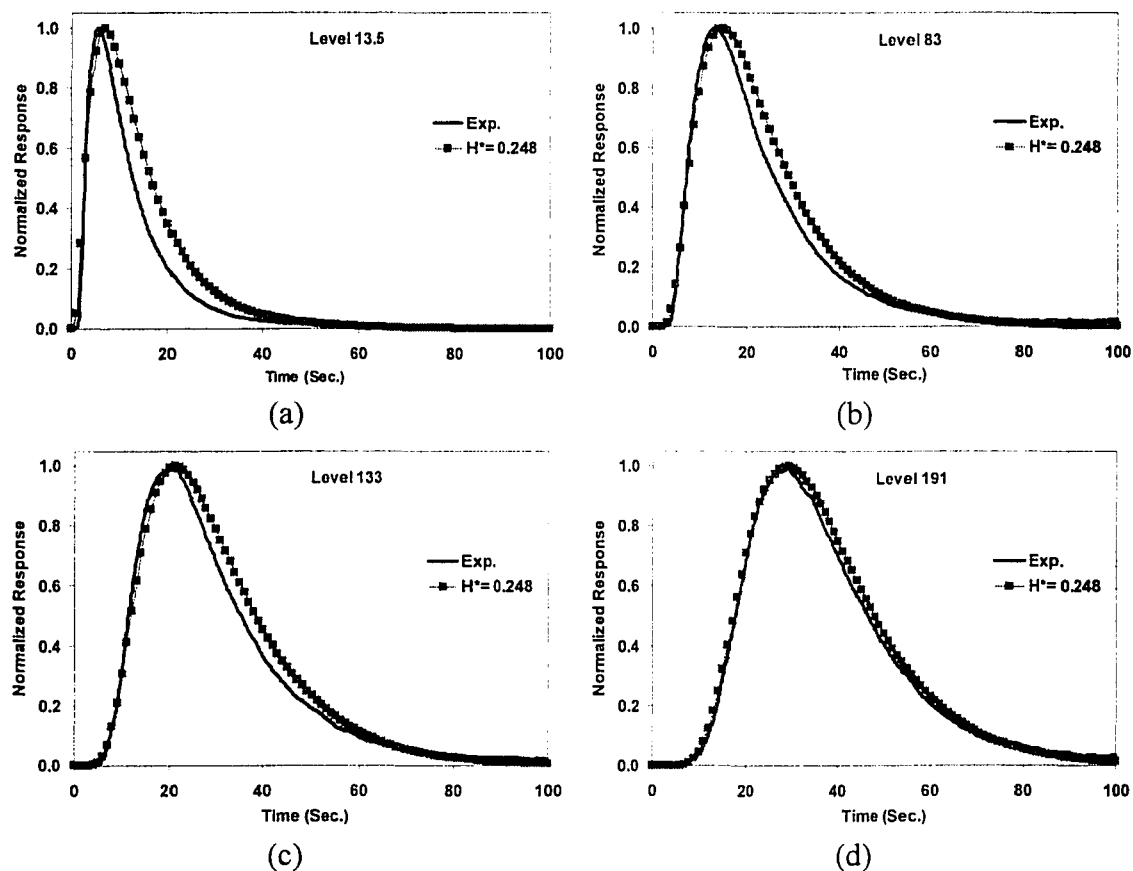


Figure 7-31. Comparison of experimental and simulated gas tracer response curves for Run 16.6 with thermodynamically estimated Henry's constant, $H^* = 0.248$.

As for Run 16.6, Figures 7-32 to 7-34 show the comparison of the simulation results with experimental data for the radioactive gas tracer injected below the gas sparger for Run 16.7. One can see from these figures that at the lowest tracer-monitoring level, the model simulations are in good agreement with the experimental responses for smaller values of the Henry's constant than predicted by thermodynamic calculations. For the middle monitoring levels, a Henry's constant of 0.15 (dimensionless) again provides the best match between data and simulations. The thermodynamically estimated Henry's constant ($H^*=0.245$) results in good predictions of the data at the middle levels and is in excellent agreement with the experimental data at the two highest levels in the column. Overall, the mismatch between simulated and experimental tracer curves is well within

the thermodynamic estimation accuracy of the Henry's constant that can have a variation of $\pm 25\text{-}50\%$. Additional figures at other levels are presented in Appendix C.

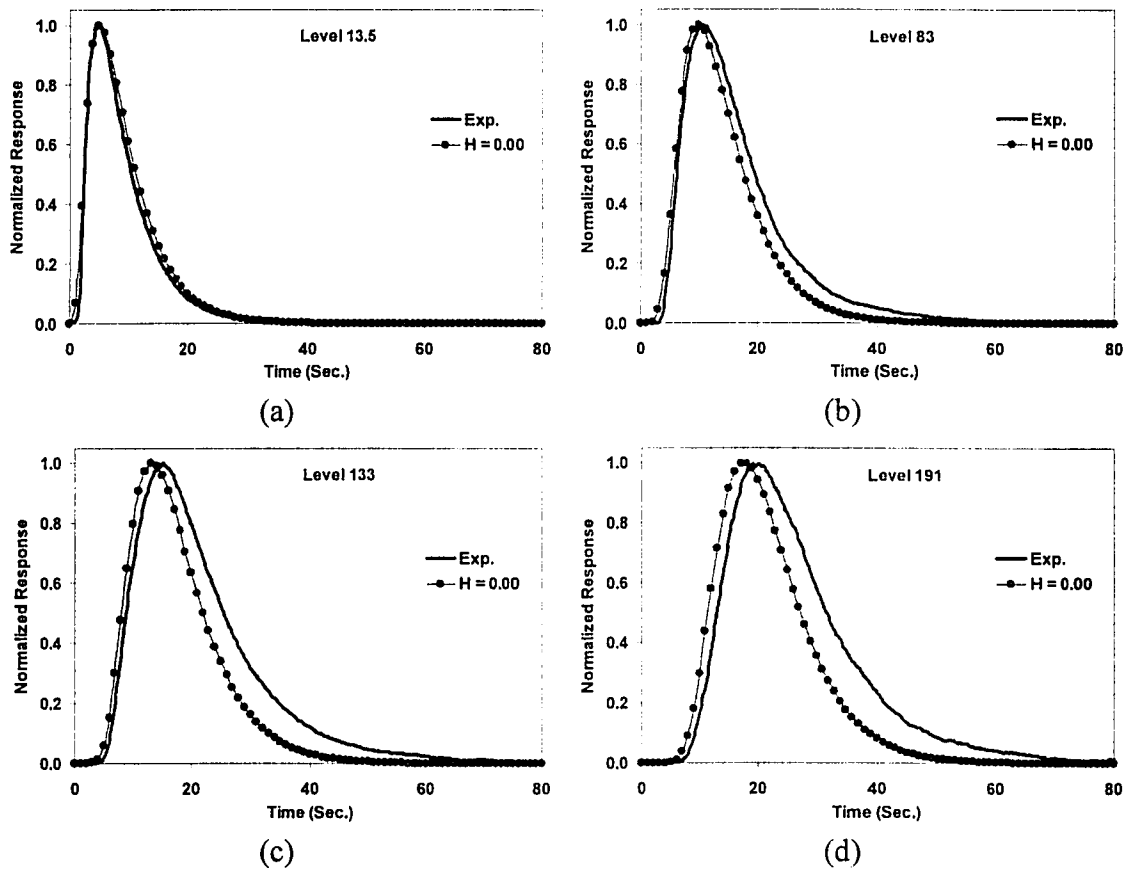


Figure 7-32. Comparison of experimental and simulated gas tracer response curves for Run 16.7 with Henry's constant, $H = 0$.

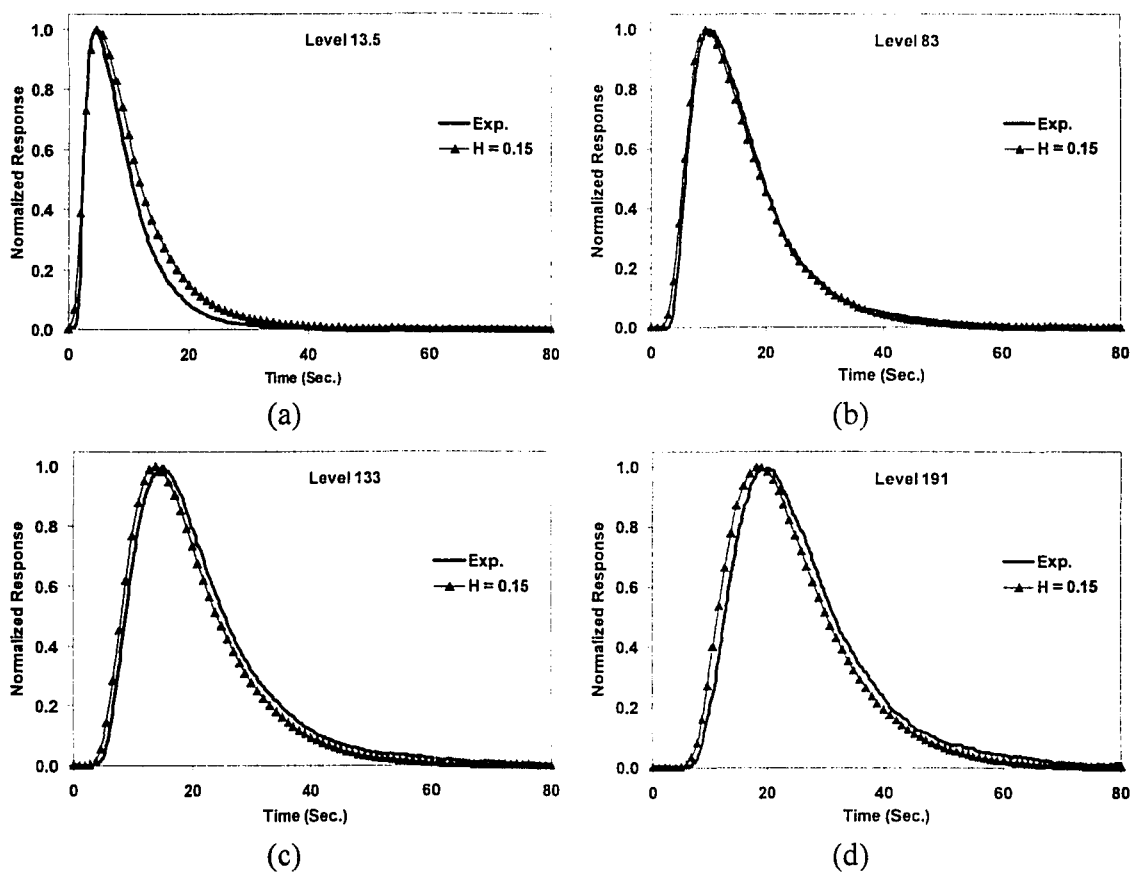


Figure 7-33. Comparison of experimental and simulated gas tracer response curves for Run 16.7 with Henry's constant, $H = 0.15$.

It is worth mentioning that the protocols for executing the tracer experiments during the FT-IV runs were improved from those that were in place when tracer tests were done during methanol synthesis (tracer data presented in Chapter 6). Additionally, the reactor used for FT-IV is considerably shorter than that used for methanol synthesis experiments. Furthermore, the superficial gas velocities employed for methanol runs were significantly higher than those used for FT-IV runs. As a result, the gas tracer for FT-IV experiments gets convected axially on a relatively longer time scale as compared to the methanol runs implying that comparatively it is more backmixed or has a lower plug flow character. As was mentioned in Chapter 6, the more a radiotracer gets mixed, the lesser the tracer broadening effect, which vanishes for a completely backmixed flow pattern.

Thus, the gas tracer responses for FT-IV have relatively lower (negligible) tracer broadening effects as compared to methanol gas tracer responses.

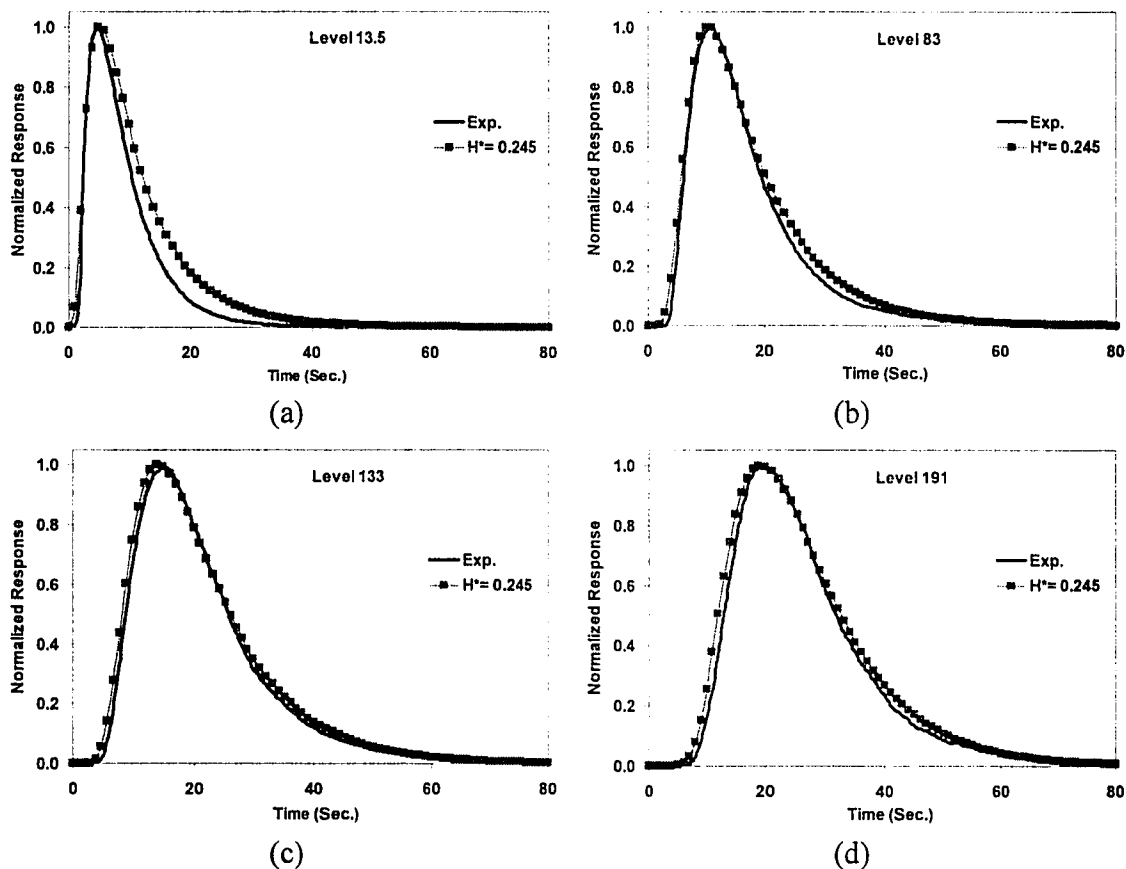


Figure 7-34. Comparison of experimental and simulated gas tracer response curves for Run 16.7 with thermodynamically estimated Henry's constant, $H^* = 0.245$.

7.3.2. Parametric Sensitivity of Simulated Gas Tracer Responses

As for the liquid/catalyst tracer experiments, Figures 7-35 and 7-36 present the effect of the various model input parameters on the computed gas tracer responses for Run 16.6 and Run 16.7 respectively. For this purpose, the normalized tracer response at level 191 inches as marked on the outside tape has been chosen. As before for the liquid responses, the gas tracer responses also show a finite but relatively insignificant effect of the radial eddy diffusivity on the computed tracer response, with the response computed

with account for the presence of internals yielding better agreement with data. Secondly, since the gas tracer is injected below the gas sparger, it is relatively well mixed radially resulting in a negligible difference between attenuated and non-attenuated responses. Thirdly, the effect of the gas holdup profile on the computed responses is negligible, however, the lower values of the exponent “ m ” provide a marginally better agreement between simulations and data. Lastly, the effect of the mixing length profile on the computed responses is also not large, with ML-1 (representative of bubbly flow as per Kumar, 1994) resulting in the greatest deviation between simulated and experimental responses.

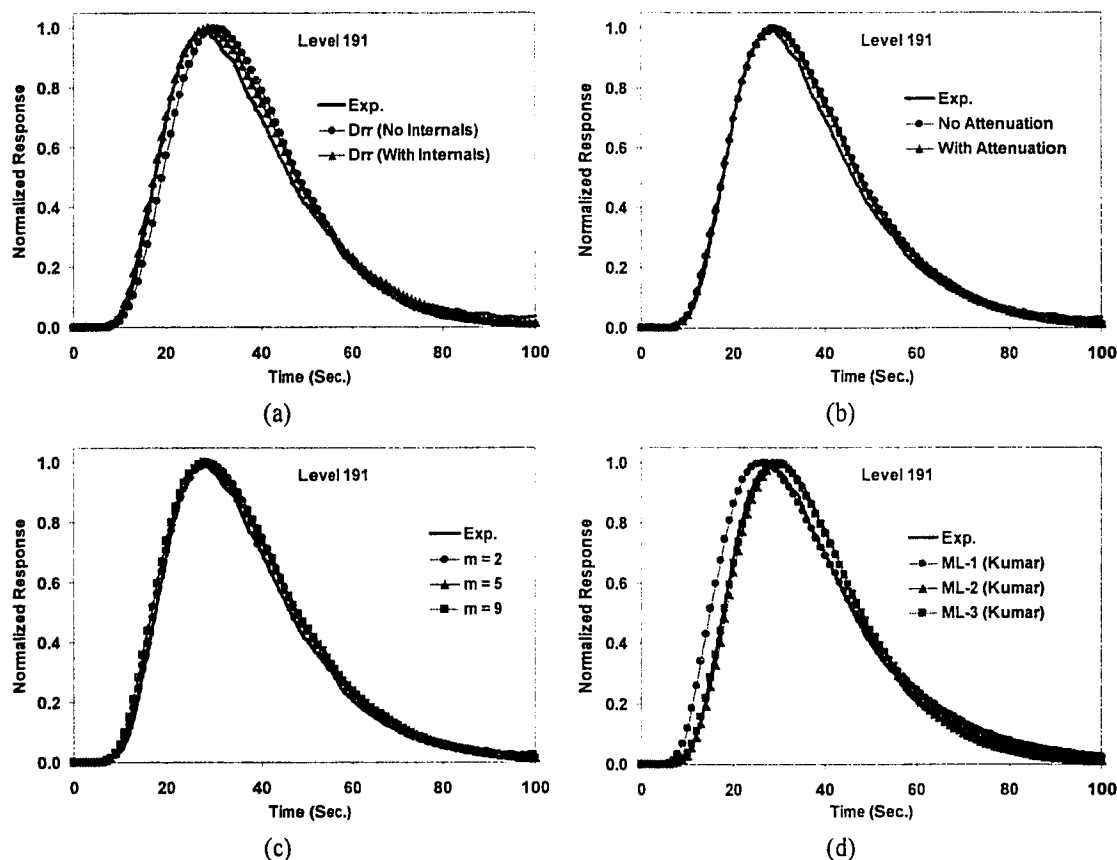


Figure 7-35. Parametric sensitivity of simulated gas tracer responses for Run 16.6

- a) Effect of D_{rr} b) Effect of radiation attenuation
 c) Effect of gas holdup profile d) Effect of mixing length profile

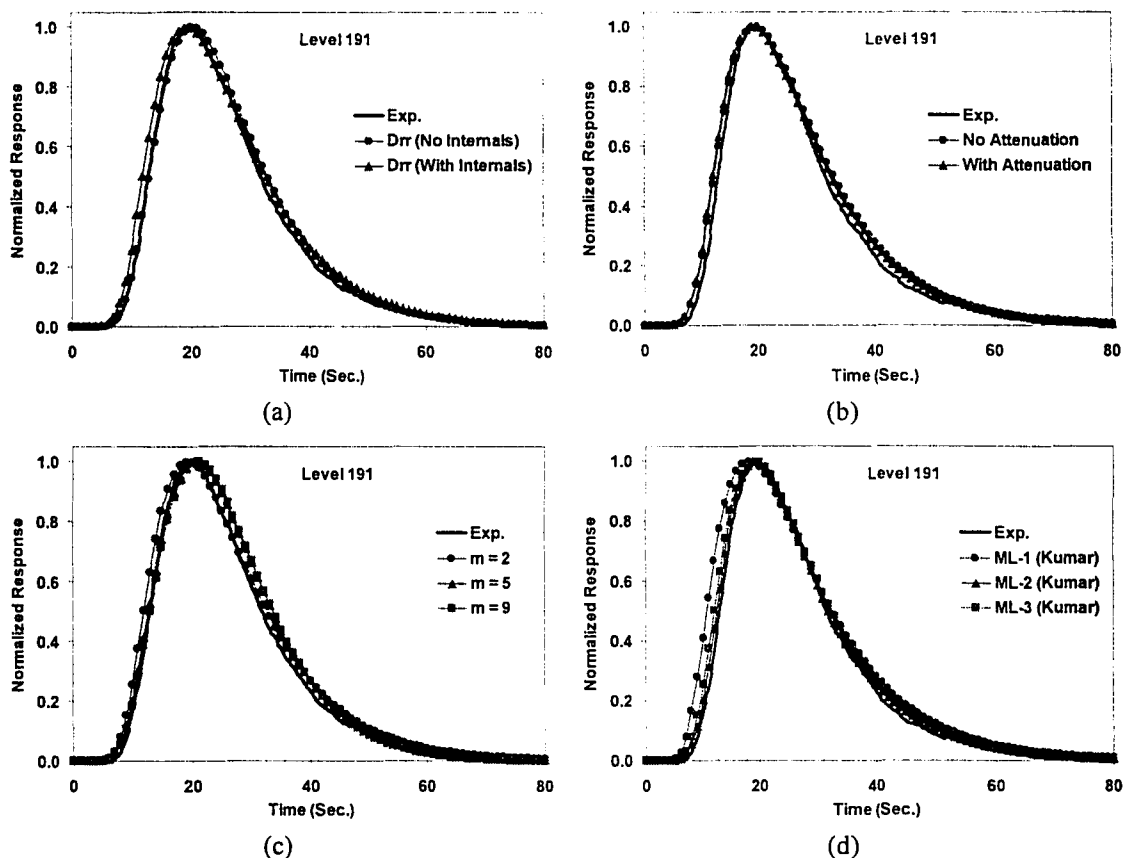


Figure 7-36. Parametric sensitivity of simulated gas tracer responses for Run 16.7

- a) Effect of D_{rr} b) Effect of radiation attenuation
 c) Effect of gas holdup profile d) Effect of mixing length profile

In conclusion, the dynamics of the gas phase mixing during the FT-IV runs is well predicted by the SBCM developed in Chapter 6. This includes not only the peak arrival times of the tracer impulse at various detector levels, but also the overall shape of the normalized responses. In general, the overall agreement between model predictions and data for FT-IV experiments is better than that for methanol runs. A possible reason for this outcome could be the relatively better known hydrodynamics (turbulence closure, drag, etc.) at the conditions of the FT-IV experiments. This points to the need for future investigations to expand the hydrodynamic database to operating conditions emulating those of the methanol runs.

7.4. Summary and Conclusions

Detailed hydrodynamic investigations on a pilot-scale FT reactor were conducted at the AFDU under reaction conditions with the scope of unraveling a few of the complexities associated with hydrodynamics of slurry bubble column reactors. This was a unique venture as most laboratory scale experiments are usually conducted under cold-flow conditions, or in cases where reaction conditions are involved, the studies are limited to relatively small vessels. However, relatively simple tasks that are taken for granted in a laboratory setup often prove to be the most challenging during a field experiment. The experience with the γ -densitometry scans at the AFDU for the present investigation is a case in point.

To summarize the evaluation of the data from the densitometry studies, one can state that it is evident that the uncertainties in the estimation of chordal averaged gas holdup from the gamma scans data are large and significant. This makes any quantitative holdup profile estimate difficult for use in a hydrodynamic model. Therefore, future gamma-scans at the La Porte AFDU should be considered only when the errors associated with source-detector misalignment are resolved with a test on a phantom of known geometry. A simple experiment was described that could be performed to achieve this objective. In the absence of a reliable and precise densitometry equipment, and until the new scanning protocols are designed and formulated, it is recommended that sectional Differential Pressure (DP) measurements be conducted together with Nuclear Densitometry Gauge (NDG) measurements to aid in the determination of the radial gas holdup profile. The NDG measurements should be performed at several axial locations around which DP measurements exist, and at least along three chordal lengths. In the past, from a single NDG line average measurement along the column diameter and DP measurements, the holdup profile was estimated assuming one of the parameters in the profile. Additional accurate chordal measurements would provide for estimation of the entire set of holdup profile parameters, *i.e.*, the values of $\bar{\epsilon}_g$, c and m .

The mixing studies using radioactive tracers provided invaluable information on the degree of backmixing in the individually traced phases. Since the temporal evolution

of tracer responses along the reactor length is dependent on the condition of flow that existed at the particular moment of injection, repeated experiments were conducted to properly assess ensemble averaged tracer responses for comparison with simulation results from mixing models. The injection of gas tracer in the gas feed line before the sparger ensured a high degree of cross-sectional uniformity of the tracer at the point of tracer entry into the column, which was the gas sparger. As a result, excellent reproducibility was achieved for gas tracer experiments under both operating conditions. It is, therefore, proposed that for future gas tracer experiments many repeated tracer injections are not necessary. It is, however, recommended that for a given operating condition, one repetition still be done as a check. On the other hand, for point tracer injections of the catalyst or Mn_2O_3 tracers, it is recommended that injections be repeated at least five times to obtain the ensemble-averaged responses. This is necessary to account for the variable flow conditions at the point of tracer injection.

Generally, it is expected that the catalyst is well suspended in the liquid phase because of the small size ($\sim 10\text{-}50\ \mu\text{m}$) of the catalyst particles in a slurry bubble column operation. During the course of the experimentation with the catalyst and “liquid” tracers at the AFDU, it was confirmed that the differences in responses from the catalyst and fine powdered Mn_2O_3 tracer injections are minimal indicating the validity of the pseudo-homogeneous assumption for the liquid (FT-wax) plus the solid (catalyst) phases. Valuable qualitative information was obtained in Run 16.6 by employing the *wrong* tracer (coarse MnO_2 particles $\sim 150\ \mu\text{m}$ were accidentally used instead of the fine Mn_2O_3 powder) which clearly demonstrated that coarse particles do settle. It is evident that because of the settling of these large MnO_2 particles, the tracer responses from MnO_2 tracer particles is dramatically different than the responses due to the catalyst or “liquid” (fine particles) tracers.

Both the gas and the liquid (slurry) tracer data was analyzed with mixing models developed at CREL (Degaleesan, 1997; Gupta *et al.*, 2001^a). The existing liquid/slurry mixing model was successfully modified by splitting the reactor domain to account for the slurry exit from the middle portion of the column as well as the slurry recycle at the bottom of the reactor. Comparison of tracer data with simulation results shows that the

responses obtained from the catalyst tracer injection in the bottom-center portion of the reactor for Run 16.6 are in reasonable agreement with the predictions of the liquid-mixing model. However, such is not the case with the tracer responses obtained from the side-wall injection in the middle portion of the reactor, since the tracer injection point is very close to the slurry exit, which results in incomplete radial mixing of the tracer before encountering the slurry outlet. Thus, model assumptions are severely violated for tracer injections very close to the slurry exit (as for the sidewall tracer injection), and this manifests itself in poor agreement between simulated and experimental data. However, the model assumptions seem to hold well for the tracer injection into the reactor bottom, and good agreement is obtained between simulated and experimental data. It is recommended that for future tracer tests on this unit with a finite slurry outflow, sidewall tracer injections into the middle portion of the reactor be avoided unless comparison with 3-D mixing models is being considered.

Similar to Run 16.6, the liquid/slurry-mixing model was used to model the liquid and catalyst tracer data acquired during the operating conditions of Run 16.7, and simulation results compare well with experimental data. The higher superficial gas velocity for Run 16.7 apparently results in relatively faster radial mixing as compared to Run 16.6. Therefore, for Run 16.7, the agreement between simulation results and experimental data for the sidewall-middle tracer injection are considerably better than for Run 16.6. Nevertheless, for future tracer studies at the AFDU, bottom-middle injection is recommended for characterization of mixing of the slurry phase for this particular reactor setup and sidewall injection should be avoided.

Correct "liquid" tracer was employed during Run 16.7 to trace the liquid phase. It appears that the fine Mn_2O_3 particles tag the liquid phase very well, and consequently the tracer responses, obtained by employing these particles as tracers, are predicted well by the mixing model which is based on the assumption of a pseudo-homogeneous slurry phase. Compared to the catalyst tracer particles, fine Mn_2O_3 tracer appears to follow the liquid even more closely as in general there is even better agreement between simulation results for the slurry (liquid) and experimental data for Mn_2O_3 tracer responses. However, at conditions of Run 16.7 the catalyst tracer also seems to follow the liquid closely. This

analysis indicates that a reliable estimate of the state of liquid mixing can be obtained by using the fine Mn_2O_3 particles.

For the analysis of gas tracer data, the gas-liquid recirculation model, based on a constant bubble size as developed in Chapter 6, was used to simulate the gas tracer responses acquired during the FT-IV operation of the AFDU. The model is able to predict the characteristic features of the observed experimental responses. The sub-model employed to compute the gas-liquid recirculation rates, for the given gas holdup profiles and operating conditions, predicts a mean bubble size of 1.6 mm for Run 16.6 and 9.4 mm for Run 16.7. These bubble sizes reflect the higher gas holdup measured during Run 16.6 as compared to Run 16.7 with the magnitude of the bubble sizes suggesting that Run 16.7 was most likely in churn-turbulent flow while Run 16.6 most likely experienced transition or even bubbly flow. For Run 16.6, the predicted tracer responses based on Henry's constant of $H = 0.15$ are in reasonable agreement with experimental data. However, the predicted response for the thermodynamically estimated Henry's constant of $H^* = 0.248$ seems to be marginally delayed in time compared to the experimental curve. On the other hand, the predicted tracer responses for Run 16.7 based on the thermodynamically predicted Henry's of $H^* = 0.245$ are in reasonably good agreement with experimental data. This could be due to the higher superficial gas velocity in Run 16.7 that most likely results in satisfying the model assumptions better as compared to Run 16.6.

Analysis of the various model parameters on the computed responses indicates that the effect of internals on the radial eddy diffusivities is significant, which consequently considerably affects the computed liquid tracer responses. This effect is more pronounced and important for responses resulting from point injection of liquid/catalyst tracer than for gas tracer responses. Comparatively, gas holdup and mixing length have relatively lower influence on the simulation results, especially for gas tracer responses. The parametric sensitivity analysis indicates that a gas holdup profile with low values of the exponent "m" and mixing length (ML-3) are good choices as the input model parameters for the FT-IV operating conditions. However, more investigations need

to be made to formulate reliable principles based on which these parameters could be chosen for a broader range of reactor sizes and operating conditions.

In conclusion, the by-and-large reasonable agreement of the simulation results with experimental data indicates that the mechanistic modeling of gas-liquid flows in slurry bubble columns, in the framework developed in Chapter 6, provides a relatively simple tool for assessing the extent of mixing to within 20% in these reactor types. It should be re-emphasized that numerous physical phenomena that affect mixing in a slurry bubble column operation result in extremely complex physics which is difficult to model precisely with the current level of understanding. In this sense, the models developed in Chapter 6 are powerful as they systematically incorporate the known physics of slurry bubble column hydrodynamics and provide a fundamentally based framework for bubble column reactor modeling.

Chapter 8. Summary, Conclusions and Recommendations

8.1. Summary and Conclusions

The work accomplished as part of this thesis contributes to both the advancement of laboratory and pilot scale experimentation as well as mechanistic modeling of bubble column flows and associated interphase scalar transport. Given the multi-faceted scope of this study, especially on the experimental side, it was somewhat challenging to provide a focused theme for the thesis. However, since good modeling efforts need to be backed up with robust experimental methods, the link among the various contributions of this work should be evident. The following summary of the major conclusions from each portion of this study also outlines the potential for future investigations.

In Chapter 3, a methodology was developed for extracting point measurements of liquid conductance in gas-liquid flows, which are needed for process identification and diagnostics as well as for the measurement of the degree of backmixing of the liquid phase. It was shown that standard filtering techniques could not provide an acceptable measured signal as they resulted in under assessment of the liquid phase conductance. To remedy the problems with the standard filtering methods, a novel software based signal filtering methodology was successfully developed, which makes it possible to cleanly extract the liquid phase tracer concentration from conductance measurements acquired in turbulent gas-liquid flows. The algorithm is based on applying soft thresholding concepts to the raw signal from a conductivity probe along with standard digital signal filters, like those available in commercial software packages like MATLABTM. A direct comparison of the new and standard filtering techniques establishes the superiority of the developed

algorithm. From the response times of the probes employed in this work, it was concluded that the present probes are 100% effective for measuring liquid conductance changes occurring at frequencies smaller than 5-10 Hz. For measuring phenomena at higher frequencies, different probes with correspondingly shorter response times are needed. The filtering method developed in this work is fully applicable for processing signals from such faster responding probes. With this filtering methodology as the basis, the technique has many potential applications in situations where liquid phase conductance in gas-liquid mixtures needs to be measured. Additionally, the developed filtering methodology could be applied to process not only conductance signals, but signals from any other measurement of multiphase gas-liquid flows that are systematically corrupted due to the presence of the bubbles.

Chapters 4 and 5 provide the details of effecting Monte Carlo simulations of scintillator detector efficiencies. These simulation techniques are integral to the Nuclear Engineering field and are important to the CARPT measurement methodology where a radioactive particle is tracked in time as the phase follower in a single or multi-phase flow situation. As part of this study, therefore, a Monte Carlo based simulation technique was developed for numerically estimating the counting efficiency of a cylindrical scintillation crystal when it is exposed to a point radioactive source with the reactor fluids and walls as the intervening media (Yang, 1997). A computationally efficient surface integration technique was implemented that made the computation of the detector efficiency *an order of magnitude faster*. The effect of the intervening media density on detector counting efficiency was investigated, using the developed simulation tool, and it was established that the ratio of the peak-to-total efficiencies is relatively independent of the intervening media. This ratio, however, showed a 10-15% variation with source location implying that this variation cannot be ignored in the Monte Carlo based particle tracking methodology.

The above technique was further *integrated* for simulation of the counting characteristics in a multi-detector setup for non-invasively tracking the motion of a radioactive tracer particle. The computational efficiency of the developed simulation procedure results in significantly reduced time requirements for generating a calibration

map during a CARPT experiment. Additionally, it provides the capability for conducting particle-tracking studies in pilot scale vessels where the traditional calibration method is most challenging, if not impossible. The results from the implementation of the Monte Carlo algorithm and the associated computationally efficient numerical technique were validated against experimental data. The validation experiments showed that the procedure developed in this work results in prediction of particle position to better than 5 mm accuracy. A sample application of the developed method was also illustrated for a high superficial gas velocity bubble column flow in a stainless steel column where the traditional CARPT reconstruction methodology proved inaccurate. It was shown that the achieved resolution in the validation experiments, as well as in bubble column experiments in opaque vessels, can be further improved by packing more detectors in the axial direction.

The second portion of this thesis focused on developing mechanistic flow models for liquid and gas phase mixing in bubble column flows with interphase transport. Towards this end, a gas-liquid recirculation model based on the two-fluid approach was developed in Chapter 6 for simulation of time-averaged *steady recirculation patterns of gas and liquid/slurry* phases for bubble column operation in churn-turbulent flow conditions. The developed model needs the radial gas holdup profile as input. Such a holdup profile can be estimated from NDG and DP measurements, or in a design situation can be based on the correlation of Wu *et al.* (2001). It was shown that the predicted liquid recirculation based on turbulence closures developed from small-scale (6" to 18") columns were reasonably accurate in prediction of liquid velocity profile in an 18" diameter column. The extension of the liquid recirculation model to predict gas recirculation was accomplished based on the two-fluid formulation with one of its outcomes being the information on bubble size, which is important for estimation of mass transport parameters.

The above recirculation flow model was integrated with mechanistic models that describe gas phase mixing and interphase mass transport. Two competing models, one based on a constant bubble size (SBCM) and the other based on a radial distribution of the mean bubble size (DBSM), were explored. Robust numerical techniques were

implemented for simulation of the model equations and simulation predictions were tested against pilot-scale tracer data. From the comparison of the two reactor models, it was concluded that the distributed-bubble class model, as developed in this work, does not offer any significant advantage over the one based on a single bubble size. Comparison of the simulation results with experimental data showed that the quality of comparison is significantly dependent on the accuracy of the Henry's constant, an important model parameter. The fundamental basis of these models makes them attractive for prediction of reactor performance when relevant kinetics is incorporated in the reaction terms.

The last part of the study dealt with applying the models developed earlier in Chapter 6 to interpret radioactive tracer data from a Pilot scale demonstration of the Fischer-Tropsch technology. Towards this goal of establishing a slurry bubble-column based FT technology, gas, liquid and catalyst mixing in a pilot scale slurry bubble column were studied via radioactive tracer measurements at the Alternate Fuels Development Unit (AFDU) in La Porte, TX. The mechanistic liquid mixing model discussed in Chapter 6 was successfully extended to account for slurry exit from the middle portion of the column and its re-entry into the reactor bottom after separation of the wax product through a filtration loop. A data collection and interpretation protocol was established for future tracer experiments at the AFDU and recommendations were made for improvements in the γ -densitometry technique applied for gas holdup measurements. The comparison of model predicted tracer responses with experimental data were in good agreement especially for Run 16.7 that was clearly in the churn-turbulent flow regime.

As evident from the above, most of the objectives set forth for this thesis work have been successfully met, and the accomplishments attained provide the foundation for future investigations. Some of these are discussed below.

8.2. Recommendations for Future Work

Suggestions for extending the work conducted in different parts of this study are listed below:

1. ***Liquid conductance measurements in gas-liquid flows:*** On the hardware side, future development efforts for the liquid conductance measurement in gas-liquid flows could explore better and faster responding miniature probes with the smallest measurement chamber possible. This should go in parallel with identifying the right conductance meters, as most often they have the largest response times among all the components of a conductance measurement system. Additionally, alternate possibilities for the probe coatings could be investigated to provide better wetting/dewetting dynamics. This would enable studying high-speed recirculatory flows in bubble columns without trays and at high gas throughputs where high gas volume-fractions are encountered. On the software side, using filters other than the Butterworth filters employed in the present study could be investigated to identify better alternatives. These include filters like the Chebyshev and other IIR (Infinite Impulse Response) as well as FIR (Finite Impulse Response) filters. For these purposes, the reader is referred to any basic DSP (Digital Signal Processing) text (Smith, 1999). The Butterworth filters employed in this study, as well as the ones mentioned above, are all based on the Fourier theory that does not consider the frequency content variations with time. Therefore, Wavelet filtering of the raw signal before thresholding could be considered as an additional alternative to be explored. With the rapid advances in software like MATLABTM, it should be possible to investigate many of the alternatives discussed herein.
2. ***Monte Carlo simulation based radioactive particle tracking:*** The simulation methodology could be further improved by possibly accounting for the buildup effect due to the presence of the vessel walls and the intervening reactor media between the moving radioactive source and the detectors. This area where multiple measurements are used to identify a single parameter (in our case, the multiple measurements are the counts from the scintillation detectors and the parameter to be identified is the

particle location) is referred to in the “Pattern Recognition” community as “Data Fusion” techniques (Filippidis, 1996). This is a relatively young area of research, however, much of the mathematics and the principles developed therein could be adopted for improving the transient particle location in a CARPT experiment. This, however, calls for dedicated research in a multi-disciplinary environment where research and development objectives are very clearly identified. Additionally, since the generation of the calibration map is the only time consuming step that requires offline processing, with the reconstruction of particle location from counts data being relatively fast, it is possible to integrate the counts acquisition procedure with on-the-fly position rendition to achieve *real-time* tracking of a tracer particle in a multiphase flow situation. This would of course require updates to the hardware and carefully planned execution.

3. ***Bubble-induced turbulent eddy viscosity:*** The model developed for predicting liquid and gas phase recirculation uses a closure for the liquid phase turbulence based on the mixing length correlations proposed in the literature. Alternatively, however, since the model provides estimation of the radial distribution of the bubble size as well as the slip velocity, the liquid phase turbulence could also be closed based on the concept of bubble-induced turbulent viscosity (Pan and Dudukovic', 1999). This might provide a better basis for closing the liquid phase turbulence and couple the calculation of the gas and liquid phase momentum balance equations which are currently solved in a de-coupled manner. The bubble-induced turbulent kinematic viscosity is generally modeled as being proportional to the product of the bubble diameter and the magnitude of the relative velocities of the gas and liquid phases. Since the above quantities are readily available as outputs from the solution of the current model equations, the calculation of the bubble-induced kinematic viscosity can be achieved by suitably choosing (or alternatively investigating the effect of) a proportionality constant. This can then be put into a feedback loop where it feeds into the turbulence closure terms of the liquid-recirculation model equations.
4. ***Extension of mechanistic reactor models:*** The phenomenological approach, based on the overall bubble column hydrodynamics, was shown to be adequate in modeling

reactor scale mixing phenomena. Further model development can expand this work to a two-dimensional case where the radial distribution of the flow parameters is incorporated without the need of reactor compartmentalization into the up-flow and down-flow zones. Degaleesan (1997) did this for the liquid phase model. The developed mechanistic models can also be further extended to account for changing gas molar flow rates in the reactor due to consumption or production under reaction conditions. This again calls for careful examination of the two-fluid model equations along with continuity for each phase to avoid pitfalls in arriving at a formulation that is physically inconsistent. There is also a need to improve the understanding of the hydrodynamic parameters (mixing length, gas holdup distribution, etc.) across a broad range of operating conditions and liquid/slurry physical properties. Subsequently, methods could be developed to estimate or predict them reliably in order to render the models to be robust and fully predictive. Once this has been reliably accomplished, the models could be extended to handle multiple species and subsequently to multiple reactions to provide as a stand-alone tool for reactor modeling of slurry bubble columns.

5. ***Pilot-scale experimentation:*** More sophisticated data analysis techniques could be sought to translate the scintillation counts data acquired from radioactive tracer measurements into tracer concentration data. Specifically, some of the tracer-response broadening effects could be captured by simulation-based relation of tracer concentration to the intensity counts received by the array of scintillation detectors. This can be accomplished by incorporating some of the physics involved in the radiation detection process as described in Chapters 4, 5 and 6. Improvements can also be sought for the implementation and interpretation of the densitometry scans so that a reliable estimate of the gas volume-fraction distribution could be achieved in a pilot-scale setup. One possibility is to achieve a reliable mechanism for mounting and positioning the radioactive source and detector/s. The other involves exploring the fan-beam scanning arrangement to achieve true reconstruction of the cross-sectional distribution of the phases.

Appendix A. Parameter Estimation of Bubble Column Hydrodynamics

This appendix describes the liquid recirculation model of Ueyama and Miyauchi (1979) as well as presents the correlations for predicting the parameters of the radial gas holdup profile and the radial and axial eddy diffusivities from the CT (Computed Tomography) and CARPT (Computer Automated Radioactive Particle Tracking) databases.

Model for Liquid Velocity Profiles (Ueyama and Miyauchi, 1979)

$$\frac{u_l + |u_w|}{u_0 + |u_w|} = \left[1 - \left(\frac{r}{R} \right)^2 \right]^2 \quad (\text{A-1})$$

$$u_0 = \frac{gD\epsilon_g}{192\nu_l} \left(\frac{4 - 3\epsilon_g}{1 - \epsilon_g} \right) + \frac{U_L}{1 - \epsilon_g} \quad (\text{A-2})$$

$$|u_w| = \frac{gD\epsilon_g}{192\nu_l} \left(\frac{2 - 3\epsilon_g}{1 - \epsilon_g} \right) - \frac{U_L}{1 - \epsilon_g} \quad (\text{A-3})$$

where,

D \equiv column diameter

g \equiv acceleration due to gravity

U_L \equiv superficial liquid velocity

u_0 \equiv centerline interstitial liquid velocity

$|u_w|$ \equiv absolute value of the interstitial axial liquid velocity near the wall.

U_L is zero if the liquid is a batch. In this approach, the velocity in the core is matched to the universal velocity profile for the laminar sub-layer at a distance δ from the column wall. With this model, some degree of empiricism is involved in extending the single-phase universal velocity relations to two-phase flows.

Model for Liquid Velocity Profiles (Anderson and Rice, 1989)

In this model, the following equation was derived relating the dimensionless pressure gradient, p' to ξ^* :

$$\xi^* = \sqrt{\bar{\varepsilon}_g / (1 - p')} \quad (\text{A-4})$$

Here, ξ^* is the dimensionless radius at which the downward liquid velocity is maximum.

They also derived the following equation for the downward maximum velocity:

$$u_l(\xi = \xi^*) = u_{\xi^*} = \frac{gR^2 \bar{\varepsilon}_g}{4\nu_m \xi^{*2}} (\xi^{*2} - 1 - 2\xi^{*2} \ln \xi^*) \quad (\text{A-5})$$

Correlations for Parameters of the Radial Gas Holdup Profiles (Wu *et al.*, 2001)

As mentioned previously, the following expression is usually used to describe the radial distribution of the gas holdup in well-developed flow zones of a bubble column:

$$\varepsilon_g(\xi) = \bar{\varepsilon}_g \left(\frac{m+2}{m+2-2c} \right) (1 - c\xi^m) \quad (\text{A-6})$$

Wu *et al.* (2001) correlated the parameters m and c in the above expression with macroscopic flow variables. These correlations are:

$$m = 2.188 \times 10^3 Re_G^{-0.598} Fr_G^{0.146} Mo_L^{-0.004} \quad (\text{A-7})$$

$$c = 4.32 \times 10^{-2} Re_G^{0.2492} \quad (\text{A-8})$$

where, $Re_G = \frac{D_c U_G (\rho_L - \rho_G)}{\mu_L}$

$$Fr_G = \frac{U_G^2}{gD_C}$$

$$Mo_L = \frac{g\mu_L^4}{(\rho_L - \rho_G)\sigma_L^3}$$

$U_G \equiv$ gas superficial velocity

$D_C \equiv$ column diameter

$\rho_L \equiv$ density of the liquid phase

$\mu_L \equiv$ molecular viscosity of the liquid phase

$\sigma_L \equiv$ surface tension of the liquid phase

$\rho_G \equiv$ density of the gas phase (dependent on operating pressure)

For estimating the cross-sectional average gas holdup, $\bar{\epsilon}_g$, an appropriate correlation could be chosen as presented by Ong (1999) and Kemoun *et al.* (2001^b).

Correlations for Radial and Axial Turbulent Eddy Diffusivities (Degaleesan, 1997)

The mixing models presented in Chapter 6 and 7 make use of the correlations developed by Degaleesan (1997) for estimating the radial (D_{rr}) and axial (D_{xx}) turbulent eddy diffusivities. These correlations are:

$$D_{rr}(\xi) = \left(-\frac{350}{D_C^{0.8}} + 13(D_C U_{Ge})^{0.3} \right) P_2(\xi) \quad (\text{A-9})$$

$$D_{xx}(\xi) = \left(-\frac{2325}{D_C^{0.8}} + 106.6(D_C U_{Ge})^{0.3} \right) P_4(\xi) \quad (\text{A-10})$$

$$P_2(\xi) = 0.1653 + 5.0717\xi - 5.0929\xi^2 \quad (\text{A-11})$$

$$P_4(\xi) = 0.5847 + 0.005035\xi + 0.4693\xi^2 + 3.2704\xi^3 - 3.4979\xi^4 \quad (\text{A-12})$$

where U_{Ge} is an equivalent superficial gas velocity based on the observed gas holdup and is given as

$$U_{Ge} = \left(\frac{\bar{\epsilon}_g}{0.07} \right)^{(0.474 - 0.000626 D_C)} \quad (\text{A-13})$$

Appendix B. Effect of Boundary Conditions on Simulation Results from Mixing Models

In this appendix, the comparison of the simulation results from the gas and liquid phase mixing models, developed in Chapters 6 and 7, with the correct (Dirichlet) and incorrect (Danckwerts') boundary conditions is presented. For a well-defined "closed" system, Danckwerts' boundary conditions consist of the Robin (mixed) boundary conditions at the inlet boundary with Neumann boundary conditions at the outlet. As was briefly mentioned in Chapter 6, it seemed natural at first to use the Danckwerts' boundary conditions for the well-developed zones in the mixing models presented earlier. However, it was subsequently realized that since the boundaries of the well-developed zones are not the *physical* boundaries of the reactor domain but only *fictitious* "ones", as pertinent to the compartmentalization of the reactor domain, the use of Danckwerts' boundary conditions for a "closed" system is *unphysical*. Therefore, the correct boundary conditions to use for the well-developed zones are the continuity of species concentration in both the gas and liquid phases, which makes the concentrations at the ends of the well-developed flow zones equal to the concentrations in the respective end zones.

To elucidate the problem with using the Danckwerts boundary conditions for the reactor compartmentalization proposed in this study, a simplified situation of a unidirectional flow with three sub-zones is presented in Figure B-1. If Danckwerts boundary conditions are imposed at the two boundaries of the axial dispersion zone (zone B), it implies that if the tracer is injected in zone C, *mathematically* it will never be able

to get into zones A or B because of the zero flux condition at the hypothetical interface between zone B and zone C. This is physically unrealistic since there are situations where the effective dispersion coefficients (in the context of the ADM) are estimated from tracer responses resulting from the injection of the tracer close to the vessel exit in a location similar to zone C. On the contrary, if Dirichlet boundary conditions are imposed at the two boundaries of the axial dispersion zone, a tracer injected into zone C will be able to diffuse into zone B and subsequently into zone A with convection having zero contribution to the tracer transport into zones A and B. Thus, by appropriately incorporating the dispersive fluxes from the axial dispersion zone into the end zone mass balance equations, with a superposition of the Dirichlet boundary conditions at the two boundaries of the axial dispersion zone, one eliminates the unphysical nature of scalar transport resulting from the use of Danckwerts' boundary conditions.

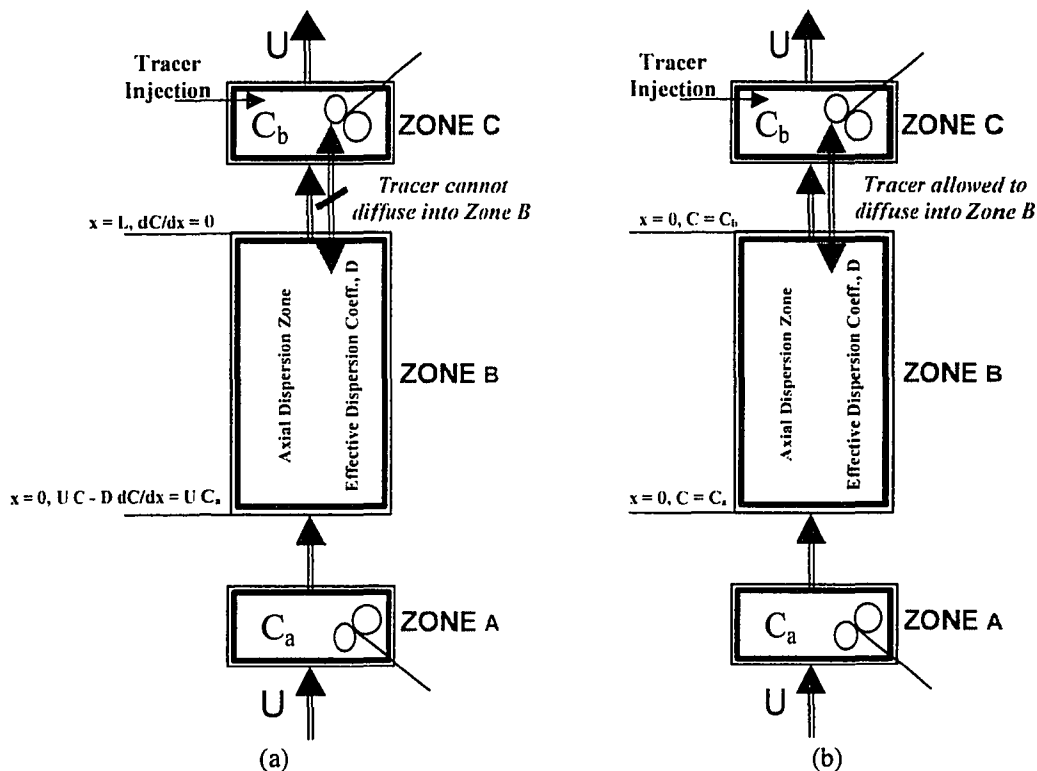


Figure B-1. Schematic of unidirectional flow with the axial dispersion zone imposed with

- a) Incorrect Danckwerts' boundary conditions
- b) Correct Dirichlet boundary conditions

Much of the earlier work reported using the mixing models presented in Chapters 6 and 7 used the improper Danckwerts' boundary conditions (Degaleesan *et al.*, 1996^a; Gupta *et al.*, 2001^a; Gupta *et al.*, 2001^b). Based on the realization of the problem associated with scalar transport arising from the use of the Danckwerts' boundary conditions (depicted in Figure B-1), a revision of the model formulation was accomplished by re-deriving the model equations and boundary conditions based on *proper* mass balance at the end zones modeled as perfectly mixed vessels. ***Fortunately, the differences in the simulated responses computed with these alternative boundary conditions are insignificant for the results presented in the earlier work.*** The reason for this is that in the simulated work reported so far, tracer injection always occurred far from the top end zones so that the Danckwerts' boundary conditions approximately hold true. However, these differences could be significant for locations of tracer injections other than the ones used in this study. It is therefore considered important to point out the differences between the correct and incorrect formulations and present example results comparing the two. Table B-1 presents the model equations for the "correct" formulation while Table B-2 does the same for the "incorrect" one.

The partial differential equations describing the species transport in the well-developed zones are not being shown, as they don't change because of the difference in the boundary conditions. These are Equations 6-1 to 6-4 for SBCM and Equations 6-19 to 6-23 for DBSM as presented in Chapter 6. However, the formulation of the mass balance in the end zones does change resulting in differences in the model equations as is evident from the two tables. It is noteworthy that the model equations for the end zone CSTs with the physically "correct" boundary conditions have a slightly uncharacteristic form. However, in the limit when the end zone volumes go to zero, the "correct" formulation yields the classical Danckwerts' boundary conditions as can be seen from Tables B-1 and B-2.

Table B-1. Model Equations with "Correct" Boundary Conditions

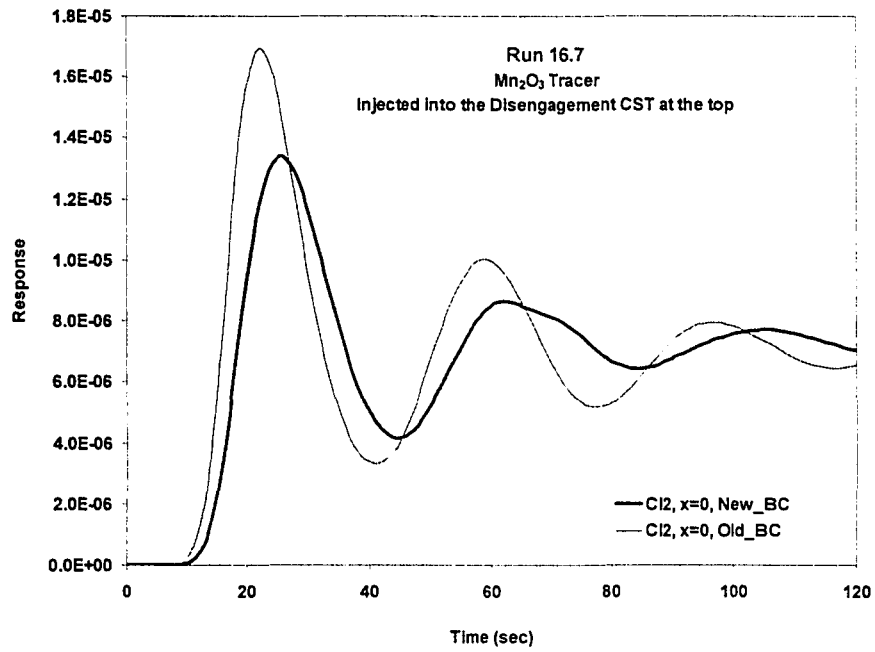
Single Bubble Class Model		Distributed Bubble Size Model	
Gas in the Distributor Zone			
$\frac{dC_{ga}}{dt} = \left\{ \begin{array}{l} \frac{U_G}{\bar{\epsilon}_g \phi_m D_C} C_{g,m} - \frac{U_G}{\bar{\epsilon}_g \phi_m D_C} C_{ga} + \frac{\bar{\epsilon}_{g1}}{\bar{\epsilon}_g \phi_m D_C} \frac{r'^2}{R^2} \bar{D}_{xx1} \frac{\partial C_{g1}}{\partial x} \Big _{x=0} \\ + \frac{\bar{\epsilon}_{g2}}{\bar{\epsilon}_g \phi_m D_C} \frac{(R^2 - r'^2)}{R^2} \bar{D}_{xx2} \frac{\partial C_{g2}}{\partial x} \Big _{x=0} - \frac{k_{CST} a_{CST}}{\bar{\epsilon}_g} (HC_{ga} - C_{la}) + R_{x,ga} \end{array} \right\}$			
Liquid in the Distributor Zone			
$\frac{dC_{la}}{dt} = \left\{ \begin{array}{l} \frac{U_L}{\bar{\epsilon}_l \phi_m D_C} C_{l,m} - \frac{U_L}{\bar{\epsilon}_l \phi_m D_C} C_{la} + \frac{\bar{\epsilon}_{l1}}{\bar{\epsilon}_l \phi_m D_C} \frac{r'^2}{R^2} \bar{D}_{xx1} \frac{\partial C_{l1}}{\partial x} \Big _{x=0} \\ + \frac{\bar{\epsilon}_{l2}}{\bar{\epsilon}_l \phi_m D_C} \frac{(R^2 - r'^2)}{R^2} \bar{D}_{xx2} \frac{\partial C_{l2}}{\partial x} \Big _{x=0} + \frac{k_{CST} a_{CST}}{\bar{\epsilon}_l} (HC_{ga} - C_{la}) + R_{x,la} \end{array} \right\}$			
Gas in the Disengagement Zone			
$\frac{dC_{gb}}{dt} = \left\{ \begin{array}{l} - \frac{\bar{\epsilon}_{g1}}{\bar{\epsilon}_g \phi_{out} D_C} \frac{r'^2}{R^2} \bar{D}_{xx1} \frac{\partial C_{g1}}{\partial x} \Big _{x=l} - \frac{k_{CST} a_{CST}}{\bar{\epsilon}_g} (HC_{gb} - C_{lb}) \\ - \frac{\bar{\epsilon}_{g2}}{\bar{\epsilon}_g \phi_{out} D_C} \frac{(R^2 - r'^2)}{R^2} \bar{D}_{xx2} \frac{\partial C_{g2}}{\partial x} \Big _{x=l} + R_{x,gb} \end{array} \right\}$			
Liquid in the Disengagement Zone			
$\frac{dC_{lb}}{dt} = \left\{ \begin{array}{l} - \frac{\bar{\epsilon}_{l1}}{\bar{\epsilon}_l \phi_{out} D_C} \frac{r'^2}{R^2} \bar{D}_{xx1} \frac{\partial C_{l1}}{\partial x} \Big _{x=l} + \frac{k_{CST} a_{CST}}{\bar{\epsilon}_l} (HC_{gb} - C_{lb}) \\ - \frac{\bar{\epsilon}_{l2}}{\bar{\epsilon}_l \phi_{out} D_C} \frac{(R^2 - r'^2)}{R^2} \bar{D}_{xx2} \frac{\partial C_{l2}}{\partial x} \Big _{x=l} + R_{x,lb} \end{array} \right\}$			
Boundary Conditions for the Well-Developed Flow Zones			
Up-Flowing Gas		Up-Flowing Gas (Small Bubbles)	
$C_{g1} _{x=0} = C_{ga}$	$C_{g1} _{x=l} = C_{gb}$	$C_{g1} _{x=0} = C_{ga}$	$C_{g1} _{x=l} = C_{gb}$
		Up-Flowing Gas (Large Bubbles)	
		$C_{g3} _{x=0} = C_{ga}$	
Up-Flowing Liquid		Up-Flowing Liquid	
$C_{l1} _{x=0} = C_{la}$	$C_{l1} _{x=l} = C_{lb}$	$C_{l1} _{x=0} = C_{la}$	$C_{l1} _{x=l} = C_{lb}$
Down-Flowing Gas		Down-Flowing Gas (Small Bubbles)	
$C_{g2} _{x=0} = C_{ga}$	$C_{g2} _{x=l} = C_{gb}$	$C_{g2} _{x=0} = C_{ga}$	$C_{g2} _{x=l} = C_{gb}$
Down-Flowing Liquid		Down-Flowing Liquid	
$C_{l2} _{x=0} = C_{la}$	$C_{l2} _{x=l} = C_{lb}$	$C_{l2} _{x=0} = C_{la}$	$C_{l2} _{x=l} = C_{lb}$

Table B-2. Model Equations with “Incorrect” Boundary Conditions

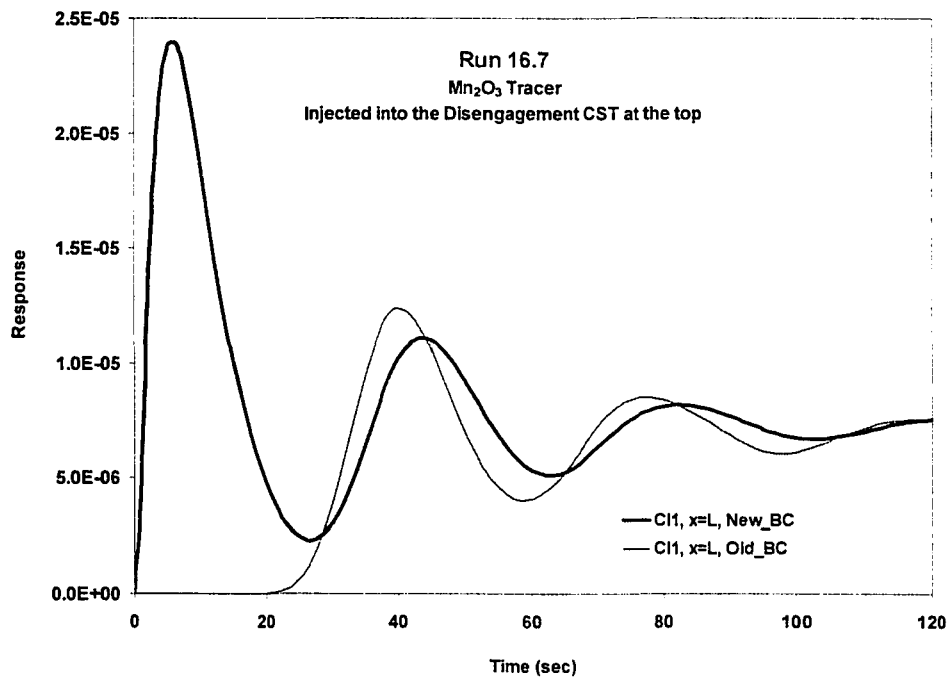
Single Bubble Class Model	Distributed Bubble Size Model
Gas in the Distributor Zone	
$\frac{dC_{gu}}{dt} = \left\{ \begin{array}{l} \frac{\bar{\epsilon}_{g2} \bar{u}_{g2}}{\bar{\epsilon}_g \phi_m D_c} \frac{(R^2 - r'^2)}{R^2} C_{g2} \Big _{x=0} - \frac{\bar{\epsilon}_{g1} \bar{u}_{g1}}{\bar{\epsilon}_g \phi_m D_c} \frac{r'^2}{R^2} C_{gu} \\ + \frac{U_G}{\bar{\epsilon}_g \phi_m D_c} C_{g,m} - \frac{k_{CST} a_{CST}}{\bar{\epsilon}_g} (HC_{gu} - C_{lu}) + R_{x,gu} \end{array} \right\}$	$\frac{dC_{gu}}{dt} = \left\{ \begin{array}{l} \frac{\bar{\epsilon}_{g2} \bar{u}_{g2}}{\bar{\epsilon}_g \phi_m D_c} \frac{(R^2 - r'^2)}{R^2} C_{g2} \Big _{x=0} - \frac{k_{CST} a_{CST}}{\bar{\epsilon}_g} (HC_{gu} - C_{lu}) \\ - \frac{(\bar{\epsilon}_{g1} \bar{u}_{g1} + \bar{\epsilon}_{g3} \bar{u}_{g3}) r'^2}{\bar{\epsilon}_g \phi_m D_c} \frac{C_{gu}}{R^2} + \frac{U_G}{\bar{\epsilon}_g \phi_m D_c} C_{g,m} + R_{x,gu} \end{array} \right\}$
Liquid in the Distributor Zone	
$\frac{dC_{lu}}{dt} = \left\{ \begin{array}{l} \frac{\bar{\epsilon}_{l2} \bar{u}_{l2}}{\bar{\epsilon}_l \phi_m D_c} \frac{(R^2 - r'^2)}{R^2} C_{l2} \Big _{x=0} - \frac{\bar{\epsilon}_{l1} \bar{u}_{l1}}{\bar{\epsilon}_l \phi_m D_c} \frac{r'^2}{R^2} C_{lu} \\ + \frac{U_L}{\bar{\epsilon}_l \phi_m D_c} C_{l,m} + \frac{k_{CST} a_{CST}}{\bar{\epsilon}_l} (HC_{gu} - C_{lu}) + R_{x,lu} \end{array} \right\}$	$\frac{dC_{lu}}{dt} = \left\{ \begin{array}{l} \frac{\bar{\epsilon}_{l2} \bar{u}_{l2}}{\bar{\epsilon}_l \phi_m D_c} \frac{(R^2 - r'^2)}{R^2} C_{l2} \Big _{x=0} - \frac{\bar{\epsilon}_{l1} \bar{u}_{l1}}{\bar{\epsilon}_l \phi_m D_c} \frac{r'^2}{R^2} C_{lu} \\ + \frac{U_L}{\bar{\epsilon}_l \phi_m D_c} C_{l,m} + \frac{k_{CST} a_{CST}}{\bar{\epsilon}_l} (HC_{gu} - C_{lu}) + R_{x,lu} \end{array} \right\}$
Gas in the Disengagement Zone	
$\frac{dC_{gb}}{dt} = \left\{ \begin{array}{l} \frac{\bar{\epsilon}_{g1} \bar{u}_{g1}}{\bar{\epsilon}_g \phi_{out} D_c} \frac{r'^2}{R^2} C_{g1} \Big _{x=L} - \frac{\bar{\epsilon}_{g2} \bar{u}_{g2}}{\bar{\epsilon}_g \phi_{out} D_c} \frac{(R^2 - r'^2)}{R^2} C_{gb} \\ - \frac{U_G}{\bar{\epsilon}_g \phi_{out} D_c} C_{g,b} - \frac{k_{CST} a_{CST}}{\bar{\epsilon}_g} (HC_{gb} - C_{lb}) + R_{x,gb} \end{array} \right\}$	$\frac{dC_{gb}}{dt} = \left\{ \begin{array}{l} \frac{\bar{\epsilon}_{g1} \bar{u}_{g1}}{\bar{\epsilon}_g \phi_{out} D_c} \frac{r'^2}{R^2} C_{g1} \Big _{x=L} + \frac{\bar{\epsilon}_{g3} \bar{u}_{g3}}{\bar{\epsilon}_g \phi_{out} D_c} \frac{r'^2}{R^2} C_{g3} \Big _{x=L} \\ - \frac{U_G}{\bar{\epsilon}_g \phi_{out} D_c} C_{g,b} - \frac{\bar{\epsilon}_{g2} \bar{u}_{g2}}{\bar{\epsilon}_g \phi_{out} D_c} \frac{(R^2 - r'^2)}{R^2} C_{gb} \\ - \frac{k_{CST} a_{CST}}{\bar{\epsilon}_g} (HC_{gb} - C_{lb}) + R_{x,gb} \end{array} \right\}$
Liquid in the Disengagement Zone	
$\frac{dC_{lb}}{dt} = \left\{ \begin{array}{l} \frac{\bar{\epsilon}_{l1} \bar{u}_{l1}}{\bar{\epsilon}_l \phi_{out} D_c} \frac{r'^2}{R^2} C_{l1} \Big _{x=L} - \frac{\bar{\epsilon}_{l2} \bar{u}_{l2}}{\bar{\epsilon}_l \phi_{out} D_c} \frac{(R^2 - r'^2)}{R^2} C_{lb} \\ - \frac{U_L}{\bar{\epsilon}_l \phi_{out} D_c} C_{lb} + \frac{k_{CST} a_{CST}}{\bar{\epsilon}_l} (HC_{gb} - C_{lb}) + R_{x,lb} \end{array} \right\}$	$\frac{dC_{lb}}{dt} = \left\{ \begin{array}{l} \frac{\bar{\epsilon}_{l1} \bar{u}_{l1}}{\bar{\epsilon}_l \phi_{out} D_c} \frac{r'^2}{R^2} C_{l1} \Big _{x=L} - \frac{\bar{\epsilon}_{l2} \bar{u}_{l2}}{\bar{\epsilon}_l \phi_{out} D_c} \frac{(R^2 - r'^2)}{R^2} C_{lb} \\ - \frac{U_L}{\bar{\epsilon}_l \phi_{out} D_c} C_{lb} + \frac{k_{CST} a_{CST}}{\bar{\epsilon}_l} (HC_{gb} - C_{lb}) + R_{x,lb} \end{array} \right\}$
Boundary Conditions for the Well-Developed Flow Zones	
Up-Flowing Gas	Up-Flowing Gas (Small Bubbles)
$\bar{u}_{g1} C_{g1} \Big _{x=0} - \bar{D}_{x1} \frac{\partial C_{g1}}{\partial x} \Big _{x=0} = \bar{u}_{g1} C_{gu} \quad \frac{\partial C_{g1}}{\partial x} \Big _{x=L} = 0$	$\bar{u}_{g1} C_{g1} \Big _{x=0} - \bar{D}_{x1} \frac{\partial C_{g1}}{\partial x} \Big _{x=0} = \bar{u}_{g1} C_{gu} \quad \frac{\partial C_{g1}}{\partial x} \Big _{x=L} = 0$
	Up-Flowing Gas (Large Bubbles)
	$C_{g3} \Big _{x=0} = C_{gu}$
Up-Flowing Liquid	Up-Flowing Liquid
$\bar{u}_{l1} C_{l1} \Big _{x=0} - \bar{D}_{x1} \frac{\partial C_{l1}}{\partial x} \Big _{x=0} = \bar{u}_{l1} C_{lu} \quad \frac{\partial C_{l1}}{\partial x} \Big _{x=L} = 0$	$\bar{u}_{l1} C_{l1} \Big _{x=0} - \bar{D}_{x1} \frac{\partial C_{l1}}{\partial x} \Big _{x=0} = \bar{u}_{l1} C_{lu} \quad \frac{\partial C_{l1}}{\partial x} \Big _{x=L} = 0$
Down-Flowing Gas	Down-Flowing Gas (Small Bubbles)
$\bar{u}_{g2} C_{g2} \Big _{x=L} + \bar{D}_{x2} \frac{\partial C_{g2}}{\partial x} \Big _{x=L} = \bar{u}_{g2} C_{gb} \quad \frac{\partial C_{g2}}{\partial x} \Big _{x=0} = 0$	$\bar{u}_{g2} C_{g2} \Big _{x=L} + \bar{D}_{x2} \frac{\partial C_{g2}}{\partial x} \Big _{x=L} = \bar{u}_{g2} C_{gb} \quad \frac{\partial C_{g2}}{\partial x} \Big _{x=0} = 0$
Down-Flowing Liquid	Down-Flowing Liquid
$\bar{u}_{l2} C_{l2} \Big _{x=L} + \bar{D}_{x2} \frac{\partial C_{l2}}{\partial x} \Big _{x=L} = \bar{u}_{l2} C_{lb} \quad \frac{\partial C_{l2}}{\partial x} \Big _{x=0} = 0$	$\bar{u}_{l2} C_{l2} \Big _{x=L} + \bar{D}_{x2} \frac{\partial C_{l2}}{\partial x} \Big _{x=L} = \bar{u}_{l2} C_{lb} \quad \frac{\partial C_{l2}}{\partial x} \Big _{x=0} = 0$

In view of Tables B-1 and B-2, one can understand the pitfalls resulting from the use of the “old” Danckwerts’ boundary conditions. To further elaborate on the problem

associated with the Danckwerts' boundary conditions similar to that depicted in Figure B-1, let us consider the transport of a non-volatile liquid tracer for the reactor compartmentalization presented in Chapter 7. To accentuate the effect of the incorrect boundary conditions on the computed response, let us further assume that there is no cross-flow exchange between the up-flowing and down-flowing liquid zones. Then, based on the imposed old Danckwerts' boundary condition at $x = L$ of $\partial C_{11}/\partial x = 0$, a liquid tracer injected into the disengagement CST at the top of the column could not propagate into the well developed up-flow region until it is transported through the down-flow region and appears into the up-flow region from the bottom. In reality, however, axial diffusion of the tracer injected into the stirred tank at the top would immediately cause it to diffuse against the flow, since the concentration at the top of the up-flow region is the same as that in the disengagement CST. This is reflected in the correct boundary condition of $C_{11} = C_{1b}$ at $x = L$. The effects described above can be clearly seen from Figure B-2 which shows the simulation results computed using the "Old" and the "New" boundary conditions for a hypothetical situation of a liquid tracer injected in the disengagement CST with the operating conditions being those during FT-IV synthesis (Run 16.7). It can be shown that for tracer injections close to the bottom of the column, however, both types of conditions lead to almost the same results.



(a)



(b)

Figure B-2. Hypothetical case of “liquid-like” (Mn₂O₃) tracer injection in the disengagement CST. Tracer concentration a) at the bottom-end of the down-flow zone b) at the top-end of the up-flow zone.

The effect of these two alternate boundary condition formulations on the computed tracer responses is further illustrated in the Figures B-3 and B-4. For the purposes of these demonstrations, the examples chosen are the simulation of the tracer responses for the FT-IV tracer tests reported in Chapter 7. Measurement levels “Lev1” (13.5” on outside tape), “Lev4” (116” on outside tape) and “Lev8” (215” on outside tape) as shown in Figure 7-7 were chosen for the purposes of this examination.

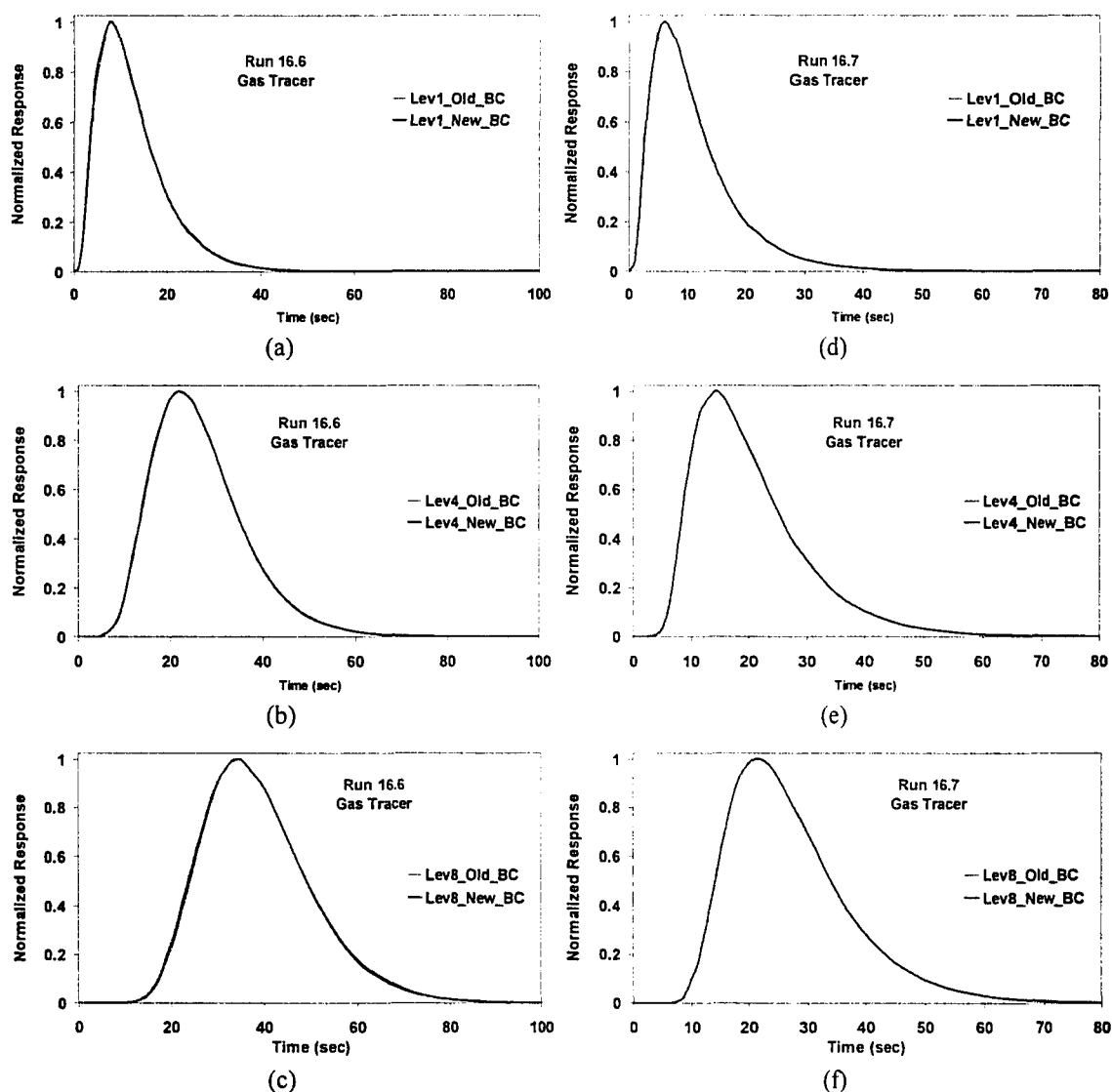


Figure B-3. Effect of alternate boundary conditions on FT-IV gas tracer responses.

In the figures showing this comparison (Figures B-3 and B-4), “Old_BC” refers to the “incorrect” Danckwerts’ boundary conditions while “New_BC” refers to the “correct” Dirichlet boundary conditions. Figure B-3 shows the effect of the “New” and “Old” boundary conditions on gas phase responses for Runs 16.6 and 16.7. It can be concluded from the figure that the change in boundary conditions has a negligible effect on simulated responses computed from the gas phase mixing model for the experimental conditions of this study.

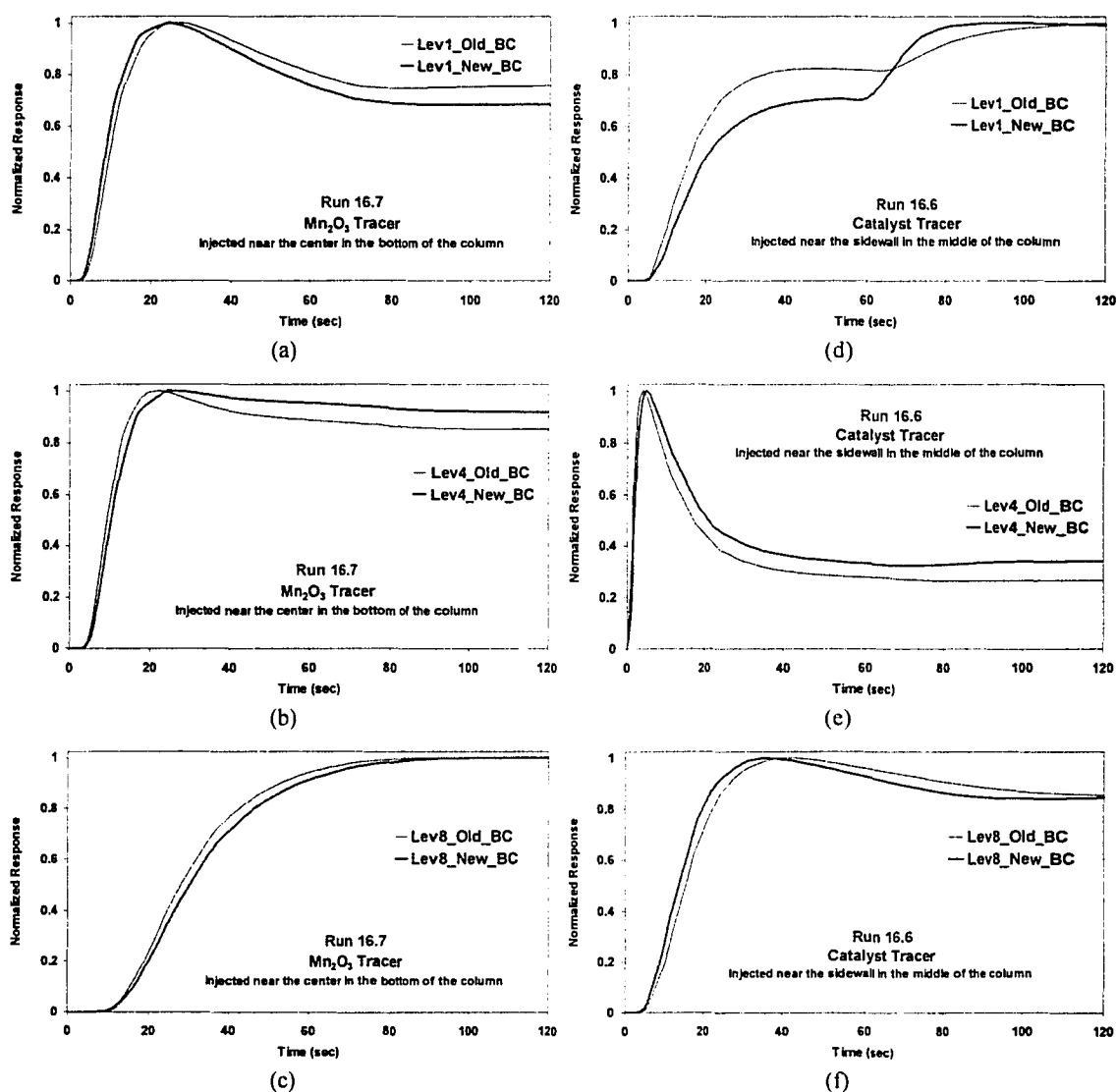


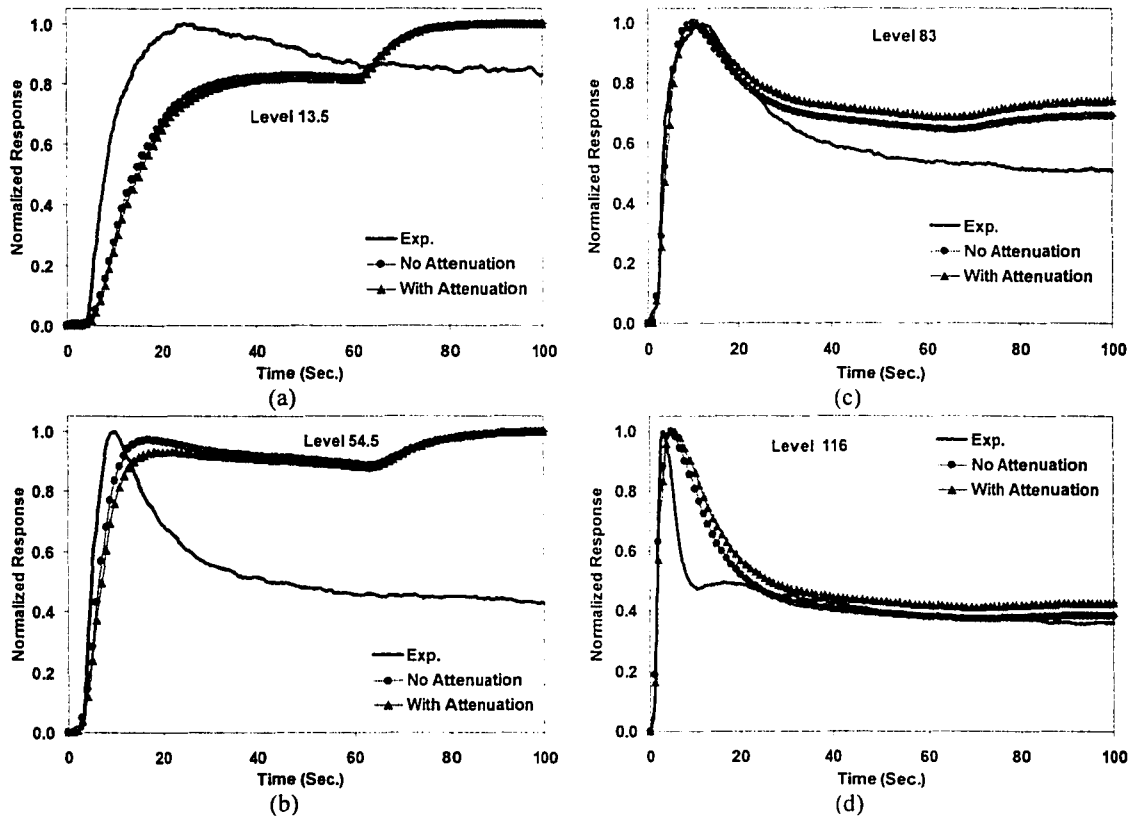
Figure B-4. Effect of alternate boundary conditions on FT-IV “liquid-like” (Mn_2O_3) and catalyst tracer responses.

Figure B-4 (a-c) show the effect of the “old” and “new” boundary conditions on the “liquid-like” tracer responses corresponding to Run 16.7 while Figure B-4 (d-f) shows those for the catalyst tracer responses corresponding to Run 16.6. It can be seen from these figures that for the liquid mixing simulations, the difference exists but is not significant except for Level-1 of Run 16.6 for the catalyst where the difference is quite pronounced. Since this was the low superficial gas velocity case, it is not surprising that the effect of improper boundary conditions is magnified due to slower mixing.

In conclusion, it can be seen that it is vital to impose correct boundary conditions at the end of the well-developed zones pertinent to the reactor compartmentalization based on the models developed in this study. The effect of the boundary conditions is insignificant when the tracer is injected into the reactor inlet, as was the case for the gas tracer injections for both the methanol as well as the FT-IV runs. However, when the tracer injection point is anywhere other than the inlet stream or the inlet CST, the effect of the use of incorrect boundary conditions would be encountered. This effect would increasingly worsen as the tracer injection point is moved closer to the outlet of the well-developed zones. For much of the earlier work reported by Degaleesan (1997) on the liquid and catalyst tracer tests during the methanol runs, since the majority of tracer mixing was due to the recirculatory flow of the liquid/slurry phase, the effect of the incorrect boundary conditions on the computed responses would be minimal. However, for unidirectional flows or recirculatory flows with no cross-mixing and tracer injection close to the exit, major problems would arise as shown in Figure B-2. Thus, realizing the problem with the use of incorrect Danckwerts’ boundary conditions, all tracer responses reported in this study were recomputed with the correct “Dirichlet” boundary conditions and contain no artifact originating from the use of Danckwerts’ boundary conditions.

Appendix C. Comparison of FT-IV Experimental Data with Simulation Results from Mixing Models

This appendix presents the comparison of simulation results from mixing models with experimental data *at every axial level* for the FT-IV tracer tests conducted at the AFDU. These are being presented here for the sake of completeness since only selected results relevant to the discussion were presented in Chapter 7.



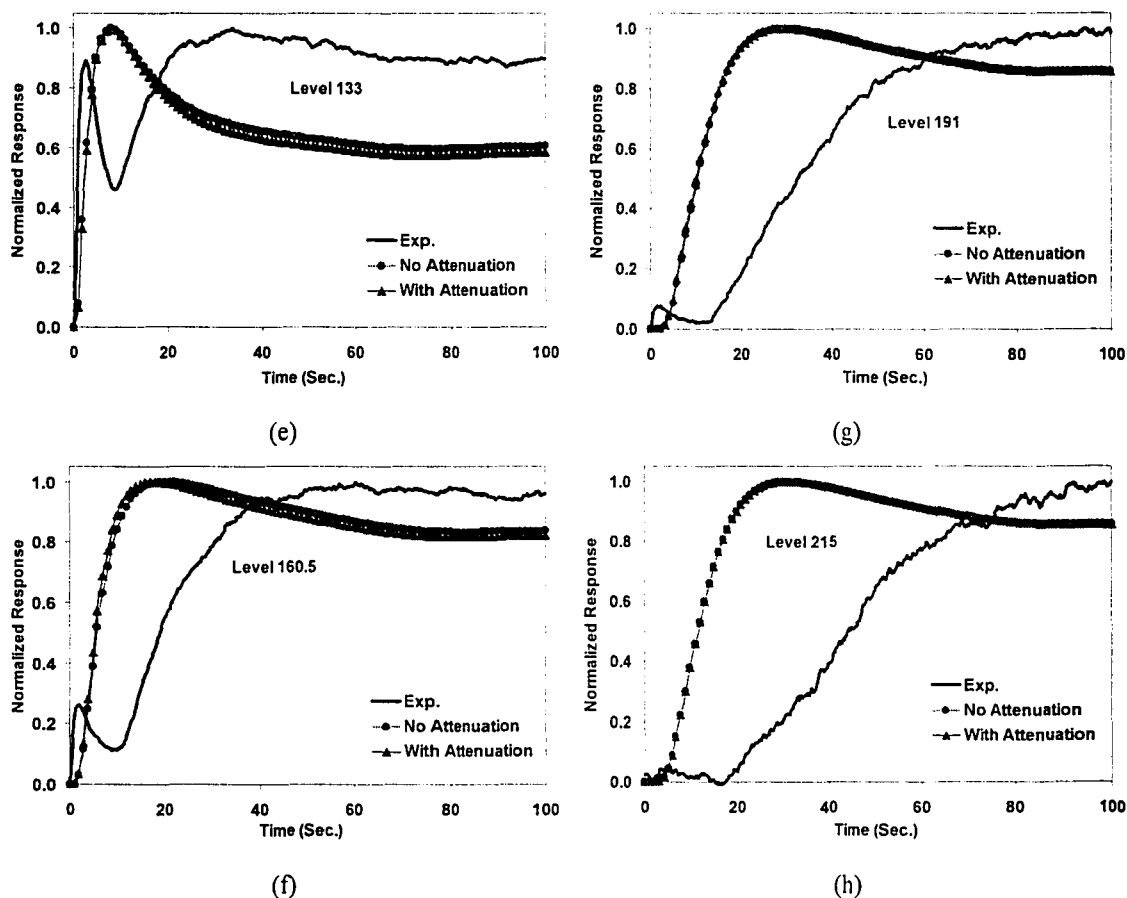
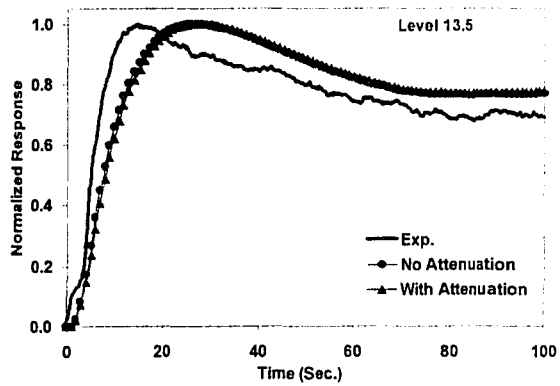
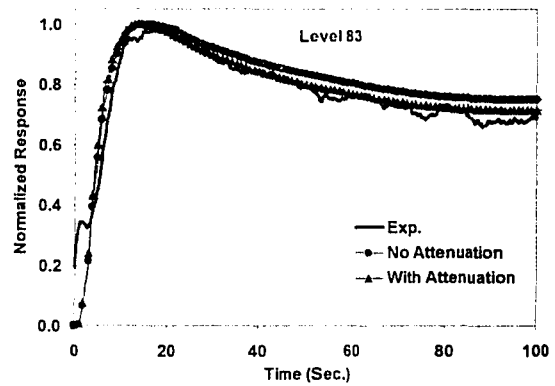


Figure C-1. Comparison of experimental and simulated tracer responses for Run 16.6 (Tracer: - Catalyst; Injection Pt.: - Sidewall-Middle).

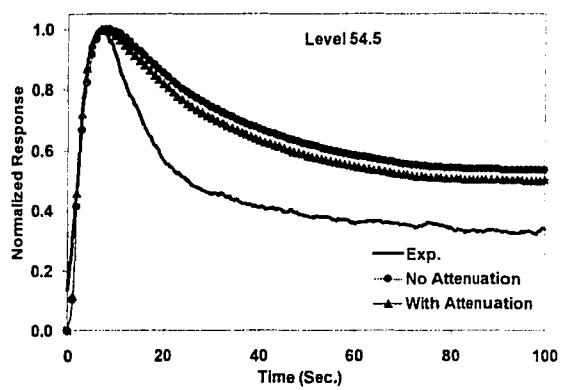
In Figure C-1 as well as in all the rest of the figures in this appendix, sub-figures (a)-(h) represent the eight detector levels where measurements were taken and comparison with simulations from mixing models are reported. From Figure C-1, it can be seen that the comparison of the simulations results with data is poor. As mentioned earlier in Chapter 7, for the sidewall injection of liquid-like or catalyst tracer and especially for the operating conditions of Run 16.6, the assumptions of mixing models are probably violated severely resulting in poor comparison of simulations with data.



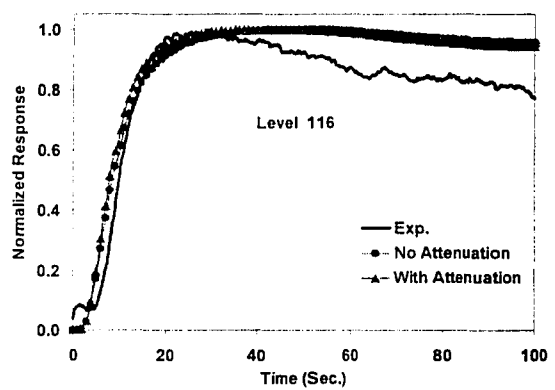
(a)



(c)



(b)



(d)

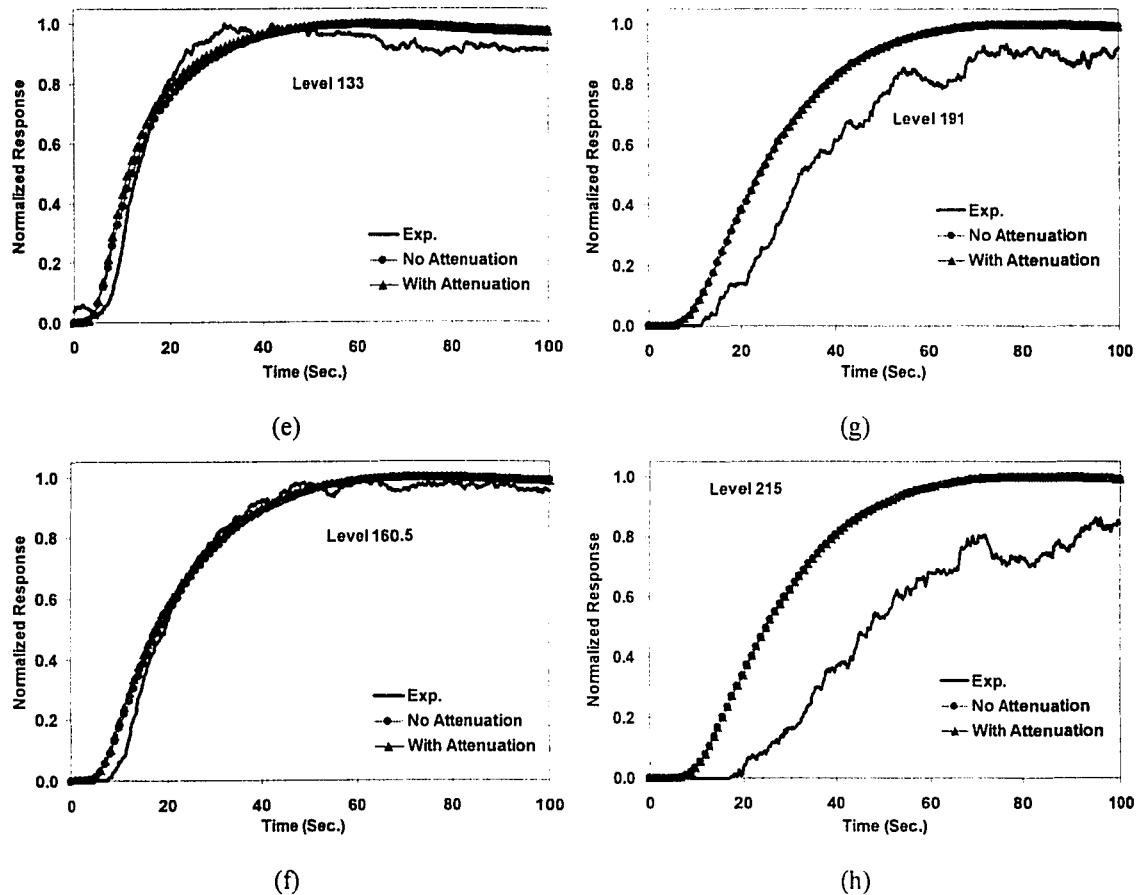
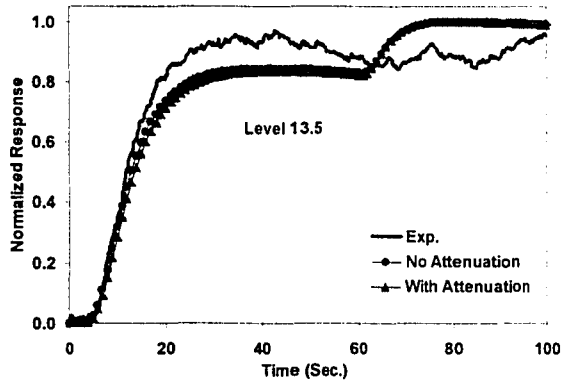
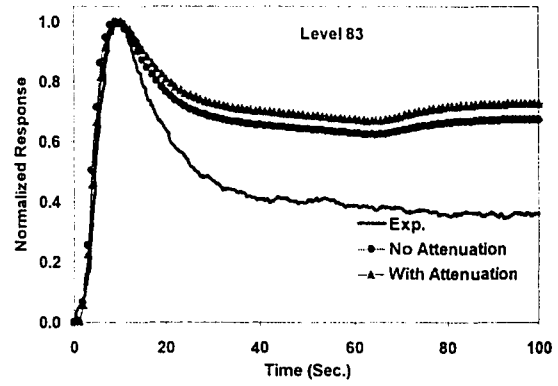


Figure C-2. Comparison of experimental and simulated tracer responses for Run 16.6 (Tracer: - Catalyst; Injection Pt.: - Center-Bottom).

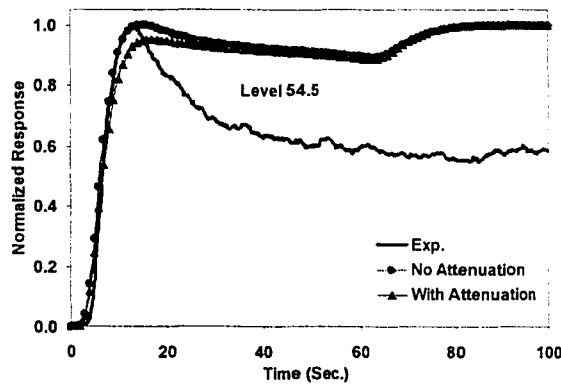
Figure C-2 shows the comparison of experimental and simulated tracer responses for the catalyst tracer injected in the bottom-center location. As mentioned earlier in Chapter 7, this is a preferred injection location as it is further away from the slurry exit. As a result, the model assumptions of axisymmetry are valid to a greater extent, and this is evident from a substantially improved agreement between simulations and data. For the two highest detector-levels (191 and 215 inches as referenced on the outside tape) however, the experimental responses are still much delayed in time compared to simulations. This points to the presence of a foamy two-phase mixture at the very top of the liquid-slurry dispersion with the density of foam increasing from level 191 to level 215.



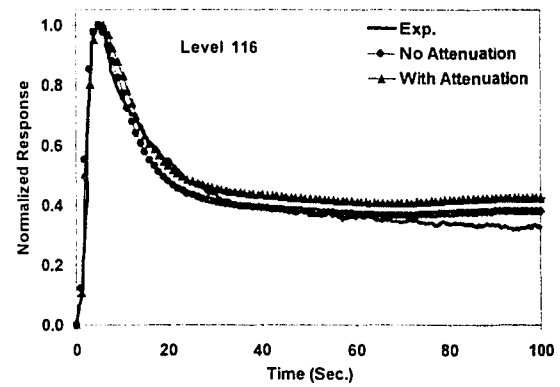
(a)



(c)



(b)



(d)

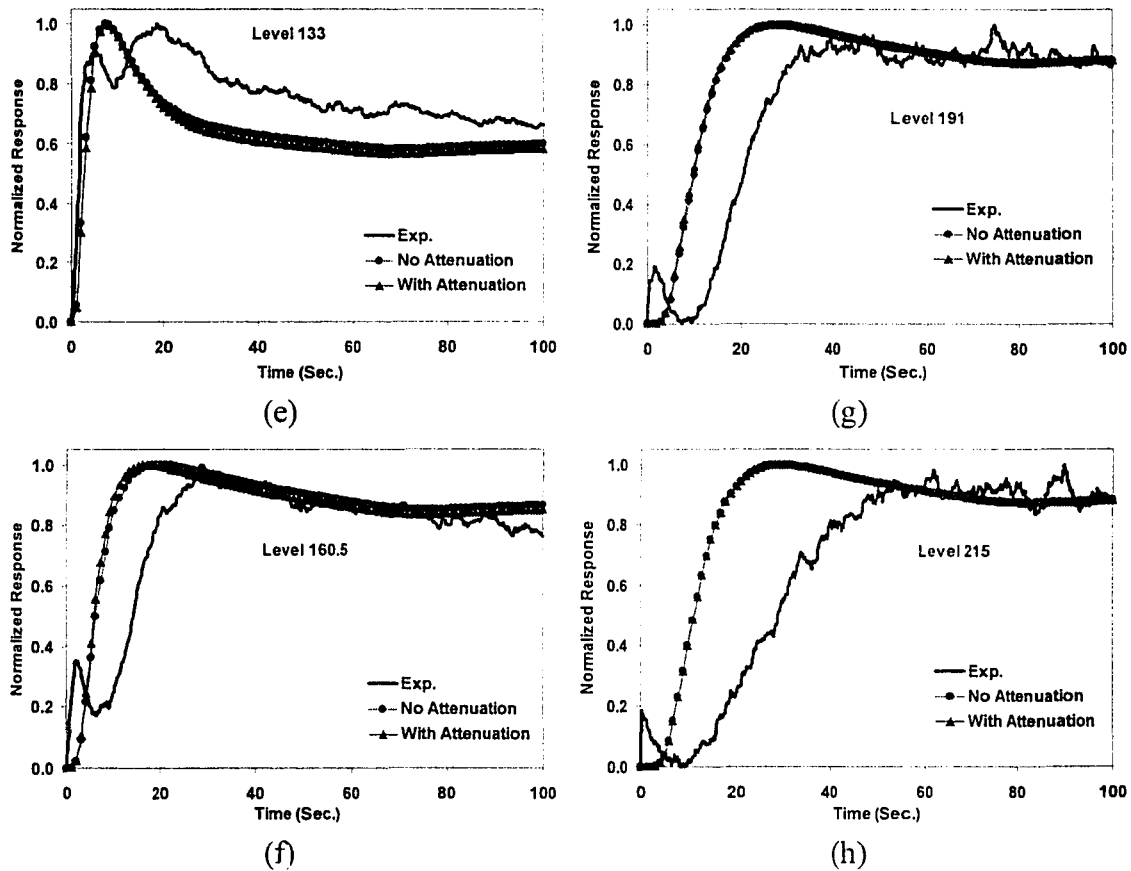
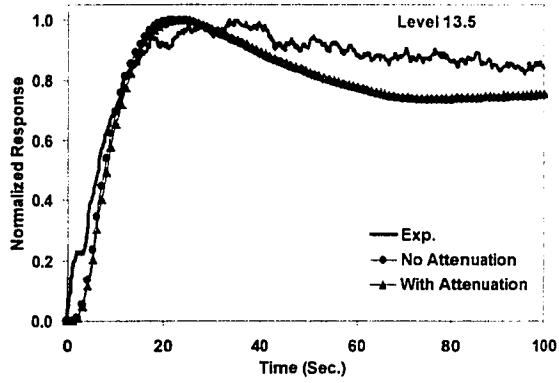
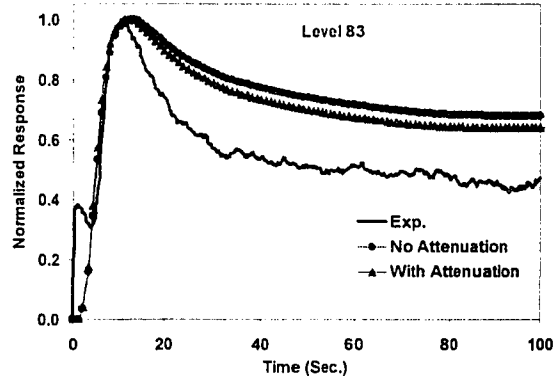


Figure C-3. Comparison of experimental and simulated tracer responses for Run 16.7 (Tracer: - Catalyst; Injection Pt.: - Sidewall-Middle).

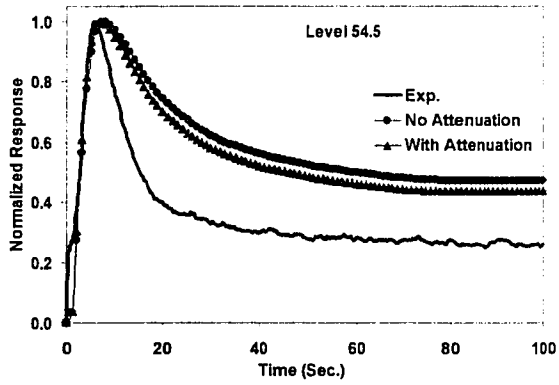
Figure C-3 shows the comparison of the experimental as simulated tracer responses for the middle-sidewall injection of the catalyst tracer during Run 16.7. As for Run 16.6, the general agreement between simulated and experimental responses is not good, however it is much better than that for run 16.6. This is due to the higher superficial gas velocity employed during Run 16.7 which results in better radial mixing and consequently better realization of the liquid mixing model assumptions compared to Run 16.6.



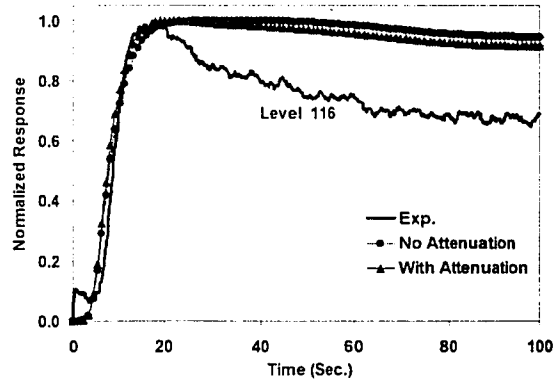
(a)



(c)



(b)



(d)

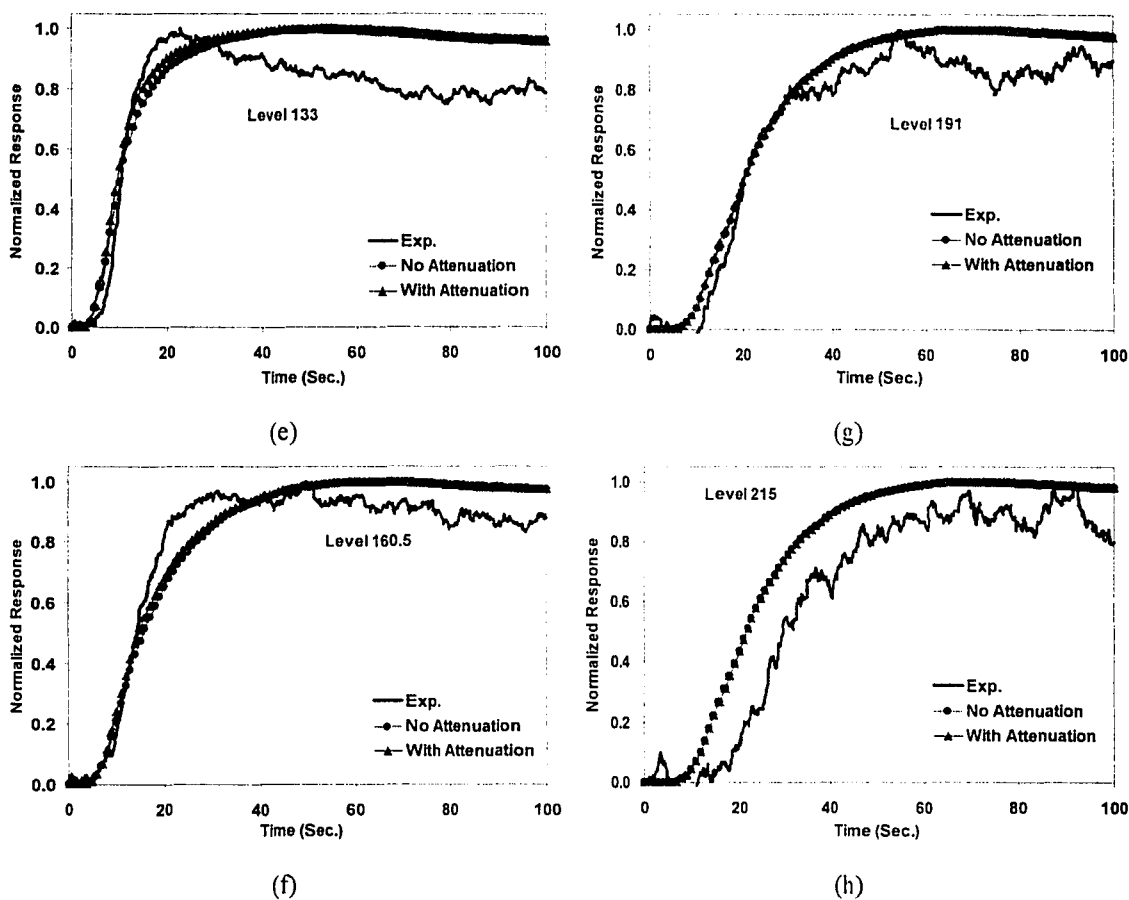
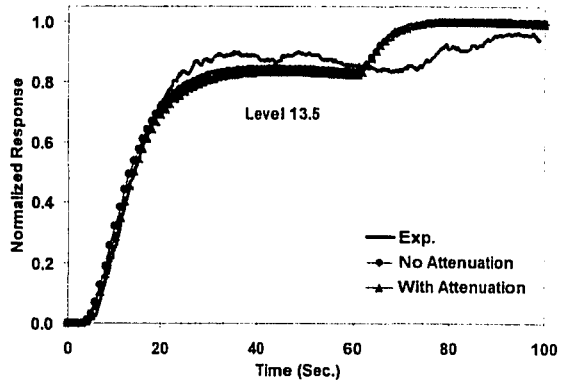
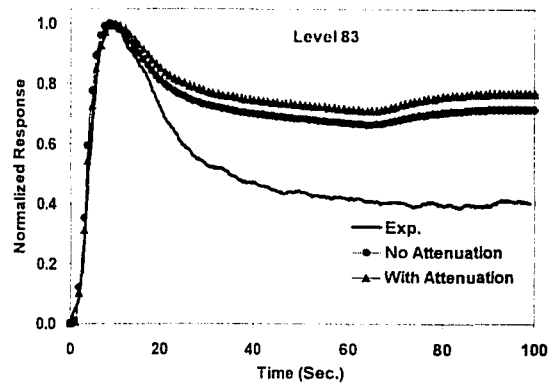


Figure C-4. Comparison of experimental and simulated tracer responses for Run 16.7 (Tracer: - Catalyst; Injection Pt.: - Center-Bottom).

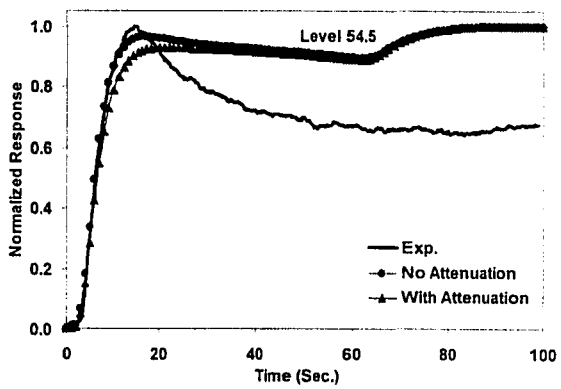
Figure C-4 provides a comparison of the experimental and simulated responses for the catalyst tracer injected into the bottom-center of the reactor. As for Run 16.6, the agreement between simulations and data is much better as compared to the middle-sidewall injection of the tracer. In addition, the higher superficial gas velocity of Run 16.7 also provides for a relatively quicker radial mixing of the tracer than that for Run 16.6. This implies that model assumptions are better satisfied in Run 16.7 than in Run 16.6 and consequently leads to better agreement between simulations and data. Furthermore, since the operating conditions of Run 16.6 may be closer to transition, there exist additional uncertainty with regards to the realization of the model assumption for this case.



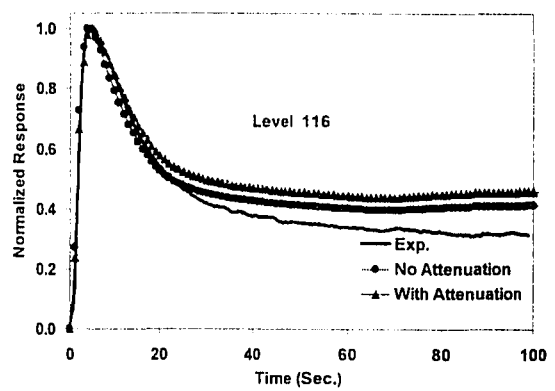
(a)



(c)



(b)



(d)

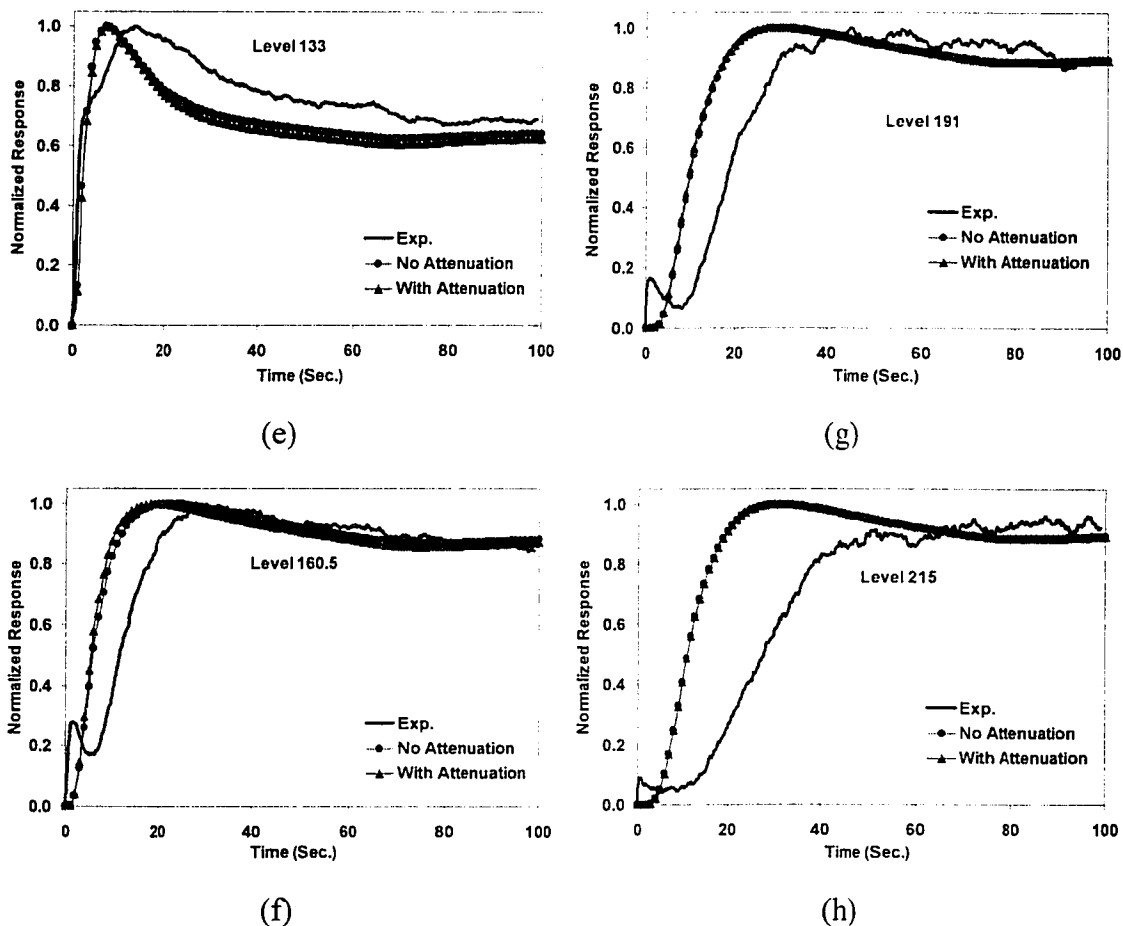
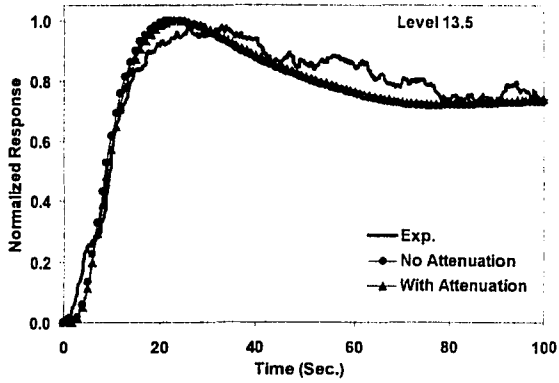
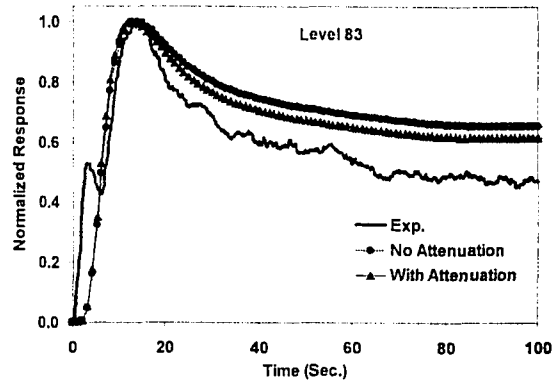


Figure C-5. Comparison of experimental and simulated tracer responses for Run 16.7 (Tracer: - Mn_2O_3 ; Injection Pt.: - Sidewall-Middle).

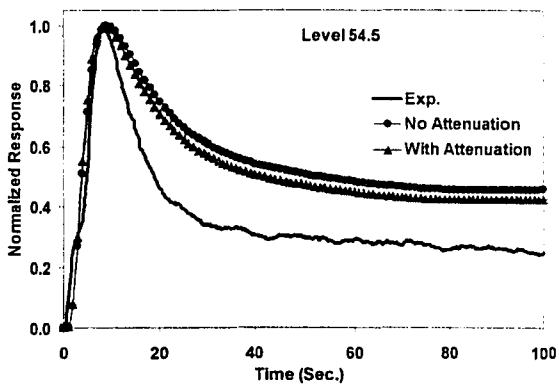
The trends in the comparison of experimental responses with simulations in Figure C-5 are a reflection of the trends observed in Figure C-3 for the same operating conditions but using the Mn_2O_3 tracer instead of the catalyst tracer. In general, the agreement between simulations and experiments is fair for the lower four levels and deteriorates for the top four levels. This is most likely due to the dynamics originating from the presence of the slurry outlet in the middle of the column as well as the possible existence of a foamy structure near the top of the gas-slurry dispersion.



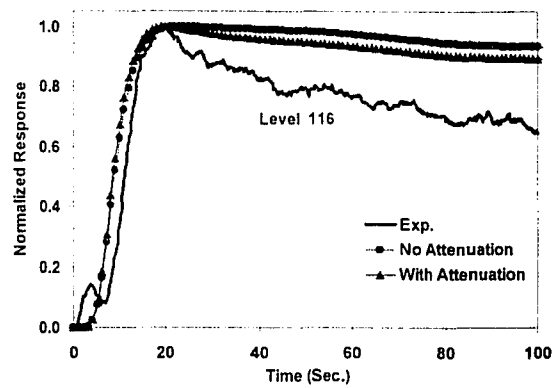
(a)



(c)



(b)



(d)

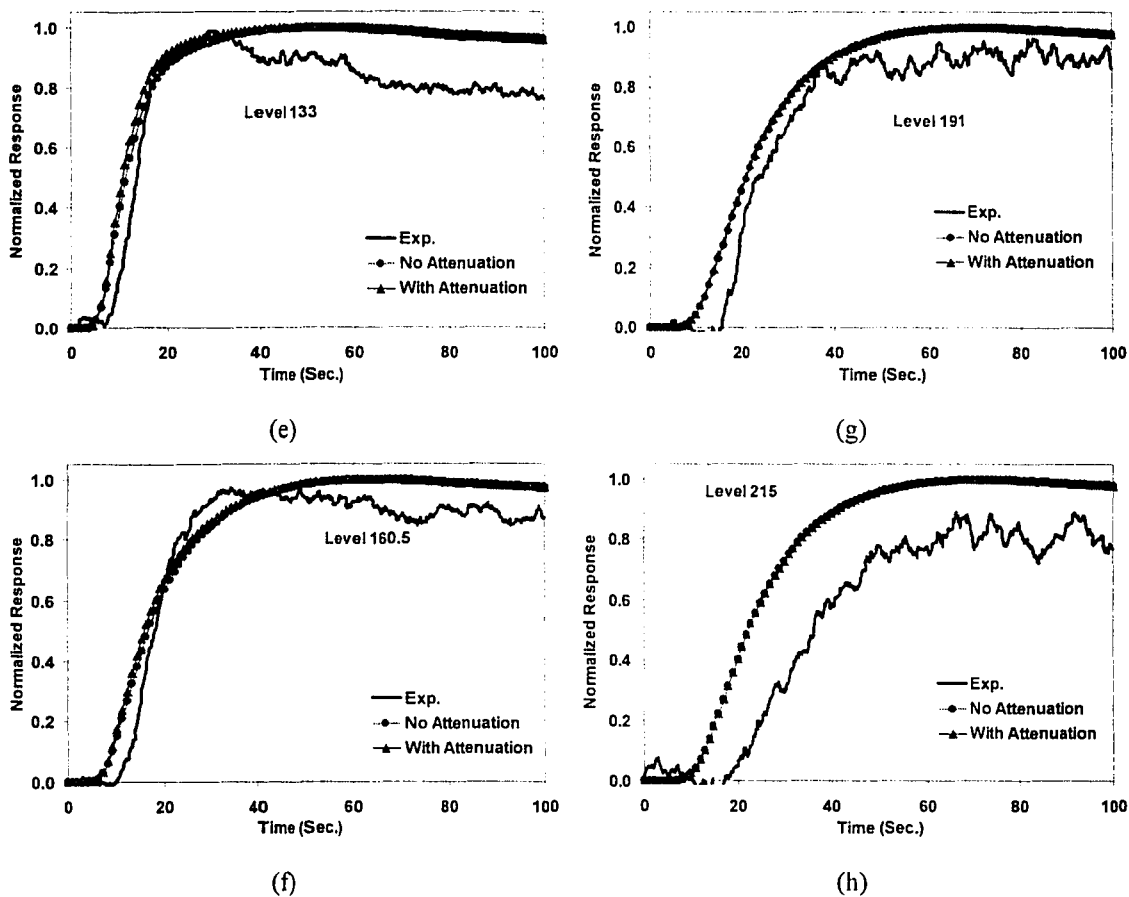
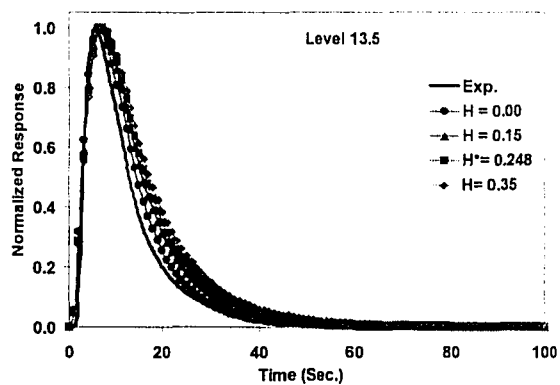


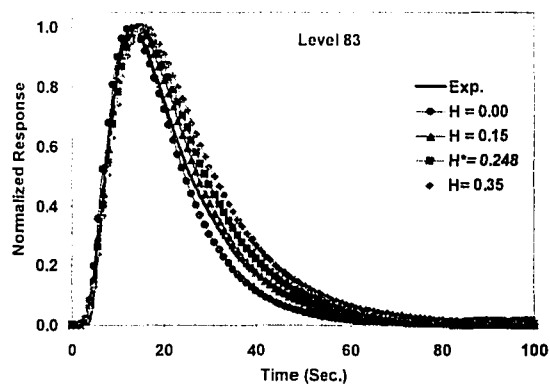
Figure C-6. Comparison of experimental and simulated tracer responses for Run 16.7 (Tracer: - Mn_2O_3 ; Injection Pt.: - Center-Bottom).

Figure C-6 provides comparison of the simulated and experimental responses for the Mn_2O_3 tracer injected into the bottom-center of the reactor. Given the nature of the tracer, the point of its injection as well as the operating conditions of Run 16.7, this experiment is the most likely to satisfy the maximum number of assumptions of the mixing model among all the liquid/catalyst tracer experiments that were performed. This is evident from the best comparison between experiments and simulations among all the liquid/catalyst tracer tests. Interestingly, even the comparison at level 191 is reasonably good, which was not the case for the catalyst tracer. This points to the better ability of the Mn_2O_3 tracer to follow the liquid phase as compared to the catalyst tracer that seems to have difficulties following the liquid/slurry phase as one approaches the top of the gas-

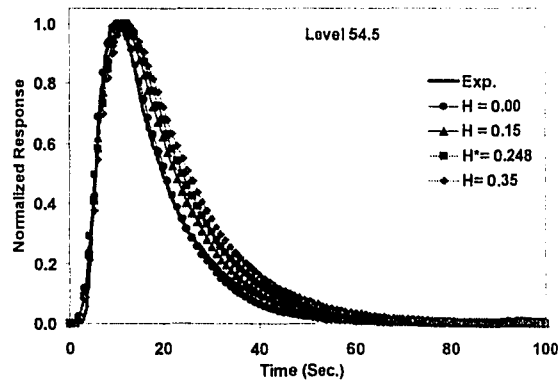
slurry dispersion. As mentioned earlier in Chapter 7, this is the result of the larger particle size of the catalyst as compared to Mn_2O_3 tracer.



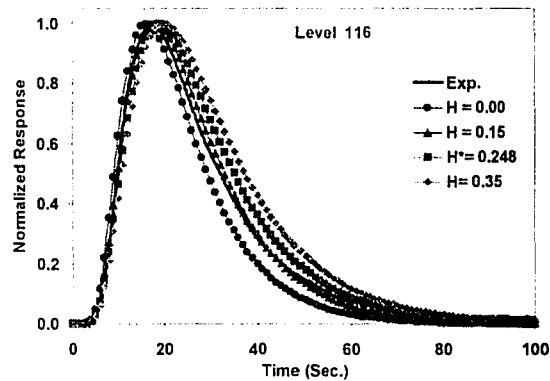
(a)



(c)



(b)



(d)

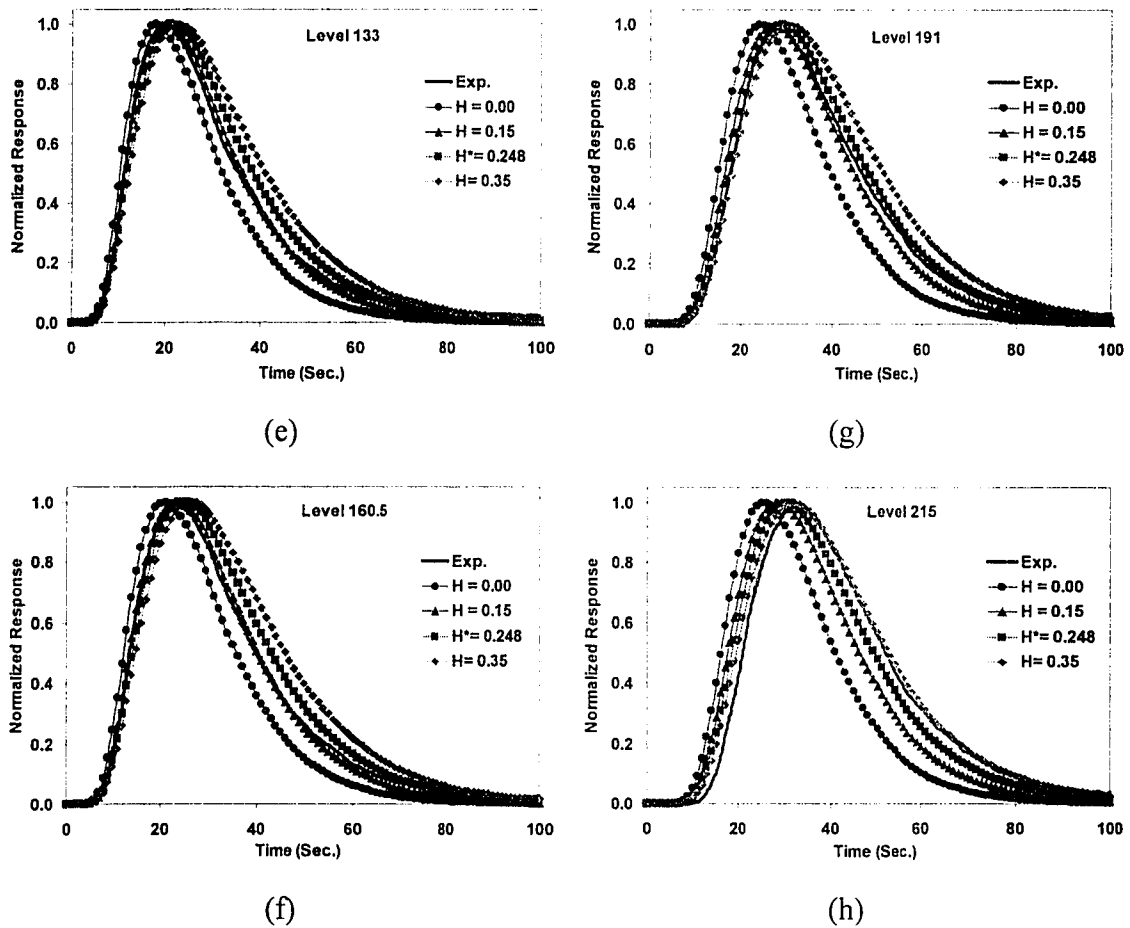
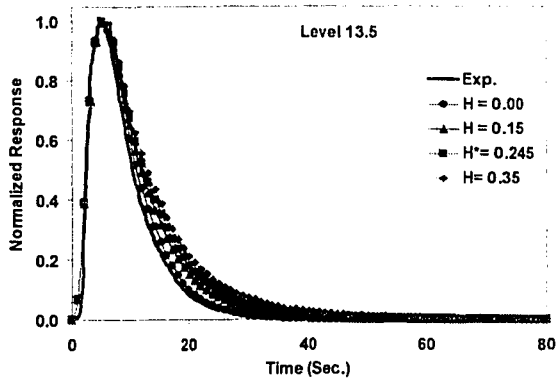
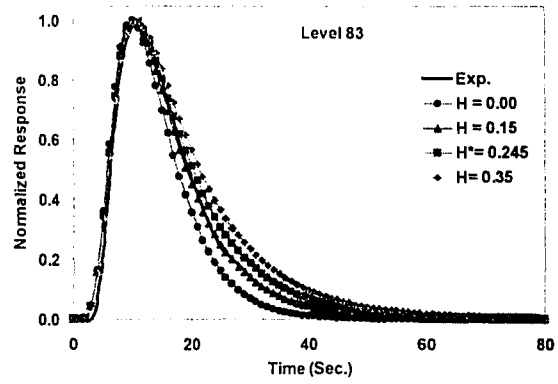


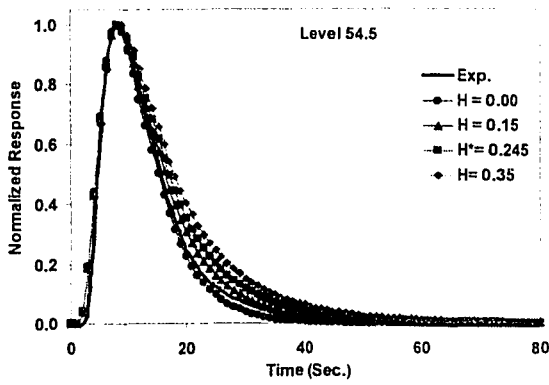
Figure C-7. Comparison of experimental and simulated gas tracer response curves for Run 16.6 for different Henry's constants.



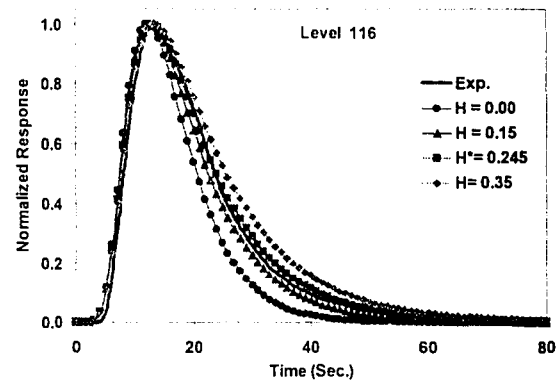
(a)



(c)



(b)



(d)

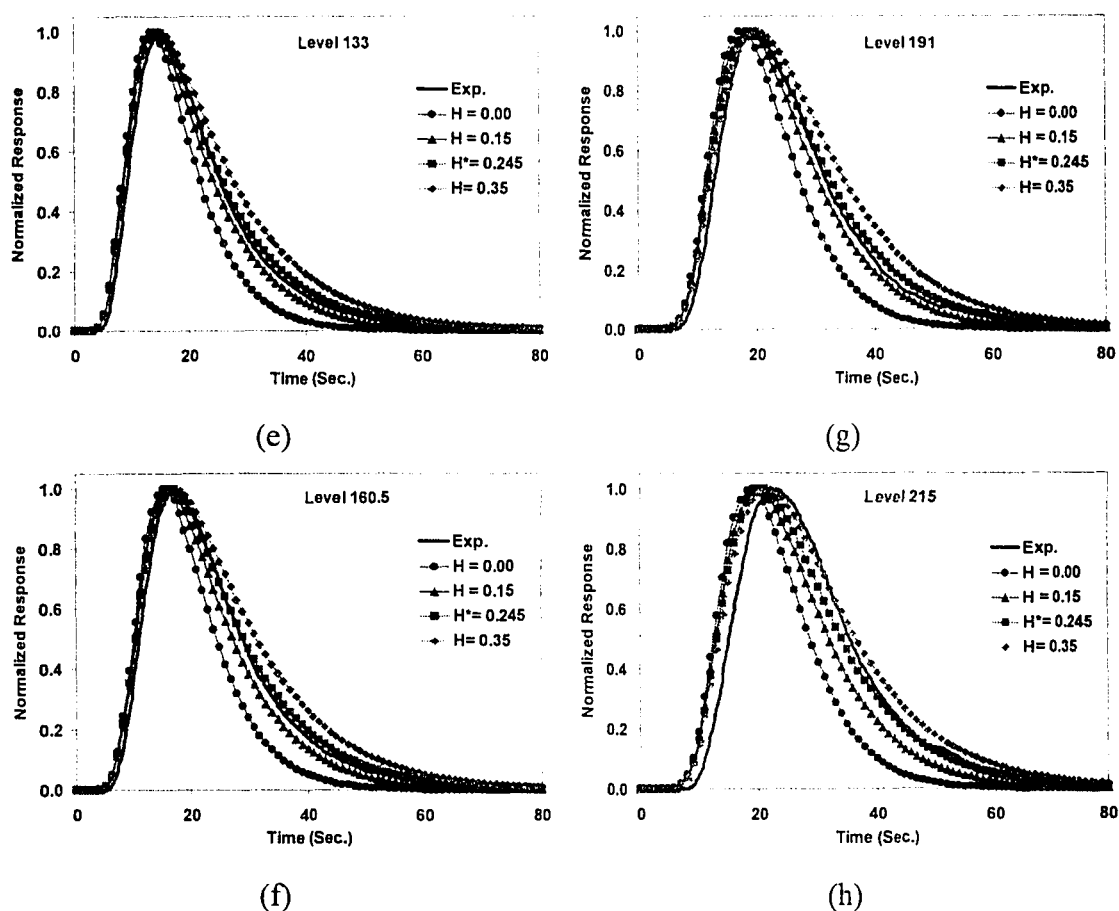


Figure C-8. Comparison of experimental and simulated gas tracer response curves for Run 16.7 for different Henry's constants.

Figures C-7 and C-8 provide a comparison of the experimental and simulated gas tracer responses for Runs 16.6 and 16.7 respectively. From the figures one can see that in general, for the thermodynamically estimated Henry's constant (H^*), the agreement between experiments and data is very good except for level 215 where the experimental response seems to have been delayed. This is observed in both Runs 16.6 and 16.7, and was also noticed in all the liquid/catalyst tracer tests, all pointing to the presence of a froth at the gas-slurry interface in the free-board region. Additionally, the simulations for Run 16.6 with $H=0.15$ indicate a better match with experimental data than those computed with $H=H^*$. As was mentioned earlier in Chapter 7, this could possibly be the

result of the uncertainties associated with the thermodynamic estimation of H given the complex molecular composition of the FT wax. Nevertheless, the good agreement between data and simulations in terms of the peak arrival time as well as the overall shape of the tracer responses indicates that given reliable inputs, the gas mixing model developed in this study is capable of predicting the dynamics of scalar gas-liquid transport in bubble and slurry bubble column reactors.

References

- Adkins, D. R., K. A., Shollenberger, T. J., O'Hern and J. R., Torczynski, 1996, 'Pressure Effects on Bubble Column Flow Characteristics', *ANS Proceedings*, 1996 National Heat Transfer Conference, **9**, 318-325.
- Akita, K., and Yoshida, F., 1973, 'Gas Holdup and Volumetric Mass Transfer Coefficient in Bubble Columns,' *Ind. Eng. Chem. Process Des. Dev.*, **12**, 76-80.
- Anderson, K. G. and Rice, R.G., 1989, 'Local Turbulence Model for Predicting Circulation Rates in Bubble Column,' *AIChE J.*, **35** (3), 514-518.
- Andreussi, P., A. Di Donfrancesco, and M. Messina, 1988, 'An Impedance Method for the Measurement of Liquid Hold-up in Two-phase Flow', *Int. J. Multiphase Flow*, **14**(6), 777-785.
- Armstrong, P.A., B. L., Bhatt, B. E., Latshaw, B. A. Toseland and R. P., Underwood, 1993, 'Isobutanol Dehydration in a Slurry-phase Reactor', *Proceedings of the Annual Int. Pittsburgh Coal Conference*, **10**, 1196-1199.
- Azbel, D., 1981, 'Two-phase Flows in Chemical Engineering', Cambridge University Press, Cambridge.
- Beam, G. B., L. Wielopolski, R. P. Gardner and K. Verghese, 1978, 'Monte Carlo Calculation of Efficiencies of Right-Circular Cylindrical NaI Detectors for Arbitrarily Located Point Sources', *Nuclear Instruments and Methods*, **154**(3), 501-508.

- Bhatt, B. L., 1999, 'Liquid Phase Fischer-Tropsch (III & IV) Demonstration in the La Porte Alternate Fuels Development Unit', *Topical report for Contract DE-FC22-95PC93052*.
- Boddem, M., and D. Mewes, 1996, 'Two-Phase Flow in the Upper Plenum of a PWR During ECC,' International Conference on Nuclear Engineering, **1**, Part B, 813-823, ASME 1996.
- Briens, C. L., C. Hudson and L. A. Briens, 1996, 'Rapid Characterization of Flow Regimes in Multiphase Reactors through Box-Counting Dimensions with an Embedding Dimension of Two,' *Chem. Eng. J.*, **64**, 169-178.
- Boisson, N. and M. R. Malin, 1996, 'Numerical Prediction of Two-Phase Flow in Bubble Columns,' *Int. J. Num. Methods in Fluids*, **23**, 1289-1310.
- Buchholz, R., W. Zakrzewski and K. Schügerl, 1981, 'Techniques for Determining the Properties of Bubbles in Bubble Columns', *Int. Chem. Eng.*, **21**(2), 180-187.
- Cameron, R. A., J. D. Kurfess, W. N. Johnson, R. L. Kinzer, R. A. Kroeger, M. D. Leising, R. J. Murphy, G. H. Share, M. S. Strickman, J. E. Grove, G. V. Jung, D. J. Grabelsky, S. M. Matz, W. R. Purcell and M. P. Ulmer, 1991, 'Operation and Performance of the OSSE Instrument', *NASA Conf. Publication* 3137, p3.
- Calderbank, P. H. and M. B., Moo-Young, 1961, 'The Continuous Phase Heat and Mass-Transfer Properties of Dispersion', *Chem. Eng. Sci.*, **16**, 39-54.
- Carbonell, M. M. and R. Guirardello, 1997, 'Modeling of a Slurry Bubble Column Reactor Applied to the Hydroconversion of Heavy Oils', *Chem. Eng. Sci.*, **52**(21/22), 4179-4185.

- Cartellier, A. and J. L. Achard, 1991, 'Local Phase Detection Probes in Fluid/Fluid Two-Phase Flows', *Rev. Sci. Instrum.*, **62**(2), 279-303.
- Cartellier, A., 1992, 'Simultaneous Void Fraction Measurement, Bubble Velocity, and Size Estimate Using a Single Optical Probe in Gas-Liquid Two-Phase Flows', *Rev. Sci. Instrum.*, **63** (11), 5442-5453.
- Chabot, J. and H. I., De Lasa, 1993, 'Gas Holdup and Bubble Characteristics in a Bubble Column Operated at High Temperature', *Ind. Eng. Chem. Res.*, **32**, 2595-2601.
- Chaouki, J., F. Larachi and M. P. Dudukovic', 1997, "Non-Invasive Monitoring of Multiphase Flows", Elsevier, New York.
- Chen, J., P., Gupta, S., Degaleesan, M. H., Al-Dahhan, M. P., Dudukovic and B. A., Toseland, 1998, 'Gas holdup distributions in large-diameter bubble columns measured by computed tomography', *Flow Measurement and Instrumentation*, **9**(2), 91-101.
- Chen, J., F., Li, S., Degaleesan, P., Gupta, M. H., Al-Dahhan, M. P., Dudukovic and B. A., Toseland, 1999, 'Fluid dynamic parameters in bubble columns with internals', *Chem. Eng. Sci.*, **54**(13-14), 2187-2197.
- Chen, R. C. and L. S., Fan, 1992, 'Particle Image Velocimetry for Characterizing the Flow Structure in three-dimensional Gas-Liquid-Solid Fluidized Beds', *Chem. Eng. Sci.*, **47**(13-14), 3615-3622.
- Chen, R. C., J., Reese and L. S., Fan, 1994, 'Flow Structure in a Three-Dimensional Bubble Column and a Three-Phase Fluidized Bed', *AIChE J.*, **40**, 1093-1104.
- Chisti, M. Y., 1989, 'Airlift Bioreactors', Elsevier Applied Science, London

- Choi, K. H. and W. K., Lee, 1990, 'Comparison of Probe Methods for Measurement of Bubble Properties', *Chem. Eng. Comm.*, **91**, 35-47.
- Choi, K. H., 1996, 'Circulation liquid velocity in external-loop airlift reactors', *Korean J. Chem. Eng.*, **13**(4), 379-383.
- Clift, R., J. R. Grace and M. E. Weber, 1978, 'Bubbles, Drops, and Particles', Academic Press, New York.
- Danckwerts, P. V., 1970, 'Gas-Liquid Reactions', McGraw Hill Co., New York.
- Dassori, C. G., 1998, 'Three-phase Reactor Modeling with Significant Backmixing in the Liquid Phase Using a Modified Cell Model (MCM)', *Comp. Chem. Eng.*, **22**, S679-S682.
- Debellefontaine, H., S. Crispel, P. Reihac, F. Perie and J. Foussard, 1999, 'Wet Air Oxidation (WAO) for the Treatment of Industrial Wastewater and Domestic Sludge. Design of Bubble Column Reactors', *Chem. Eng. Sci.*, **54**(21), 4953-4959.
- Deckwer, W. D., Louisi, Y., Zaidi, A., and Ralek, M., 1980, 'Hydrodynamic Properties of the Fischer-Tropsch Slurry Process,' *Ind. Eng. Chem. Process Des. Dev.*, **19**, 699-708.
- Deckwer, W. -D., 1981, 'Access of Hydrodynamic Parameters Required in the Design and Scale-Up of Bubble Column Reactors', *ACS Symp. Ser.*, **168**(Chem. React.), 213-41.
- Deckwer, W. -D., Nguyen-Tien, K., Kelkar, B. G. and Shah, Y. T., 1983, 'Applicability of axial dispersion model to analyze mass transfer measurements in bubble columns', *AIChE J.*, **29**(6), 915

Deckwer, W., 1992, 'Bubble Column Reactors', John Wiley & Sons.

Degaleesan, S., M. P. Dudukovic', B. L. Bhatt and B. A. Toseland, 1996^a, 'Slurry Bubble Column Hydrodynamics: Tracer Studies of the La Porte AFDU Reactor During Methanol Synthesis', *Fourth quarterly report for Contract DOE-FC 2295 PC 95051*.

Degaleesan, S., S. Roy, S. B. Kumar and M. P. Dudukovic', 1996^b, 'Liquid Backmixing Based on Convection and Turbulent Dispersion in Bubble Columns', *Chem. Eng. Sci.*, **51**, 1967-1976.

Degaleesan, S., 1997, *Fluid Dynamic Measurements and Modeling of Liquid Mixing in Bubble Columns*, D.Sc. Thesis, Washington University, Saint Louis, Missouri.

Degaleesan, S. and M. P. Dudukovic', 1999, 'Liquid Backmixing in Bubble Columns and the Axial Dispersion Coefficient', *AIChE J.*, **44**(11), 2369-2378.

Delnoij, E., F. A., Lammers, J. A. M., Kuipers and W. P. M., van Swaaij, 1997, 'Dynamic Simulation of Dispersed Gas-Liquid Two-Phase Flow Using a Discrete Bubble Model', *Chem. Eng. Sci.*, **52**, 1429-1458.

de Swart, J. W. A., 1996, *Scale-up of a Fischer-Tropsch Slurry Reactor*, Ph.D. Thesis, University of Groningen, The Netherlands.

Devanathan, N., D. Moslemian and M. P. Dudukovic', 1990, 'Flow Mapping in Bubble Columns Using CARPT', *Chem. Engng. Sci.*, **45**, 2285-2291.

Devanathan, N., 1991, *Investigation of Liquid Hydrodynamics in Bubble Columns via a Computer Automated Radioactive Particle Tracking (CARPT) Facility*, D.Sc. Thesis, Washington University, St. Louis, Missouri.

Dicken, F. J., R. A., Williams and M. S., Beck, 1993, 'Determination of Composition and Motion of Multicomponent Mixtures in Process Vessels Using Electrical Impedance Tomography - I. Principles and Process Engineering Applications', *Chem. Eng. Sci.*, **48**, 1883-1897.

Drew, D. A., 1983, 'Mathematical Modeling of two-phase flows', *Ann. Rev. Fluid Mech.*, **15**, 261-291.

Drew, D. A. and S. L. Passman, 1998, 'Theory of Multicomponent Fluids', Springer, New York.

Dudukovic, M. P., 1999^a, 'Trends in catalytic reaction engineering', *Catal. Today*, **48**(1-4), 5-15.

Dudukovic, M. P., 1999^b, 'Multiphase Opaque Systems: Experiments and Simulations', *AIChE Symp. Ser.*, **321**(Advanced Technologies for Fluid-Particle Systems), 30-35.

Dunn, W. L. and R. P. Gardner, 1972, 'The Determination of Intrinsic Gamma-Ray Detection Efficiencies for Cylindrical Geiger-Muller Tubes by Monte Carlo Methods', *Nuclear Instruments and Methods*, **103**, 373-384.

Fair, J. R., 1967, 'Designing Gas-Sparged Reactors', *Chem. Eng.*, **74**, 67

Fan, L. S., 1989, 'Gas-Liquid Solid Fluidization', Butterworth, Boston.

Fan, L. S., G. Q., Yang, D. J., Lee, K., Tsuchiya and X., Luo, 1999, 'Some Aspects of High Pressure Phenomena of Bubbles in Liquids and Liquid-Solid Suspensions', *Chem. Eng. Sci.*, **54**(21), 4681-4709.

- Filippidis, A., 1996, 'Data fusion using sensor data and a priori information', *Control Engineering Practice*, **4**(1), 43-53.
- Fossa, M., 1998, 'Design and Performance of a Conductance Probe for Measuring the Liquid Fraction in Two-Phase Gas-Liquid Flows', *Flow Meas. Instrum.*, **9**(2), 103-109.
- Geary, N. W. and R. G. Rice, 1992, 'Circulation and Scale-up in Bubble Columns', *AIChE J.*, **38**(1), 76-81.
- Grienberger, J. and H., Hoffman, 1992, 'Investigations and Modelling of Bubble Columns', *Chem. Eng. Sci.*, **47**(9-11), 2215-2220.
- Groen, J. S., R. F., Mudde and H. E. A., van den Akker, 1995, 'Time Dependent Behavior of the Flow in a Bubble Column,' *Trans. Inst. Chem. Engrs.*, A9-A16.
- Groen, J., S., R. G. C., Oldeman, R. F., Mudde and H. E. A., van den Akker, 1996, 'Coherent Structures and Axial Dispersion in Bubble Column Reactors', *Chem. Eng. Sci.*, **51**(10), Part A, 2511-2520.
- Gharat, S. D. and J. B. Joshi, 1992, 'Transport Phenomena in Bubble Columns I: Flow Pattern', *Chem. Eng. J. & Biochem. Eng. J.*, **48**(3), 141-152.
- Gunn, D. J. and H. H. Al-Doori, 1985, 'The Measurement of Bubble Flows in Fluidized Beds by Electrical Probe', *Int. J. Multiphase Flow*, **11**(4), 535-551.
- Gupta, P., B. Ong, M. H. Al-Dahhan and M. P. Dudukovic', 1999, 'Investigation of Liquid Mixing in Churn-Turbulent Bubble Columns Using Conductivity Probes', *Oral Presentation, North American Mixing Forum-Mixing XVII*, Banff, Alberta, Canada.

Gupta, P., M. H., Al-Dahhan, M. P., Dudukovic and P. L., Mills, 2000, 'A novel signal filtering methodology for obtaining liquid phase tracer responses from conductivity probes', *Flow Measurement and Instrumentation*, **11**(2), 123-131.

Gupta, P., B., Ong, M. H., Al-Dahhan, M. P., Dudukovic and B. A., Toseland, 2001^a, 'Hydrodynamics of churn turbulent bubble columns: gas-liquid recirculation and mechanistic modeling', *Catalysis Today*, **64**(3-4), 253-269.

Gupta, P., M. H., Al-Dahhan, M. P., Dudukovic and B. A., Toseland, 2001^b, 'Comparison of single- and two-bubble class gas-liquid recirculation models - application to pilot-plant radioactive tracer studies during methanol synthesis', *Chem. Eng. Sci.*, **56**(3), 1117-1125.

Hassan, Y. A. and G. C. Rush, 1985, 'A New Technique for Estimation of Void Fraction From Conductivity Probe Signals in a Small Break Loss-of-Coolant Accident Test Facility', *The American Society of Mechanical Engineers*, Presented at the Winter Annual Meeting, Miami Beach, Florida – Nov. 17-21.

Hikita, H., Asai, S., Tanigawa, K., Segawa, K., and Kitao, M., 1981, 'The Volumetric Liquid-Phase Mass Transfer Coefficient in Bubble Columns', *Chem. Eng. J.*, **22**, 61

Hillmer, G., L. Weismantel and H. Hofmann, 1994, 'Investigations and Modeling of Slurry Bubble Columns', *Chem. Eng. Sci.*, **49**(6), 837-842.

Hills, J. H., 1974, 'Radial non-uniformity of velocity and voidage in a bubble column', *Trans. Inst. Chem. Engrs.*, **52**(1), 1-9.

Hu, Z., B. Yu and Y. Wang, 1985, 'Studies on the Local Hold-Up and Liquid Velocity Distribution in G-L-S Three Phase Fluidized Bed', *Chem. Reaction Eng. Tech.*, **1**(3), 66-73.

- Jakobsen, H. A., B. H., Sannaes, S., Grevskott and H. F., Svendsen, 1997, 'Modeling of Vertical Bubble-Driven Flows', *Ind. Eng. Chem. Res.*, **36**, 4052-4074.
- Jiang, P, Lin, T. J., Luo, X., and Fan, L. S., 1995, 'Flow Visualization of High-Pressure (21 MPa) Bubble Column: Bubble Characteristics,' *Trans IChemE*, **73**, Part A, 269-274.
- Joshi, J. B., 1980, 'Axial Mixing in Multiphase Contactors - A Unified Correlation', *Trans. Inst. Chem. Engrs*, **58**(3), 155-165.
- Joshi, J. B. and Y. T. Shah, 1981, 'Hydrodynamic and Mixing Models for Bubble Column Reactors', *Chem. Eng. Commun.*, **11**(1-3), 165-199.
- Joshi, J. B., 1982, Gas dispersion in bubble columns, *Chem. Eng. J.*, **24**, 213
- Joshi, J. B., U. Parasu Veera, Ch. V. Prasad, D. V. Phanikumar, N. S. Deshpande, S. S. Thakre and B. N. Thorat, 1998, 'Gas Holdup Structure in Bubble Column Reactors', *PINSA-A, Proc. Indian Natl. Sci. Acad., Part A*, **64**(14), 441-567.
- Kang, Y., J. S., Shim, S. H., Cho, M. J., Choi and K. W., Lee, 1995, 'Dehydration of Ortho-Boric Acid in a Three-Phase Bubble Column Reactor Operating at Low Pressure', *J. Chem. Tech. Biotechnology*, **63**, 313-320.
- Kang, Y., Y. J., Cho, K. I., Woo, Kim and S. D., Kim, 2000, 'Bubble Properties and Pressure Fluctuations in Pressurized Bubble Columns,' *Chem. Eng. Sci.*, **55**, 411-419.
- Kastanek, F., Zahradnik, J., Kratochvil, J. and Cermak, J., 1984, 'Frontiers in Chemical Reaction Engineering', **1**, 330-344, Wiley Eastern Ltd., New Delhi.

- Kastanek, F., J. Zahradnik, J. Kratochvil and J. Cermak, 1993, *Chemical Reactions for Gas-Liquid Systems*, Ellis Horwood, New York.
- Kawase, Y., Halard, B., and Young, M. M., 1987, 'Theoretical Prediction of Volumetric Mass Transfer Coefficients in Bubble Columns for Newtonian and Non-Newtonian Fluid', *Chem. Eng. Sci.*, **42**, 1609
- Keane, R. D. and R. J., Adrian, 1992, 'Theory of cross-correlation analysis of PIV images', *Journal of Applied Scientific Research*, **49**, 191-215.
- Kemoun, A., N., Rados, F., Li, M. H., Al-Dahhan, M. P., Dudukovic', P. L., Mills, T. M. Leib and J. J., Lerou, 2001^a, 'Gas holdup in a trayed cold-flow bubble column', *Chem. Eng. Sci.*, **56**(3), 1197-1205.
- Kemoun, A., B. C., Ong, P., Gupta, M. H., Al-Dahhan and M. P., Dudukovic', 2001^b, 'Gas Holdup in Bubble Columns at Elevated Pressure via Computed Tomography', *International Journal of Multiphase Flows*, **27**(5), 929-946.
- Knoll, G. F., 1989, 'Radiation Detection and Measurement', John Wiley and Sons, NY.
- Kohler, M. A., 1986, 'Comparison of Mechanically Agitated and Bubble Column Slurry Reactors', *Appl. Catal.*, **22**(1), 21-53.
- Kojima, H., B., Okumura and A., Nakamura, 1997, 'Effect of Pressure on Volumetric Mass Transfer Coefficient and Gas Holdup in Bubble Column', *Chem. Eng. Sci.*, **52** (21/22), 4111-4116.
- Kölbel, H., Borchers, E., and Langemann, H., 1961, 'Größenverteilung der Gasblasen in Blasensäulen. Teil 1: Einflüsse von Flüssigkeitsviskosität und Säuleninnendruck,' *Chem. Ing. Tech.*, **33**, 668-675.

- Krishna, R. and S. T., Sie, 1994, 'Strategies for multiphase reactor selection', *Chem. Eng. Sci.*, **54**, 4029-4065.
- Krishna, R. and Ellenberger, J., 1995, 'A unified approach to the scale-up of fluidized multiphase reactors', *Trans. I. Chem. E.*, **73(A)**, 217
- Krishna, R. and J., Ellenberger, 1996, 'Gas Holdup in Bubble Column Reactors Operating in the Churn-Turbulent Flow Regime', *AIChE J.*, **42**, 9, 2627-2634.
- Krishna, R., J. M. van Baten and J., Ellenberger, 1998, 'Scale effects in fluidized multiphase reactors', *Powder Tech.*, **100**, 137-146.
- Krishna, R., M. I., Urseanu, J. M. van Baten and J., Ellenberger, 1999^a, 'Rise velocity of a swarm of large bubbles in liquids', *Chem. Eng. Sci.*, **54**, 171-183.
- Krishna, R., M. I. Urseanu, J. M. van Baten and J. Ellenberger, 1999^b, 'Influence of Scale on the Hydrodynamics of Bubble Columns operating in the Churn-Turbulent Regime: Experiments vs. Eulerian Simulations', *Chem. Eng. Sci.*, **54(21)**, 4903-4911.
- Krishna, R., M. I., Urseanu, J. M. van Baten and J., Ellenberger, 1999^c, 'Wall effects on the rise of single gas bubbles in liquids', *Int. Comm. Heat Mass Transfer*, **26(6)**, 781-790.
- Krishna, R., J. M., van Baten, M. I. Urseanu and J., Ellenberger, 2000^a, 'Rise velocity of single circular-cap bubbles in two-dimensional beds of powders and liquids', *Chemical Engineering and Processing*, **39**, 433-440.
- Krishna, R., J. M. van Baten and M. I., Urseanu, 2000^b, 'Three-phase Eulerian simulations of bubble column reactors operating in the churn-turbulent regime: a scale up strategy', *Chem. Eng. Sci.*, **55**, 3275-3286.

- Krishna, R., M. I. Urseanu and A. J., Dreher, 2000^c, 'Gas hold-up in bubble columns: influence of alcohol addition versus operation at elevated pressures', *Chemical Engineering and Processing*, **39**, 371-378.
- Krishna, R., M. I., Urseanu, J. M. van Baten and J., Ellenberger, 2000^d, 'Liquid phase dispersion in bubble columns operating in the churn-turbulent flow regime', *Chemical Engineering Journal*, **78**, 43-51.
- Krishna, R., J., Ellenberger, M. I., Urseanu and F. J., Keil, 2000^e, 'Utilisation of bubble resonance phenomena to improve gas-liquid contact', *Naturwissenschaften*, **87**, 455-459.
- Krishna, R., A. J. Dreher and M. I., Urseanu, 2000^f, 'Influence of alcohol addition on gas hold-up in bubble columns: development of a scale up model', *Int. Comm. Heat Mass Transfer*, **27**(4), 465-472.
- Krishna, R., M. I., Urseanu, J. W. A. de Swart and J., Ellenberger, 2000^g, 'Gas holdup in bubble columns: operation with concentrated slurries versus high viscosity liquid', *Can. J. Chem. Eng.*, **78**, 442-448.
- Krishna, R., 2000^h, 'A scale-up strategy for a commercial scale bubble column slurry reactor for Fischer-Tropsch synthesis', *Oil & Gas Science and Technology – Rev. IFP*, **55**, 359-393.
- Krishna, R., J. M., van Baten, M. I. Urseanu and J., Ellenberger, 2001, 'Design and scale up of a slurry reactor for Fischer-Tropsch synthesis', *Chem. Eng. Sci.*, **56**, 537-545.
- Kuipers, J. A. M. and W. P. M. Van Swaaij, 1998, 'Computational Fluid Dynamics Applied to Chemical Reaction Engineering', *Adv. Chem. Eng.*, **24**, 227-328.

- Kumar, S. B., 1994, *Computed tomographic measurements of void fraction and modeling of the flow in bubble columns*, Ph.D. Thesis, Florida Atlantic University.
- Kumar, S. B., N. Devanathan, D. Moslemian and M. P. Dudukovic', 1994, 'Effect of Scale on Liquid Recirculation in Bubble Columns', *Chem. Engng., Sci.*, **49**(24B), 5637-5652.
- Kumar, S. B., Moslemian, D., and Dudukovic', M. P., 1995, A Gamma Ray Tomographic Scanner for Imaging Void Fraction Distribution in Bubble Columns, *Flow Meas. Instr.*, **6**(1), 61-73.
- Kumar, S. B., D. Moslemian and M. P. Dudukovic', 1997, 'Gas Holdup Measurements in Bubble Columns Using Computed Tomography', *AIChE J.*, **43**(6), 1414-1425.
- Lage, P. and L. C., Espósito, 1999, 'Experimental Determination of Bubble Size Distributions in Bubble Columns: Prediction of Mean Bubble Diameter and Gas Holdup', *Powder Technology*, **101**, 142-150.
- Lapin, A., and Lubbert, A., 1994, 'Numerical Simulation of the Dynamics of Two-Phase Gas-Liquid Flows in Bubble Columns,' *Chem. Engng. Sci.*, **49**, 3661-3674.
- Larachi, F., G. Kennedy and J. Chaouki, 1994, 'A γ -ray Detection System for 3-D Particle Tracking in Multiphase Reactors', *Nuclear Instruments and Methods in Physics Research A.*, **338**, 568-576.
- Lasdon, L. S., A. D. Warren, A. Jain and M. Ratner, 1978, 'Design and Testing of a Generalized Reduced Gradient Code for Nonlinear Programming', *ACM Transactions on Mathematical Software*, **4**(1), 34-50.

- Letzel, H. M., 1997, *Hydrodynamics and Mass Transfer in Bubble Columns at Elevated Pressures*, Ph.D. Thesis, University of Amsterdam, The Netherlands.
- Letzel, H. M., J. C. Schouten, R. Krishna and C. M. van den Bleek, 1997, 'Characterization of Regimes and Regime Transitions in Bubble Columns by Chaos Analysis of Pressure Signals', *Chem. Eng. Sci.*, **52**(24), 4447-4459.
- Letzel, H. M., J. C., Schouten, C. M. van den Bleek and R., Krishna, 1999, 'Gas Holdup and Mass Transfer in Bubble Column Reactors Operated at Elevated Pressure', *Chem. Eng. Sci.*, **54**, 2237-2246.
- Limtrakul, S., 1996, *Hydrodynamics of Liquid Fluidized Beds and Gas-Liquid Fluidized Beds*, D.Sc. Thesis, Washington University, Saint Louis, Missouri.
- Lin, J. S., Chen, M. M., and Chao, B. T., 1985, 'A novel radioactive particle tracking facility for measurement of solids motion in gas fluidized beds,' *AIChE J.*, **31** (3), 465-473.
- Lin, T. J., Tsuchiya, K., and Fan, L. S., 1998, 'Bubble Flow Characteristics in Bubble Columns at Elevated Pressure and Temperature,' *AIChE J.*, **44** (3), 545-560.
- Lockett, M. J. and R. D. Kirkpatrick, 1975, 'Ideal Bubbly Flow and Actual Flow in Bubble Columns', *Trans. I. Chem. E.*, **53**, 267-273.
- Lopez de Bertodano, M., R. T. Lahey Jr. and O. C. Jones, 1994, 'Phase Distribution in Bubbly Two-Phase Flow in Vertical Ducts', *Int. J. Multiphase Flow*, **20**(5), 805-18.
- Luo, H. and H. F. Svendsen, 1991, 'Turbulent Circulation in Bubble Columns from Eddy Viscosity Distributions of Single-Phase Pipe Flow', *Can. J. Chem. Eng.*, **69**, 1389-94.

Luo, H., 1993, *Coalescence, breakup and liquid circulation in bubble column reactors*, Ph.D. Thesis, Universitetet i Trondheim, Norges Tekniske Høgskole.

Luo, X., D. J. Lee, R. Lau, G. Yang, G. and L. S. Fan, 1999, 'Maximum Stable Bubble Size and Gas Holdup in High-Pressure Slurry Bubble Columns', *AIChE J.*, **45**(4), 665-680.

Maretto, C. and R. Krishna, 1999, 'Modelling of a bubble column slurry reactor for Fischer-Tropsch synthesis', *Catalysis Today*, **52**, 279-289.

MATLAB, 1997, Version 5, The MATH WORKS Inc., Boston, MA.

Mashelkar, R. A., 1970, 'Bubble columns', *Brit. Chem. Eng.*, **15**(10), 1297-304.

Menzel, T., T. in der Weide, O. Staudacher, O. Wein and U. Onken, 1990, 'Reynolds Shear Stress for Modelling of Bubble Column Reactors', *Ind. Eng. Chem. Res.*, **29**, 988-994.

Mitra-Majumdar, D., B. Farouk, and Y. T. Shah, 1997, 'Hydrodynamic Modeling of Three-Phase Flows through a Vertical Column', *Chem. Eng. Sci.*, **52**(4), 4485-4497.

Modak, S. Y., V. A. Juvekar and V. C. Rane, 1993, 'Dynamic of the Gas Phase in Bubble Columns', *Chem. Eng. Technol.*, **16**, 303-306.

Modak, S. Y., V. A. Juvekar and V. C. Rane, 1994, 'Comparison of the Single-Bubble-Class and Modified Two-Bubble-Class Models of Bubble Column Reactors', *Chem. Eng. Technol.*, **16**, 313-322.

- Moens, L., J. De Donder, X. Lin, F. De Corte, A. De Wispelaere, A. Simonits and J. Hoste, 1981, 'Calculation of the Absolute Peak Efficiency of Gamma-Ray Detectors for Different Counting Geometries', *Nuclear Instruments and Methods*, **187**, 451-472.
- Molerus, O. and Kurtin, M., 1986, 'Modeling of residence time distributions of the gas phase in bubble columns in liquid circulation regime', *Chem. Eng. Sci.*, **41**, 2693
- Mosslemian, D., Devanathan, N. and M. P. Dudukovic', 1992, 'Radioactive Particle Tracking Technique for Investigation of Phase Recirculation and Turbulence in Multiphase Systems', *Rev. Sci. Instrum.*, **63**(10), 4361-4372.
- Mudde, R. F., J. S. Groen and H. E. A. Van Den Akker, 1997, 'Liquid Velocity Field in a Bubble Column: LDA Experiments', *Chem. Eng. Sci.*, **52**(21/22), 4217-4224.
- Mudde, R. F., J. S. Groen and H. E. A. Van Den Akker, 1998, 'Application of LDA to Bubbly Flows', *Nucl. Eng. Des.*, **184**(2-3), 329-338.
- Myers, K. J., M. P. Dudukovic' and P. A. Ramachandran, 1987, 'Modeling of Churn-Turbulent Bubble Columns – I: Liquid Phase Mixing', *Chem. Eng. Sci.*, **42**(10), 2301-2311.
- Nakanoh, M., and Yoshida, F., 1980, 'Gas Adsorption by Newtonian and Non-Newtonian Liquids in a Bubble Column,' *Int. Eng. Chem. Process Des. Dev.*, **19**, 190-195.
- Nardi, E., 1970, 'A Note on Monte Carlo Calculations in NaI Crystals', *Nuclear Instruments and Methods*, **83**, 331-332.
- Nottenkamper, R., A. Steiff and P. -M. Weinspach, 1983, 'Experimental Investigation of Hydrodynamics of Bubble Column', *Ger. Chem. Eng.*, **6**, 147-155.

- Ong, B. C., 1999, *Characterization of Gas-Liquid Churn-Turbulent Flow in Bubble Columns at Elevated Pressure*, D.Sc. Proposal, Washington University, Saint Louis, Missouri.
- Oyevaar, M. H., and Westerterp, K. R., 1989, 'Mass Transfer Phenomena and Hydrodynamics in Agitated Gas-Liquid Reactors and Bubble Columns at Elevated Pressures: State of the Art,' *Chem. Eng. Process.*, **25**, 85-98.
- Ozturk, S. S., Schumpe, A., and Deckwer, W. D., 1987, 'Organic Liquids in Bubble Columns: Hold-ups and Mass Transfer Coefficients', *AIChE J.*, **33**, 1473
- Pan, Y., M. P. Dudukovic' and M. Chang, 1999, 'Dynamic Simulation of Bubbly Flow in Bubble Columns', *Chem. Eng. Sci.*, **54**(13), 2481-2489.
- Pilhofer, T. H., 1980, 'Effects of plate geometry on gas hold-up in bubble columns', *Chem. Eng. Comm.*, **5**, 69-72.
- Poulsen, B. R. and J. J. L. Iversen, 1998, 'Characterization of Gas Transfer and Mixing in a Bubble Column Equipped with a Rubber Membrane Diffuser', *Biotechnology and Bioengineering*, **58**(6), 633-641.
- Press, W. H., S. A. Teukolsky, W. T. Vetterling and B. P. Flannery, 1992, 'Numerical Recipes in Fortran 77: The Art of Scientific Computing', Cambridge University Press, Cambridge.
- Prince, M. J. and Blanch, H. W., 1990, 'Bubble coalescence and break-up in air-sparged bubble columns', *AIChE J.*, **36**(10), 1485
- Ramachandran, P. A. and R. V., Chaudhari, 1983, 'Three-Phase Catalytic Reactors', Gordon and Breach Science Publishers.

- Ranade, V. V., 1995, 'Computational Fluid Dynamics for Reaction Engineering', *Reviews in Chem. Eng.*, **11**(3), 229-289.
- Ranade, V. V., 1997, 'Modeling of Turbulent Flow in A Bubble Column Reactors', *Trans. Inst. Chem. Eng.*, **75**, 14
- Reilly, I. G., D. S., Scott, T. J. W., De Bruijn and D. MacIntyre, 1994, 'The Role of Gas Phase Momentum in Determining Gas Holdup and Hydrodynamic Flow Regimes in Bubble Column Operations', *Can. J. Chem. Eng.*, **72**, 3
- Rice, R. G. and N. W. Geary, 1990, 'Prediction of Liquid Circulation in Viscous Bubble Columns', *AIChE J.*, **36** (9), 1339-1348.
- Romanainen, J. J., 1997, 'Numerical approach to modeling of dynamic bubble columns', *Chem. Eng. Processing*, **36**, 1-15.
- Rustemeyer, U., J. Pauli, T. Menzel, R. Buchholz and U. Onken, 1989, 'Liquid-Phase Mixing Model for Hydrodynamics of Bubble Columns', *Chem. Eng. Process.*, **26**, 165-172.
- Saito, K. and S. Moriuchi, 1981, 'Monte Carlo Calculation of Accurate Response Functions for a NaI (TI) Detector for Gamma Rays', *Nuclear Instruments and Methods*, **185**, 299-308.
- Sandler, S. I., 1989, "Chemical and Engineering Thermodynamics", John Wiley & Sons, New York, 381-440.
- Saxena, S. C., 1995, 'Bubble column reactors and Fischer-Tropsch synthesis', *Catal. Rev.*, **37**(2), 227

- Schibler, J. A., December 1997, 'Improving Precision and Accuracy with Software-Based Signal Filtering', *American Laboratory*, 52-54.
- Schlichting, H., 1979, 'Boundary Layer Theory', McGraw Hill, New York, 602-609.
- Schlueter, S., A Steiff, and P. M. Weinspach, 1992, 'Modeling and Simulation of Bubble Column Reactors', *Chem. Eng. Process.*, **31**(2), 91-117.
- Schlueter, S., 1995, 'Simulation of Bubble Column Reactors with the BCR Computer Code', *Chem. Eng. Process.*, **34**(2), 127-136.
- Schulzke, T., S. Schlueter and P. M. Weinspach, 1998, 'Experimental Studies and Simulation of the Dynamic Behavior of Bubble Column Reactors', *Comp. Chem. Eng.*, **22**, S667-S670.
- Shah, Y. T., G. J. Stiegel and M. M. Sharma, 1978, 'Backmixing in Gas-Liquid Reactors', *AIChE J.*, **24**(3), 369-400.
- Shah, Y. T., 1981, 'Bubble Column. An Overview', *ACS Symp. Ser.*, **168**(Chem. React.), 203-11.
- Shah, Y. T., B. G. Kelkar, S. P. Godbole and W. D. Deckwer, 1982, 'Design Parameter Estimations for Bubble Column Reactors', *AIChE J.*, **28**(3), 353-379.
- Shah, Y. T., Joseph, S., Smith, D. N. and Reuther, J. A., 1985, 'Two-bubble class model for churn-turbulent bubble column reactor', *Ind. Eng. Chem. Process Des. & Dev.*, **24**, 1096-1104.
- Shetty, S. A., Kantak, M. V. and Kelkar, M. G., 1992, 'Gas-phase backmixing in bubble column reactors', *AIChE J.*, **38**, 1013

- Shollenberger, K. A., Torczynski, J. R., Adkins, D. R., O'Hern, T. J., and Jackson, N. B., 1997, 'Gamma-Densitometry Tomography of Gas Holdup Spatial Distribution in Industrial-Scale Bubble Columns,' *Chem. Eng. Sci.*, **52** (13), 2037-2048.
- Shultis, J. K. and R. E. Faw, 1996, "Radiation Shielding", Prentice Hall, New Jersey.
- Sie, S. T. and R. Krishna, 1999, 'Fundamentals and Selection of Advanced Fischer-Tropsch Reactors', *Applied Catalysis A*, **186**, 55-70.
- Sokolichin, A. and G., Eigenberger, 1994, 'Gas-Liquid Flow in Bubble Columns and Loop Reactors: Part 1. Detailed Modelling Numerical Simulation', *Chem. Eng. Sci.*, **24**, 5735-5746.
- Sokolichin, A. and G. Eigenberger, 1999, 'Applicability of the Standard k- ϵ Turbulence Model to the Dynamic Simulation of Bubble Columns: Part I. Detailed Numerical Simulations,' *Chem. Eng. Sci.*, **54** (13-14), 2273-2284.
- Sokolov, M. and M. Mashaal, 1990, 'Velocity Measurements in Slow Flow by the Conductance-Tracer Method', *Experiments in Fluids*, **9**, 252-256.
- Sotelo, J. L., Benitez, F. J., Beltran-Heredia, J. and Rodriguez, C., 1994, 'Gas hold-up and mass transfer coefficients in bubble columns. 1. Porous glass-plate diffusers', *Int. Chem. Eng.*, **34**(1), 82
- Stern, D., A. T. Bell and H. Heinemann, 1985, 'A Theoretical Model for the Performance of Bubble-Column Reactors Used for Fischer-Tropsch Synthesis', *Chem. Eng. Sci.*, **40**(9), 1665-1677.

- Steyn, J. J., R. Huang and D. W. Harris, 1973, 'Monte Carlo Calculation of Clad NaI (TI) Scintillation Crystal Response to Gamma', *Nuclear Instruments and Methods*, **107**, 465-475.
- Svendson, H. F., H. Luo, K. W. Hjarbo and H. A. Jakobsen, 1998, 'Experimental determination and modeling of bubble size distributions in bubble columns', *Chinese J. of Chem. Eng.*, **6**(1), 29-41.
- Tassin, A. L. and D. E., Nikitopoulos, 1995, 'Non-intrusive Measurements of Bubble Size and Velocity', *Experiments in Fluids*, **19**, 121-132.
- Thakre, S. S. and J. B. Joshi, 1999, 'CFD Simulation of Bubble Column Reactors: Importance of Drag Force Formulation', *Chem. Eng. Sci.*, **54**(21), 5055-5060.
- Tomiyama, A., I. Kataoka and T. Sakaguchi, 1995, 'Drag Coefficients of Bubbles (1st report, Drag Coefficients of a Single Bubble in a Stagnant Liquid)', *Trans. JSME Part B*, **61**(587), 2357-2364.
- Tsoufanidis, N., 1983, "Measurement and Detection of Radiation", McGraw Hill, New York.
- Tsochatzidis, N. A., T. D. Karapantsios, M. V. Kostoglou and A. J. Karabelas, 1992, 'A Conductance Probe for Measuring Liquid Fraction in Pipes and Packed Beds', *Int. J. Multiphase Flow*, **18**(5), 653-667.
- Tzeng, J. -W., R. C. Chen and L. -S., Fan, 1993, 'Visualization of flow characteristics in a 2-D bubble column and three-phase fluidized bed', *AIChE J.*, **39**(5), 733-744.
- Ueyama, K. and T. Miyauchi, 1979, 'Properties of Recirculating Turbulent Two-Phase Flow in Gas Bubble Columns', *AIChE J.*, **25** (2), 258-266.

- Vermeer, D. J. and R. Krishna, 1981, 'Hydrodynamics and Mass Transfer in Bubble Columns Operating in the Churn-Turbulent Regime', *Ind. Engng. Chem. Process Design & Dev.*, **20**(3), 475-482.
- Wang, Q., 1996, *Modeling of Gas and Liquid Phase Mixing with Reaction in Bubble Column Reactors*, M. S. Thesis, Washington University, Saint Louis, Missouri.
- Wender, I., 1996, 'Reactions of synthesis gas', *Fuel Processing Technology*, **48**, 189-297.
- Werther, J. and O. Molerus, 1973, 'The Local Structure of Gas Fluidized Beds – I. A Statistically Based Measuring System', *Int. J. Multiphase Flow*, **1**, 103-122.
- Wilkinson, P. M., 1991, *Physical aspects and scale-up of high pressure bubble columns*, Ph. D. Thesis, University of Groningen, The Netherlands.
- Wilkinson, P. M., A. P. Spek, and L. L. van Dierendonck, 1992, 'Mass transfer and bubble size in a column under pressure', *AIChE J.*, **38**, 544
- Wilkinson, P. M., Haringa, H. and van Dierendonck, L. L., 1994, 'Design parameters estimation for scale-up of high pressure bubble columns', *Chem. Eng. Sci.*, **49**, 1417
- Wu, Y., B. C. Ong and M. H. Al-Dahhan, 2001, 'Predictions of radial gas holdup profiles in bubble column reactors,' *Chem. Eng. Sci.*, **56**, 1207-1210.
- Yang, Y. B., N. Devanathan and M. P. Dudukovic', 1993, 'Liquid Mixing in Bubble Columns via Computer Automated Radioactive Particle Tracking (CARPT)', *Expt. in Fluids*, **16**, 1-9.

- Yang, Y., 1997, 'Monte Carlo Simulations for CARPT Calibrations', Chapter 4 in Novel Techniques for Slurry Bubble Column Hydrodynamics, *Annual Tech. Report*, **2** (July 1996-June 1997) to DOE from Chemical Reaction Engineering Laboratory (DOE-FG2295 PC 95212), 20-39.
- Yao, B. P., C. Zheng, H. E. Gasche and H. Hofmann, 1991, 'Bubble Behavior and Flow Structure of Bubble Columns', *Chem. Eng. Process.*, **29**, 25-75.
- Yu, Y. H., and Kim, S. D., 1991, 'Bubble Properties and Local Liquid Velocity in the Radial Direction of Cocurrent Gas-Liquid Flow,' *Chem. Eng. Sci.*, **46** (1), 313-320.
- Zhao, Y., R. R. Schehl, R. R. Anderson and R. D. Chi, 1987, 'A Multicomponent Axial Dispersion Model of Bubble Column Slurry Reactor for the Fischer-Tropsch Synthesis', *Huaxue Fanying Gongcheng Yu Gongyi*, **3**(2), 22-33.
- Zrymiak, T. L. and G. A. Hill, 1986, 'Probe for Measuring Local Gas Holdups in Saline Potash Pulps', *Can. J. Chem. Eng.*, **64**(2), 341-345.

VITA

Name	Puneet Gupta
Date of Birth	June 13, 1972
Place of Birth	Ajmer, India.
Degrees	B. Tech. in Chem. Eng., July 1994 Indian Institute of Technology, Bombay, India. MS in Chemical Engineering, December 1996 Washington University, Saint Louis, MO, USA. D.Sc. Chemical Engineering, May 2002 Washington University, Saint Louis, MO, USA.
Industrial Experience	Summer Intern at Savita Chemicals, Bombay, India, (1993). Summer Intern at MEMC Electronic Materials Inc., Saint Peters, MO, USA (1995).
Professional Societies	American Institute of Chemical Engineers American Society of Mechanical Engineers Institute for Multifluid Science and Technology

Publications

“Gas Holdup in Bubble Columns at Elevated Pressure via Computed Tomography”, Kemoun, A., Ong, B. C., Gupta, P., Al-Dahhan, M. H. and Dudukovic', M. P., *International Journal of Multiphase Flows*, 27(5), 929-946 (2001).

“Comparison of single- and two-bubble class gas-liquid recirculation models - application to pilot-plant radioactive tracer studies during methanol synthesis”, Gupta, P.,



Al-Dahhan, M. H., Dudukovic, M. P. and Toseland, B. A., *Chem. Eng. Sc.*, **56**(3), 1117-1125 (2001).

“Hydrodynamics of Churn-Turbulent Bubble Columns: Gas-Liquid Recirculation and Mechanistic Modeling”, Gupta, P., Ong, B., Al-Dahhan, M.H., Dudukovic, M. P., and Toseland, B. A., *Catalysis Today*, **64** (3-4), 253-269 (2001).

“A novel signal filtering methodology for obtaining liquid phase tracer responses from conductivity probes”, Gupta, P., Al-Dahhan, M. H., Dudukovic, M. P. and Mills, P. L., *Flow Measurement and Instrumentation*, **11**(2), 123-131 (2000).

“Fluid Dynamic Parameters in Bubble Columns with Internals”, Chen, J., Li, F., Degaleesan, S., Gupta, P., Al-Dahhan, M. H., Dudukovic, M. P., and Toseland, B. A., *Chemical Engineering Science*, **54** (13-14), 2187 (1999).

“Non-Invasive Flow Monitoring in Opaque Multiphase Reactors Via CARPT and CAT”, Roy, S., Chen, J., Degaleesan, S., Gupta, P., Al-Dahhan, M. H., and Dudukovic, M. P., *Proceedings of the Fluids Engineering Division Summer Meeting (FEDSM)* (1998).

“Gas Holdup Distributions in Large-Diameter Bubble Columns Measured by Computed Tomography”, Chen, J., Gupta, P., Degaleesan, S., Al-Dahhan, M. H., Dudukovic, M. P., and Toseland, B. A., *Flow Measurement and Instrumentation*, **9**, 91 (1998).

“Fluid Dynamics in Churn-Turbulent Bubble Columns: Measurements and Modeling”, Dudukovic, M. P., Degaleesan, S., Gupta, P., and Kumar, S. B., *Proceedings of the Fluids Engineering Division Summer Meeting (FEDSM)* (1997).

Presentations

“Comparison of single- and two-bubble class gas-liquid recirculation models - application to pilot-plant radioactive tracer studies during methanol synthesis”, Gupta, P., Al-Dahhan, M. H., Dudukovic, M. P. and Toseland, B. A., *Poster Presentation, ISCRE 16*, Cracow, Poland (2000)

“Hydrodynamics of Churn-Turbulent Bubble Columns: Gas-Liquid Recirculation and Mechanistic Modeling”, Gupta, P., Ong, B., Al-Dahhan, M.H., Dudukovic, M. P., and Toseland, B. A., *Oral Presentation, 16th Canadian Symposium On Catalysis*, Banff, Alberta, Canada (2000).

“Gas Holdup in a High Pressure Bubble Column by Computed Tomography”, Kemoun, A., Ong, B. C., Gupta, P., Al-Dahhan, M. H., and Dudukovic, M. P., *Oral Presentation, AIChE Annual Meeting*, Dallas, Texas (1999).

“Investigation of Liquid Mixing in Churn-Turbulent Bubble Columns Using Conductivity Probes”, Gupta, P., Ong, B. C., Al-Dahhan, M. H., and Dudukovic’, M. P., *Oral Presentation, North American Mixing Forum-Mixing XVII*, Banff, Alberta, Canada (1999).

“Monte Carlo Simulations for Determining NaI (Tl) Efficiencies for Tracking of Radioactive Particle as a Phase Follower in Multiphase Flows”, Gupta, P., Yang, Y., and Dudukovic’, M. P., *Oral Presentation, AIChE Annual Meeting, Miami Beach, Florida* (1998).

“Gas Holdup Distributions In Large Diameter Bubble Columns Measured by Computer Tomography” Gupta, P., Chen, J., Degaleesan, S., Al-Dahhan, M. H., Dudukovic’, M. P., and Toseland, B. A., *Poster Presentation, Engineering Foundation Conference – Frontiers in Industrial Process Tomography -II, Delft, Netherlands* (1997).

“1-D Phenomenological Modeling of Bubble Columns” Gupta, P., Al-Dahhan, M. H., and Dudukovic’, M. P., *Poster Presentation, Engineering Foundation Conference – Computational Fluid Dynamics, San Diego, California* (1996).

May, 2002